



ISSN 1580-3155

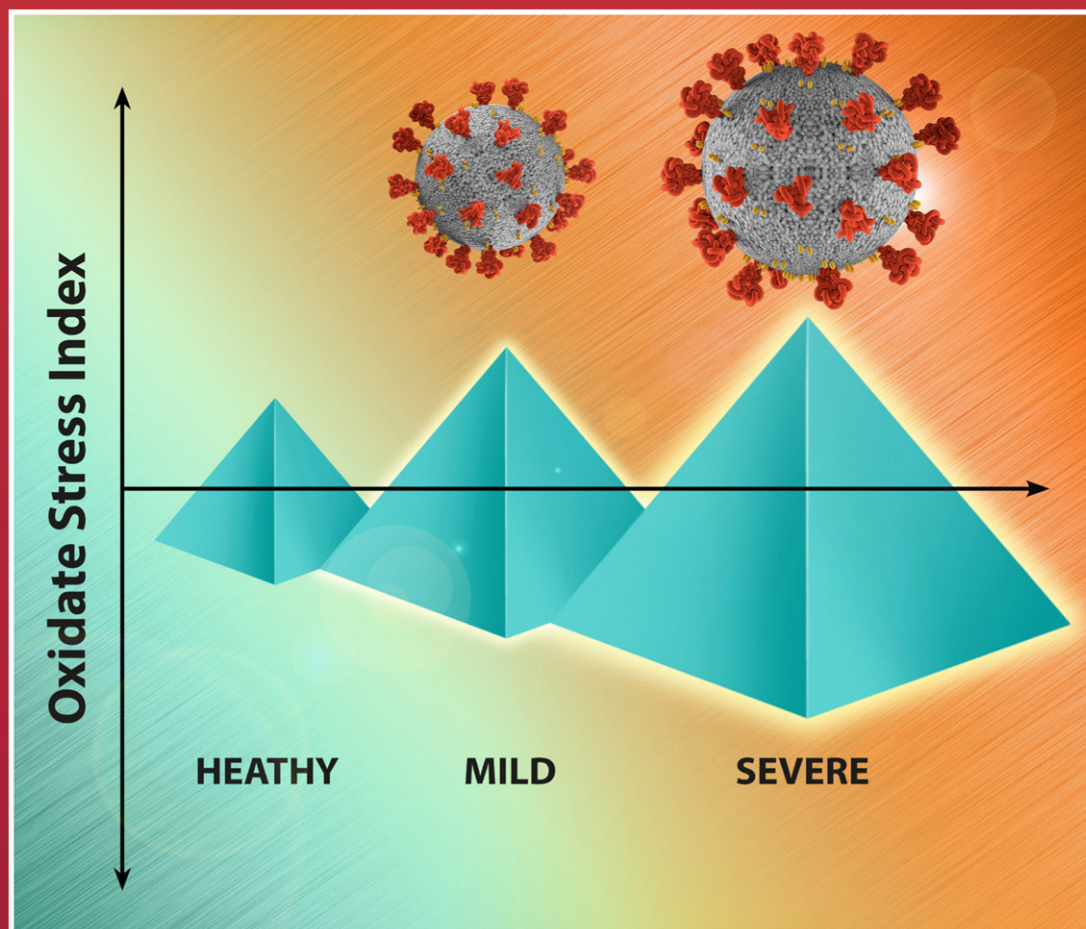
Pages 507–733 ■ Year 2022, Vol. 69, No. 3

Slovensko kemijsko društvo  
Slovenian Chemical Society



# Acta Chimica Slo Acta Chimica Slo Slovenica Acta C 3

69/2022



---

## EDITOR-IN-CHIEF

KSENIJA KOGEJ

University of Ljubljana, Faculty of Chemistry and Chemical Technology, Večna pot 113, SI-1000 Ljubljana, Slovenija

E-mail: ACSi@fkk.uni-lj.si, Telephone: (+386)-1-479-8538

## ASSOCIATE EDITORS

Alen Albreht, National Institute of Chemistry, Slovenia

Aleš Berlec, Jožef Stefan Institute, Slovenia

Janez Cerkovnik, University of Ljubljana, Slovenia

Mirela Dragomir, Jožef Stefan Institute, Slovenia

Ksenija Kogej, University of Ljubljana, Slovenia

Krištof Kranjc, University of Ljubljana, Slovenia

Matjaž Kristl, University of Maribor, Slovenia

Franč Perdih, University of Ljubljana, Slovenia

Aleš Ručigaj, University of Ljubljana, Slovenia

Helena Prosen, University of Ljubljana, Slovenia

Irena Vovk, National Institute of Chemistry, Slovenia

## ADMINISTRATIVE ASSISTANT

Marjana Gantar Albreht, National Institute of Chemistry, Slovenia

Eva Mihalinec, Slovenian Chemical Society, Slovenia

---

## EDITORIAL BOARD

Wolfgang Buchberger, Johannes Kepler University, Austria

Alojz Demšar, University of Ljubljana, Slovenia

Stanislav Gobec, University of Ljubljana, Slovenia

Marko Goličnik, University of Ljubljana, Slovenia

Günter Grampp, Graz University of Technology, Austria

Wojciech Grochala, University of Warsaw, Poland

Danijel Kikelj, University of Ljubljana

Janez Košmrlj, University of Ljubljana, Slovenia

Blaž Likozar, National Institute of Chemistry, Slovenia

Mahesh K. Lakshman, The City College and

The City University of New York, USA

Janez Mavri, National Institute of Chemistry, Slovenia

Friedrich Sreenc, University of Minnesota, USA

Walter Steiner, Graz University of Technology, Austria

Jurij Svete, University of Ljubljana, Slovenia

David Šarlah, University of Illinois at Urbana-Champaign, USA;  
Università degli Studi di Pavia, Italy

Ivan Švancara, University of Pardubice, Czech Republic

Jiri Pinkas, Masaryk University Brno, Czech Republic

Gašper Tavčar, Jožef Stefan Institute, Slovenia

Ennio Zangrando, University of Trieste, Italy

---

## ADVISORY EDITORIAL BOARD

### Chairman

Branko Stanovnik, Slovenia

### Members

Udo A. Th. Brinkman, The Netherlands

Attilio Cesaro, Italy

Vida Hudnik, Slovenia

Venc̃eslav Kaučič, Slovenia

Željko Knez, Slovenia

Radovan Komel, Slovenia

Stane Pejovnik, Slovenia

Anton Perdih, Slovenia

Slavko Pečar, Slovenia

Andrej Petrič, Slovenia

Boris Pihlar, Slovenia

Milan Randić, Des Moines, USA

Jože Škerjanc, Slovenia

Đurđa Vasić-Rački, Croatia

Marjan Veber, Slovenia

Gorazd Vesnaver, Slovenia

Jure Zupan, Slovenia

Boris Žemva, Slovenia

Majda Žigon, Slovenia

*Acta Chimica Slovenica* is indexed in: Academic Search Complete, Central & Eastern European Academic Source, Chemical Abstracts Plus, Chemical Engineering Collection (India), Chemistry Citation Index Expanded, Current Contents (Physical, Chemical and Earth Sciences), Digitalna knjižnica Slovenije (dLib.si), DOAJ, ISI Alerting Services, PubMed, Science Citation Index Expanded, SciFinder (CAS), Scopus and Web of Science. Impact factor for 2021 is IF = 1.524.



Articles in this journal are published under the  
Creative Commons Attribution 4.0 International License

### Izdaja – Published by:

SLOVENSKO KEMIJSKO DRUŠTVO – SLOVENIAN CHEMICAL SOCIETY

Naslov redakcije in uprave – Address of the Editorial Board and Administration

Hajdrihova 19, SI-1000 Ljubljana, Slovenija

Tel.: (+386)-1-476-0252; Fax: (+386)-1-476-0300; E-mail: chem.soc@ki.si

### Izdajanje sofinancirajo – Financially supported by:

National Institute of Chemistry, Ljubljana, Slovenia

Jožef Stefan Institute, Ljubljana, Slovenia

Faculty of Chemistry and Chemical Technology, University of Ljubljana, Slovenia

Faculty of Chemistry and Chemical Engineering, University of Maribor, Slovenia

University of Nova Gorica, Slovenia

Slovensko kemijsko društvo  
Slovenian Chemical Society

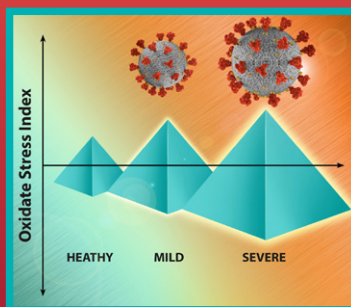


*Acta Chimica Slovenica* izhaja štirikrat letno v elektronski obliki na spletni strani <http://acta.chem-soc.si>. V primeru posvečenih števil izhaja revija tudi v tiskani obliki v omejenem številu izvodov.

*Acta Chimica Slovenica* appears quarterly in electronic form on the web site <http://acta.chem-soc.si>. In case of dedicated issues, a limited number of printed copies are issued as well.

Transakcijski račun: 02053-0013322846 Bank Account No.: SI56020530013322846-Nova Ljubljanska banka d. d., Trg republike 2, SI-1520 Ljubljana, Slovenia, SWIFT Code: LJBA SI 2X

Oblikovanje ovitka – Design cover: KULT, oblikovalski studio, Simon KAJTNA, s. p. Grafična priprava za tisk: OSITO, Laura Jankovič, s.p.



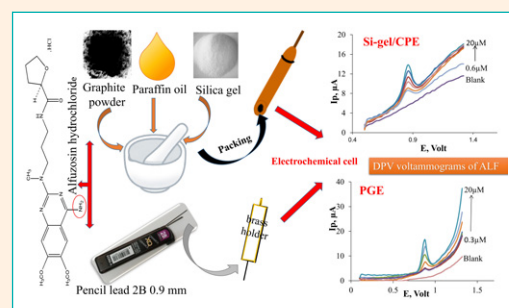
## SCIENTIFIC PAPER

507–518

Analytical chemistry

### Development of Green Differential Pulse Voltammetric Strategy for the Determination of Alfuzosin Hydrochloride at Pencil Graphite and Modified Carbon Paste Electrodes

Youstina Mekhail Metias, Emad Mohamed Hussien, Mervat Mohamed Hosny, and Magda Mohamed Ayad

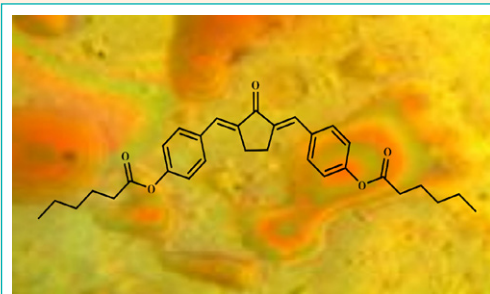


519–525

Organic chemistry

### Synthesis, Characterization, and Investigation of Mesomorphic Properties of a New 2,5-Bis-(4-alkanoyloxybenzylidene)cyclopentan-1-one

Abdullah Hussein Kshash, Omar Jamal Mahdi Al-Asafi and Hanaa Kaen Salih

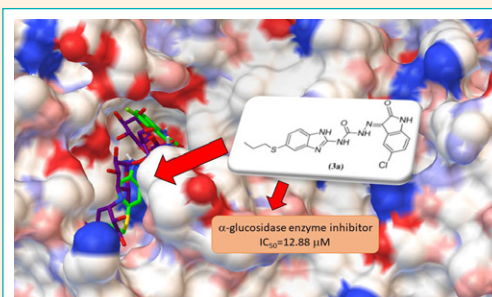


526–535

Organic chemistry

### Synthesis, Molecular Docking Studies and ADME Prediction of Some New Albendazole Derivatives as $\alpha$ -Glucosidase Inhibitors

Sevil Şenkardeş, Necla Kulabaş and Ş. Güniz Küçükgülzel



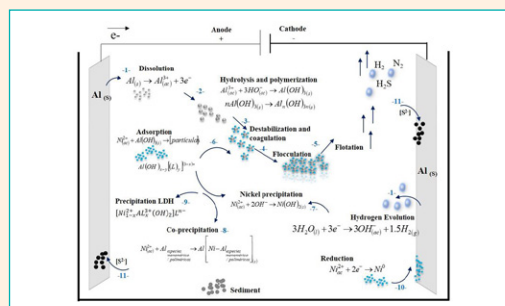


536–551

Chemical, biochemical and environmental engineering

## Nickel Removing by Electrocoagulation of Ni(II)-NH<sub>3</sub>-CO<sub>2</sub>-SO<sub>2</sub>-H<sub>2</sub>O System. Kinetics, Isothermal, Mechanism and Estimated Cost of Operation

Armando Rojas Vargas, Margarita Penedo Medina, Alba González Vives, Nouredine Barka and Aymara Ricardo Riverón

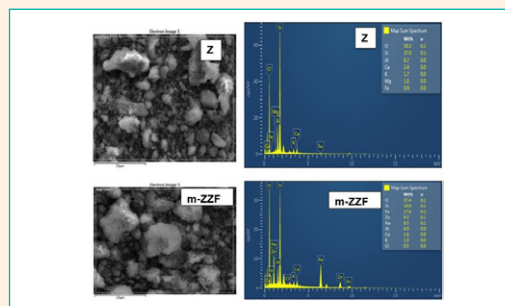


552–563

Chemical, biochemical and environmental engineering

## Decolorization of Direct Black 22 by Photo Fenton like Method Using UV Light and Zeolite Modified Zinc Ferrite: Kinetics and Thermodynamics

Serap Findik

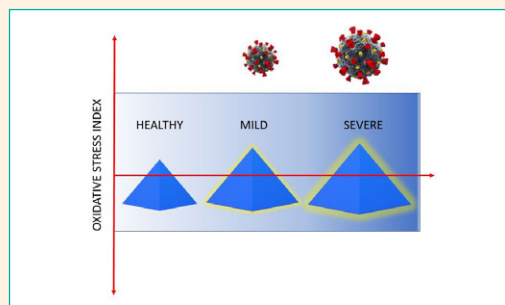


564–570

Biomedical applications

## The Predictive Value of Oxidative Stress Index in Patients with Confirmed SARS-COV-2 Infection

Joško Osredkar, Sara Puck, Milica Lukić, Teja Fabjan, Elizabeta Božnar Alič, Kristina Kumer, Maria Martin Rodriguez and Matjaž Jereb

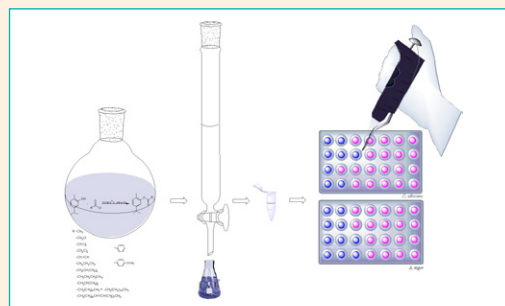


571–583

Organic chemistry

## Carvacrol Derivatives as Antifungal Agents: Synthesis, Antimicrobial Activity and *in Silico* Studies on Carvacryl Esters

Jelena Lazarević, Ana Marković, Andrija Šmelcerović, Gordana Stojanović, Pierangela Ciuffreda and Enzo Santaniello

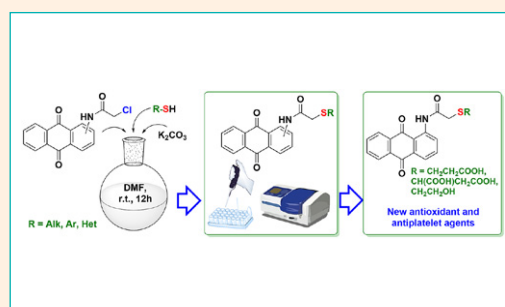


584–595

Organic chemistry

## N-(9,10-Dioxo-9,10-dihydroanthracen-1(2)-yl)-2-(R-thio) Acetamides: Synthesis, Antioxidant and Antiplatelet Activity

Maryna Stasevych, Viktor Zvarych, Olena Yaremkevych, Mykhaylo Vovk, Alla Vaskevych, Tetiana Halenova and Olexii Savchuk



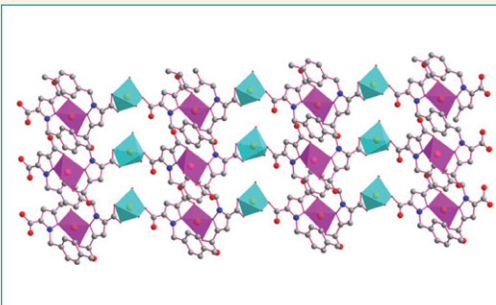


596–603

Inorganic chemistry

## A New Zn(II) Two-dimensional Coordination Polymer: Synthesis, Structure, Highly Efficient Fluorescence and DFT Study

Fen-Fang Li



604–618

Inorganic chemistry

## Ternary Transition Metal Complexes with an Azo-Imine Ligand and 2,2'-Bipyridine: Characterization, Computational Calculations, and Acetylcholinesterase Inhibition Activities

Kerim Serbest, Turan Dural, Demet Kızıl, Mustafa Emirik, Ali Zengin and Barbaros Dinçer

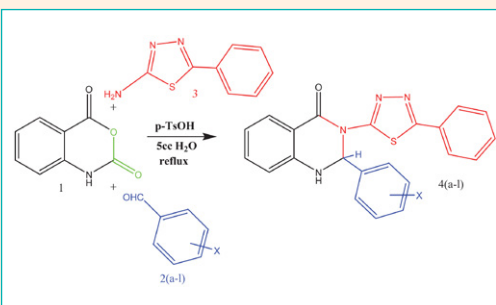


619–628

Organic chemistry

## Synthesis, Antimicrobial and Molecular Docking Studies of Some New Derivatives of 2,3-Dihydroquinazolin-4(1H)-one

Karim Zahmatkesh, Karim Akbari Dilmaghani and Yasin Sarveahrabi

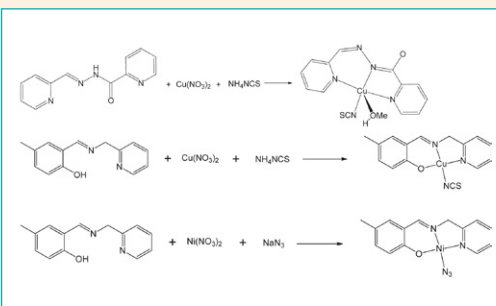


629–637

Organic chemistry

## Synthesis, Crystal Structures and Urease Inhibition of Mononuclear Copper(II) and Nickel(II) Complexes with Schiff Base Ligands

Jian Jiang, Peng Liang, Huiyuan Yu and Zhonglu You

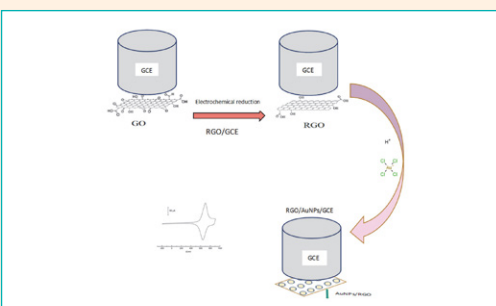


638–646

Analytical chemistry

## Electroanalytical Determination of Ziram by Differential Pulse Voltammetry with Reduced Graphene Oxide/Gold Nanoparticles Modified Glassy Carbon Electrode

Nazife Aslan, Sema Bilge Ocak and Uğur Gökmen



647–656

Physical chemistry

## Electronic Structures and Reactivities of COVID-19 Drugs: A DFT Study

Seyda Aydogdu and Arzu Hatipoglu

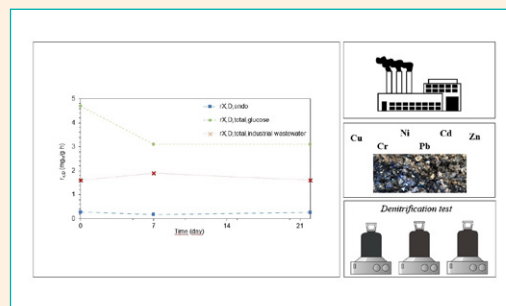


657–664

Chemical, biochemical and environmental engineering

## Industrial Wastewater as a Source of External Organic Carbon for the Biological Nutrient Removal

Bibiána Kožárová, Ronald Zakhar, Zuzana Imreová, Hana Hanuljaková, Ines Karlovská and Miloslav Drtil

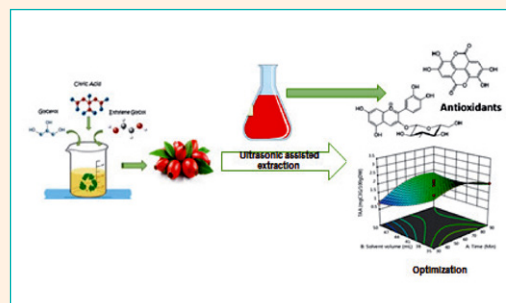


665–673

Chemical, biochemical and environmental engineering

## Environmentally Friendly Extraction of Bioactive Compounds from *Rosa canina* L. fruits Using Deep Eutectic Solvent (DES) as Green Extraction Media

Hyrije Koraqi, Bujar Qazimi, Cengiz Çesko and Anka Trajkovska Petkoska

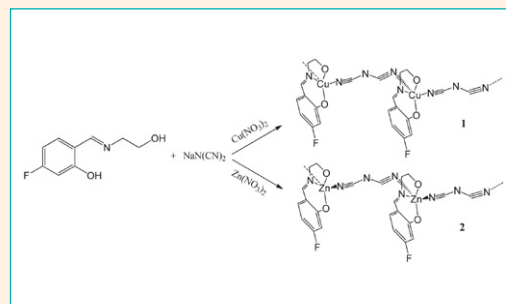


674–680

Inorganic chemistry

## Syntheses, Characterization and Crystal Structures of Dicyanamide Bridged Polynuclear Copper(II) and Zinc(II) Complexes with Urease Inhibitory Activity

Li Zhang, Yuqing Gu, Xinhui Feng, Ting Yang, Xiaoyan Li, Jing Wang and Zhonglu You

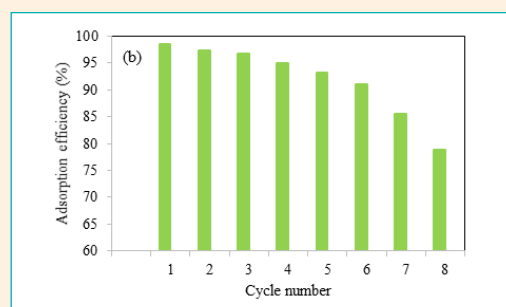


681–693

Chemical, biochemical and environmental engineering

## Phosphate Ion Removal from Synthetic and Real Wastewater Using $\text{MnFe}_2\text{O}_4$ Nanoparticles: ...

Widodo Brontowiyono, Indrajit Patra, Shaymaa Abed Hussein, Alimuddin, Ahmed B. Mahdi, Samar Emad Izzat, Dhuha Mohsin Al-Dhalemi, Ahmed Kareem Obaid Aldulaim, Rosario Mireya Romero Parra, Luis Andres Barboza Arenas and Yasser Fakri Mustafa

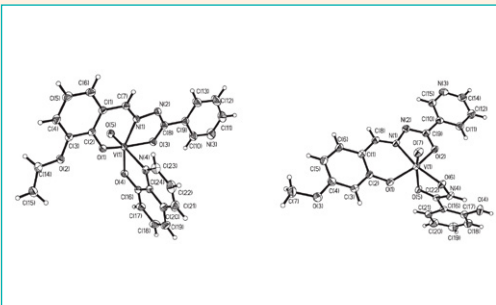


694–699

Inorganic chemistry

## Syntheses, Structures and Insulin-Like Activity of Two Oxidovanadium(V) Complexes with Similar Nicotinothiohydrazone Ligands

Gao-Qi Zhou, Xiao-Yang Qiu, Shu-Juan Liu, Chu-Yi Wang

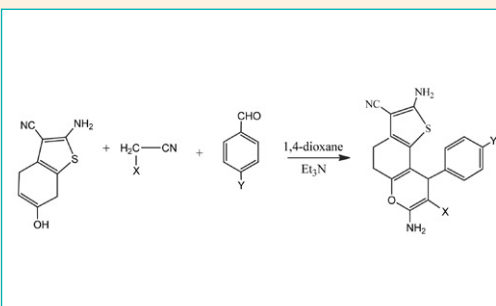


700–713

Organic chemistry

## Antiproliferative and Antiprostata Cancer Activities of Heterocyclic Compounds Derived from Cyclohexane-1,4-dione

Nadia Y. Megally Abdo and Rafat Milad Mohareb

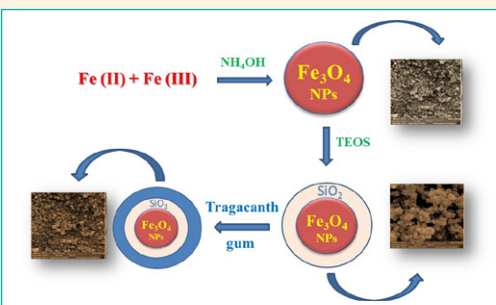


714–721

Analytical chemistry

## Superparamagnetic Tragacanth Coated $\text{Fe}_3\text{O}_4@\text{SiO}_2$ Nanoparticles for the Loading and Delivery of Metformin

Fereshte Farajian and Payman Hashemi

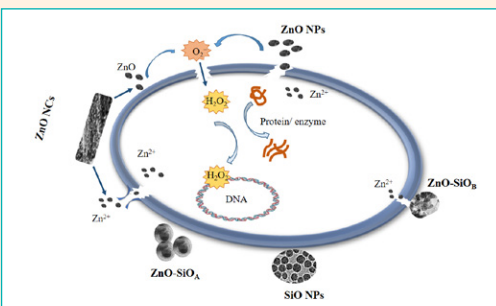


722–733

Materials science

## Investigation of Biological and Prooxidant Activity of Zinc Oxide Nanoclusters and Nanoparticles

Iliana A. Ivanova, Elitsa L. Pavlova, Aneliya S. Kostadinova, Radostina D. Toshkovska, Lyubomira D. Yocheva, Kh El-Sayed, Mohamed A. Hassan, Heba El-Sayed El-Zorkany and Hisham A. Elshoky







Scientific paper

# Development of Green Differential Pulse Voltammetric Strategy for the Determination of Alfuzosin Hydrochloride at Pencil Graphite and Modified Carbon Paste Electrodes

Youstina Mekhail Metias,<sup>1,2</sup> Emad Mohamed Hussien,<sup>3,\*</sup>  
Mervat Mohamed Hosny,<sup>1</sup> and Magda Mohamed Ayad<sup>1</sup>

<sup>1</sup> Department of Analytical Chemistry, Faculty of Pharmacy, Zagazig University 44519, Zagazig, Egypt.

<sup>2</sup> Department of Applied Chemistry, Graduate School of Engineering, Kyushu University, Moto-oka 744, Nishi-ku, Fukuoka-shi, Fukuoka 819-0395, Japan.

<sup>3</sup> Department of Pharmaceutical Chemistry, National Organization for Drug Control and Research (NODCAR), Giza, Egypt.

\* Corresponding author: E-mail: emadhussien@yahoo.com  
Tel.: +2 02 3749 6077

Received: 06-14-2022

## Abstract

A sensitive and inexpensive differential pulse voltammetric technique was applied to investigate the electrochemical behavior of alfuzosin hydrochloride at two different working electrodes: silica gel modified carbon paste and pencil graphite electrodes (PGE). The voltammetric conditions were optimized using cyclic voltammetry, showing an irreversible anodic peak in Britton-Robinson buffered medium (pH 6) at 0.86–0.90 V. The electrochemical responses were linearly correlated with alfuzosin concentrations ( $R^2 > 0.999$ ) in the ranges of 0.6–20 and 0.3–20  $\mu\text{M}$ , exhibiting higher electrocatalytic activity at PGE with a low detection limit/ detectability of 0.099  $\mu\text{M}$ . In addition, this study was a successful attempt for the drug determination in tablets and spiked urine samples with green profile evaluation, employing the National Environmental Methods Index, analytical Eco-Scale score, and Green Analytical Procedure Index.

**Keywords:** Alfuzosin hydrochloride; carbon paste electrode; cyclic voltammetry; differential pulse voltammetry; pencil graphite electrode.

## 1. Introduction

Alfuzosin hydrochloride (ALF), a selective  $\alpha_1$ -adrenoceptor antagonist, is defined as (2RS) -N- [3-[(4-Amino- 6,7 dimethoxyquinazolin-2-yl) methylamino] propyl] tetrahydrofuran-2-carboxamide hydrochloride.<sup>1</sup> The action of ALF as a vasodilator may be less frequent, but it acts more selectively on the smooth muscle tone within the prostate and bladder neck, causing relaxation of these muscles. Therefore, it results in symptomatic relief of the benign prostatic hyperplasia, a common progressive disease encountered in aging men, within weeks.<sup>2</sup> It alleviates the symptoms of urinary obstruction after oral administration of sustained release ALF by reducing outflow resistance and enhancing bladder emptying.

Several analytical methods were published for ALF determination either alone or in combinations, including

micellar flow injection analysis with fluorescence detection,<sup>3</sup> kinetic colorimetric,<sup>4</sup> and UV-spectrophotometric methods.<sup>5</sup> Spectrofluorimetric methods adopting utilization of ortho-phthalaldehyde<sup>6</sup> and micellar matrix<sup>7</sup> for ALF assay in biological fluids and stability indicating spectroscopic studies were also developed.<sup>8</sup> In addition, chromatographic methods such as HPLC with UV,<sup>9</sup> MS/MS,<sup>10</sup> and fluorescence<sup>11, 12</sup> detections, chiral HPLC,<sup>13</sup> UPLC,<sup>14</sup> and stability indicating HPTLC<sup>15</sup> were developed.

Different electrochemical techniques were also established for potentiometric,<sup>16</sup> conductometric,<sup>17</sup> and voltammetric analysis of ALF by linear sweep and normal pulse polarography,<sup>18</sup> Coulometric fast Fourier transform linear sweep voltammetry,<sup>19</sup> and differential pulse<sup>20,21</sup> and square-wave voltammetry.<sup>22</sup>

To our knowledge from the literature review, few analytical studies were performed to investigate the elec-

trochemical behavior of ALF, as depicted in Figure 1. Meanwhile, most of the reported researches were directed towards the chromatographic and spectroscopic analysis of the drug, which required expensive instrumentations, high amounts of solvents, hazardous reagents, prolonged analysis time, or complicated steps for sample pretreatment. Therefore, the development of analytical methods with simpler, greener, lower-cost and faster procedures, and achieving the validation criteria such as higher sensitivity and selectivity is widely demanded for drug analysis. The electrochemical techniques such as voltammetric methods are considered a satisfactory alternative<sup>23</sup> among the available approaches and an appealing choice for pharmaceutical analysis<sup>24</sup>. Although ALF is an electroactive compound, few voltammetric studies were reported for its electrochemical analysis, employing various working electrodes such as Hg electrode,<sup>18</sup> bare<sup>22</sup> and modified glassy carbon electrodes with hybrid of ionic liquid-ZrO<sub>2</sub> in graphene oxide,<sup>19</sup> and multiwall carbon nanotubes sensors incorporated with the ionic liquid 1-hexylpyridinium hexafluorophosphate<sup>20</sup> and nickel oxide nanoparticles.<sup>21</sup>

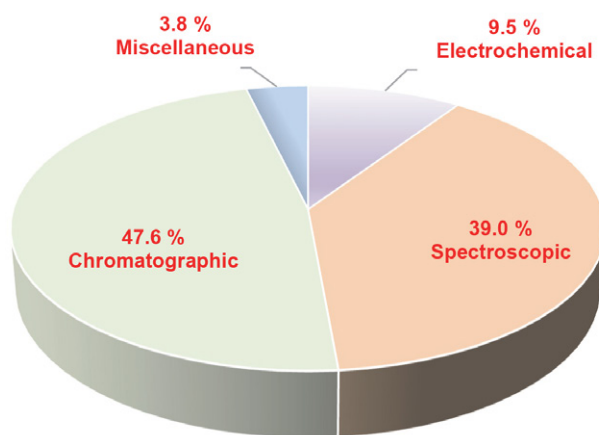


**Figure 1:** Classification of the analytical techniques reported for ALF determination.

However, the reported voltammetric methods showed good sensitivity and satisfactory analytical performance, the applied electrodes exhibited some drawbacks such as mercuric toxicity, and the use of expensive nanomaterials which also required complicated and time consuming procedures for preparation of these modified electrodes. Therefore, the continuous development and chemical modification of the electrochemical sensors with low-cost, easily-prepared, and eco-friendly modifiers have received an extensive interest to enhance their performance as chemical and biological sensors in electroanalysis.

The carbon paste electrode (CPE), a widely applicable electrochemical sensor, has been employed in the areas of electrochemistry and electroanalysis due to its

attractive characteristics, including simple preparation, affordable implementation, easy surface renewal, a low background current, and a wide range of potential window.<sup>23,25</sup> In addition, CPE can be easily modified and simply manipulated in order to obtain a stable response with the possibility of lowering the overpotential, and to increase the sensitivity and selectivity of some electroactive species.<sup>26</sup> Thus, the feasibility of CPE modification with different modifiers were utilized in previous studies, such as sephadex modifier,<sup>27</sup> and rosaniline,<sup>28</sup> phthalo blue,<sup>29</sup> glycine,<sup>30</sup> and helianthium dye<sup>31</sup> which were electropolymerized on CPE for their effective functioning, exhibiting linearity for the studied analytes over the ranges of 0.005–1, 1–3.5, 0.25–1.25, 0.06–1, and 0.06–0.15 mM, respectively.

In the present work, chemically modified graphite electrode with silica gel was employed to investigate the electrochemical behavior of ALF. Silica gel is a granular and porous form of silicon dioxide and can be easily incorporated into the carbon paste as an inexpensive and effective modifier. It possesses some attractive electrochemical properties which is extremely useful for electroanalytical purposes, such as high surface area, strong adsorption capacity, insolubility in most solvents, high thermal stability, and readily surface modification.<sup>32–34</sup>

In recent years, disposable sensors composed of convenient matrices for surface renewal, such as pencil graphite electrodes (PGE), gained a large applicability to quantitative assays.<sup>35–37</sup> PGE stand as an excellent versatile tool in the electroanalysis having favorable advantages over the traditional electrodes of being simple, cheap, commercially available, easily modified, low technology, and good mechanical rigidity. Moreover, the preparation of PGE for each measurement is faster and easier than the procedures required for other conventional carbon electrodes, including tedious hand mixing and polishing, and hazardous steps.<sup>38</sup>

Differential pulse voltammetry (DPV) is a simple pulse voltammetric technique that is widely applicable for the determination of various pharmaceuticals.<sup>24</sup> Herein, we employ DPV to study the electrochemical oxidation of ALF at two different electrochemical sensors: silica gel modified carbon paste and pencil graphite electrodes, with a comparison of their performance.

Thus, our study aims to develop an easy, simple, and rapid DPV method for highly sensitive estimation of ALF in tablets and biological samples. As far as we know, it is the first report to employ a disposable pencil graphite electrode for the voltammetric assessment of ALF and to demonstrate the practical usefulness of two simple electrodes of low cost for the direct assay of ALF in urine samples. Moreover, the ecological impact of the proposed method was also evaluated using three metrics, namely, the National Environmental Methods Index (NEMI), analytical Eco-Scale score, and Green Analytical Procedure Index (GAPI).



## 2. Experimental

### 2. 1. Instrumentation

The electroanalytical study was performed using a SP-150 potentiostat (Bio-Logic Science Instrument, France) connected to a Lenovo computer provided with EC-Lab for windows v11.02 software. The cell potentials were measured with respect to the Ag/AgCl/3.0 M KCl reference electrode (BAS, USA) in a glass cell, comprising a working electrode and platinum wire (BAS, USA) as an auxiliary electrode.

A digital analyzer pH meter (Jenway 3510, USA) and ultrasonic bath sonicator (UCI-750, RAYPA, Spain) were also used.

### 2. 2. Working Electrodes

Voltammetric measurements were performed using two different electrodes:

#### 2. 2. 1. Modified Carbon Paste Electrode

Silica gel modified carbon paste electrode (Si-gel/CPE) was prepared by thoroughly hand-mixing of 0.2 g silica gel and 0.8 g graphite powder with 0.6 mL paraffin oil by a ceramic pestle in a glass mortar to obtain a homogeneous paste. The preparation of the bare (plain or unmodified) CPE was likewise done by blending of 1.0 g graphite powder with 0.6 mL paraffin oil. The resulting paste was packed into the electrode body hole, and then the external surface of the electrode was polished on a soft paper with figure-eight motions in order to remove the excess of the paste and obtain a shiny appearance prior to using. In addition, subsequent renewal of the carbon paste surface for the each measurement should be performed, where a small portion of the paste at the electrode tip was scraped out and replaced by a new portion then repolished to generate a fresh electrode surface.

#### 2. 2. 2. Pencil Graphite Electrode

XQ pencil leads of 2B grade with 0.9 mm diameter and 60 mm length from the local bookstore were employed for the voltammetric measurements of ALF. An insulating tape was used for wrapping PGE gently, where 25 mm of the pencil lead at one end was inserted into a home-designed brass holder for the electrical connection with the device. Meanwhile, the exposed surface of PGE at the other end was only 10 mm devoted as the sensitive part for the voltammetric assay and was gently polished before each recording using a cloth felt pad.

### 2. 3. Materials and Reagents

Pure sample of ALF was generously provided by Eva Pharma, Egypt (lot no. 1422R118) with purity of 100.80% according to the comparison method.<sup>1</sup>

Bi-distilled water obtained from a Milli-Q water purification system and chemical reagents of highest purity were used in this study. Graphite powder, paraffin oil, Sephadex G-50, C18 silica gel, and chitosan were supplied from Sigma-Aldrich. Methanol, sodium hydroxide, glacial acetic acid, boric acid, phosphoric acid, and hydrochloric acid were obtained from El Nasr Pharmaceutical Chemicals CO. (Cairo, Egypt).

Britton-Robinson buffer (B-R buffer), a widely used multi-buffer system in the voltammetric studies, was employed as a non-complexing supporting electrolyte for the voltammetric measurements of ALF. The multi-acid B-R buffer system is consisted of three different buffering components of diminishing strength, so a linear pH response is obtained from pH 2.5 to pH 9.2 upon adding the alkali. Thus, it was easily prepared at the desired pH value without changing the chemical composition of the buffered components. It was prepared from a mixture of 0.04 M of each acid; boric, phosphoric and acetic acids, and the desired pH was adjusted using NaOH.

### 2. 4. Pharmaceutical Formulation

Prostetrol® modified release tablets (10 mg of ALF/tablet), a product of Eva Pharma with batch no. (10)190238, were purchased from the Egyptian market to be analyzed by the proposed method.

### 2. 5. Stock and Working Standard Solutions

A stock standard solution of ALF ( $1.0 \times 10^{-2}$  M) was prepared using methanol for dissolving 42.59 mg of ALF into a 10 mL volumetric flask. Further dilution was carried out by transferring 0.25 mL of the prepared solution into a 25 mL volumetric flask and completing the final volume with bi-distilled water to obtain a standard solution of  $1.0 \times 10^{-4}$  M. The ALF working solutions were made by further dilution of the standard solution with B-R buffer solution to cover the concentration ranges of  $6 \times 10^{-7}$  to  $2 \times 10^{-5}$  M and  $3 \times 10^{-7}$  to  $2 \times 10^{-5}$  M at Si-gel/CPE and PGE, respectively.

### 2. 6. General Procedure

#### 2. 6. 1. Voltammetric Procedures

The surface of the working electrode was conditioned at first by performing successive anodic cyclic voltammetry (CV) scans within the potential of 0 up to 1.6 V in an electrochemical cell containing B-R buffer solution of pH 6. After achieving stable background and response, an appropriate volume of the ALF standard solution was added to the cell, and then the solution was stirred for 1 min at an open circuit potential followed by a rest period for 30 s. The voltammograms were then recorded at a scan rate of  $200 \text{ mVs}^{-1}$  and ambient temperature.

### 2. 6. 2. Construction of Calibration Curves

The quantitative determination of ALF was performed using the DPV method within a potential range of 0 to 1.3 V, employing the optimum parameters of 50 mV pulses and step height, 50 ms pulses width, and 100 ms step time. Different aliquots of the ALF standard solution ( $1.0 \times 10^{-4}$  M) were transferred by a micropipette into an electrochemical cell containing 10 mL buffer of pH 6, and then the peak currents were measured after stirring of the cell content for 1 min. The oxidation current peak ( $\mu$ A) that developed at each working electrode was plotted against its corresponding drug concentration ( $\mu$ M) to construct two calibration curves, covering the concentration ranges of 0.6–20 and 0.3–20  $\mu$ M at Si-gel/CPE and PGE, respectively, and being fit with two linear regression equations.

### 2. 6. 3. Assay of Pharmaceutical Preparations

Ten Prostetrol® tablets were finely pulverized, and an equivalent amount to  $1.0 \times 10^{-2}$  M ALF was accurately weighed, transferred into a 25 mL volumetric flask, and dissolved in 20 mL methanol by sonication for 30 min in an ultrasonic bath. The final volume was made up using the same solvent, and then the flask content was well mixed and allowed to settle for 15 min before filtering the supernatant.<sup>39</sup> Further dilution was done with bi-distilled water to obtain  $1.0 \times 10^{-4}$  M solution of ALF. Different aliquots from the prepared solution were investigated for ALF quantification in its dosage form, applying the procedures described under construction of calibration curves section and the percentage recoveries were calculated from the corresponding regression equation.

### 2. 6. 4. ALF Assay in Spiked Human Urine

Human urine samples, collected from a healthy donor and stored at  $-20$  °C, were allowed to be partially thawed at room temperature to collect a clear supernatant. In order to reduce the matrix effect, the urine supernatant underwent fifty and twenty fold dilutions with the B-R buffer of pH 6 for the voltammetric measurements at Si-gel/CPE and PGE, respectively. 10 mL of the sample solution was transferred into the voltammetric cell and its voltammogram was recorded as a blank solution for subsequent measurements. Appropriate aliquots of  $1.0 \times 10^{-4}$  M of ALF solution were then spiked for their direct analysis in urine matrix, using the procedures described under construction of calibration curves section for the recovery studies of the spiked urine samples.

## 3. Results and Discussion

The electrochemical behavior of ALF was investigated at two different electrodes: CPE and PGE using CV technique, where different chemical and electrochemical

parameters were thoroughly studied for optimization its voltammetric performance. The voltammograms of the studied drug were recorded from 0 to 1.6 V in the B-R buffer solution as the supporting electrolyte. ALF exhibited a well-defined anodic peak current at around 0.90 V without a cathodic peak on the reverse scan, indicating the irreversible electro-oxidation process of ALF. The reasonable oxidation mechanism, as postulated by the previous electrochemical studies of ALF,<sup>20,22</sup> might occur at the electroactive nitrogen atom in the amine group of the pyrimidine moiety, followed by deprotonation and dimerization.

### 3. 1. Optimization of the Experimental Conditions Using Cyclic Voltammetry

#### 3. 1. 1. Effect of the Solution pH

The pH of the supporting electrolyte has an important impact on the voltammetric behavior of the drug. Therefore, the change in the pH range of B-R buffer from 3 to 9 was studied using CV method and the electro-oxidation peak potential and peak current of 10  $\mu$ M ALF were assessed. Upon increasing the pH values, the anodic peak potential shifted in the less positive direction due to the proton dependent electro-oxidation mechanism of ALF on the working electrode and followed linear regression equation 1 (Figure 2B):

$$E_{pa} = -0.0561\text{pH} + 1.3287 \quad (R^2 = 0.9900) \quad (1)$$

where:  $E_{pa}$  is the anodic peak potential of 10  $\mu$ M ALF as a function of the applied pH of B-R buffer.

In addition, the slope of 0.0561 V/pH is close to the theoretical value of 0.059 V /pH of the Nernst equation, indicating that equal number of electrons and protons participated in the process of drug oxidation. Moreover, the anodic peak current of ALF enhanced in less acidic medium, reaching the optimum at pH 6. Meanwhile, badly-defined oxidation peaks and a gradual decrease in the peak height were observed with the further increase in the pH values. This might be attributed to the dissociation constant of the studied drug, where the pKa values of ALF are 2.26 and 5.56.<sup>40</sup> Therefore, the pH of the solution could affect the existing form of ALF as the drug would exist in its protonated (water soluble) form in the acidic medium, while at higher pH values, it would be deprotonated to its barely soluble form. Thus, the decrease in the peak currents was observed at higher pH values ( $>$  pKa values of ALF). As can be seen in Figure 2, B-R buffer of pH 6 was fit for all subsequent measurements of ALF.

#### 3. 1. 2. Effect of Surfactants as Electrolyte Additives

The impact of surfactant addition to the supporting electrolyte was investigated in the present study, as sur-

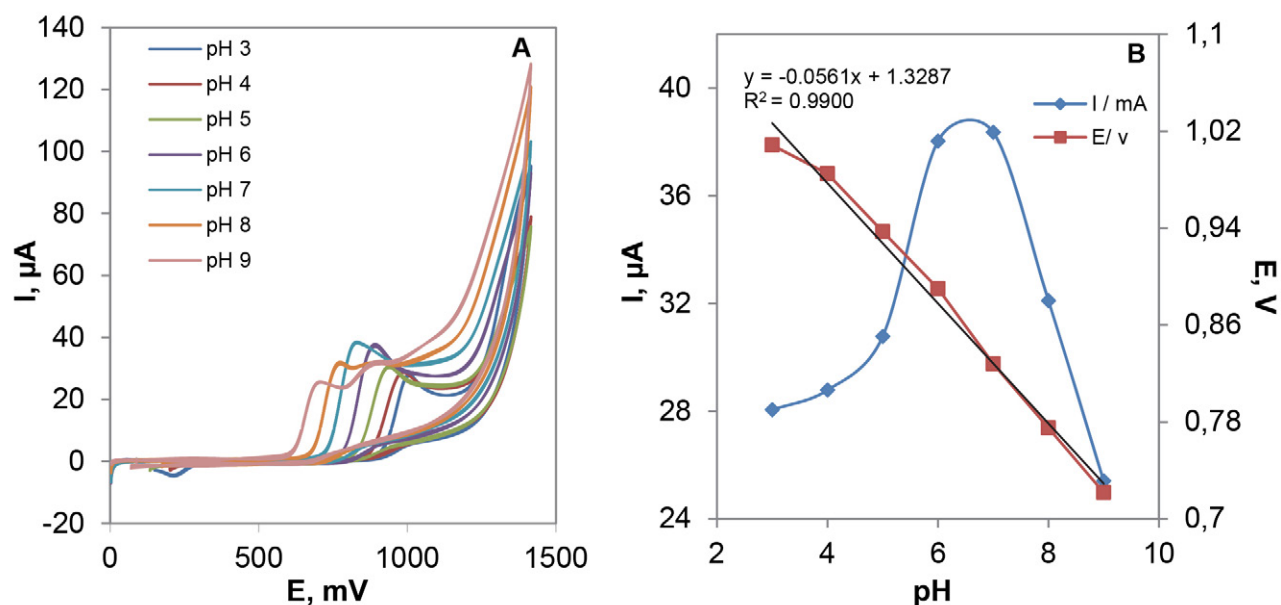


**Figure 2:** (A) Cyclic voltammograms of 10 μM ALF recorded at different pH values (3–9) of B-R buffer at 200 mV/s scan rate; (B) Dependence of the anodic peak potential and peak current on the pH values.

factants are widely used in electroanalysis for enhancing the electrochemical performance of some analytes. Therefore, the oxidation behavior of ALF was studied in the presence of different types of surfactants, including SDS, CTAB, and Brij-35 as anionic, cationic, and nonionic surfactants, respectively. The aqueous electrolytic solution of B-R buffer showed the best response as can be seen in Figure S1, meanwhile no distinct effect was noticed upon adding the surfactants to the analyte in the B-R buffer solution of pH6.

### 3. 1. 3. Effect of the Stirring Time

The anodic peak current of ALF in dependence of the stirring time was studied at different time intervals from 0 to 3 min using CV, where the voltammograms were recorded after stirring the solution at 400 rpm, followed by 30 s quiescent time at an open circuit potential. As shown in Figure S2, the oxidation peak current improved after the solution stirring for 1 min, then became stable up to 3 min.

### 3. 1. 4. Effect of the Carbon Paste Composition

The incorporation of different modifiers such as silica gel, chitosan, sephadex and iron nanoparticles into the carbon paste composition were investigated to attain highly responsive sensor. The oxidation peak current of the studied drug enhanced upon modifying CPE with silica gel which exhibited a higher electrocatalytic activity and sensitivity towards ALF oxidation, Figure S3. The effect of silica gel content was also checked by recording the voltammetric responses of CPE containing various

proportions of silica gel. The addition of silica gel in the ratio of 20% w/w of the paste total mass showed an efficient synergistic effect for improving the oxidation peak current of ALF, Figure S4.

### 3. 1. 5. Effect of the Pencil Graphite Types

Different types and diameters of disposable PGE were examined using CV for B-R solution containing 5 μM ALF. Pencil leads are usually marked with either H (hardness), B (blackness), or HB letters which mainly differ in their composition ratio of graphite and clay. PGE of the soft B type containing more graphite and with larger diameter are appropriate for quantitative assay as this type provides an easy electronic transfer which generates higher signals.<sup>38</sup> PGE from different commercial manufacturers such as HB, rotring, faber castle, and XQ were also investigated, where electroactive species may show different voltammetric behavior on PGE produced from different manufacturers with the same hardness due to different interactions of the analyte with common components of PGE.<sup>38</sup> 2B XQ pencil lead of 0.9 mm diameter was the optimum which gave the best electrochemical response with relatively low noise, Figure S5.

### 3. 1. 6 Optimization of the Scan Rate

Studying the scan rate effect gave valuable information about the electrochemical behavior of the studied drug at the working electrode, whether the electro-oxidation process would be under diffusion or adsorption con-



trolled mechanism. The variation in the peak current ( $i_p$ ) and peak potential ( $E_p$ ) of 10  $\mu\text{M}$  ALF in B-R buffer solution (pH 6) at Si-gel/CPE was examined by the CV mode at different scan rates. Upon increasing the scan rate from 25 up to 300 mV/s, the anodic peak current grew gradually and the oxidation peak potential shifted slightly towards more positive direction, indicating the irreversible oxidation process. The scan rate of 200 mV/s was selected for the successive voltammetric measurements, exhibiting a well-shaped peak with relatively narrow width and high sensitivity, Figure 3 A.

A direct relationship was found between the oxidation peak current of ALF and square root of the scan rate

( $v^{1/2}$ ) over the scan rate range of 25–200 mV/s<sup>-1</sup>, based on  $I(\mu\text{A}) = 2.7885 v^{1/2} (\text{mV/s}) + 2.0843 (R^2 = 0.9816)$ . Thus, the electrochemical oxidation of ALF was controlled by a diffusion process, Figure 3 B.

Moreover, plotting the logarithm of the peak current versus logarithm of the scan rate exhibited a straight line following equation 2 (Figure 3 C):

$$\log I_p (\mu\text{A}) = 0.4932 \log v (\text{mV/s}) + 0.4922, R^2 = 0.9799 \quad (2)$$

where  $I_p$  represents the anodic peak current and  $v$  is the scan rate.

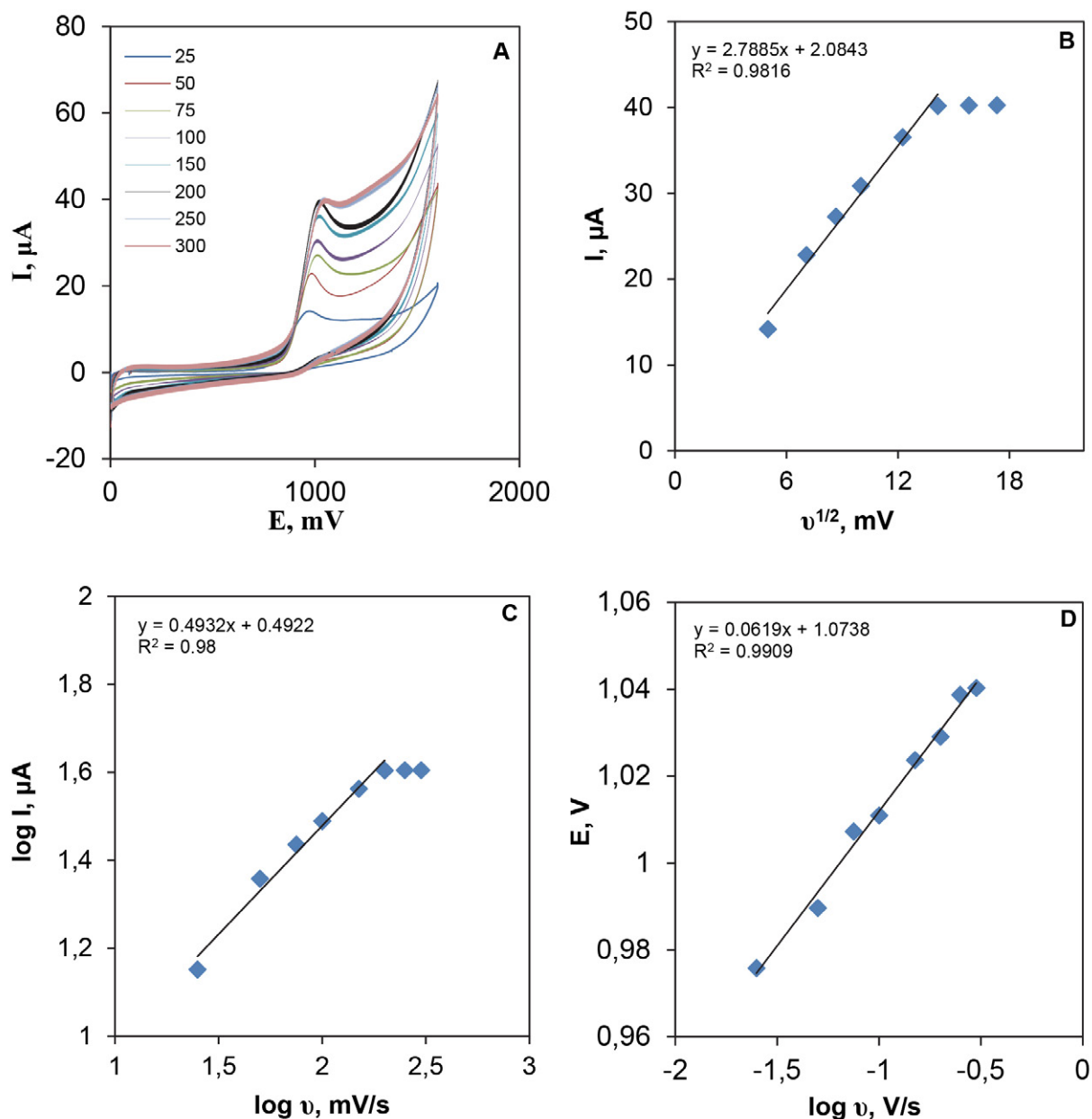


**Figure 3:** (A) Cyclic voltammograms of 10  $\mu\text{M}$  ALF in B-R buffer of pH 6 at different scan rates; (B) Linear plot of the peak current versus square root of the scan rate; (C) Dependence of the logarithm of the peak current on logarithm of the scan rate; (D) Linear plot of the peak potential as function of logarithm of the scan rate.

The obtained slope value of 0.4932 was close to the theoretical value of 0.5 for the diffusion-controlled electrode process.<sup>41</sup> Furthermore, the relationship between the peak potential and logarithm of the scan rate was found to be linear according to equation 3 (Figure 3 D):

$$E_{pa}(V) = 0.0619 \log v (V/s) + 1.0738, R^2 = 0.9909 \quad (3)$$

where  $E_{pa}$  represents the anodic peak potential and  $v$  is the scan rate.

In accordance with Laviron's equation given for an irreversible electrochemical process, the number of electrons transferred at the surface of the electrode due to ALF oxidation was calculated as follows:<sup>42</sup>

$$E_p = E^\circ + \frac{2.303RT}{\alpha nF} \left( \log \frac{RTk^\circ}{\alpha nF} \right) + \frac{2.303RT}{\alpha nF} \log v \quad (4)$$

Herein, the following elements in equation 4 possess their conventional meanings: the electron transfer coefficient ( $\alpha$ ), the number of electrons transferred ( $n$ ), temperature ( $T = 298 \text{ K}$ ), gas constant ( $R = 8.314 \text{ J K mol}^{-1}$ ), Faraday constant ( $F = 96485 \text{ C mol}^{-1}$ ), and the voltammetric scan rate ( $v$ ).  $k^\circ$  denotes the standard heterogeneous rate constant of the surface reaction,  $E^\circ$  represents the formal redox potential, and  $E_p$  is the anodic peak potential.

The  $E^\circ$  value can be obtained from the intercept of  $E_p$  against  $v$  on the ordinate by extrapolating the line to the vertical axis at  $v = 0$ . From the linear relationship between  $E_{pa}$  versus  $\log v$ , the value of  $\alpha n$  can be deduced from the slope and found to be 0.0619. The supposed value of  $\alpha$  equals 0.5 for the irreversible electrochemical process,<sup>43</sup> thus the  $n$  value was calculated to be 1.911 (approximately 2.0). This value referred to the participation of two electrons and protons in the electro-oxidation reaction of ALF which coincided with previously published results.<sup>20,21</sup>

## 3. 2. Method Validation

The developed DPV method at two different electrodes was validated according ICH guidelines<sup>44</sup> with regard to the following parameters:

### 3. 2. 1. Linearity and Ranges

Under the optimum conditions, the linearity of ALF was investigated in the concentration ranges of  $6 \times 10^{-7}$ – $2 \times 10^{-5} \text{ M}$  at Si-gel/CPE and  $3 \times 10^{-7}$ – $2 \times 10^{-5} \text{ M}$  at PGE using DPV, Figure 4. Statistical data analysis was performed by plotting the peak current height ( $\mu\text{A}$ ) as a function of concentration ( $\mu\text{M}$ ), fitting the resulting calibration graphs into linear regression equations as follows:

$$\text{Si-gel/CPE: } I = 0.2501 C + 2.7407 (R^2 = 0.9995) \quad (5)$$

$$\text{PGE: } I = 0.6057 C + 3.3274 (R^2 = 0.9996) \quad (6)$$

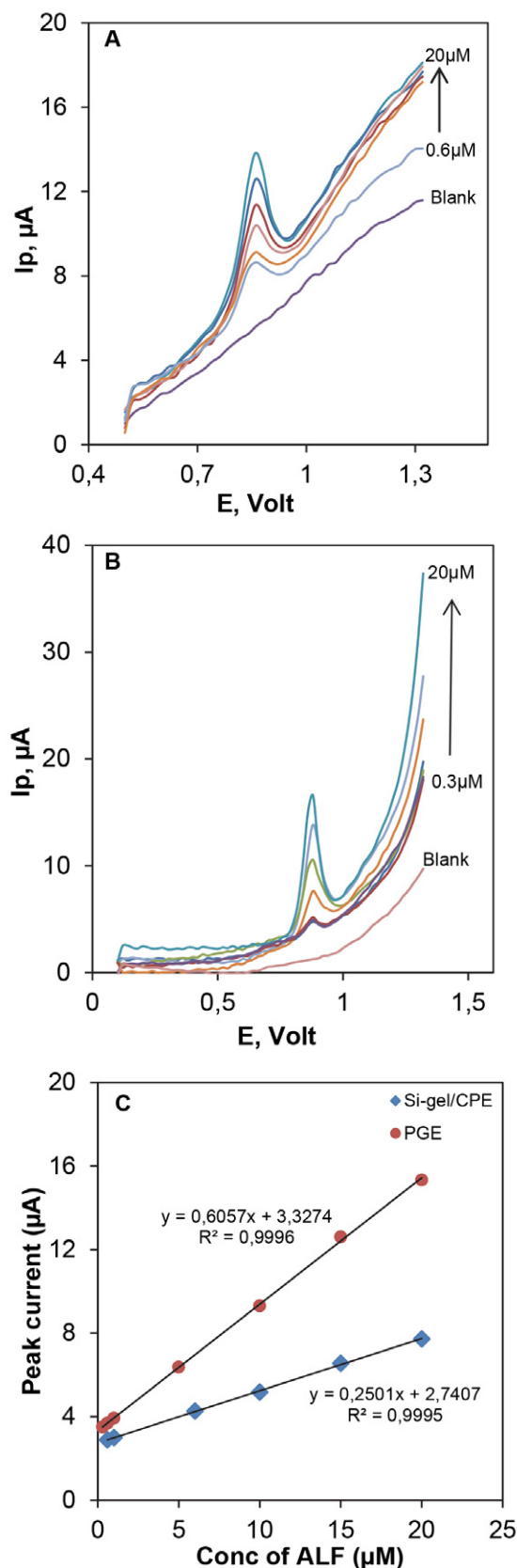


**Figure 4:** DPV voltammograms of (A) 0.6–20  $\mu\text{M}$  of ALF at Si-gel/CPE; (B) 0.3–20  $\mu\text{M}$  of ALF at PGE in B-R buffer solution of pH 6. (C) Calibration plot of the peak current versus concentration.

**Table 1.** Regression and analytical performance data of ALF assay by DPV method at two different electrodes.

Parameters	Si-gel/CPE	PGE
Linearity range ( $\mu\text{M}$ )	0.6–20	0.3–20
Intercept	2.7407	3.3274
Slope	0.2501	0.6057
Correlation Coefficient( $R^2$ )	0.9995	0.9996
LOD ( $\mu\text{M}$ )	0.17	0.099
LOQ ( $\mu\text{M}$ )	0.53	0.299
<b>Accuracy</b>		
(mean recovery% $\pm$ Er%)	100.85 $\pm$ 0.85	98.97–1.03
	97.57–2.43	99.74–0.26
	98.99–1.01	100.94 $\pm$ 0.94
Precision (RSD%)		
Repeatability <sup>[a]</sup>	1.756	1.399
Intermediate precision <sup>[b]</sup>	1.794	1.788

<sup>[a]</sup> The intra-day and <sup>[b]</sup> inter-day RSD ( $n=9$ ) of 1, 10, and 20  $\mu\text{M}$  ALF at Si-gel/CPE and 1, 10, and 15  $\mu\text{M}$  ALF at PGE within the same day and in three successive days.

The obtained data with high correlation coefficients were indicative of good linearity of the proposed method at the two applied electrodes, Table 1.

### 3. 2. 2. Sensitivity

The limits of detection (LOD) and quantification (LOQ) were calculated according to the ICH guidelines:<sup>44</sup>  $\text{LOD} = 3.3 \sigma/s$  and  $\text{LOQ} = 10 \sigma/s$ , where,  $\sigma$  is the standard deviation of the responses of four replicated blanks obtained at the same potential applied for the sample and  $s$  is the slope of the calibration graph. The obtained values of LOD and LOQ indicated the sensitivity of the proposed method at the applied electrodes, as shown in Table 1.

### 3. 2. 3. Accuracy and Precision

The accuracy of the proposed method was examined using nine samples of three different concentrations of the pure drug selected to cover the low, medium and high ranges of the calibration graph. The mean percentage recoveries of these ALF concentrations were calculated, as shown in Table 1.

The precision was also evaluated through triplicate determinations of three different concentrations of pure drug within the same day (intra-day) and on three different days (inter-day). The obtained results in Table 1 exhibited acceptable values of relative standard deviation (RSD%) and percentage relative error (Er%).

### 3.2.4. Specificity

The specificity of the proposed method was confirmed by ALF assay in its tablet formulation and urine samples. The selectivity of DPV at the applied electrodes was also tested in the presence of commonly used exci-

ents in tablets, such as silica, lactose, PVP, talc, and magnesium stearate. The excipients were added to ALF at the same concentration ( $10^{-5}$  M) and analyzed under optimum conditions.

Table 2 exhibits sufficiently good recoveries with no interference, while lactose showed a slight decrease in the electrochemical response of ALF.

**Table 2:** Voltammetric analysis of ALF in the presence of some common excipients by DPV at two different electrodes.

Excipients Added <sup>[a]</sup> ( $1 \times 10^{-5}$ M)	Recovery % <sup>[b]</sup>	
	Si-gel/CPE ( $1 \times 10^{-5}$ M)	PGE ( $1 \times 10^{-5}$ M)
Silica	103.40	101.88
Lactose	95.00	94.23
Povidone k30	102.87	97.67
Talc	100.10	100.40
Magnesium stearate	101.18	101.71

<sup>[a]</sup> Drug: excipients in the ratio of 1: 1 M.

<sup>[b]</sup> Average of three determinations.

### 3. 3. Statistical Analysis

The results of DPV at both electrodes were statistically examined using the Student's t-test and variance ratio F-test at the 95% confidence level. The obtained results were compared with those of the official potentiometric method for the ALF assay<sup>1</sup> and showed no significant differences, Table 3.

**Table 3.** Statistical analysis of the results obtained by DPV at two different electrodes and the pharmacopeial method for ALF assay.

	Si-gel/CPE	PGE	Comparison method [1] <sup>[a]</sup>
Mean $\pm$ SD	100.10 $\pm$ 1.58	99.39 $\pm$ 1.40	100.80 $\pm$ 1.42
Variance	2.508	1.970	2.016
n	6	7	3
Student-t-test	0.642 (2.365) <sup>[b]</sup>	1.549 (2.306) <sup>[b]</sup>	–
F-test	1.244 (5.790) <sup>[b]</sup>	1.023 (5.140) <sup>[b]</sup>	–

<sup>[a]</sup> Potentiometric official method for ALF assay.

<sup>[b]</sup> The corresponding theoretical values for t and F tests at  $p = 0.05$ .

### 3. 4. Analytical Applications

The employed electrodes showed satisfactory results for the ALF assay in Prostetrol<sup>®</sup> tablets and spiked urine samples using DPV. The recovery values of the target analyte and the standard deviations (SD) proved the suitability of the proposed method for fast routine analysis of ALF in its tablets and human urine samples (Table 4).

Thus, the proposed DPV method exhibited simpler, time saving, greener, and good practical applicability for



ALF analysis in real samples with acceptable percentage recoveries. As compared to the voltammetric performance of ALF at Si-gel/CPE, PGE showed a better response with a smaller background current, good conductivity, sharp oxidation peaks, and higher sensitivity (Figure 4) due to the presence of  $sp^2$  hybridized carbon of graphite bound with clay in the pencil lead composition. Herein, clay, an aggregate of minerals and colloidal substances, contributed to the good sensing performance of PGE because of its highly attractive characteristics such as chemical and mechanical stability, strong sorption properties revealed in high ionic exchange capabilities, and porosity which exhibits beneficial ionic conductivity and electrocatalytic activity.<sup>45</sup> Table 1 ascertains the good electrocatalytic activity of PGE towards the ALF oxidation, where the sensitivity obtained at PGE was two times higher than that at Si-gel/CPE with a lower LOD of 0.099  $\mu\text{M}$ .

### 3. 5. Greenness profile of the Proposed Method

The assessment of the analytical method procedures from the green perspective has recently attracted the authors' concern in the field of green analytical chemistry (GAC). Electroanalytical techniques mostly comply with the GAC principles as they are free of hazardous chemicals and organic solvents, and do not produce large volumes of analytical waste compared to the classical chromatographic methods.

To deepen this view, the greenness profile of the developed method was established using three assessment tools: NEMI, Analytical Eco-Scale, and GAPI methods. The applied metrics introduced more easier and visible information on the environmental impact of the applied analytical procedures.

NEMI labeling is considered as one of the oldest tools for qualitative greenness assessment of the analytical

procedures. The NEMI pictogram is symbolized by a circle divided into four fields that reflect four different criteria of the described analytical methodology: persistence, bioaccumulation potential, and toxicity (PBT), hazardous chemicals, corrosiveness, and waste. Each field is filled with green when its required criterion is met by the developed method.<sup>46</sup> Adopting these criteria, the pictogram of the applied method showed green-colored quadrants due to satisfaction with their requirements as shown in Table 5, except for the hazardous quadrant due to methanol usage, regardless of the minute amount used per sample.

From a glance at the NEMI symbol, general information about environmental impact of the analytical procedure can be easily read with no significance to energy consumption or the quantity of chemicals.

Thus, the analytical Eco-Scale approach was employed for the greenness assessment in a more quantitative way, where a numerical score was given for the developed method. The analytical Eco-Scale score was calculated by subtraction of the total penalty points from the basis of 100 points (ideal green analysis). The penalty points of the analytical procedure were assigned to four main categories: the amount and type of chemicals, energy consumption, occupational hazard, and amount of generated waste, and the way for its treatment. The score was ranked on a scale, where the method greenness was excellent if the score is higher than 75, acceptable if it is higher than 50, and inadequate if it is less than 50.<sup>47</sup> The DPV method scored 80 at Si-gel/CPE and 82 at PGE (higher than 75), so it ranked as an excellent green method. As can be seen in Table 5, the analytical Eco-Scale scores were calculated in detail for assessing its greenness profile more clearly than that obtained by NEMI.

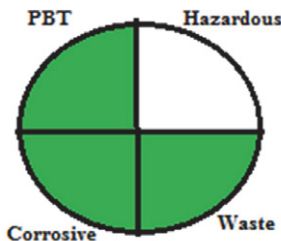
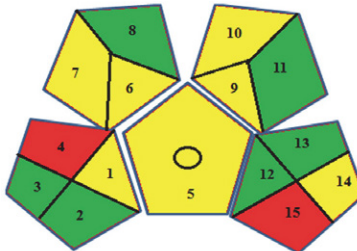
A recent assessment tool known as GAPI was also employed, showing a specific symbol with five pentagrams segmented into 15 zones to encompass five main categories: sample handling, general method type, sample prepa-

**Table 4.** Analytical application of the DPV method for ALF determination in tablets formulation and spiked urine samples at two different electrodes.

Parameters	Si-gel/CPE						PGE					
	Prostetrol <sup>®</sup> modified release tablets			Urine samples			Prostetrol <sup>®</sup> modified release tablets			Urine samples		
	Taken $\mu\text{M}$	Found $\mu\text{M}$	Recover $y^{[a]}\%$	Taken $\mu\text{M}$	Found $\mu\text{M}$	Recover $y^{[a]}\%$	Taken $\mu\text{M}$	Found $\mu\text{M}$	Recover $y^{[a]}\%$	Taken $\mu\text{M}$	Found $\mu\text{M}$	Recover $y^{[a]}\%$
	5	4.02	101.92	3	3.08	102.57	0.6	0.59	98.43	5	5.10	102.01
	7	4.49	99.96	5	5.12	102.36	5	4.89	97.74	7	7.19	102.66
	13	6.05	101.72	10	10.10	100.95	7	6.97	99.61	10	10.02	100.24
	16	6.82	101.97	15	15.15	101.03	10	10.04	100.43	12	11.80	98.85
	20	7.84	102.00				12	11.65	97.10			
Mean $\pm$ SD	101.51 $\pm$ 0.88			101.73 $\pm$ 0.85			98.66 $\pm$ 1.36			100.94 $\pm$ 1.73		
N	5			4			5			4		
SE	0.392			0.427			0.607			0.866		
V	0.767			0.729			1.842			2.997		

<sup>[a]</sup> Average of three determinations.

Table 5. Greenness assessment of the proposed method by the Analytical Eco-Scale, NEMI, and GAPI approaches.

Analytical Eco-Scale score parameters	Penalty points (PPs)		NEMI pictograms
	Si-gel/CPE	PGE	
<b>I-Reagents/ word sign /no of pictograms</b>			
Bi-distilled water/ – / 0		0	
Methanol/ danger / 2		4	
1M NaOH/ danger / 1		2	
Silica gel / – / 0	0	–	
Paraffin oil/ danger / 1	2	–	
Graphite/ – / 0		0	
0.04 M acetic acid / danger / 1		2	
0.04 M orthophosphoric acid/ danger / 1		2	
0.04 M boric acid/ danger / 1		2	
	$\Sigma = 14$	$\Sigma = 12$	
<b>II-Instruments a-Energy</b>			
Potentiostat		0	
pH meter		0	
Vortex mixer		0	
Sonicator		0	
<b>b-Occupational hazards</b>		3	
<b>c-Waste</b>		3	
	$\Sigma = 6$		
<b>Total PPs</b>	20	18	
<b>Analytical eco-scale score = 100- total PPs</b>	80	82	
	Excellent green analysis		

\* Red zones depict high ecological impact; yellow zones represent lower impact; and green zones represent more safe effect to the environment.

ration, reagents/solvents used and instrumentation. Thus, the GAPI approach evaluates 15 criteria covering every step in the whole analytical procedure using a color code: green, yellow, and red signifying low, medium, and high adherence to GAC standards, respectively. Color codes given to each segment were specified according to the detailed information described in a report by Wasylka<sup>48</sup>. As shown in Table 5, the environmental impact of employing two different electrodes in the proposed method for ALF assay was the same in all evaluation parameters represented in one GAPI pictogram. The visual inspection of the first eight segments of the pictogram refers to few simple steps required for the sample preparation in every analytical procedure, including the use of green solvents and reagents without macro-extraction or derivatization steps since the red zone represents special storage conditions of urine samples. Meanwhile, the segments from 9 to 11 reflects the use of lower amount of less hazardous solvents and reagents. In addition, the lower energy consumption of our instrumentation with lower waste production per sample were represented on the last pentagram that also exhibits one red zone due to no treatment applied for the generated waste. Therefore, the resulting GAPI pictogram of the DPV method showed (6) green (7) yellow, and (2) red shaded zones that reflects its lower impact on the environment.

Overall, our simple study is shed light on the merits of the applied voltammetric method as a green and safe

practice for ALF quantification that can be used in routine work and quality control purposes in pharmaceutical industries.

### 3. 6. Perspectives

Development of the voltammetric techniques is a growing trend in the electroanalytical field to attain more affordable, greener, easily used, and highly sensitive electrochemical methods. Recently, the chemical modification of electrochemical sensors and the use of disposable and multiplexed electrodes received a great deal of attention to attain stable and rapid responses with high sensitivity, accurate selectivity, and reliability. Thus, incorporation of different modifiers and fabrication of new applicable sensors have been utilized to construct electrodes with high conductivity, great catalytic activity, lower toxicity, and effortless synthesis. Combination of the nanotechnology with electrochemical techniques have been applied, such as the application of multi-walled carbon nanotubes and metal nanoparticles for enhancing the electrocatalytic activity of the sensors. As a result, the continuous development of the sensor technology based on the electrochemical technique have been applied to gas sensors, environmental monitoring sensors, biosensors, *etc.*, which can be employed in different aspects such as forensic medicine and evidence science. In addition, further modifications have been widely proposed to be reasonably integrated

with portable voltammetric analyzers for on-site analysis. Moreover, the growing interest in green analytical chemistry also requires a fresh perspective for the appropriate modification and selection of the electrochemical sensors. Thus, development and exploration of electrochemical sensors with specific selectivity, good conductivity, and economic feasibility for an eco- and user-friendly voltammetric assay is an urgent task.

## 4. Conclusion

In the proposed study, a differential pulse voltammetric method was developed for rapid determination of ALF at two different electrodes with an evaluation of their green-profile. Carbon paste electrode modified with silica gel and pencil graphite electrode proved to be high efficient and sensitive; nevertheless, they are simpler and more economic than those employed in the previously reported methods. The electrochemical behavior of ALF was studied in B-R buffer solution and exhibited well-defined and irreversible anodic peaks with an optimal current density at pH 6. The electrochemical activity of ALF towards PGE was superior to that at Si-gel/CPE which demonstrated as a two fold increase in the sensitivity with no need for its surface modification. The analytical procedures were fully validated and successfully applied for ALF assay in tablets formulation and human urine samples with satisfactory recoveries. This is the first report to apply a simple disposable PGE for fast green analysis and perform a direct voltammetric assay of ALF in urine sample which required no hazardous chemicals, extraction or tedious separation steps.

## 5. References

- BP, Her Majesty's Stationery Office, London, **2021**, pp. 96–98.
- S. C. Sweetman, Book Martindale : the complete drug reference The Pharmaceutical Press, London; Chicago, **2014**.
- N. A. Mohamed, S. Ahmed and S. A. El Zohry, *J. Fluoresc.* **2013**, 23, 1301–1311. <http://dx.doi.org/10.1007/s10895-013-1264-0> DOI:10.1007/s10895-013-1264-0
- S. A. Al-Tamimi, F. A. Aly and A. M. Almutairi, *J. Anal. Chem.* **2013**, 68, 313–320. DOI:10.1134/S1061934813040102
- M. A. Tantawy, S. A. Weshahy, M. Wadie and M. R. Rezk, *Curr. Pharm. Anal.* **2020**, 16, 1–11. DOI:10.2174/1573412916999200730005740
- M. A. Omar, A.-M. I. Mohamed, S. M. Derayea, M. A. Ham-mad and A. A. Mohamed, *Spectrochim. Acta Part A: Mol. Bi-omol. Spectrosc.* **2018**, 195, 215–222. DOI:10.1016/j.saa.2018.01.077
- H. S. Elama, S. M. Shalan, Y. El-Shabrawy, M. I. Eid and A. M. Zeid, *Spectrochim. Acta Part A: Mol. Biomol. Spectrosc.* **2022**, 266, 120420 DOI:10.1016/j.saa.2021.120420
- A. S. Fayed, M. A. Shehata, N. Y. Hassan and S. A. Weshahy, *Pharmazie* **2007**, 62, 830–835. DOI:10.1691/ph.2007.11.7082.
- P. D. Satpute, S. B. Jadhav, M. P. Rathod and P. S. Naykodi, *Pharm. J. Reson.* **2018**, 1, 21–25.
- E. M. Moustapha, R. M. El Gamal and M. Kamal, *J. Anal. Chem.* **2021**, 76, 1327–1335. DOI:10.1134/S1061934821110095
- YAO Hong-wei, Y. Jin, J. Li, Y.-f. Zhang, X.-n. Ding and S.-y. Xu, *Chin. J. Pharm. Anal.* **2002**, 22, 127–128.
- A. K. Shakya, T. A. Arafat, A. Abuawaad, H. Al-Hroub and M. Melhim, *Jordan J. Pharm. Sci.* **2010**, 3, 25–36.
- M. Wadie, E. M. Abdel-Moety, M. R. Rezk and M. A. Tantawy, *Microchem. J.* **2021**, 165, 106095. DOI:10.1016/j.microc.2021.106095
- M. N. Brinda, V. K. Reddy and E. S. Goud, *Int. J. Pharm. Biol. Sci.* **2014**, 4, 54–60.
- M. A. Tantawy, S. A. Weshahy, M. Wadie and M. R. Rezk, *Microchem. J.* **2020**, 157, 104905. DOI:10.1016/j.microc.2020.104905
- M. E. B. Mohamed, E. Y. Frag and Y. M. Gamal Eldin, *J. Iran. Chem. Soc.* **2020**, 17, 2257–2265. DOI:10.1007/s13738-020-01922-1
- S. Ashour and M. Khateeb, *Can. Chem. Trans.* **2013**, 1, 292–304.
- C. E. Xin and Z. Y. Huai, *Chin. J. Pharm.* **2001**, 32, 362–364.
- H. Rashedi, P. Norouzi and M. R. Ganjali, *Int. J. Electrochem. Sci.* **2013**, 8, 2479–2490.
- M. R. Baezzat, F. Banavand and F. Fasihi, *J. Mol. Liq.* **2017**, 233, 391–397. DOI:10.1016/j.molliq.2017.02.119
- Z. Pourghobadi and R. Pourghobadi, *J. Electrochem. Soc.* **2019**, 166, B76–B83. DOI:10.1149/2.0651902jes
- B. Uslu, *Electroanalysis* **2002**, 14, 866–870. DOI:10.1002/1521-4109(200206)14:12<866::AID-ELAN866>3.0.CO;2-Y
- J. Wang, Book Analytical Electrochemistry, Wiley-VCH, New York, **2006**. DOI:10.1002/0471790303
- V. K. Gupta, R. Jain, K. Radhapyari, N. Jadon and S. Agarwal, *Anal. Biochem.* **2011**, 408, 179–196. DOI:10.1016/j.ab.2010.09.027
- I. Švancara, K. Vytrás, K. Kalcher, A. Walcarius and J. Wang, *Electroanalysis* **2009**, 21, 7–28. DOI:10.1002/elan.200804340
- A. A. Al-rashdi, O. A. Farghaly and A. H. Naggar, *J. Chem. Pharm. Res.* **2018**, 10, 21–43. DOI:10.13140/RG.2.2.15392.23047.
- E. M. Hussien, H. Saleh, M. El Henawee, A. Abou El Khair and N. Ahmed, *Acta Chim. Slov.* **2020**, 67, 757–763. DOI:10.17344/acsi.2019.5686
- J. G. Manjunatha, B. E. K. Swamy and M. Deraman, *Anal. Bioanal. Electrochem.* **2013**, 5, 426–38.
- J. G. Manjunathaa, M. Deraman, N. H. Basri and I. Talib: Ad-vanced Materials Research, Trans Tech Publ, 2014, pp. 447–451. DOI:10.4028/www.scientific.net/AMR.895.447
- C. Raril and J. G. Manjunatha, *Anal. Bioanal. Electrochem.* **2018**, 10, 488–98.
- N. Hareesha and J. G. Manjunatha, *J. Iran. Chem. Soc.* **2020**, 17, 1507–1519. DOI:10.1007/s13738-020-01876-4
- Z. Nasri and E. Shams, *Electrochim. Acta* **2009**, 54, 7416–7421.

- DOI:10.1016/j.electacta.2009.07.089
33. M. Jaafarías, E. Shams and M. K. Amini, *Electrochim. Acta* **2011**, 56, 4390–4395. DOI:10.1016/j.electacta.2010.12.052
  34. H. E. Zaazaa, N. N. Salama, S. M. Azab, S. A. Atty, N. M. El-Kosy and M. Y. Salem, *RSC Adv.* **2015**, 5, 48842–48850. DOI:10.1039/C5RA06292F
  35. H. T. Purushothama, Y. A. Nayaka, M. M. Vinay, P. Manjunatha, R. O. Yathisha and K. V. Basavarajappa, *J. Sci.: Adv. Mater. Devices* **2018**, 3, 161–166. DOI:10.1016/j.jsamd.2018.03.007
  36. I. Y. L. d. Macêdo, M. F. Alecrim, J. R. Oliveira Neto, I. M. S. Torres, D. V. Thomaz and E. d. S. Gil, *Braz. J. Pharm. Sci.* **2020**, 56, e17344. DOI:10.1590/s2175-97902019000317344.
  37. P. T. Pinar, *Acta Chim. Slov.* **2020**, 67, 212–220. DOI:10.17344/acsi.2019.5367
  38. I. G. David, D.-E. Popa and M. Buleandra, *J. Anal. Methods Chem.* **2017**, 2017, 1905968. DOI:10.1155/2017/1905968
  39. USP, The United States Pharmacopeial Convention, Rockville, **2013**, pp. 2366–2369, 4314–4317, 5137–5139, 5318–5321.
  40. <https://www.drugbank.ca/drugs>, (accessed: June 5, 2022)
  41. D. K. Gosser, *Synthesis and Reactivity in Inorganic and Metal-Organic Chemistry* **1994**, 24, 1237–1238. DOI:10.1080/00945719408001398
  42. E. Laviron and L. Roullier, *J. Electroanal. Chem. Interfacial Electrochem.* **1980**, 115, 65–74. DOI:10.1016/S0022-0728(80)80496-7
  43. B. Hatamluyi, F. Lorestani and Z. Es'haghi, *Biosens. Bioelectron.* **2018**, 120, 22–29. DOI:10.1016/j.bios.2018.08.008
  44. International conference on harmonization, Geneva, Switzerland, incorporated in November 2005.
  45. E. Skowron, K. Spilarewicz-Stanek, D. Guziejewski, K. Koszelska, R. Metelka and S. Smarzewska, *Molecules* **2022**, 27, 2037. DOI:10.3390/molecules27072037
  46. L. H. Keith, L. U. Gron and J. L. Young, *Chemical Reviews* **2007**, 107, 2695–2708. DOI:10.1021/cr068359e
  47. A. Gałuszka, Z. M. Migaszewski, P. Konieczka and J. Namieśnik, *TrAC Trends Anal. Chem.* **2012**, 37, 61–72. DOI:10.1016/j.trac.2012.03.013
  48. J. Płotka-Wasyłka, *Talanta* **2018**, 181, 204–209. DOI:10.1016/j.talanta.2018.01.013

## Povzetek

Uporabljena je bila občutljiva in poceni diferencialna pulzna voltametrična tehnika za raziskovanje elektrokemičnega obnašanja alifuzosin hidroklorida na dveh različnih delovnih elektrodah: ogljikova pasta, modificirana s silikagelom, in svinčnikova grafitna elektroda (PGE). Voltametrični pogoji so bili optimizirani s ciklično voltametrijjo, ki je pokazala ireverzibilni anodni vrh v Britton-Robinsonovem pufrskem mediju (pH 6) pri 0,86–0,90 V. Elektrokemični odzivi so bili linearno odvisni od koncentracije alifuzosina ( $R^2 > 0,999$ ) v razponu od 0,6–20 in 0,3–20  $\mu\text{M}$ , ki kaže večjo elektrokatalitsko aktivnost pri PGE z nizko mejo zaznave 0,099  $\mu\text{M}$ . Poleg tega je bila ta študija uspešen poskus določanja zdravila v tabletah in vzorcih urina z dodatkom učinkovine z vrednotenjem zelenega profila z uporabo Nacionalnega indeksa okoljskih metod, analitične ocene Eco-Scale in Indeksa zelenih analitičnih postopkov.



Except when otherwise noted, articles in this journal are published under the terms and conditions of the Creative Commons Attribution 4.0 International License

# Synthesis, Characterization, and Investigation of Mesomorphic Properties of a New 2,5-Bis-(4-alkanoyloxybenzylidene)cyclopentan-1-one

Abdullah Hussein Kshash,<sup>1,\*</sup> Omar Jamal Mahdi Al-Asafi<sup>2</sup>  
and Hanaa Kaen Salih<sup>2</sup>

<sup>1</sup> Department of Chemistry, Education College for Pure Science, University Of Anbar, Anbar, Iraq

<sup>2</sup> Department of Chemistry, College of Science, University of Tikrit, Tikrit, Iraq

\* Corresponding author: E-mail: drabdullahkshash@gmail.com

Received: 01-14-2022

## Abstract

A new set of cyclopentanone chalcone esters 2,5-bis-(4-alkanoyloxybenzylidene)cyclopentan-1-one (**B2–B10**) has been synthesized and monitored by TLC. Structures of these compounds were determined by spectroscopic techniques (FTIR, <sup>1</sup>H NMR, and mass spectrometry). Differential scanning calorimetry (DSC) and polarized optical microscopy were used to evaluate their transition temperatures and mesophase properties (POM) throughout heating and cooling scans. The thermal data indicate that the compounds **B5–B10** have mesomorphic properties with thermal stabilities; the data also reveal that the compounds **B6–B10** are monotropic, whereas **B5** is enantiotropic. **B6**, **B7**, and **B9** only have a nematic phase, but **B8** and **B10** have a smectic phase followed by a nematic phase, and **B5** only has a smectic phase. In addition, the study reveals that the inclusion of an acyl group as a terminal chain had the opposite effect on isotropization temperatures for compounds **B6**, **B8**, and **B10**, resulting in an increase in transition temperatures and a decrease in mesophase stability. The lack of a smectic phase in **B7** and **B9** compounds could be attributed to the narrow phase temperature range, which makes examination difficult, or to the molecules' lack of lateral attraction.

**Keywords:** Cyclopentanone chalcone, nematic, smectic, enantiotropic, monotropic.

## 1. Introduction

Chalcone is the common name for flavonoids, the name chalcone comes from the Greek word “chalcos”, which means “bronze”, because most natural chalcones have a bronze color.<sup>1</sup> Chalcones have two aromatic rings linked by an unsaturated  $\alpha,\beta$ -ketone. Chemically, they are open-chain flavonoids with two aromatic rings bonded by a three-carbon atom (unsaturated carbonyl) system (Figure 1). In other words, “chalcones are structural derivatives of 1,3-diphenylprop-2-en-1-one”.<sup>2–4</sup>

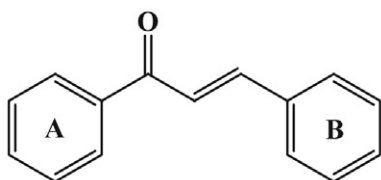


Figure 1: General structure of a chalcone

The Claisen–Schmidt condensation reaction is often used to prepare chalcones, which involves the condensation of aldehydes and ketones in the presence of a base or acid catalyst, followed by a dehydration process.<sup>5</sup> Chalcones have recently received a lot of attention, not only from the synthetic and biosynthetic standpoint, but also because of their biological activities,<sup>6</sup> which include anti-cancer,<sup>7–9</sup> GSK-3 inhibition and antimicrobial activity,<sup>10</sup> anti-HIV,<sup>11</sup> and antimalarial properties.<sup>12</sup> The target of this study is to synthesize cyclopentanone chalcone esters and investigate their liquid crystal properties and the influence of chain length on these properties.

## 2. Experimental Section

### 2. 1. Materials

All chemicals were purchased from Sigma–Aldrich and were used without further purification. Melting points



were determined in an open capillary tube and are uncorrected. A Tensor 27 Bruker, Germany spectrometer was used to record infrared spectra as ATR (range 4000–600  $\text{cm}^{-1}$ ). The  $^1\text{H}$  NMR spectra were recorded on a Bruker Ultraschield 400 MHz NMR spectrometer, Germany, using  $\text{DMSO}-d_6$  as the solvent. The chemical shifts are reported as  $\delta$  values (in ppm). Mass spectrum analyses were performed by the Agilent Technology MS 5973 device. POM equipped with a hot stage and Mettler Toledo DSC 823 (DSC) at a heating rate of  $20\text{ }^\circ\text{C min}^{-1}$  was used for the investigation of phase transition temperatures.

## 2. 2. Synthesis of 2,5-Bis((*E*)-4-hydroxybenzylidene)cyclopentan-1-one (A)

In a 250 mL round-bottom flask containing 100 mL of ethanol, cyclopentanone (40 mmol) and 4-hydroxybenzaldehyde (80 mmol) were introduced and thoroughly mixed. Then, 40% sodium hydroxide solution (10 mL) was added slowly, and the reaction mixture was stirred overnight at room temperature. Thereafter, the reaction mixture was poured into a beaker containing crushed ice to quench the reaction and then neutralized with 10% HCl. The precipitate was filtered and recrystallized from absolute ethanol.

Green solid, yield 76%; mp  $> 280\text{ }^\circ\text{C}$  (lit.  $> 300\text{ }^\circ\text{C}$ ),  $R_f = 0.8$  (acetone:hexane 5:5). IR (ATR)  $\nu$  3289 (O-H phenol), 3046 (C-H aromatic), 2973 ( $\nu$  C-H<sub>al</sub>), 1668 ( $\nu$  C=O), 1561, 1509 (aromatic ring)  $\text{cm}^{-1}$ .  $^1\text{H}$  NMR (400 MHz)  $\delta$  10.06 (lit. 10.06) (s, 2H, H<sub>1</sub>, H<sub>1'</sub>), 7.53 (d, 4H, H<sub>2,2'</sub>, H<sub>2',2'</sub>), 7.34 (lit. 7.34) (s, 2H, H<sub>3</sub>, H<sub>3'</sub>), 6.83–6.90 (d, 4H, H<sub>4,4'</sub>, H<sub>4',4'</sub>), 3.01 (lit. 3.01) (t, 4H, H<sub>5,5'</sub>, H<sub>5',5'</sub>).

## 2. 2. Synthesis of (1*E*,1'*E*)-(2-Oxocyclopentane-1,3-diylidene)bis(methaneylylidene)bis(4,1-phenylene) dialkanoate B2–B10

To a 50 mL round-bottomed flask immersed in an ice bath and containing 20 mL of pyridine and compound A (1.7 mmol), an appropriate acid chloride (3.4 mmol) was added. The mixture was stirred at room temperature overnight. Thereafter, the mixture was poured into a beaker containing crushed ice, acidified with 10% HCl, and the solid product was filtered, washed with water, and recrystallized from absolute ethanol. TLC was performed using acetone-hexane (3:7) as the eluent solution.

## 2. 3. Characterization of Products B2–B10

### ((1*E*,1'*E*)-(2-Oxocyclopentane-1,3-diylidene)bis(methaneylylidene))bis(4,1-phenylene) diacetate (B2)

Yellow solid, yield 77%; mp  $200\text{--}202\text{ }^\circ\text{C}$  (decomp.),  $R_f = 0.62$ , IR (ATR)  $\nu$  3110 (C-H aromatic), 2981 (C-H<sub>al</sub>), 1763 ( $\nu$  C=O<sub>ester</sub>), 1671 ( $\nu$  C=O<sub>ketone</sub>), 1594, 1505 (aro-

matic ring)  $\text{cm}^{-1}$ .  $^1\text{H}$  NMR (400 MHz)  $\delta$  6.78–7.95 (d, 8H, Ar-H), 7.65 (s, 2H, CH=CH), 3.00 (t, 4H, saturated five membered ring), 2.40 (s, 6H, CH<sub>3</sub> groups).

### ((1*E*,1'*E*)-(2-Oxocyclopentane-1,3-diylidene)bis(methaneylylidene))bis(4,1-phenylene) dipropionate (B3)

Yellow solid, yield 48%; mp  $280\text{--}282\text{ }^\circ\text{C}$ ,  $R_f = 0.81$ , IR (ATR)  $\nu$  3114 (C-H aromatic), 2975 (C-H<sub>al</sub>), 1759 ( $\nu$  C=O<sub>ester</sub>), 1675 ( $\nu$  C=O<sub>ketone</sub>), 1577, 1504 (aromatic ring), 752 ( $\gamma$  CH<sub>2</sub>)  $\text{cm}^{-1}$ .  $^1\text{H}$  NMR (400 MHz)  $\delta$  7.67–6.76 (d, 8H, Ar-H), 7.47 (s, 2H, CH=CH), 2.95–3.00 (t, 4H, saturated five membered ring), 1.25–2.52 (m, 10H, alkyl groups).

### ((1*E*,1'*E*)-(2-Oxocyclopentane-1,3-diylidene)bis(methaneylylidene))bis(4,1-phenylene) dibutyrate (B4)

Yellow solid, yield 71%; mp  $164\text{ }^\circ\text{C}$  (decomp.),  $R_f = 0.76$ , IR (ATR)  $\nu$  3123 (C-H aromatic), 2978 (C-H<sub>al</sub>), 1754 ( $\nu$  C=O<sub>ester</sub>), 1672 ( $\nu$  C=O<sub>ketone</sub>), 1564, 1505 (aromatic ring), 743 ( $\gamma$  CH<sub>2</sub>)  $\text{cm}^{-1}$ .  $^1\text{H}$  NMR (400 MHz)  $\delta$  7.73–6.85 (d, 8H, Ar-H), 7.40 (s, 2H, CH=CH), 2.55–3.09 (t, 4H, saturated five membered ring), 0.89–2.50 (m, 14H, alkyl groups). MS  $m/z$  434.3.

### ((1*E*,1'*E*)-(2-Oxocyclopentane-1,3-diylidene)bis(methaneylylidene))bis(4,1-phenylene) dipentanoate (B5)

Deep yellow solid, yield 45%; mp  $197\text{--}199\text{ }^\circ\text{C}$ ,  $R_f = 0.72$ , IR (ATR)  $\nu$  3119 (C-H aromatic), 2963 (C-H<sub>al</sub>), 1752 ( $\nu$  C=O<sub>ester</sub>), 1687 ( $\nu$  C=O<sub>ketone</sub>), 1594, 1504 (aromatic ring), 754 ( $\gamma$  CH<sub>2</sub>)  $\text{cm}^{-1}$ .  $^1\text{H}$  NMR (400 MHz)  $\delta$  7.25–7.74 (d, 8H, Ar-H), 7.46 (s, 2H, CH=CH), 3.10 (t, 4H, saturated five membered ring), 0.95–2.50 (m, 18H, alkyl groups). MS  $m/z$  460.7.

### ((1*E*,1'*E*)-(2-Oxocyclopentane-1,3-diylidene)bis(methaneylylidene))bis(4,1-phenylene) dihexanoate (B6)

Yellow solid, yield 53%; mp  $169\text{--}171\text{ }^\circ\text{C}$ ,  $R_f = 0.74$ , IR (ATR)  $\nu$  3057 (C-H aromatic), 2957 (C-H<sub>al</sub>), 1753 ( $\nu$  C=O<sub>ester</sub>), 1688 ( $\nu$  C=O<sub>ketone</sub>), 1593, 1504 (aromatic ring), 736 ( $\gamma$  CH<sub>2</sub>)  $\text{cm}^{-1}$ .  $^1\text{H}$  NMR (400 MHz)  $\delta$  6.32–7.00 (d, 8H, Ar-H), 6.99 (s, 2H, CH=CH), 1.94–2.05 (t, 4H, saturated five membered ring), 0.30–1.11 (m, 22H, alkyl groups). MS  $m/z$  490.4.

### ((1*E*,1'*E*)-(2-Oxocyclopentane-1,3-diylidene)bis(methaneylylidene))bis(4,1-phenylene) diheptanoate (B7)

Brown solid, yield 28%; mp  $170\text{--}172\text{ }^\circ\text{C}$ ,  $R_f = 0.67$ , IR (ATR)  $\nu$  3116 (C-H aromatic), 2987 (C-H<sub>al</sub>), 1759 ( $\nu$  C=O<sub>ester</sub>), 1669 ( $\nu$  C=O<sub>ketone</sub>), 1597, 1509 (aromatic ring), 769 ( $\gamma$  CH<sub>2</sub>)  $\text{cm}^{-1}$ .  $^1\text{H}$  NMR (400 MHz)  $\delta$  6.88–7.98 (d, 8H, Ar-H), 7.51 (s, 2H, CH=CH), 2.46–3.43 (t, 4H, saturated five membered ring), 0.86–1.66 (m, 26H, alkyl groups).

### ((1*E*,1'*E*)-(2-Oxocyclopentane-1,3-diylidene)bis(methaneylylidene))bis(4,1-phenylene) dioctanoate (B8)

Brown solid, yield 46%; mp  $178\text{--}180\text{ }^\circ\text{C}$ ,  $R_f = 0.71$ , IR (ATR)  $\nu$  3080 (C-H aromatic), 2956 (C-H<sub>al</sub>), 1748 ( $\nu$

C=O<sub>ester</sub>), 1669 (ν C=O<sub>ketone</sub>), 1597, 1509 (aromatic ring), 748 (γ CH<sub>2</sub>) cm<sup>-1</sup>. <sup>1</sup>H NMR (400 MHz) δ 6.90–7.98 (d, 8H, Ar-H), 7.46 (s, 2H, CH=CH), 2.78–3.30 (t, 4H, saturated five membered ring), 0.86–2.38 (m, 30H, alkyl groups).

**((1E,1'E)-(2-Oxocyclopentane-1,3-diylidene)bis(methaneylylidene))bis(4,1-phenylene) dinonanoate (B9)**

Brown solid, yield 84%; mp 162–164 °C, *R*<sub>f</sub> = 0.71, IR (ATR) ν 3057 (C-H aromatic), 2957 (C-H<sub>al</sub>), 1752 (ν C=O<sub>ester</sub>), 1690 (ν C=O<sub>ketone</sub>), 1594, 1503 (aromatic ring), 747 (γ CH<sub>2</sub>) cm<sup>-1</sup>. <sup>1</sup>H NMR (400 MHz) δ 6.88–7.75 (d, 8H, Ar-H), 7.40 (s, 2H, CH=CH), 2.50–3.35 (t, 4H, saturated five membered ring), 0.86–1.65 (m, 34H, alkyl groups).

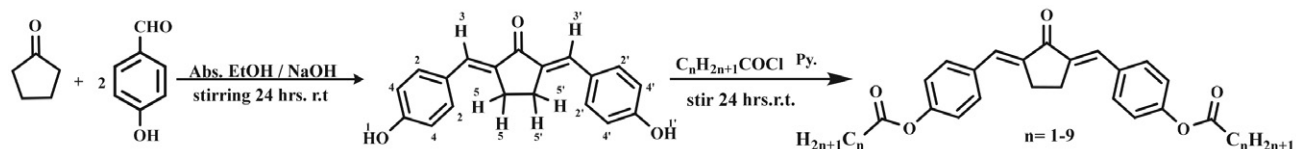
**((1E,1'E)-(2-Oxocyclopentane-1,3-diylidene)bis(methaneylylidene))bis(4,1-phenylene) bis(decanoate) (B10)**

Brown solid, yield 81%; mp 175–177 °C, *R*<sub>f</sub> = 0.61, IR (ATR) ν 3101 (C-H aromatic), 2958 (C-H<sub>al</sub>), 1752 (ν C=O<sub>ester</sub>), 1690 (ν C=O<sub>ketone</sub>), 1596, 1503 (aromatic ring), 741 (γ CH<sub>2</sub>) cm<sup>-1</sup>. <sup>1</sup>H NMR (400 MHz) δ 6.89–7.73 (d, 8H, Ar-H), 7.32 (s, 2H, CH=CH), 2.52–3.07 (t, 4H, saturated five membered ring), 0.87–1.64 (m, 38H, alkyl groups). MS *m/z* 600.5.

### 3. Result and Discussion

#### 3.1. Chemistry

Target ester compounds B2–B10 were synthesized using the method presented in scheme 1.



**Scheme 1.** Synthetic route for synthesis of compounds B2–B10

The presence of α-hydrogen atoms on both sides of the carbonyl group in the cyclopentanone molecule was used in the Claisen–Schmidt condensation reaction of cyclopentanone with 4-hydroxybenzaldehyde to produce two α,β-unsaturated groups of the chalcone compound 2,5-bis((E)-4-hydroxybenzylidene)cyclopentan-1-one (**A**). While esters **B2–B10** were synthesized by reacting phenolic hydroxyl groups in chalcone **A** as a nucleophile with acid chlorides in the presence of pyridine as a solvent. This reaction was carried out in two steps. The nucleophile (OH) first attacks the carbonyl carbon atom of an acyl chloride, forming a tetrahedral intermediate that can eliminate the chloride as a leaving group.

#### 3.2. Characterization

TLC was used to monitor the synthesis of chalcone **A**, with changes in product color and melting point serving

as a preliminary evidence.<sup>13</sup> Thereafter, the FTIR spectrum (Figure 2) for compound **A** revealed a broad absorption band at 3289 cm<sup>-1</sup> attributed to the O–H group, a medium absorption at 3046 cm<sup>-1</sup> attributed to the aromatic C–H, a strong absorption band at 2973 cm<sup>-1</sup> attributed to the C–H<sub>asy</sub>(aliphatic) and the absorption at 2935 cm<sup>-1</sup> that can be assigned to the C–H<sub>sy</sub>(aliphatic), while the C=O group stretching vibration for ketone was observed at 1668 cm<sup>-1</sup>.

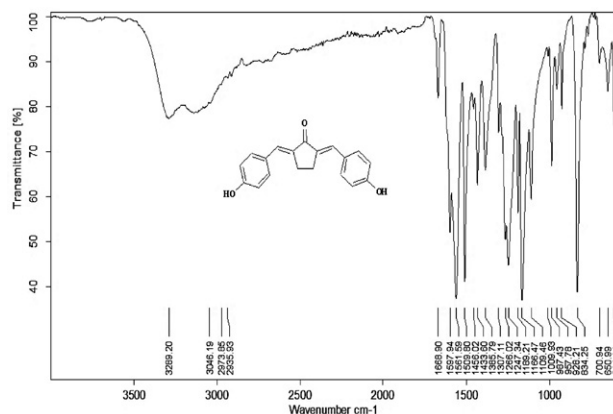


**Figure 2:** FT IR spectrum for chalcone **A**.

The <sup>1</sup>H NMR (Figure 3) spectrum of chalcone **A** reveals three distinct regions of chemical shifts. The signal of the hydroxyl proton appears as a singlet at δ 10.09 ppm, aromatic protons (8H) signals appear as two doublets in

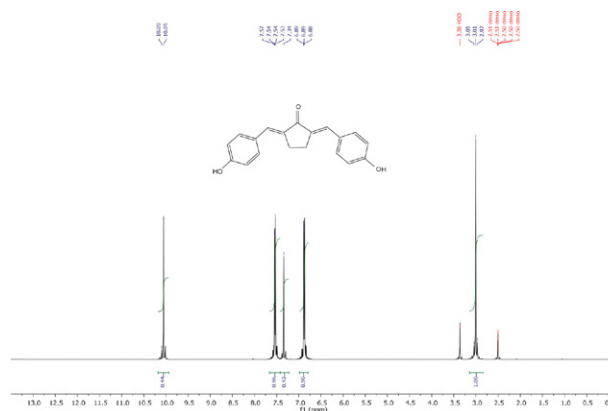


**Figure 3:** <sup>1</sup>H NMR spectrum for chalcone **A**.

the regions of δ 7.57–7.53 and 6.89–6.88 ppm, β-protons signal was observed as a singlet at δ 7.34 ppm, while a triplet signal at δ 3.01 ppm was ascribed to the two methylene groups in cyclopentane.

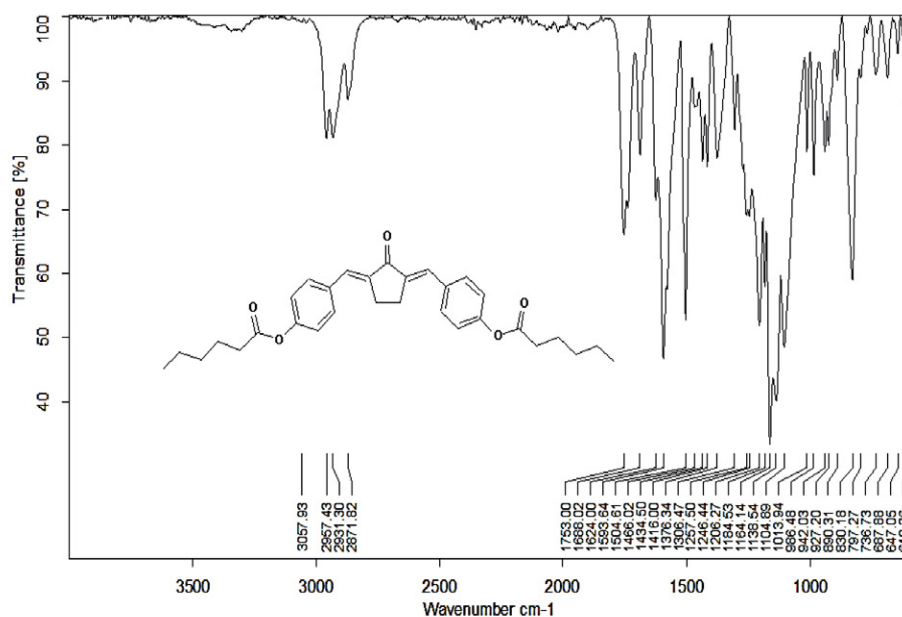


Figure 4: FT IR spectrum for chalcone **B6**.

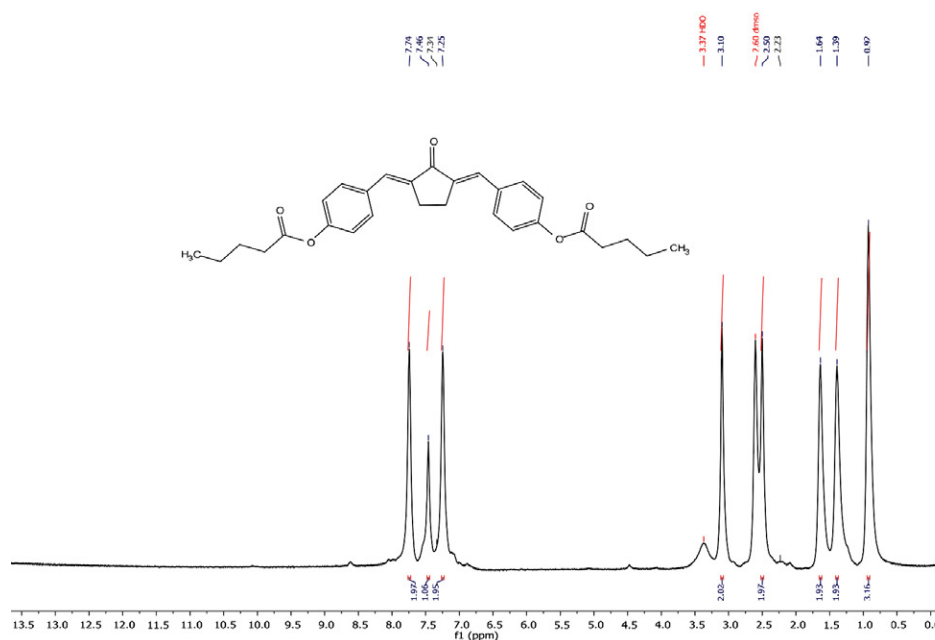


Figure 5:  $^1\text{H}$  NMR spectrum for compound **B5**.

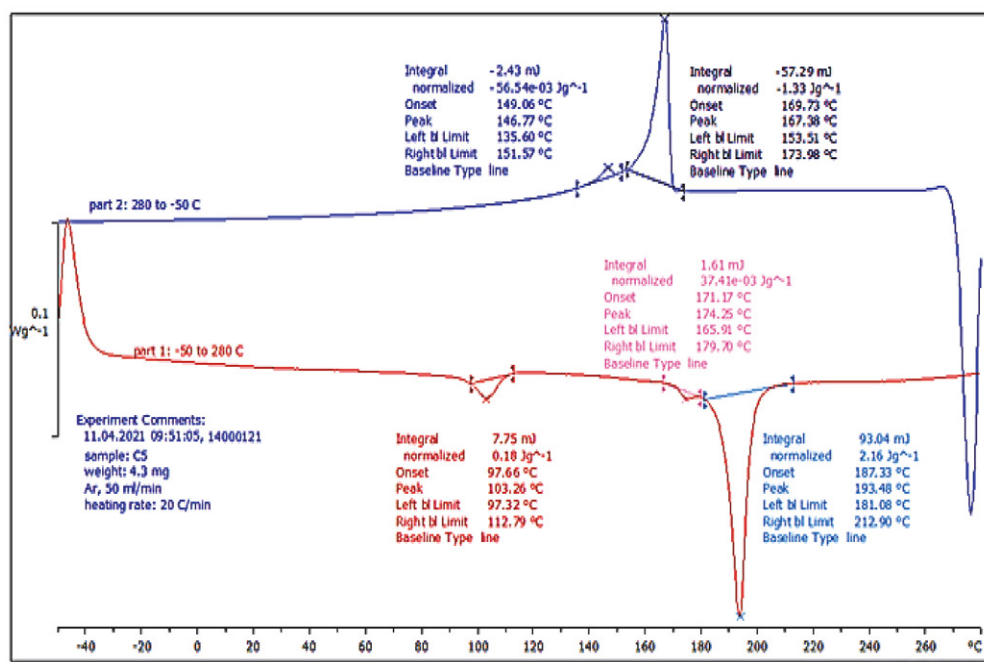
The FTIR spectra for compounds **B2–B10** (see Figure 4 for a representative case of **B6**) show the disappearance of the OH band for chalcone, and the appearance of an absorption band within the range of  $3123\text{--}3110\text{ cm}^{-1}$  that is attributable to the aromatic C–H, a strong absorption band within the range of  $1762\text{--}1748\text{ cm}^{-1}$  that is attributable to the C=O group of ester, and absorption band within the range of  $1690\text{--}1669\text{ cm}^{-1}$  assigned to the C=O group for ketone.

According to  $^1\text{H}$  NMR spectra for compounds **B2–B10**, the OH signal at 10.09 ppm attributable to compound

**A** has disappeared, aromatic proton signals were observed within the range  $\delta\ 6.32\text{--}7.79\text{ ppm}$ , while proton signals for alkyl groups were observed within the range  $\delta\ 0.25\text{--}3.23\text{ ppm}$ . See Figure 5 for a representative case of a  $^1\text{H}$  NMR spectrum for compound **B5**.

### 3. 3. Mesomorphic Properties

The DSC and POM were utilized to investigate the characteristics of the phases of the 2,5-bis-(4-alkanoyloxybenzylidene)cyclopentan-1-one compounds **B2–B10**

Figure 6: DSC of compound **B5** during heating/cooling cyclesTable 1. Phase transitions and transition enthalpy for chalcone esters **B5–B10** under heating and cooling cycle

Comp.	Transition Temperatures, °C ( $\Delta H$ , kJ mol <sup>-1</sup> )	
	Heating	Cooling
B5	Cr 103.26 (0.0829) S <sub>A</sub> 174.25 (17.22) S <sub>C</sub> 193.48 (0.994) I Cr 70.99/0.0002 S <sub>A</sub> 19.23/ 0.038 S <sub>C</sub> -/ 0.002 I	I 167.38 (0.61) S <sub>C</sub> 146.77 (26.0) Cr
B6	Cr 68.62 (3.058) N 168.70 (23.01) I Cr 100.08/0.008 N -/ 0.052 I	I 100.89 (10.26) Cr
B7	Cr 103.91 (3.39) N 164.10 (17.59) I Cr 60.19/ 0.009 N - / 0.040 I	I 142.23 (9.55) Cr
B8	Cr <sub>1</sub> 87.88 (6.30) Cr <sub>2</sub> 106.95 (1.08) S <sub>A</sub> 134.28 (0.71) N 173.42 (16.94) I Cr <sub>1</sub> 19.07/ 0.017 Cr <sub>2</sub> 27.33/ 0.002 S <sub>A</sub> 39.14 / 0.0004 N - / 0.037 I	I 147.54 (13.51) Cr
B9	Cr <sub>1</sub> 122.92 (1.72) Cr <sub>2</sub> 132.27 (0.36) N 166.99 (23.15) I Cr <sub>1</sub> 9.35/0.0043 Cr <sub>2</sub> 34.72/0.0009 N -/0.0526 I	I 150.77 (17.63) Cr
B10	Cr <sub>1</sub> 21.01/0.0096 Cr <sub>2</sub> 51.25/0.0019 S <sub>A</sub> 32.78/0.018 S <sub>C</sub> 8.84/0.0273 N -/0.0055 I	I 145.58 (10.51) Cr

upon heating and cooling, by tracing the thermal transitions in the DSC and confirming mesophases type by observing the texture using POM. Figure 6 shows the DSC thermogram for the compound **B5** after a heating and cooling scan.

The transition temperatures, enthalpies, and entropies of the chalcone ester compounds **B5–B10** from DSC are presented in Table 1.

The phase behavior investigation of chalcone ester compounds revealed that the compounds **B5–B10** exhibit liquid crystal properties with thermal stabilities. Compounds **B6–B10** were monotropic, while **B5** was enantiotropic. Compounds **B6**, **B7**, and **B9** have only a nematic phase, while **B8** and **B10** have a smectic phase followed by a

nematic phase, and **B5** has only a smectic phase (Figure 7).

According to thermal degradation studies, compounds having odd methylene groups in the terminal alkoxy chain are more stable than those with even number of methylene groups.<sup>14</sup> While the study of the data in Table 1 revealed that the introduction of an acyl group as a terminal chain had the opposite effect on isotropization temperatures for compounds **B6**, **B8**, and **B10**, increasing transition temperatures and decreasing their mesophase stability (Figure 6).

The lack of a smectic phase in compounds **B7** and **B9** could be due to the phase's narrow temperature range, which causes investigation difficulties, or to the molecules' lack of lateral attraction.

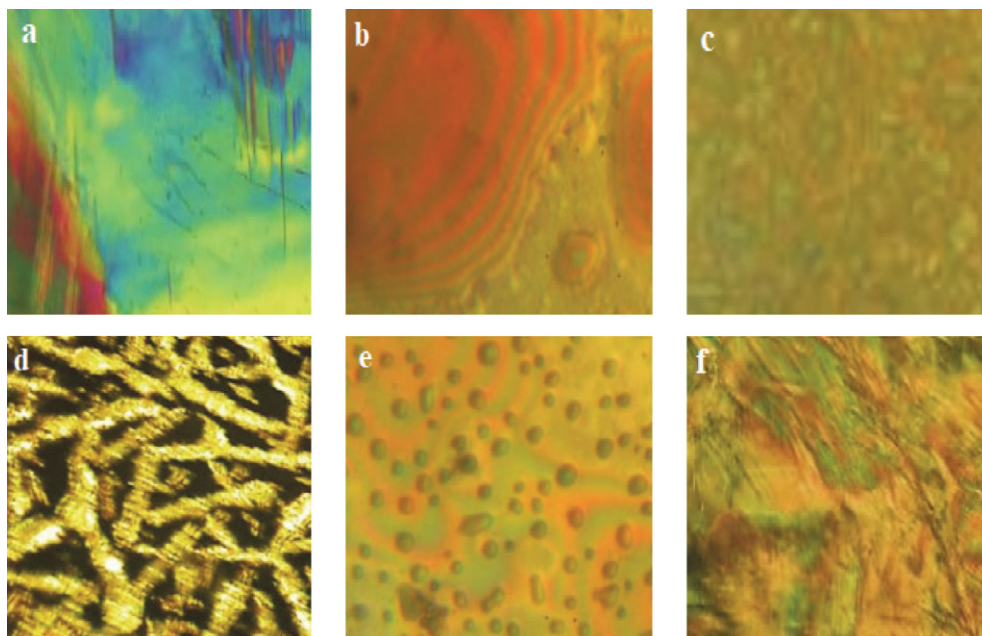


Figure 7: Polarized optical micrographs for: (a) compound B5 (SC at 174.25 °C); (b) compound B6 (N, at 68.62 °C); (c) compound B7 (N, mosaic at 103.91 °C), (d) compound B8 (SA, at 106.95 °C); (e) compound B9 (N, Schlieren, at 132.27 °C); (f) compound B10 (N, mosaic at 164.30 °C).

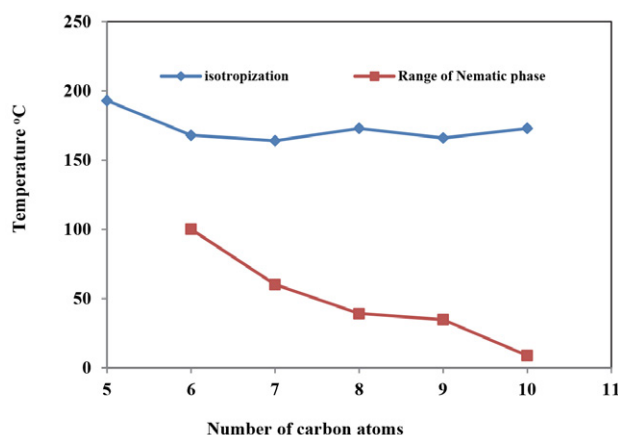


Figure 8: Relationship of isotropization and nematic phase range with the number of carbon atoms

## 4. Conclusion

The chalcone esters of cyclopentanone were successfully synthesized, and FTIR and  $^1\text{H}$  NMR were used to characterize them. According to thermal data, compounds with 2–4 carbon atoms are non-mesogenic materials, while those with 5–10 carbon atoms are mesogenic materials. For compounds with 6, 8, and 10 carbon atoms, adding an acyl group as a terminal chain had the opposite impact on isotropization temperatures, causing an increase in transition temperatures and a decrease in mesophase stability.

## Acknowledgements

The authors are grateful to Ms. Ala'a Adnan Rashad of Al-Nahrain University for her assistance with the study's thermal analysis..

## 5. References

1. N. K. Sahu, S. S. Balbhadra, J. Choudhary, D. V. Kohli, *Curr. Med. Chem.* **2012**, *19*, 209–225. DOI:10.2174/092986712803414132
2. G. L. Santosh, U. N. Vignesh, *Res. Chem. Intermed.* **2017**, *43*, 6043–6077. DOI:10.1007/s11164-017-2977-5
3. C. Mustafa, F. Esra, *Synth. Commun.* **2009**, *39*, 1046–1054. DOI:10.1007/s10701-009-9315-8 DOI:10.1080/00397910802474974
4. S. N. Bukhari, M. Jasamai, I. Jantan, *Mini Rev Med. Chem.* **2012**, *12*, 1394–403. DOI:10.2174/13895575112091394
5. L. Claisen, A. Claparede, *Ber. Dtsch. Chem. Ges.* **1881**, *14*, 2460–2468. DOI:10.1002/cber.188101402192
6. R. Marinov, N. Markova, S. Krumova, K. Yotovska, M. M. Zaharieva, P. Genova-Kalou, *Pharmacia*. **2020**, *67*, 325–337. DOI:10.3897/pharmacia.67.e53842
7. X. Ma, D. Wang, G. Wei, Q. Zhou, X. Gan, *Synth. Commun.* **2021**, *51*, 1363–1372. DOI:10.1080/00397911.2021.1881124
8. F. Gao, G. Huang, J. Xiao, *Med. Res. Rev.* **2020**, *40*, 2049–2084. DOI:10.1002/med.21698
9. K. L. Wang, Y. C. Yu, S. M. Hsia, *Cancers* **2021**, *13*, 115. DOI:10.3390/cancers13010115
10. T. Pritam, P. U. Sunil, Z. S. William, S. Vikas, G. Prajwal, L. S. Eung, S. Ram, S. Mukut, *Bioorg. Chem.* **2021**, *108*, 104681. DOI:10.1016/j.bioorg.2021.104681



11. N. Turkovic, B. Ivkovic, J. Kotur-Stevuljevic, M. Tasic, B. Marković, Z. Vujic, *Curr. Pharm. Des.* **2020**, *26*, 802–814. DOI:10.2174/1381612826666200203125557
12. M. Xu, P. Wu, F. Shen, J. Ji, K. P. Rakesh, *Bioorg. Chem.* **2019**, *91*, 103133. DOI:10.1016/j.bioorg.2019.103133
13. F. Zhao, H.-H. Dong, Y.-H. Wang, T.-Y. Wang, Z.-H. Yan, F. Yan, D.-Z. Zhang, Y.-Y. Cao, Y.-S. Jin, *Med. Chem. Commun.* **2017**, *8*, 1093–1102. DOI:10.1039/C6MD00649C
14. G. Lisa, E.-R. Cioancă, N. Tudorachi, I. Cârlescu, D. Scutaru, *Thermochim. Acta* **2011**, *524*, 179–185. DOI:10.1016/j.tca.2011.07.013

## Povzetek

Sintetizirali smo novo serijo ciklopentanonskih halkonskih estrov 2,5-bis-(4-alkanoiloksibenziliden)ciklopentan-1-onov (**B2–B10**); reakcije smo nadzorovali s TLC. Strukture teh spojin smo določili s spektroskopskimi tehnikami (FTIR, <sup>1</sup>H NMR in masna spektrometrija). Diferenčna dinamična kalorimetrija (DSC) in polarizirana optična mikroskopija sta bili uporabljeni za določanje temperatur prehoda in mezofaznih lastnosti (POM) v celotnem območju segrevanja in ohlajanja vzorcev. Podatki termičnih analiz kažejo, da imajo spojine **B5–B10** mezomorfne lastnosti in da so termično stabilne; podatki tudi kažejo, da so spojine **B6–B10** monotropne, medtem ko je spojina **B5** enantiotropna. Spojine **B6**, **B7** in **B9** imajo samo nematsko fazo; pri spojinah **B8** in **B10** pa smektični fazi sledi nematska faza; spojina **B5** ima samo smektično fazo. Študije so tudi razkrile, da ima vključitev acilne skupine na terminalno mesto verige nasprotni učinek na izotropno temperaturo za spojine **B6**, **B8** in **B10**, kar povzroči povečanje temperatur prehoda in zmanjšanje mezofazne stabilnosti. Dejstvo, da spojin **B7** in **B9** nimata smektične faze, lahko pripišemo ozkim temperaturnim intervalom faznih prehodov, kar povzroča eksperimentalne težave, ali pa pomanjkanju lateralnih privlačnih sil med molekulami v teh dveh primerih.



Except when otherwise noted, articles in this journal are published under the terms and conditions of the Creative Commons Attribution 4.0 International License

# Synthesis, Molecular Docking Studies and ADME Prediction of Some New Albendazole Derivatives as $\alpha$ -Glucosidase Inhibitors

Sevil Şenkardeş,<sup>1,\*</sup> Necla Kulabaş<sup>1</sup> and Ş. Güniz Küçükgülzel<sup>2</sup>

<sup>1</sup> Marmara University, Faculty of Pharmacy, Department of Pharmaceutical Chemistry, Maltepe, Başibüyük, 34854, Istanbul, Turkey

<sup>2</sup> Fenerbahçe University, Faculty of Pharmacy, Department of Pharmaceutical Chemistry, Ataşehir, 34758, Istanbul, Turkey

\* Corresponding author: E-mail: sevil.aydin@marmara.edu.tr  
Tel. +90-216-777 52 00

\* This study was partly presented at the International Congress on Biological and Health Sciences on 26–28 February 2021 (Online), Turkey

Received: 01-28-2022

## Abstract

A series of novel 2-(substituted arylidene)-*N*-(5-(propylthio)-2,3-dihydro-1*H*-benzo[d]imidazol-2-yl)hydrazine-1-carboxamide derivatives **3a–i** were synthesized *via* condensation of *N*-(5-(propylthio)-1*H*-benzo[d]imidazol-2-yl) hydrazinecarboxamide (**2**), with the corresponding ketone or aldehydes. The chemical structures of the compounds prepared were confirmed by analytical and spectral data. The compounds were screened for their  $\alpha$ -glucosidase inhibitory activity and all of them showed better inhibition than acarbose, except **3h**. In particular, compound **3a** proved to be the most active compound among all synthetic derivatives having  $IC_{50}$  value  $12.88 \pm 0.98 \mu M$ . Also, molecular docking studies were carried out for the compounds to figure out the binding interactions. Compound **3a** has exhibited the highest binding energy ( $\Delta G = -9.4$  kcal/mol) and the most hydrogen bond interactions with active sites. Eventually, *in silico* studies were in good agreement with *in vitro* studies.

**Keywords:** Benzimidazole; antidiabetic; albendazole;  $\alpha$ -glucosidase; semicarbazone; docking study

## 1. Introduction

Diabetes Mellitus (DM), known simply as diabetes, is a major health problem as a metabolic disease and is characterized by a failure of insulin production. It can be classified into two broad categories; type 1 and type 2 diabetes. Type 2 diabetes ranks as the most common type of diabetes worldwide among all reported cases.<sup>1</sup> This form of diabetes results from a combination of insulin resistance and insulin secretion defects.<sup>2</sup> Insulin plays an important role in the regulation of blood glucose levels and energy metabolism.<sup>3</sup> If diet and exercise fail to adequately control blood glucose levels, it is recommended to start oral drug therapy such as  $\alpha$ -glucosidase inhibitors.

$\alpha$ -Glucosidase is a key enzyme in carbohydrate digestion, released from mucosal cells and plays a significant role in carbohydrate metabolism.<sup>4</sup> The enzyme has

important functions in diabetes, viral infections, and cancer.  $\alpha$ -Glucosidase inhibitors delay the hydrolysis of carbohydrates and this action reduces the glucose absorption. Acarbose, miglitol, and voglibose are used in the clinic as  $\alpha$ -glucosidase inhibitors. Nevertheless, side effects such as diarrhea, hepatotoxicity and flatulence are observed in the long-term treatment with these inhibitors.<sup>5,6</sup> Hence, developing novel  $\alpha$ -glucosidase inhibitors with minimum side effects is always a promising medicinal chemistry effort.

Benzimidazoles are important nitrogen-containing heterocyclic compounds and literature review showed that there are a great number of studies on  $\alpha$ -glucosidase inhibitory activity of benzimidazole derivatives. Zawawi *et al.*<sup>7</sup> and Ozil *et al.*<sup>8</sup> have reported that a novel series of benzimidazole derivatives **I–II** (Figure 1) act as a new class of  $\alpha$ -glucosidase inhibitors.

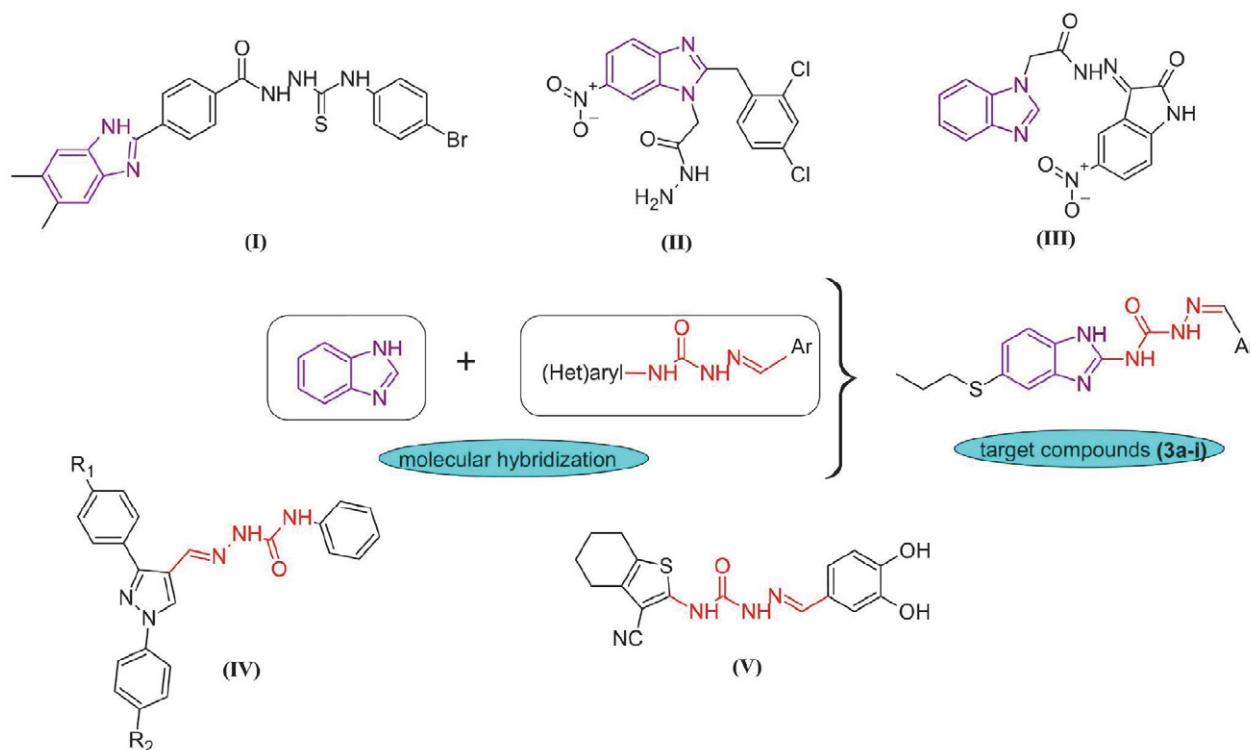


Figure 1. Designing of target molecules *via* molecular hybridization strategy

Ahmad *et al.*<sup>9</sup> provided an overview about the  $\alpha$ -glucosidase inhibitory potential of a variety of benzimidazole derivatives **III** (Figure 1).

On the other hand, semicarbazones, as medicinally significant scaffolds, are imine derivatives formed by condensation reaction between aldehyde/ketone functional groups and the  $-NH_2$  group of semicarbazides. These derivatives are known to have a broad range of biological properties including antidiabetic activity.<sup>10–14</sup> For instance, pyrazole-phenyl semicarbazone derivatives were reported by Azimi *et al.* as potent  $\alpha$ -glucosidase inhibitors **IV** (Figure 1) with  $IC_{50}$  values in the range of 65.1–695.0  $\mu M$  comparing with acarbose ( $IC_{50} = 750.0 \mu M$ ).<sup>14</sup> More recently, a (*E*)-2-benzylidene-*N*-(3-cyano-4,5,6,7-tetrahydrobenzo[*b*]thiophen-2-yl) hydrazine-1-carboxamide derivative (**V**) has been reported for its  $\alpha$ -glucosidase inhibitory potential<sup>15</sup> (Figure 1).

From the literature survey, we revealed that molecules containing benzimidazole and semicarbazone moiety have gained a huge interest as potent  $\alpha$ -glucosidase inhibitors.

## 2. Experimental

### 2.1. General

All the reagents used were analytical reagent grade. All melting points were determined on a Thermo Scientific 9300 melting point apparatus and are

uncorrected. The IR spectra were recorded on a Shimadzu FTIR 8400S spectrophotometer. NMR spectra were measured on a Bruker Avance 300 spectrometer in DMSO- $d_6$  solutions using TMS as the internal standard. Elemental analyses were determined on CHNS-932 (LECO) analyzer. The liquid chromatographic system consists of an Agilent Technologies 1100 series instrument equipped with a quaternary solvent delivery system and a model Agilent series G1315 A photodiode array detector. The chromatographic data were collected and processed using Agilent Chemstation Plus software. Chromatographic separation was performed at ambient temperature using a reverse phase Zorbax C8 (4.0×250 mm) column. All experiments were performed using acetonitrile-water gradient mobile phase (50:50 from 0 to 3 min; 75:25 to 50:50 from 3 to 6 min; 100:0 to 75:25 from 6 to 12 min; the flow rate was 1.0 mL/min).

## 2.2. Chemistry

### 2.1.1. Synthesis of *N*-(5-(Propylthio)-1*H*-benzo[*d*]imidazol-2-yl) Hydrazinecarboxamide (**2**)

*N*-(5-(Propylthio)-1*H*-benzo[*d*]imidazol-2-yl) hydrazinecarboxamide (**2**) was prepared by heating hydrazine hydrate and Albendazole (**1**) in methanol. The product was purified by recrystallization from methanol yielding white solid.

## 2. 1. 2. General Procedure for the Synthesis of 2-(Substituted Arylidene)-N-(5-(propylthio)-2,3-dihydro-1H-benzo[d]imidazol-2-yl)hydrazine-1-carboxamides 3a–i

A mixture of *N*-(5-(propylthio)-1H-benzo[d]imidazol-2-yl) hydrazinecarboxamide (**2**) (0.001 mol) and various aromatic aldehydes or ketones (0.001 mol) in absolute ethanol (20 mL), in the presence of a catalytic amount of glacial acetic acid, was refluxed for 6–7 hours. The reaction mixture was allowed to cool to room temperature and then poured onto crushed ice. The precipitated compound was filtered and washed with water and recrystallized from absolute ethanol.

### 2-(5-Chloro-2-oxoindolin-3-ylidene)-N-(5-(propylthio)-2,3-dihydro-1H-benzo[d]imidazol-2-yl)hydrazine-1-carboxamide (**3a**)

Yield 79%; m.p. 296–297 °C; HPLC  $t_R$  (min): 6.32; FT-IR:  $\nu$  3327 (NH), 1681 (C=O), 1630 (C=N), 1608 (C=C)  $\text{cm}^{-1}$ ;  $^1\text{H}$  NMR (300 MHz, DMSO- $d_6$ )  $\delta$  0.96 (t, 3H, -S-CH<sub>2</sub>CH<sub>2</sub>CH<sub>3</sub>), 1.56 (m, 2H, -S-CH<sub>2</sub>CH<sub>2</sub>CH<sub>3</sub>), 2.88 (t, 2H, -S-CH<sub>2</sub>CH<sub>2</sub>CH<sub>3</sub>), 7.15–8.34 (m, 6H, Ar-H), 10.92 (s, 1H, NH), 11.24 (s, 1H, NH), 11.61 (s, 1H, NH), 11.65 (s, 1H, NH);  $^{13}\text{C}$  NMR (75.5 MHz, DMSO- $d_6$ )  $\delta$  13.5 (CH<sub>3</sub>), 22.5 (CH<sub>2</sub>), 36.9 (CH<sub>2</sub>), 112.5, 117.1, 124.8, 126.2, 128.1, 132.0, 135.6, 136.2, 142.6, 148.8 (C=N), 153.6 (C=O), 165.0 (C=O). Anal. calcd for C<sub>19</sub>H<sub>17</sub>ClN<sub>6</sub>O<sub>2</sub>S<sub>4</sub>/3H<sub>2</sub>O: C, 50.39; H, 4.38; N, 18.56; S, 7.08. Found: C, 50.51; H, 4.69; N, 18.65; S, 7.02. LC/MS (ESI)  $m/z$  429 [M+H]<sup>+</sup>.

### 2-(2-Fluorobenzylidene)-N-(5-(propylthio)-2,3-dihydro-1H-benzo[d]imidazol-2-yl)hydrazine-1-carboxamide (**3b**)

Yield 72%; m.p. 196–197 °C; HPLC  $t_R$  (min): 5.27; FT-IR:  $\nu$  3321 (NH), 1678 (C=O), 1631 (C=N), 1556 (C=C);  $^1\text{H}$  NMR (300 MHz, DMSO- $d_6$ )  $\delta$  0.96 (t, 3H, -S-CH<sub>2</sub>CH<sub>2</sub>CH<sub>3</sub>), 1.56 (m, 2H, -S-CH<sub>2</sub>CH<sub>2</sub>CH<sub>3</sub>), 2.86 (t, 2H, -S-CH<sub>2</sub>CH<sub>2</sub>CH<sub>3</sub>), 7.24–8.41 (m, 8H, Ar-H and CH=N), 10.65 (s, 1H, NH), 11.34 (s, 1H, NH), 11.93 (s, 1H, NH);  $^{13}\text{C}$  NMR (75.5 MHz, DMSO- $d_6$ )  $\delta$  13.5 (CH<sub>3</sub>), 22.6 (CH<sub>2</sub>), 37.2 (CH<sub>2</sub>), 116.2, 122.1, 122.3, 124.5, 125.0, 125.1, 127.1, 127.6, 131.9, 132.0, 135.5, 135.6, 148.5 (C=N), 153.8 (C=O), 159.7 and 162.2 (C-F,  $J$  = 248 Hz). Anal. calcd for C<sub>18</sub>H<sub>18</sub>FN<sub>5</sub>OS: C, 58.21; H, 4.88; N, 18.86; S, 8.63. Found: C, 58.60; H, 4.92; N, 18.74; S, 8.58. LC/MS (ESI)  $m/z$  372 [M+H]<sup>+</sup>, 394 [M+Na]<sup>+</sup>.

### 2-(3-Fluorobenzylidene)-N-(5-(propylthio)-2,3-dihydro-1H-benzo[d]imidazol-2-yl)hydrazine-1-carboxamide (**3c**)

Yield 85%; m.p. 188–190 °C; HPLC  $t_R$  (min): 4.94; FT-IR:  $\nu$  3348 (NH), 1674 (C=O), 1627 (C=N), 1552 (C=C);  $^1\text{H}$  NMR (300 MHz, DMSO- $d_6$ )  $\delta$  0.96 (t, 3H, -S-CH<sub>2</sub>CH<sub>2</sub>CH<sub>3</sub>), 1.54 (m, 2H, -S-CH<sub>2</sub>CH<sub>2</sub>CH<sub>3</sub>), 2.86

(t, 2H, -S-CH<sub>2</sub>CH<sub>2</sub>CH<sub>3</sub>), 7.11–8.01 (m, 8H, Ar-H and CH=N), 11.32 (s, 1H, NH), 11.89 (s, 1H, NH), 11.92 (s, 1H, NH);  $^{13}\text{C}$  NMR (75.5 MHz, DMSO- $d_6$ )  $\delta$  13.5 (CH<sub>3</sub>), 22.6 (CH<sub>2</sub>), 37.2 (CH<sub>2</sub>), 113.2, 113.4, 116.7, 116.9, 124.5, 124.6, 125.9, 127.0, 131.0, 137.3, 141.7, 148.5 (C=N), 153.7 (C=O), 161.8 and 164.2 (C-F,  $J$  = 242 Hz). Anal. calcd for C<sub>18</sub>H<sub>18</sub>FN<sub>5</sub>OS: C, 58.21; H, 4.88; N, 18.86; S, 8.63. Found: C, 58.40; H, 4.72; N, 18.14; S, 8.11. LC/MS (ESI)  $m/z$  372 [M+H]<sup>+</sup>, 394 [M+Na]<sup>+</sup>.

### 2-(2,5-Difluorobenzylidene)-N-(5-(propylthio)-2,3-dihydro-1H-benzo[d]imidazol-2-yl)hydrazine-1-carboxamide (**3d**)

Yield 74%; m.p. 202–204 °C; HPLC  $t_R$  (min): 5.20; FT-IR:  $\nu$  3335 (NH), 1674 (C=O), 1631 (C=N), 1552 (C=C);  $^1\text{H}$  NMR (300 MHz, DMSO- $d_6$ )  $\delta$  0.96 (t, 3H, -S-CH<sub>2</sub>CH<sub>2</sub>CH<sub>3</sub>), 1.56 (m, 2H, -S-CH<sub>2</sub>CH<sub>2</sub>CH<sub>3</sub>), 2.86 (t, 2H, -S-CH<sub>2</sub>CH<sub>2</sub>CH<sub>3</sub>), 7.11–8.45 (m, 7H, Ar-H and CH=N), 10.88 (s, 1H, NH), 11.44 (s, 1H, NH), 11.98 (s, 1H, NH);  $^{13}\text{C}$  NMR (75.5 MHz, DMSO- $d_6$ )  $\delta$  13.5 (CH<sub>3</sub>), 22.5 (CH<sub>2</sub>), 37.2 (CH<sub>2</sub>), 113.5, 117.7, 117.9, 118.0, 118.3, 118.5, 123.9, 124.0, 124.5, 127.1, 134.4, 148.4 (C=N), 153.7 (C=O), 155.9 and 158.4 (C-F,  $J$  = 243 Hz), 157.8 and 160.2 (C-F,  $J$  = 238 Hz). Anal. calcd for C<sub>18</sub>H<sub>17</sub>F<sub>2</sub>N<sub>5</sub>OS: C, 55.52; H, 4.40; N, 17.98; S, 8.23. Found: C, 55.91; H, 4.76; N, 17.80; S, 8.22. LC/MS (ESI)  $m/z$  390 [M+H]<sup>+</sup>, 428 [M+K]<sup>+</sup>.

### 2-(4-Methylbenzylidene)-N-(5-(propylthio)-2,3-dihydro-1H-benzo[d]imidazol-2-yl)hydrazine-1-carboxamide (**3e**)

Yield 82%; m.p. 199–200 °C; HPLC  $t_R$  (min): 3.19; FT-IR:  $\nu$  3335 (NH), 1681 (C=O), 1625 (C=N), 1556 (C=C);  $^1\text{H}$  NMR (300 MHz, DMSO- $d_6$ )  $\delta$  0.96 (t, 3H, -S-CH<sub>2</sub>CH<sub>2</sub>CH<sub>3</sub>), 1.53 (m, 2H, -S-CH<sub>2</sub>CH<sub>2</sub>CH<sub>3</sub>), 2.35 (s, 3H, CH<sub>3</sub>), 2.86 (t, 2H, -S-CH<sub>2</sub>CH<sub>2</sub>CH<sub>3</sub>), 7.10–7.99 (m, 8H, Ar-H and CH=N), 10.29 (s, 1H, NH), 11.15 (s, 1H, NH), 11.91 (s, 1H, NH);  $^{13}\text{C}$  NMR (75.5 MHz, DMSO- $d_6$ )  $\delta$  13.6 (CH<sub>3</sub>), 21.5 (CH<sub>2</sub>), 22.6 (CH<sub>3</sub>), 37.5 (CH<sub>2</sub>), 124.5, 126.6, 127.0, 127.1, 127.8, 128.8, 129.6, 129.9, 131.9, 139.9, 143.3, 148.3 (C=N), 153.3 (C=O). Anal. calcd for C<sub>19</sub>H<sub>21</sub>N<sub>5</sub>OS $\cdot$ 1/4H<sub>2</sub>O: C, 61.35; H, 5.83; N, 18.83; S, 8.62. Found: C, 61.52; H, 6.24; N, 18.56; S, 8.69. LC/MS (ESI)  $m/z$  368 [M+H]<sup>+</sup>, 390 [M+Na]<sup>+</sup>.

### 2-(2,4-Dichlorobenzylidene)-N-(5-(propylthio)-2,3-dihydro-1H-benzo[d]imidazol-2-yl)hydrazine-1-carboxamide (**3f**)

Yield 78%; m.p. 177–179 °C; HPLC  $t_R$  (min): 4.22; FT-IR:  $\nu$  3317 (NH), 1680 (C=O), 1631 (C=N), 1556 (C=C);  $^1\text{H}$  NMR (300 MHz, DMSO- $d_6$ )  $\delta$  0.95 (t, 3H, -S-CH<sub>2</sub>CH<sub>2</sub>CH<sub>3</sub>), 1.53 (m, 2H, -S-CH<sub>2</sub>CH<sub>2</sub>CH<sub>3</sub>), 2.51 (t, 2H, -S-CH<sub>2</sub>CH<sub>2</sub>CH<sub>3</sub>), 7.05–8.53 (m, 7H, Ar-H and CH=N), 10.56 (s, 1H, NH), 11.17 (s, 1H, NH), 11.45 (s, 1H, NH);  $^{13}\text{C}$  NMR (75.5 MHz, DMSO- $d_6$ )  $\delta$  13.5 (CH<sub>3</sub>), 22.5 (CH<sub>2</sub>), 37.2 (CH<sub>2</sub>), 114.5, 115.8, 116.2, 124.5, 127.2,

128.0, 129.5, 131.0, 133.7, 135.0, 137.8, 138.5, 148.5 (C=N), 154.6, 156.5 (C=O). Anal. calcd for  $C_{18}H_{17}Cl_2N_5OS$ : C, 51.19; H, 4.06; N, 16.79; S, 7.59. Found: C, 51.04; H, 4.04; N, 16.79; S, 7.59. LC/MS (ESI)  $m/z$  422 [M+H]<sup>+</sup>.

**2-(3,4-Dimethylbenzylidene)-N-(5-(propylthio)-2,3-dihydro-1H-benzo[d]imidazol-2-yl)hydrazine-1-carboxamide (3g)**

Yield 81%; m.p. 191–193 °C; HPLC  $t_R$  (min): 6.02; FT-IR:  $\nu$  3332 (NH), 1681 (C=O), 1627 (C=N), 1556 (C=C); <sup>1</sup>H NMR (300 MHz, DMSO-*d*<sub>6</sub>)  $\delta$  0.96 (t, 3H, -S-CH<sub>2</sub>CH<sub>2</sub>CH<sub>3</sub>), 1.54 (m, 2H, -S-CH<sub>2</sub>CH<sub>2</sub>CH<sub>3</sub>), 2.25 (s, 3H, -CH<sub>3</sub>), 2.26 (s, 3H, -CH<sub>3</sub>), 2.85 (t, 2H, -S-CH<sub>2</sub>CH<sub>2</sub>CH<sub>3</sub>), 7.11–7.96 (m, 7H, Ar-H and CH=N), 10.35 (s, 1H, NH), 11.16 (s, 1H, NH), 11.93 (s, 1H, NH); <sup>13</sup>C NMR (75.5 MHz, DMSO-*d*<sub>6</sub>)  $\delta$  13.5 (CH<sub>3</sub>), 19.7 (CH<sub>2</sub>), 19.9 (CH<sub>3</sub>), 22.6 (CH<sub>3</sub>), 37.2 (CH<sub>2</sub>), 124.4, 125.4, 126.9, 127.1, 127.4, 128.5, 130.2, 130.7, 132.2, 137.0, 138.7, 139.6, 143.6, 148.4 (C=N), 153.4 (C=O). Anal. calcd for  $C_{20}H_{23}N_5OS$ : C, 62.71; H, 6.24; N, 17.92; S, 8.21. Found: C, 63.04; H, 5.96; N, 17.67; S, 7.99. LC/MS (ESI)  $m/z$  382 [M+H]<sup>+</sup>, 404 [M+Na]<sup>+</sup>.

**2-(5-Bromo-2-methoxybenzylidene)-N-(5-(propylthio)-2,3-dihydro-1H-benzo[d]imidazol-2-yl)hydrazine-1-carboxamide (3h)**

Yield 81%; m.p. 198–200 °C; HPLC  $t_R$  (min): 5.86; FT-IR:  $\nu$  3348 (NH), 1681 (C=O), 1627 (C=N), 1556 (C=C); <sup>1</sup>H NMR (300 MHz, DMSO-*d*<sub>6</sub>)  $\delta$  0.96 (t, 3H, -S-CH<sub>2</sub>CH<sub>2</sub>CH<sub>3</sub>), 1.54 (m, 2H, -S-CH<sub>2</sub>CH<sub>2</sub>CH<sub>3</sub>), 2.86 (t, 2H, -S-CH<sub>2</sub>CH<sub>2</sub>CH<sub>3</sub>), 3.84 (s, 3H, -OCH<sub>3</sub>), 7.04–8.50 (m, 7H, Ar-H and CH=N), 10.65 (s, 1H, NH), 11.26 (s, 1H, NH), 11.95 (s, 1H, NH); <sup>13</sup>C NMR (75.5 MHz, DMSO-*d*<sub>6</sub>)  $\delta$  13.5 (CH<sub>3</sub>), 22.6 (CH<sub>2</sub>), 37.2 (CH<sub>2</sub>), 56.7 (OCH<sub>3</sub>), 113.3, 114.4, 116.6, 124.5, 124.8, 127.0, 128.8, 130.3, 130.4, 133.6, 136.9, 138.9, 148.4 (C=N), 153.4 (C-OCH<sub>3</sub>), 156.9 (C=O). Anal. calcd for  $C_{19}H_{20}BrN_5O_2S$ : C, 49.36; H, 4.36; N, 15.15; S, 6.94. Found: C, 49.56; H, 4.36; N, 14.35; S, 6.55. LC/MS (ESI)  $m/z$  462 [M+H]<sup>+</sup>, 484 [M+Na]<sup>+</sup>.

**2-(4-Trifluoromethylbenzylidene)-N-(5-(propylthio)-2,3-dihydro-1H-benzo[d]imidazol-2-yl)hydrazine-1-carboxamide (3i)**

Yield 75%; m.p. 208–210 °C; HPLC  $t_R$  (min): 6.72; FT-IR:  $\nu$  3348 (NH), 1681 (C=O), 1614 (C=N), 1539 (C=C); <sup>1</sup>H NMR (300 MHz, DMSO-*d*<sub>6</sub>)  $\delta$  0.96 (t, 3H, -S-CH<sub>2</sub>CH<sub>2</sub>CH<sub>3</sub>), 1.54 (m, 2H, -S-CH<sub>2</sub>CH<sub>2</sub>CH<sub>3</sub>), 2.86 (t, 2H, -S-CH<sub>2</sub>CH<sub>2</sub>CH<sub>3</sub>), 7.11–8.15 (m, 8H, Ar-H and CH=N), 11.38 (s, 1H, NH, other NH proton not observed). <sup>13</sup>C NMR (75.5 MHz, DMSO-*d*<sub>6</sub>)  $\delta$  13.5 (CH<sub>3</sub>), 22.6 (CH<sub>2</sub>), 37.2 (CH<sub>2</sub>), 115.6, 120.6, 123.3, 125.8, 125.9, 126.0, 126.2, 127.2 (q, CF<sub>3</sub>,  $J$  = 265 Hz), 128.3, 128.7, 129.2, 130.1, 138.7, 141.3, 148.6 (C=N), 153.9 (C=O). Anal. calcd for  $C_{19}H_{18}F_3N_5OS$ : C, 54.15; H, 4.30; N, 16.62; S, 7.61. Found: C, 54.12; H, 4.33; N, 16.62; S, 7.43. LC/MS (ESI)  $m/z$  422 [M+H]<sup>+</sup>, 444 [M+Na]<sup>+</sup>.

## 2. 3. $\alpha$ -Glucosidase Assay

The  $\alpha$ -glucosidase inhibitor activity was evaluated as described by Ramakrishna *et al.* with slight modifications described by Sen *et al.*<sup>16</sup> Each concentration had three replicates when preliminary screened and inhibition percentages were calculated using the following formula.

$$\% \text{ Inhibition} = \frac{A_{\text{control}} - A_{\text{sample}}}{A_{\text{control}}} \cdot 100$$

where *A* is the absorbance.

Finally, IC<sub>50</sub> values were also determined for the compounds having 50% or above inhibition values.

## 2. 4. Molecular Docking

Molecular docking simulations were performed against  $\alpha$ -glucosidase by using AutoDock Vina software.<sup>17</sup> The protein data of  $\alpha$ -glucosidases (PDB ID: 4J5T) was referenced from Protein Data Bank.<sup>18</sup>

The target protein was prepared in three steps using the AutoDock Tools program<sup>19</sup> for docking studies: (1) were removed water molecules; (2) were added polar hydrogen to  $\alpha$ -glucosidase macromolecule; (3) the obtained structure was energy-minimized.

The synthesized compounds **3a–i** and reference ligands were prepared in two steps for docking studies: (1) were drawn with the Spartan 04 software (SPARTAN 04, Wavefunction, Inc., Irvine, USA)<sup>20</sup> and optimized for each compound by using the semi-empirical PM3 method; (2) the docking input files of the most stable conformation were generated using the AutoDock Tools program.

The grid box size was determined as 78 Å × 69 Å × 104 Å within 0.375 Å grid spacing and center\_x = −18.44, center\_y = −20.91, center\_z = 8.22 dimensions were used in  $\alpha$ -glucosidase enzyme docking studies, appropriate to the literature.<sup>18</sup> The Vina parameter “exhaustiveness” was set to the value of 10.

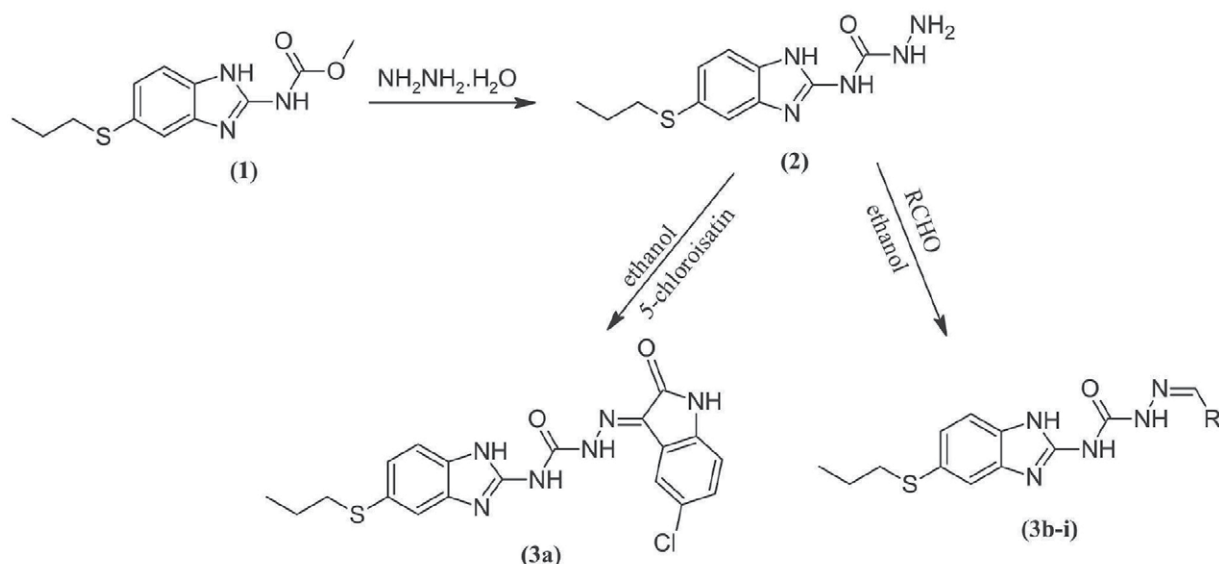
The reference ligands used in validation studies include sugars that form part of the biological substrate, as well as known inhibitors (acarbose, glucose, miglitol, deoxynojirimycin, and kojibiose). During study of validations as well as our docking of ligands were used flexible ligands in rigid protein. The resulting files were analyzed using Accelrys Discovery Studio Visualizer 4.0 program.

## 3. Results and Discussion

### 3. 1. Chemistry

Scheme 1 shows the synthetic route for the target compounds. Albendazole (**1**) was reacted with hydrazine hydrate, affording **2** according to the similar method reported in the literature.<sup>21</sup> The new derivatives **3a–i** were obtained by the reaction of **2** with appropriate aromatic





Scheme 1. Synthetic route to target derivatives 3a–i

aldehydes or ketone in the presence of acid according to the literature procedures.<sup>22,23</sup> The structures of the desired target compounds were confirmed by FT-IR, <sup>1</sup>H NMR, and elemental analysis.

In the IR spectra of the studied compounds, the less intense broad bands around 3317–3348 cm<sup>−1</sup> are assigned to ν(N–H) vibrations of the NHCO group. The band around 1674–1681 cm<sup>−1</sup> corresponds to the carbonyl group of CONH. The azomethine band is observed at 1625–1631 cm<sup>−1</sup>. <sup>1</sup>H NMR spectrum revealed three signals around 10.29–11.98 ppm assigned to three NH protons. In

the <sup>1</sup>H NMR spectrum of compound 3i, the NH proton was seen as a singlet at δ 11.38 ppm and two NH protons were not observed.

### 3.2. α-Glucosidase Inhibitory Activity

We have synthesized benzimidazoles bearing semicarbazones 3a–i and evaluated them for α-glucosidase inhibitory potential. All derivatives showed excellent inhibitory activities having IC<sub>50</sub> values ranging between 12.88–44.35 μM as compared to the standard acarbose

Table 1. α-Glucosidase inhibitory activity (IC<sub>50</sub>) of albendazole derivatives 3a–i

Compound	-Ar	IC <sub>50</sub> (μM) <sup>a</sup>	Compound	-Ar	IC <sub>50</sub> (μM) <sup>a</sup>
3a		12.88±0.98	3f		31.16±0.17
3b		30.80±0.27	3g		28.72±1.32
3c		13.68±0.65	3h		44.35±0.21
3d		30.30±0.89	3i		28.36±0.50
3e		14.54±0.25	Acarbose <sup>b</sup>		40.06±2.14

<sup>a</sup>Data represents means SD of triplicate samples obtained from the dose inhibition curve. <sup>b</sup>Standard drug

(IC<sub>50</sub> = 40.06 µM) (Table 1). Their possibly potent inhibitory potential may be due to the benzimidazole core bearing a semicarbazone entity.

The isatin moiety of the most active compound **3a**, was determined to be important for biological activity, suggesting intramolecular hydrogen bond formation.

### 3. 3. ADME Prediction

The potent inhibitors **3a–i** were evaluated *in silico* for selected ADME properties using the SwissADME online tool (<http://www.swissadme.ch/>). Table 2 shows the ADME prediction results of the compounds. Topological Polar Surface Area (TPSA) shows the surface belonging to polar atoms in the compound and lower TPSA values are appropriate for drug-likeness properties. The absorption percentage was also calculated by using the following formula:

$$\%Abs = 109 - [0.345 \cdot TPSA]$$

as given in the literature<sup>24,25</sup> and showed a good absorption profile.

According to Lipinski's rule of five, drug candidate should have log *P* less than 5, its polar surface area within 140 Å<sup>2</sup>, it should have less than 10 H bond acceptors, it should have less than 5 H bond donors and its molecular weight should be below 500 Dalton.<sup>26</sup> Also, the more negative the skin permeability (log *K<sub>p</sub>*) value is, the less possible for the compound to penetrate the skin barrier. The tool predicted that derivatives have suitable skin permeability with log *K<sub>p</sub>* values of –5.24 to –5.90 cm/s.

Eventually, all of the molecules were shown to comply best with these properties used to predict drug-likeness (Table 2).

To reveal the capability of intestinal absorption and permeability of the blood–brain barrier (BBB), the boiled-egg model of the molecules was predicted using SwissADME (Figure 2). Molecules that fall in the yellow field de-

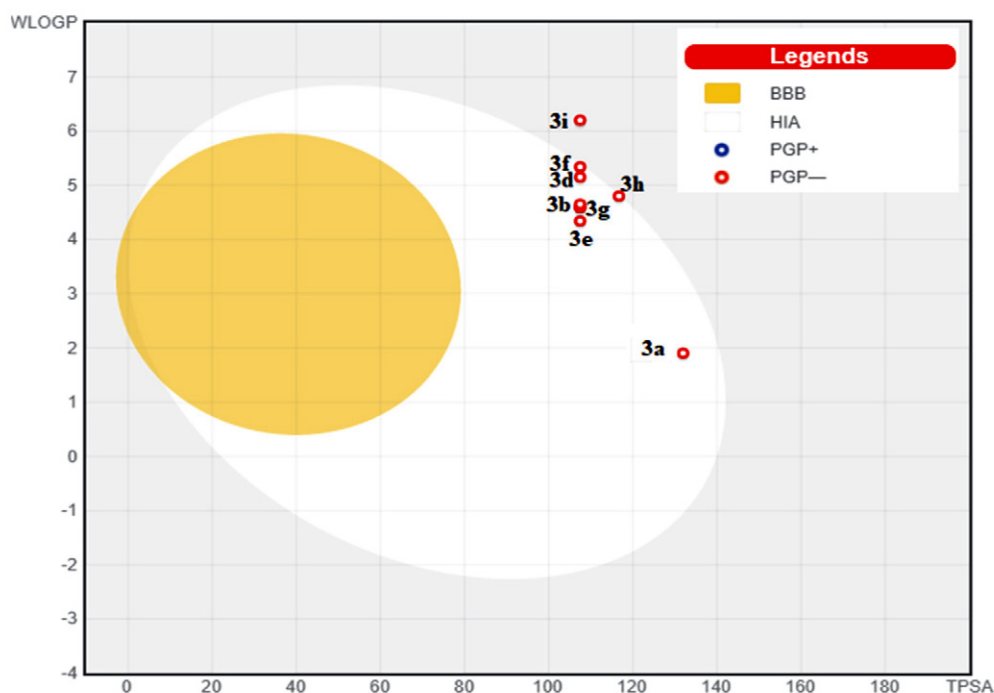


Figure 2. The boiled-egg plot of compounds **3a–i**. HIA: Human Intestinal Absorption; BBB: Blood–Brain Barrier; PGP: Permeability Glycoprotein.

Table 2. ADME results of the albendazole derivatives **3a–i**

ADME properties	<b>3a</b>	<b>3b</b>	<b>3c</b>	<b>3d</b>	<b>3e</b>	<b>3f</b>	<b>3g</b>	<b>3h</b>	<b>3i</b>
Molecular weight (g/mol)	428.903	371.439	371.439	389.429	367.476	422.339	381.503	462.371	421.446
Num.H-bond acceptors	8	6	6	6	6	6	6	7	6
Num.H-bond donors	4	3	3	3	3	3	3	3	3
Num.rotatable bonds	7	8	8	8	8	8	8	9	9
logP	2.86	3.63	3.63	4.01	3.47	4.24	3.70	3.55	4.08
TPSA (Å <sup>2</sup> )	131.95	107.47	107.47	107.47	107.47	107.47	107.47	116.70	107.47
Absorption (%)	63.48	71.92	71.92	71.92	71.92	71.92	71.92	68.73	71.92
Log <i>K<sub>p</sub></i> (skin permeation (cm/s))	–5.65	–5.75	–5.75	–5.79	–5.54	–5.24	–5.37	–5.90	–5.50

pict the BBB permeation, whereas the white eclipse region symbolizes gastrointestinal absorption. According to the boiled-egg plot, all of the compounds are BBB-impermea-

ble and have good absorption, except compound **3i**. P-glycoprotein (P-gp) plays a significant role in drug absorption and disposition. Compounds **3a–i** are non substrates of

**Table 3.** Types of interactions of the compounds **3a–i** and small reference ligands with the binding site residues of  $\alpha$ -glucosidase enzyme.

Compounds <sup>a</sup>	Binding energy $\Delta G$ (kcal/mol)	Binding site	Distance (Å)	Hydrogen bond Interactions (A/D) <sup>b</sup>
<b>3a</b>	−9.3	A	2.80	Asp392 (A)
			1.80	Arg428 (D)
			2.59	Arg428 (D)
			2.66	Arg428 (D)
<b>3b</b>	−7.7	A	2.50	Arg428 (D)
<b>3c</b>	−8.4	A	2.25	Arg428 (D)
<b>3d</b>	−7.9	A	2.88	Trp391 (D)
			2.49	Arg428 (D)
			2.25	Arg428 (D)
<b>3e</b>	−8.4	A	2.31	Arg428 (D)
			2.97	Val446 (A)
			2.78	Gln447 (D)
<b>3f</b>	−7.3	A	2.87	Glu429 (A)
<b>3g</b>	−7.9	A	2.87	Arg428 (D)
<b>3h</b>	−7.3	A	2.84	Arg428 (D)
<b>3i</b>	−8.4	A	2.71	Trp391 (D)
			2.27	Asp568 (A)
			3.02	Glu771(A) <sup>c</sup>
<b>ACB</b>	−8.1	A	3.09	Glu443 (A)
			3.16	Val446 (A)
			3.09	Asp568 (A)
			1.97	Trp710 (D)
			3.33	Glu771 (A)
<b>GLC</b>	−5.5	A	1.84	Trp391 (D)
			2.26	Arg428 (D)
			2.73	Arg428 (D)
			2.46	Gly566 (A)
			2.72	Asp568 (D)
<b>DNJ</b>	−5.4	A	2.54	Trp391 (D)
			2.13	Gly566 (A)
			2.69	Gly566 (A)
			1.98	Trp710 (D)
			2.37	Trp710 (D)
<b>MGL</b>	−5.5	A	2.27	Gly566 (A)
<b>KJB</b>	−6.1	A	2.41	Ile362 (A)
			2.75	Glu429 (A)
			2.66	Leu50 (A)
	−6.4	B	2.21	His51 (A)
			2.44	Phe56 (A)
			2.46	Asp61 (A)
			1.96	Arg209 (D)
			2.33	Arg209 (D)
			2.62	Arg209 (D)

<sup>a</sup> ACB: Acarbose; GLC: Glucose; DNJ: Deoxynojirimycin; MGL: Miglitol; KJB: Kojibiose. <sup>b</sup> A: H-bond acceptor; D: H-bond donor. <sup>c</sup> Halogen bond.

P-gp, therefore it can be theorized that they may possibly act as inhibitors of P-gp.

### 3. 3. Molecular Modeling

The molecular docking analysis was carried out to investigate the binding mode of novel  $\alpha$ -glucosidase inhibitors compounds **3a–i** within the binding pocket of the target enzyme, and to further understand their structure-activity relationship. Firstly, we examined the interactions

of the known inhibitors (acarbose, glucose, miglitol, deoxynojirimycin, and kojibiose) with  $\alpha$ -glucosidase active site to compare with our synthesized compounds **3a–i**. The binding energies and interactions with the active site of the reference ligands and compounds **3a–i** are given in Table 3.

As shown in Figure 3, one of the two binding sites of  $\alpha$ -glucosidase has been defined as “site A” containing a glutamate (Glu771) and an aspartate (Asp568), while the other is “site B”.<sup>18</sup> It was determined that among the known

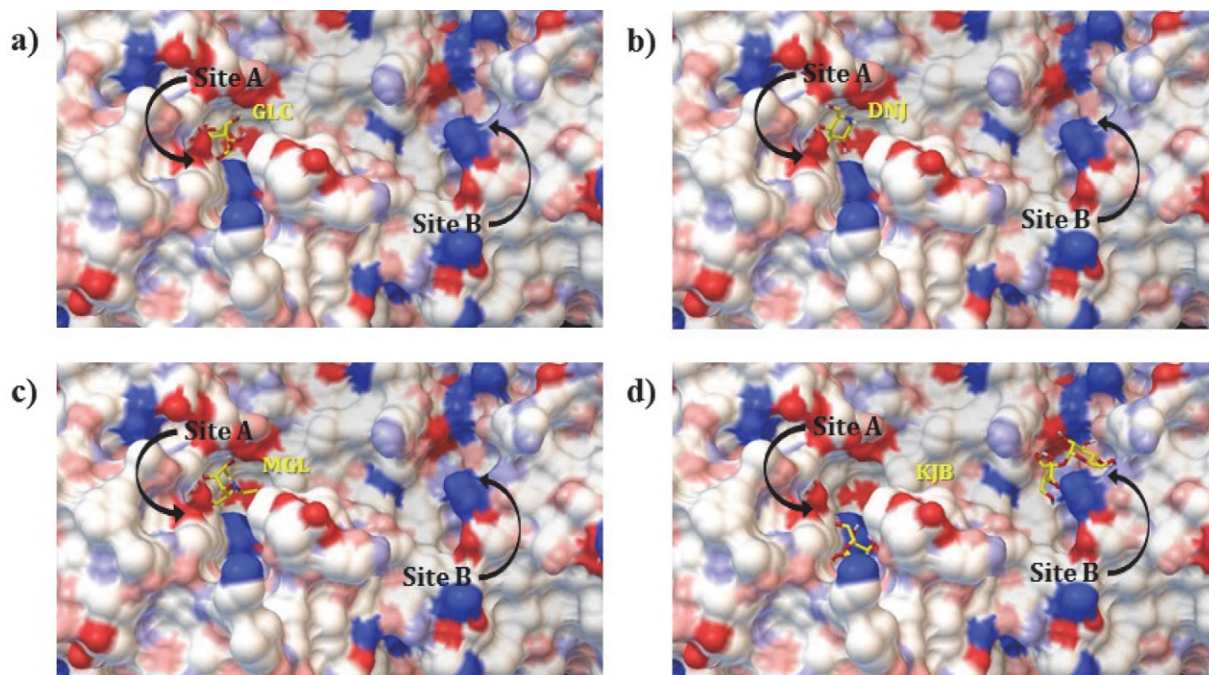


**Figure 3.** For  $\alpha$ -glucosidase enzyme small references ligands a) GLC is in binding site A, b) DNJ is in binding site A, c) MGL is in binding site A, and d) KJB is in both binding sites A and B. A surface representation of  $\alpha$ -glucosidase shown as the DG color scheme (neutral oxygen (pink), nitrogen atoms (light blue), charged oxygen (red) and nitrogen atoms (dark blue)).

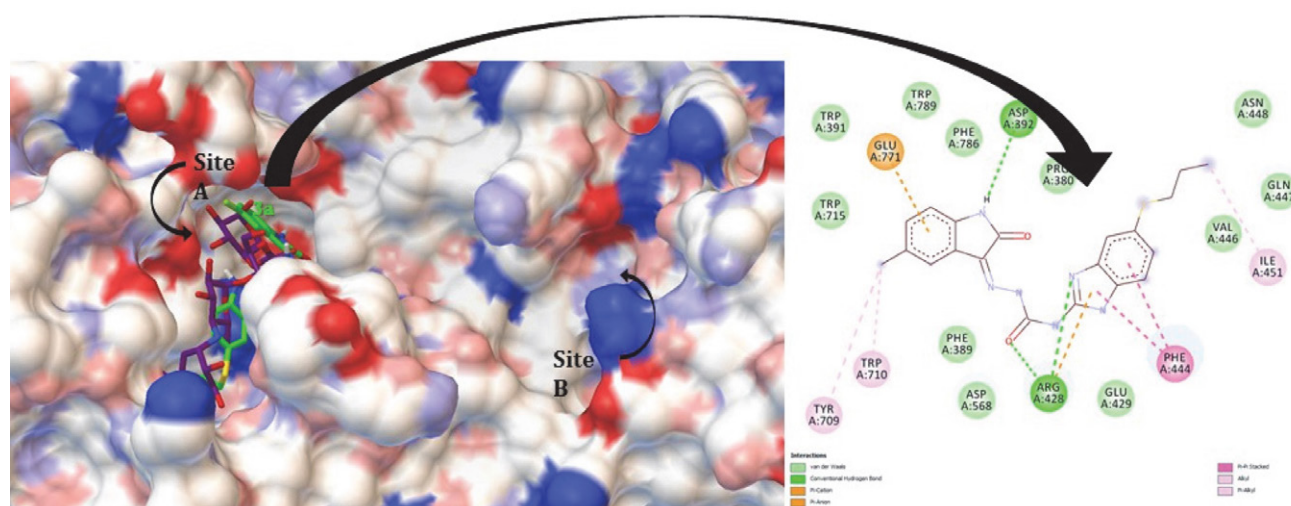


**Figure 4.** A surface representation of  $\alpha$ -glucosidase shown as the DG color scheme (neutral oxygen (pink), nitrogen atoms (light blue), charged oxygen (red) and nitrogen atoms (dark blue)). Positions of compound **3a** (green) and acarbose (purple) in the binding site A of  $\alpha$ -glucosidase enzyme and 2D interactions of the compound **3a** with active site residues.

ligands ACB, GLC, DNJ and MGL are docked into “site A” of  $\alpha$ -glucosidase, while KJB docked into both of the sites.

According to the *in silico* molecular modeling studies, it has been determined that the synthesized compounds **3a–i** interact with the binding site A. Binding energies of these compounds have been determined to be between  $-7.3$  kcal/mol and  $-9.3$  kcal/mol as higher than the known inhibitors GLC, DNJ, MGL and KJB. Compared with the binding energy of ACB ( $-8.1$  kcal/mol) used in *in vitro* inhibition studies, compound **3a** was found to be remarkable with the value of  $-9.3$  kcal/mol, while the other synthesized compounds showed similar results. These findings supports the results of *in vitro* enzyme inhibition studies. All of the synthesized novel benzimidazole derivatives, except **3f** and **3i** have exhibited hydrogen bond (H-bond) interaction with Arg428, like reference ligand GLC. Also, it was detected that compound **3a** exhibited  $\pi$ -anion interaction with active site residue Glu771, while compound **3i** exhibited halogen bond interaction.

Compound **3a**, which was found to be the most effective compound according to both *in vitro* and *in silico* studies, exhibited three H-bond interactions with Arg428. One of the three H-bond interactions were detected with =N- atom of benzimidazole moiety and the others with CO group of semicarbazone moiety. Moreover, a H-bond interaction between the NH group of 2-oxoindolin structure and Asp392 has been detected. Additionally, hydrophobic interactions have been determined between Arg428, Glu771 residues and benzimidazole ( $\pi$ -cation), 2-oxoindolin ( $\pi$ -anion) rings, respectively. These hydrophobic interactions were supported by the  $\pi$ - $\pi$  stacking interactions of the benzimidazole ring with Phe444 besides other hydrophobic interactions between compound **3a** and Ile451, Leu563, Trp709 and Trp710 (Figure 4). Finally, it has been detected that the compound **3a** exhibits more hydrophobic interactions than all reference ligands and synthesized compounds and these findings contribute to having the highest binding energy.

## 4. Conclusions

The targeted 2-(substituted arylidene)-*N*-(5-(propylthio)-2,3-dihydro-1*H*-benzo[d]imidazol-2-yl)hydrazine-1-carboxamides **3a–i** were synthesized in good yields. All of the molecules demonstrated encouraging inhibitory activity against  $\alpha$ -glucosidase which was also supported by molecular docking studies. Docking studies revealed that compound **3a** is the most active compound with the highest binding energy value of  $-9.3$  kcal/mol. As a result, it has been determined that the findings obtained from *in vitro* and *in silico*  $\alpha$ -glucosidase enzyme inhibition studies were compatible. These compounds revealed also reasonable *in silico* physicochemical and pharmacokinetic parameters (ADME). The present findings may invite researchers to work in the area of development of the  $\alpha$ -glucosidase inhibitors.

## Conflict of Interest

Authors declare no conflict of interest.

## 5. References

- G. Wang, M. Chen, J. Qiu, Z. Xie, A. Cao, *Bioorg. Med. Chem. Lett.* **2018**, 28, 113–116. DOI:10.1016/j.bmcl.2017.11.047
- J. Zhang, H. Xie, Y. Li, K. Wang, Z. Song, K. Zhu, L. Fang, J. Zhang, C. Jiang, *Bioorg. Med. Chem. Lett.* **2017**, 52, 1–5. DOI:10.1016/j.bmcl.2017.09.048
- E. S. Moghadam, M. H. Tehrani, R. Abdel-Jalil, M. A. Faramarzi, M. Amini, *Polycycl. Aromat. Compd.* **2021**, 1–19. DOI:10.1080/10406638.2021.1962369
- H. Bischoff, *Clin. Invest. Med.* **1995**, 18, 303–311. DOI:10.1007/978-3-322-89194-5\_2
- A. J. Krentz, C. J. Bailey, *Drugs*. **2005**, 65, 385–411. DOI:10.2165/00003495-200565030-00005
- S.-H. Hsiao, L.-H. Liao, P.-N. Cheng, T.-J. Wu, *Ann. Pharmacother.* **2006**, 40, 151–154. DOI:10.1345/aph.1G336
- N. K. N. A. Zawawi, M. Taha, N. Ahmat, A. Wadood, N. H. Ismail, F. Rahim, S. S. Azam, N. Abdullah, *Bioorg. Chem.* **2016**, 64, 29–36. DOI:10.1016/j.bioorg.2015.11.006
- M. Özl, C. Parlak, N. Baltaş, *Bioorg. Chem.* **2018**, 76, 468–477. DOI:10.1016/j.bioorg.2017.12.019
- M. U. Ahmad, M. Rafiq, B. Zahra, M. Islam, M. Ashraf, M. al-Rashida, A. Khan, J. Hussain, Z. Shafiq, A. Al-Harrasi, *Drug Dev. Res.* **2021**, 82, 1033–1043. DOI:10.1002/ddr.21807
- F. Carrasco, W. Hernández, O. Chupayo, C. M. Álvarez, S. Oramas-Royo, E. Spodine, C. Tamariz-Angeles, P. Oliveira-Gonzales, J. Z. Dávalos, *J. Chem.* **2020**, 7157281. DOI:10.1155/2020/7157281
- L. Ma, H. Wang, J. Wang, L. Liu, S. Zhang, M. Bu, *Molecules*. **2020**, 25, 1209. DOI:10.3390/molecules25051209
- R. B. de Oliveira, E. M. de Souza-Fagundes, R. P. P. Soares, A. A. Andrade, A. U. Krettli, C. L. Zani, *Eur. J. Med. Chem.* **2008**, 43, 1983–1988. DOI:10.1016/j.ejmech.2007.11.012
- S. N. Pandeya, S. S. Panda, A. Pandeya, J. P. Stables, *Indian J. Chem.* **2003**, 42, 2657–2661.
- F. Azimi, J. B. Ghasemi, H. Azizian, M. Najafi, M. A. Faramarzi, L. Saghaei, H. Sadeghi-aliabadi, B. Larijani, F. Hassan-zadeh, M. Mahdavi, *Int. J. Biol. Macromol.* **2021**, 166, 1082–1095. DOI:10.1016/j.ijbiomac.2020.10.263
- J. H. Zhang, H. X. Xie, Y. Li, K. M. Wang, Z. Song, K. K. Zhu, L. Fang, J. Zhang, C. S. Jiang, *Bioorg. Med. Chem. Lett.* **2021**, 52, 128413. DOI:10.1016/j.bmcl.2021.128413
- A. Sen, M. Kurkcuoglu, I. Senkardes, L. Bitis, K. H. C. Baser, *J. Essent. Oil-Bearing Plants*. **2019**, 22, 1048–1057. DOI:10.1080/0972060X.2019.1662333
- O. Trott, A. J. Olson, *J. Comput. Chem.* **2010**, 31, 455–461. DOI:10.1002/jcc.21334
- M. K. Barker, D. R. Rose, *J. Biol. Chem.* **2013**, 288, 13563–13574. DOI:10.1074/jbc.M113.460436
- G. M. Morris, R. Huey, W. Lindstrom, M. F. Sanner, R. K. Belew, D. S. Goodsell, A. J. Olson, *J. Comput. Chem.* **2009**, 30, 2785–2791. DOI:10.1002/jcc.21256



20. J. J. P. Stewart, *J. Mol. Model.* **2007**, *13*, 1173–1213. DOI:10.1007/s00894-007-0233-4
21. B. S. Rani, K. B. Priyanka, G. Sammaiah, *Int. J. Pharm. Bio. Sci.* **2014**, *4*, 29–34.
22. S. Şenkardeş, Ö. Erdoğan, Ö. Çevik, G. Küçükgülzel, *Synth. Commun.* **2021**, *51*, 2634–2643. DOI:10.1080/00397911.2021.1945105
23. S. Şenkardeş, A. Türe, S. Ekrek, A. T. Durak, M. Abbak, Ö. Çevik, B. Kaşkatepe, İ. Küçükgülzel, G. Küçükgülzel, *J. Mol. Struct.* **2021**, *1223*, 128962. DOI:10.1016/j.molstruc.2020.128962
24. Y. H. Zhao, M. H. Abraham, J. Le, A. Hersey, C. N. Luscombe, G. Beck, B. Sherborne, I. Cooper, *Pharm. Res.* **2002**, *19*, 1446–1457. DOI:10.1023/A:1020444330011
25. S. Şenkardeş, N. Kulabaş, Ö. Bingöl Özakpınar, S. Kalayci, F. Şahin, İ. Küçükgülzel, G. Küçükgülzel, *Turkish J. Pharm. Sci.* **2020**, *17*, 81–93. DOI:10.4274/tjps.galenos.2018.59389
26. C. A. Lipinski, F. Lombardo, B. W. Dominy, P. J. Feeney, *Adv. Drug Deliv. Rev.* **2012**, *64*, 4–17. DOI:10.1016/j.addr.2012.09.019

## Povzetek

S pomočjo kondenzacije *N*-(5-(propiltio)-1*H*-benzo[*d*]imidazol-2-il) hidrazinkarboksamidov (**2**) z ustreznimi ketoni ali aldehidi smo sintetizirali serijo novih 2-(substituiranih ariliden)-*N*-(5-(propiltio)-2,3-dihidro-1*H*-benzo[*d*]imidazol-2-il)hidrazin-1-karboksamidnih derivatov **3a–i**. Kemijske strukture pripravljenih spojin smo potrdili z analitskimi in spektroskopskimi metodami. Za pripravljene spojine smo določili njihovo inhibitorno aktivnost na  $\alpha$ -glukozidazo; vse spojine, razen **3h**, so se izkazale kot boljši inhibitorji od akarboze. Še posebej zanimiva je spojina **3a**, ki je pokazala največjo aktivnost ( $IC_{50}$  vrednost  $12.88 \pm 0.98 \mu M$ ) izmed vseh sintetiziranih derivatov. Da bi raziskali vezavne interakcije, smo izvedli tudi študije molekulskega sidranja. Spojina **3a** je pokazala največjo vezno energijo ( $\Delta G = -9.4$  kcal/mol) in največje število interakcij z aktivnim mestom z vodikovimi vezmi. Tudi rezultati *in silico* študij se dobro ujemajo z rezultati *in vitro* raziskav.



Except when otherwise noted, articles in this journal are published under the terms and conditions of the Creative Commons Attribution 4.0 International License

Scientific paper

# Nickel Removing by Electrocoagulation of Ni(II)-NH<sub>3</sub>-CO<sub>2</sub>-SO<sub>2</sub>-H<sub>2</sub>O System. Kinetics, Isothermal, Mechanism and Estimated Cost of Operation

Armando Rojas Vargas,<sup>1,\*</sup> Margarita Penedo Medina,<sup>2</sup> Alba González Vives,<sup>3</sup>  
Noureddine Barka<sup>4</sup> and Aymara Ricardo Riverón<sup>5</sup>

<sup>1</sup> Empresa de Servicios Técnicos de Computación, Comunicaciones y Electrónica “Rafael Fausto Orejón Forment”,  
Nicaro, Holguín, Cuba

<sup>2</sup> Universidad de Oriente, Facultad de Ingeniería Química, Santiago de Cuba, Cuba

<sup>3</sup> POLYMAT, Departamento de Ciencia y Tecnología de Polímeros, Universidad del País Vasco, España

<sup>4</sup> Sultan Moulay Slimane University of Beni Mellal, Multidisciplinary Research and Innovation Laboratory, FP Khouribga,  
BP.145, 25000, Khouribga, Morocco.

<sup>5</sup> Centro de Investigaciones del Níquel “Alberto Fernández Montes de Oca”, Nicaro, Holguín, Cuba

\* Corresponding author: E-mail: arojas@eros.moa.minem.cu)  
Tel: +53-24-51-6695

Received: 02-09-2022

## Abstract

This study reports nickel removing by electrocoagulation of Ni(II)-NH<sub>3</sub>-CO<sub>2</sub>-SO<sub>2</sub>-H<sub>2</sub>O system at laboratory scale. Experiments were done using Al/Al pair electrodes at initial nickel concentration between 293 and 1356 mg L<sup>-1</sup> and under operation parameters of pH 8.6, current density 9.8 mA cm<sup>-2</sup>, electrolysis time 30 min, and temperature 60 °C. The obtained results show removal efficiencies between 97.7 and 99.7%. Kinetics modeling suggested combined effects of external diffusion and nucleation, and as controlling step the chemical reaction and a possible autocatalytic contribution. The process followed the Langmuir's isotherm with a maximum adsorption capacity of 7519 mg g<sup>-1</sup>. ICP-OES, XRD and FTIR characterization of the precipitates indicated a typical Ni-Al layered double hydroxide structures with 33.4–40.7% nickel and 6.3–7.0% aluminum depending on initial nickel concentration. The operation costs of energy and electrode consumption were 320–537 \$ t<sup>-1</sup> of removed nickel.

**Keywords:** Electrocoagulation – isotherm – kinetic – layered double hydroxides – mechanism – nickel removing

## 1. Introduction

In the production plant located in Punta-Gorda Cuba, the Ammoniacal Carbonate Leaching Technology is used for the selective recovering of nickel and cobalt from lateritic ore. In the distillation effluents a suspension of basic nickel carbonate is obtained.<sup>1</sup> After sedimentation of this suspension, the clear liquor contained several ionic species with composition according to the following proportions: 1.8 < Ni/S < 3.2, 1.5 < NH<sub>3</sub>/CO<sub>2</sub> < 2.0, 10.4 < CO<sub>2</sub>/S < 13.8 of the Ni(II)-NH<sub>3</sub>-CO<sub>2</sub>-SO<sub>2</sub>-H<sub>2</sub>O system. The temperature of the liquor is between 70 and 85 °C and the pH from 7.4 to 9.0.<sup>2</sup>

The dissolved nickel in the clear liquor reaches concentrations between 0.2 and 1.0 g L<sup>-1</sup> in the form of hydroxide and coordination compounds.<sup>1,2</sup> It precipitates with NH<sub>4</sub>HS in a piston flow reactor leading to nickel sulfide.<sup>3</sup> The reagents used in this process are toxic, corrosive and of high hazard for the environment. For these reasons, the possibility of substituting chemical precipitation by electrocoagulation (EC) process was analyzed in our previous study.<sup>4</sup>

The EC consists of the destabilization of suspended, emulsified or dissolved compounds in an electrolytic cell facilitating their removal.<sup>5</sup> In relation to the mechanisms of the process, the fundamental stages have been reported:<sup>6–12</sup>

- 1 – Electrolytic reactions on the surface of the electrodes.
- 2 – Formation of coagulants in the aqueous phase.
- 3 – Destabilization and adsorption of pollutants on coagulants (coagulation).
- 4 – Aggregation of destabilized particles and formation of flocs (flocculation).
- 5 – Removal of contaminating material by means of secondary treatment.

It also refers to the contribution of mechanisms functioning synergistically and benefit the removal efficiency such as: chemistry precipitation by the formation of the pollutant metal hydroxides, reduction of metal ions, non-metal anions and gases formation at the cathode surface, co-precipitation and complexation of anions and organic compounds.<sup>8,9,11,13</sup>

The parameters that influence the efficiency of the EC process can be classified into two categories: design parameters and operational parameters. The most important design parameters are related with material, shape, arrangement and spacing of electrodes, as well as type of power supply; either direct current (DC), alternating current (AC) or alternating pulsed current (APC). The operational parameters are current density, electrocoagulation time, aqueous solution pH, temperature, agitation speed, initial ions concentration and supporting electrolyte.<sup>4,7,8,10,13,14,15</sup>

The most favorable conditions for the nickel removal from Ni(II)-NH<sub>3</sub>-CO<sub>2</sub>-SO<sub>2</sub>-H<sub>2</sub>O system by EC using Al/Al pair electrodes were determined through a full-factorial experimental design.<sup>4</sup> The optimum efficiency of 95% was achieved for a current density of 9.8 mA cm<sup>-2</sup>, temperature of 60 °C, solution pH of 8.65 and 660 mg L<sup>-1</sup> of initial nickel concentration. This resulted in a specific energy consumption of 5.41 kWh per kg of Ni.

Many authors have identified the formation of Hydrotalcite-like layered double hydroxides (LDHs) during EC process. Zhao (2010) proposed the formation of Mg/Al-F-LDH as one of the mechanisms for EC defluoridation in systems containing both F<sup>-</sup> and Mg<sup>2+</sup>.<sup>16</sup> Mendoza, et al. (2018) in-situ synthesized Mg/Al-LDH using synthetic water under laboratory-scale conditions, with aluminum and AZ31 magnesium alloys electrodes at 5 mA cm<sup>-2</sup>, the coagulants were generated through electrochemical oxidation of the electrodes.<sup>17</sup> Jiang (2021) in-situ synthesized Zn/Al-LDH for the removal of strontium in a simulated liquid radioactive waste.<sup>18</sup> Finally, Ou (2021) fabricated Ni/Fe-LDH using nickel-plating wastewater.<sup>19</sup>

LDHs are represented by the general formula  $[M^{2+}_{1-x}M^{3+}_x(OH)_2]^{x+}(A^{n-})_{x/n}mH_2O$ , where M<sup>2+</sup> is a divalent cation (Mg<sup>2+</sup>, Ca<sup>2+</sup>, Mn<sup>2+</sup>, Co<sup>2+</sup>, Ni<sup>2+</sup>, Cu<sup>2+</sup>, Zn<sup>2+</sup>), M<sup>3+</sup>, is a trivalent cation (Al<sup>3+</sup>, Cr<sup>3+</sup>, Mn<sup>3+</sup>, Fe<sup>3+</sup>, Co<sup>3+</sup>, Ni<sup>3+</sup>), A<sup>n-</sup>, interlayer anion (Cl<sup>-</sup>, NO<sub>3</sub><sup>-</sup>, ClO<sub>4</sub><sup>-</sup>, CO<sub>3</sub><sup>2-</sup>, SO<sub>4</sub><sup>2-</sup>, S<sub>2</sub>O<sub>3</sub><sup>2-</sup> and other organic compounds), and x is the charge density for the molar ratio M<sup>3+</sup> (M<sup>2+</sup> + M<sup>3+</sup>)<sup>-1</sup> which varied from 0.2 and 0.35.<sup>20–31</sup> These compounds have been extensively investigated due to their improved

microstructure, increased active electrochemical sites and their wide applications.

In the case of Ni/Al-LDH, it has been reported as highly efficient in the adsorption of metals (Au, Cd, Cu, Pb, Se),<sup>28,32</sup> anions (F<sup>-</sup>, IO<sub>3</sub><sup>-</sup>)<sup>33,34</sup> and organic compounds.<sup>24–26,29,35,36</sup> Ni-based LDHs in the energy storage and conversion field are still limited by their intrinsically poor conductivity, aggregation, limited active sites and stability.<sup>23,31</sup> Ni/Al-LDH exhibits a specific capacitance 2128 F g<sup>-1</sup> at 1 A g<sup>-1</sup> and coulombic efficiency above 80% during 1000 cycles (Ni/Al:3).<sup>37,38</sup> In order to improve the electrochemical performance, nanostructured Ni/Al-LDH have been synthesized using different routes.<sup>23,39,40,41</sup> This compound, followed by controlled thermal decomposition, represents an appropriate material for the preparation of ceramic pigments with different properties.<sup>42</sup> Carbonate intercalated with a c-axis preferred orientation, show excellent anticorrosive performance with polarization current density of 10<sup>-9</sup> A cm<sup>-2</sup>.<sup>43</sup> It is active for the photocatalytic conversion of CO<sub>2</sub> to CO in water, under UV light irradiation,<sup>44</sup> and promising catalyst precursors for fine CO<sub>2</sub> removal from hydrogen-rich gas streams through the methanation reaction and methane dry reforming.<sup>45,46</sup> Moreover, the combination of nickel and aluminum finds applications in the production of superalloys (53.3 ≤ Ni ≤ 73.0%, 1.2 ≤ Al ≤ 6.0%) and permanent magnets (15 ≤ Ni ≤ 26%, 8 ≤ Al ≤ 12%).

It was assumed that the thermodynamics, kinetics, equilibrium analysis through adsorption isotherms, characterization of the adsorbent, and the analysis of chemical-physical interactions through Stern's electrical double layer model, coordination surface and the electrode processes, provide elements to propose the removal mechanism by electrocoagulation.<sup>30,47,48</sup>

The purpose of this work was to determine the reaction kinetics, the adsorption isotherm, the mechanism and the preliminary cost of operation for the nickel removing by electrocoagulation from the Ni(II)-NH<sub>3</sub>-CO<sub>2</sub>-SO<sub>2</sub>-H<sub>2</sub>O system, at different concentrations of dissolved nickel in the initial liquor. The resulted precipitate was characterized by ICP-OES, DXR, and FTIR in order to elucidate the removal mechanics.

## 2. Materials and Methods

### 2.1. Materials

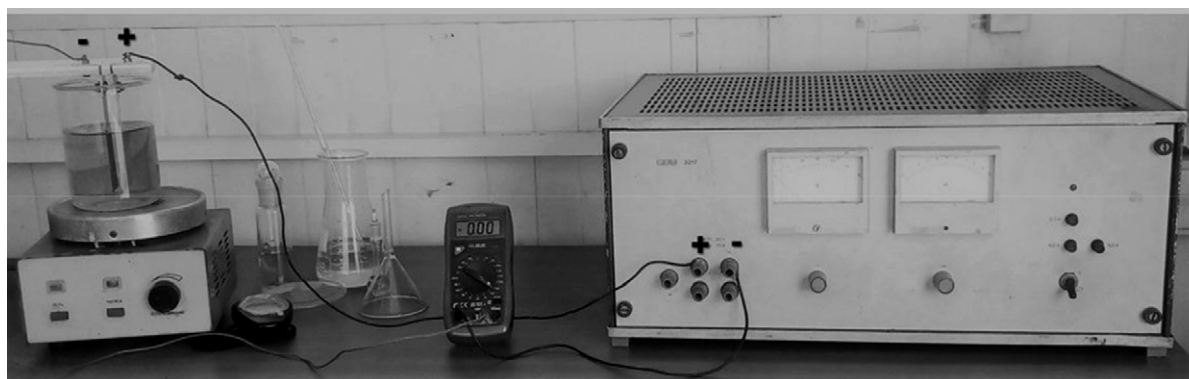
The liquor used in the electrocoagulation experiments was sampled spot in the distillation columns discharge at the production plant in Punta-Gorda Cuba. The pH was adjusted with ammonium carbonate solution (pH 11.7) or a mixture of hydrochloric and nitric acid. The initial nickel concentration was adjusted by dilution of the liquor using distilled water. The resulting concentrations for each sample are shown in Table 1. The material used as electrode was aluminum with a composition of 98.98% Al, 0.5% Mg, 0.33% Fe and 0.114% Si.

**Table 1.** Characterization of the liquor fed to the electrocoagulation cell

Ni (mg L <sup>-1</sup> )	NH <sub>3</sub> (g L <sup>-1</sup> )	CO <sub>2</sub> (g L <sup>-1</sup> )	S (g L <sup>-1</sup> )	[SO <sub>4</sub> ] <sup>2-</sup> (g L <sup>-1</sup> )
293	0.51	0.33	2.70	3.59
379	0.92	0.50	2.14	3.52
474	1.10	0.25	2.43	3.53
505	1.08	0.29	2.31	3.46
646	1.40	0.30	2.73	5.70
775	1.20	0.35	3.00	3.46
953	1.21	0.35	3.47	6.83
1356	4.70	3.27	3.20	6.82

## 2. 2. Methods

EC experiments were done in an electrochemical cell consisted of a discontinuous cylindrical glass reactor, with a useful capacity of 500 mL. It was equipped with a pair of flat electrodes, arranged vertically, in parallel, 10 mm spacing, submerged 57 mm in the liquor with a total area of  $5.6 \cdot 10^{-3} \text{ m}^2$  and an effective area of  $4.6 \cdot 10^{-3} \text{ m}^2$ . The cell was alimanted by Direct current source of 0.01 - 30 V, maximum amperage 10 A, power supply  $220 \pm 10\%$ , 50 Hz and 250 W. The current density was monitored using a multimeter. The positive terminal of the current source was connected directly to the electrode (anode) and the negative terminal to the multimeter and from this (COM) to the cathode. The source allowed to regulate the voltage to keep the electric current amperage constant (Fig.1).

**Figure 1.** Experimental installation of electrocoagulation

The overflow liquor from the basic nickel carbonate settler tank was first adjusted to the desired pH using a Philips PW-9420 pH meter and the temperature was controlled ASCON KR3 controller. The it was fed to the reactor and continually stirred at 100 rpm using a hot plate stirrer with thermal control.

The nickel removal experiments by electrocoagulation consisted in assuming the current density of  $9.8 \text{ mA cm}^{-2}$ , pH 8.6, temperature  $60^\circ \text{C}$  and electrolysis time 30 min, according to the most favorable conditions for the

nickel removal from the Ni(II)-NH<sub>3</sub>-CO<sub>2</sub>-SO<sub>2</sub>-H<sub>2</sub>O system.<sup>4</sup>

The nickel removal, electrode mass and electric power consumption were determined at different concentration of nickel [Ni] dissolved in the initial liquor.

After each experiment, samples were removed from the reactor to a volumetric flask. Then, they were covered and allowed to settle for 24 h. Finally, the aliquot required for chemical analysis was pipetted. Residual nickel concentration was measured by atomic absorption spectroscopy (AAS) using a SP-9 Spectrophotometer.

The preparation of the electrodes consisted of polishing the surface with coarse and fine sandpaper, and washing with distilled water. After electrocoagulation, they were cleaned with phosphoric acid solution, sodium hexametaphosphate and distilled water until the deposited layer was removed. Later these electrodes were weighed. Each anode was used for at most two experiments. an Optical emission spectrometer GS 1000-II was used to characterize the electrodes.

The resulting precipitate was characterized using Inductively Coupled Plasma Optical Emission Spectrometry (ICP-OES), Spectro ARCOS FHX. X-ray diffraction (XRD), Bruker D8 Advance equipment, Cu anode lamp (CuK $\alpha$  radiation) and wavelength  $1.5405 \text{ \AA}$ , constant scanning at a measurement interval of  $2\theta$  between  $5 - 6$  to  $100^\circ$  with a step of  $0.05^\circ$  measured every 5 min, and Fourier transform infrared spectroscopy (FTIR), Nicolet 6700 Spectrometer, range between  $4000$  and  $400 \text{ cm}^{-1}$ , resolution of  $4 \text{ cm}^{-1}$ .

## 2. 3. Adsorption Kinetics Models

The adsorption capacity ( $Q_t$ ) or amount of adsorbate adsorbed per adsorbent unit ( $\text{mg g}^{-1}$ ) was determined by Eq. (1).

$$Q_t = (C_0 - C_t) \cdot \frac{V}{\Delta M_F} \quad (1)$$

where  $C_0$  ( $\text{mg L}^{-1}$ ) is the initial concentration of nickel,  $C_t$  ( $\text{mg L}^{-1}$ ) is the concentration of nickel in the liquid phase in each time interval,  $V$  (L) is the volume of solution,  $\Delta M_F$

(g) is the amount of metal in solution according to Faraday's Law, Eq. (2).

$$\Delta M_F = \frac{I \cdot M \cdot t}{n \cdot F} \quad (2)$$

where,  $I$  (A) is the current intensity,  $M$  the molecular weight of [Al] 26.98 g mol<sup>-1</sup>,  $t$  (s) the electrocoagulation time,  $n$  number of electrons for aluminum (3),  $F$  Faraday constant (96487 C mol<sup>-1</sup>).

When the duration of the process is long enough,  $Q_t$  is constant and determines the charge or adsorption capacity ( $Q_e$ , mg L<sup>-1</sup>) corresponding to the concentration at equilibrium ( $C_e$ , mg L<sup>-1</sup>).

Kinetics data were correlated to pseudo-second order, Avrami, Elovich, Bangham and Weber-Morris intra-particle diffusion models.<sup>48,49,50</sup> The parameters were adjusted with StatGraphic 5.1 and Microsoft Excel and the best quality of fit was decided by the highest coefficient of determination ( $R^2$ ).

The pseudo-second order kinetic model is presented by Eq. (3) and its linear form is given by Eq. (4):

$$\frac{dQ_t}{dt} = k_2 \cdot (Q_e - Q_t)^2 \quad (3)$$

$$\frac{t}{Q_t} = \frac{1}{k_2 \cdot Q_e^2} + \frac{1}{Q_e} \cdot t = \frac{1}{h} + \frac{1}{Q_e} \cdot t \quad (4)$$

where  $k_2$  (g mg<sup>-1</sup> min<sup>-1</sup>) is the adsorption rate constant while  $h$  (g<sup>-1</sup> mg min<sup>-1</sup>) is assumed as the initial reaction rate.

Avrami's fractional kinetic model is based on the Johnson-Mehl-Avrami-Erofeev-Kolmogorov (JMAEK) theory,<sup>51</sup> and consist of phase transformations via homogeneous and spontaneous nucleation and growth of a crystal as a function of crystallization time. Although it has been assumed as an empirical model for the analysis of adsorption kinetic data.<sup>47</sup> It is represented by Eq. (5), integrated form (6) and linearized form (7).

$$\frac{dQ_t}{dt} = k_{av}^{n_{av}} \cdot t^{n_{av}-1} \cdot (Q_e - Q_t) \quad (5)$$

$$Q_t = Q_e \cdot \{1 - \exp[-(k_{av} \cdot t)^{n_{av}}]\} \quad (6)$$

$$\ln \left[ -\ln \left( 1 - \frac{Q_t}{Q_e} \right) \right] = n_{av} \cdot \ln k_{av} + n_{av} \cdot \ln t \quad (7)$$

where,  $k_{av}$  (min<sup>-1</sup>) is the kinetic constant or global constant,  $n_{av}$  (/) fractional reaction order, which refers to the nucleation, growth and orientation of crystallites or possible changes in the adsorption mechanism.

The Elovich kinetic model in its nonlinear and linear form is expressed by the Eq. (8) and (9), respectively.

$$\frac{dQ_t}{dt} = \alpha \cdot \exp(\beta \cdot Q_t) \quad (8)$$

$$Q_t = \frac{1}{\beta} \cdot \ln(\alpha \cdot \beta) + \frac{1}{\beta} \cdot \ln(t) \quad (9)$$

where,  $\alpha$  (mg g<sup>-1</sup> min<sup>-1</sup>) is a constant related to adsorption rate,  $\beta$  (g mg<sup>-1</sup>) is a constant which depicts the extent of surface coverage.

Bangham's equation was used to evaluate whether the adsorption is pore-diffusion controlled, it is represented by Eq. (10).

$$\ln \ln \left( \frac{C_0}{C_0 - Q_t \cdot W} \right) = \ln \left( k_B \cdot W \cdot \frac{1}{V} \right) + \alpha \cdot \ln t \quad (10)$$

where,  $C_0$  (mg·L<sup>-1</sup>) is initial concentration,  $V$  (mL) volume of the solution,  $W$  (g L<sup>-1</sup>) weight of the adsorbent,  $k_B$  (mL g<sup>-1</sup> L) and  $\alpha$  (/) the constants.

The Weber and Morris intraparticle diffusion model can be expressed by Eq. (11) and its linear form by Eq. (12).

$$\frac{dQ_t}{dt} = \frac{1}{2} \cdot k_3 \cdot t^{-1/2} \quad (11)$$

$$Q_t = k_3 \cdot \sqrt{t} + c \quad (12)$$

where,  $k_3$  (mg g<sup>-1</sup> min<sup>-0.5</sup>) the intra-particle diffusion rate constant,  $c$  (mg g<sup>-1</sup>) is the intercept.

In addition, the goodness of fit of several integral equations for the reaction kinetics was evaluated, in order to investigate the controlling mechanism in the nickel removing by electrocoagulation, regarding the individual or simultaneous contribution of the resistances: external diffusion, internal diffusion, nucleation, chemical reaction, autocatalysis (Table 2).<sup>52,53,54</sup> The algorithm followed consisted of assuming a controlling mechanism, calculating the fraction of incomplete conversion and adjusting the model with StatGraphic 5.1 and Microsoft Excel, the best quality of fit was decided by the highest coefficient of determination ( $R^2$ ) and the lowest estimated error, Eq. (13).

$$I = 1 - x = 1 - \left( \frac{C_0 - C_t}{C_0} \right) \quad (13)$$

where,  $I$  (/) fraction of incomplete conversion and  $x$  fractional conversion (/).

## 2. 4. Adsorption Isotherm Models

The Langmuir, Freundlich, Temkin, Toth, Koble – Carrigan and Redlich – Peterson adsorption isotherm models were evaluated.<sup>10,25,35,48,49,50</sup>

Langmuir's isotherm in the linear form is shown in Eq. (29), and the equilibrium parameter is defined in Eq. (30).

$$\frac{C_e}{Q_e} = \frac{C_e}{q_m} + \frac{1}{q_m \cdot K_L} \quad (29)$$

$$R_L = \frac{1}{1 + K_L \cdot C_0} \quad (30)$$

where,  $q_m$  (mg g<sup>-1</sup>) is the maximum monolayer adsorption capacity,  $K_L$  (L mg<sup>-1</sup>) the Langmuir adsorption constant that defines the affinity of the adsorbate for the adsorbent,

**Table 2.** Models used in the kinetic analysis to investigate the controlling mechanism in the nickel removing by electrocoagulation

Name	$g(I, x)$	Eq.
<b>External diffusion</b>		
1-D	$1 - I$	(14)
2-D	$1 - I^{\frac{1}{2}}$	(15)
3-D	$1 - I^{\frac{1}{3}}$	(16)
Boundary layer	$1 - I^{\frac{2}{3}}$	(17)
<b>Internal diffusion</b>		
1-D	$x^2$	(18)
2-D	$I \cdot \ln(I) + x$	(19)
3-D (Jander)	$\left(1 - I^{\frac{1}{3}}\right)^2$	(20)
3-D (Ginstling – Brounshtein)	$1 - \frac{2}{3} \cdot x - I^{\frac{2}{3}}$	(21)
<b>Nucleation</b>		
Avrami	$[-\ln(I)]^{\frac{1}{2}}$	(22)
Erofeév	$[-\ln(I)]^{\frac{1}{3}}$	(23)
Avrami – Erofeév	$\ln \cdot \left[ \ln \left( \frac{1}{I} \right) \right]$	(24)
JMAEK	$5 \cdot [-\ln(I)]^{\frac{1}{5}}$	(25)
<b>Autocatalysis</b>		
Roginskii-Shultz	$\frac{2}{x^3} \cdot \frac{2}{I^3}$	(26)
Kolmogorov	$\frac{2}{x^3} \cdot \frac{4}{I^3}$	(27)
<b>Chemical reaction</b>		
Power law	$1 - I^{\frac{1}{3}}$	(28)

and  $R_L$  is the equilibrium parameter of the Langmuir's isotherm.

Freundlich's isotherm is applicable to adsorption processes that occur on heterogenous surfaces, its linear form is expressed by Eq. (31).

$$\ln Q_e = \frac{1}{n} \cdot \ln C_e + \ln K_f \quad (31)$$

where,  $K_f$  ( $\text{mg g}^{-1}/(\text{mg L}^{-1})^n$ ) is related to the adsorption capacity and  $n$  (dimensionless) is related to the adsorption intensity; it also indicates the relative distribution of the energy and the heterogeneity of the adsorbate sites.

Temkin isotherm model takes into account the effects of indirect adsorbate/adsorbate interactions on the adsorption process, Eq. (32) and (33).

$$Q_e = B \cdot \ln C_e + B \cdot \ln K_T \quad (32)$$

$$b_T = \frac{R \cdot T}{B} \quad (33)$$

where,  $b_T$  ( $\text{J mol}^{-1}$ ) is Temkin constant which is related to the heat of sorption and  $K_T$  ( $\text{L mg}^{-1}$ ) is Temkin isotherm constant,  $T$  (K) the absolute temperature,  $R$  is the gas constant  $8.31 \text{ J mol}^{-1} \text{ K}^{-1}$ .

The Toth's isotherm is an empirical modification of the Langmuir equation, Eq. (34) and (35).

$$\frac{Q_e}{q_m} = \theta = \frac{K_h \cdot C_e}{[1 + (K_h \cdot C_e)^n]^{1/n}} \quad (34)$$

$$\ln \frac{Q_e^n}{q_m^n - Q_e^n} = n \cdot \ln(K_h) + n \cdot \ln(C_e) \quad (35)$$

where,  $K_h$  ( $\text{mg g}^{-1}$ ) is Toth isotherm constant and  $n$  ( $\text{mg g}^{-1}$ ) is the Toth constant.

Koble-Carrigan isotherm model is a three-parameter equation which incorporates both Langmuir and Freundlich isotherms for representing equilibrium adsorption data, Eq. (36).

$$\frac{1}{Q_e} = \left( \frac{1}{A_k \cdot C_e^n} \right) + \frac{B_k}{A_k} \quad (36)$$

where,  $A_k$  ( $\text{L}^n \text{ mg}^{1-n} \text{ g}^{-1}$ ),  $B_k$ , ( $\text{L mg})^n$ ,  $n$  (dimensionless) are Koble - Carrigan's isotherm constants.

The Redlich-Peterson isotherm is a mix of the Langmuir and Freundlich isotherms. Its linear form can be expressed by the Eq. (37).

$$\ln \left( \frac{C_e}{Q_e} \right) = \beta \cdot \ln(C_e) - \ln K_R \quad (37)$$

where,  $K_R$  ( $\text{L g}^{-1}$ ) is Redlich-Peterson isotherm constant,  $\beta$ (dimensionless) is constant.

The verification of the consistency of adsorption models and the theoretical assumptions of adsorption models was made by Average Relative Error (ARE) and Marquardt's Percent Standard Deviation (MPSD) calculated by Eq. (38) and (39) respectively.<sup>35</sup>

$$ARE = \frac{100}{n} \cdot \sum_{i=1}^n \left[ \left( \frac{Q_{e,i,cal} - Q_{e,i,exp}}{Q_{e,i,exp}} \right) \right] \quad (38)$$

$$MPSD = \sqrt{\frac{1}{n-P} \cdot \sum_{i=1}^n \left[ \left( \frac{Q_{e,i,cal} - Q_{e,i,exp}}{Q_{e,i,exp}} \right) \right]^2} \quad (39)$$

where,  $n$  is the number of data points and  $P$  the number of parameters.

## 2. 5. Operating Cost Estimate

The operating cost per kg of nickel removed was calculated by Eq. (40).

$$C_{op} = [a \cdot C_{en} + b \cdot \Delta M_{exp}] \cdot \frac{1}{m_{Ni}} \quad (40)$$

where,  $C_{op}$  ( $\text{\$ kg}^{-1}$ ) operating cost,  $a$  ( $\text{\$ 0.090 / kWh}$ ) cost



of electricity,  $C_{en}$  (kWh) power consumption,  $b$  (1.445 \$  $\text{kg}^{-1}$ ) cost of the aluminum electrode;  $\Delta M_{exp}$  (g) experimental weight loss of the electrodes,  $m_{Ni}$  (kg) mass of nickel removed.

After transforming, the operating cost can be expressed as Eq. (41):

$$C_{op} = \left[ a \cdot U \cdot I \cdot t \cdot \frac{1}{60} + b \cdot \Delta M_{exp} \right] \cdot \frac{1}{[Ni] \cdot V \cdot x_{Ni}} \quad (41)$$

where,  $U$  (V) voltage,  $I$  (A) current intensity,  $t$  (min) electrocoagulation time,  $[Ni]$  ( $\text{g L}^{-1}$ ) initial concentration of dissolved nickel,  $V$  (0.5 L) useful volume of the cell,  $x_{Ni}$  fraction converted or nickel removing.

The current efficiency ( $\eta$ ) and the specific energy consumption per kg electrode dissolved (SEC,  $\text{kW-h kg}^{-1}$ ) were determined by Eq. (42) and (43), respectively.

$$\eta = \frac{\Delta M_{exp}}{\Delta M_F} \quad (42)$$

$$SEC = \frac{n \cdot F \cdot U}{3600 \cdot M \cdot \eta} \quad (43)$$

### 3. Results and Discussion

#### 3.1 Adsorption Kinetics

The study of adsorption kinetics provides information on the mechanisms involved in the process. For the experimental conditions of 9.8  $\text{mA cm}^{-2}$ , 60 °C, pH 8.6, 30 min of electrolysis and initial concentration  $293 \leq [Ni] \leq 953 \text{ mg L}^{-1}$ , the nickel removal efficiency was between 99.0  $\leq X \leq 99.7\%$  (Table 3).

**Table 3.** Efficiency of nickel removal by electrocoagulation

Ni ( $\text{mg L}^{-1}$ )	293	379	474	505	646	775	953	1356 <sup>1</sup>
X (%)	99.7	99.3	99.3	99.5	99.0	99.0	99.0	97.7

<sup>1</sup>40 min of electrolysis

A model was obtained that relates the conversion time ( $t$ ) as a function of the fractional conversion ( $x$ ), nickel initial concentration ( $\text{mg L}^{-1}$ ), mass of aluminum  $[Al]$  and the coefficients or constants  $a$ ,  $b$ ,  $c$ ,  $d$ ,  $e$ ,  $f$ , Eq. (44).

$$t = \left\{ \begin{array}{l} a \cdot [1 - (1 - x)^{\frac{1}{2}}] \\ + b \cdot [5 \cdot [-\ln(1 - x)]^{\frac{1}{5}}] \\ + c \cdot [1 - (1 - x)^{\frac{1}{3}}] \\ + d \cdot [x^{\frac{2}{3}} \cdot (1 - x)^{\frac{2}{3}}] \end{array} \right\} \cdot [Ni]^e \cdot [Al_t]^f \quad (44)$$

From Faraday's law to determine the mass of dissolved aluminum, Eq. (45) is obtained.

$$t^n = \left\{ \begin{array}{l} a \cdot [1 - (1 - x)^{\frac{1}{2}}] \\ + b \cdot [5 \cdot [-\ln(1 - x)]^{\frac{1}{5}}] \\ + c \cdot [1 - (1 - x)^{\frac{1}{3}}] \\ + d \cdot [x^{\frac{2}{3}} \cdot (1 - x)^{\frac{2}{3}}] \end{array} \right\} \cdot [Ni]^e \cdot k_{Al} \quad (45)$$

where, the constant ( $n$ ) refers to the conversion time, the resistance coefficient to external diffusion ( $a$ ), nucleation ( $b$ ), chemical reaction ( $c$ ) and its autocatalytic contribution ( $d$ ), the nickel exponent ( $e$ ), and the coefficient ( $k_{Al}$ ) for the estimate of dissolved aluminum by Faraday's Law.

The parameters of the conversion time (CVT) model (45) are shown in Table 4 for the concentration ranges:  $293 \leq Ni \leq 646 \text{ mg L}^{-1}$ ;  $775 \leq Ni \leq 1356 \text{ mg L}^{-1}$ ;  $293 \leq Ni \leq 1356 \text{ mg L}^{-1}$ . It reflects between 99.18 and 99.88% of the variability in nickel removal. The coefficient of determination ( $R^2$ ) adjusted by the degrees of freedom (g.l.) allows compare this model with others with the same number of independent variables.

CVT model expresses that the nickel removing is determined by the combined effect of the resistances of the mechanisms:

- External diffusion ( $a$ ), in the film or boundary layer to the adsorbent surface, by the two-dimensional (2-D) diffusion model.
- Nucleation and crystallization ( $b$ ), by the JMAEK equation, which refers to the random formation and growth of the adsorption surface due to the hydrolysis and polymerization reactions of aluminum, giving rise to the species monomeric, polymeric, oligomeric aluminum and  $\text{Al(OH)}_3$ , where the contaminants adsorption occurs ( $\text{Ni}^{2+}$ ,  $\text{S}_x\text{O}_y^{z-}$ ,  $\text{CO}_3^{2-}$ ,  $\text{NH}_3$ ) in the active centers by electrostatic interaction and coordination surface, and subsequent crystallization; in competition with that nucleation that occurs when the deposits grow on the electrodes.

**Table 4.** CVT model constants by Eq. (45) and quality of fit

	$n$	$a$	$b$	$c$	$d$	$e$	$k_{Al} \cdot 10^{-2}$	$R^2$	$R^2$ (g. l.)
<sup>1</sup>	0.2938	8.8582	1.1429	12.4190	10.4680	0.3054	1.4834	99.41	99.18
<sup>2</sup>	0.3029	0.9418	1.7497	16.7428	18.7548	0.2812	1.5661	99.91	99.88
<sup>3</sup>	0.2985	9.9782	2.6673	13.2262	20.1508	0.2337	1.5250	99.35	99.24

<sup>1</sup>[Ni] between 293 and 646  $\text{mg L}^{-1}$ ; <sup>2</sup>[Ni] 775 - 1356  $\text{mg L}^{-1}$ ; <sup>3</sup>[Ni] 293 - 1356  $\text{mg L}^{-1}$ .

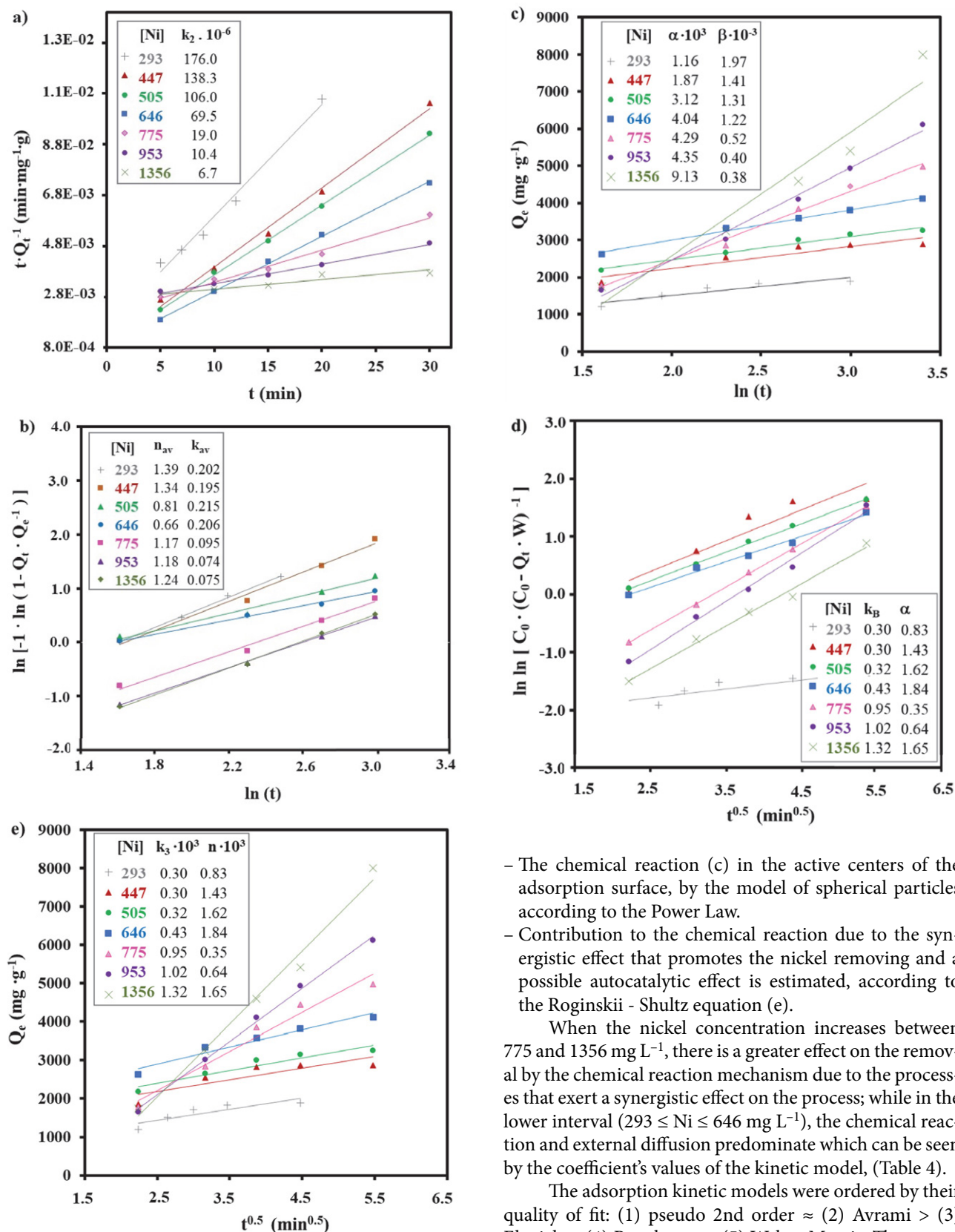


**Figure 2.** Adsorption of nickel with the electrode pair Al/Al at 9.8 mA cm<sup>-2</sup>, 60 °C, pH 8.6, a) Pseudo-second order kinetic model, b) Avrami's model, c) Elovich's model, d) Bangham's model, e) Weber and Morris's model.

- The chemical reaction (c) in the active centers of the adsorption surface, by the model of spherical particles according to the Power Law.
- Contribution to the chemical reaction due to the synergistic effect that promotes the nickel removing and a possible autocatalytic effect is estimated, according to the Roginskii - Shultz equation (e).

When the nickel concentration increases between 775 and 1356 mg L<sup>-1</sup>, there is a greater effect on the removal by the chemical reaction mechanism due to the processes that exert a synergistic effect on the process; while in the lower interval (293 ≤ Ni ≤ 646 mg L<sup>-1</sup>), the chemical reaction and external diffusion predominate which can be seen by the coefficient's values of the kinetic model, (Table 4).

The adsorption kinetic models were ordered by their quality of fit: (1) pseudo 2nd order ≈ (2) Avrami > (3) Elovich ≈ (4) Bangham >> (5) Weber-Morris. These were used to validate the conversion time model, Eq. (45).

The pseudo-second order (PSO) model showed a high quality of fit (96.1 ≤ R<sup>2</sup> ≤ 99.8%). As the initial nickel

concentration increased, (Fig.2 a), the rate constant  $k_2$  ( $\text{g mg}^{-1} \text{min}^{-1}$ ) decreased. This result can be attributed to the progressive saturation of the active sites in the adsorption surface with the cation  $[\text{Ni}^{2+}]$  and causes an increase in the necessary electrocoagulation time.

The Avrami's model was representative of dates because of its high quality of fit. The removal rate ( $k_{av}$ ) for initial nickel concentration between 293 and  $646 \text{ mg L}^{-1}$  was assumed constant and equal to  $0.20 (+/- 0.01) \text{ min}^{-1}$  ( $97.94 \leq R^2 \leq 99.62\%$ ); but in the range of 775 to  $1356 \text{ mg L}^{-1}$  the kinetic behavior changed and  $k_{av}$  decreased between 50 and 60% ( $98.82 \leq R^2 \leq 99.75\%$ ) due to the increase in adsorbate concentration. It was regarded that in the first interval the contribution of the mechanism of external diffusion influenced in the higher value of  $k_{av}$  while in the second interval  $k_{av}$  was lower under the mechanism control the chemical reaction resistance (Fig.2 b) (Table 4).

With respect to the lines slopes that reflect the fractional order ( $n_{av}$ ) of Avrami's model, in the interval  $293 \leq [\text{Ni}^{2+}] \leq 646 \text{ mg L}^{-1}$  decreased from 1.39 to 0.66 with the increase of the cation  $[\text{Ni}^{2+}]$ . This is attributed to the progressive saturation of the active adsorption sites because there is a greater amount of adsorbate that reaches the adsorbent surface and therefore a longer electrocoagulation time is required. Also, the interactions augment and the tendency to change the controlling mechanism. In the interval of  $775 \leq [\text{Ni}^{2+}] \leq 1356 \text{ mg L}^{-1}$ , the exponential constant ( $n_{av}$ ) increased to 1.21 ( $+/- 0.05$ ). According to Eq. (44), it may be associated with the controlling mechanism of chemical reaction resistance.

The Elovich's model ( $95.5 \leq R^2 \leq 99.62\%$ ) suggests that the adsorbent active sites are heterogeneous and therefore exhibit different activation energies. This suggests that more than one mechanism incises the removal process such as transport in the solution phase (bulk diffusion) and surface diffusion.<sup>48,49,50</sup> The initial rate kinetic constant ( $\alpha$ ) ( $\text{mg g}^{-1} \text{min}$ ) increased proportionally to the concentration of  $[\text{Ni}^{2+}]$ . In addition, the constant ( $\beta$ ) ( $\text{g mg}^{-1}$ ) related to the chemisorption activation energy and the extension of the adsorption surface, decreased with the increase of cation  $[\text{Ni}^{2+}]$  throughout the interval (Fig.2 c).

The Bangham and Weber-Morris's models were less representatives of the data due to their lower quality of fit, in correspondence with the CVT model, Eq. (45) where internal diffusion resistance could be omitted from the process due to low statistical significance. The Bangham's model is applied to investigate pore activation for adsorbate diffusion. The fit quality was obtained in the interval  $95.0 \leq R^2 \leq 99.3\%$ , which indicates that both intra-particle diffusion and pore diffusion are not controlling in the process (Fig.2 d).<sup>50</sup> With regard to the Weber and Morris's model, it reflects the influence of external mass transfer followed by intra-particle diffusion in pores of different sizes.<sup>48,50</sup> The plot of  $Q_t$  versus  $t^{0.5}$  did not result in a linear relationship with intercept at the origin of coordinates ( $86.5 \leq R^2 \leq 99.1$ ) (Fig.2 e). This result suggests that diffu-

sion is not a limiting step in the mechanism. Furthermore, the intra-particle kinetic rate constant was not directly proportional to the adsorbate concentration, suggesting that the process is not controlled by adsorption in the pores.

### 3. 2 Nickel Adsorption Isotherms

The equilibrium concentration ( $C_e$ ,  $\text{mg L}^{-1}$ ) corresponding to each initial nickel concentration ( $C_0$ ,  $\text{mg L}^{-1}$ ), and the equilibrium adsorption capacity ( $Q_e$ ,  $\text{mg g}^{-1}$ ) were determined. From Fig.3 it can be seen that by increasing the initial concentration, the adsorption capacity at equilibrium increased. For  $[\text{Ni}^{2+}] > 953 \text{ mg L}^{-1}$ , the formation of a plateau was obtained, which indicates saturation of the adsorption sites and a decrease in the removal efficiency at the experimental conditions studied.

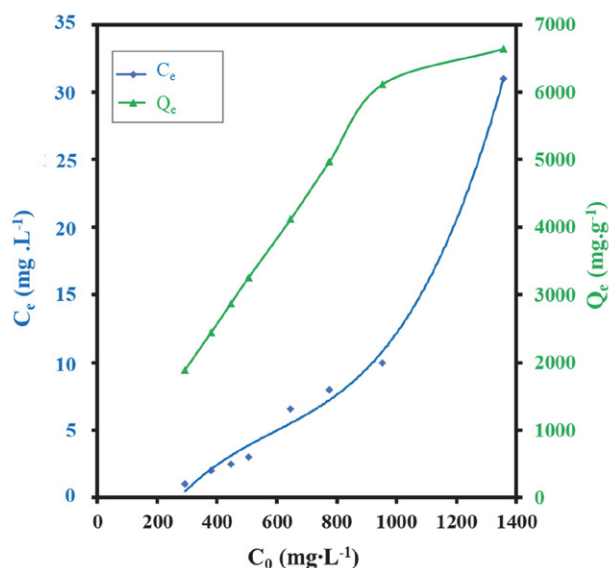


**Figure 3.** Equilibrium concentration ( $C_e$ ) and adsorption capacity ( $Q_e$ ) versus the initial concentration ( $C_0$ ) for nickel removing at  $9.8 \text{ mA cm}^{-2}$ ,  $60^\circ \text{C}$  and  $\text{pH } 8.6$ .

Table 5 shows the isotherm constants for the adsorption of  $\text{Ni(II)}$  calculated for each isotherm model. That table indicates that the order of goodness-of-fit ( $R^2$ ) of the adsorption isotherm models was: Langmuir ( $99.3\%$ )  $>$  Redlich - Peterson ( $97.3\%$ )  $>$  Koble - Carrigan ( $96.1\%$ )  $\approx$  ToTh ( $96.1\%$ )  $>$  Temkin ( $93.8\%$ )  $\approx$  Freundlich ( $93.7\%$ ).

The Langmuir isotherm was more representative of the data, this presented the highest quality of fit determined by the coefficient of determination ( $R^2$ ), the lower ARE 7.6 and MPSD 0.013. This result suggests monolayer adsorption in a specific number and fixed of accessible sites on the adsorbent surface, all active sites have the same energy. Once an adsorbate occupies a site, no farther adsorption can occur on that site and there is not interaction

between adsorbate species.<sup>48,49,50</sup> The maximum adsorption capacity ( $q_m$ ) was 7519 mg g<sup>-1</sup>, the constant ( $K_L$ ) was 0.216 L mg<sup>-1</sup> and the equilibrium parameter  $0.003 \leq R_L \leq 0.013$ .

The Redlich-Peterson's isotherm ( $K_R$  4.84 10<sup>-4</sup> L g<sup>-1</sup>; beta-β 0.61) and the Koble-Carrigan's isotherm ( $A_k$  1429 L<sup>n</sup> mg<sup>1-n</sup> g<sup>-1</sup>,  $B_k$  0.14 (L mg)<sup>n</sup>, n 1.08) refers that adsorption is a mixture (Langmuir and Freundlich) and not precisely the ideal adsorption monolayer. While the Toth's isotherm ( $K_h$  0.251 mg g<sup>-1</sup>, n 5.5 mg g<sup>-1</sup>) is a modification of the Langmuir's equation and suggest a heterogeneous adsorption (n > 1).

**Table 5.** Isotherm constants for the adsorption of Ni(II)

Parameter	Value
<b>Langmuir</b>	
$q_m$ (mg g <sup>-1</sup> )	7519
$K_L$ (L mg <sup>-1</sup> )	0.216
$R^2$	99.30
ARE	7.60
MPSD	0.013
<b>Redlich - Paterson</b>	
$K_R$ (L g <sup>-1</sup> )	4.84 10 <sup>-4</sup>
(/)	0.61
$R^2$ (/)	97.30
ARE	8.50
MPSD	0.017
<b>Koble - Carrigan</b>	
$A_k$ (L <sup>n</sup> mg <sup>1-n</sup> g <sup>-1</sup> )	1429
$B_k$ (L mg) <sup>n</sup>	0.14
n (/)	1.08
$R^2$ (/)	96.10
ARE	8.52
MPSD	0.026
<b>Toth</b>	
$q_m$ (mg g <sup>-1</sup> )	6650
$K_h$ (mg g <sup>-1</sup> )	0.251
n (mg g <sup>-1</sup> )	5.50
$R^2$ (/)	96.10
ARE	10.00
MPSD	0.081
<b>Temkin</b>	
$K_T$ (L mg <sup>-1</sup> )	2.88
$b_T$ (J mol <sup>-1</sup> )	1.79
$R^2$ (/)	93.80
ARE	8.30
MPSD	0.015
<b>Freundlich</b>	
n (/)	2.51
$K_f$ (mg g <sup>-1</sup> )/(mg L <sup>-1</sup> ) <sup>n</sup>	2001
$R^2$ (/)	93.70
ARE	8.31
MPSD	0.015

The Temkin's model assumes linear rather than logarithm decrease of heat of adsorption while ignoring extremely low and very high concentration. It also assumes uniform distribution of bounding energy up to some maximum bonding energy.<sup>35,50</sup> The heat of adsorption,  $b_T$ , is equal to 1.79 J mol<sup>-1</sup> and  $K_T$  was 2.88 L mg<sup>-1</sup>.

Eventually, the lower value of the determination coefficient corresponded to the Freundlich's isotherm, which assumes a heterogeneous distribution of active sites and energy on the surface, applicable to multilayer adsorption.<sup>48,50</sup>  $K_f$  was 2001 (mg g<sup>-1</sup>)/(mg L<sup>-1</sup>)<sup>n</sup> and n was 2.51.

Thus, the kinetic and equilibrium analyses suggest the control of chemisorption on a monolayer, at a fixed and specific number of accessible sites on the adsorbent surface. Although, it does not specifically follow the ideal adsorption monolayer at identical sites. The interaction between the molecules is not neglected, due to the action of electrostatic forces and exchange reactions in the active sites of the coordination surface. In addition, the transport of solute through the internal structure of the adsorbent pores and the diffusion in the solid are neglected.

### 3. 3 Analysis of the Precipitate

In order to investigate the nickel removal mechanism by electrocoagulation the precipitate was analyzed. The ICP-OES, DXR and FTIR analysis showed the formation of Ni/Al layered double hydroxide [Ni/Al-LDH] intercalated by [NH<sub>3</sub>], [SO<sub>4</sub><sup>2-</sup>] and [CO<sub>3</sub><sup>2-</sup>] as the main product, and accompanied by phases impurities.

From XRD patterns (Fig. 4a), the largest diffraction peaks were obtained at 2θ (2θ) Bragg angles of 10.745°, 22.101°, 34.922° and 61.067°, which are assigned to the crystalline planes, according to the Miller indices (hkl): (003), (006), (012), (110) respectively, are also of interest at 46.43° (018) and 72.676° (119). These diffraction peaks are indexed on a hexagonal system with rhombohedral symmetry, special group R-3m (polytype of three layers). The presence of 0kl peaks anticipates the presence of stacked layers (JCPDS file 15-0087).<sup>22,27,28,34,39,55</sup>

The XRD pattern also showed phases impurities. By comparison of the characteristic reflection pattern in Fig. 4a to a reference library of samples, the low intensity peaks can be attributed to the bayerite polymorphs Al(OH)<sub>3</sub> and aluminum hydroxide or gibbsite [γ-Al(OH)<sub>3</sub>], (JCPDS 33-0018, JCPDS 20-0011, JCPDS 24-0006).<sup>15,40,56</sup> Also nickel hydroxide [Ni(OH)<sub>2</sub>] indexed to the hexagonal [β-Ni(OH)<sub>2</sub>], the [Ni(OH)<sub>2</sub>·0.75H<sub>2</sub>O], nickel oxy-hydroxides corresponding to [β-NiOOH] and [γ-NiOOH] phases can be identified (JCPDS 14-0117, JCPDS 38-0715, JCPDS 06-0141, JCPDS 06-0075).<sup>57,58,59–61</sup> The presences of nickel aluminate were also identified: [NiAl<sub>2</sub>O<sub>4</sub>], [NiAl<sub>26</sub>O<sub>40</sub>], [NiAl<sub>32</sub>O<sub>49</sub>] and [Ni<sub>2</sub>Al<sub>18</sub>O<sub>29</sub>] (JCPDS 10-0339, JCPDS 20-0776, JCPDS 20-0777, JCPDS 22-0451).<sup>62,63</sup> These phases may be a consequence of the decrease in pH during the process from 8.53 (+/-0.07) to 8.35 (+/-0.08).

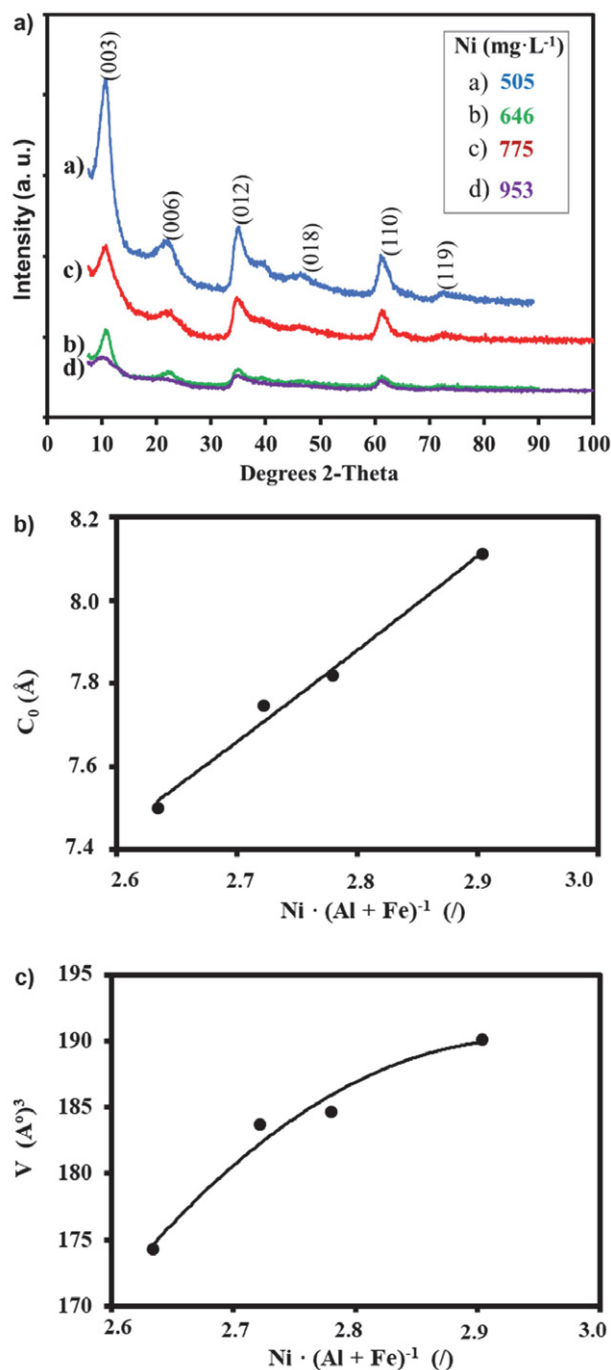


**Figure 4.** XRD of Ni/Al-LDH, Cu K $\alpha$ 1,  $\lambda=1.540598$  Å, at 9.8 mA/cm<sup>2</sup>, 30 min, 60 °C and pH 8.6. a) Diffraction intensity for various Bragg reflection angles. b) Interaction of the basal axis  $c_0$  with the molar ratio M(II)/M(III). c) Crystallite volume interaction  $V$  (Å<sup>3</sup>) with M(II)/M(III).

Fourier transform infrared spectroscopy (FTIR) spectra of the samples are illustrated in Fig.5. The broad bands that can be seen in the region from 3423 to 3465 cm<sup>-1</sup> are assigned to the stretching vibrations hydroxyl group ( $\nu_{\text{OH}}$ ) in the Ni/Al-LDH, Ni(OH)<sub>2</sub>, Al(OH)<sub>3</sub> and

the water molecules adsorbed in the interlayer.<sup>25,26,27,36,55</sup> The peaks observed between 2077.9 and 2084.7 cm<sup>-1</sup> are associated with stretching vibration of the N-H bond.<sup>55</sup> The characteristic bands between 1629 and 1641 cm<sup>-1</sup> are attributed the deformation ( $\delta\text{H-O-H}$ ) angle of water molecule ( $\delta\text{H-O-H}$ ) which confirms the presence of water in the Ni/Al-LDH interlayer.<sup>17,21,25,26,36</sup> The spectra also shows intense bands located from 1364 to 1368 cm<sup>-1</sup> and represent symmetric stretching vibrations carbon-oxygen bond (C-O) of carbonate ions  $\text{n}_3(\text{CO}_3^{2-})$ .<sup>20,21,55,60</sup> The adsorption peaks from 1108 to 1115 cm<sup>-1</sup> corresponded to S-O stretching vibrations of the sulfate anion  $\text{n}_3(\text{SO}_4^{2-})$ .<sup>20,24</sup> The characteristic band at 1041 cm<sup>-1</sup> represents the vibration  $\nu(\text{Al-OH})$ . Furthermore, in the region between 615 and 617 cm<sup>-1</sup> the bands can be assigned to the stretching vibration of metal (M) - oxygen (Ni-O; Al-O; Ni-O-Al), related to the oxides and aluminates determined by DXR.<sup>25,36</sup> The peaks between 409.8 and 410.8 cm<sup>-1</sup> are assigned to nickel oxides and nickel hydroxides [Ni-O; Ni-O-H<sup>-</sup>]; and the bands between 566 – 567 cm<sup>-1</sup> are attributed to stretching vibrations [Ni<sup>3+</sup>-O] in [ $\gamma$ -NiOOH].<sup>14,25,60</sup>

The elemental analysis of the precipitates is given in Table 6. The precipitate had a nickel concentration between 33.40 and 40.68%, aluminum from 6.43 to 7.0% and charge density ( $x$ ) from 0.256 to 0.36. When the initial concentration of nickel increased, there was a tendency to increase Ni in the precipitate. The table also shows that sulfate anion was predominant.

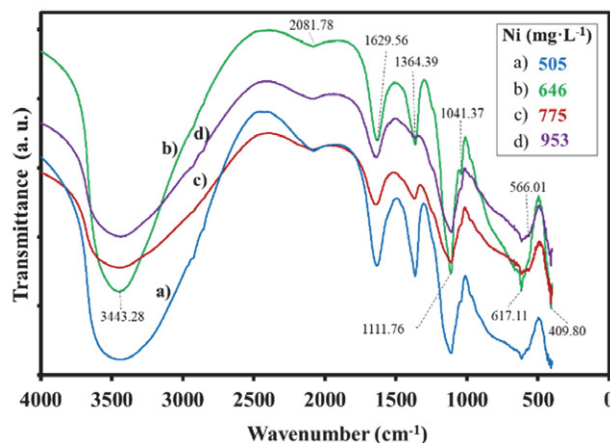


**Figure 5.** FTIR spectral of Ni/Al-LDH from different nickel concentration, a) 505 mg L<sup>-1</sup>, b) 646 mg L<sup>-1</sup>, c) 775 mg L<sup>-1</sup>, d) 953 mg L<sup>-1</sup>

From the DXR analysis, the spacing ( $d_{\text{hkl}}$ ) of the LDHs, the crystal lattice parameters ( $a$ ,  $c$ ) and the crystallite size ( $D_{\text{hkl}}$ ) were determined (Table 7). Parameters “ $a$ ” and “ $c$ ” were calculated using the relationship between the spacing ( $d_{\text{hkl}}$ ) in the planes ( $hkl$ ): (003), (012), (110) and the lattice parameters ( $a$ ,  $b$ ,  $c$ ) for the hexagonal crystal system ( $b=c$ ). The data was adjusted using the Statgraphic 5.1 software in the nonlinear regression option.

**Table 6.** Characterization of Ni/Al-LDH and estimated chemical formulas

[Ni <sup>2+</sup> ]	Concentration (%w/w)				Chemical formulas	Ni/(Al+Fe) (molar)
	Ni	Al	S	Fe		
447	33.40	8.64	7.10	0.13	[Ni <sub>0.640</sub> Al <sub>0.360</sub> (OH) <sub>2</sub> ] (SO <sub>4</sub> ) <sub>0.156</sub> (CO <sub>3</sub> ) <sub>0.024</sub> xH <sub>2</sub> O	1.76
505	37.39	6.30	5.62	0.03	[Ni <sub>0.732</sub> Al <sub>0.268</sub> (OH) <sub>2</sub> ] (SO <sub>4</sub> ) <sub>0.113</sub> (CO <sub>3</sub> ) <sub>0.021</sub> xH <sub>2</sub> O	2.72
646	38.47	6.67	5.72	0.09	[Ni <sub>0.726</sub> Al <sub>0.274</sub> (OH) <sub>2</sub> ] (SO <sub>4</sub> ) <sub>0.123</sub> (CO <sub>3</sub> ) <sub>0.014</sub> xH <sub>2</sub> O	2.63
775	39.21	6.41	5.12	0.05	[Ni <sub>0.738</sub> Al <sub>0.262</sub> (OH) <sub>2</sub> ] (SO <sub>4</sub> ) <sub>0.107</sub> (CO <sub>3</sub> ) <sub>0.024</sub> xH <sub>2</sub> O	2.80
953	40.68	6.43	4.37	0.02	[Ni <sub>0.744</sub> Al <sub>0.256</sub> (OH) <sub>2</sub> ] (SO <sub>4</sub> ) <sub>0.115</sub> (CO <sub>3</sub> ) <sub>0.013</sub> xH <sub>2</sub> O	2.90
1356*	39.20	7.00	3.75	0.05	[Ni <sub>0.720</sub> Al <sub>0.280</sub> (OH) <sub>2</sub> ] (SO <sub>4</sub> ) <sub>0.068</sub> (CO <sub>3</sub> ) <sub>0.071</sub> xH <sub>2</sub> O	2.57

\*Sample analyzed after electrocoagulation for 40 min

**Table 7.** Lattice parameters and size of Ni/Al-LDH crystallites

Sample Ni (g mL <sup>-1</sup> )	Spacing (Å)			Cell parameters (Å)		V (Å) <sup>3</sup>	Crystallite size (nm)	
	d <sub>003</sub>	d <sub>012</sub>	d <sub>110</sub>	a = b	D		D	D <sub>003</sub>
505	8.227	2.567	1.516	3.02	23.237	184	5.40	8.45
646	8.305	2.560	1.513	3.00	24.336	174	5.69	8.92
775	8.266	2.546	1.511	3.02	23.460	185	6.35	9.90
953	8.632	2.585	1.507	3.00	22.495	190	6.71	10.5

The distance between ( $d_{003}$  planes) of the LDH, also called d spacing, basal distance or thickness of the interlayer gallery was calculated using Bragg's Law. The obtained values were similar to those of the compounds synthesized by coprecipitation reported in the literature: [Ni/Al-SO<sub>4</sub><sup>2-</sup>] ( $8.01 \leq d_{003} \leq 8.59$  Å) and [Ni/Al-NO<sub>3</sub><sup>-</sup>] ( $7.82 \leq d_{003} \leq 8.76$  Å). The variation in the basal distance is due to the variation in the amount (intercalation degree) and type of anions (atom size and valence) in the LDH interlayer.<sup>24,26,64</sup>

The average values of the lattice parameters (+/- standard deviation) were:  $a=b=3.01$  Å (+/-0.013) and "c" equal to  $23.4$  Å (+/-0.76), with a fit quality greater than 99.7%, confirming that it is a hexagonal crystalline system. The parameter "a" is equivalent to the average distance between the center of adjacent cations in the lattice; and "c" is the basal axis, which is related to the distance between neighboring atoms and the interlayer distance. These parameters are comparable to the parameters reported for the compounds obtained by coprecipitation: [Ni/Al-SO<sub>4</sub><sup>2-</sup>]-LDH values of "a"  $3.03$  Å and "c"  $24.05$  Å; and for [Ni/Al-CO<sub>3</sub><sup>2-</sup>]-LDH in the following ranges:  $3.02 \leq a \leq 3.08$  Å and  $22.2 \leq c \leq 24.05$  Å.<sup>21,24,28</sup>

The basal axis cell parameter for n-layers is  $c=n c_0$ . For the polytype 3R with rhombohedral symmetry  $n=3$ , and with the lowest reflection (0 0 n)  $c_0$  (Å) was calculated. An increase in the basal axis as the molar ratio [Ni<sup>2+</sup> / (Al<sup>3+</sup> + Fe<sup>3+</sup>)] increases was observed with a coefficient of determination ( $R^2$ ) equal to 97.42%. This is because the nickel has a larger ionic radius than iron and aluminum ( $0.69$  Å  $> 0.55$  Å  $> 0.535$  Å), (Figure 4 b).<sup>21,26</sup>

The unit cell volume ( $V=0.866 a^2 c$ ) was  $183$  Å<sup>3</sup> (+/-6.58), similar to other [CO<sub>3</sub><sup>2-</sup>]-LDH obtained by co-pre-

cipitation such as [Zn/Al]  $189$  Å<sup>3</sup>, [Ni/Al]  $187.6$  Å<sup>3</sup> y [Mg/Al]  $180$  Å<sup>3</sup> and by the sol-gel method [Ni/Al]  $148$ - $163$  Å<sup>3</sup>. the lower the molar ratio [Ni<sup>2+</sup> / (Al<sup>3+</sup> + Fe<sup>3+</sup>)] the smaller the volume, (Figure 4 c).<sup>21,28</sup>

The crystallite size ( $D_{hkl}$ ) was calculated using the Scherrer equation and the mean size (D) by the Williamson-Hall "SSP" method. Both sizes reached lower values than other Ni/Al-LDHs synthesized by coprecipitation, but those were similar to the LDHs obtained by the sol-gel technique [Ni/Al-CO<sub>3</sub><sup>2-</sup>] ( $2.69 \leq D_{003} \leq 8.11$  nm). Crystallinity increased with increasing temperature, current density and constant alkaline pH.<sup>21,34,65</sup>

In that order of ideas, the average size of the crystallites (D) presented an inversely proportional relationship with the reaction rate constant ( $k_{av}$ ) of the Avrami's model, following a linear function ( $R^2$  95.92%). Regarding the fractional reaction order ( $n_{av}$ ), it was related to the preferential orientation of the crystallites, according to the peak intensity in the  $I_{003}/I_{012}$  ratio ( $1.43 \leq I_{003}/I_{012} \leq 1.82$ ) with an inverse relationship and linear trend ( $R^2$  98.0%). Liu (2015) used the ratio  $I_{003}/I_{012}$  in the interval  $0.2 \leq I_{003}/I_{012} \leq 2.7$  to evaluate the orientation of Ni/Al-CO<sub>3</sub>-LDH. He referred that a higher  $I_{003}/I_{012}$  value indicates that the LDH has a c-axis preferred orientation, while a lower value demonstrates preferentially ab-oriented. Based on this criterion, it was supposed that when the fractional reaction order ( $n_{av}$ ) increases the crystallites have a greater tendency to ab-orientation.<sup>43</sup>

### 3. 4 Nickel Removal Mechanism Analysis

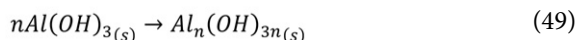
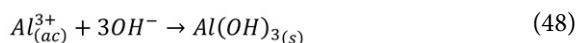
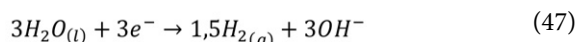
Taking into account the results of the kinetic and equilibrium analysis, the characterization of the product,



as well as the information consulted in the literature, it is considered that the following reactions control the nickel removing by electrocoagulation of Ni(II)-NH<sub>3</sub>-CO<sub>2</sub>-SO<sub>2</sub>-H<sub>2</sub>O system, (Fig. 6).<sup>6,7,10,11,15,66</sup>

- Precipitation of nickel hydroxide.
- Co-precipitation of Ni in spinels [Ni<sub>x</sub>Al<sub>y</sub>O<sub>z</sub>].
- Precipitation of layered double hydroxides.
- Cathodic electro-reduction to form metallic nickel

Where, the anionic ligands [CO<sub>3</sub><sup>2-</sup>], [S<sub>x</sub>O<sub>y</sub><sup>z-</sup>], [NO<sub>3</sub><sup>2-</sup>] on the coordination surface, depending on the dissolved Ni concentration, activate a synergism on the process that benefits the removal.



Nickel compounds and other contaminants, either colloids, suspended or dissolved material begin to destabilize due to:<sup>6,7,11,13</sup>

- 1) Compression of the diffuse double layer around the charged species because of the physical-chemical interactions with the generated ionic species, by the electrochemical dissolution of the sacrificial electrode (anode).

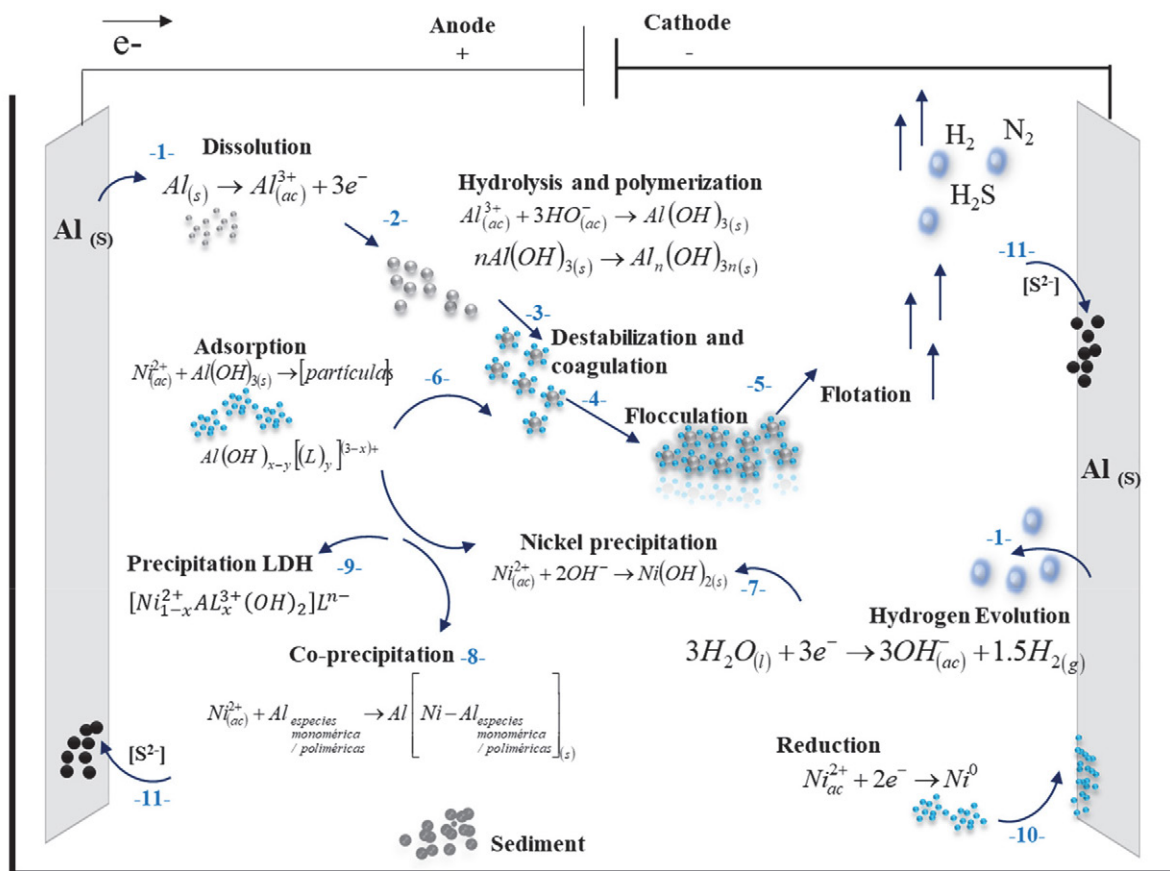


Figure 6. Schematic representation of the nickel removal mechanism by electrocoagulation of the Ni(II)-NH<sub>3</sub>-CO<sub>2</sub>-SO<sub>2</sub>-H<sub>2</sub>O system.

Due to the simultaneous electrolytic reactions that occur on the surface of the electrodes (step 1 Fig. 6), the electro-coagulant aluminum cation [Al<sup>3+</sup>] and the hydroxide anion [OH<sup>-</sup>] are produced, Eq. (46) and (47). These diffuse in the solution and spontaneously the hydrolysis of aluminum occurs to form several monomeric and polymeric species, oligomeric complexes and aluminum hydroxide, Eq. (48) and (49), Step 2.<sup>67</sup>



These affect the potential difference between the surface of the particles and the solution, thus decreasing the interparticle repulsive forces.

- 2) Charge neutralization of the ionic species present in the solution due to the ions of opposite charge generated at the anode and the processes of adsorption, precipitation and co-precipitation; thus, the interparticle repulsive electrostatic forces decrease, instead the Van der Waals attraction forces predominate and as a result, coagulation occurs. While monomeric aluminum species neutralize

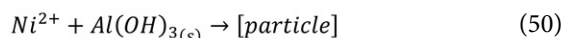
the charge of contaminants by adsorbing on their surface and binding to their ionized groups, polymeric species can bind several contaminant particles (or molecules) at once, Step 3.

3) Following destabilization, flocs are formed as a result of aggregation of the destabilized particles, leading to sludge formation (flocculation), Step 4.

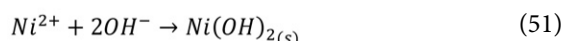
4) The hydrogen released in the cathodic reaction (2), enables the electro-flotation of the flocculated particles, which is also favored by the removal of sulfur in the form of hydrogen sulfide (H<sub>2</sub>S), Step 5.

In parallel, mechanisms occur that favor the removal of nickel, as explained below:

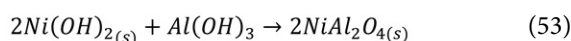
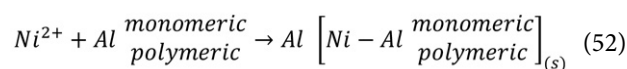
Adsorption of [Ni<sup>2+</sup>] in the active centers of the surface of the aluminum species and fundamentally, on [Al(OH)<sub>3</sub>] in interaction with other ions present in solution provided by the compounds CO<sub>2</sub> - SO<sub>2</sub> - NH<sub>3</sub>. This process happens by two mechanisms: electrostatic attraction and coordination surface, Eq. (50), Step 6.



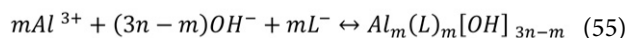
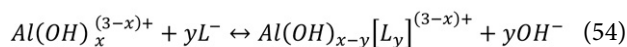
Result of simultaneous reactions at the anode and cathode, hydroxide ion is released and nickel hydroxide precipitates, Eq. (51), Step 7.



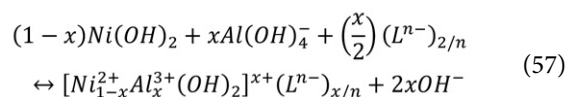
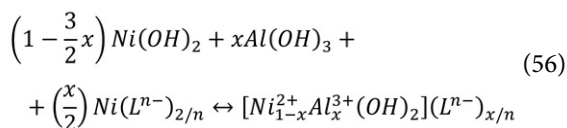
Through sequential co-precipitation, [Ni(OH)<sub>2</sub>] is incorporated into the crystal structure of [Al(OH)<sub>3</sub>] and forms spinel: NiAl<sub>2</sub>O<sub>4</sub>, [NiAl<sub>26</sub>O<sub>40</sub>], [NiAl<sub>32</sub>O<sub>49</sub>], [Ni<sub>2</sub>Al<sub>18</sub>O<sub>29</sub>], Eq. (52) and (53), Step 8.



Anions in solution are attracted by electrostatic forces to balance charges and adsorbed on the active centers of the coordination surface, where (L) represents anionic ligands such as [CO<sub>3</sub><sup>2-</sup>], [S<sub>x</sub>O<sub>y</sub><sup>z-</sup>], [NO<sub>3</sub><sup>2-</sup>], [OH<sup>-</sup>], Eq. (54) and (55).<sup>65,68</sup>



Subsequently, the adsorbed ions can be displaced by other competing ions in the solution (exchange adsorption), due to the interactions between the ions on the charged surface and in the diffuse layer around the surface, and the nickel removal by formation of Ni-Al/LDH is promoted. LDH of high purity at alkaline pH and maximum temperature of 80 °C has been prepared by co-precipitation, Eqs. (56) - (57), Step 9.<sup>24,26,31,69,70</sup>

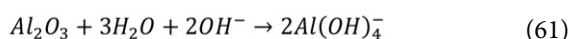
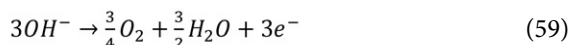


The hydrogen evolution reaction (HER) (2) occurs at the cathode to a standard potential of -0.826 V with the release of gaseous H<sub>2</sub>; and the nickel reduction on the cathode surface to a more positive standard reduction potential of -0.25 V, Eq. (58), Step 10.



The precipitation of [Ni(OH)<sub>2</sub>], [Ni/Al-LDH] and the co-precipitation of spinels Ni-Al cause a synergistic effect in the process, achieving high efficiency of nickel removing. A greater effect is reached as the initial nickel concentration in dissolution increases, which is reflected by the kinetic model TCV Eq. (45).

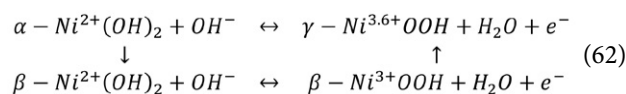
The possibility of an electrocatalytic effect of Ni<sup>2+</sup>/Al<sup>3+</sup>-LDH and the pair Ni(OH)<sub>2</sub>/[β-Ni<sup>3+</sup>OOH] on the anodic reaction of water electrolysis with oxygen evolution (OER) is also considered. The OER presupposes the absorption in the anode deposits of the hydroxide radicals generated by the hydrogen evolution (HER) in the cathode (0.404 V), Eq. (59).<sup>71</sup> The OER can promote the aluminum oxidation and the formation of LDH, Eq. (60) and (61).



The intercalation of molecules (H<sub>2</sub>O, NH<sub>3</sub>) and anions [S<sub>x</sub>O<sub>y</sub><sup>z-</sup>], [CO<sub>3</sub><sup>2-</sup>] in the LDH interlayer let to more electrons could being transferred to the surface of the active sites of LDH [Ni<sub>1-x</sub>Al<sub>x</sub>OOH], stabilizing their high-valence states and increases the activity for the OER from the reversible redox pair Ni<sup>2+</sup>/Ni<sup>3+</sup>. Zhou et al. (2018) showed that intercalated anions with strong reducing ability modify the electronic structure of surface metal sites and significantly improve the performance of the corresponding LDH for the OER with a linear relationship<sup>64</sup>, in the case of ions [S<sub>x</sub>O<sub>y</sub><sup>z-</sup>] it increases from [S<sub>2</sub>O<sub>8</sub><sup>2-</sup>] to [SO<sub>3</sub><sup>2-</sup>].

Regarding NiOOH, it is a catalyst for OER under alkaline conditions and acts as an active center in the pair [Ni(OH)<sub>2</sub>]/[β-NiOOH] for the adsorption of [OH<sup>-</sup>]. Nickel is capable of acquiring valences (+2, +3, +3.6) making it susceptible to various electronic transitions and phase transformations, Eq. (62). The Ni(OH)<sub>2</sub> has a large specific surface which favors contact between the active material

and the electrolytic dissolution.<sup>59,72,73,74</sup>



Reactions of sulfide formation (NiS, Al<sub>2</sub>S<sub>3</sub>), the release of irritating gases (H<sub>2</sub>S) and the formation of deposits on the surface of the electrodes are considered. These deposits exert resistance to the passage of electrical current, reduce charge transfer, affect the efficiency of the process and the stability of the operation, Step 11.

### 3. 5 Result of the Operating Cost Estimate

The operating cost was estimated for electrode and electrical energy consumption for initial nickel concentration in the range  $0.474 \leq \text{Ni} \leq 0.953 \text{ g L}^{-1}$ , 9.8 mA cm<sup>-2</sup>, 60 °C, pH 8.6 and 98% nickel removal, for a remainder between 6 and 19 mg L<sup>-1</sup> (Table 8).

**Table 8.** Estimated operating costs for nickel removal by electrocoagulation Base: 98% removing, 9.8 mA cm<sup>-2</sup>, 60 °C, pH 8.6

Ni (mg L <sup>-1</sup> )	379	447	505	646	775	953
Cost (\$ t <sup>-1</sup> Ni)	320	382	509	521	537	534
SEC (kW h kg <sup>-1</sup> Al)	5.26	6.33	6.75	5.11	3.45	2.76

The operating cost amounted to between 320 and 537 \$ t<sup>-1</sup> of nickel removed, regarding the specific energy consumption (SEC), it was between 2.76 and 6.75 kW h kg<sup>-1</sup> of aluminum. The increase in nickel concentration in the initial liquor augments the electrocoagulation time necessary to achieve high removal efficiency and therefore also increases energy and electrode consumption. The higher the concentration of ionic species in the liquor, the conductivity is favored and SEC decreases.

According to the analyzed aspects of the removal mechanism, it is possible to reduce costs by designing a reactor with favorable geometric and hydrodynamic conditions to achieve adequate mass transfer between the phases. It also suggests recycling a suspension of the product obtained at the non-saturation conditions of the adsorption sites, according to the isotherm model to be followed.

## 4. Conclusions

The nickel removing by electrocoagulation from the liquor effluent of the nickel production plant in Punta-Gorda Cuba, was studied in Ni(II)-NH<sub>3</sub>-CO<sub>2</sub>-SO<sub>2</sub>-H<sub>2</sub>O system. The reaction kinetics, the adsorption isotherm, the mechanism and the preliminary cost of operation at different concentrations of dissolved nickel in the initial liquor were evaluated. In the interval defined for the operating

variables, a removing efficiency between 97.7 and 99.7% was obtained. A kinetic model of conversion time was proposed, which suggests that the process is determined by the combined effect of the resistances of the mechanisms: external diffusion, nucleation, and as controlling step the chemical reaction and a possible autocatalytic contribution. The removal was characterized by monolayer chemisorption at a finite number of specific adsorption sites, following the Langmuir isotherm. The precipitate had between 33.4 and 40.7% nickel and from 6.3 to 7.0% aluminum, with a typical structure of Ni/Al-LDH and phases impurities Al(OH)<sub>3</sub>, Ni(OH)<sub>2</sub>/NiOOH and nickel-aluminum spinels. The operating costs were between 320 and 537 \$ t<sup>-1</sup> of removed nickel, considering the energy and electrode consumption. The research represents the opportunity to diversify production, in-situ synthesize Ni/Al-LDH, improve its properties and evaluate its applications for the projection of an industrial process.

## Acknowledgment

Thanks to Nélida Powery Ebanks, NICAROTEC Co.; and colleagues of the Chemical Analysis Laboratory, CED-INIQ-Nicaragua Cuba, for their collaboration.

## Conflict of Interest

The authors declare no conflict of interest

## 5. References

1. A. R. Vargas; M. E. T. Nieves; Y. G. Díaz. *Acta Chimica Slovenica*, **2020**, 67, 1239–1249. DOI:10.17344/acsi.2020.6147
2. A. R. Vargas, M. E. M. Haynes, A. R. Riveron. *Rev. Metal. (Madrid, Spain)*, **2019**, 55, DOI:10.3989/revmetalm.149
3. L. C. Lamorú, A. O. C. Navarro, Y. A. Arias. *Minería y Geología*, **2018**, 34, 422–439.
4. A. R. Vargas, A. R. Riverón, M. P. Medina, E. O. Armaignac. *Tecnol. Quim.*, **2020**, 40, 363–382.
5. L. M. Irions, A. R. Vargas, et al. *Tecnol. Quim.*, **2020**, 40, 19–36.
6. A. S. Naje, S. Chelliapan, Z. Zakaria, M. A. Ajeel, P. A. Alaba. *Rev. Chem. Eng.*, **2016**, 33, 263–292. DOI:10.1515/revce-2016-0019
7. J. N. Hakizimana, B. Gourich, M. Chafi, et al. *Desalination*, **2017**, 404, 1–21. DOI:10.1016/j.desal.2016.10.011
8. S. García-Segura, M. M. S. G. Eiband, J. Vieira de Melo, C. A. M. Huitle. *J. Electroanal. Chem.*, **2017**, 801, 267–299. DOI:10.1016/j.jelechem.2017.07.047
9. Z. Al-Qodah, M. Al-Shannag, K. Bani-Melhem, et al. *Environ. Chem. Lett.*, **2018**, 16, 695–714. DOI:10.1007/s10311-018-0711-1
10. Z. Al-Qodah, M. Al-Shannag. *Sep. Sci. Technol.*, **2017**, 52, 2649–2676. DOI:10.1080/01496395.2017.1373677
11. S. M. Didar; U. I. Islam. *Sustain. Water Resour. Manag.*, **2019**, 5, 359–380. DOI:10.1007/s40899-017-0152-1

12. K. Dermentzis, K. Karakosta, R. Kosheleva, N. Kokkinos. *J. Eng. Sci. Tech. Rev.*, **2020**, *13*. DOI:10.25103/jestr.136.04
13. D. Ghernaout, A. Alghamdi, B. Ghernaout. *J. Environ. Sci. Allied. Res.* **2019**, 51–67.
14. T. S. Pertile, E. J. Birriel. *Korean J. Chem. Eng.* **2017**, *34*, 2631–2640. DOI:10.1007/s11814-017-0178-y
15. X. Chen, P. Ren, Tao Li, et al. *Chem. Eng. Journal.* **2018**, *31*, 358–367. DOI:10.1016/j.cej.2018.05.099
16. H. Zhao, B. Zhao, W. Yang, T. Li. *Environ. Sci. Technol.* **2010**, *44*, 9112–9116. DOI:10.1021/es102540t
17. M. M. Mendoza, D. D. Victoria, N. M. Cabrales. *MethodsX.* **2018**, *5*, 915–923. DOI:10.1016/j.mex.2018.07.019
18. L. Jiang, G. Huang, L. Shao, J. Huang, S. Peng, X. Yang. *Colloids Surf.* **2021**, *608*, 125589. DOI:10.1016/j.colsurfa.2020.125589
19. Ou, J. Yan, T. Xu, Z. Jiang, H. Tan, S. He, B. Hu, G. Yu. *J. Mol. Liq.* **2021**, *335*, 116246. DOI:10.1016/j.molliq.2021.116246
20. Y. Zhao, F. Xiao, Q. Jiao. *J. Nanotechnol.* **2011**. DOI:10.1155/2011/646409
21. M. Jitianu, D. C. Gunness, D. E. Aboagye, M. Zaharescu, A. Jitianu. *Mater. Res. Bull.* **2013**, *48*, 1864–1873. DOI:10.1016/j.materresbull.2013.01.030
22. T. D. Nguyen, Q. T. P. Bui, H. Q. H. Phan. *J. Mater. Sci. Surf. Eng.* **2016**, *4*, 488–491.
23. L. Li, K. S. Hui, K. N. Hui, et al. *J. Alloys Compd.* **2017**. DOI:10.1016/j.jallcom.2017.06.062
24. F. Z. Mahjoubi, A. Khalidi, M. Abdennouri, N. Barka. *Desalin. Water Treat.* **2015**, *1*–13. DOI:10.1080/19443994.2015.1124055
25. F. Z. Mahjoubi, A. Elhalil, R. Elmoubarki, et al. *JASI.* **2017a**, *2(1-3)*, 1–11.
26. F. Z. Mahjoubi, A. Khalidi, O. Cherkaoui, et al. *J. Water Reuse Desalin.* **2017b**. DOI:10.2166/wrd.2016.041
27. S. Jaerger, S. F. Zawadzki, A. Leuteritz, F. Wypych. *J. Braz. Chem. Soc.* **2017**, *28*, 2391–2401. DOI:10.21577/0103-5053.20170093
28. W. M. A. El Rouby, S. I. El-Dek, M. E. Goher, S. G. Noaemy. *Environ. Sci. Pollut. Res.* **2018**. DOI:10.1007/s11356-018-3257-7
29. O. Rahmanian, M. H. Maleki, M. Dinari. *J. Phys. Chem. Solids.* **2017**, *110*, 195–201. DOI:10.1016/j.jpcs.2017.06.018
30. N. Taoufik, W. Boumya, A. Elhalil, et al. *Int. J. Environ. Anal. Chem.* **2020**. DOI:10.1080/03067319.2020.1863387
31. M. Mousazadeh, S. M. Alizadeh, Z. Frontistis, et al. *Water.* **2021**, *13*, 656. DOI:10.3390/w13050656
32. Z. Tang, Z. Qiu, S. Lu, X. Shi. *Nanotechnol. Rev.* **2020**, *9*, 800–819. DOI:10.1515/ntrev-2020-0065
33. H. Lu, Q. Li, H. Xiao, et al. *Am. J. Anal. Chem.* **2014**, *5*, 547–558. DOI:10.4236/ajac.2014.59062
34. L. Yang, Z. Liu, S. Zhu, L. Feng, W. Xing. *Materials Today Physics.* **2021**, *16*, 100292. DOI:10.1016/j.mtphys.2020.100292
35. N. Ayawei, A. N. Ebelegi, D. J. Wankasi. *J. Chem.* **2017**. DOI:10.1155/2017/3039817
36. M. Mamat, N. Roslan, K. H. K. Bulat, et al. *Mater. Sci. Eng.* **2018**, *440*. DOI:10.1088/1757-899X/440/1/012013
37. G. Li, X. Zhang, D. Qiu. *Adv. Electron. Mater.* **2019**, *5*, 1900215. DOI:10.1002/aelm.201900215
38. X. Zhang, C. B. Cockreham, E. Yilmaz. *ChemRxiv.* **2020**. DOI:10.26434/chemrxiv.11919804.v2
39. J. Wang, Y. Song, Z. Li. *Energy Fuels.* **2010**, *24*, 6463–6467. DOI:10.1021/ef101150b
40. W. Wang, N. Zhanga, Z. Shia. *Chem. Eng. J.* **2018**, *338*, 55–61. DOI:10.1016/j.cej.2018.01.024
41. Q. Xie, Z. Cai, P. Li, et al. *Nano Res.* **2018**, *11*, 4524–4534. DOI:10.1007/s12274-018-2033-9
42. M. Gabrovskaa, D. Nikolova, M. Shopska, et al. W. E. Lee et al. (eds.), *Proceedings of the III Advanced Ceramics and Applications Conference.* **2016**. DOI:10.2991/978-94-6239-157-4\_15
43. Y. Liu, T. Yu, R. Cai. *RSC Adv.* **2015**, *5*, 29552. DOI:10.1039/C5RA01969A
44. S. Iguchi, S. Kikkawa, K. Teramura, et al. *Phys. Chem. Chem. Phys.* **2016**, *18*, 13811–13819. DOI:10.1039/C6CP01646D
45. M. Gabrovskaa, R. E. Kardjieva, D. Crisan, et al. *Reac. Kinet. Mech. Cat.* **2012**, *105*, 79–99. DOI:10.1007/s11144-011-0378-0
46. F. Touahra, M. Sehailia, W. Ketir, et al. *Appl. Petrochem. Res.* **2016**, *6*, 1–13. DOI:10.1007/s13203-015-0109-y
47. E. C. Lima, A. R. Cestari, M. A. Adebayo. *Desalin. Water Treat.* **2015**, *56*, 19566–19571. DOI:10.1080/19443994.2015.1095129
48. H. N. Tran, S. J. Youb, A. H. Bandegharai, H. P. Chao. *Water Res.* **2017**, *120*, 88–116. DOI:10.1016/j.watres.2017.04.014
49. A. I. Adeogun, R. B. Balakrishnan. *Appl. Water Sci.* **2015**, *7*, 1711–1723. DOI:10.1007/s13201-015-0337-4
50. A. A. Inyinbor, F. A. Adekola, G. A. Olatunji. *Water Resour. Ind.* **2016**, *15*, 4–27. DOI:10.1016/j.wri.2016.06.001
51. N. A. Oladoja. *Desalin. Water Treat.* **2015**, *57*, 15813–15825. DOI:10.1080/19443994.2015.1076355
52. A. R. Vargas. *Tecnol. Quim.* **2021**, *42*, 114–130.
53. I. Avramov, J. Sestak. Generalized kinetics of overall phase transition explicit to crystallization. *J. Therm. Anal. Calorim.* **2014**, *118*, 1715–1720. DOI:10.1007/s10973-014-4144-1
54. L. Shi-Yong, Z. Jia-yun, Z. Tu-ping. Computer prediction system on solid / solid reaction kinetic. *Trans. Nonferrous Met. Soc. China.* **2001**, *11(3)*, 466–470. DOI: 1003-6326(2001) 03-0466-05.
55. X. Xue, S. Zhang, H. Zhang. *Am. J. Anal. Chem.* **2015**, *6*, 334–341. DOI:10.4236/ajac.2015.64032
56. N. F. M. Salleh, A. A. Jalila, S. Triwahyonoc, et al. *Appl. Surf. Sci.* **2015**, *349*, 485–495. DOI:10.1016/j.apsusc.2015.05.048
57. P. Lu, F. Liu, D. Xue, et al. *Electrochim. Acta.* **2012**, *78*, 1–10. DOI:10.1016/j.electacta.2012.03.183
58. D. S. Hall, David; D. J. Lockwood, C. Bock, B. R. MacDougall. *Proc. R. Soc. A.* **2015**, *471*. DOI:10.1098/rspa.2014.0792
59. M. H. Syafiq, O. M. Rozali. *Int. J. Electrochem. Sci.* **2018**, *8*, 4747–4760.
60. A. A. Lobinsky, V. P. Tolstoy, I. A. Kodinzev. *Nanosyst.: Phys., Chem., Math.* **2018**, *9*, 669–675. DOI:10.17586/2220-8054-2018-9-5-669-675
61. A. Khan, R. A. Senthil, J. Pan, Y. Sun. *Chin. J. Chem. Eng.* **2019**. DOI:10.1016/j.cjche.2019.01.025

62. C. G. Anchietta, L. Tochetto, H. B. Madalosso. *Cerámica*. **2015**, 61, 477–481. DOI:10.1590/0366-69132015613601925
63. C. Ragupathi, J. J. Vijaya, J. L. Kennedy. *J. Saudi Chem. Soc.* **2017**, 21, 231–239. DOI:10.1016/j.jscs.2014.01.006
64. D. Zhou, Z. Cai, Y. Bi. *Nano Res.* **2018**. DOI:10.1007/s12274-017-1750-9
65. Y. T. Prabhu, K. V. Rao, V. S. Kumar, B. S. Kumari. *World J. Nano Sci. Eng.* **2014**, 4, 21–28. DOI:10.4236/wjnse.2014.41004
66. E. Nariyan, M. Sillanpää, C. Wolkersdorfer. *Sep. Purif. Technol.* **2017**, 177, 363–373. DOI:10.1016/j.seppur.2016.12.042
67. B. Lekhlif, L. Oudrhiri, F. Zidane, et al. *J. Mater. Environ. Sci.* **2014**, 5, 111–120.
68. M. A. Sandoval, J. L. Nava, O. Coreño, et al. *Int. J. Electrochem. Sci.* **2017**, 12, 1318–1330. DOI:10.20964/2017.02.08
69. J. J. Bravo-Suárez, E. A. Páez-Mozo, S. T. Oyama. *Quim. Nova*, **2004**, 27, 601–614. DOI:10.1590/S0100-40422004000400015
70. R. Bloom, N. Hondow, V. Dupont, M. V. Twigg, S. J. Milne. *Energy Rep.* **2018**, 4, 733–743. DOI:10.1016/j.egyr.2018.10.008
71. Y. Cheng, S. P. Jiang. *Prog. Nat. Sci.: Mater. Int.* **2015**, 25, 545–553. DOI:10.1016/j.pnsc.2015.11.008
72. D. E. Pissinis, L. E. Sereno, J. M. Marioli. *Open J. Phys. Chem.* **2012**, 2, 23–33. DOI:10.4236/ojpc.2012.21004
73. V. Kotok, V. Kovalenko, V. Malyshev. *East. Eur. J. Enterp. Technol.* **2017**, 89, 5–12. DOI:10.15587/1729-4061.2017.109770
74. Y. H. Chung, I. Jang, J. H. Jang. *Sci. Rep.* **2017**, 7, 8236. DOI:10.1038/s41598-017-08296-0

## Povzetek

Raziskava poroča o odstranjevanju niklja z elektrokoagulacijo sistema Ni(II)-NH<sub>3</sub>-CO<sub>2</sub>-SO<sub>2</sub>-H<sub>2</sub>O v laboratorijskem merilu. Poskusi so bili izvedeni z Al/Al par elektrodami pri začetni koncentraciji niklja med 293 in 1356 mg L<sup>-1</sup> in pri obratovalnih parametrih pH 8,6, gostoti toka 9,8 mA cm<sup>-2</sup>, času elektrolize 30 min in temperaturi 60 °C. Dobljeni rezultati kažejo na učinkovitost odstranjevanja med 97,7 in 99,7 %. Kinetično modeliranje je predlagalo kombinirane učinke zunanje difuzije in nukleacije ter kemično reakcijo in možen avtokatalitični prispevek kot kontrolni korak. Postopek je sledil Langmuirjevi izotermi z največjo adsorpcijsko zmogljivostjo 7519 mg g<sup>-1</sup>. ICP-OES, XRD in FTIR karakterizacija oborin je pokazala tipične plastne Ni-Al dvojne hidroksidne strukture s 33,4–40,7 % niklja in 6,3–7,0 % aluminija, odvisno od začetne koncentracije niklja. Operativni stroški porabe energije in elektrod so bili 320–537 \$ t<sup>-1</sup> odstranjenega niklja.



Except when otherwise noted, articles in this journal are published under the terms and conditions of the Creative Commons Attribution 4.0 International License

# Decolorization of Direct Black 22 by Photo Fenton like Method Using UV Light and Zeolite Modified Zinc Ferrite: Kinetics and Thermodynamics

Serap Findik\*

Hitit University, Engineering Faculty, Chemical Engineering Department, Kuzey Yerleskesi, Çevre Yolu Bulvarı, 19030, Çorum, Türkiye

\* Corresponding author: E-mail: serapfindik@hitit.edu.tr

Received: 02-24-2022

## Abstract

In this study, a heterogeneous catalyst was prepared to enhance photo-Fenton like oxidation of Direct Black-22 (DB-22). Zeolite modified with zinc ferrite was used as a catalyst. The prepared catalyst was characterized using FTIR, SEM, EDS and XRD. The effect of various parameters like catalyst modification with HCl,  $\text{H}_2\text{O}_2$  amount, catalyst amount,  $\text{CaCl}_2$  amount, initial pH, initial concentration and temperature on the decolorization of DB-22 was studied under UV light. Kinetic and thermodynamic properties were investigated. The highest decolorization of DB-22 was found to be 93.3% under the following conditions: initial concentration: 0.070 g/L, initial temperature: 25 °C, original pH,  $\text{H}_2\text{O}_2$  amount: 2.78 g/L, m-ZZF amount: 3 g/L,  $\text{CaCl}_2$  amount: 3.75 g/L, reaction time: 60 min and UV light. The activation energy was found to be  $-14.76$  kJ/mol under the studied conditions. The decolorization reaction was an exothermic reaction, and the calculated reaction enthalpy was  $-17.31$  kJ/mol. The activation entropy was calculated to be  $-0.326$  kJ/mol. The standard Gibbs free energy change of the activation had a positive value, and it increased with increasing temperature.

**Keywords:** Direct black 22, photo-Fenton process, UV, zeolite, zinc ferrite

## 1. Introduction

Textile dyes account for more than half of the total dye production in the world. The dyes used in the dyeing process cause the formation of textile wastewater. This wastewater causes coloration in natural water resources, as well as damaging living organisms and preventing the passage of sunlight. In addition, when mixed with drinking water, it harms human life due to its carcinogenic nature. Removing these dyes from water is important to prevent environmental damage.<sup>1</sup>

Conventional treatment methods such as biological treatment, coagulation, adsorption, chemical precipitation, solvent extraction, filtration, and electrochemical treatment are ineffective for decolorization of dyes.<sup>2,3</sup> They also have some disadvantages such as incomplete destruction of dye, high energy consumption, high operating cost, poor selectivity, incomplete ion removal, and generation of toxic sludge and waste product. Advanced oxidation methods are preferred for dye removal because of their simplicity and effectiveness.<sup>2,4,5</sup> Advanced oxidation methods are based on the production of the  $\text{OH}\cdot$  radicals.

The homogeneous Fenton process is a Fenton reaction in which iron salts are used as catalysts. In this process, hydrogen peroxide, which is used as an oxidant, and iron ions, which are used as a catalyst, react to produce  $\text{OH}\cdot$  radicals.<sup>6</sup> The use of  $\text{H}_2\text{O}_2$  and Fenton reagents with UV light has been known as photo-Fenton oxidation system. UV light irradiation and Fenton reagents cause an increase in the  $\text{OH}\cdot$  formation rate. Additional  $\text{OH}\cdot$  radicals are formed by either photoreduction of ferric ions ( $\text{Fe}^{3+}$ ) to ferrous ions ( $\text{Fe}^{2+}$ ) or hydrogen peroxide photolysis.<sup>2,3,6</sup>

Fenton oxidation systems based on the homogeneous Fenton reagent ( $\text{Fe}^{2+}/\text{Fe}^{3+}/\text{H}_2\text{O}_2$ ) have some disadvantages such as narrow pH range, removal of sludge containing iron ions, and requirement of large amount of chemicals.<sup>2-4,6</sup> Therefore, heterogeneous Fenton reactions are preferred to eliminate the negative effects of homogeneous Fenton reactions.

In the heterogeneous catalyst, the iron is stabilized into the catalyst interlayer space. Hydroxyl radicals are produced by oxidation of hydrogen peroxide with neither pH control nor precipitation of iron hydroxide.<sup>6</sup>



In heterogeneous Fenton-like processes, spinel ferrites ( $\text{MFe}_2\text{O}_4$ ) can be used as a heterogeneous catalyst. The term M in spinel ferrite structure refers to the divalent metal ions such as  $\text{Ni}^{2+}$ ,  $\text{Mn}^{2+}$ ,  $\text{Co}^{2+}$ ,  $\text{Mg}^{2+}$ ,  $\text{Cu}^{2+}$ ,  $\text{Zn}^{2+}$  etc. Spinel ferrites such as  $\text{ZnFe}_2\text{O}_4$ ,  $\text{CoFe}_2\text{O}_4$ , and  $\text{NiFe}_2\text{O}_4$  are used in medicines, sensors, and catalyst carriers thanks to their high mechanical strength, magnetic properties, unique structure, and catalytic performance.<sup>7,8</sup>

The use of zeolites modified with semiconductors can be an alternative catalyst for a variety of important reactions.<sup>1,2</sup> Zeolites are crystalline aluminosilicates with cavities, unique structures and chemical compositions, uniform pores and channels, high surface area, thermal stability, and an excellent adsorption ability. Conventional zeolites are constructed by tetrahedral  $\text{SiO}_4$  and  $\text{AlO}_4$  units.<sup>1,9,10</sup> There are at least 41 known types of natural zeolite.<sup>1</sup> Some of the most known and abundant types of natural zeolite are clinoptilolite, phillipsite, heulandite, mordenite, chabazite, and ferrierite.<sup>11</sup>

Azo dyes are the most important synthetic dyes with  $-\text{N}=\text{N}-$  bonds in their molecular structure. They can be classified according to number of azo groups, such as monoazo, diazo, triazo, polyazo, and azoic.<sup>12</sup>

Direct black 22 (DB-22) is one of the tetra azo dyes used in textile industry for dyeing cellulosic fibers such as cotton, wool, viscose, rayon, and paper. The high concentration of DB-22 in wastewater harms the environment with its carcinogenic properties, toxicity, organic matter content, and strong color.<sup>13</sup> For this reason, wastewater containing DB-22 should be released to the environment after being treated. There are few studies in the literature on DB-22 removal. In their study, Hien et al.<sup>13</sup> investigated the catalytic ozonation of DB-22 using different metal slags. Carvalho et al.<sup>14</sup> examined the removal of DB-22 using microaerated upflow anaerobic sludge blanket (UASB) reactors. Gomes et al.<sup>15</sup> investigated the degradation of DB-22 using homogeneous and heterogeneous photo-Fenton advanced oxidation process. They used LED light as a source of radiation, and ferrous sulfate and iron residue as catalysts. In another study, Menezes et al.<sup>16</sup> investigated the effect of the combination of anaerobic process and micro-aeration (continuous and intermittent) on DB-22 removal. Shu et al.<sup>17</sup> examined the decolorization of DB-22 using the  $\text{UV}/\text{H}_2\text{O}_2$  process, ozonation, and pre-ozonation coupled with  $\text{UV}/\text{H}_2\text{O}_2$ . Moreover, some other studies focused on the photoelectrochemical oxidation of DB-22 under elevated oxygen pressure and the adsorption of DB-22 using polymeric adsorbent.<sup>18,19</sup>

The aim of this study is to investigate photo-Fenton like oxidation of DB-22 using zeolite modified zinc ferrite. Kinetic and thermodynamic properties of the DB-22 decolorization and the effects of the reaction parameters such as catalyst modification with HCl, catalyst amount,  $\text{H}_2\text{O}_2$  amount, salt addition, pH, initial dye concentration, temperature were also investigated. The zeolite and synthesized catalysts were characterized using FTIR, SEM, EDS and XRD.

## 2. Materials and Methods

### 2.1. Materials and Equipments

The zeolite with a particle size of 23  $\mu$  was procured from a company in Balıkesir, Turkey. It was a commercial product and used without purification. HCl and NaOH were procured from Tekkim, DB-22 (commercial name Direct Black 22 VSF 1600) from a company named “HNY” in Turkey,  $\text{H}_2\text{O}_2$  (34.5–36.5 w/w %, Cas no: 7722-84-1) from Sigma,  $\text{CaCl}_2$  from Emir Kimya,  $\text{FeSO}_4\cdot 7\text{H}_2\text{O}$  (Cas no: 7782-63-0) from Merck and  $\text{ZnSO}_4\cdot 7\text{H}_2\text{O}$  (Art no: 8881) from Merck.

A magnetic stirrer (HSD-180), pH meter (C561, Consort), digital scale (Ohaus), centrifuge (Nuve, NF 200), and incubator (Ecocell) were used in the study. UV- spectrophotometer (Hach, DR-2400) was used to measure the absorbance of the sample. A COD reactor (Hach DRB 200) was used to heat the samples before measuring the COD value. A UV lamp (Light Tech GPH212T5L/4, 10 W) with a wavelength of 254 nm was used in the photocatalytic decolorization of DB-22.

### 2.2. Preparation of the Catalyst

The catalyst, zeolite/Zn/Fe was prepared by chemical coprecipitation method. First, iron II sulphate heptahydrate ( $\text{FeSO}_4\cdot 7\text{H}_2\text{O}$ ) and zinc sulphate heptahydrate ( $\text{ZnSO}_4\cdot 7\text{H}_2\text{O}$ ) with a molar ratio of 2:1 were dissolved in 200 ml distilled water. Then, zeolite was added to the solution and heated to 65–70 °C while stirring with a magnetic stirrer. The mixture was stirred for 30 min using a magnetic stirrer. 3 M NaOH solution was added dropwise to the solution, and pH of the solution was adjusted to 12. After addition of NaOH solution, stirring was continued for one hour at 100 °C. The prepared catalyst was left for one day at room conditions, and then placed in water bath for 4 h at 95 °C. After that, it was dried at 95 °C for 90 h. The dried composite was soaked in 0.1 N HCl solution at room temperature for 24 hour, and then filtered and washed using distilled water. Finally, it was dried at 95 °C for 60 hours. The catalysts treated with and without HCl were coded as m-ZZF and ZZF, respectively.

### 2.3. Characterization

The catalysts used in the study were characterized by XRD, FTIR, SEM and EDS. The crystalline structure of the samples was determined by XRD analysis using Rigaku Smart Lab with Cu-K $\alpha$  radiation at 40kV and 30mA. The samples were scanned from 5°– 90° at a rate of 2°/min, and with a step size of 0.01. FTIR (PerkinElmer, Spectrum Two) was used to identify the functional groups of the adsorbents before and after adsorption in the range of 400–4000  $\text{cm}^{-1}$ . SEM and EDS analysis were performed using Tescan, MAIA3 XMU.

## 2. 4. Experimental

In the study, a cylindrical glass reactor with a volume of 250 ml, a height of 20 cm, and a diameter of 5 cm was used. The reactor was filled with 200 ml of DB-22 solution with a known concentration, and the catalyst was added, then magnetically stirred for 30 min in the dark to ensure a complete equilibration of adsorption/desorption of DB-22 on the catalyst surface. In order to find the amount of dye adsorbed on the catalyst surface in the dark, a sample was taken from the dye solution and its absorbance was measured. Then, a UV lamp with a quartz tube was placed in the center of the reactor at a distance of 2 cm from the bottom. The surface of the reactor was covered with aluminum foil to prevent light penetration. While the DB 22 solution was stirred continuously, the UV lamp was switched on and the reaction time was started immediately. Stirring rate was kept constant at 800 rpm in all experiments. The experiments were carried out at the original pH of the dye solution, except for the experiments in which the pH effect was examined. The samples taken from the reactor at regular intervals were centrifuged at 5000 rpm for 10 minutes. Then, the absorbance of the dye solution was recorded at 481 nm using UV-spectrophotometer to calculate decolorization. Decolorization of DB-22 dye was calculated using the Eq. 1

$$\text{Decolorization, \%} = \frac{(C_0 - C)}{C_0} * 100 \quad (1)$$

where,  $C_0$  and  $C$  represent the concentration of the DB-22 at the beginning of the reaction and at corresponding time, respectively.

COD was measured using Hach DR 2400 spectrophotometer, Hach COD reactor and test kits in the range 0–1500 ppm. Instructions for the Hach higher range test followed.

The DB-22 solution temperature was not controlled in the experiments. The reaction was started at a room temperature of 25 °C, except for the experiments in which the effect of temperature was examined, and a temperature

increase of 15 °C was observed at the end of 60 minutes. No temperature control was done to constitute a natural environment and to save on cooling water cost.

## 3. Results and Discussion

### 3.1. Catalyst Characterization

The XRD pattern of the zeolite (Z) and m-ZZF are shown in Fig.1. As can be seen in the Fig.1, all diffraction peaks were apparent and strong. This indicates that the Z and m-ZZF samples were in crystalline form.

According to XRD data, zeolite (Z) was identified by its characteristic X-ray diffraction peaks at  $2\theta$ : 11.15°, 16.87°, 20.84°, 22.34°, 22.73°, 26.02°, 26.6°, 29.85°. These XRD peaks of the Z coded sample are compatible with the clinoptilolite with PDF card no 00-013-0304. This result shows that the zeolite was composed of clinoptilolite. As shown in Fig.1-b, all peaks of natural zeolite accept 26.74° disappeared after the preparation of m-ZZF. According to the PDF card, peaks appear at 34.96°, 52.74° and 61.97° matchwell with PDF card 00-010-0467 (Franklinite,  $\text{Zn-Fe}_2\text{O}_4$ ). Spinel ferrite  $\text{ZnFe}_2\text{O}_4$  coats the surface of zeolite. This improves the photocatalytic activity of m-ZZF.

Figure 2 shows the SEM images and EDS results of zeolite (Z) and m-ZZF. As can be seen in SEM image of Z, particles had an irregular shape and porous surface. In m-ZZF image, zinc ferrite agglomerated on the surface of the zeolite. According to EDS results, zeolite was mainly composed of O, Si, and Al, in addition to small amounts of K, Mg, Ca and Fe. The percentage of iron and zinc considerably increased in m-ZZF.

Figure 3 shows the FTIR spectra of zeolite, ZZF, m-ZZF, and m-ZZF after being used in DB-22 decolorization. As can be seen in Fig. 3, the zeolite had bands around 800, 1030, and 1630  $\text{cm}^{-1}$ . The band between 450 and 1100  $\text{cm}^{-1}$  was related to the active zeolite lattice bands.<sup>20</sup> The band at 800  $\text{cm}^{-1}$  corresponds to the stretching vibration of Si-O-Si. The absorption bands around 1030  $\text{cm}^{-1}$

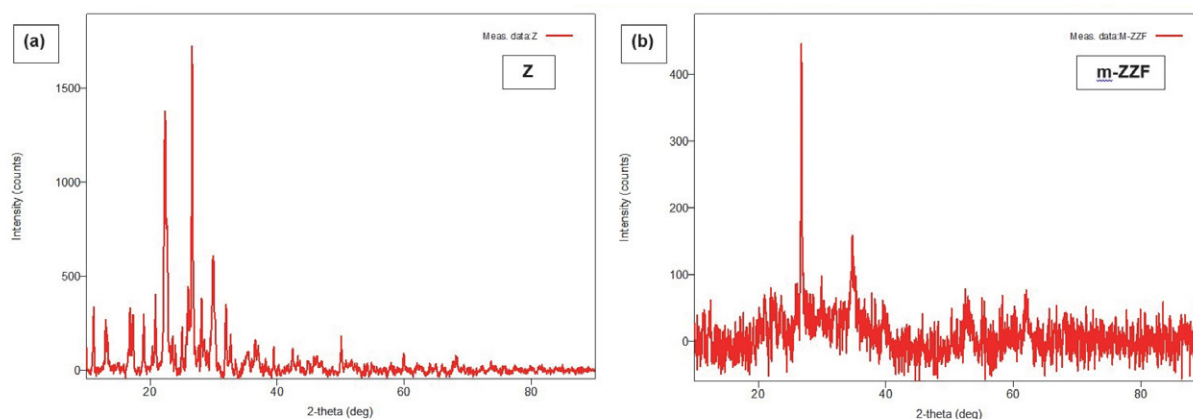


Fig. 1. XRD analysis of (a) Z and (b) m-ZZF

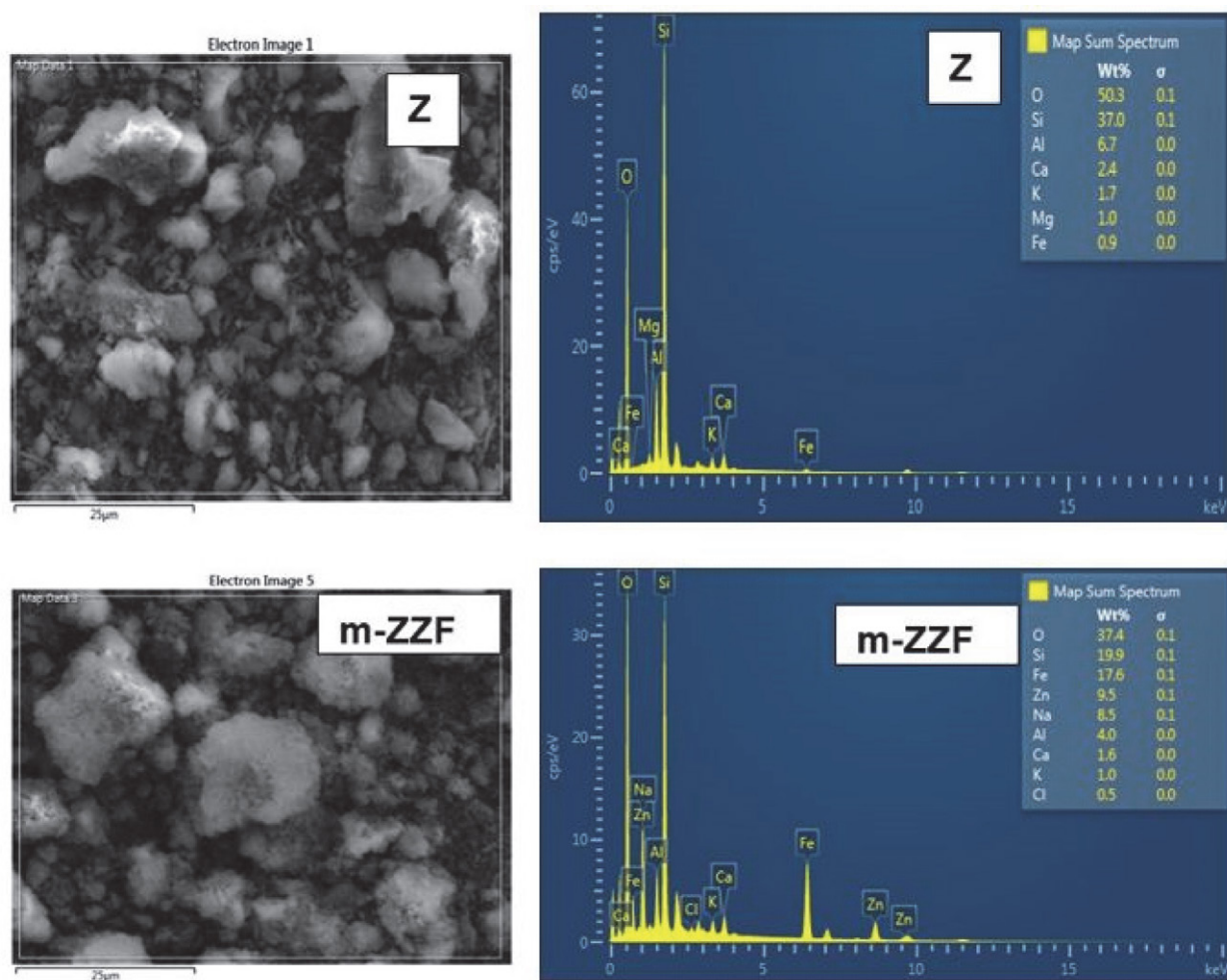


Fig. 2. SEM image and EDS results of zeolit and m-ZZF

were due to asymmetric stretching vibrations of Al and/or Si bonding with oxygen. The peak at  $1030\text{ cm}^{-1}$  is the proof that the zeolite was composed of alumina silicate. The peak at  $1030\text{ cm}^{-1}$  is sensitive to the change in Si and Al content. The band at  $1630\text{ cm}^{-1}$  is related to the O-H stretching vibrations and the adsorbed  $\text{H}_2\text{O}$  molecules.<sup>20–23</sup> As seen in Fig. 3, there were a few differences between Z, ZZF, and m-ZZF spectrum. In ZZF and m-ZZF, the peaks at  $800\text{ cm}^{-1}$

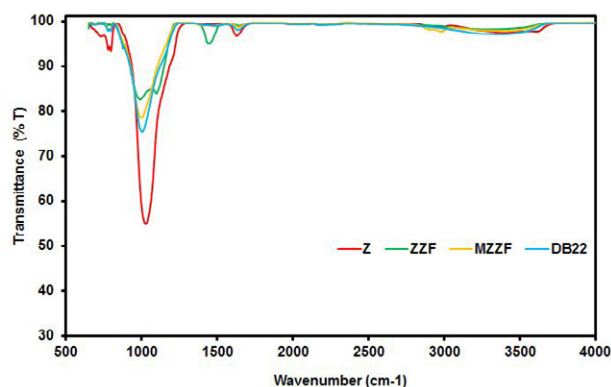


Fig. 3. FTIR analysis of the Z, ZZF, m-ZZF and m-ZZF after being used in DB-22 decolorization

$\text{cm}^{-1}$  and  $1630\text{ cm}^{-1}$  disappeared. The peak at  $1000\text{ cm}^{-1}$  in m-ZZF was the result of the shift of the peak at  $1030\text{ cm}^{-1}$  in Z, and the transmittance at  $1000\text{ cm}^{-1}$  increased. With the addition of zinc ferrite to the structure of the zeolite, the ratio of Al and Si changed. Maybe that is why, the transmittance increased. The FTIR spectrum of m-ZZF after it was used in DB-22 decolorization was similar to that before it was used and only the transmittance at  $1000\text{ cm}^{-1}$  decreased.

### 3.2. The effect of HCl Modification of Catalyst on Photocatalytic Decolorization of DB-22

In order to determine the effective catalyst in the photocatalytic degradation of DB-22, the experiments were performed under the following reaction conditions: initial dye concentration:  $0.04\text{ g/L}$ , catalyst loading:  $4\text{ g/L}$ , original pH, and UV lamp. As seen in Fig. 4-a, in the presence of ZZF and m-ZZF, the decolorization rate was higher with using UV lamp than without UV lamp. The catalyst modified with HCl (m-ZZF) gave better results than ZZF. Mesopores formed as a result of acid treatment of zeolite

are active surfaces for the adsorption and catalysis of relatively large molecules.<sup>22</sup> The decolorization of DB-22 using UV light and 4 g/L m-ZZF was 10.9% and 14.6% at the end of 30 min and 60 min, respectively. On the other hand, a decolorization of 6.4% and 12.8% was observed in the experimental set up with UV light and 4 g/L ZZF at the reaction times of 30 min and 60 min respectively. So, the decolorization rate increased in the system using UV light and m-ZZF. Considering the individual m-ZZF and UV processes, it is seen that the photocatalytic activity of m-ZZF is very poor.

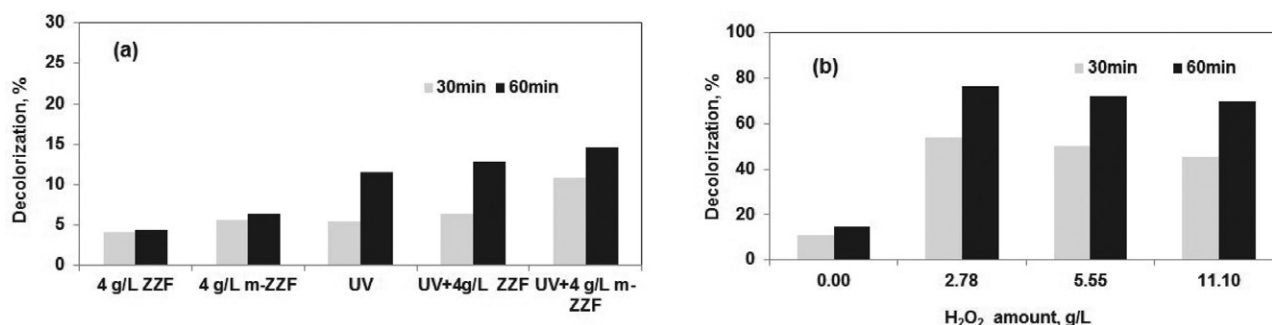
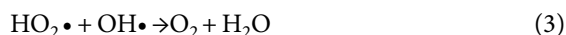
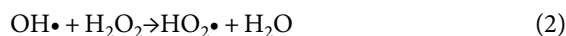


Fig. 4. Effect of (a) HCl modification of catalyst (initial dye concentration: 0.04 g/L, initial temperature: 25 °C, catalyst amount: 4 g/L, original pH) and (b) H<sub>2</sub>O<sub>2</sub> concentration (initial dye concentration: 0.04 g/L, initial temperature: 25 °C, m-ZZF amount: 4 g/L, original pH, UV light) on the decolorization of DB-22

### 3.3. Effect of Hydrogen Peroxide Amount

The effect of hydrogen peroxide amount on the decolorization of DB-22 was studied with the H<sub>2</sub>O<sub>2</sub> amounts of 2.78 g/L, 5.55 g/L, and 11.1 g/L while keeping all other parameters constant (initial DB-22 concentration: 0.04 g/L, m-ZZF amount: 4 g/L, UV light, and original pH). The results are presented in Fig. 4-b. As seen in Fig. 4-b, the decolorization of DB-22 without the addition of H<sub>2</sub>O<sub>2</sub> was less than that with the addition of H<sub>2</sub>O<sub>2</sub>. The photocatalytic decolorization of the DB-22 enhanced when the H<sub>2</sub>O<sub>2</sub> amount was introduced to the Fenton system due to the accelerated generation of hydroxyl radicals (OH•).<sup>24</sup> According to our results, the decolorization rate decreased with increasing H<sub>2</sub>O<sub>2</sub> concentration. In 60 min, the decolorization rate increased from 69.5% to 76.4% when the H<sub>2</sub>O<sub>2</sub> concentration decreased from 5.55 g/L to 2.78 g/L.

At high H<sub>2</sub>O<sub>2</sub> concentrations, excess hydrogen peroxide reacts with the produced OH• radicals and causes the formation of less reactive radicals like hydrogen dioxide.<sup>21,25</sup> The reactions between OH• radicals and excess hydrogen peroxide are given by the equations below<sup>26</sup>:



A similar result was reported by Abharya et al.<sup>24</sup> They reported that photocatalytic degradation decreased after the

H<sub>2</sub>O<sub>2</sub> concentration of 0.0389 M and when the amount of H<sub>2</sub>O<sub>2</sub> was above the critical value, the reaction between excess H<sub>2</sub>O<sub>2</sub> and the generated OH• radicals caused a decrease in photocatalytic activity over time. In another study, Badvi and Javanbakht<sup>21</sup> reported similar results for the photocatalytic degradation of methylene blue. They found that the dye degradation decreased when the H<sub>2</sub>O<sub>2</sub> concentration was increased from 250 to 750 mg/L. Moreover, they asserted that when H<sub>2</sub>O<sub>2</sub> concentration exceeded a certain level, hydrogen peroxide acted as a scavenger of the photo produced holes and caused a decrease in the efficiency of dye degradation.

### 3.4. Effect of Catalyst Amount

In order to examine the effect of the amount of catalyst and to find the optimum amount of catalyst, experiments were carried out by changing the amount of catalyst between 1 g/L and 6 g/L while keeping the other parameters constant (H<sub>2</sub>O<sub>2</sub> amount: 2.78 g/L, initial DB-22 concentration: 0.04 g/L, UV light, original pH and initial temperature: 25 °C). The results are presented in Fig. 5-a.

As can be seen in Fig. 5-a, as the catalyst amount was increased from 1 g/L to 3 g/L, the decolorization rate of DB-22 increased from 78.0% to 80.8%. After the catalyst loading of 3 g/L, the decolorization rate decreased. Under the studied conditions, the optimum catalyst amount was found to be 3 g/L. This means that, the catalyst amounts higher than the optimum value may decrease the light transmittance. Abharya et al.<sup>24</sup> investigated the photocatalytic treatment of methylene blue and obtained similar results. They reported that the number of reactive sites increased with increasing catalyst loading and after the optimum catalyst amount, the catalyst particles tended to agglomerate, causing a decrease in the number of reactive sites and an increase in light scattering. In another study, Gan and Li<sup>27</sup> investigated the decolorization of Rhodamine B using catalyst by Fenton like process. They reported that the decolorization of Rhodamine B increased with increasing the catalyst amount from 0.5 g/dm<sup>3</sup> to 1 g/dm<sup>3</sup>, but after 1 g/dm<sup>3</sup>, it started to decrease. They also reported that, after the optimum catalyst amount (1 g/dm<sup>3</sup>), the catalyst surface area decreased due to the aggregation between particles, and as a result, color removal decreased.

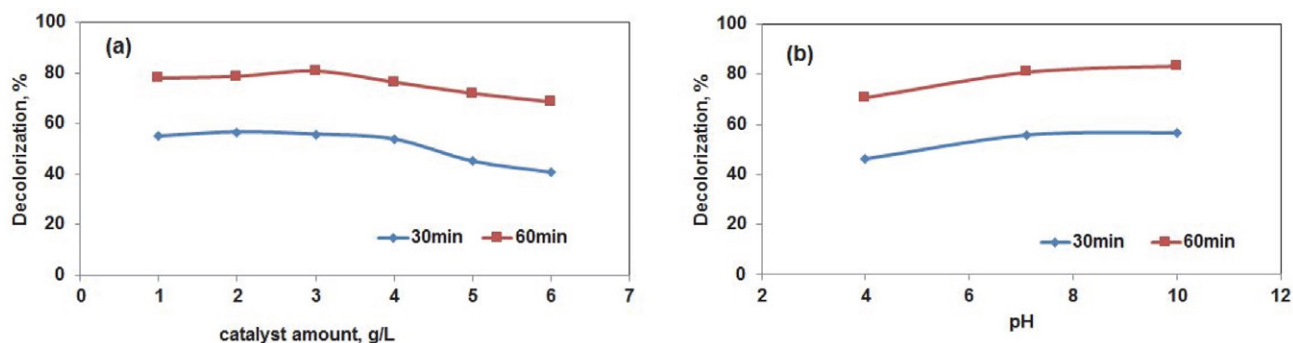


Fig. 5. Effect of (a) m-ZZF amount (initial dye concentration: 0.04 g/L, initial temperature: 25 °C, original pH, H<sub>2</sub>O<sub>2</sub> amount 2.78 g/L, UV light) (b) pH (initial dye concentration: 0.04 g/L, initial temperature: 25 °C, H<sub>2</sub>O<sub>2</sub> amount 2.78 g/L, m-ZZF amount: 3 g/L, UV light) on the decolorization of DB-22

Ejhieh and Khorsandi<sup>1</sup> investigated the photocatalytic decolorization of Eriochrome Black T using NiS-P zeolite. They reported that the decolorization of Eriochrome Black T increased with increasing the catalyst amount from 0.1 g/L to 0.8 g/L, but after 0.8 g/L, it started to decrease. They asserted that as the amount of catalyst increased, the solid particles blocked the photon penetration. In another study, Ji et al.<sup>28</sup> investigated the decolorization of methylene blue using catalyst and heterogeneous photo Fenton system and reported that the decolorization of methylene blue increased with increasing the catalyst from 0.25 to 1.5 g/L. As the amount of catalyst increases, the number of active sites increases. In the catalyst amounts higher than 1.5 g/L, the catalyst particles prevented the transmission of UV light into the solution. Therefore, with the increase of the amount of catalyst from 1.5 to 2 g/L, the rate of decolorization decreased.

### 3.5. Effect of Initial pH

The effect of pH on the decolorization of DB-22 was studied at the initial pHs of 4, ≈7.1, and 10. ≈7.1 is the original pH of the dye solution. The pH of the DB-22 solution was adjusted at the beginning of the experiment. pH control was not done during the reaction. Fig. 5-b shows the results.

The decolorization of DB-22 increased when the pH was increased from 4 to 10. The decolorization of DB-22 was found to be 70.8%, 80.2%, and 83.3% at the pH values of 4, 7.1, and 10 respectively. Karimi-Shamsabadi et al.<sup>29</sup> obtained similar results for the photocatalytic degradation of Eriochrome black T using NiO-ZnO doped nanozeolite X. They reported that at the basic pH, due to higher concentration of hydroxyl ions, the concentration of hydroxyl radicals increased, which enhanced the photocatalytic degradation rate. In another study by Ejhieh and Khorsandi<sup>1</sup>, it was asserted that the degradation of Eriochrome Black T increased with increasing the initial pH. Under the acidic conditions, Cl<sup>-</sup> ions and hydroxyl radicals combine to form inorganic radical ions (ClO<sup>-•</sup>). They reported that the reactivity of ClO<sup>-•</sup> anions was less than that of hydrox-

yl radicals, therefore, these radicals did not involve in the decolorization reactions. Under basic conditions, due to the increase in the number hydroxyl radicals, the decolorization rate increased.

### 3.6. Effect of Salt Addition

The effect of salt on the decolorization of DB-22 was investigated using CaCl<sub>2</sub>. The results obtained for different CaCl<sub>2</sub> amounts are given in Fig. 6. As can be seen in Fig. 6, the decolorization rate of DB-22 increased with the addition of CaCl<sub>2</sub>. When the CaCl<sub>2</sub> amount was increased from 2.5 to 5 g/L, no significant change was observed in the decolorization rate at the reaction time of 60 min. In the reaction time of 30 min, while the decolorization of DB-22 was found to be 83.2% in the case of the addition of 2.5 g/L CaCl<sub>2</sub>, it was 90.1% in the case of the addition of 3.75 g/L CaCl<sub>2</sub>. 3.75 g/L CaCl<sub>2</sub> was chosen due to the higher decolorization rate at 30 min. The results show that m-ZZF is effective in the presence of CaCl<sub>2</sub>.

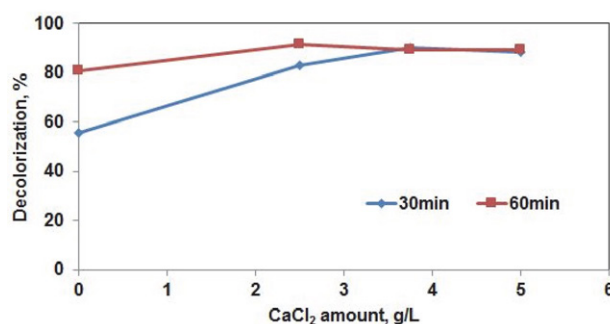


Fig. 6. Effect of CaCl<sub>2</sub> amount on the decolorization of DB-22 (initial dye concentration: 0.040 g/L, initial temperature: 25 °C, original pH, H<sub>2</sub>O<sub>2</sub> amount: 2.78 g/L, m-ZZF amount: 3 g/L, UV light)

Gan et al.<sup>27</sup> reported similar results in their study investigating the effect of ionic strength using different concentrations of NaCl. According to their results, increasing NaCl from 0.05 M to 0.1M did not change the degradation rate. The ionic strength for the adsorption of dye on oxide surface can influence the electrostatic interactions



between the oxide surface and the dye species. In heterogeneous catalytic systems, the presence of excess anions may affect the equilibria between the dye molecules and the catalyst surface.<sup>27</sup>

When low concentrations of salt are used,  $\text{Cl}\cdot$  radicals with high oxidizing potential are formed and they oxidize organic materials.  $\text{Cl}\cdot$  radicals have a high affinity for a hole and they can also prevent electron-hole recombination, thus enhancing the efficiency of reactive species formation. If the salt amount is more than the optimum value, the dye removal efficiency decreases. This is because the  $\text{Cl}^-$  competes with the dye molecules for the limited catalyst surface and the surface is deactivated.<sup>30</sup>

### 3. 7. Effect of Initial Dye Concentration and Reaction Time

In the study, the effects of initial dye concentration and reaction time on DB-22 decolorization were also investigated. The experiments were done within the initial concentration range of 0.025–0.070 g/L with a m-ZZF amount of 3 g/L,  $\text{H}_2\text{O}_2$  amount of 2.78 g/L, and  $\text{CaCl}_2$  amount of 3.75 g/L, at original pH, at an initial temperature of 25 °C and under UV light. Fig. 7 shows the effect of initial dye concentration and reaction time on the decolorization of DB-22.

The experimental results showed that the decolorization rate of DB-22 was faster in the first 10 min. After 10 min, decolorization rate slowed down and remained almost constant after the reaction time of 30 min. As seen in Fig. 7, the decolorization of DB-22 increased with the increasing initial concentrations. The decolorization of DB-22 for the reaction time of 60 min was found to be 81.3%, 90.2%, 90.5%, 91%, and 93.3% at the initial dye concentrations of 0.025, 0.040, 0.050, 0.060, and 0.070 g/L, respectively. In the literature, Ejhieh and Khorsandi<sup>1</sup> reported similar results for the photocatalytic decolorization of Eriochrome Black T using NiS-P zeolite. They found that the decolorization of Eriochrome Black T increased with increasing the initial concentration from 10 mg/L to 40 mg/L. Having a lifetime as short as a few nanoseconds, hydroxyl radicals react immediately after formation.

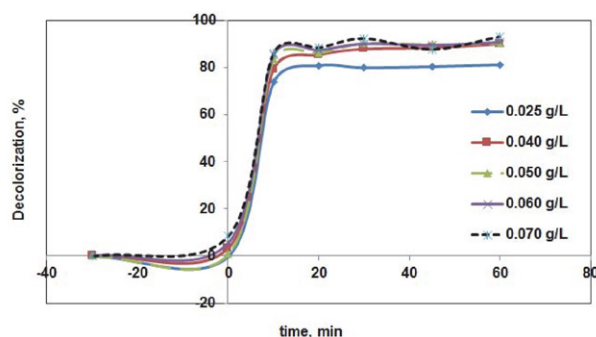


Fig. 7. Effect of initial dye concentration on the decolorization of DB-22 (pH: original, initial temperature: 25 °C,  $\text{H}_2\text{O}_2$  amount: 2.78 g/L, m-ZZF amount: 3 g/L,  $\text{CaCl}_2$  amount: 3.75 g/L, UV light)

As the number of dye molecules per unit volume increases, so does the probability of collisions between organic matter and oxidizing species. As a result, decolorization rate increases. In their study, Gan and Li<sup>27</sup> found that the decolorization of Rhodamine B increased with increasing the initial concentration from 2.5 to 50 mg/L using rice-hull based silica supported catalyst by Fenton like process. The probability of collision between dye molecules and near-surface activating species increases with the increase of dye concentration per volume.

### 3. 8. Effect of Temperature

The effect of temperature on the decolorization of DB-22 was investigated at 25 °C, 35 °C, and 45 °C while keeping other parameters constant (initial concentration of dye: 0.040 g/L, initial pH: original,  $\text{H}_2\text{O}_2$  amount: 2.78 g/L, m-ZZF amount: 3 g/L,  $\text{CaCl}_2$  amount: 3.75 g/L, UV light). As mentioned in the experimental section, the experiments were performed without cooling, and a temperature increase was observed. Initial decolorization rate was calculated for the reaction time of 10 min. An increase of 2 °C from the initial temperature was observed in 10 min.

Figure 8 shows the effect of temperature on the initial decolorization rate. As can be seen in Fig. 8, the initial decolorization of DB-22 in 10 min decreased with increasing temperatures. The decrease in the decolorization rate with the increasing temperatures shows that the reaction occurred under exothermic conditions. An increase in the reaction temperature causes a decrease in the oxygen solubility in the solution. The rate of electron withdrawal from the surface of the photocatalyst decreases due to the decrease in dissolved oxygen concentration.<sup>31</sup> Andreozzi et al.<sup>3</sup> investigated the effect of temperature on the photocatalytic degradation of 4-nitrophenol and reported that temperature had a negative effect on the degradation at pH 3. The presence of oxygen is important to keep high the concentration of photogenerated  $\text{OH}\cdot$  radicals on the surface of the catalyst. The concentration of the photogenerated holes decreases due to the decrease in oxygen solubility at high reaction temperatures.

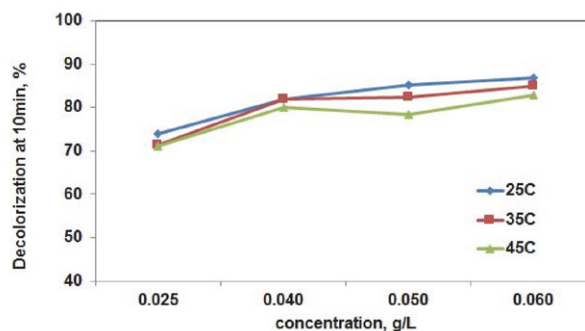


Fig. 8. Effect of temperature on the initial decolorization rate of DB-22 (initial pH: original,  $\text{H}_2\text{O}_2$  amount: 2.78 g/L, m-ZZF amount: 3 g/L,  $\text{CaCl}_2$  amount: 3.75 g/L, UV light)



### 3. 9. Decolorization of DB-22 using Different Processes

Decolorization of DB-22 was investigated at 0.040 g/L initial dye concentration and 25 °C initial temperature using different processes. The results are given in Fig. 9. Decolorization rate using 3 g/L m-ZZF and (3 g/L m-ZZF + 2.78 g/L H<sub>2</sub>O<sub>2</sub>) processes were 2.4% and 5.7% respectively. The effect of UV light was studied using processes such as, 3g/L m-ZZF, 2.5g/L CaCl<sub>2</sub> and (3 g/L m-ZZF + 2.5 g/L CaCl<sub>2</sub>). Decolorization of (UV + 3 g/L m-ZZF + 2.5 g/L CaCl<sub>2</sub>) process was greater than that of the individual processes such as UV, (UV + 3g/L m-ZZF) and (UV + 2.5g/L CaCl<sub>2</sub>). Decolorization rate was 76.1 % at 30 min and 82.3 % at 60 min using (UV + 3 g/L m-ZZF + 2.5 g/L CaCl<sub>2</sub>) process. To identify the effect of the H<sub>2</sub>O<sub>2</sub>, experiments were also done using (UV + 2.78 g/L H<sub>2</sub>O<sub>2</sub>), (UV + 2.78 g/L H<sub>2</sub>O<sub>2</sub> + 2.5 g/L CaCl<sub>2</sub>), (UV + 2.78 g/L H<sub>2</sub>O<sub>2</sub> + 3 g/L m-ZZF) and (UV + 2.78 g/L H<sub>2</sub>O<sub>2</sub> + 3 g/L m-ZZF + 2.5 g/L CaCl<sub>2</sub>). (UV + 2.78 g/L H<sub>2</sub>O<sub>2</sub>) and (UV + 2.78 g/L H<sub>2</sub>O<sub>2</sub> + 3 g/L m-ZZF) processes provided nearly the same decolorization rate as 82% at 60 min. Decolorization rate at 60 min using (UV + 2.78 g/L H<sub>2</sub>O<sub>2</sub> + 3 g/L m-ZZF + 2.5 g/L CaCl<sub>2</sub>) process was found to be 91.5%.

The decolorization of DB-22 for the reaction time of 30 min was found to be 76.1% at (UV+ 3 g/L m-ZZF + 2.5 g/L CaCl<sub>2</sub>) process. Addition of H<sub>2</sub>O<sub>2</sub> increased the color removal and decolorization of DB-22 at 30 min was found to be 83.2% at (UV + 2.78 g/L H<sub>2</sub>O<sub>2</sub> + 3 g/L m-ZZF + 2.5 g/L CaCl<sub>2</sub>) process. With increasing CaCl<sub>2</sub> amount from

2.5 to 3.75 g/L, decolorization rate increased from 83.2% to 90.1% in 30 min reaction time. With the synergetic effect of UV, m-ZZF, H<sub>2</sub>O<sub>2</sub> and CaCl<sub>2</sub>, the highest color removal was achieved in 30 minutes. Ionic strength effects the electrostatic interaction between the catalyst surface and dye molecules. Addition of anions might allow the neutralization of the positive sites on catalyst surface. Nonelectrostatic interaction between dye molecules and neutral sites could occur due to van der Waals forces or low energetic H-bonds.<sup>27</sup> According to Sudrajat and Babel<sup>30</sup>, the Cl• radicals formed as a result of the surface chain transfer reaction of the chlorine ion oxidizes the organic compounds.

Considering these results, the possible decolorization mechanism of DB-22 over m-ZZF may consist of the following steps: Due to the non-electrostatic interaction between the dye molecules and the neutral sites, dye molecules may be adsorbed on the catalyst surface in the presence of Cl<sup>-</sup> ions.<sup>27</sup> Electron/hole pairs are generated on the m-ZZF surface under UV light. Electrons on m-ZZF react with H<sub>2</sub>O<sub>2</sub> to produce both OH<sup>-</sup> ions and OH• radicals. Photogenerated holes could react with OH<sup>-</sup> ions or adsorbed water to generate OH• radicals.<sup>33,34</sup> In the presence of salt, the Cl• radicals could oxidize dye molecules.<sup>30</sup> The generated radicals react with DB-22 and degradation products are formed.

### 3. 10. COD Removal

The COD value represents the amount of oxygen required for oxidation of organics into CO<sub>2</sub> and water. It is

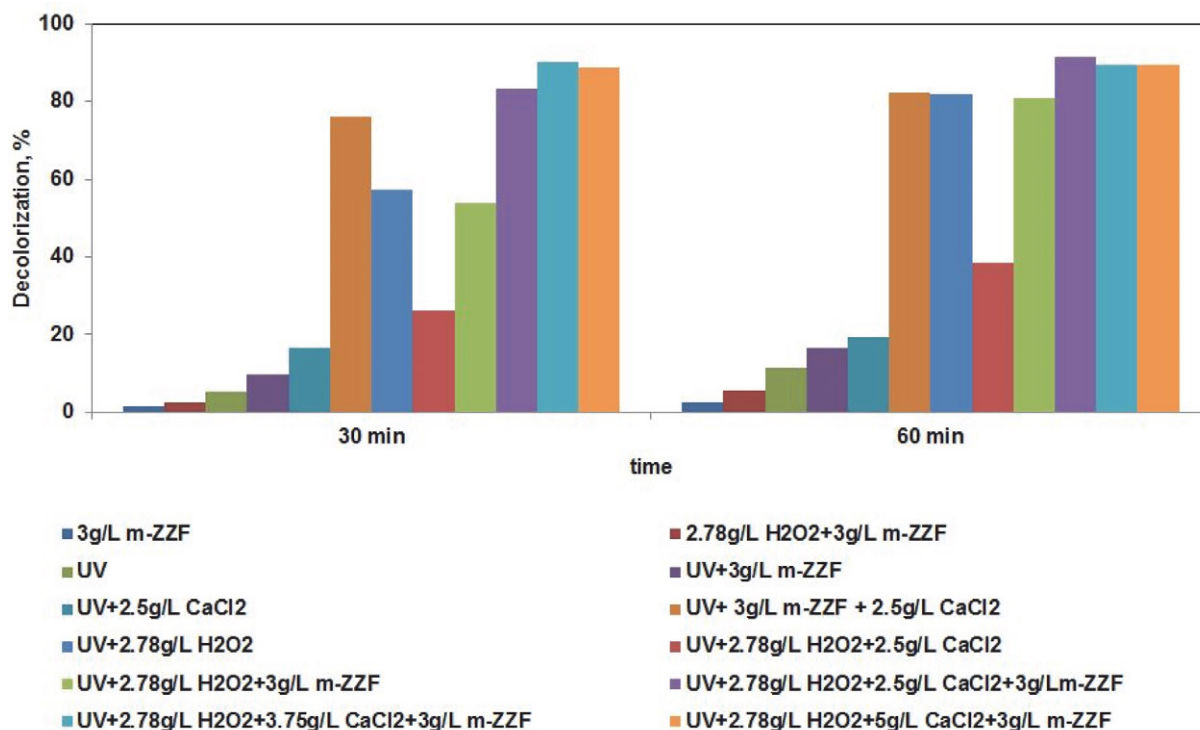


Fig. 9. Comparison of different processes

related with total organic compounds in the wastewater. In the study, the variation of COD with time was investigated under the following reaction conditions: initial dye concentration: 0.04 g/L, m-ZZF amount: 3 g/L, H<sub>2</sub>O<sub>2</sub> amount: 2.78 g/L, CaCl<sub>2</sub> amount 3.75 g/L, original pH, and UV lamp. As seen from Fig. 10, COD removal increases with increasing time. 26.9% COD removal was obtained at the end of 60 min reaction time. While the decolorization of DB-22 was found to be 79.5% and 90.1% at the 10 min and 30 min reaction time respectively, low COD removal was achieved under the studied conditions. COD removal showed the partial oxidation of the organic pollutants to CO<sub>2</sub> and H<sub>2</sub>O. The colorless intermediates were formed as a result of DB-22 oxidation. These intermediates cause low COD removal.<sup>34</sup> According to results, photo-Fenton like process is more useful for decolorization of DB-22 than COD removal.

The operating cost of the photo-Fenton process includes cost of chemicals and energy. Electricity is used in the UV lamp and mixing the process. According to Çalık<sup>35</sup>, operating cost of the photo-Fenton process changed between 13.46–20.13 €/m<sup>3</sup> for the used chemicals and electrical energy for treatment of textile wastewater.

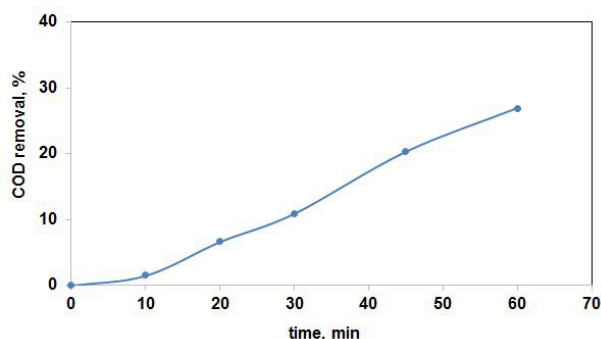


Fig. 10. Variation of COD with time (initial dye concentration: 0.04g/L, pH: original, initial temperature: 25 °C, H<sub>2</sub>O<sub>2</sub> amount:2.78 g/L, m-ZZF amount: 3 g/L, CaCl<sub>2</sub> amount: 3.75 g/L, UV light)

### 3. 11. Kinetic and Thermodynamic Studies

The initial rate equation for decolorization of dye is as follows:

$$r_o = \left(-\frac{dC}{dt}\right)_o = k_{app} C_o^n \quad (5)$$

where  $k_{app}$  is the overall observed rate constant for the reaction,  $n$  is the order of the reaction with respect to concentration. Eq. 5 is linearized by taking the natural logarithm and Eq. 6 is obtained.

$$\ln(r_o) = \ln k_{app} + n \ln C_o \quad (6)$$

If  $\ln(r_o)$  is plotted against  $C_o$ , the slope of the straight line gives the degree of reaction ( $n$ ) and intercept gives the

$\ln k_{app}$  value. Fig. 11 shows the plot of  $\ln(r_o)$  against  $\ln C_o$  for 25 °C, 35 °C, and 45 °C. The initial decolorization rate of DB-22 was calculated for the initial 10 min. The calculated  $n$  and  $k_{app}$  values were listed in Table 1. A high regression coefficient indicates a good compatibility. The values of  $n$  were 1.08, 1.12, and 1.16 at 25 °C, 35 °C and 45 °C respectively. It can be said that, the reaction order of the photocatalytic decolorization of DB-22 was 1.1 under the studied conditions.

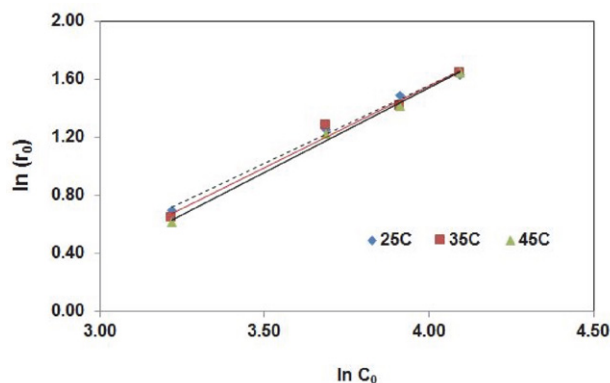


Fig. 11.  $\ln(r_o)$  versus  $\ln C_o$  (initial pH: original, H<sub>2</sub>O<sub>2</sub> amount: 2.78 g/L, m-ZZF amount: 3 g/L, CaCl<sub>2</sub> amount: 3.75 g/L, UV light)

Table 1. The reaction orders and rate constants

T (K)	n	$k_{app} \text{ (mg/L)}^{-0.1}/\text{min}$	R <sup>2</sup>
298	1.08	0.064	0.9946
308	1.12	0.053	0.9847
318	1.16	0.044	0.9949

The activation energy of the reaction was calculated using Arrhenius equation<sup>36</sup>.

$$k_{app} = A e^{-E_a/RT} \quad (7)$$

where  $k_{app}$  is the apparent reaction rate constant,  $A$  is the Arrhenius factor,  $E_a$  is the activation energy (J/mol),  $R$  is the ideal gas constant (8.314 J/molK), and  $T$  is the temperature (K). The logarithmic form of Eq. 7 can be written as:

$$\ln k_{app} = \ln A - E_a/RT \quad (8)$$

When  $\ln k_{app}$  is plotted against  $1/T$ , the slope gives  $-E_a/R$ . The Arrhenius plot is presented in Fig. 12-a. Activation energy,  $E_a$  was calculated to be -14.76 kJ/mol under the studied conditions. This result showed that the decolorization rate decreased with increasing temperature, as mentioned in the section 3.4. The activation energy is the minimum energy required to break the bonds of the species participating in the reaction and to form new bonds. A low activation energy indicates that less energy is required to break bonds.<sup>37</sup>

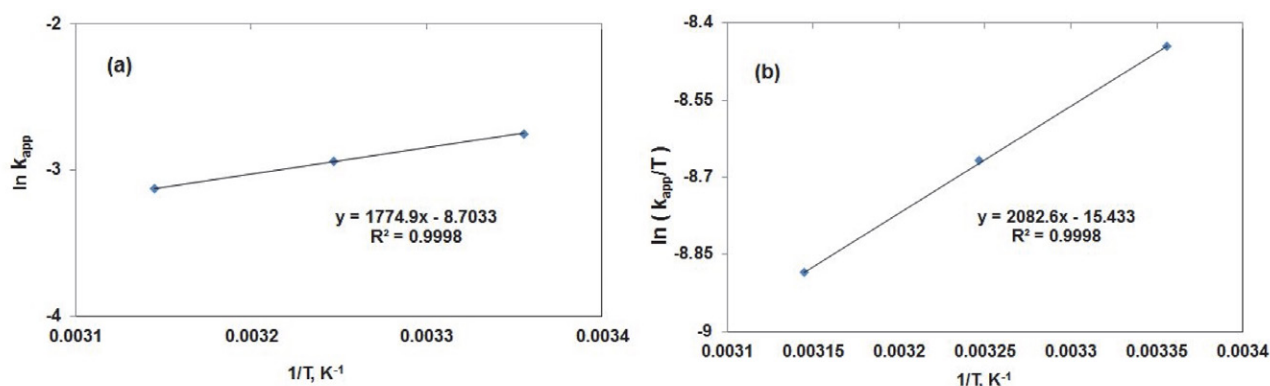


Fig. 12. (a) Arrhenius plot of  $\ln k_{app}$  against  $1/T$  (b)  $\ln(k_{app}/T)$  versus  $1/T$

The activation enthalpy ( $\Delta H^0$ ) and the activation entropy ( $\Delta S^0$ ) were calculated by plotting  $\ln(k_{app}/T)$  against  $1/T$  according to the equation below<sup>27</sup>:

$$\ln \frac{k_{app}}{T} = \ln \frac{R}{N_A h} + \frac{\Delta S^0}{R} - \frac{\Delta H^0}{RT} \quad (9)$$

where  $N_A$  is Avogadro constant ( $6.022 \times 10^{23} \text{ mol}^{-1}$ ) and  $h$  is Planck constant ( $6.626 \times 10^{-34} \text{ Js}$ ).

The slopes of this line gives  $-\Delta H^0/R$  and the intercept gives  $\ln \frac{R}{N_A h} + \frac{\Delta S^0}{R}$ . Fig. 12-b shows the plot of  $\ln \frac{k_{app}}{T}$  vs  $1/T$ . The reaction enthalpy was calculated to be  $-17.31 \text{ kJ/mol}$ . The sign of the enthalpy indicates an exothermic reaction. The value of activation entropy was calculated as  $-0.326 \text{ kJ/molK}$ . The negative value of  $\Delta S^0$  indicated that the photocatalytic decolorization of DB-22 was less random and the transition state formed in the degradation process had a lower structural freedom compared to the reactants, and this also confirms that the process was irreversible.<sup>37,38</sup>

The lowest absolute values of  $E_a$ ,  $\Delta H^0$ , and  $\Delta S^0$  found for the catalyst used in the study are indicative of its highest catalytic activity. According to the literature, the value of the activation energy determines whether the reaction is diffusion or reaction rate controlled. If the activation energy is lower than  $29 \text{ kJ/mol}$ , this indicates that the reaction is controlled by diffusion process.<sup>39,40</sup> In this study, a low activation energy was obtained; so it can be said that the photocatalytic decolorization of DB-22 using m-ZZF was a diffusion controlled process.

The standard Gibbs free energy was calculated using Eq. 10<sup>36,38</sup>

$$\Delta G^0 = \Delta H^0 - T\Delta S^0 \quad (10)$$

Table 2 gives the thermodynamic parameters. As can be seen in Table 2, standard Gibbs free energy change ( $\Delta G^0$ ) had a positive value and it increased with increasing temperatures. This result indicated no spontaneous processes and weak adsorption of dye molecules on m-ZZF.<sup>36</sup>

Table 2. Kinetic and thermodynamic parameters of the photocatalytic degradation of DB-22

T (K)	$k_{app}$ (mg/L) <sup>-0.1</sup> /min	$E_a$ (kJ/mol)	$\Delta H^0$ (kJ/mol)	$\Delta S^0$ (kJ/molK)	$\Delta G^0$ (kJ/mol)
298	0.064	-14.76	-17.31	-0.326	84.02
308	0.053				87.28
318	0.044				90.36

## 4. Conclusions

In this study, decolorization of Direct Black 22 was investigated using photo Fenton-like method. UV lamp was used as a source of light. Zeolite modified with zinc ferrite (m-ZZF) was used as a heterogeneous catalyst. m-ZZF was prepared by coprecipitation method. The zeolite and m-ZZF were characterized using XRD, SEM, EDS, and FTIR analysis. Zeolite surface was successfully coated with zinc ferrite.

The results showed that under UV light, the decolorization of DB-22 was higher with m-ZZF than with ZZF. The effect of various parameters (initial pH, initial dye concentration, catalyst amount, hydrogen peroxide concentration,  $\text{CaCl}_2$  amount, temperature) on the DB-22 decolorization was analysed, kinetic and thermodynamic investigations were performed as well. The decolorization of DB-22 was found to be 93.3% under the following reaction conditions: initial concentration:  $0.070 \text{ g/L}$ , initial temperature:  $25^\circ\text{C}$ , original pH,  $\text{H}_2\text{O}_2$  amount:  $2.78 \text{ g/L}$ , m-ZZF amount:  $3 \text{ g/L}$ ,  $\text{CaCl}_2$  amount  $3.75 \text{ g/L}$ , reaction time: 60 min, and under UV light. The activation energy was found to be  $-14.76 \text{ kJ/mol}$ . The decolorization reaction was exothermic and the calculated reaction enthalpy was  $-17.31 \text{ kJ/mol}$ . The value of activation entropy was calculated to be  $-0.326 \text{ kJ/mol}$ . The standard Gibbs free energy change of activation had a positive value, and it increased with increasing temperatures. Although high decolorization of DB-22 was achieved with the photo Fenton like process, low COD removal was observed at the studied conditions.

## Acknowledgement

The author thank to Hitit University for their financial support of this project under contract of MUH19001.21.003.

## 5. References

1. A. S. Ejhieh, M. Khorsandi, *J Haz Mat.* **2010**, *176*, 629–637. DOI:10.1016/j.jhazmat.2009.11.077
2. M. Tekbas, H.C. Yatmaz, N. Bektas, *Mic. Mes. Mat.* **2008**, *115*, 594–602. DOI:10.1016/j.micromeso.2008.03.001
3. N. Demir, G. Gündüz, M. Dükkancı, *Env. Sc. Poll. Res.* **2015**, *22*, 3193–3201. DOI:10.1007/s11356-014-2868-x
4. L. G. Devi, K. S. A. Raju, S. G. Kumar, K. E. Rajashekhar, *J Taiw. Inst. Chem. Eng.* **2011**, *42*, 341–349. DOI:10.1016/j.jtice.2010.05.010
5. F. Alakhras, E. Alhajri, R. Haounati, H. Ouachtak, A. Ait Addi, T. A. Saleh, *Sur. Int.* **2020**, *20*, 100611. DOI:10.1016/j.surfin.2020.100611
6. S. R. Pouran, A. Abdul Raman, W. M. Wan Daud, *J Cl. Prod.* **2014**, *64*, 24–35. DOI:10.1016/j.jclepro.2013.09.013
7. F. Sun, Q. Zeng, W. Tian, Y. Zhu, W. Jiang, *J Env. Chem. Eng.* **2019**, *7*, 103011. DOI:10.1016/j.jece.2019.103011
8. J. Gao J, S. Ma, Z. Du, F. Cheng, P. Li, *Wat. Sc. Tech.* **2021**, *83*(2), 425–434. DOI:10.2166/wst.2020.590
9. F. F. Brites-Nóbregaa, I. A. Lacerda, S. V. Santosa, C. C. Amorim, V. S. Santana, N. R. C. Fernandes-Machadoc, J. D. Ardisson, A. B. Henriques, M. D. Leão, *Cat. Tod.* **2015**, *240*, 168–175. DOI:10.1016/j.cattod.2014.06.036
10. G. Hu, J. Yang, X. Duan, R. Farnood, C. Yang, J. Yang, W. Liu, Q. Liu, *Chem. Eng. J.* **2021**, *417*, 129209. DOI:10.1016/j.cej.2021.129209
11. M. R. Abukhadra, A. S. Mohamed, *Silicon*, **2019**, *11*, 1635–1647. DOI:10.1007/s12633-018-9980-3
12. S. Benkhaya, S. M'rabet, A. El Harfi, *Heliyon*, **2020**, *6*(1), e03271. DOI:10.1016/j.heliyon.2020.e03271
13. N. T. Hien, L. H. Nguyen, H. T. Van, T. D. Nguyen, T. H. V. Nguyen, T. H. H. Chu, T. V. Nguyen, V. T. Trinh, X.H. Vu, K. H. H. Aziz, *Sep. Pur. Tech.* **2020**, *233*, 115961. DOI:10.1016/j.seppur.2019.115961
14. J. R. S. Carvalho, F. M. Amaral, L. Florencio, M. T. Kato, T. P. Delforno, S. Gavazza, *Chem.* **2020**, *242*, 125157. DOI:10.1016/j.chemosphere.2019.125157
15. R. K. M. Gomes, R. M. R. Santana, N. F. S. Moraes, S. G. S. Júnior, A. A. Lucena, L. E. Zaidan, D. R. M. Elihimas, D. C. Napoleao, *Chem. Pap.* **2021**, *75*, 1993–2005. DOI: 10.1007/s11696-020-01451-4
16. O. Menezes, R. Brito, F. Hallwass, L. Florêncio, M. T. Kato, S. Gavazza, *Chem Eng Res Des.* **2019**, *146*, 369–378. DOI:10.1016/j.cherd.2019.04.020
17. H-Y. Shu, M-C. Chang, *J Haz Mat.* **2005**, *B121*, 127–133. DOI:10.1016/j.jhazmat.2005.01.020
18. A. B. Isaev, Z. M. Aliev, N. A. Adamadzieva, *Russ. J App. Chem.* **2012**, *85*(5), 765–769. DOI:10.1134/S107042721205014X
19. N. M. Mahmoodi, F. Najafi, S. Khorramfar, F. Amini, M. Arami, *J Haz. Mat.* **2011**, *198*, 87–94. DOI:10.1016/j.jhazmat.2011.10.018
20. M. Moosavifar, S. M. Heidari, L. Fathyunes, M. Ranjbar, Y. Wang, H. Arandiyar, *J Inorg. Org. Poly. Mat.* **2020**, *30*, 1621–1628. DOI:10.1007/s10904-019-01277-y
21. K. Badvi, V. Javanbakht, *J Clean. Prod.* **2021**, *280*, 124518. DOI:10.1016/j.jclepro.2020.124518
22. A. B. Rakhym, G. A. Seilkhanova, Y. Mastai, *Mic. Mes. Mat.* **2021**, *318*, 111020. DOI:10.1016/j.micromeso.2021.111020
23. T. Rashid, D. Iqbal, A. Hazafa, S. Hussain, F. Sher, F. Sher, *J Env. Chem. Eng.* **2020**, *84*(2), 104023. DOI:10.1016/j.jece.2020.104023
24. A. Abharya, A. Gholizadeh, *Cer. Int.* **2021**, *47*(9), 12010–12019. DOI:10.1016/j.ceramint.2021.01.044
25. S. R. Pouran, A. Bayrami, M. A. Shafeeyan, A. A. Abdul Raman, W. M. A. Wan Daud, *Acta Chim. Slov.* **2018**, *65*(1), 166–171. DOI:10.17344/acs.2017.3732
26. Ö. Dönmez, M. Dükkancı, G. Gündüz, *J Env. Hea. Sci. Eng.* **2020**, *18*, 835–851. DOI:10.1007/s40201-020-00507-7
27. P. P. Gan, S. F. Yau Li, *Chem. Eng. J.* **2013**, *229*, 351–363. DOI:10.1016/j.cej.2013.06.020
28. F. Ji, C. Li, J. Zhang, L. Deng, *J. Haz. Mat.* **2011**, *186*, 1979–1984. DOI:10.1016/j.jhazmat.2010.12.089
29. M. Karimi-Shamsabadi, M. Behpoura, A.K. Babaheidari, Z. Saberi, *J Photoch. Photobio. A: Chem.* **2017**, *346*, 133–143. DOI:10.1016/j.jphotochem.2017.05.038
30. H. Sudrajat, S. Babel, *J Wat. Proc. Eng.* **2017**, *16*, 309–318. DOI:10.1016/j.jwpe.2016.11.006
31. D. S. Bhatkhande, V. G. Pangarkar, A. A. Beenackers, *J Chem. Tech. Biotech.* **2002**, *77*(1), 102–116. DOI:10.1002/jctb.532
32. R. Andreeozzi, V. Caprio, A. Insola, G. Longo, V. Tufano, *J Chem. Tech. Biotech.* **2000**, *75*, 131–136. DOI:10.1002/(SICI)1097-4660(200002)75:2%3C131::AID-JCTB191%3E3.0.CO;2-F
33. S. Ahmed, Z. Ahmad, *Env. Nan. Mon. Tech.* **2020**, *14*, 100321. DOI:10.1016/j.enmm.2020.100321
34. D. Uzunoglu, M. Ergüt, P. Karacabey, A. Özer, *Des. Wat. Treat.* **2019**, *172*, 96–105. DOI:10.5004/dwt.2019.24942
35. D. Çalık, D.I. Cifci, *J Env. Man.* **2022**, *304*, 114234. DOI:10.1016/j.jenvman.2021.114234
36. Z. Ghasemi, H. Younesi, A.A. Zinatizadeh, *J Taiw. Inst. Chem. Eng.* **2016**, *65*, 357–366. DOI:10.1016/j.jtice.2016.05.039
37. U. J. Ahile, R. A. Wuana, A. U. Itodo, R. Sha'Ato, R. F. Dantas, *J Wat. Proc. Eng.* **2020**, *36*, 101320. DOI:10.1016/j.jwpe.2020.101320
38. T. M. Jawad, M. R. AL-Lami, A. S. Hasan, J. A. Al-Hilfi, R. K. Mohammad, L. M. Ahmed, *Egy. J Chem.* **2021**, *64*(9), 4857–4865. DOI:10.21608/EJCHEM.2021.67501.3459
39. R. Saleh, A. Taufik, *Sep. Pur. Tech.* **2019**, *210*, 563–573. DOI:10.1016/j.seppur.2018.08.030
40. Y. Wang, J. Fang, J.C. Crittenden, C. Shen, *J Haz. Mat.* **2017**, *329*, 321–329. DOI:10.1016/j.jhazmat.2017.01.041

## Povzetek

Pripravljen je bil heterogeni katalizator za izboljšanje foto-Fentonove oksidacije barvila DB-22 (Direct Black-22). Kot katalizator je bil uporabljen zeolit, modificiran s cinkovim feritom. Pripravljeni katalizator je bil okarakteriziran z uporabo FTIR, SEM, EDS in XRD. Pod vplivom UV svetlobe je bil preučevan vpliv različnih parametrov na razbarvanje DB-22, kot so modifikacija katalizatorja s HCl, količina  $\text{H}_2\text{O}_2$ , količina katalizatorja, količina  $\text{CaCl}_2$ , začetni pH, začetna koncentracija in temperatura. Raziskane so bile kinetične in termodinamične lastnosti. Najvišje razbarvanje DB-22 je bilo 93,3 % pod sledečimi pogoji: začetna koncentracija: 0,070 g/L, začetna temperatura: 25 °C in prvotni pH, količina  $\text{H}_2\text{O}_2$ : 2,78 g/L, količina m-ZZF: 3 g/L, količina  $\text{CaCl}_2$ : 3,75 g/L, reakcijski čas: 60 min in UV svetloba. Aktivacijska energija določena pri preučevanih pogojih je bila –14,76 kJ/mol, reakcija razbarvanja pa je eksotermna z reakcijsko entalpijo –17,31 kJ/mol. Izračunana vrednost aktivacijske entropije je –0,326 kJ/mol. Standardna Gibbsova sprememba proste energije za aktivacijo ima pozitivno vrednost in se z naraščanjem temperature viša.



Except when otherwise noted, articles in this journal are published under the terms and conditions of the Creative Commons Attribution 4.0 International License

# The Predictive Value of Oxidative Stress Index in Patients with Confirmed SARS-COV-2 Infection

Joško Osredkar,<sup>1,3,\*</sup> Sara Pucko,<sup>1,3</sup> Milica Lukić,<sup>2</sup> Teja Fabjan,<sup>1,3</sup>  
Elizabeta Božnar Alič,<sup>1</sup> Kristina Kumer,<sup>1,3</sup> Maria Martin Rodriguez<sup>4</sup>  
and Matjaž Jereb<sup>2,5</sup>

<sup>1</sup> University Medical Centre Ljubljana, Clinical Institute of Clinical Chemistry and Biochemistry, Zaloška cesta 2, 1000 Ljubljana, Slovenia

<sup>2</sup> University Medical Centre Ljubljana, Infectious Diseases Department, Zaloška cesta 2, 1000 Ljubljana, Slovenia

<sup>3</sup> University Ljubljana, Faculty of Pharmacy, Aškerčeva 7, 1000 Ljubljana, Slovenia

<sup>4</sup> University of Alcalá, Faculty of Pharmacy, Carretera Madrid-Barcelona, Km.33,600 28871 Alcalá de Henares (Madrid), Spain

<sup>5</sup> University Ljubljana, Medical Faculty, Vrazov trg 1, 1000 Ljubljana, Slovenia

\* Corresponding author: E-mail: josko.osredkar@kclj.si

Received: 05-27-2022

## Abstract

Disbalance balance between oxidants and antioxidants is called oxidative stress and could be presented as oxidative stress index (OSI). OSI is determined by the reactive oxygen metabolites test (d-ROM test) to assess oxidants and the plasma antioxidant capacity test (PAT test) to measure antioxidants. The aim of the study was to evaluate the predictive value of OSI in the disease COVID-19. d-ROMs results were the highest in the SARS-CoV-2 POSITIVE group (365+/-112), lower in the SARS-CoV-2 NEGATIVE group (314+/-72.4), and the lowest in an INTENSIVE CARE UNIT group (ICU) (277+/-142). U.Carr. PAT test values were the lowest in the SARS-CoV-2 POSITIVE group (2762+/-387), higher in the ICU group (2772 +/-786), and the highest in the SARS-CoV-2 NEGATIVE group (2808+/-470), and are not statistically significantly different ( $P > 0.05$ ), while OSI was: healthy with average value of 49 and the critical ill with average value of 109 ( $P = 0.016$ ). Cut-offs for predicting ICUs admission was at OSI 62, with 80.0% sensitivity and 68.2% specificity.

**Keywords:** Oxidative stress; SARS-CoV-2; OSI Index

## 1. Introduction

Oxidative stress in cells and tissues is caused by an imbalance between the formation of reactive oxygen species (ROS) and the ability to detoxify ROS with the antioxidant system. The balance of ROS and antioxidants may be disturbed by the increased formation of ROS and/or decreased antioxidant activity. This imbalance leads to many spontaneous oxidations in the cell and, because ROS can be reducers of almost all cellular components, oxidation of biological macromolecules such as lipids, proteins, and nucleotides. Oxidation of macromolecules leads to their denaturation and, consequently, changes in their physiological functions. The chronic production of ROS causes

toxic effects that lead to cell damage, long-term oxidative stress, accelerated aging, and many diseases including dementia, inflammation, cancer, diabetes, and cardiovascular disease. In contrast to these diseases, short-term acute oxidative stress does not yield typical clinical signs to divulge its presence. Symptoms of oxidative stress usually come to the fore only when chronic diseases develop.<sup>1,2</sup>

Although abnormal levels of ROS are detrimental, small amounts of ROS production occur normally and have physiological roles. In a homeostatic state, slightly more oxidants are present than antioxidants because small amounts of ROS are formed as by-products of oxygen metabolism. Normal levels of ROS can assist with cellular signaling by changing gene and protein expression, syn-



thesizing certain hormones, and defending against infections.<sup>3</sup>

Inflammation is the body's normal response to injuries, pathogens, irritants, and other toxins. The cells of the immune system that are involved in this process include neutrophils and monocytes during acute inflammation, and macrophages, especially in chronic inflammation. These phagocytes use very strong oxidants from ROS and reactive nitrogen species (RNS) groups when microbes invade.<sup>1</sup> The sudden production of large amounts of reactive species produced by phagocytes is called an oxidative eruption. This process is usually limited to the acute response to a pathogen, but if chronic inflammation occurs, it can cause chronic oxidative stress. In chronic inflammation, the increasing amounts of ROS and RNS lead to the oxidation of cellular components and, thus, damage and apoptosis.

The entry of a virus into the cell first triggers the activation of innate immune cells (macrophages, neutrophils) that arrive at the site of infection and trigger an inflammatory response. Macrophages secrete cytokines and produce several oxidants that they use to defend themselves against the virus. Production of oxidants by macrophages depends on NADPH oxidase, which leads to the formation of O<sub>2</sub>, and on myeloperoxidase, which catalyzes the formation of hypochlorous acid. ROS can activate epithelial cells and alveolar macrophages to generate chemotactic molecules that further attract neutrophils and, especially, monocytes and lymphocytes into the lungs, providing an ideal environment for the development of chronic inflammation. Inflammation is key in the progression of COVID-19 pathology. Presentations of SARS-CoV-2 infection have ranged from asymptomatic or mildly symptomatic to severe disease and death. Common symptoms include fever, headache, cough, and shortness of breath. Other symptoms, such as malaise and acute respiratory distress syndrome (ARDS), have also been described.<sup>4</sup>

Particular laboratory features have been associated with a more severe course of the disease and worse outcomes. A progressive decline in the lymphocyte count and rise in the D-dimer concentration was observed in those who succumbed to the disease, compared with survivors who exhibited more stable levels of the D-dimer.<sup>5</sup>

In severe cases of COVID-19, it is common to observe prolonged prothrombin time, elevated levels of lactate dehydrogenase, deficient cellular immune response, activation of coagulation, and damage to the heart, liver, and kidneys.<sup>6,7</sup>

The immune response plays a key role in controlling the SARS-CoV-2 infection, but excessive and uncontrolled activation of the immune response can contribute to a more severe course of the disease.<sup>8</sup>

Preclinical studies suggest that increased ROS production and decreased antioxidant responses play an important role in the pathogenesis of viral infection and also in disease progression and severity. The severe course of COVID-19 disease involves the connection of sever-

al pathophysiological processes such as cytokine storm, inflammation, cellular apoptosis, and redox imbalance, which contribute to the poor outcomes of COVID-19.<sup>9</sup>

Lymphocyte infiltration into the lungs may explain the lymphopenia and elevated neutrophil to lymphocyte ratio observed in critically ill COVID-19 patients. The elevated neutrophil to lymphocyte ratio is also used to predict the death of critically ill COVID-19 patients. The consequence of increased ROS secreted by neutrophils, macrophages, and other immune cells has so far had two outcomes: 1) ROS damages erythrocytes, which release heme into the bloodstream, which is broken down by heme oxygenase, which releases free iron; and 2) an oxidative eruption occurs, leading to the formation of a superoxide radical and hydrogen peroxide. Furthermore, oxidative stress and free iron convert fibrinogen into abnormal fibrin clots, leading to the formation of micro thromboses in the vascular system and pulmonary microcirculation.<sup>7,10</sup>

Increased ROS production also directly or indirectly triggers the NF- $\kappa$ B signaling pathway, and studies suggest that its activation is responsible for the more severe course of COVID-19 disease. NF- $\kappa$ B is one of the major mediators of cytokine and chemokine induction and is a central coordinator of the innate and adaptive immune responses.<sup>7,11,12</sup>

If over-activation of all these pathways occurs, likely depending on the amount of virus present, a cytokine storm can develop, leading to ARDS. The cytokine storm is triggered via these oxidative stress-signaling pathways by activated leukocytes, including B and T cells, macrophages, monocytes, neutrophils, dendritic cells, as well as epithelial and endothelial cells.<sup>13–15</sup>

Hydroperoxides are formed by the oxidation of various biological molecules such as amino acids, peptides, proteins, nucleotides, and, to the greatest extent, by the oxidation of lipids. Peroxides are only one of the groups of reactive oxygen species, but they are an early marker of lipid oxidation as they are formed in the initial stages of oxidative stress unlike other markers (malondialdehyde, isoprostane). Therefore, peroxides are early indicators of oxidative stress.<sup>16–18</sup> In this study, we wanted to investigate how the OSI index may be a good predictor of the severity of COVID-19 disease.

## 2. Materials and Methods

### 2.1. Patients

Measurements of oxidants and antioxidants were performed on 171 (M/F = 42/129) samples taken at University Medical Centre Ljubljana (UMCL). Subjects were divided into 3 groups according to the course of the disease.

Group 1 (SARS-CoV-2 NEGATIVE): employees of UMCL who had a negative PCR test for SARS-CoV-2 infection (79).

Group 2 (SARS-CoV-2 POSITIVE): employees of UMCL who had a positive PCR test for SARS-CoV-2 infection without symptoms (51).

Group 3 (INTENSIVE CARE): A group of people who were hospitalized in the intensive care unit (ICU) of UMCL due to a severe course of COVID-19 (41).

## 2. 2. Methods

We used d-ROMs to measure oxidants and a PAT test to measure serum antioxidants. From the values of both tests, we then calculated the values of the oxidative stress index (OSI index) according to the FRAS5 analyzer algorithm, which summarizes the values of d-ROMs and PAT tests into one value to facilitate the evaluation of oxidative stress.

d-ROMs fast is a photometric test that gives us the status of oxidants in a biological sample by measuring hydroperoxides (ROOH).

The d-ROMs fast test is based on the Fenton reaction. Measurement with a FRAS5 photometer was performed at 505–546 nm. The color intensity was directly proportional to the ROS concentration in the sample.

The PAT test is a method that evaluates the antioxidant power of a biological sample. Measuring the antioxidant power of a sample is important as antioxidants are the first line of defense in the fight against oxidative damage.<sup>16,18</sup>

The PAT test is used to quantify water-soluble antioxidants in a biological sample by measuring its ability to reduce ferric ions ( $\text{Fe}^{3+}$ ) to  $\text{Fe}^{2+}$  ions. The measured antioxidants represent the main components of plasma in defense against oxidation: vitamin C, vitamin E, uric acid, and bilirubin.

The values of the OSI index are obtained by a certain arithmetic transformation and enable easier interpretation of oxidative stress for an individual sample. The OSI index does not have to replace the results of d-ROMs and PAT test, but complements them and presents the state of oxidative stress in the body.<sup>19</sup>

## 2. 3. Statistics

Statistical analyses were performed with IBM SPSS (version 22). We first established whether our data sets were normally distributed with the Shapiro-Wilk test for normality and established that the distribution of the oxidative stress index was nonparametric. The data were logarithmically transformed and a follow-up Shapiro-Wilk test determined that the logarithmically-transformed data were normally distributed. We used the one-factor ANOVA parametric test and the post hoc Bonferroni test and Dunn's Method test for further analysis of statistical significance. For descriptive statistics, we used mean and standard deviation (SD) to summarize our data.

## 3. Results and Discussion

**Table 1:** Basic statistics of d-ROMs, PAT, and OSI tests.

	N	d-ROMs [U. Carr]	PAT [U. Cor]	OSI Median (IRQ)
<b>SARS-CoV-2 NEGATIVE</b>	79			
	Mean	314	2808	46
	SD	72.4	470	(28–61)
<b>SARS-CoV-2 POSITIVE</b>	51			
	Mean	365	2762	56
	SD	112	387	(31–84)
<b>INTENSIVE CARE</b>	41			
	Mean	277	2772	109
	SD	142	786	(60–134)

\* d-ROMs - ROS concentration assay

PAT- antioxidant concentration assay

OSI - index of oxidative stress

SARS-CoV-2 - SARS-associated coronavirus

### 3. 1. Comparison of Groups in the Coordinate System

We used a coordinate system to show where certain groups of patients are concentrated based on their OSI (Figure 1). The purpose of the OSI index is to integrate a single value based on d-ROMs and PAT test results despite different units of measure and different value ranges. With the OSI index, we can show exactly what the disease state of each group is, for example, the levels of d-ROMs = 500 U.Carr and PAT = 1800 U.Cor can show us the same OSI value (142) as the result d-ROMs = 95 U.Carr and PAT = 3900 U.Cor, although these are completely different conditions. Namely, the OSI value serves as a rough picture of oxidative stress; if the values are normal (below 40) we can ascertain that the patient's redox ratio is balanced, otherwise, when the values are higher (above 40) it is necessary to investigate the cause and look at the values of oxidants and antioxidants. We can most reliably interpret the patient's condition based on the results of all 3 parameters, clinical laboratory tests, and when the sample was taken during the patient's illness.

We entered d-ROMs test values on the y-axis and PAT test values on the x-axis. Based on these two tests, with the help of OB Manager Online copyright © H&D S.r.l. In: 2.0.16 calculated oxidative stress index values.

### 3. 2. The Interpretation of the Results in Specific Quadrants

The first quadrant includes individuals with normal or high values of d-ROMs test and normal or high values of PAT test:

– High values of d-ROMs and normal PAT values indicate

													<40	Normality				
													41-65	Borderline				
													66-120	Alert				
													>121	Critical; evident unbalance				
d-ROMs II.																		I.
700	271	265	259	254	250	247	245	244	243	244	245	247	250	254	259	265	271	278
675	258	251	246	241	237	233	231	230	229	230	231	233	237	241	246	251	258	265
650	245	239	232	227	223	219	217	215	215	215	217	219	223	227	232	239	245	253
625	233	226	219	214	209	205	203	201	200	201	203	205	209	214	219	226	233	241
600	220	213	206	200	195	191	188	186	186	186	188	191	195	200	206	213	221	229
575	208	200	193	187	181	177	174	172	171	172	174	177	181	187	193	200	209	218
550	197	188	181	174	168	163	160	158	157	158	160	163	168	174	181	188	197	207
525	186	177	168	161	155	150	146	144	143	144	146	150	155	161	168	177	186	196
500	175	165	156	148	145	136	132	129	129	129	132	136	142	148	156	165	175	186
475	165	154	145	136	129	123	118	115	114	115	118	123	129	136	145	154	165	176
450	155	144	134	124	116	109	104	101	100	101	104	109	116	124	134	144	156	167
425	146	135	123	113	104	97	91	87	86	87	91	97	104	113	123	135	147	159
400	138	126	114	103	93	84	77	73	71	73	77	84	93	103	114	126	139	152
375	132	118	106	94	82	72	64	59	57	59	64	72	82	94	106	118	132	146
350	126	112	99	86	73	62	52	45	43	45	52	62	73	86	99	112	127	141
325	122	108	93	79	66	53	41	32	29	32	41	53	66	79	93	108	122	137
300	119	105	90	75	61	47	33	21	14	21	33	47	61	75	90	105	120	135
275	119	104	89	74	59	44	30	15	0	15	30	44	59	74	89	104	119	134
250	119	105	90	75	61	47	33	21	14	21	33	47	61	75	90	105	120	135
225	122	108	93	79	66	53	41	32	29	32	41	53	66	79	93	108	122	137
200	126	112	99	86	73	62	52	45	43	45	52	62	73	86	99	112	127	141
175	132	118	106	94	82	72	64	59	57	59	64	72	82	94	106	118	132	146
150	138	126	114	103	93	84	77	73	71	73	77	84	93	103	114	126	139	152
125	146	135	123	113	104	97	91	87	86	87	91	97	104	113	123	135	147	159
100	155	144	134	124	116	109	104	101	100	101	104	109	116	124	134	144	156	167
75	165	155	145	137	129	123	119	116	115	116	119	123	129	137	145	155	165	176
50	175	166	157	149	142	137	132	130	129	130	132	137	142	149	157	166	175	186
25	186	177	169	161	155	150	146	144	143	144	146	150	155	161	169	177	186	196
PAT	1000	1200	1400	1600	1800	2000	2200	2400	2600	2800	3000	3200	3400	3600	3800	4000	4200	4400
III																		IV

**Figure 1:** Coordinate system representing OSI and four different quadrants for interpretation. OSI values less than 40 represent normal levels. Values between 41-65 are borderline alert and normal. Values ranging from 66-120 signify a concerning imbalance between oxidants and antioxidants. Values above 121 signify a critical imbalance of oxidants and antioxidants.

\* OSI - index of oxidative stress

an initial oxidative outbreak due to an innate immune response, but the patient still maintains a good antioxidant defense.

- High values of d-ROMs and high values of PAT are the result of an increase in oxidant species and an anomalous increase of the antioxidant reserve that might reflect a state of cellular destruction and release in circulation. The second quadrant includes individuals with normal or high values for d-ROMs test and normal or low values for the PAT test:
- High values of d-ROMs and low values of PAT indicate the increase of the antioxidant species and the decrease of the antioxidant response, signs of possible inflammation onset, and hospitalization.
- The interpretation of high values of d-ROMs and normal PAT values remain the same as for the first quadrant. The third quadrant includes individuals with normal or low values of d-ROMs and normal or low values of PAT:
- Low values of d-ROMs and normal PAT values indicate a long-term infection and exhaustion of the body. Thus, the body is unable to form normal ROS, the efficacy of the innate immune response declines, and antioxidant defenses decline due to pre-existing damage indicating a loss of redox signaling power.
- Low values of d-ROMs and low PAT values show the exhaustion of the ROS system and the antioxidant network. The fourth quadrant is comprised of individuals with normal or low d-ROMs and normal or high PAT test

values.

- Low values of d-ROMs and normal PAT values in the fourth quadrant indicate the same conditions as for the third quadrant.
- Low values of d-ROMs and high values of PAT indicate a long-term infection, which involves extensive inflammation and tissue damage.

For the statistical comparison of groups, we used the parametric test one-factor ANOVA and Bonferroni post hoc test. We first performed a test of homogeneity of variances and found that there was no statistically significant difference between all three groups; variances were homogeneous ( $P = 0.395$ ). This indicated that we could go forward with the one-factor ANOVA and Bonferroni test. The ANOVA result showed that there was a statistically significant difference ( $P = 0.016$ ) between the individual groups, as shown in Table 2.

**Table 2:** Calculated differences between groups.

Group comparison for OSI		P
SARS-CoV-2 POSITIVE	SARS-Cov-2 NEGATIVE	<b>0.272</b>
SARS-CoV-2 POSITIVE	INTENSIVE CARE	<b>0.471</b>
SARS-Cov-2 NEGATIVE	INTENSIVE CARE	<b>0.024</b>

\*OSI - index of oxidative stress

SARS-CoV-2 - SARS-associated coronavirus

We did not prove a statistically significant difference between the SARS-Cov-2 positive and negative groups ( $P = 0.272$ ). The average oxidative stress index of the positive group was 17 units higher than the negative group. According to the reference table, a value of 17 is a concerning value, whereas the control group is in the range of the oxidative stress borderline state. Due to the less stressful course of the disease (from asymptomatic patients to patients with mild symptoms, which did not require hospitalization of patients), there was no critically impaired state of oxidants/antioxidants.

We demonstrated a statistically significant difference between the ICU COVID-19 patients and the SARS-Cov-2 negative group ( $P = 0.024$ ). This difference was expected as the redox ratio of hospitalized persons in ICU was severely disrupted. Some patients had a very high amount of oxidants present, yet others had a very low amount of oxidants, both indicative of oxidative stress. Normal amounts of oxidants are necessary for the normal functioning of the patient.

We did not prove statistically significant differences between the SARS-Cov-2 positive group and the ICU group ( $P = 0.471$ ). The SARS-CoV-2 positive group without symptoms had more oxidative stress than the SARS-CoV-2 negative group, but much less than the patients hospitalized in ICU.

### 3. 2. Interpretation of OSI Values for SARS-Cov-2 NEGATIVE Group:

The vast majority of patients had normal values of d-ROMs and PAT, and, consequently, the largest share of them (43.7%) had OSI values below 40, while only 2.3% had OSI above 121. These slight deviations were likely caused by other underlying conditions (such as obesity and differences in physical activity).

### 3. 3. Interpretation of OSI Values for SARS-CoV-2 POSITIVE Group:

Individuals from this group were concentrated in approximately the same part of the coordinate system, namely in quadrants I and II. Normal or high values of d-ROMs and normal or high values of PAT were measured. Most individuals (41.5%) of this group had an oxidative stress index below 40, i.e. they had normal levels without oxidative stress. Furthermore, 26.8% of them had values between 66–120 (alert state) and 22% of individuals had values between 41–65 (borderline). The last group of 66–120, which is already considered a warning state, included the fewest individuals (9.7%). The results, which were slightly above normal but not critical, were in agreement with the symptoms of the participants, which were mild although they tested positive for SARS-CoV-2. We hypothesize that the cause of high values of d-ROMs is an oxidative outbreak due to the innate immune response, while the antioxidant system also functions to fight high amounts of ROS.

### 3. 4. Interpretation of OSI Values for INTENSIVE CARE Group:

We observed the most diverse patient conditions in this group. The majority of individuals had OSI values below 40 (33.3%) and above 121 (26.7%). Based on the results of d-ROMs, PAT tests, and OSI values, this large variation in patient condition was expected in the ICU group. We observed very diverse values in intensive care patients and most (66.7%) completely disturbed the balance of oxidants/antioxidants. In quadrant II were individuals who had mostly elevated values from the d-ROMs test and normal or decreased values from the PAT test. Based on these two results, we concluded that these patients were in the initial stage of COVID-19 disease and had just been admitted to ICU.

Individuals in quadrants I and II were patients with very high values of d-ROMs and normal or elevated PAT values. The first quadrant includes patients who were in the initial stage of the disease. In those who had elevated levels of d-ROMs and PAT, there was an extensive immune response that triggered an oxidative outburst and consequently an increased response of antioxidants.

Individuals in quadrants III and IV +/- were patients with very low d-ROMs scores and normal PAT scores, and patients with very low d-ROMs scores and high PAT scores. In both cases, these are samples taken during hospitalization in the ICU after the COVID-19 infection had been going on for some time. At this point during infection, the body is already exhausted and unable to form ROS, nor is there an effective innate immune response. The antioxidant system is also active, trying to remove the damage. In the group with low d-ROMs and high PAT scores, high PAT values indicated inadequate redox signaling and increasingly severe tissue damage.

Individuals in quadrant IV were critically ill patients with low d-ROMs and high PAT values. As in the above example, there was an increasing amount of tissue damage and slow organ failure.

The frequency of the OSI index is shown in Figure 2.

A receiver operating characteristics (ROC) curve was constructed and Youden Index was used to determine the optimal cut-off for predicting intensive care unit (ICU) admission. The ROC curve is presented in Figure 3.

## 4. Conclusions

The oxidative stress index serves as a predictor for the course of COVID-19 disease. Based on our data, it is reasonable to think that OSI is a good predictive index for ICU admission where a cut-off of 62 was identified.

The very low d-ROMs level observed in patients 1 and 2 can be explained by the pathological status of the subjects. In contrast, high PAT levels can be explained by hemolysis processes, through which a high amount of glutathione (GSH) is released from red blood cells. Simul-

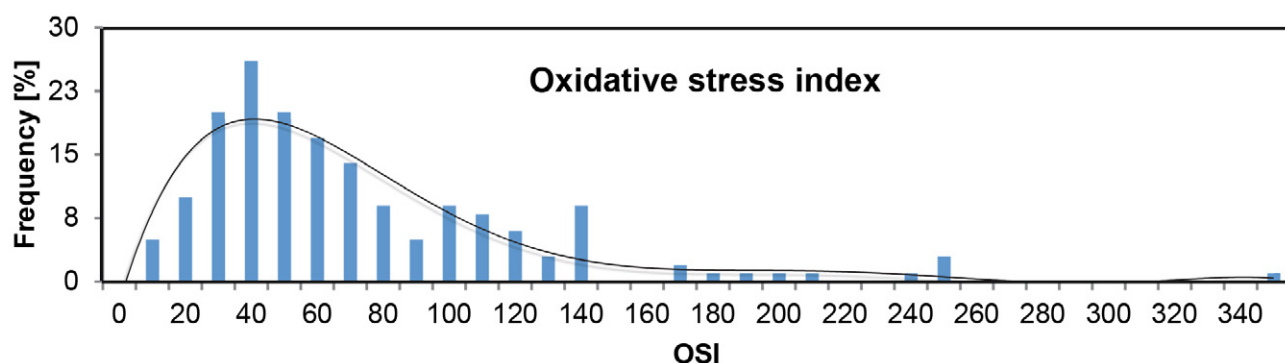


Figure 2: Calculated OSI of the whole study group.

\* OSI - index of oxidative stress

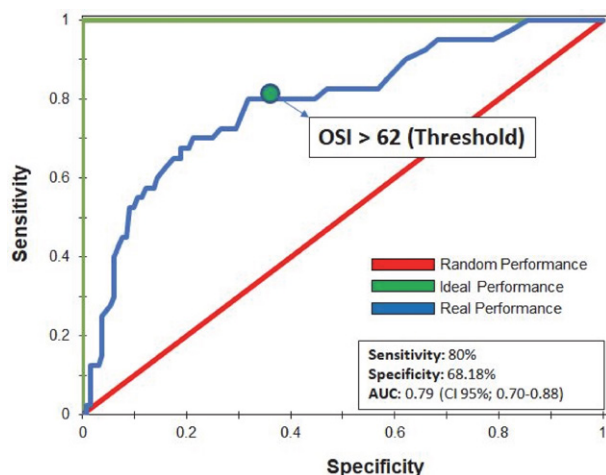


Figure 3: ROC curve for predicting ICU admission for COVID-19 positive patients.

\* OSI - index of oxidative stress    AUC - area under the ROC curve

taneously, the antioxidants are not used by the individual due to the lack of ROS species, which could contribute to why PAT levels are quite high in some cases. Moreover, this could be the reason why statistically significant differences in d-ROMs and PAT were not identified in the patients analyzed since the levels strongly depend upon the time course of the disease, and pathology can occur with low or high ratios of d-ROMs/PAT.

With the help of the coordinate system, we evaluated the disease status of the patients. We found that the PCR negative group was concentrated approximately in the middle of the coordinate system, signifying that most of the values of the measured parameters were within normal reference limits. The PCR positive group was primarily found in quadrants I and II, and the values of oxidative stress parameters indicated a shift from the normal reference limits. A wide variety of disease conditions were present in the ICU group, some of which were in the initial stage of the disease and had just been admitted to the ICU, and the results of d-ROMs, PAT, OSI were not as severe as in individuals with long-term hospitalization.

A comparison of the oxidative stress index in two ICU patients with biochemical and hematological parameters (supplemental data) showed that the values of the OSI index correlated very well with the patients' disease state and the inflammatory parameters. We compared CRP, lymphocyte and neutrophil count, IL-6, and oxidative stress index. The latter varied with a lag compared to the others, but this is consistent with studies by test manufacturers d-ROMs and PAT, where we found that oxidant levels rise when there is actual oxidative damage and thus reflect the current state of the body.

Doğan et al. published a study in which they calculated the OSI index from the parameters total oxidant status (TOS) and total antioxidant status (TAS). The calculated OSI levels were significantly different between severe moderate and mild groups of patients infected with SARS-CoV-2.<sup>20</sup>

The same method for calculating OSI was also used by Çakırca et al. Their results revealed that the increase in oxidative stress and decrease in antioxidant levels in COVID-19-infected patients were associated with worsening of disease.<sup>21</sup> The results of our study, in which we calculated OSI based on d-ROM and PAT determinations, are comparable to the results of both of these studies, which used TOS and TAS to calculate OSI.

In our study of oxidative stress, our results suggest that OSI could be a predictor of the course of SARS-CoV-2 infection and warrants further investigation. Our studies were conducted on a small number of samples so further research with more samples is necessary.

## Acknowledgments

### Funding

The study was funded by the research program of the Research Agency of the Republic of Slovenia (P3-0124).

### Author Contributions

Conceptualization JO; Writing – Original draft Preparation JO; Clinical data of the Patients ML, MJ; Laboratory Analysis SP, TF, EBA; Statistics TF; Writing – Review & Editing MJ.



## Institutional Review Board Statement

The study was conducted according to the guidelines of the Declaration of Helsinki, and approved by the National Ethics Committee; protocol number – 012-60/2021/5.

## Conflicts of interest

The authors declare no conflict of interest.

## 5. References

1. J. Mravljak, *Farm. Vestn.* **2015**, *66*, 127–132. DOI:10.1016/j.intermet.2015.07.002
2. G. Pizzino, N. Irrera, M. Cucinotta, G. Pallio, F. Mannino, V. Arcoraci, F. Squadrito, D. Altavilla, A. Bitto, *Oxid. Med. Cell. Longev.* **2017**, *2017*. DOI:10.1155/2017/8416763
3. J. Osredkar, *Zdr. Vestn.* **2012**, *81*, 393–406. DOI:10.3982/ECTA10449
4. M. Merad, J. C. Martin, *Nat. Rev. Immunol.* **2020**, *20*, 355–362. DOI:10.1038/s41577-020-0331-4
5. D. Wang, B. Hu, C. Hu, F. Zhu, X. Liu, J. Zhang, B. Wang, H. Xiang, Z. Cheng, Y. Xiong, et al., *J. Am. Med. Assoc.* **2020**, *323*, 1061–1069. DOI:10.1001/jama.2020.1585
6. B. Vellingiri, K. Jayaramayya, M. Iyer, A. Narayanasamy, V. Govindasamy, B. Giridharan, S. Ganesan, A. Venugopal, D. Venkatesan, H. Ganesan, et al., *Sci. Total Environ.* **2020**, *725*. DOI:10.1016/j.scitotenv.2020.138277
7. R. Cecchini, A. L. Cecchini, *Med. Hypotheses* **2020**, *143*. DOI:10.1016/j.mehy.2020.110102
8. Y. R. Guo, Q. D. Cao, Z. S. Hong, Y. Y. Tan, S. D. Chen, H. J. Jin, K. Sen Tan, D. Y. Wang, Y. Yan, *Mil. Med. Res.* **2020**, *7*.
9. L. Delgado-Roche, F. Mesta, *Arch. Med. Res.* **2020**, *51*, 384–387. DOI:10.1016/j.arcmed.2020.04.019
10. M. Laforge, C. Elbim, C. Frère, M. Hémadi, C. Massaad, P. Nuss, J. J. Benoliel, C. Becker, *Nat. Rev. Immunol.* **2020**, *20*, 515–516. DOI:10.1038/s41577-020-0407-1
11. D. Samir, *J. Infect. Dis. Epidemiol.* **2020**, *6*. DOI:10.23937/2474-3658/1510121
12. O. A. Khomich, S. N. Kochetkov, B. Bartosch, A. V. Ivanov, *Viruses* **2018**, *10*. DOI:10.3390/v10080392
13. D. F. van den Berg, A. A. te Velde, *Front. Immunol.* **2020**, *11*. DOI:10.3389/fimmu.2020.01580
14. A. Nasi, S. McArdle, G. Gaudernack, G. Westman, C. Melief, J. Rockberg, R. Arens, D. Kouretas, J. Sjölin, S. Mangsbo, *Toxicol. Reports* **2020**, *7*, 768–771. DOI:10.1016/j.toxrep.2020.06.003
15. N. Kelley, D. Jeltama, Y. Duan, Y. He, *Int. J. Mol. Sci.* **2019**, *20*. DOI:10.3390/ijms20133328
16. T. Fabjan, E. Vrtačnik-Bokal, K. Kumer, J. Osredkar, *J. Lab. Med.* **2018**, *42*, 51–58. DOI:10.1515/labmed-2017-0106
17. H&D srl, Colorimetric determination of reactive oxygen metabolites (ROMs), [https://innovaticslabs.com/wp-content/uploads/2018/04/d-ROMLab-test-specification\\_ENG-1.pdf](https://innovaticslabs.com/wp-content/uploads/2018/04/d-ROMLab-test-specification_ENG-1.pdf), (assessed: March 31, 2019).
18. H&D srl, Colorimetric determination of biological antioxidant potential, [https://innovaticslabs.com/wp-content/uploads/2018/04/PATLab-test-specification\\_ENG-1.pdf](https://innovaticslabs.com/wp-content/uploads/2018/04/PATLab-test-specification_ENG-1.pdf), (assessed: May 10, 2019).
19. H&D srl, Oxidative stress index OSI, [https://innovaticslabs.com/wp-content/uploads/2018/04/OSI\\_Oxidative-Stress-Index.pdf](https://innovaticslabs.com/wp-content/uploads/2018/04/OSI_Oxidative-Stress-Index.pdf), (assessed: March 21, 2019).
20. S. Dogan, T. Bal, M. Çabalak, N. Dikmen, H. Yaqoobi, O. Özcan, *Turkish J. Biochem.* **2021**, *46*, 349–357. DOI: <https://doi.org/10.1515/tjb-2021-0013>
21. G. Çakırca, T. D. Çakırca, M. Üstünel, A. Torun, İ. Koyuncu, *Ir. J. Med. Sci.* **2021**, 1–6.

## Povzetek

Neravnovesje med oksidanti in antioksidanti imenujemo oksidativni stres in ga lahko prikažemo kot indeks oksidativnega stresa (OSI). OSI določimo s testom reaktivnih presnovkov kisika (d-ROM) za oceno oksidantov in testom plazemske antioksidativne kapacitete (PAT) za merjenje antioksidantov. Namen študije je bil oceniti napovedno vrednost OSI pri boleznih COVID-19. Rezultati testa d-ROM so bili najvišji v skupini SARS-CoV-2 pozitivni (365±112), nižji v skupini SARS-CoV-2 negativni (314±72,4) in najnižji v skupini kritično bolnih v enoti za intenzivno nego (ICU) (277±142) U.Carr. Vrednosti testa PAT so bile najnižje v skupini SARS-CoV-2 pozitivni (2762±387), višje v skupini kritično bolnih (2772±786) in najvišje v skupini SARS-CoV-2 negativni (2808±470). Skupine se med sabo statistično značilno ne razlikujejo ( $P>0,05$ ). OSI se statistično značilno razlikuje med zdravimi s povprečno vrednostjo 49 in kritično bolnimi s povprečno vrednostjo 109 ( $P = 0,016$ ). Določili smo mejno vrednost za napovedovanje sprejema pacienta v enoto intenzivne nege na osnovi analize OSI, in sicer 62, z 80,0 % občutljivostjo in 68,2 % specifičnostjo.



Except when otherwise noted, articles in this journal are published under the terms and conditions of the Creative Commons Attribution 4.0 International License



Scientific paper

# Carvacrol Derivatives as Antifungal Agents: Synthesis, Antimicrobial Activity and *in Silico* Studies on Carvacryl Esters

Jelena Lazarević,<sup>1,\*</sup> Ana Marković,<sup>2</sup> Andrija Šmelcerović,<sup>1</sup> Gordana Stojanović,<sup>3</sup> Pierangela Ciuffreda<sup>4</sup> and Enzo Santaniello<sup>5</sup>

<sup>1</sup> Department of Chemistry, Faculty of Medicine, University of Niš, Bulevar dr Zorana Đinđića 81, 18000, Niš, Serbia

<sup>2</sup> Department of Pharmacy, Faculty of Medicine, University of Niš, Bulevar dr Zorana Đinđića 81, 18000, Niš, Serbia

<sup>3</sup> Department of Chemistry, Faculty of Science and Mathematics, University of Niš, Višegradska 33, 18000, Niš, Serbia

<sup>4</sup> Dipartimento di Scienze Biomediche e Cliniche "L. Sacco", Università degli Studi di Milano, Via G.B. Grassi 74, 20157 Milano, Italy

<sup>5</sup> Faculty of Medicine, University of Milan, Italy

\* Corresponding author: E-mail: jelena217@yahoo.com; jelena.lazarevic@medfak.ni.ac.rs  
Tel: +381 63 1045128; fax: +381-18-42-38-770

Received: 03-03-2022

## Abstract

Chemical modifications of natural monoterpenoids to various derivatives have been reported to result in enhancement of biological activities when compared to parent compounds. In this context a well-known biocide and food additive, carvacrol, served as a basic scaffold onto which a phenolic functionality transformation by introducing acyl groups was performed. By using this simple methodology, we obtained a small series of 25 esters. For each of the obtained compounds we have performed structural characterization, *in vitro* antimicrobial testing and *in silico* calculation of physico-chemical, pharmacokinetic and toxicological properties. Despite numerous data on the synthesis and bioactivity of carvacryl ester lower homologues, there are scarce data on esters with acid components higher than C<sub>9</sub>, so that among 25 compounds, 10 were reported for the first time (spectral characterization for 12 are herein the first reported). Our research is also the first comprehensive study of carvacryl esters antifungal and of medium/long chain fatty acid esters antibacterial activities. Interesting result is that all the synthesized esters, regardless the nature of the R residue, have shown activity on fungal strain *Aspergillus niger* and on yeast *Candida albicans* comparable to carvacrol. Besides presented experimental data, implementation of *in silico* calculation of physico-chemical, pharmacokinetic and toxicological properties on the prepared compounds, may be valuable information in further research.

**Keywords:** chemical transformation; carvacrol esters; *in vitro* antimicrobial activity; *in silico* calculation

## 1. Introduction

Natural products and their scaffolds have a long history of application as valuable starting points for medicinal chemistry and drug discovery.<sup>1</sup> Their structural modification, when compared to parent compounds, has often afforded structures with enhanced pharmacological activities and outstanding therapeutic possibilities.<sup>2,3</sup>

Carvacrol (2-methyl-5-(1-methylethyl)-phenol), a monoterpenoid phenol biosynthetically related to *pa-*

*ra*-cymene, frequently occurs in essential oils of many Lamiaceae (*Origanum*, *Thymbra*, *Thymus*, *Satureja*) and Verbenaceae (*Lippia*) plants usually used as spices and for therapy/prevention purposes in folk medicine.<sup>4</sup> A variety of biological properties including antioxidant, antimicrobial, antiviral, insecticidal, antiparasitic, antihypertensive, immunomodulatory and antitumor, resulted from numerous studies overtaken in past 20 years, recently reviewed by Rathod *et al.* and Sharifi-Rad *et al.*<sup>5,6</sup> Moreover, the European Commission has included carvacrol in the list of

chemical flavors and Food and Drug Administration (FDA) approved carvacrol, together with carvacryl ethyl ether, carvacryl acetate and carvacryl propanoate, considering them safe from a toxicological point of view for their use as additives in food products.<sup>7,8</sup>

Although carvacrol is well known as effective in controlling infection diseases, the molecular mechanisms involved in antimicrobial action are not yet completely elucidated. The antibacterial activity of carvacrol has been attributed to its considerable effects on the structural and functional properties of cytoplasmatic membrane, involving outer- and inner membrane disruption and interaction with membrane proteins and intracellular targets.<sup>9,10</sup> The most recent study by Niu *et al.*<sup>11</sup> reported carvacrol could trigger *Candida albicans* apoptosis, causing membrane disruption, inducing ROS production and mitochondrial dysfunction.

Carvacryl derivatives, either natural or synthetic, have also been employed in biological testing with vast range of activities, such as antimicrobial,<sup>12–15</sup> antiinflammatory,<sup>16</sup> antioxidant,<sup>17–21</sup> anticancer,<sup>17,19,20</sup> larvicidal,<sup>22,23</sup> antihelmintic,<sup>24,25</sup> also acting as enzyme inhibitors (acetylcholinesterase and butyrylcholinesterase,<sup>26</sup> mushroom tyrosinase,<sup>27</sup> *Mycobacterium tuberculosis* chorismate mutase<sup>28</sup>).

There are also a large number of reports on the synthesized esters of carvacrol and on their biological activities.<sup>15,16,22,23,27,29–36</sup> Antimicrobial assays have evaluated activity of a few carvacryl esters of straight chain lower carboxylic acid homologues and diverse heteroaromatic carboxylic acids.<sup>15,29,30,34,37</sup> Interestingly, versus plentiful data on the synthesis and bioactivity of lower homologues, there are sporadic or no data on carvacryl esters with acid components higher than C<sub>9</sub> (except for C<sub>12</sub> reported in Bassanetti *et al.*<sup>34</sup>).

In the context of diverse biological activities of carvacrol and rich number of promising studies on carvacrol derivatives, a one-step transformation of phenolic functionality by introducing an acyl group was made. We have obtained a series of 25 compounds (**3a–y**), which, after structural characterization, have been involved in *in vitro* antimicrobial testing. This research is the first comprehensive study of the antifungal activity of the synthesized carvacrol derivatives and the first study on antimicrobial activity of carvacryl ester medium/higher homologues. Along with experimental data we provided *in silico* predictions of physico-chemical, pharmacokinetic and toxicological properties for entire group of the synthesized derivatives. Current paper also complements our work on modifying the phenolic function of a few most active natural biocides found in essential oils.<sup>38,39</sup>

## 2. Experimental

### 2. 1. Chemicals

All chemicals used were of analytical reagent grade. Unless specified otherwise, all reagents and standards were purchased from Merck (Darmstadt, Germany).

### 2. 1. 1. General Synthetic Procedures

Acetyl, benzoyl, palmitoyl, stearoyl and oleoyl chloride were purchased from Sigma-Aldrich and were used directly in the synthesis of carvacryl esters. For other acyl chlorides used in the study we have utilized two synthetic approaches depending on whether the transformed acids had less (together with 2-chloroacetyl and trichloroacetyl chloride)<sup>40</sup> or more than 10 carbon atoms,<sup>41</sup> both described by Lazarević *et al.*<sup>38</sup> and Lazarević *et al.*<sup>39</sup>

The material obtained following the above protocols was used directly in the synthesis of esters that was performed as reported in Paolini *et al.*<sup>42</sup> The synthesis of carvacryl (5-isopropyl-2-methylphenyl) esters **3a–y** is represented in Scheme 1. The obtained esters **3a–y** were purified by column chromatography, stationary phase Silica Gel 60 (70–230 mesh), mobile phase (hexane/diethyl ether, gradient 9:1 to 7:3). Data on yields are given in Table 1.

### 2. 2. Identification of Synthetized Compounds

#### 2. 2. 1. GC-MS Analysis

MS spectra of samples of the synthesized compounds were recorded on a 7890/7000B GC/MS/MS triple quadrupole system (Agilent Technologies, USA, equipped with a Combi PAL auto sampler). The fused silica capillary column HP-5MS (5% phenylmethylsiloxane, 30 m × 0.25 mm, film thickness 0.25 μm, Agilent Technologies, Palo Alto, CA, USA) was used. The injector, source and interface operated at 250, 230 and 300 °C, respectively. The temperature program: from 60 for 5 min isothermal to 300 °C at a heating rate of 8 °C/min and on 300 °C for 5 min isothermal. The solutions in hexane were injected in split ratio 10:1. The carrier gas was helium with a flow of 1.0 mL/min. Post run: back flash for 1.89 min, at 280 °C, with helium at 50 psi. MS conditions were as follows: ionization voltage of 70 eV, acquisition mass range 50–650, scan time 0.32 s. Semi-quantitative analysis was carried out directly from peak areas in the GC profile. Linear retention indices (RI) were determined based on the retention times of C<sub>8</sub>–C<sub>40</sub> alkanes run on HP-5MS column, using the above mentioned temperature programme.<sup>43</sup>

#### 2. 2. 2. NMR Analysis

NMR spectra were registered on a Bruker AVANCE 500 spectrometer equipped with a 5 mm broadband reverse probe with field z-gradient operating at 500.13 and 125.76 MHz for <sup>1</sup>H and <sup>13</sup>C, respectively. All NMR spectra were recorded at 298 K in CDCl<sub>3</sub> (isotopic enrichment 99.95%) solution. Chemical shifts are reported on the δ (ppm) scale and are relative to the residual CHCl<sub>3</sub> signals (7.24 for <sup>1</sup>H and 77.0 ppm, central line, for <sup>13</sup>C spectra, respectively), and scalar coupling constants are reported in Hertz. The experimental error in the measured <sup>1</sup>H–<sup>1</sup>H coupling constants was ±0.5 Hz. The signals assignment was given by a combination of 1D and 2D COSY, HSQC

and HMBC experiments, using standard Bruker pulse programs. Acquisition parameters for 1D were as follows:  $^1\text{H}$  spectral width of 5000 Hz and 32k data points providing a digital resolution of ca. 0.305 Hz per point, relaxation delay 2 s;  $^{13}\text{C}$  spectral width of 29412 Hz and 64k data points providing a digital resolution of ca. 0.898 Hz per point, relaxation delay 2.5 s. The experiments were performed through standard pulse sequences. gCOSY-45 experiments were acquired with 512 t1 increments; 2048 t2 points; spectral/spectrum width 10.0 ppm. The acquisition data for gHSQC and gHMBC experiments were obtained with 512 t1 increments; 2048 t2 points; spectral/spectrum width 10.0 ppm for  $^1\text{H}$  and 220 ppm for  $^{13}\text{C}$ . Delay values were optimized for  $^1J_{\text{C,H}}$  140.0 Hz and  $^nJ_{\text{C,H}}$  3.0 Hz. Zero filling in F1 to 1k, p/2 shifted sine-bell squared (for gHSQC) or sinebell (for gHMBC) apodization functions were used for processing.

## 2. 3. Antimicrobial Activity

### 2. 3. 1. Microbial Strains

Antimicrobial activity of the synthesized compounds was tested *in vitro* against a panel of laboratory control strains belonging to the American Type Culture Collection Maryland, USA: Gram-positive: *Bacillus subtilis* ATCC 6633 and *Staphylococcus aureus* ATCC 6538; Gram-negative: *Escherichia coli* ATCC 8739 and *Salmonella typhimurium* ATCC 14028, fungal organisms: *Aspergillus niger* ATCC 16404 and *Candida albicans* ATCC 10231. The Gram-negative bacteria *Salmonella* abony NCTC 6017 was obtained from the National Collection of Type Cultures. All microorganisms were maintained at  $-20\text{ }^\circ\text{C}$  under appropriate conditions and regenerated twice before use in the manipulations.

### 2. 3. 2. Screening of Antimicrobial Activity

The minimal inhibitory concentration (MIC) of esters was determined based on a broth microdilution method performed in 96-well microtitre plates.<sup>44</sup> The inocula of the bacterial strains were prepared from overnight broth cultures and suspensions were adjusted to 0.5 McFarland

standard turbidity. Dimethyl sulphoxide (10% aqueous solution) was used to dissolve and to dilute samples to the highest concentration to be tested (stock concentrations 2 mg/mL). A serial doubling dilution of the samples was prepared in a 96-well microtiter plate, using the method of Sarker *et al.*,<sup>45</sup> with slight modifications. The minimal bactericidal/fungicidal concentration (MBC/MFC) was evaluated as the lowest concentration of tested samples at which inoculated microorganisms were 99.9% killed. Tests were carried out in triplicate. The procedure is described in detail by Lazarević *et al.*<sup>46</sup>

## 2. 4. *In Silico* Physico-chemical, Pharmacokinetic, and Toxicological Properties of the Synthesized Compounds

Together with experimental data we provided an *in silico* study on physico-chemical, pharmacokinetic and toxicological properties of the synthesized compounds **3a–y**. *In silico* predictions were accomplished using the Molinspiration,<sup>47</sup> admetSAR,<sup>48</sup> DataWarrior,<sup>49</sup> and Toxtree<sup>50</sup> tools.

## 3. Results and Discussion

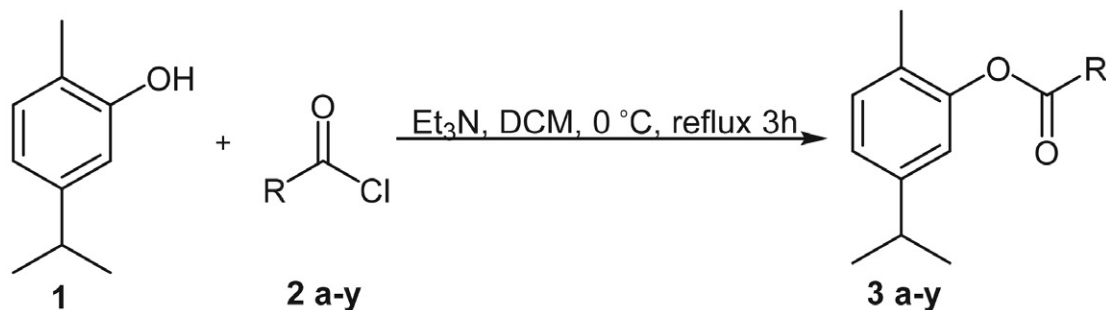
### 3. 1. Chemical Synthesis

A small focused library of 25 carvacryl esters was synthesized according to previously published standard methodology, given in Scheme 1, with yields ranging from 95 to 52% (Table 1). To the best of our knowledge compounds **3m**, **3o–w** are new (Table 1). For solid compounds **3t**, **3v**, **3x** and **3y** melting points were determined in a Stuart Scientific SMP3 apparatus and are uncorrected.

### 3. 2. Spectral Data on Synthesized Compounds

#### 3. 2. 1. Carvacryl Acetate (**3a**)<sup>22,30</sup>

Chromatographic purification gave colorless oil.  $\text{C}_{12}\text{H}_{16}\text{O}_2$  ( $M = 192.25$ ); yield 87%; RI (HP5-MS): 1384;  $^1\text{H}$



**Scheme 1.** Synthesis of the assayed esters **3a–y**. Reagents and conditions: **2a–y** solution was added dropwise to the solution of **1** and triethylamine ( $\text{Et}_3\text{N}$ ), all previously dissolved in dichloromethane ( $\text{DCM}$ ). During the addition, temperature was maintained at  $0\text{ }^\circ\text{C}$ . After reaching room temperature, the reaction mixture was refluxed for 3 h.<sup>42</sup> For structures and **3a–y** designations, see Table 1.

**Table 1.** Carvacryl esters **3a–y**, mass (g), yield (%) and entry. The reference is related to the previously reported synthesis/antimicrobial research.

Entry	Structure of R in carvacryl esters 3	Mass (g)	Yield (%)	References
<b>3a</b>	CH <sub>3</sub>	0.59	87	22, 30
<b>3b</b>	CH <sub>2</sub> Cl	0.63	83	22, 27
<b>3c</b>	CCl <sub>3</sub>	0.89	91	22, 51
<b>3d</b>	CH <sub>2</sub> CH <sub>3</sub>	0.59	86	22, 30, 52
<b>3e</b>	CH=CH <sub>2</sub>	0.50	74	53
<b>3f</b>	CH <sub>2</sub> CH <sub>2</sub> CH <sub>3</sub>	0.65	89	52, 54
<b>3g</b>	CH(CH <sub>3</sub> ) <sub>2</sub>	0.62	85	30
<b>3h</b>	CH <sub>2</sub> (CH <sub>2</sub> ) <sub>2</sub> CH <sub>3</sub>	0.63	82	52, 44
<b>3i</b>	CH <sub>2</sub> CH(CH <sub>3</sub> ) <sub>2</sub>	0.63	81	30
<b>3j</b>	CH <sub>2</sub> (CH <sub>2</sub> ) <sub>3</sub> CH <sub>3</sub>	0.70	85	23
<b>3k</b>	CH <sub>2</sub> (CH <sub>2</sub> ) <sub>4</sub> CH <sub>3</sub>	0.79	91	52*
<b>3l</b>	CH <sub>2</sub> (CH <sub>2</sub> ) <sub>5</sub> CH <sub>3</sub>	0.78	85	52*
<b>3m</b>	CH <sub>2</sub> (CH <sub>2</sub> ) <sub>6</sub> CH <sub>3</sub>	0.79	82	current study
<b>3n</b>	CH <sub>2</sub> (CH <sub>2</sub> ) <sub>7</sub> CH <sub>3</sub>	0.83	83	
<b>3o</b>	CH <sub>2</sub> (CH <sub>2</sub> ) <sub>8</sub> CH <sub>3</sub>	0.91	87	current study
<b>3p</b>	CH <sub>2</sub> (CH <sub>2</sub> ) <sub>9</sub> CH <sub>3</sub>	0.86	78	34
<b>3q</b>	CH <sub>2</sub> (CH <sub>2</sub> ) <sub>10</sub> CH <sub>3</sub>	0.93	81	current study
<b>3r</b>	CH <sub>2</sub> (CH <sub>2</sub> ) <sub>11</sub> CH <sub>3</sub>	0.90	76	current study
<b>3s</b>	CH <sub>2</sub> (CH <sub>2</sub> ) <sub>12</sub> CH <sub>3</sub>	0.91	74	current study
<b>3t</b>	CH <sub>2</sub> (CH <sub>2</sub> ) <sub>13</sub> CH <sub>3</sub>	1.12	92	current study
<b>3u</b>	CH <sub>2</sub> (CH <sub>2</sub> ) <sub>14</sub> CH <sub>3</sub>	0.97	73	current study
<b>3v</b>	CH <sub>2</sub> (CH <sub>2</sub> ) <sub>15</sub> CH <sub>3</sub>	1.17	85	current study
<b>3w</b>	CH <sub>2</sub> (CH <sub>2</sub> ) <sub>6</sub> CH=CHCH <sub>2</sub> (CH <sub>2</sub> ) <sub>6</sub> CH <sub>3</sub>	0.71	52	current study
<b>3x</b>	Ph	0.80	95	22, 23, 30, 54
<b>3y</b>	CH <sub>3</sub> O-Ph	0.89	95	23

\* spectral data are presented in the current paper for the first time

NMR (CDCl<sub>3</sub>, 500.13 MHz)  $\delta$  7.14 (d,  $J$  = 8.0 Hz, 1H, Ar-H), 7.04 (d,  $J$  = 8.0 Hz, 1H, Ar-H), 6.89 (s, 1H, Ar-H), 2.90 (spt,  $J$  = 6.9 Hz, 1H, CH), 2.34 (s, 3H, CH<sub>3</sub>), 2.16 (s, 3H, CH<sub>3</sub>), 1.25 (d,  $J$  = 6.9 Hz, 6H, CH<sub>3</sub>). <sup>13</sup>C NMR (CDCl<sub>3</sub>, 125.76 MHz)  $\delta$  169.3 (C=O), 149.3 (C<sub>Ar</sub>), 148.1 (C<sub>Ar</sub>), 130.9 (C<sub>Ar</sub>), 127.2 (C<sub>Ar</sub>), 124.2 (C<sub>Ar</sub>), 119.8 (C<sub>Ar</sub>), 33.6 (CH), 23.9 (2  $\times$  CH<sub>3</sub>), 20.8 (CH<sub>3</sub>), 15.8 (CH<sub>3</sub>-Ar); MS (EI):  $m/z$  (%): 192 (M<sup>+</sup>) (8.0), 151 (6.4), 150 (55.2), 136 (9.7), 135 (100), 105 (6.8), 105 (5.2), 91 (18.5), 79 (6.6), 77 (9.9), 43 (10.1).

### 3. 2. 2. Carvacryl 2-Chloroacetate (**3b**)<sup>22,27</sup>

Chromatographic purification gave colorless oil. C<sub>12</sub>H<sub>15</sub>ClO<sub>2</sub> ( $M$  = 226.70); yield 83%; RI (HP5-MS): 1598; <sup>1</sup>H NMR (CDCl<sub>3</sub>, 500.13 MHz)  $\delta$  7.19 (d,  $J$  = 7.6 Hz, 1H, Ar-H), 7.08 (dd,  $J$  = 8.0, 1.7 Hz, 1H, Ar-H), 6.93 (d,  $J$  = 1.7 Hz, 1H, Ar-H), 4.34 (s, 2H, CH<sub>2</sub>), 2.91 (m, 1H, CH), 2.19 (s, 3H, CH<sub>3</sub>), 1.26 (d,  $J$  = 6.9 Hz, 6H, 2  $\times$  CH<sub>3</sub>). <sup>13</sup>C NMR (CDCl<sub>3</sub>, 125.76 MHz)  $\delta$  165.7 (C=O), 148.8 (C<sub>Ar</sub>), 148.3 (C<sub>Ar</sub>), 131.1 (C<sub>Ar</sub>), 126.9 (C<sub>Ar</sub>), 124.7 (C<sub>Ar</sub>), 119.3 (C<sub>Ar</sub>), 40.7 (CH<sub>2</sub>), 33.6 (CH), 23.9 (2  $\times$  CH<sub>3</sub>), 15.7 (CH<sub>3</sub>-Ar); MS (EI):  $m/z$  (%): 226 (M<sup>+</sup>) (14.5), 151 (8.2), 150 (80.9), 136 (8.8), 135 (100), 133 (6.5), 105 (10.0), 91 (9.9), 79 (6.8), 77 (18.4).

### 3. 2. 3. Carvacryl Trichloroacetate (**3c**)<sup>22,51</sup>

Chromatographic purification gave colorless oil. C<sub>12</sub>H<sub>13</sub>Cl<sub>3</sub>O<sub>2</sub> ( $M$  = 295.59); yield 91%; RI (HP5-MS): 1731; <sup>1</sup>H NMR (CDCl<sub>3</sub>, 500.13 MHz)  $\delta$  7.23 (m, 1H, Ar-H), 7.14 (dd,  $J$  = 8.0 Hz, 1.4 Hz, 1H, Ar-H), 7.03 (s, 1H, Ar-H), 2.95 (spt,  $J$  = 6.9 Hz, 1H, CH), 2.27 (s, 3H, Ar-CH<sub>3</sub>), 1.29 (d,  $J$  = 6.9 Hz, 6H, CH(CH<sub>3</sub>)<sub>2</sub>). <sup>13</sup>C NMR (CDCl<sub>3</sub>, 125.76 MHz)  $\delta$  160.4 (C=O), 149.0 (C<sub>Ar</sub>), 148.7 (C<sub>Ar</sub>), 131.4 (C<sub>Ar</sub>), 126.8 (C<sub>Ar</sub>), 125.3 (C<sub>Ar</sub>), 118.6 (C<sub>Ar</sub>), 89.9 (C), 33.7 (CH), 23.9 (2  $\times$  CH<sub>3</sub>), 15.5 (CH<sub>3</sub>-Ar); MS (EI):  $m/z$  (%): 296 (23.0), 294 (24.2), 283 (29.8), 281 (92.1), 279 (M<sup>+</sup>) (100.0), 133 (63.1), 117 (35.9), 105 (32.3), 91 (43.6), 77 (21.0).

### 3. 2. 4. Carvacryl Propanoate (**3d**)<sup>22,30,52</sup>

Chromatographic purification gave colorless oil. C<sub>13</sub>H<sub>18</sub>O<sub>2</sub> ( $M$  = 206.28); yield 86%; RI (HP5-MS): 1479; <sup>1</sup>H NMR (CDCl<sub>3</sub>, 500.13 MHz)  $\delta$  7.17 (d,  $J$  = 7.6 Hz, 1H, Ar-H), 7.03 (dd,  $J$  = 7.6, 1.7 Hz, 1H, Ar-H), 6.88 (d,  $J$  = 1.7 Hz, 1H, Ar-H), 2.93–2.88 (m, 1H, CH), 2.64 (q, 2H,  $J$  = 7.4 Hz, CH<sub>2</sub>), 2.15 (s, 3H, CH<sub>3</sub>), 1.33 (t,  $J$  = 7.4 Hz, 3H, CH<sub>3</sub>), 1.26 (d,  $J$  = 6.9 Hz, 6H, CH<sub>3</sub>). <sup>13</sup>C NMR (CDCl<sub>3</sub>, 125.8 MHz)  $\delta$  172.7 (C=O), 149.3 (C<sub>Ar</sub>), 148.0 (C<sub>Ar</sub>), 130.9 (C<sub>Ar</sub>), 127.1 (C<sub>Ar</sub>), 124.0 (C<sub>Ar</sub>), 119.8 (C<sub>Ar</sub>), 33.6 (CH), 27.7 (CH<sub>2</sub>), 23.9 (2  $\times$  CH<sub>3</sub>), 15.8 (CH<sub>3</sub>-Ar), 9.3 (CH<sub>3</sub>); MS (EI):

$m/z$  (%): 206 ( $M^+$ ) (8.3), 151 (7.8), 150 (67.6), 136 (9.9), 135 (100), 133 (6.1), 105 (7.5), 91 (18.6), 79 (6.8), 77 (10.2), 57 (23.7).

### 3. 2. 5. Carvacryl Acrylate (3e)<sup>53</sup>

Chromatographic purification gave colorless oil.  $C_{13}H_{18}O_2$  ( $M = 204.27$ ); yield 74%; RI (HP5-MS): 1466;  $^1H$  NMR ( $CDCl_3$ , 500.13 MHz)  $\delta$  7.19 (d,  $J = 7.8$  Hz, 1H, Ar-H), 7.06 (dd,  $J = 6.2$ , 1.6 Hz, 1H, Ar-H), 6.95 (s, 1H, Ar-H), 6.65 (dd,  $J = 6.9$ , 1.3 Hz, 1H,  $CH_2=CH$ ), 6.4 (dd,  $J = 10.4$ , 6.9 Hz, 1H,  $CH=CH_2$ ), 6.05 (dd,  $J = 9.2$ , 1.4 Hz, 1H,  $CH_2=CH$ ), 2.88–2.97 (m, 1H,  $J = 6.9$  Hz,  $CH(CH_3)_2$ ), 2.18 (s, 3H,  $CH_3$ -Ar), 1.28 (d,  $J = 6.9$  Hz, 6H,  $CH_3$ ).  $^{13}C$  NMR ( $CDCl_3$ , 125.76 MHz)  $\delta$  164.3 (C=O), 149.1 ( $C_{Ar}$ ), 148.1 ( $C_{Ar}$ ), 132.3 (=C), 130.9 ( $C_{Ar}$ ), 127.9 (=C<), 127.2 ( $C_{Ar}$ ), 124.2 ( $C_{Ar}$ ), 119.8 ( $C_{Ar}$ ), 33.6 (CH), 23.9 ( $2 \times CH_3$ ), 15.7 ( $CH_3$ -Ar); MS (EI):  $m/z$  (%): 204 ( $M^+$ ) (25.6), 189 (5.6), 150 (44.7), 149 (5.5), 135 (43.6), 105 (7.1), 91 (15.6), 79 (5.8), 77 (9.2), 57 (100).

### 3. 2. 6. Carvacryl Butanoate (3f)<sup>52,54</sup>

Chromatographic purification gave colorless oil.  $C_{14}H_{20}O_2$  ( $M = 220.31$ ); yield 89%; RI (HP5-MS): 1570;  $^1H$  NMR ( $CDCl_3$ , 500.13 MHz)  $\delta$  7.17 (d,  $J = 7.6$  Hz, 1H, Ar-H), 7.04 (d,  $J = 8.0$  Hz, 1H, Ar-H), 6.88 (s, 1H, Ar-H), 2.93–2.88 (m, 1H, CH), 2.59 (t,  $J = 7.5$  Hz, 2H,  $CH_2$ ), 2.16 (s, 3H,  $CH_3$ ), 1.85 (sxt,  $J = 7.5$  Hz, 2H,  $CH_2$ ), 1.27–1.25 (m, 6H,  $CH_3$ ), 1.08 (t,  $J = 7.5$  Hz, 3H,  $CH_3$ ).  $^{13}C$  NMR ( $CDCl_3$ , 125.76 MHz)  $\delta$  171.9 (C=O), 149.3 ( $C_{Ar}$ ), 148.0 ( $C_{Ar}$ ), 130.9 ( $C_{Ar}$ ), 127.1 ( $C_{Ar}$ ), 124.0 ( $C_{Ar}$ ), 119.3 ( $C_{Ar}$ ), 36.2 ( $CH_2$ ), 33.6 (CH), 23.9 ( $2 \times CH_3$ ), 18.6 ( $CH_2$ ), 15.8 ( $CH_3$ -Ar), 13.8 ( $CH_3$ ); MS (EI):  $m/z$  (%): 220 ( $M^+$ ) (8.1), 151 (10.6), 150 (91.2), 136 (10.0), 135 (100), 105 (8.6), 91 (19.7), 77 (9.8), 71 (16.8), 43 (19.6).

### 3. 2. 7. Carvacryl 2-Methylpropanoate (3g)<sup>30</sup>

Chromatographic purification gave colorless oil,  $C_{14}H_{20}O_2$  ( $M = 220.31$ ); yield 85%; RI (HP5-MS): 1524;  $^1H$  NMR ( $CDCl_3$ , 500.13 MHz)  $\delta$  7.17 (d,  $J = 8.0$  Hz, 1H, Ar-H), 7.04 (dd,  $J = 7.8$ , 1.9 Hz, 1H, Ar-H), 6.87 (d,  $J = 1.7$  Hz, 1H, Ar-H), 2.93–2.84 (m, 2H, CH), 2.16 (s, 3H,  $CH_3$ ), 1.38 (d,  $J = 6.9$  Hz, 6H,  $2 \times CH_3$ ), 1.26 (d,  $J = 6.9$  Hz, 6H,  $2 \times CH_3$ );  $^{13}C$  NMR ( $CDCl_3$ , 125.76 MHz)  $\delta$  175.3 (C=O), 149.3 ( $C_{Ar}$ ), 148.0 ( $C_{Ar}$ ), 130.9 ( $C_{Ar}$ ), 127.1 ( $C_{Ar}$ ), 123.9 ( $C_{Ar}$ ), 119.8 ( $C_{Ar}$ ), 34.2 (CH), 33.6 (CH), 23.9 ( $2 \times CH_3$ ), 19.1 ( $2 \times CH_3$ ), 15.8 ( $CH_3$ -Ar); MS (EI):  $m/z$  (%): 220 (13.6), 151 (11.1), 150 (100), 136 (8.6), 135 (91.7), 105 (8.5), 91 (18.9), 77 (9.5), 71 (22.8), 43 (32.8).

### 3. 2. 8. Carvacryl Pentanoate (3h)<sup>52,44</sup>

Chromatographic purification gave colorless oil.  $C_{15}H_{22}O_2$  ( $M = 234.34$ ); yield 82%; RI (HP5-MS): 1670;  $^1H$

NMR ( $CDCl_3$ , 500.13 MHz)  $\delta$  7.17 (d,  $J = 8.0$  Hz, 1H, Ar-H), 7.04 (dd,  $J = 8.0$ , 1.7 Hz, 1H, Ar-H), 6.88 (d,  $J = 1.7$  Hz, 1H, Ar-H), 2.93–2.88 (m, 1H, CH), 2.61 (t,  $J = 7.5$  Hz, 2H,  $CH_2$ ), 2.16 (s, 3H,  $CH_3$ ), 1.79 (quin,  $J = 7.5$  Hz, 2H,  $CH_2$ ), 1.5 (dq,  $J = 15$ , 7.4 Hz, 2H,  $CH_2$ ), 1.26 (d,  $J = 6.9$  Hz, 6H,  $2 \times CH_3$ ), 1.0 (t,  $J = 7.5$  Hz, 3H,  $CH_3$ ).  $^{13}C$  NMR ( $CDCl_3$ , 125.76 MHz)  $\delta$  172.1 (C=O), 149.3 ( $C_{Ar}$ ), 148.0 ( $C_{Ar}$ ), 130.9 ( $C_{Ar}$ ), 127.1 ( $C_{Ar}$ ), 124.0 ( $C_{Ar}$ ), 119.8 ( $C_{Ar}$ ), 34.0 ( $CH_2$ ), 33.6 (CH), 27.2 ( $CH_2$ ), 23.9 ( $2 \times CH_3$ ), 22.4 ( $CH_2$ ), 15.8 ( $CH_3$ -Ar), 13.8 ( $CH_3$ ); MS (EI):  $m/z$  (%): 234 (6.8), 151 (11.7), 150 (100), 136 (8.5), 135 (86.5), 105 (8.0), 91 (17.2), 85 (11.6), 77 (8.1), 57 (28.9).

### 3. 2. 9. Carvacryl 3-Methylbutanoate (3i)<sup>30</sup>

Chromatographic purification gave colorless oil.  $C_{15}H_{22}O_2$  ( $M = 234.34$ ); yield 81%; RI (HP5-MS): 1619;  $^1H$  NMR ( $CDCl_3$ , 500.13 MHz)  $\delta$  7.17 (d,  $J = 7.6$  Hz, 1H, Ar-H), 7.04 (dd,  $J = 7.6$ , 1.7 Hz, 1H, Ar-H), 6.87 (d,  $J = 1.7$  Hz, 1H, Ar-H), 2.93–2.88 (m, 1H, CH), 2.49 (d,  $J = 6.9$  Hz, 2H,  $CH_2$ ), 2.34–2.26 (m, 1H, CH), 2.17 (s, 3H,  $CH_3$ ), 1.26 (d,  $J = 6.9$  Hz, 6H,  $CH_3$ ), 1.11 (d,  $J = 6.6$  Hz, 6H,  $CH_3$ ).  $^{13}C$  NMR ( $CDCl_3$ , 125.76 MHz)  $\delta$  171.4 (C=O), 149.3 ( $C_{Ar}$ ), 148.0 ( $C_{Ar}$ ), 130.9 ( $C_{Ar}$ ), 127.2 ( $C_{Ar}$ ), 124.0 ( $C_{Ar}$ ), 119.9 ( $C_{Ar}$ ), 43.3 ( $CH_2$ ), 33.6 (CH), 25.8 (CH), 23.9 ( $2 \times CH_3$ ), 22.5 ( $2 \times CH_3$ ), 15.9 ( $CH_3$ -Ar); MS (EI):  $m/z$  (%): 234 ( $M^+$ ) (8.1), 151 (12.0), 150 (100), 136 (7.9), 135 (80.2), 105 (8.5), 91 (17.9), 85 (13.2), 77 (8.5), 57 (40.3), 41 (7.1).

### 3. 2. 10. Carvacryl Hexanoate (3j)<sup>23</sup>

Chromatographic purification gave colorless oil,  $C_{16}H_{24}O_2$  ( $M = 248.37$ ); yield 85%; RI (HP5-MS): 1770;  $^1H$  NMR ( $CDCl_3$ , 500.13 MHz)  $\delta$  7.17 (d,  $J = 8.0$  Hz, 1H, Ar-H), 7.05 (dd,  $J = 7.6$ , 1.7 Hz, 1H, Ar-H), 6.89 (d,  $J = 1.7$  Hz, 1H, Ar-H), 2.94–2.88 (m, 1H, CH), 2.61 (t,  $J = 7.5$  Hz, 2H,  $CH_2$ ), 2.17 (s, 3H,  $CH_3$ ), 1.85–1.79 (m, 2H,  $CH_2$ ), 1.48–1.38 (m, 4H,  $2 \times CH_2$ ), 1.36–1.26 (m, 6H,  $2 \times CH_3$ ), 0.99–0.91 (m, 3H,  $CH_3$ ).  $^{13}C$  NMR ( $CDCl_3$ , 125.76 MHz)  $\delta$  172.1 (C=O), 149.3 ( $C_{Ar}$ ), 148.0 ( $C_{Ar}$ ), 130.9 ( $C_{Ar}$ ), 127.2 ( $C_{Ar}$ ), 124.0 ( $C_{Ar}$ ), 119.8 ( $C_{Ar}$ ), 34.3 ( $CH_2$ ), 33.6 (CH), 31.4 ( $CH_2$ ), 24.8 ( $CH_2$ ), 23.9 ( $2 \times CH_3$ ), 22.4 ( $CH_2$ ), 15.8 ( $CH_3$ -Ar), 13.9 ( $CH_3$ ); MS (EI):  $m/z$  (%) 248 ( $M^+$ ), 151 (11.9), 150 (100), 135 (73.1), 105 (8.4), 99 (8.8), 91 (17.9), 77 (8.4), 71 (13.1), 55 (8.9), 43 (21.3).

### 3. 2. 11. Carvacryl Heptanoate (3k)<sup>52</sup>

Chromatographic purification gave colorless oil.  $C_{17}H_{26}O_2$  ( $M = 262.39$ ); yield 91%; RI (HP5-MS): 1873;  $^1H$  NMR ( $CDCl_3$ , 500.13 MHz)  $\delta$  7.17 (d,  $J = 7.6$  Hz, 1H, Ar-H), 7.04 (dd,  $J = 7.8$ , 1.9 Hz, 1H, Ar-H), 6.89 (d,  $J = 1.7$  Hz, 1H, Ar-H), 2.96–2.88 (m, 1H, CH), 2.61 (t,  $J = 7.5$  Hz, 2H,  $CH_2$ ), 2.17 (s, 3H,  $CH_3$ ), 1.81 (quin,  $J = 7.5$  Hz, 2H,  $CH_2$ ), 1.50–1.44 (m, 2H,  $CH_2$ ), 1.39–1.37 (m, 4H,  $2 \times CH_2$ ), 1.27 (d,  $J = 6.9$  Hz, 6H,  $CH_3$ ), 0.96–0.91 (m, 3H,

CH<sub>3</sub>). <sup>13</sup>C NMR (CDCl<sub>3</sub>, 125.76 MHz)  $\delta$  172.1 (C=O), 149.3 (C<sub>Ar</sub>), 148.0 (C<sub>Ar</sub>), 130.9 (C<sub>Ar</sub>), 127.2 (C<sub>Ar</sub>), 124.0 (C<sub>Ar</sub>), 119.8 (C<sub>Ar</sub>), 34.3 (CH<sub>2</sub>), 33.6 (CH), 31.5 (CH<sub>2</sub>), 28.9 (CH<sub>2</sub>), 25.1 (CH<sub>2</sub>), 23.9 (2  $\times$  CH<sub>3</sub>), 22.5 (CH<sub>2</sub>), 15.8 (CH<sub>3</sub>-Ar), 14.1 (CH<sub>3</sub>); MS (EI):  $m/z$  (%) 262 (M<sup>+</sup>) 151 (14.3), 150 (100), 135 (67.2), 113 (8.7), 105 (10.4), 91 (22.1), 77 (11.4), 55 (13.6), 43 (31.8), 41 (12.1).

### 3. 2. 12. Carvacryl Octanoate (3l)<sup>52</sup>

Chromatographic purification gave colorless oil. C<sub>18</sub>H<sub>28</sub>O<sub>2</sub> ( $M$  = 276.42); yield 85%; RI (HP5-MS): 1978; <sup>1</sup>H NMR (CDCl<sub>3</sub>, 500.13 MHz)  $\delta$  7.17 (d,  $J$  = 7.6 Hz, 1H, Ar-H), 7.04 (dd,  $J$  = 7.8, 1.6 Hz, 1H, Ar-H), 6.89 (d,  $J$  = 1.7 Hz, 1H, Ar-H), 2.94–2.88 (m, 1H, CH), 2.61 (t,  $J$  = 7.5 Hz, 2H, CH<sub>2</sub>), 2.17 (s, 3H, CH<sub>3</sub>), 1.82 (quin,  $J$  = 7.5 Hz, 2H, CH<sub>2</sub>), 1.48–1.31 (m, 8H, 4  $\times$  CH<sub>2</sub>), 1.27 (d,  $J$  = 6.9 Hz, 6H, CH<sub>3</sub>), 0.94 (m, 3H, CH<sub>3</sub>). <sup>13</sup>C NMR (CDCl<sub>3</sub>, 125.76 MHz)  $\delta$  172.1 (C=O), 149.3 (C<sub>Ar</sub>), 148.0 (C<sub>Ar</sub>), 130.9 (C<sub>Ar</sub>), 127.2 (C<sub>Ar</sub>), 124.0 (C<sub>Ar</sub>), 119.8 (C<sub>Ar</sub>), 34.3 (CH<sub>2</sub>), 33.6 (CH), 31.7 (CH<sub>2</sub>), 29.2 (CH<sub>2</sub>), 29.0 (CH<sub>2</sub>), 25.1 (CH<sub>2</sub>), 23.9 (2  $\times$  CH<sub>3</sub>), 22.6 (CH<sub>2</sub>), 15.8 (CH<sub>3</sub>-Ar), 14.1 (CH<sub>3</sub>); MS (EI):  $m/z$  (%) 276 (M<sup>+</sup>) 151 (12.3), 150 (100), 135 (52.3), 105 (7.3), 91 (14.4), 77 (6.3), 57 (22.7), 55 (14.0), 43 (11.4), 41 (8.5).

### 3. 2. 13. Carvacryl Nonanoate (3m)

Chromatographic purification gave colorless oil. C<sub>19</sub>H<sub>30</sub>O<sub>2</sub> ( $M$  = 290.45); yield 82%; RI (HP5-MS): 2082; <sup>1</sup>H NMR (CDCl<sub>3</sub>, 500.13 MHz)  $\delta$  7.17 (d,  $J$  = 7.6 Hz, 1H, Ar-H), 7.04 (dd,  $J$  = 8.0, 1.7 Hz, 1H, Ar-H), 6.9 (d,  $J$  = 1.7 Hz, 1H, Ar-H), 2.94–2.88 (m, 1H, CH), 2.61 (t,  $J$  = 7.6 Hz, 2H, CH<sub>2</sub>), 2.17 (s, 3H, CH<sub>3</sub>), 1.82 (quin,  $J$  = 7.5 Hz, 2H, CH<sub>2</sub>), 1.50–1.44 (m, 2H, CH<sub>2</sub>), 1.41–1.33 (m, 8H, 4  $\times$  CH<sub>2</sub>), 1.27 (d,  $J$  = 6.9 Hz, 6H, CH<sub>3</sub>), 0.93 (m, 3H, CH<sub>3</sub>). <sup>13</sup>C NMR (CDCl<sub>3</sub>, 125.76 MHz)  $\delta$  172.1 (C=O), 149.3 (C<sub>Ar</sub>), 148.0 (C<sub>Ar</sub>), 130.9 (C<sub>Ar</sub>), 127.2 (C<sub>Ar</sub>), 124.0 (C<sub>Ar</sub>), 119.8 (C<sub>Ar</sub>), 34.3 (CH<sub>2</sub>), 33.6 (CH), 31.8 (CH<sub>2</sub>), 29.2 (2  $\times$  CH<sub>2</sub>), 29.2 (CH<sub>2</sub>), 25.1 (CH<sub>2</sub>), 23.9 (2  $\times$  CH<sub>3</sub>), 22.7 (CH<sub>2</sub>), 15.8 (CH<sub>3</sub>-Ar), 14.1 (CH<sub>3</sub>); MS (EI):  $m/z$  (%) 290 (M<sup>+</sup>) 151 (12.2), 150 (100), 136 (4.3), 135 (43.9), 109 (3.9), 91 (6.8), 71 (6.4), 57 (9.0), 55 (7.3), 43 (5.7).

### 3. 2. 14. Carvacryl Decanoate (3n)

Chromatographic purification gave colorless oil. C<sub>20</sub>H<sub>32</sub>O<sub>2</sub> ( $M$  = 304.47); yield 83%; RI (HP5-MS): 2186; <sup>1</sup>H NMR (CDCl<sub>3</sub>, 500.13 MHz)  $\delta$  7.17 (d,  $J$  = 8.0 Hz, 1H, Ar-H), 7.03 (dd,  $J$  = 8.0 Hz, 1.4 Hz, 1H, Ar-H), 6.88 (s, 1H, Ar-H), 2.93–2.88 (m, 1H, CH), 2.61 (t,  $J$  = 7.5 Hz, 2H, CH<sub>2</sub>), 2.17 (s, 3H, CH<sub>3</sub>), 1.81 (quin,  $J$  = 7.5 Hz, 2H, CH<sub>2</sub>), 1.49–1.29 (m, 14H, 7  $\times$  CH<sub>2</sub>), 1.27 (d,  $J$  = 6.9 Hz, 6H, CH<sub>3</sub>), 0.93 (m, 3H, CH<sub>3</sub>). <sup>13</sup>C NMR (CDCl<sub>3</sub>, 125.76 MHz)  $\delta$  172.1 (C=O), 149.3 (C<sub>Ar</sub>), 148.0 (C<sub>Ar</sub>), 130.9 (C<sub>Ar</sub>), 127.2 (C<sub>Ar</sub>), 124.0 (C<sub>Ar</sub>), 119.8 (C<sub>Ar</sub>), 34.3 (CH<sub>2</sub>), 33.6 (CH), 31.9 (CH<sub>2</sub>), 29.5 (CH<sub>2</sub>), 29.3 (2  $\times$  CH<sub>2</sub>), 29.3 (CH<sub>2</sub>), 25.1 (CH<sub>2</sub>),

23.9 (2  $\times$  CH<sub>3</sub>), 22.7 (CH<sub>2</sub>), 15.8 (CH<sub>3</sub>-Ar), 14.1 (CH<sub>3</sub>); MS (EI):  $m/z$  (%) 304 (M<sup>+</sup>) 151 (12.5), 150 (100), 136 (3.8), 135 (39.0), 109 (4.1), 91 (5.8), 71 (4.5), 57 (5.4), 55 (7.0), 43 (6.1).

### 3. 2. 15. Carvacryl Undecanoate (3o)

Chromatographic purification gave colorless oil. C<sub>21</sub>H<sub>34</sub>O<sub>2</sub> ( $M$  = 318.50); yield 87%; RI (HP5-MS): 2287; <sup>1</sup>H NMR (CDCl<sub>3</sub>, 500.13 MHz)  $\delta$  7.17 (d,  $J$  = 7.6 Hz, 1H, Ar-H), 7.04 (dd,  $J$  = 7.6, 1.7 Hz, 1H, Ar-H), 6.88 (d,  $J$  = 1.7 Hz, 1H, Ar-H), 2.9 (quin,  $J$  = 7.5 Hz, 1H, CH), 2.6 (t,  $J$  = 7.5 Hz, 2H, CH<sub>2</sub>), 2.16 (s, 3H, CH<sub>3</sub>), 1.81 (quin,  $J$  = 7.5 Hz, 2H, CH<sub>2</sub>), 1.49–1.28 (m, 16H, 8  $\times$  CH<sub>2</sub>), 1.26 (d,  $J$  = 6.9 Hz, 6H, CH<sub>3</sub>), 0.92 (m, 3H, CH<sub>3</sub>). <sup>13</sup>C NMR (CDCl<sub>3</sub>, 125.76 MHz)  $\delta$  172.1 (C=O), 149.3 (C<sub>Ar</sub>), 148.0 (C<sub>Ar</sub>), 130.9 (C<sub>Ar</sub>), 127.2 (C<sub>Ar</sub>), 124.0 (C<sub>Ar</sub>), 119.8 (C<sub>Ar</sub>), 34.3 (CH<sub>2</sub>), 33.6 (CH), 31.9 (CH<sub>2</sub>), 29.6 (CH<sub>2</sub>), 29.5 (CH<sub>2</sub>), 29.3 (CH<sub>2</sub>), 29.3 (CH<sub>2</sub>), 29.2 (CH<sub>2</sub>), 25.1 (CH<sub>2</sub>), 23.9 (2  $\times$  CH<sub>3</sub>), 22.7 (CH<sub>2</sub>), 15.8 (CH<sub>3</sub>-Ar), 14.1 (CH<sub>3</sub>); MS (EI):  $m/z$  (%) 318 (M<sup>+</sup>) 151 (13.0), 150 (100), 136 (3.4), 135 (34.9), 109 (4.7), 105 (2.5), 91 (4.6), 57 (6.0), 55 (6.3), 43 (4.9).

### 3. 2. 16. Carvacryl Dodecanoate (3p)<sup>34</sup>

Chromatographic purification gave colorless oil. C<sub>22</sub>H<sub>36</sub>O<sub>2</sub> ( $M$  = 332.53); yield 78%; RI (HP5-MS): 2388; <sup>1</sup>H NMR (CDCl<sub>3</sub>, 500.13 MHz)  $\delta$  7.17 (d,  $J$  = 8.0 Hz, 1H, Ar-H), 7.04 (dd,  $J$  = 7.8, 1.6 Hz, 1H, Ar-H), 6.88 (d,  $J$  = 1.4 Hz, 1H, Ar-H), 2.90 (m, 1H, CH), 2.60 (t,  $J$  = 7.6 Hz, 2H, CH<sub>2</sub>), 2.16 (s, 3H, CH<sub>3</sub>), 1.81 (quin,  $J$  = 7.5 Hz, 2H, CH<sub>2</sub>), 1.49–1.43 (m, 2H, CH<sub>2</sub>), 1.4–1.29 (m, 14H, 7  $\times$  CH<sub>2</sub>), 1.27 (d,  $J$  = 6.9 Hz, 6H, CH<sub>3</sub>), 0.92 (t,  $J$  = 6.8 Hz, 3H, CH<sub>3</sub>). <sup>13</sup>C NMR (CDCl<sub>3</sub>, 125.76 MHz)  $\delta$  172.1 (C=O), 149.3 (C<sub>Ar</sub>), 148.0 (C<sub>Ar</sub>), 130.9 (C<sub>Ar</sub>), 127.2 (C<sub>Ar</sub>), 124.0 (C<sub>Ar</sub>), 119.8 (C<sub>Ar</sub>), 34.3 (CH<sub>2</sub>), 33.6 (CH), 31.9 (CH<sub>2</sub>), 29.6 (2  $\times$  CH<sub>2</sub>), 29.5 (CH<sub>2</sub>), 29.4 (CH<sub>2</sub>), 29.3 (CH<sub>2</sub>), 29.2 (CH<sub>2</sub>), 25.1 (CH<sub>2</sub>), 23.9 (2  $\times$  CH<sub>3</sub>), 22.7 (CH<sub>2</sub>), 15.8 (CH<sub>3</sub>-Ar), 14.1 (CH<sub>3</sub>); MS (EI):  $m/z$  (%) 332 (M<sup>+</sup>) 151 (12.8), 150 (100), 136 (3.1), 135 (32.1), 109 (5.2), 91 (4.3), 71 (2.6), 57 (7.0), 55 (7.2), 43 (5.2).

### 3. 2. 17. Carvacryl Tridecanoate (3q)

Chromatographic purification gave colorless oil. C<sub>23</sub>H<sub>38</sub>O<sub>2</sub> ( $M$  = 346.55); yield 81%; RI (HP5-MS): 2491; <sup>1</sup>H NMR (CDCl<sub>3</sub>, 500.13 MHz)  $\delta$  7.18 (m, 1H, Ar-H), 7.04 (dd,  $J$  = 7.8, 1.6 Hz, 1H, Ar-H), 6.88 (s, 1H, Ar-H), 2.91 (m, 1H, CH), 2.6 (t,  $J$  = 7.5 Hz, 2H, CH<sub>2</sub>), 2.16 (s, 3H, CH<sub>3</sub>), 1.81 (quin,  $J$  = 7.5 Hz, 2H, CH<sub>2</sub>), 1.49–1.43 (m, 2H, CH<sub>2</sub>), 1.38–1.28 (m, 16H, 8  $\times$  CH<sub>2</sub>), 1.27 (d,  $J$  = 6.9 Hz, 6H, CH<sub>3</sub>), 0.92 (t,  $J$  = 6.8 Hz, 3H, CH<sub>3</sub>). <sup>13</sup>C NMR (CDCl<sub>3</sub>, 125.76 MHz)  $\delta$  172.1 (C=O), 149.3 (C<sub>Ar</sub>), 148.0 (C<sub>Ar</sub>), 130.9 (C<sub>Ar</sub>), 127.2 (C<sub>Ar</sub>), 124.0 (C<sub>Ar</sub>), 119.8 (C<sub>Ar</sub>), 34.3 (CH<sub>2</sub>), 33.6 (CH), 31.9 (CH<sub>2</sub>), 29.7 (2  $\times$  CH<sub>2</sub>), 29.5 (CH<sub>2</sub>), 29.4 (CH<sub>2</sub>), 29.3 (CH<sub>2</sub>), 29.2 (CH<sub>2</sub>), 29.1 (CH<sub>2</sub>), 25.1 (CH<sub>2</sub>), 23.9 (2  $\times$



CH<sub>3</sub>), 22.7 (CH<sub>2</sub>), 15.8 (CH<sub>3</sub>-Ar), 14.1 (CH<sub>3</sub>); MS (EI): *m/z* (%) 346 (M<sup>+</sup>) 151 (13.3), 150 (100), 136 (2.8), 135 (28.9), 109 (5.2), 91 (3.6), 71 (2.9), 57 (6.4), 55 (6.6), 43 (4.8).

### 3. 2. 18. Carvacryl Tetradecanoate (3r)

Chromatographic purification gave colorless oil. C<sub>24</sub>H<sub>40</sub>O<sub>2</sub> (*M* = 360.58); yield 76%; RI (HP5-MS): 2590; <sup>1</sup>H NMR (CDCl<sub>3</sub>, 500.13 MHz) δ 7.17 (d, *J* = 7.6 Hz, 1H, Ar-H), 7.04 (dd, *J* = 7.8, 1.6 Hz, 1H, Ar-H), 6.88 (s, 1H, Ar-H), 2.9 (m, 1H, CH), 2.6 (t, *J* = 7.6 Hz, 2H, CH<sub>2</sub>), 2.16 (s, 3H, CH<sub>3</sub>), 1.81 (quin, *J* = 7.5 Hz, 2H, CH<sub>2</sub>), 1.49–1.43 (m, 2H, CH<sub>2</sub>), 1.4–1.28 (m, 18H, 9 × CH<sub>2</sub>) 0.91 (t, *J* = 6.9 Hz, 3H, CH<sub>3</sub>). <sup>13</sup>C NMR (CDCl<sub>3</sub>, 125.76 MHz) δ 172.1 (C=O), 149.3 (C<sub>Ar</sub>), 148.0 (C<sub>Ar</sub>), 130.9 (C<sub>Ar</sub>), 127.2 (C<sub>Ar</sub>), 124.0 (C<sub>Ar</sub>), 119.8 (C<sub>Ar</sub>), 34.3 (CH<sub>2</sub>), 33.6 (CH), 31.9 (CH<sub>2</sub>), 29.7 (2 × CH<sub>2</sub>), 29.6 (2 × CH<sub>2</sub>), 29.5 (CH<sub>2</sub>), 29.4 (CH<sub>2</sub>), 29.3 (CH<sub>2</sub>), 29.2 (CH<sub>2</sub>), 25.1 (CH<sub>2</sub>), 23.9 (2 × CH<sub>3</sub>), 22.7 (CH<sub>2</sub>), 15.9 (CH<sub>3</sub>-Ar), 14.1 (CH<sub>3</sub>); MS (EI): *m/z* (%) 360 (M<sup>+</sup>) 151 (12.4), 150 (100), 135 (27.7), 109 (6.0), 91 (4.5), 71 (3.8), 69 (3.7), 57 (9.0), 55 (10.0), 43 (8.3).

### 3. 2. 19. Carvacryl Pentadecanoate (3s)

Chromatographic purification gave colorless oil. C<sub>25</sub>H<sub>42</sub>O<sub>2</sub> (*M* = 374.61); yield 74%; RI (HP5-MS): 2694; <sup>1</sup>H NMR (CDCl<sub>3</sub>, 500.13 MHz) δ 7.17 (d, *J* = 7.6 Hz, 1H, Ar-H), 7.04 (dd, *J* = 8.0, 1.7 Hz, 1H, Ar-H), 6.88 (d, *J* = 1.7 Hz, 1H, Ar-H), 2.9 (m, 1H, CH), 2.6 (t, *J* = 7.5 Hz, 2H, CH<sub>2</sub>), 2.16 (s, 3H, CH<sub>3</sub>), 1.81 (quin, *J* = 7.5 Hz, 2H, CH<sub>2</sub>), 1.49–1.44 (m, 2H, CH<sub>2</sub>), 1.4–1.28 (m, 20H, 10 × CH<sub>2</sub>), 1.26 (d, *J* = 6.9 Hz, 3H, CH<sub>3</sub>), 0.92 (t, *J* = 6.9 Hz, 3H, CH<sub>3</sub>). <sup>13</sup>C NMR (CDCl<sub>3</sub>, 125.76 MHz) δ 172.1 (C=O), 149.3 (C<sub>Ar</sub>), 148.0 (C<sub>Ar</sub>), 130.9 (C<sub>Ar</sub>), 127.2 (C<sub>Ar</sub>), 124.0 (C<sub>Ar</sub>), 119.8 (C<sub>Ar</sub>), 34.3 (CH<sub>2</sub>), 33.6 (CH), 31.9 (CH<sub>2</sub>), 29.7 (3 × CH<sub>2</sub>), 29.6 (CH<sub>2</sub>), 29.5 (CH<sub>2</sub>), 29.4 (CH<sub>2</sub>), 29.3 (2 × CH<sub>2</sub>), 29.2 (CH<sub>2</sub>), 25.1 (CH<sub>2</sub>), 23.9 (2 × CH<sub>3</sub>), 22.7 (CH<sub>2</sub>), 15.8 (CH<sub>3</sub>-Ar), 14.1 (CH<sub>3</sub>); MS (EI): *m/z* (%) 374 (M<sup>+</sup>) 151 (12.5), 150 (100), 135 (25.2), 109 (6.1), 91 (3.9), 71 (3.6), 69 (3.6), 57 (8.6), 55 (9.1), 43 (7.4).

### 3. 2. 20. Carvacryl Hexadecanoate (3t)

Chromatographic purification gave amorphous white solid. Mp 31–32 °C. C<sub>26</sub>H<sub>44</sub>O<sub>2</sub> (*M* = 388.63); yield 92%; RI (HP5-MS): 2804; <sup>1</sup>H NMR (CDCl<sub>3</sub>, 500.13 MHz) δ 7.17 (d, *J* = 7.9 Hz, 1H, Ar-H), 7.04 (dd, *J* = 7.7, 1.7 Hz, 1H, Ar-H), 6.88 (d, *J* = 1.6 Hz, 1H, Ar-H), 2.90 (m, 1H, CH), 2.60 (t, *J* = 7.6 Hz, 2H, CH<sub>2</sub>), 2.16 (s, 3H, CH<sub>3</sub>), 1.81 (quin, *J* = 7.6 Hz, 2H, CH<sub>2</sub>), 1.47–1.28 (bm, 24H, 12 × CH<sub>2</sub>), 1.26 (d, *J* = 7.0 Hz, 6H, CH<sub>3</sub>), 0.9 (m, 3H, CH<sub>3</sub>). <sup>13</sup>C NMR (CDCl<sub>3</sub>, 125.76 MHz) δ 172.1 (C=O), 149.3 (C<sub>Ar</sub>), 148.0 (C<sub>Ar</sub>), 130.8 (C<sub>Ar</sub>), 127.1 (C<sub>Ar</sub>), 124.0 (C<sub>Ar</sub>), 119.8 (C<sub>Ar</sub>), 34.3 (CH<sub>2</sub>), 33.6 (CH), 31.9 (CH<sub>2</sub>), 29.7 (4 × CH<sub>2</sub>), 29.6 (CH<sub>2</sub>), 29.5 (CH<sub>2</sub>), 29.4 (CH<sub>2</sub>), 29.3 (CH<sub>2</sub>), 29.2

(CH<sub>2</sub>), 29.1 (CH<sub>2</sub>), 25.1 (CH<sub>2</sub>), 23.9 (2 × CH<sub>3</sub>), 22.7 (CH<sub>2</sub>), 15.8 (CH<sub>3</sub>-Ar), 14.1 (CH<sub>3</sub>); MS (EI): *m/z* (%) 388 (M<sup>+</sup>) 151 (18.7), 150 (100), 136 (2.9), 135 (29.4), 109 (6.8), 71 (2.8), 69 (2.7), 57 (5.5), 55 (5.4), 43 (3.7).

### 3. 2. 21. Carvacryl Heptadecanoate (3u)

Chromatographic purification gave colorless oil. C<sub>27</sub>H<sub>46</sub>O<sub>2</sub> (*M* = 402.66); yield 73%; RI (HP5-MS): 2902; <sup>1</sup>H NMR (CDCl<sub>3</sub>, 500.13 MHz) δ 7.17 (d, *J* = 8.0 Hz, 1H, Ar-H), 7.04 (dd, *J* = 7.6, 1.7 Hz, 1H, Ar-H), 6.88 (bs, 1H, Ar-H), 2.9 (m, 1H, CH), 2.60 (t, *J* = 7.6 Hz, 2H, CH<sub>2</sub>), 2.16 (s, 3H, CH<sub>3</sub>), 1.81 (quin, *J* = 7.5 Hz, 2H, CH<sub>2</sub>), 1.48–1.28 (bm, 26H, 13 × CH<sub>2</sub>), 1.26 (d, *J* = 6.9 Hz, 6H, CH<sub>3</sub>), 0.92 (t, *J* = 6.9 Hz, 3H, CH<sub>3</sub>). <sup>13</sup>C NMR (CDCl<sub>3</sub>, 125.76 MHz) δ 172.1 (C=O), 149.3 (C<sub>Ar</sub>), 148.0 (C<sub>Ar</sub>), 130.9 (C<sub>Ar</sub>), 127.2 (C<sub>Ar</sub>), 124.0 (C<sub>Ar</sub>), 119.8 (C<sub>Ar</sub>), 34.3 (CH<sub>2</sub>), 33.6 (CH), 32.0 (CH<sub>2</sub>), 29.7 (6 × CH<sub>2</sub>), 29.6 (CH<sub>2</sub>), 29.5 (CH<sub>2</sub>), 29.4 (CH<sub>2</sub>), 29.3 (CH<sub>2</sub>), 29.2 (CH<sub>2</sub>), 25.1 (CH<sub>2</sub>), 23.9 (2 × CH<sub>3</sub>), 22.7 (CH<sub>2</sub>), 15.8 (CH<sub>3</sub>-Ar), 14.1 (CH<sub>3</sub>); MS (EI): *m/z* (%) 402 (M<sup>+</sup>) 151 (14.0), 150 (100), 135 (21.9), 109 (6.0), 91 (2.6), 71 (2.9), 69 (2.9), 57 (6.4), 55 (6.3), 43 (4.8).

### 3. 2. 22. Carvacryl Octadecanoate (3v)

Chromatographic purification gave amorphous white solid. Mp 61 °C. C<sub>28</sub>H<sub>48</sub>O<sub>2</sub> (*M* = 416.69); yield 85%; RI (HP5-MS): 2945; <sup>1</sup>H NMR (CDCl<sub>3</sub>, 500.13 MHz) δ 7.17 (d, *J* = 7.8 Hz, 1H, Ar-H), 7.04 (dd, *J* = 7.8, 1.9 Hz, 1H, Ar-H), 6.88 (d, *J* = 1.8 Hz, 1H, Ar-H), 2.9 (hept, *J* = 6.9 Hz, 1H, CH), 2.6 (t, *J* = 7.6 Hz, 2H, CH<sub>2</sub>), 2.16 (s, 3H, CH<sub>3</sub>), 1.81 (quin, *J* = 7.5 Hz, 2H, CH<sub>2</sub>), 1.51–1.28 (m, 28H), 1.26 (d, *J* = 6.9 Hz, 6H, 2 × CH<sub>3</sub>), 0.92 (t, *J* = 6.9 Hz, 3H, CH<sub>3</sub>). <sup>13</sup>C NMR (CDCl<sub>3</sub>, 125.76 MHz) δ 172.1 (C=O), 149.3 (C<sub>Ar</sub>), 148.0 (C<sub>Ar</sub>), 130.8 (C<sub>Ar</sub>), 127.1 (C<sub>Ar</sub>), 124.0 (C<sub>Ar</sub>), 119.8 (C<sub>Ar</sub>), 34.3 (CH<sub>2</sub>), 33.6 (CH), 32.0 (CH<sub>2</sub>), 29.7 (7 × CH<sub>2</sub>), 29.6 (CH<sub>2</sub>), 29.5 (CH<sub>2</sub>), 29.4 (CH<sub>2</sub>), 29.3 (CH<sub>2</sub>), 29.2 (CH<sub>2</sub>), 25.1 (CH<sub>2</sub>), 23.9 (2 × CH<sub>3</sub>), 22.7 (CH<sub>2</sub>), 15.8 (CH<sub>3</sub>-Ar), 14.1 (CH<sub>3</sub>); MS (EI): *m/z* (%) 416 (M<sup>+</sup>), 151 (12.5), 150 (100), 135 (25.6), 109 (7.0), 91 (5.1), 69 (5.5), 57 (13.5), 55 (14.0), 43 (15.9), 41 (5.2).

### 3. 2. 23. Carvacryl Oleate (3w)

Chromatographic purification gave colorless oil. C<sub>28</sub>H<sub>46</sub>O<sub>2</sub> (*M* = 414.67); yield 52%; RI (HP5-MS): 2936; <sup>1</sup>H NMR (CDCl<sub>3</sub>, 500.13 MHz) δ 7.17 (d, *J* = 7.8 Hz, 1H, Ar-H), 7.03 (dd, *J* = 7.8, 1.8 Hz, 1H, Ar-H), 6.87 (d, *J* = 1.8 Hz, 1H, Ar-H), 5.43–5.34 (m, 2H, CH=CH *Z*-configuration), 2.9 (hept, *J* = 7.0 Hz, 1H, CH), 2.6 (t, *J* = 7.5 Hz, 2H, CH<sub>2</sub>), 2.16 (s, 3H, CH<sub>3</sub>), 2.10–2.01 (m, 4H, 2 × CH<sub>2</sub>), 1.81 (quin, *J* = 7.5 Hz, 2H, CH<sub>2</sub>), 1.61 – 1.53 (m, 2H, CH<sub>2</sub>), 1.51–1.41 (m, 2H, CH<sub>2</sub>), 1.36 (d, *J* = 7.5 Hz, 6H, 2 × CH<sub>3</sub>), 1.33–1.23 (m, 16H, 8 × CH<sub>2</sub>), 0.91 (t, *J* = 6.9 Hz, 3H, CH<sub>3</sub>). <sup>13</sup>C NMR (CDCl<sub>3</sub>, 125.76 MHz) δ 172.0 (C=O), 149.3 (C<sub>Ar</sub>), 148.0 (C<sub>Ar</sub>), 130.8 (C<sub>Ar</sub>), 130.0 (=C-), 129.7 (=C-),

127.1 (C<sub>Ar</sub>), 124.0 (C<sub>Ar</sub>), 119.8 (C<sub>Ar</sub>), 34.3 (CH<sub>2</sub>), 33.6 (CH), 31.9 (CH<sub>2</sub>), 29.8 (CH<sub>2</sub>), 29.7 (CH<sub>2</sub>), 29.5 (CH<sub>2</sub>), 29.3 (CH<sub>2</sub>), 29.2 (2 × CH<sub>2</sub>), 29.1 (CH<sub>2</sub>), 27.7 (CH<sub>2</sub>), 27.3 (CH<sub>2</sub>), 27.2 (CH<sub>2</sub>), 25.1 (CH<sub>2</sub>), 23.9 (2 × CH<sub>3</sub>), 22.7 (CH<sub>2</sub>), 15.8 (CH<sub>3</sub>-Ar), 14.1 (CH<sub>3</sub>); MS (EI): *m/z* (%) 414.40 (M<sup>+</sup>) 151 (12.3), 150 (100), 135 (26.4), 109 (6.1), 83 (4.4), 69 (8.0), 67 (6.3), 57 (4.9), 55 (17.3), 43 (6.1).

### 3. 2. 24. Carvacryl Benzoate (3x)<sup>22,23,30,54</sup>

Chromatographic purification gave amorphous white solid. Mp 31 °C. C<sub>17</sub>H<sub>18</sub>O<sub>2</sub> (*M* = 254.33); yield 95%; RI (HP5-MS): 1991; <sup>1</sup>H NMR (CDCl<sub>3</sub>, 500.13 MHz) δ 8.26 (d, *J* = 7.6 Hz, 2H, Ar-H), 7.68 (m, 1H, Ar-H), 7.56 (m, 2H, Ar-H), 7.23 (d, *J* = 8.0 Hz, 1H, Ar-H), 7.09 (d, *J* = 8.0 Hz, 1H, Ar-H), 7.04 (s, 1H, Ar-H), 2.94 (m, 1H, CH), 2.23 (s, 3H, CH<sub>3</sub>), 1.29 (d, *J* = 6.9 Hz, 6H, 2 × CH<sub>3</sub>). <sup>13</sup>C NMR (CDCl<sub>3</sub>, 125.76 MHz) δ 164.9 (C=O), 149.5 (C<sub>Ar</sub>), 148.2 (C<sub>Ar</sub>), 133.5 (C<sub>Ar</sub>), 130.9 (C<sub>Ar</sub>), 130.2 (2 × C<sub>Ar</sub>), 129.6 (C<sub>Ar</sub>), 129.1 (C<sub>Ar</sub>), 128.6 (2 × C<sub>Ar</sub>), 127.4 (C<sub>Ar</sub>), 124.2 (C<sub>Ar</sub>), 119.9 (C<sub>Ar</sub>), 33.6 (CH), 24.0 (2 × CH<sub>3</sub>), 15.9 (CH<sub>3</sub>-Ar); MS (EI): *m/z* (%): 254 (M<sup>+</sup>) (7.3), 106 (7.7), 105 (100), 91 (5.1), 79 (2.1), 78 (3.3), 77 (34.8), 65 (1.2), 51 (6.2), 50 (1.4).

### 3. 2. 25. Carvacryl 4-Methoxybenzoate (3y)<sup>23</sup>

Chromatographic purification gave amorphous white solid. Mp 31–32 °C. C<sub>17</sub>H<sub>18</sub>O<sub>2</sub> (*M* = 284.35); yield 95%; RI (HP5-MS): 2302; <sup>1</sup>H NMR (CDCl<sub>3</sub>, 500.13 MHz) δ 8.21 (d, *J* = 8.9 Hz, 2H, Ar-H), 7.21 (d, *J* = 7.8 Hz, 1H, Ar-H), 7.07 (d, *J* = 7.8 Hz, 1H, Ar-H), 7.03 (s, 1H, Ar-H), 7.01 (d, 2H, Ar-H), 3.93 (s, 3H, CH<sub>3</sub>), 3.51 (q, *J* = 7.0 Hz, 2H contamination EtOAc), 2.93 (m, 1H, CH), 2.21 (s, 3H, CH<sub>3</sub>), 1.29 (d, *J* = 6.9 Hz, 6H, 2 × CH<sub>3</sub>), 1.24 (t, *J* = 7.0 Hz, 3H contamination EtOAc); <sup>13</sup>C NMR (CDCl<sub>3</sub>, 125.76 MHz) δ 164.6 (C<sub>Ar</sub>-O), 163.8 (C=O), 149.6 (C<sub>Ar</sub>-OCO), 148.1 (C<sub>Ar</sub>), 132.2 (2 × C<sub>Ar</sub>), 130.9 (C<sub>Ar</sub>), 127.4 (C<sub>Ar</sub>), 124.0 (C<sub>Ar</sub>), 122.0 (C<sub>Ar</sub>), 120.0 (C<sub>Ar</sub>), 113.9 (2 × C<sub>Ar</sub>), 55.5 (C-O), 33.6 (CH), 23.9 (2 × CH<sub>3</sub>), 15.8 (CH<sub>3</sub>-Ar); MS (EI): *m/z* (%): 284 (M<sup>+</sup>) (2.6), 136 (8.7), 135 (100), 107 (6.2), 92 (9.0), 91 (3.8), 79 (2.0), 77 (147), 64 (3.4), 63 (2.0).

## 3. 3. Antimicrobial Activity

The antimicrobial activity was evaluated by determining the minimum inhibitory concentration (MIC) and the minimum microbicidal concentration, which includes minimum bactericidal (MBC) and minimum fungicidal concentrations (MFC), using the broth microdilution method. The obtained results are given in Table 2. The assayed samples were less effective than antibiotic/antimycotic used as reference standard, and if observed, activity was never greater than the values acquired for the parent compound **1** (MIC/MBC/MFC never exceeded 0.031 mg/mL). The panel of bacterial strains, represented by Gram-positive (*B. subtilis* and *S. aureus*) and Gram-nega-

tive (*E. coli*, *S. abony* and *S. typhimurium*) microorganisms, were completely resistant to the synthesized compounds at tested concentration (Table 2), except for compound **3b** that inhibited growth of *B. subtilis* and *S. aureus* at 0.5 and 1 mg/mL, respectively, and inhibited the growth/had cidal effect on *S. typhimurium* at concentrations comparable to **1** (0.50 / 0.25 mg/mL). On the other hand, an interesting experimental fact is that the representatives of the synthesized homologues, regardless of the nature of the R residue, have shown activity on fungal strain *Aspergillus niger* and on yeast *Candida albicans* (for MIC/MFC, see Table 2, entries **3a–y**), being antimicrobials comparable to carvacrol.

Compounds **3a,d,g,i,x** from our study are matching samples to those tested by Mathela and collaborators,<sup>30</sup> who were making evaluation of antibacterial activity on *Streptococcus mutans* (MTCC 890), *S. aureus* (MTCC 96), *B. subtilis* (MTCC 121), *S. epidermidis* (MTCC 435) and *E. coli* (MTCC 723) and also reported attenuation of the activity in comparison to **1**. Compound **3p** is identical to the sample tested by Bassanetti *et al.*<sup>34</sup> on *E. coli* (isolate and ATCC 25922), *S. typhimurium* (isolate and ATCC 23564), *S. enteritidis* (isolate and ATCC 49220) and *Clostridium perfringens* (isolate and ATCC 13124), with identical observations (regardless of the bacterial strain involved) related to attenuation of the synthetic compound activity in comparison to the parent compound **1**. None of two previous studies did include fungi/yeast strains in antimicrobial bioassays. Moreover, according to the authors' best knowledge and based on the literature search,<sup>55</sup> only one study assaying antifungal (*Botrytis cinerea*) and activity against yeast (*Saccharomyces cerevisiae*), involving only one of the prepared compounds (carvacryl acetate), exists.<sup>37</sup>

Veldhuizen *et al.*<sup>56</sup> comparing **1** with carvacrol-related compounds, indicated structural requirements in exerting antimicrobial activity against pathogenic bacteria such as *E. coli* and *S. aureus*. Further investigations emphasized the correlation between the free-hydroxyl group in the phenolic ring and the antimicrobial potency on ester derivatives obtained by replacing hydroxyl group with acyl moieties. Ultee *et al.*<sup>9</sup> suggested that the crucial role for efficacy of phenolic compounds (*e.g.* carvacrol) is attributed to the presence of OH functional group and to a system of delocalized electrons, allowing compounds to act as proton exchanger, thus reducing the gradient across the cytoplasmic membrane (resulting collapse of the proton-motive force and depletion of the ATP pool lead eventually to cell death, as reported by Ultee *et al.*<sup>9</sup>). The delocalized electron system present in carvacryl derivatives implies that they are proton acceptors, however unable to release a proton through the acyl group to act as a proton exchanger.<sup>37</sup> So far obtained data emphasized that the insertion of acyl groups in the carvacrol aromatic ring results in a weaker antibacterial activity,<sup>57</sup> which was also the result confirmed by Mathela *et al.*<sup>30</sup> and by our current study. However, this single structural modification of phe-

**Table 2.** The minimal inhibitory (MIC) and minimal bactericidal/fungicidal (MBC/MFC) concentrations of the carvacrol (1) and the synthesised 3a–y esters. The initial concentration of the derivatives applied in broth microdilution assay were 2 mg/mL.

Compound	Bacterial strains					Fungal strains	
	Gram-positive		Gram-negative			<i>A. niger</i>	<i>C. albicans</i>
	<i>B. subtilis</i>	<i>S. aureus</i>	<i>E. coli</i>	<i>S. abony</i>	<i>S. typhimurium</i>		
<b>1</b>	MIC = 0.25 MBC = 0.50	MIC = 0.25 MBC = 0.50	MIC = 0.25 MBC = 0.50	MIC = 0.50 MBC = 1.0	MIC = 0.25 MBC = 0.50	MIC = 0.031 MFC = 0.50	MIC = MFC = 0.125
<b>3a</b>	na	na	na	na	na	MIC = 0.25 MFC = 0.50	MIC = MFC = 0.50
<b>3b</b>	MIC = 0.50	MIC = 1.0	na	na	MIC = 0.25 MBC = 0.50	MIC = 0.25 MFC = 0.50	MIC = 0.125 MFC = 0.50
<b>3c</b>	na	na	na	na	na	MIC = 0.25 MFC = 0.50	MIC = 1.0
<b>3d</b>	na	na	na	na	na	MIC = 0.25 MFC = 0.50	MIC = 1.0
<b>3e</b>	na	na	na	na	na	MIC = MFC = 0.50	MIC = 1.0
<b>3f</b>	na	na	na	na	na	MIC = 0.25 MFC = 0.50	MIC = 1.0
<b>3g</b>	na	na	na	na	na	MIC = 0.25 MFC = 1.0	MIC = 1.0
<b>3h</b>	na	na	na	na	na	MIC = 0.25 MFC = 1.0	MIC = 1.0
<b>3i</b>	na	na	na	na	na	MIC = 0.25 MFC = 1.0	MIC = 0.25
<b>3j</b>	na	na	na	na	na	MIC = 0.50 MFC = 1.0	MIC = 0.50
<b>3k</b>	na	na	na	na	na	MIC = MFC = 1.0	MIC = 0.50 MFC = 1.0
<b>3l</b>	na	na	na	na	na	MIC = 0.25 MFC = 0.50	MIC = MFC = 1.0
<b>3m</b>	na	na	na	na	na	MIC = 0.50	MIC = 1.0
<b>3n</b>	na	na	na	na	na	MIC = 0.25 MFC = 0.50	MIC = 1.0
<b>3o</b>	na	na	na	na	na	MIC = 0.25 MFC = 0.50	MIC = 1.0
<b>3p</b>	na	na	na	na	na	MIC = 0.25 MFC = 0.50	MIC = 0.50
<b>3q</b>	na	na	na	na	na	MIC = MFC = 0.50	MIC = 0.50 MFC = 1.0
<b>3r</b>	na	na	na	na	na	MIC = MFC = 0.25	MIC = 1.0
<b>3s</b>	na	na	na	na	na	MIC = MFC = 0.25	MIC = 0.25 MFC = 1.0
<b>3t</b>	na	na	na	na	na	MIC = 0.25 MFC = 1.0	MIC = 0.25 MFC = 1.0
<b>3u</b>	na	na	na	na	na	MIC = 0.25 MFC = 0.50	MIC = 0.50
<b>3v</b>	na	na	na	na	na	MIC = 0.5	MIC = 0.5

Compound	Bacterial strains					Fungal strains	
	Gram-positive		Gram-negative			<i>A. niger</i>	<i>C. albicans</i>
	<i>B. subtilis</i>	<i>S. aureus</i>	<i>E. coli</i>	<i>S. abony</i>	<i>S. typhimurium</i>		
						MFC = 1.0	MFC = 1.0
<b>3w</b>	na	na	na	na	na	MIC = 0.5 MFC = 1.0	MIC = 0.5 MFC = 1.0
<b>3x</b>	na	na	na	na	na	MIC = 0.25 MFC = 0.50	MIC = 1.0
<b>3y</b>	na	na	na	na	na	MIC = 0.25 MFC = 0.50	MIC = 1. 0
Positive control (referent standard)							
Doxycycline ( $\mu\text{g/mL}$ )	MIC C = MB = 1.56	MIC = 6.25 MBC = 0.78	MIC = MBC = 0.78	MIC = MBC = 12.5	MIC = MBC = 6.25	nt	nt
Nystatin ( $\mu\text{g/mL}$ )	nt	nt	nt	nt	nt	MIC = MBC = 6.25	MIC = MBC = 0.78
Negative control (solvent used)							
DMSO 10% aqueous solution	na	na	na	na	na	na	na

“na” not active, “nt” not tested, “MIC” minimum inhibitory concentration as the lowest concentration of an antimicrobial agent (synthetic compound) needed to inhibit the visible in vitro growth of a challenge microorganism, “MBC” minimum bactericidal concentration and “MFC” minimum fungicidal concentration; concentrations were evaluated as the lowest concentration at which 99.9% of the inoculated microorganisms were killed.

nolic functionality seems to have different effect on fungi/yeasts (*A. niger* and *C. albicans*) compared to bacteria (Table 2, antibacterial vs. antifungal/anticandidal activity). Introducing an acyl group to the carvacrol results in increased lipophilicity of the synthesized compound (Table S1, see octanol–water partition coefficient calculation, represented as  $m_i\text{LogP}$ ). Except preserved *A. niger* antifungal potential, for which no remarkable oscillations in values were observed, no significant (balanced) correlations were detected between increased lipophilicity (the chain length) and the antifungal activity (MIC/MFC) among tested carvacryl ester derivatives. Slight (negligible) loss of anti-*A. niger* potential could be observed in those compounds where the parent phenolic (**1**) is substituted with butanoyl, 2-methylpropanoyl, pentanoyl, 3-methylbutanoyl, hexanoyl, octadecanoyl and oleoyl moieties (Table 2, entries **3g–k,v,w**). As for *C. albicans*, the strongest anticandidal activity, except for **1**, was observed for the introduced methanoyl and 2-chloromethanoyl moieties (Table 2, entries **3a,b**). There are no striking differences in anticandidal potential of the homologues higher than  $\text{C}_3$ , and from the Table 2 we can notice that there is anticandidal activity evidenced in all of the synthesized compounds (**3a–y**). Interestingly, Damiens *et al.*<sup>36</sup> have observed and stated the importance of (a balanced) hydrophilicity/lipophilicity ratio, though in sesamol derivatives, against a phyto-pathogen fungi *Zymoseptoria tritici* (modulating lipophilicity proved to increase the antifungal biological activity for sesamol derivatives). The phenomena noticed in our research and in Damiens *et al.*<sup>36</sup> does not

have to be an isolated incident, it could also be a regularity based on subtle structural changes that would, within certain limits, by enhancing lipophilicity affect bioactivity. It is certain that this aspect deserves further research.

It is interesting to recall and compare the results of the antimicrobial assay we have obtained for acylated thymol (positional isomer of carvacrol) derivatives.<sup>38</sup> Unlike esters of thymol, which effected only growth of *C. albicans*, carvacrol ester derivatives are strongly affecting growth of both, *A. niger* and *C. albicans*, with a more pronounced (cidal) effect on *A. niger*. The stronger effect is most probably related to the orientation/position of the groups in (acylated) positional isomer homologs, and this item could also be worth of further research.

### 3. 4. In Silico Study

#### 3. 4. 1. Physico-chemical Properties

Physico-chemical properties of the studied compounds predicted by the Molinspiration tool<sup>47</sup> are shown in Table S1. It can be seen that **1** and seven synthesized compounds (**3a,b,d,f,g,e,i**) fulfilled all Lipinski's and Veber's rules ( $m_i\text{LogP} \leq 5$ ,  $\text{TPSA} \leq 140 \text{ \AA}^2$ ,  $\text{nON} \leq 10$ ,  $\text{nOHNH} \leq 5$ ,  $\text{nroth} \leq 10$ ,  $M_r \leq 500$ ) indicating their good oral bioavailability *in vivo*. However, eight compounds (**3c,h,j–m,x,y**) were predicted with one deviation ( $m_i\text{LogP} > 5$ ), and ten compounds (**3n–w**) were predicted with two deviations ( $m_i\text{LogP} > 5$ ,  $\text{nroth} > 10$ ) from the Lipinski's and Veber's rules, indicating their poorer bioavailability.

### 3. 4. 2. Pharmacokinetic Properties

Absorption properties of the studied compounds predicted by admetSAR<sup>48</sup> are shown in Table S2. All compounds tested were predicted as compounds permeable across Caco-2 cells, capable of being absorbed by intestine, as well as compounds able to pass through blood-brain barrier and penetrate into the central nervous system. None of the tested compounds was predicted as a P-glycoprotein substrate, while a small number (**3r–w,y**) was predicted as a P-glycoprotein inhibitor.

Metabolic properties of the studied compounds predicted by admetSAR<sup>48</sup> are shown in Table S3. According to the results, the tested compounds differ from each other in their metabolic properties, depending on whether they are potential substrates and/or inhibitors of certain CYP450 isoenzymes. No compound was predicted as CYP450 3A4 substrate or CYP450 2D6/3A4 inhibitor. Only the parent compound **1** was predicted as CYP450 2C9/2D6 substrate. The only compound envisaged as CYP450 2C9 inhibitor is **3x**. Most compounds (19 of 25) are potential inhibitors of CYP450 2C19, and all are potential inhibitors of CYP450 1A2.

### 3. 4. 3. Toxicological Properties

Toxicological properties of the studied compounds predicted by DataWarrior<sup>49</sup> are shown in Table S4. It can be seen that most of the studied compounds were predicted as non-mutagenic, non-tumorigenic and non-reproductive effective (22, 21 and 22 out of 25 compounds, respectively). Compounds **3b,c,e** were predicted as highly mutagenic, compounds **3b** and **3c** and highly reproductive effective, while compounds **3b,e,j** were predicted as highly tumorigenic. All 25 compounds tested were predicted as highly irritant. The results obtained by predicting organ toxicity, organ system toxicity, genotoxicity and ecotoxicity of the studied compounds using admetSAR<sup>48</sup> are shown in Tables S5–S8.

Most of the studied compounds were predicted as potentially non-hepatotoxic, with no risk of eye corrosion or eye irritation, but with the possibility of human ether-à-go-go inhibition. According to the risk of acute oral toxicity, the studied compounds were predicted as category III, or slightly toxic compounds, with LD50 values of 500–5000 mg/kg. Only one compound (**3b**) was predicted as category II, or moderately toxic compound, with LD50 value of 50–500 mg/kg (Table S5).

The results obtained by predicting the compound ability to interact with the hormonal system showed that the studied compounds have low predispositions for estrogen receptor, aromatase and glucocorticoid receptor binding, slightly higher predispositions for thyroid receptor binding and high predispositions for peroxisome proliferator-activated receptor  $\gamma$  binding (Table S6).

Regarding genotoxicity, all of the studied compounds were predicted as non-genotoxic (Table S7), and regarding

ecotoxicity, all compounds tested were predicted as non-toxic to avian, but toxic to fish, honey bee and *Tetrahymena pyriformis*. More than a half were predicted as toxic to crustaceans. Finally, the majority was predicted as biodegradable compounds (Table S8).

Structural alerts for DNA and protein binding for the studied compounds, predicted by Toxtree,<sup>50</sup> are presented in Table S9. All of the compounds tested showed at least one structural alert for DNA or protein binding.

## 4. Conclusion

By chemical synthesis, we have obtained a series of 25 esters, among which 10 compounds are reported for the first time. All of the synthesized compounds were employed in antimicrobial bioassay, exhibiting the greatest activity on fungal strain *A. niger* and on yeast *C. albicans*, where was found that all could be antimicrobials, comparable to carvacrol, and can also be considered as activity holders. While the phenolic hydroxyl group of carvacrol is essential for action against bacteria, it seems that lipophilicity plays an important role in antifungal activity. The pronounced antimicrobial selectivity is certainly a subject deserving more thorough examination either through the mechanism of action or through a greater number of diverse compounds involved in establishing a detailed structure-activity correlation.

Based on our *in silico* study seven compounds (**1** and **3a,b,d,f,g,e,i**) fulfilled all Lipinski's and Veber's rules and were predicted to have good oral bioavailability. All compounds were recognized as compounds able to pass through blood-brain barrier, capable of being absorbed by intestine and permeable across Caco-2 cells. Metabolic properties differ within the studied compounds, depending on whether they act as substrates and/or inhibitors of various CYP450 enzymes. All compounds were predicted as non-genotoxic, and most were predicted as non-mutagenic, non-tumorigenic, non-reproductive effective and non-hepatotoxic. Regarding the risk of acute oral toxicity, they were predicted as slightly toxic compounds. However, some of the compounds showed predispositions to act as potential endocrine disruptors, and all of them showed at least one structural alert for DNA or protein binding.

Taking in consideration the overall results, carvacryl esters are another type of phenolics that, from the aspect of enhanced lipophilicity (improved membrane permeability), could be useful in fungal control.

## Acknowledgements

The work was funded by the Ministry of Science and Technological Development of Serbia (Projects 451-03-821/2012-14, 451-03-68/2022-14/200113 and 451-03-9/2022-14/200124).

## 5. References

1. T. Rodrigues, D. Reker, P. Schneider, G. Schneider, *Nat. Chem.* **2016**, 8, 531–541. DOI:10.1038/nchem.2479
2. S. Bernardini, A. Tiezzi, V. Laghezza Masci, E. Ovidi, *Nat. Prod. Res.* **2018**, 32, 1926–1950. DOI:10.1080/14786419.2017.1356838
3. A. G. Atanasov, S. B. Zotchev, V. M. Dirsch, *Nat. Rev. Drug Discov.* **2021**, 20, 200–216. DOI:10.1038/s41573-020-00114-z
4. K. H. C. Baser, *Curr. Pharm. Des.* **2008**, 14, 3106–3119. DOI:10.2174/138161208786404227
5. N. B. Rathod, P. Kulawik, F. Ozogul, J. M. Regenstien, Y. Ozogul, *Trends Food Sci. Tech.* **2021**, 116, 733–748. DOI:10.1016/j.tifs.2021.08.023
6. M. Sharifi-Rad, E. M. Varoni, M. Iriti, M. Martorell, W. N. Setzer, M. Del Mar Contreras, B. Salehi, A. Soltani-Nejad, S. Rajabi, M. Tajbakhsh, J. Sharifi-Rad, *Phytother. Res.* **2018**, 32, 1675–1687. DOI:10.1002/ptr.6103
7. Commission European (2012) COMMISSION IMPLEMENTING REGULATION (EU) No 872/2012 of 1 October 2012 adopting the list of flavouring substances provided for by regulation (EC) No 2232/96 of the European parliament and of the council, introducing it in Annex I to Regulation (EC) No 1334. Off J Eur Union L 267:161.
8. FDA (2017) CFR-Code of federal regulations title 21 FOOD AND DRUGS, volume 3 CITE: 21CFR172.515. CHAPTER I - FOOD AND DRUG ADMINISTRATION DEPARTMENT OF HEALTH AND HUMAN SERVICES SUBCHAPTER B - FOOD FOR HUMAN CONSUMPTION (CONTINUED) PART 172 - FOOD ADDITIVES PERMITTED FOR DIRECT ADDITION TO FOOD FOR HUMAN CONSUMPTION.
9. A. Ultee, M. H. J. Bennik, R. Moezelaar, *Appl. Environ. Microbiol.* **2002**, 68, 1561–1568. DOI:10.1128/AEM.68.4.1561-1568.2002
10. A. Ait-Ouazzou, L. Espina, T. K. Gelaw, S. de Lamo-Castellví, R. Pagán, D. García-Gonzalo, *J. Appl. Microbiol.* **2013**, 114, 173–185. DOI:10.1111/jam.12028
11. C. Niu, C. Wang, Y. Yang, R. Chen, J. Zhang, H. Chen, Y. Zhuge, J. Li, J. Cheng, K. Xu, M. Chu, C. Ren, C. Zhang, C. Jia, *Front. Cell. Infect. Microbiol.* **2020**, 10, 192. DOI:10.3389/fcimb.2020.00192
12. L. Marinelli, A. Di Stefano, I. Cacciatore, *Phytochem. Rev.* **2018**, 17, 903–921. DOI:10.1007/s11101-018-9569-x
13. P. F. Pinheiro, L. A. P. Menini, P. C. Bernardes, S. H. Saraiva, J. W. M. Carneiro, A. V. Costa AV, T. R. Arruda, M. R. Lage, P. M. Gonçalves, C. O. Bernardes, E. S. Alvarenga, L. Menini, *J. Agric. Food Chem.* **2018**, 66, 323–330. DOI:10.1021/acs.jafc.7b04418
14. J. U. Patil, K. C. Suryawanshi, P. B. Patil, S. R. Chaudhary, N. S. Pawar, *J. Asian Nat. Prod. Res.* **2010**, 12, 129–133. DOI:10.1080/10286020903455907
15. K. Wang, S. Jiang, Y. Yang, L. Fan, F. Su, M. Ye, *Nat. Prod. Res.* **2019**, 33, 1924–1930. DOI:10.1080/14786419.2018.1480618
16. S. R. B. Damasceno, F. R. A. M. Oliveira, N. S. Carvalho, C. F. C. Brito, I. S. Silva, F. B. M. Sousa, R. O. Silva, D. P. Sousa, A. L. R. Barbosa, R. M. Freitas, J.-V. R. Medeiros, *Life Sci.* **2014**, 94, 58–66. DOI:10.1016/j.lfs.2013.11.001
17. J. Mastelić, I. Jerković, I. Blazević, M. Poljak-Blazi, S. Borović, I. Ivancić-Baće, V. Smrecki, N. Zarković, K. Brcić-Kostić, D. Vikić-Topić, N. Müller, *J. Agric. Food Chem.* **2008**, 56, 3989–3996. DOI:10.1021/jf073272v
18. E. M. Alvarenga, N. A. Sousa, S. de Araújo, J. L. P. Júnior, A. R. Araújo, B. Iles, D. M. Pacífico, G. A. C. Brito, E. P. Souza, D. P. Sousa, J. V. R. Medeiros, *J. Pharm. Pharmacol.* **2017**, 69, 1773–1785. DOI:10.1111/jphp.12818
19. J. D. Rajput, S. D. Bagul, R. M. Bendre, *Res. Chem. Intermed.* **2017a**, 43, 4893–4906. DOI:10.1007/s11164-017-2919-2
20. J. D. Rajput, S. D. Bagul, A. A. Hosamani, M. M. Patil, R. S. Bendre, *Res. Chem. Intermed.* **2017b**, 43, 5377–5393. DOI:10.1007/s11164-017-2933-4
21. M. M. de Souza, M. C. Andreolla, T. C. Ribeiro, A. E. Gonçalves, A. R. Medeiros, A. S. de Souza, L. L. G. Ferreira, A. D. Andricopulo, R. A. Yunesco, A. S. de Oliveira, *RSC Med. Chem.* **2020**, 11, 307–316. DOI:10.1039/D0MD00009D
22. V. B. Silva, D. L. Travassos, A. Nepel, A. Barison, E. V. Costa, L. Scotti, M. T. Scotti, F. J. B. Mendonça-Junior, R. La Corte Dos Santos, S. C. de Holanda Cavalcanti, *J. Arthropod. Borne Dis.* **2017**, 11, 315–330.
23. B. M. de Mesquita, P. G. G. do Nascimento, L. G. S. Souza, I. F. de Farias, R. A. C. da Silva, T. L. G. de Lemos, F. J. Q. Monte, M. T. S. Trevisan, H. C. da Silva, G. M. P. Santiago, *Quím. Nova.* **2018**, 41, 412–416. DOI:10.21577/0100-4042.20170189
24. W. P. P. Andre, W. L. C. Ribeiro, G. S. Cavalcante, J. M. L. dos Santos, I. T. F. Macedo, H. C. B. de Paula, R. M. de Freitas, S. M. de Moraes, J. V. de Melo, C. M. L. Bevilacqua, *Vet. Parasitol.* **2016**, 218, 52–58. DOI:10.1016/j.vetpar.2016.01.001
25. W. P. P. André, J. R. de Paiva Junior, G. S. Cavalcante, W. L. C. Ribeiro, J. V. de Araújo Filho, J. M. L. dos Santos, A. P. N. N. Alves, J. P. Monteiro, S. M. de Moraes, I. N. G. da Silva, L. M. B. de Oliveira, F. O. M. da Silva Abreu, C. M. L. Bevilacqua, *Rev. Bras. Parasitol. Vet.* **2020**, 29, e013119. DOI:10.1590/s1984-29612019098
26. B. Z. Kurt, I. Gazioglu, A. Dag, R. E. Salmas, G. Kayık, S. Durdagi, F. Sonmez, *Bioorg. Med. Chem.* **2017**, 25, 1352–1363. DOI:10.1016/j.bmc.2016.12.037
27. Z. Ashraf, M. Rafiq, H. Nadeem, M. Hassan, S. Afzal, M. Wa-seem, K. Afzal, J. Latip, *PLoS One* **2017**, 12, e0178069. DOI:10.1371/journal.pone.0178069
28. R. Alokam, V. U. Jeankumar, J. Padma Sridevi, S. Sai Matikonda, S. Peddi, M. Alvala, P. Yogeewari, D. Sriram, *J. Enzyme Inhib. Med. Chem.* **2014**, 29, 547–554. DOI:10.3109/14756366.2013.823958
29. V. P. Nikumbh, V. S. Tare, P. P. Mahulikar, *JSIR* **2003**, 62, 1086–1089. DOI:10.1093/jnen/62.10.1086
30. C. S. Mathela, K. K. Singh, V. K. Gupta, *Acta Pol. Pharm.* **2010**, 67, 375–380.
31. L. F. Pires, L. M. Costa, O. A. Silva, A. A. de Almeida, G. S. Cerqueira, D. P. de Sousa, R. M. de Freitas, *Pharmacol. Biochem. Behav.* **2013**, 112, 42–48. DOI:10.1016/j.pbb.2013.09.001
32. M. T. de Santana, V. B. Silva, R. G. de Brito, dos Santos PL, S.



- C. de Holanda Cavalcanti, E. O. Barreto, J. N. de Souza Ferro, M. R. V. dos Santos, A. A. de Sousa Araújo, L. J. Quintans-Júnior, *Inflammation* **2014**, 37, 1575–1587. DOI:10.1007/s10753-014-9884-3
33. L. F. Pires, L. M. Costa, A. A. de Almeida, O. A. Silva, G. Santos Cerqueira, D. P. de Sousa, R. M. Pires, P. Satyal, R. M. de Freitas, *Chem.-Biol. Interact.* **2015**, 226, 49–57. DOI:10.1016/j.cbi.2014.12.001
34. I. Bassanetti, M. Carcelli, A. Buschini, S. Montalbano, G. Leonardi, P. Pelagatti, G. Tosi, P. Massi, L. Fiorentini, D. Rogolino, *Food Cont.* **2017**, 73, 606–612. DOI:10.1016/j.foodcont.2016.09.010
35. Y. Song, L. B. Wang, Y. Bei, D.-X. Qin, L.-Y. Ai, Q.-Z. Maa, P.-Y. Lina, *Food Funct.* **2020**, 11, 1754–1763. DOI:10.1039/C9FO02037C
36. A. Damiens, M. T. Alebrahim, E. Léonard, A. Fayeulle, C. Furman, J.-L. Hilbert, A. Siah, M. Billamboz, *Pest. Manag. Sci.* **2021**, 77, 2403–2414. DOI:10.1002/ps.6269
37. A. Ben Arfa, S. Combes, L. Preziosi-Belloy, N. Gontard, P. Chalier, *Lett. Appl. Microbiol.* **2006**, 43, 149–154. DOI:10.1111/j.1472-765X.2006.01938.x
38. J. Lazarević, A. Kolarević, A. Đorđević, G. Stojanović, A. Šmelcerović, P. Ciuffreda, E. Santaniello, *Acta Chim. Slov.* **2017**, 64, 603–612. DOI:10.17344/acsi.2017.3356
39. J. Lazarević, A. Kolarević, G. Stojanović, A. Šmelcerović, P. Ciuffreda, E. Santaniello, *Acta Chim. Slov.* **2018**, 65, 801–810. DOI:10.17344/acsi.2018.4380
40. H. C. Brown, *J. Am. Chem. Soc.* **1938**, 60, 1325–1328. DOI:10.1021/jo701630a
41. W. G. Rose, *J. Am. Chem. Soc.* **1947**, 69, 1384–1387. DOI:10.1021/ja01198a043
42. J. Paolini, A. Muselli, A. F. Bernardini, A. Bighelli, J. Casanova, J. Costa, *Flavour Fragr. J.* **2007**, 22, 479–487. DOI:10.1016/j.chroma.2005.03.131
43. H. Van den Dool, P. D. Kratz, *J. Chromatogr. A* **1963**, 11, 463–471. DOI:10.1016/S0021-9673(01)80947-X
44. NCCLS, Performance Standards for Antimicrobial Susceptibility Testing: Eleventh Informational Supplement, M100-S11. **2003**, National Committee for Clinical Laboratory Standards, Wayne, PA.
45. S. A. Sarker, L. Nahar, Y. Kumarasamy, *Methods* **2007**, 42, 321–324. DOI:10.1016/j.ymeth.2007.01.006
46. J. Lazarević, A. Đorđević, D. Kitić, B. Zlatković, G. Stojanović, *Chem. Biodivers.* **2013**, 10, 1335–1349. DOI:10.1002/cbdv.201200332
47. Molinspiration Cheminformatics, www.molinspiration.com; Accessed May 2020.
48. admetSAR, http://lmmd.ecust.edu.cn/admetSar2; Accessed June 2020.
49. DataWarrior, www.openmolecules.org/datawarrior; Accessed May 2020.
50. ToxTree, v.2.6.13; Accessed May 2020.
51. P. J. Rice, J. R. Coats, *J. Econ. Entomol.* **1994**, 87, 1172–1179. DOI:10.1093/jee/87.5.1172
52. A. B. Sen, S. S. Parmar, *J. Indian Chem. Soc.* **1953**, 30, 61–63.
53. F. J. Xavier, K. A. Rodrigues, R. G. de Oliveira, C. G. Lima Junior, J. da Câmara Rocha, T. S. L. Keesen, M. R. de Oliveira, F. P. L. Silva, M. L. A. de Almeida Vasconcellos, *Molecules* **2016**, 21, 1483. DOI:10.3390/molecules21111483
54. M. A. M. Mansilla, C. A. R. Vasquez, K. S. Rikardsen, K. Fyrand, B. Wrege, B. O. Hjelstuen, Anti-sea lice compositions and their use, WO2012/001668, PTC/IB2011/052922.
55. SciFinder. Chemical Abstracts Service, n.d. https://scifinder.cas.org; Accessed December 12, 2021.
56. E. J. A. Veldhuizen, J. L. M. Tjeerdsmā-Van Bokhoven, C. Zweijter, S. A. Burt, H. P. Haagsman, *J. Agric. Food Chem.* **2006**, 54, 1874–1879. DOI:10.1021/jf052564y
57. A. Marchese, C. R. Arciola, E. Coppo, R. Barbieri, D. Barreca, S. Chebaibi, E. Sobarzo-Sánchez, S. F. Nabavi, S. M. Nabavi, M. Daglia, *Biofouling*. **2018**, 34, 630–656. DOI:10.1080/08927014.2018.1480756

## Povzetek

Iz literature so poznane kemijske modifikacije naravnih monoterpenoidov v različne derivate, kar lahko okrepi njihove biološke aktivnosti v primerjavi z matičnimi spojinami. Skladno s tem smo karvakrol, znan biocid in dodatek k hrani, uporabili kot ogrodje za uvedbo acilne skupine na prvotno fenolno skupino. S to enostavno metodologijo smo pripravili majhno serijo 25 estrov. Za vsako pripravljeno spojino smo izvedli strukturno karakterizacijo, določili *in vitro* antimikrobno učinkovitost ter *in silico* izračunali nekatere fizikalnokemijske, farmakokinetične ter toksikološke lastnosti. Čeprav obstajajo mnogi podatki o sintezah in bioaktivnostih nižjih karvakrolnih estrskih homologov, so podatki o estrih z daljšimi karboksilnimi kislinami (več kot C<sub>9</sub>), zelo redki; izmed 25 spojin jih je kar 10 opisanih prvič (spektroskopske karakterizacije pa so prvič opisane za 12 spojin). Naša raziskava predstavlja prvo podrobno študijo karvakrolnih estrov kot učinkovin proti glivam ter prvo, kjer so karvakrolni estri, sestavljeni iz srednjedolgih ali dolgih verig maščobnih kislin, izkazovali antibakterijske aktivnosti. Zanimivo je, da vse pripravljene spojine, ne glede na naravo ostanka R, izkazujejo aktivnost proti glivi *Aspergillus niger* ter proti kvasovki *Candida albicans*, ki je primerljiva z aktivnostjo karvakrola. Poleg predstavljenih eksperimentalnih podatkov, je tudi uporaba *in silico* računskih metod za določanje fizikalnokemijskih, farmakokinetičnih ter toksikoloških lastnosti pripravljenih spojin, pomembna informacija za nadaljnje raziskave.



Except when otherwise noted, articles in this journal are published under the terms and conditions of the Creative Commons Attribution 4.0 International License

Scientific paper

# ***N*-(9,10-Dioxo-9,10-dihydroanthracen-1(2)-yl)-2-(*R*-thio) Acetamides: Synthesis, Antioxidant and Antiplatelet Activity**

Maryna Stasevych,<sup>1,\*</sup> Viktor Zvarych,<sup>1</sup> Olena Yaremkevych,<sup>1</sup> Mykhaylo Vovk,<sup>2</sup>  
Alla Vaskevych,<sup>2</sup> Tetiana Halenova<sup>3</sup> and Olexii Savchuk<sup>3</sup>

<sup>1</sup> Department of Technology of Biologically Active Substances, Pharmacy, and Biotechnology,  
Lviv Polytechnic National University, 79013 Lviv, Ukraine

<sup>2</sup> Department of Chemistry of Functional Heterocyclic Systems, Institute of Organic Chemistry of National Academy  
of Sciences of Ukraine, 02660 Kyiv, Ukraine

<sup>3</sup> Educational and Scientific Center “Institute of Biology and Medicine”, Taras Shevchenko National University of Kyiv,  
01601 Kyiv, Ukraine

\* Corresponding author: E-mail: maryna.v.stasevych@lpnu.ua

Received: 03-11-2022

## **Abstract**

The synthesis of new *N*-(9,10-dioxo-9,10-dihydroanthracen-1(2)-yl)-2-(*R*-thio) acetamides was carried out using reaction of 2-chloro-*N*-(9,10-dioxo-9,10-dihydroanthracen-1(2)-yl)acetamides with functionalized thiols in the presence of potassium carbonate in *N,N*-dimethylformamide (DMF) at room temperature. Evaluation of the synthesized compounds on such indicators of radical scavenging activity as lipid peroxidation (LP) and oxidative modification of proteins (OMP) *in vitro* in rat liver homogenate was carried out. It was determined that the compounds with a substituent in the first position of anthracenedione core showed better antioxidant properties than their isomers with a substituent in the second position. The compounds **6** and **7** with the best indicators of radical-scavenging activity were determined. Antioxidant effect in OMP processes was also determined for compound **10**. The antiplatelet activity study *in vitro* revealed compound **10** with the inhibited effect of ADP-induced aggregation.

**Keywords:** *N*-(9,10-dioxo-9,10-dihydroanthracen-1(2)-yl)-2-(*R*-thio) acetamides; free-radical oxidation markers; antioxidant activity; antiplatelet activity; structure-activity relationship

## **1. Introduction**

Arterial thrombosis is one of the critical factors determining the outcome of cardiovascular and oncological diseases,<sup>1–4</sup> which share the first place among all diseases, both in Ukraine and in the world.<sup>5</sup> They cause sudden death in myocardial infarction, vascular complications of diabetes mellitus, cancer chemotherapy.<sup>6</sup> Also, it lowers the effectiveness of surgical treatment of coronary artery disease, etc. There are several mechanisms of thrombosis formation:<sup>7–9</sup> the activation of platelet and coagulation chains of homeostasis, disruption of synthesis for some blood coagulation factors II (Prothrombin), VII (Proconvertin), IX (Christmas factor), and X (Stuart–Prower factor), a decrease of fibrinolytic activity of blood, activation of lipid

peroxidation, disruption of endothelium functional activity, etc.<sup>10</sup> Modern antiplatelet and anticoagulant drugs influence the thrombocyte aggregation and blood coagulation system. However, their effectiveness often does not satisfy clinicians. Numerous clinical studies show that the use of modern antiplatelet drugs is often accompanied by such side effects as resistance to their action, an increased risk of uncontrolled bleeding, as well as the development of serious systemic complications.<sup>11</sup> The high cost and the listed side effects of these drugs indicate the need for further research in the pursue for new, more effective, and safe substances and the development of antiplatelet drugs based on them.

In recent years, the important role of lipid peroxidation in the pathogenesis of thrombus formation has

been shown. The influence of free radical mechanisms on the development of various types of cancer, atherosclerosis and its thrombotic consequences (heart attack, stroke), diabetes mellitus, chronic nonspecific lung diseases, diseases of the reproductive system, as well as radiation injury, hepatitis, decreased cellular and humoral immunity, etc. has been studied.<sup>12–14</sup> Therefore, there has been a constant search for antioxidants, both natural and synthetic.<sup>15–16</sup>

The quinoid system is the structural block of many natural biologically active molecules, such as vitamins K and E, as well as compounds directly involved in oxidative metabolism, such as coenzyme Q10. Many antioxidants contained in food products are quinones (for example, flavonoids). The derivatives from quercetin (contained in vegetables and fruits), resveratrol (red vine), catechins and epicatechin (chocolate and tea) and also compounds obtained from tyrosine and tryptophan aminoacids (hydroxytyrosol, 5-hydroxytryptophan and pyrroloquinoline quinone) are considered to be quinone compounds.<sup>17</sup> The main advantage of quinones is their aromatic nature, which implies the stability necessary for functioning in an oxidative environment and actively participating in redox reactions.<sup>18</sup>

Many natural anthracenediones extracted from plants demonstrate antioxidant properties.<sup>19–21</sup> Among the synthetic derivatives of 9,10-anthracenedione were discovered compounds with antioxidant properties<sup>22–24</sup> and oxidative stress and cytotoxicity ability.<sup>25</sup> It was demonstrated that the amount and position of substituents in the anthracenedione's ring influence antioxidant properties.<sup>26–28</sup> The scientists<sup>29,30</sup> discovered some compounds among anthracenedione derivatives with antiplatelet and anticoagulant action. Dutch scientists obtained 1,4- and 1,8-derivatives of 9,10-anthracenedione included in oligodeoxynucleotides to investigate the influence on coagulation time of fibrinogen in the blood. The investigation showed better anticoagulation properties for 1,8-anthracenedione products.<sup>31</sup> Some sulfur-containing derivatives of 9,10-anthracenedione demonstrated high antioxidant activity.<sup>32</sup> There are studies dedicated to researching antithrombotic drugs in Ukraine as well.<sup>33,34</sup>

Therefore, the purpose of the present work is to carry out the synthesis of new derivatives of 2-chloro-*N*-(9,10-dioxo-9,10-dihydroanthracen-1(2)-yl)-acetamides using functionalization by thio fragments and *in vitro* study of obtained derivatives for antioxidant and antiplatelet effects.

## 2. Experimental

### 2.1. Chemistry

Melting points were measured in open to air-glass capillaries using a Büchi B-540 melting point apparatus and are uncorrected. Elemental analysis was performed

on Perkin–Elmer 2400 CHN-analyzer, and the results were found to be in good agreement with the calculated values. <sup>1</sup>H and <sup>13</sup>C NMR spectra in DMSO-*d*<sub>6</sub> were recorded on Varian Mercury-400 spectrometer with TMS as an internal standard. Mass spectra were recorded on Agilent 1100 Series G1956B LC/MSD SL LCMS system (Zorbax SBC18 column, 4.6×15 mm, 1.8 μm (PN 82(c) 75-932); solvent dimethylsulfoxide), using electrospray ionization at atmospheric pressure (70 eV). Infrared spectra were recorded on a Perkin–Elmer Spectrum Two FT-IR Spectrometer equipped with an UATR (HR Single-Reflection with a diamond sensor) using Perkin–Elmer Spectrum 10 Spectroscopy Software with an ATR absorbance correction for Spectrum Two UATR spectra. All chemicals were of reagent grade and used without further purification. The solvents were purified according to the standard procedures.<sup>35</sup>

2-Chloro-*N*-(9,10-dioxo-9,10-dihydroanthracen-1(2)-yl)-acetamides **1** and **2** were obtained by published methods.<sup>36,37</sup>

### General Procedure for the Preparation of *N*-(9,10-Dioxo-9,10-dihydroanthracen-1(2)-yl)-2-(*R*-thio) Acetamides **3–20**

To 0.5 g (1.668 mmol) of chloroacetamide **1** or **2** in 40 mL of DMF, 1.835 mmol of the corresponding thiol and 0.507 g (3.67 mmol) of potassium carbonate were added under stirring. The reaction mixture was kept under stirring and at room temperature for 12 hours. Then, the reaction mixture was poured into 200 mL of water, acidified with 10% HCl solution to pH 6, and left overnight. The mixture was filtered off. The precipitate was washed with 20 mL of cold water and dried. As a result, target sulfide derivatives **3–20** were obtained with 60–93% yields.

**2-((2-((9,10-Dioxo-9,10-dihydroanthracen-1-yl)amino)-2-oxoethyl)thio)acetic Acid (3).** Yield 0.551 g (93%), mp 217 °C dec. FT-IR (UATR diamond)  $\nu_{\max}$  3196.07, 2928.41, 1751.23, 1670.84, 1652.32, 1590.18, 1517.03, 1420.10, 1345.29, 1281.09, 1169.65, 1021.33, 801.68, 705.48 cm<sup>-1</sup>. <sup>1</sup>H NMR (400 MHz, DMSO-*d*<sub>6</sub>)  $\delta$  12.70 (br. s, 1H, OH), 12.43 (s, 1H, NH), 8.88 (d, *J* = 7.7 Hz, 1H<sub>Ar</sub>), 8.08 (dd, *J* = 23.9, 6.1 Hz, 2H<sub>Ar</sub>), 7.84 (d, *J* = 10.0 Hz, 3H<sub>Ar</sub>), 7.79 (d, *J* = 7.4 Hz, 1H<sub>Ar</sub>), 3.67 (s, 2H, CH<sub>2</sub>), 3.46 (s, 2H, CH<sub>2</sub>). <sup>13</sup>C NMR (100 MHz, DMSO-*d*<sub>6</sub>)  $\delta$  186.45, 182.35, 171.26, 169.08 (C=O), 141.28, 135.97, 135.10, 135.02, 134.01, 133.87, 132.48, 127.40, 126.79, 125.83, 122.41, 118.29 (C<sub>Ar</sub>), 37.65, 34.35 (CH<sub>2</sub>). LC-MS, *m/z* (*I*<sub>rel</sub>): 356 (M+H, 100). Anal. Calcd for C<sub>18</sub>H<sub>13</sub>NO<sub>5</sub>S: C, 60.84; H, 3.69; N, 3.94; S, 9.02. Found: C, 60.77; H, 3.60; N, 3.88; S, 9.12.

**Methyl 2-((2-((9,10-Dioxo-9,10-dihydroanthracen-1-yl)amino)-2-oxoethyl)thio)acetate (4).** Yield 0.554 g (90%), mp 120 °C dec. FT-IR (UATR diamond)  $\nu_{\max}$  3193.96, 2955.61, 1754.54, 1695.98, 1652.48, 1594.73, 1516.00, 1411.04, 1340.64, 1280.24, 709.26 cm<sup>-1</sup>. <sup>1</sup>H NMR

(400 MHz, DMSO- $d_6$ )  $\delta$  12.41 (br. s, 1H, NH), 8.87 (d,  $J = 7.7$  Hz, 1H<sub>Ar</sub>), 8.07 (dd,  $J = 22.8, 6.6$  Hz, 2H<sub>Ar</sub>), 7.82 (dd,  $J = 18.2, 7.6$  Hz, 4H<sub>Ar</sub>), 3.68 (s, 2H, CH<sub>2</sub>), 3.59 (s, 3H, CH<sub>3</sub>), 3.56 (s, 2H, CH<sub>2</sub>). <sup>13</sup>C NMR (100 MHz, DMSO- $d_6$ )  $\delta$  186.48, 182.32, 170.40, 168.96 (C=O), 141.26, 136.01, 135.11, 135.04, 134.03, 133.85, 132.50, 127.37, 126.81, 125.77, 122.44, 118.24 (C<sub>Ar</sub>), 52.55 (CH<sub>3</sub>), 37.78, 33.84 (CH<sub>2</sub>). LC-MS,  $m/z$  ( $I_{rel}$ ): 370 (M+H, 100). Anal. Calcd for C<sub>19</sub>H<sub>15</sub>NO<sub>5</sub>S: C, 61.78; H, 4.09; N, 3.79; S, 8.68. Found: C, 61.69; H, 4.20; N, 3.60; S, 8.77.

**2-((2-((9,10-Dioxo-9,10-dihydroanthracen-1-yl)amino)-2-oxoethyl)thio)propanoic Acid (5).** Yield 0.566 g (92%), mp 182 °C dec. FT-IR (UATR diamond)  $\nu_{max}$  3135.98, 2985.20, 2933.81, 1749.97, 1673.73, 1652.70, 1593.52, 1520.90, 1283.63 cm<sup>-1</sup>. <sup>1</sup>H NMR (400 MHz, DMSO- $d_6$ )  $\delta$  12.94 (br. s, 1H, OH), 12.46 (s, 1H, NH), 8.84 (d,  $J = 7.3$  Hz, 1H<sub>Ar</sub>), 8.04 (d,  $J = 6.5$  Hz, 1H<sub>Ar</sub>), 7.98 (d,  $J = 6.7$  Hz, 1H<sub>Ar</sub>), 7.85–7.79 (m, 2H<sub>Ar</sub>), 7.74 (q,  $J = 7.5, 7.0$  Hz, 2H<sub>Ar</sub>), 3.73–3.63 (m, 2H, CH<sub>2</sub>), 3.57 (q,  $J = 6.7$  Hz, 1H, CH), 1.41 (d,  $J = 6.9$  Hz, 3H, CH<sub>3</sub>). <sup>13</sup>C NMR (100 MHz, DMSO- $d_6$ )  $\delta$  186.29, 182.20, 173.84, 169.06 (C=O), 141.16, 135.90, 135.03, 134.95, 133.88, 133.74, 132.34, 127.32, 126.72, 125.70, 122.36, 118.14 (C<sub>Ar</sub>), 41.62 (CH), 36.88 (CH<sub>2</sub>), 17.38 (CH<sub>3</sub>). LC-MS,  $m/z$  ( $I_{rel}$ ): 370 (M+H, 100). Anal. Calcd for C<sub>19</sub>H<sub>15</sub>NO<sub>5</sub>S: C, 61.78; H, 4.09; N, 3.79; S, 8.68. Found: C, 61.71; H, 4.22; N, 3.63; S, 8.81.

**3-((2-((9,10-Dioxo-9,10-dihydroanthracen-1-yl)amino)-2-oxoethyl)thio)propanoic Acid (6).** Yield 0.443 g (72%), mp 227 °C dec. FT-IR (UATR diamond)  $\nu_{max}$  3183.89, 1739.22, 1679.84, 1655.50, 1594.52, 1521.37, 1339.16, 1282.47, 709.32 cm<sup>-1</sup>. <sup>1</sup>H NMR (400 MHz, DMSO- $d_6$ )  $\delta$  13.18 (br. s, 1H, OH), 12.46 (s, 1H, NH), 8.87 (d,  $J = 7.8$  Hz, 1H), 8.08 (d,  $J = 6.8$  Hz, 1H), 8.02 (d,  $J = 7.4$  Hz, 1H<sub>Ar</sub>), 7.84 (q,  $J = 6.5, 4.0$  Hz, 2H<sub>Ar</sub>), 7.78 (q,  $J = 8.5$  Hz, 2H<sub>Ar</sub>), 3.59 (s, 2H, CH<sub>2</sub>), 2.84 (t,  $J = 7.1$  Hz, 2H, CH<sub>2</sub>), 2.62 (t,  $J = 7.1$  Hz, 2H, CH<sub>2</sub>). <sup>13</sup>C NMR (100 MHz, DMSO- $d_6$ )  $\delta$  186.39, 182.27, 173.27, 169.69 (C=O), 141.25, 135.95, 135.05, 134.97, 133.97, 133.81, 132.42, 127.37, 126.74, 125.67, 122.37, 118.17 (C<sub>Ar</sub>), 37.43, 34.43, 27.86 (CH<sub>2</sub>). LC-MS,  $m/z$  ( $I_{rel}$ ): 370 (M+H, 100). Anal. Calcd for C<sub>19</sub>H<sub>15</sub>NO<sub>5</sub>S: C, 61.78; H, 4.09; N, 3.79; S, 8.68. Found: C, 61.75; H, 4.01; N, 3.72; S, 8.77.

**2-((2-((9,10-Dioxo-9,10-dihydroanthracen-1-yl)amino)-2-oxoethyl)thio)succinic Acid (7).** Yield 0.613 g (89%), mp 167 °C dec. FT-IR (UATR diamond)  $\nu_{max}$  3193.78, 3014.84, 1992.55, 1739.80, 1677.70, 1654.32, 1593.35, 1575.24, 1281.58, 1242.10, 708.99 cm<sup>-1</sup>. <sup>1</sup>H NMR (400 MHz, DMSO- $d_6$ )  $\delta$  12.72 (br. s, 1H, OH), 12.57 (br. s, 1H, OH), 12.45 (s, 1H, NH), 8.87 (d,  $J = 7.9$  Hz, 1H<sub>Ar</sub>), 8.06 (dd,  $J = 23.3, 7.8$  Hz, 2H<sub>Ar</sub>), 7.93 (s, 1H<sub>Ar</sub>), 7.86–7.78 (m, 3H<sub>Ar</sub>), 3.76 (d,  $J = 3.8$  Hz, 2H, CH<sub>2</sub>), 3.70 (dd,  $J = 10.2, 5.1$  Hz, 1H, CH), 2.85–2.76 (m, 2H, CH<sub>2</sub>). <sup>13</sup>C NMR (100 MHz, DMSO- $d_6$ )  $\delta$  186.38, 182.30, 172.64, 172.15, 168.84

(C=O), 141.16, 135.94, 135.07, 135.00, 133.98, 133.85, 132.43, 127.37, 126.76, 125.84, 122.44, 118.32 (C<sub>Ar</sub>), 42.19 (CH), 36.97, 36.23 (CH<sub>2</sub>). LC-MS,  $m/z$  ( $I_{rel}$ ): 414 (M+H, 100). Anal. Calcd for C<sub>20</sub>H<sub>15</sub>NO<sub>7</sub>S: C, 58.11; H, 3.66; N, 3.39; S, 7.76. Found: C, 58.16; H, 3.76; N, 3.48; S, 7.65.

**2-((2-((9,10-Dioxo-9,10-dihydroanthracen-1-yl)amino)-2-oxoethyl)thio)benzoic Acid (8).** Yield 0.64 g (92%), mp 250–252 °C dec. FT-IR (UATR diamond)  $\nu_{max}$  3254.37, 1711.64, 1675.22, 1646.37, 1593.72, 1540.41, 1339.99, 1276.95 cm<sup>-1</sup>. <sup>1</sup>H NMR (400 MHz, DMSO- $d_6$ )  $\delta$  13.18 (br. s, 1H, OH), 12.62 (s, 1H, NH), 8.92 (d,  $J = 8.1$  Hz, 1H<sub>Ar</sub>), 8.15 (d,  $J = 7.5$  Hz, 1H<sub>Ar</sub>), 8.11 (d,  $J = 6.5$  Hz, 1H<sub>Ar</sub>), 7.93–7.87 (m, 4H<sub>Ar</sub>), 7.84 (t,  $J = 8.0$  Hz, 1H<sub>Ar</sub>), 7.50 (t,  $J = 7.6$  Hz, 1H<sub>Ar</sub>), 7.43 (d,  $J = 7.7$  Hz, 1H<sub>Ar</sub>), 7.20 (t,  $J = 7.5$  Hz, 1H<sub>Ar</sub>), 4.16 (m, 2H, CH<sub>2</sub>). <sup>13</sup>C NMR (100 MHz, DMSO- $d_6$ )  $\delta$  186.46, 182.48, 169.09, 167.90 (C=O), 141.05, 139.90, 136.05, 135.09, 134.24, 133.99, 132.97, 132.63, 131.51, 129.03, 127.42, 126.84, 125.84, 125.04, 122.57, 118.52 (C<sub>Ar</sub>), 37.59 (CH<sub>2</sub>). LC-MS,  $m/z$  ( $I_{rel}$ ): 418 (M+H, 100). Anal. Calcd for C<sub>23</sub>H<sub>15</sub>NO<sub>5</sub>S: C, 66.18; H, 3.62; N, 3.36; S, 7.68. Found: C, 66.05; H, 3.65; N, 3.44; S, 7.84.

**2-((2-((9,10-Dioxo-9,10-dihydroanthracen-1-yl)amino)-2-oxoethyl)thio)nicotinic Acid (9).** Yield 0.635 g (91%), mp 192 °C dec. FT-IR (UATR diamond)  $\nu_{max}$  3492.52, 3217.87, 3085.59, 2926.78, 1698.96, 1672.50, 1643.98, 1581.67, 1558.28, 1519.99, 1466.38, 1411.38, 1338.67, 1313.37, 1274.00, 1246.80, 1236.69, 1157.46, 1068.96, 708.93 cm<sup>-1</sup>. <sup>1</sup>H NMR (400 MHz, DMSO- $d_6$ )  $\delta$  13.57 (br. s, 1H, OH), 12.44 (s, 1H, NH), 8.86 (d,  $J = 5.4$  Hz, 1H<sub>Ar</sub>), 8.60 (d,  $J = 3.1$  Hz, 1H<sub>Ar</sub>), 8.24 (d,  $J = 5.9$  Hz, 1H<sub>Ar</sub>), 8.02 (t,  $J = 9.2$  Hz, 2H<sub>Ar</sub>), 7.96–7.91 (m, 1H<sub>Ar</sub>), 7.83 (t,  $J = 7.1$  Hz, 2H<sub>Ar</sub>), 7.78–7.76 (m, 1H<sub>Ar</sub>), 7.23 (dd,  $J = 7.8, 4.7$  Hz, 1H<sub>Ar</sub>), 4.10 (s, 2H, CH<sub>2</sub>). <sup>13</sup>C NMR (100 MHz, DMSO- $d_6$ )  $\delta$  186.26, 182.32, 169.50, 166.76 (C=O), 159.59, 152.44, 141.29, 139.61, 135.88, 134.98, 134.92, 134.04, 133.86, 132.48, 127.22, 126.72, 125.76, 124.23, 122.20, 120.06, 118.13 (C<sub>Ar</sub>), 35.89 (CH<sub>2</sub>). LC-MS,  $m/z$  ( $I_{rel}$ ): 419 (M+H, 100). Anal. Calcd for C<sub>22</sub>H<sub>14</sub>N<sub>2</sub>O<sub>5</sub>S: C, 63.15; H, 3.37; N, 6.70; S, 7.66. Found: C, 63.17; H, 3.37; N, 6.59; S, 7.73.

**N-(9,10-Dioxo-9,10-dihydroanthracen-1-yl)-2-((2-hydroxyethyl)thio)acetamide (10).** Yield 0.467 g (82%), mp 145 °C dec. FT-IR (UATR diamond)  $\nu_{max}$  3460.15, 2945.84, 1689.32, 1652.84, 1590.36, 1521.72, 1414.92, 1342.11, 1277.93, 1171.80, 707.98 cm<sup>-1</sup>. <sup>1</sup>H NMR (400 MHz, DMSO- $d_6$ )  $\delta$  12.53 (s, 1H, NH), 8.92 (d,  $J = 7.9$  Hz, 1H<sub>Ar</sub>), 8.13 (d,  $J = 8.1$  Hz, 1H<sub>Ar</sub>), 8.06 (d,  $J = 6.5$  Hz, 1H<sub>Ar</sub>), 7.89–7.79 (m, 4H<sub>Ar</sub>), 4.87 (t,  $J = 5.1$  Hz, 1H, OH), 3.65–3.58 (m, 4H, 2CH<sub>2</sub>), 2.73 (t,  $J = 6.6$  Hz, 2H, CH<sub>2</sub>). <sup>13</sup>C NMR (100 MHz, DMSO- $d_6$ )  $\delta$  186.07, 182.00, 169.55 (C=O), 140.91, 135.57, 134.68, 134.59, 133.70, 133.52, 132.12, 126.98, 126.38, 125.30, 121.97, 117.91 (C<sub>Ar</sub>), 60.46 (CH<sub>2</sub>-OH), 37.27, 34.80 (CH<sub>2</sub>). LC-MS,  $m/z$  ( $I_{rel}$ ): 342 (M+H, 100).

Anal. Calcd for  $C_{18}H_{15}NO_4S$ : C, 63.33; H, 4.43; N, 4.10; S, 9.39. Found: C, 63.32; H, 4.29; N, 4.01; S, 9.47.

**2-((2,3-Dihydroxypropyl)thio)-N-((9,10-dioxo-9,10-dihydroanthracen-1-yl) Acetamide (11).** Yield 0.446 g (72%), mp 162 °C dec. FT-IR (UATR diamond)  $\nu_{\max}$  3380.05, 3190.26, 3106.35, 2988.43, 2934.29, 2845.55, 2780.01, 1674.85, 1647.56, 1591.37, 1575.92, 1515.35, 1476.80, 1408.66, 1337.05, 1280.48, 1238.14, 1172.97, 1021.33, 706.82  $cm^{-1}$ .  $^1H$  NMR (400 MHz, DMSO- $d_6$ )  $\delta$  12.61 (s, 1H, NH), 8.96 (dd,  $J$  = 14.4, 6.6 Hz, 1H<sub>Ar</sub>), 8.21 (dd,  $J$  = 5.1, 2.4 Hz, 1H<sub>Ar</sub>), 8.16–8.12 (m, 2H<sub>Ar</sub>), 7.95–7.89 (m, 3H<sub>Ar</sub>), 4.89 (t,  $J$  = 6.1 Hz, 1H, OH), 4.66–4.60 (m, 2H, CH<sub>2</sub>), 4.25 (dd,  $J$  = 13.6, 4.2 Hz, 1H, CH), 4.12–3.90 (m, 2H), 3.61 (d,  $J$  = 3.0 Hz, 2H, CH<sub>2</sub>), 2.78 (dd,  $J$  = 13.3, 4.6 Hz, 2H, CH<sub>2</sub>).  $^{13}C$  NMR (100 MHz, DMSO- $d_6$ )  $\delta$  186.51, 182.52, 170.04 (C=O), 141.37, 136.03, 135.18, 135.07, 134.15, 133.99, 132.55, 127.47, 126.83, 125.78, 122.40, 118.41 (C<sub>Ar</sub>), 71.67 (CH-OH), 64.92 (CH<sub>2</sub>-OH), 36.51, 34.43 (CH<sub>2</sub>). LC-MS,  $m/z$  ( $I_{rel}$ ): 372 (M+H, 100). Anal. Calcd for  $C_{19}H_{17}NO_5S$ : C, 61.44; H, 4.61; N, 3.77; S, 8.63. Found: C, 61.40; H, 4.52; N, 3.68; S, 8.72.

**2-((2-((9,10-Dioxo-9,10-dihydroanthracen-2-yl)amino)-2-oxoethyl)thio)acetic Acid (12).** Yield 0.432 g (73%), mp 136 °C dec. FT-IR (UATR diamond)  $\nu_{\max}$  3589.84, 3516.18, 3296.49, 3203.80, 3102.15, 3064.54, 2957.96, 1719.69, 1675.77, 1656.88, 1644.88, 1589.23, 1574.78, 1548.17, 1425.65, 1332.17, 1302.35, 1226.20, 1192.26, 1133.81, 712.54  $cm^{-1}$ .  $^1H$  NMR (400 MHz, DMSO- $d_6$ )  $\delta$  11.36 (br. s, 1H, OH), 10.69 (s, 1H, NH), 8.28–8.26 (m, 1H<sub>Ar</sub>), 8.05 (d,  $J$  = 7.8 Hz, 2H<sub>Ar</sub>), 8.01 (d,  $J$  = 8.4 Hz, 1H<sub>Ar</sub>), 7.94 (d,  $J$  = 7.7 Hz, 1H<sub>Ar</sub>), 7.83–7.79 (m, 2H<sub>Ar</sub>), 3.48 (d,  $J$  = 11.6 Hz, 4H, 2CH<sub>2</sub>).  $^{13}C$  NMR (100 MHz, DMSO- $d_6$ )  $\delta$  182.66, 181.58, 171.50, 168.81 (C=O), 144.79, 134.88, 134.54, 134.40, 133.42, 133.38, 128.81, 128.35, 127.08, 127.01, 124.12, 124.04, 116.24 (C<sub>Ar</sub>), 36.46, 34.27 (CH<sub>2</sub>). LC-MS,  $m/z$  ( $I_{rel}$ ): 356 (M+H, 100). Anal. Calcd for  $C_{18}H_{13}NO_5S$ : C, 60.84; H, 3.69; N, 3.94; S, 9.02. Found: C, 60.79; H, 3.64; N, 3.88; S, 9.10.

**Methyl 2-((2-((9,10-Dioxo-9,10-dihydroanthracen-2-yl)amino)-2-oxoethyl)thio)acetate (13).** Yield 0.486 g (79%), mp 180 °C dec. FT-IR (UATR diamond)  $\nu_{\max}$  3328.94, 3297.88, 3237.78, 3104.62, 2966.01, 2921.55, 1726.79, 1709.91, 1670.16, 1651.28, 1583.47, 1538.40, 1345.28, 1293.99, 1171.15, 1126.35, 713.52  $cm^{-1}$ .  $^1H$  NMR (400 MHz, DMSO- $d_6$ )  $\delta$  10.69 (s, 1H, NH), 8.35–8.31 (m, 1H<sub>Ar</sub>), 8.13–8.05 (m, 3H<sub>Ar</sub>), 7.98 (d,  $J$  = 7.5 Hz, 1H<sub>Ar</sub>), 7.86–7.83 (m, 1H<sub>Ar</sub>), 3.67–3.60 (m, 3H, CH<sub>3</sub>), 3.56–3.54 (m, 2H, CH<sub>2</sub>), 3.52–3.48 (m, 2H, CH<sub>2</sub>).  $^{13}C$  NMR (100 MHz, DMSO- $d_6$ )  $\delta$  182.69, 181.61, 170.60, 168.67 (C=O), 144.77, 134.91, 134.57, 134.44, 133.45, 133.41, 128.86, 128.39, 127.09, 127.02, 124.12, 116.24 (C<sub>Ar</sub>), 52.59 (CH<sub>3</sub>), 36.49, 33.68 (CH<sub>2</sub>). LC-MS,  $m/z$  ( $I_{rel}$ ): 370 (M+H, 100). Anal. Calcd for  $C_{19}H_{15}NO_5S$ : C, 61.78; H, 4.09; N, 3.79; S, 8.68. Found: C, 61.93; H, 4.00; N, 3.78; S, 8.57.

**2-((2-((9,10-Dioxo-9,10-dihydroanthracen-2-yl)amino)-2-oxoethyl)thio)propanoic Acid (14).** Yield 0.462 g (75%), mp 138 °C dec. FT-IR (UATR diamond)  $\nu_{\max}$  3563.85, 3480.16, 3175.69, 3102.14, 3056.23, 2990.48, 2942.47, 1729.97, 1676.97, 1589.49, 1576.80, 1548.81, 1423.12, 1349.47, 1333.52, 1303.10, 1180.68, 851.93, 713.74  $cm^{-1}$ .  $^1H$  NMR (400 MHz, DMSO- $d_6$ )  $\delta$  12.70 (s, 1H, OH), 10.74 (s, 1H, NH), 8.29–8.27 (m, 1H<sub>Ar</sub>), 8.06–8.03 (m, 2H<sub>Ar</sub>), 8.00 (d,  $J$  = 8.5 Hz, 1H<sub>Ar</sub>), 7.94 (d,  $J$  = 9.1 Hz, 1H<sub>Ar</sub>), 7.82–7.79 (m, 2H<sub>Ar</sub>), 3.62 (q,  $J$  = 6.7 Hz, 1H, CH), 3.56 (d,  $J$  = 3.3 Hz, 2H, CH<sub>2</sub>), 1.38 (d,  $J$  = 7.1 Hz, 3H, CH<sub>3</sub>).  $^{13}C$  NMR (100 MHz, DMSO- $d_6$ )  $\delta$  182.16, 181.08, 173.64, 168.34 (C=O), 144.32, 134.37, 134.03, 133.90, 132.93, 132.89, 128.30, 127.85, 126.58, 126.51, 123.64, 115.76 (C<sub>Ar</sub>), 41.12 (CH), 35.42 (CH<sub>2</sub>), 17.28 (CH<sub>3</sub>). LC-MS,  $m/z$  ( $I_{rel}$ ): 370 (M+H, 100). Anal. Calcd for  $C_{19}H_{15}NO_5S$ : C, 61.78; H, 4.09; N, 3.79; S, 8.68. Found: C, 61.69; H, 4.17; N, 3.82; S, 8.80.

**3-((2-((9,10-Dioxo-9,10-dihydroanthracen-2-yl)amino)-2-oxoethyl)thio)propanoic Acid (15).** Yield 0.542 g (88%), mp 149 °C dec. FT-IR (UATR diamond)  $\nu_{\max}$  3066.41, 3014.57, 2980.94, 2934.81, 1745.47, 1724.84, 1667.40, 1651.21, 1644.45, 1589.56, 1573.68, 1511.50, 1417.25, 1385.74, 1332.89, 1279.43, 1239.20, 1162.90, 1081.52, 707.49  $cm^{-1}$ .  $^1H$  NMR (400 MHz, DMSO- $d_6$ )  $\delta$  12.32 (s, 1H, OH), 10.90 (s, 1H, NH), 8.42–8.40 (m, 1H<sub>Ar</sub>), 8.14–8.12 (m, 2H<sub>Ar</sub>), 8.10–8.09 (m, 1H<sub>Ar</sub>), 8.04 (d,  $J$  = 8.4 Hz, 1H<sub>Ar</sub>), 7.87 (t,  $J$  = 8.0 Hz, 2H<sub>Ar</sub>), 3.43–3.42 (m, 2H, CH<sub>2</sub>), 2.84 (t,  $J$  = 7.0 Hz, 2H, CH<sub>2</sub>), 2.59 (t,  $J$  = 7.0 Hz, 2H, CH<sub>2</sub>).  $^{13}C$  NMR (100 MHz, DMSO- $d_6$ )  $\delta$  182.77, 181.70, 173.32, 169.56 (C=O), 144.95, 134.95, 134.62, 134.52, 133.50, 133.47, 128.87, 128.41, 127.13, 127.05, 124.20, 116.27 (C<sub>Ar</sub>), 35.98, 34.51, 27.54 (CH<sub>2</sub>). LC-MS,  $m/z$  ( $I_{rel}$ ): 370 (M+H, 100). Anal. Calcd for  $C_{19}H_{15}NO_5S$ : C, 61.78; H, 4.09; N, 3.79; S, 8.68. Found: C, 61.71; H, 4.10; N, 3.80; S, 8.72.

**2-((2-((9,10-Dioxo-9,10-dihydroanthracen-2-yl)amino)-2-oxoethyl)thio)succinic Acid (16).** Yield 0.386 g (56%), mp 185 °C dec. FT-IR (UATR diamond)  $\nu_{\max}$  3335.94, 3008.21, 2786.81, 1717.18, 1675.41, 1589.10, 1543.68, 1468.67, 1417.92, 1339.34, 1299.14, 1235.29, 1177.40, 711.15  $cm^{-1}$ .  $^1H$  NMR (400 MHz, DMSO- $d_6$ )  $\delta$  12.81 (br. s, 1H, OH), 12.51 (br. s, 1H, OH), 10.98 (s, 1H, NH), 8.47 (d,  $J$  = 8.1 Hz, 1H<sub>Ar</sub>), 8.16–8.08 (m, 3H<sub>Ar</sub>), 7.97–7.94 (m, 1H<sub>Ar</sub>), 7.83–7.76 (m, 2H<sub>Ar</sub>), 3.91–3.89 (m, 1H, CH), 3.69–3.58 (d,  $J$  = 7.6 Hz, 2H, CH<sub>2</sub>), 2.70–2.59 (m, 2H, CH<sub>2</sub>).  $^{13}C$  NMR (100 MHz, DMSO- $d_6$ )  $\delta$  182.18, 181.22, 171.68, 171.29, 168.72 (C=O), 142.77, 133.92, 133.44, 133.35, 132.62, 127.58, 127.11, 123.53, 116.01 (C<sub>Ar</sub>), 42.30 (CH), 36.17, 34.78 (CH<sub>2</sub>). LC-MS,  $m/z$  ( $I_{rel}$ ): 414 (M+H, 100). Anal. Calcd for  $C_{20}H_{15}NO_7S$ : C, 58.11; H, 3.66; N, 3.39; S, 7.76. Found: C, 58.18; H, 3.59; N, 3.27; S, 7.70.

**2-((2-((9,10-Dioxo-9,10-dihydroanthracen-2-yl)amino)-2-oxoethyl)thio)benzoic Acid (17).** Yield 0.557

g (80%), mp 237 °C dec. FT-IR (UATR diamond)  $\nu_{\max}$  3568.41, 3506.01, 3244.18, 3173.85, 3101.99, 3061.49, 2931.53, 2882.55, 1671.01, 1643.70, 1590.20, 1576.63, 1541.84, 1466.10, 1331.88, 1299.86, 1259.74, 1159.88, 1119.05, 710.97  $\text{cm}^{-1}$ .  $^1\text{H}$  NMR (400 MHz, DMSO- $d_6$ )  $\delta$  12.73 (br. s, 1H, OH), 10.94 (s, 1H, NH), 8.37–8.32 (m, 1H<sub>Ar</sub>), 8.13–8.04 (m, 2H<sub>Ar</sub>), 7.98 (d,  $J$  = 8.7 Hz, 2H<sub>Ar</sub>), 7.92 (d,  $J$  = 7.7 Hz, 2H<sub>Ar</sub>), 7.87–7.80 (m, 2H<sub>Ar</sub>), 7.57–7.52 (m, 2H<sub>Ar</sub>), 7.24 (t,  $J$  = 6.6 Hz, 1H<sub>Ar</sub>), 3.96–3.93 (m, 2H, CH<sub>2</sub>).  $^{13}\text{C}$  NMR (100 MHz, DMSO- $d_6$ )  $\delta$  182.25, 181.20, 167.88, 167.45 (C=O), 144.24, 140.26, 134.47, 134.13, 134.03, 133.01, 132.97, 132.52, 131.02, 128.44, 128.05, 127.91, 126.65, 126.58, 125.74, 124.40, 123.75, 115.83 (C<sub>Ar</sub>), 36.71 (CH<sub>2</sub>). LC-MS,  $m/z$  ( $I_{\text{rel}}$ ): 418 (M+H, 100). Anal. Calcd for C<sub>23</sub>H<sub>15</sub>NO<sub>5</sub>S: C, 66.18; H, 3.62; N, 3.36; S, 7.68. Found: C, 66.05; H, 3.65; N, 3.44; S, 7.84.

**2-((2-((9,10-Dioxo-9,10-dihydroanthracen-2-yl)amino)-2-oxoethyl)thio)nicotinic Acid (18).** Yield 0.523 g (75%), mp 180 °C dec. FT-IR (UATR diamond)  $\nu_{\max}$  3588.77, 3528.34, 3241.81, 3174.17, 3102.68, 3000.36, 2636.05, 1670.57, 1648.96, 1632.10, 1590.54, 1575.51, 1556.74, 1543.53, 1419.68, 1389.13, 1331.30, 1301.77, 1252.08, 1233.62, 1156.54, 1129.87, 1070.10, 710.97  $\text{cm}^{-1}$ .  $^1\text{H}$  NMR (400 MHz, DMSO- $d_6$ )  $\delta$  12.60 (br. s, 1H, OH), 10.90 (s, 1H, NH), 8.57 (s, 1H<sub>Ar</sub>), 8.37 (s, 1H<sub>Ar</sub>), 8.23 (d,  $J$  = 7.1 Hz, 1H<sub>Ar</sub>), 8.10–7.99 (m, 5H<sub>Ar</sub>), 7.83 (s, 2H<sub>Ar</sub>), 7.26–7.21 (m, 1H<sub>Ar</sub>), 4.09 (s, 2H, CH<sub>2</sub>).  $^{13}\text{C}$  NMR (100 MHz, DMSO- $d_6$ )  $\delta$  182.71, 181.59, 168.67, 166.96 (C=O), 160.38, 152.02, 145.04, 139.45, 134.84, 134.50, 134.45, 133.41, 128.81, 128.19, 127.05, 126.98, 124.42, 124.07, 119.67, 116.17 (C<sub>Ar</sub>), 35.74 (CH<sub>2</sub>). LC-MS,  $m/z$  ( $I_{\text{rel}}$ ): 419 (M+H, 100). Anal. Calcd for C<sub>22</sub>H<sub>14</sub>N<sub>2</sub>O<sub>5</sub>S: C, 63.15; H, 3.37; N, 6.70; S, 7.66. Found: C, 63.09; H, 3.23; N, 6.78; S, 7.77.

**N-(9,10-Dioxo-9,10-dihydroanthracen-2-yl)-2-((2-hydroxyethyl)thio)acetamide (19).** Yield 0.484 g (85%), mp 187 °C dec. FT-IR (UATR diamond)  $\nu_{\max}$  3589.84, 3516.18, 3296.49, 3203.80, 3102.15, 3064.54, 2957.96, 1719.69, 1675.77, 1656.88, 1644.88, 1589.23, 1574.78, 1548.17, 1425.65, 1352.14, 1332.17, 1302.35, 1226.20, 1192.26, 1167.14, 1151.73, 1133.81, 931.71, 712.54  $\text{cm}^{-1}$ .  $^1\text{H}$  NMR (400 MHz, DMSO- $d_6$ )  $\delta$  10.70 (s, 1H, NH), 8.40–8.37 (m, 1H<sub>Ar</sub>), 8.14–8.12 (m, 2H<sub>Ar</sub>), 8.11–8.09 (m, 1H<sub>Ar</sub>), 8.01 (d,  $J$  = 8.4 Hz, 1H<sub>Ar</sub>), 7.87 (t,  $J$  = 7.6 Hz, 2H<sub>Ar</sub>), 4.88 (t,  $J$  = 5.3 Hz, 1H, OH), 3.60 (q,  $J$  = 6.1 Hz, 2H, CH<sub>2</sub>), 3.40–3.39 (m, 2H, CH<sub>2</sub>), 2.74 (t,  $J$  = 6.6 Hz, 2H, CH<sub>2</sub>).  $^{13}\text{C}$  NMR (100 MHz, DMSO- $d_6$ )  $\delta$  182.34, 181.25, 169.21 (C=O), 144.48, 134.51, 134.17, 134.10, 133.08, 133.05, 128.47, 127.99, 126.69, 126.61, 123.73, 123.65, 115.82, 115.74 (C<sub>Ar</sub>), 60.44 (CH<sub>2</sub>-OH), 35.90, 34.62 (CH<sub>2</sub>). LC-MS,  $m/z$  ( $I_{\text{rel}}$ ): 342 (M+H, 100). Anal. Calcd for C<sub>18</sub>H<sub>15</sub>NO<sub>4</sub>S: C, 63.33; H, 4.43; N, 4.10; S, 9.39. Found: C, 63.20; H, 4.30; N, 4.09; S, 9.29.

**2-((2,3-Dihydroxypropyl)thio)-N-((9,10-dioxo-9,10-dihydroanthracen-2-yl) Acetamide (20).** Yield 0.501

g (81%), mp 163 °C dec. FT-IR (UATR diamond)  $\nu_{\max}$  3335.95, 3104.86, 3069.88, 2927.97, 1675.70, 1589.96, 1542.74, 1419.12, 1340.62, 1299.62, 1237.15, 933.59, 711.60  $\text{cm}^{-1}$ .  $^1\text{H}$  NMR (400 MHz, DMSO- $d_6$ )  $\delta$  11.06 (s, 1H, NH), 8.45 (d,  $J$  = 2.3 Hz, 1H<sub>Ar</sub>), 8.20–8.12 (m, 2H<sub>Ar</sub>), 8.04 (dd,  $J$  = 8.6, 2.3 Hz, 1H<sub>Ar</sub>), 7.91–7.86 (m, 3H<sub>Ar</sub>), 5.21 (dd,  $J$  = 19.7, 5.4 Hz, 1H, CH), 4.83 (t,  $J$  = 6.3 Hz, 1H, OH), 4.09 (t,  $J$  = 12.6 Hz, 1H, OH), 3.43 (d,  $J$  = 5.0 Hz, 2H, CH<sub>2</sub>), 3.24–3.00 (m, 2H, CH<sub>2</sub>), 2.99–2.77 (m, 2H, CH<sub>2</sub>).  $^{13}\text{C}$  NMR (100 MHz, DMSO- $d_6$ )  $\delta$  182.65, 181.64, 165.00 (C=O), 144.34, 134.96, 134.63, 134.46, 133.41, 128.87, 128.68, 127.10, 127.03, 124.30, 116.38 (C<sub>Ar</sub>), 66.76 (CH-OH), 59.23 (CH<sub>2</sub>-OH), 36.27, 34.66 (CH<sub>2</sub>). LC-MS,  $m/z$  ( $I_{\text{rel}}$ ): 372 (M+H, 100). Anal. Calcd for C<sub>19</sub>H<sub>17</sub>NO<sub>5</sub>S: C, 61.44; H, 4.61; N, 3.77; S, 8.63. Found: C, 61.32; H, 4.57; N, 3.69; S, 8.52.

## 2. 2. Antioxidant Activity

### 2. 2. 1 Method of Study of Lipid Peroxidation (LP) and Oxidative Modification of Proteins (OMP) of Thioether Acetamides

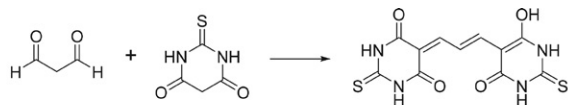
The LP and OMP processes study was performed *in vitro* on rat's liver homogenate according to the Lushchak's method.<sup>38</sup> The amount of protein in the sample was determined due to the Lowry method. This method is based on LP activation by ferrous iron ions to a level recorded spectrophotometrically by reaction with thiobarbituric acid. The degree of OMP was evaluated calculating the amount of additional CGs formed in the side chains of aminoacids under the reaction with 2,4-dinitrophenylhydrazine. The methanol solutions served as control, while the standard of measurement was 10<sup>-6</sup> M solution of quercetin. Experimental data were analyzed considering the arithmetic mean  $M$  and standard error  $m$  in the form of ( $M \pm m$ ),  $n = 5$ . Differences between experimental data were determined via Tukey's test of one-way analysis (ANOVA), and the differences were considered to be statistically significant at  $P < 0.05$ .<sup>39</sup>

At the beginning of our experiment, to 0.3 g of rat liver homogenate 0.3 mL methanol solutions of sulfur-containing derivatives of 2-chloro-*N*-(9,10-dioxo-9,10-dihydroanthracen-1(2)-yl)-acetamides (10<sup>-6</sup> M concentration) was poured. Iron(II) sulfate solution (0.3 mL of 2.8%) was introduced to the obtained solution. The reaction of LP was induced within 10 minutes. Then 0.3 mL of 4% solution of hydrogen peroxide was added, and the solution was incubated for 2 hours. The reaction was stopped after introducing 1.2 mL of 40% trichloroacetic acid, precipitating polypeptides. Reaction mixture was centrifuged for 10 minutes at 5·10<sup>3</sup> RPM. Bioactive compounds' influence analyses on FRO were conducted for a single sample. Carbonyl groups were determined in the sediment, and products of lipids interaction with TBA were determined from the supernatant.



## 2. 2. 2. Determination of the Content of Products of Lipids Interaction with TBA in the Supernatant

1.5 mL of 0.8% TBA was added to the supernatant separated from the sediment. The reaction between TBA and MDA proceeds during the heating of this solution to 100 °C for about 1 hour. The formation of the pinky colored complex allows determining the content of TBA-active products:



After cooling, 3 mL of butanol was added to the reaction mass and was left for 2 hours. After, the formation of two phases was observed. Determination of the extinction coefficient was determined from the butanol fraction at  $\lambda = 532$  nm.

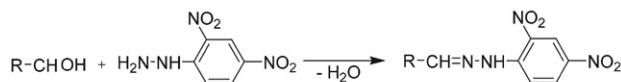
Calculation of TBA-active products was performed according to:

$$[\text{TBA} - \text{active products}] = \frac{E \cdot V_1 \cdot V_2}{\epsilon \cdot V \cdot C}, \text{ } \mu\text{mol/mg of protein} \quad (1)$$

where  $E$  – extinction coefficient of the test sample;  $\epsilon$  – millimolar extinction coefficient ( $\epsilon = 156 \text{ cm}^2/\mu\text{mol}$ );  $V_1$  – a volume of butanol (mL);  $V_2$  – sample volume (mL);  $V$  – supernatant volume (mL);  $C$  – protein concentration in the supernatant ( $\mu\text{mol}$ ).

## 2. 2. 3. Determination of CGs Proteins in the Precipitate

To the formed precipitate 1 mL of 1% 2,4-dinitrophenylhydrazine solution was added.



The resulting solution was incubated for an hour, then centrifuged at  $5 \cdot 10^3$  RPM for 10 minutes. The precipitate was washed three times with the addition of 1 mL of ethanol-ethyl acetate solution (1:1) and centrifuged. Then 3 mL of 50% urea solution was added to the precipitate, centrifuged, and the additional CG was determined using a spectrophotometer ( $\lambda = 370$  nm).

## 2. 3. Anti-platelet Activity

### 2. 3. 1. Preparation of Rabbit Platelet-rich Plasma

Platelet-rich plasma (PRP) was obtained from at least 3 different healthy adult rabbits. The Scientific Ethics Committee of Taras Shevchenko National University of Kyiv, Ukraine approved the study protocol.

Rabbit blood was collected from the ear artery into a polyethylene tube with 3.8% sodium citrate in the ratio 9:1. PRP was obtained by centrifugation of stabilized blood

at 300 g for 10 min. The supernatant (PRP) was carefully separated and used further in the aggregation assay. Platelet-pure plasma (PPP) was prepared by further centrifugation of the remained stabilized blood at 1,500 g for 30 min.

### 2. 3. 2. Platelet Aggregation Assay

Platelet aggregation was assessed within the first 3 h after blood sampling using photo-optical aggregometer AT-02 (Medtech, Russia). Before the assessment, the platelet count in PRP was adjusted with PPP to about  $230 \times 10^3$ – $250 \times 10^3$  cells/ $\mu\text{L}$ .

The studied compounds were dissolved in pure dimethyl sulfoxide (DMSO) and their test concentrations were prepared using distilled water. The final DMSO concentration in all experiments was fixed at 1% to minimize the effect of DMSO on the platelet aggregation.

Primary screening for anti-aggregation activity of compounds **3–20** was performed *in vitro*: PRP was incubated with studied compounds (final concentration was 50  $\mu\text{M}$ ) in a cuvette for 2 min at 37 °C with constant stirring (500 rpm). PRP incubated with DMSO alone was used as a control. ADP (Sigma, USA) in the final concentration of  $5 \times 10^{-6}$  M was added to the sample, and the change of light transmission was monitored for 8 minutes ADP to induce platelet aggregation. In this experiment the level of spontaneous aggregation induced by addition of the tested compounds to PRP was studied. The degree of platelet aggregation (the maximal level of light transmission of PRP after addition of inducer) was evaluated. The degree of inhibition of ADP-dependent aggregation under the action of obtained derivatives **3–20** relative to control, which was taken as 100%, was calculated.

## 3. Results and Discussion

### 3. 1. Synthesis of *N*-(9,10-Dioxo-9,10-dihydroanthracen-1(2)-yl)-2-(*R*-thio) Acetamides

In continuation of the previous studies of our group on the functionalization of 9,10-anthracenedione,<sup>36,37,40–46</sup> a structural modification of 2-chloro-*N*-(9,10-dioxo-9,10-dihydroanthracen-1(2)-yl)acetamides **1**, **2** by pharmacophore fragments, namely, sulfur-containing substituents was carried out. In this work, the reaction of chloroacetamides **1**, **2** with a number of alkyl(aryl/heteroaryl)thiols, additionally functionalised with mercapto, hydroxy, carboxy and carboxylate groups was carried out (Scheme 1). It can be a key aspect for improving biological activity, including antiplatelet and antioxidant actions, as well as bioavailability due to an increase in the polarity of the obtained compounds and better water solubility.

Modification of chloroacetamides **1**, **2** with the corresponding thiols was carried out using their interaction at

room temperature in the presence of potassium carbonate in DMF (Scheme 1). As a result, the corresponding sulfide derivatives **3–20** were obtained in good and high yields of up to 93%.

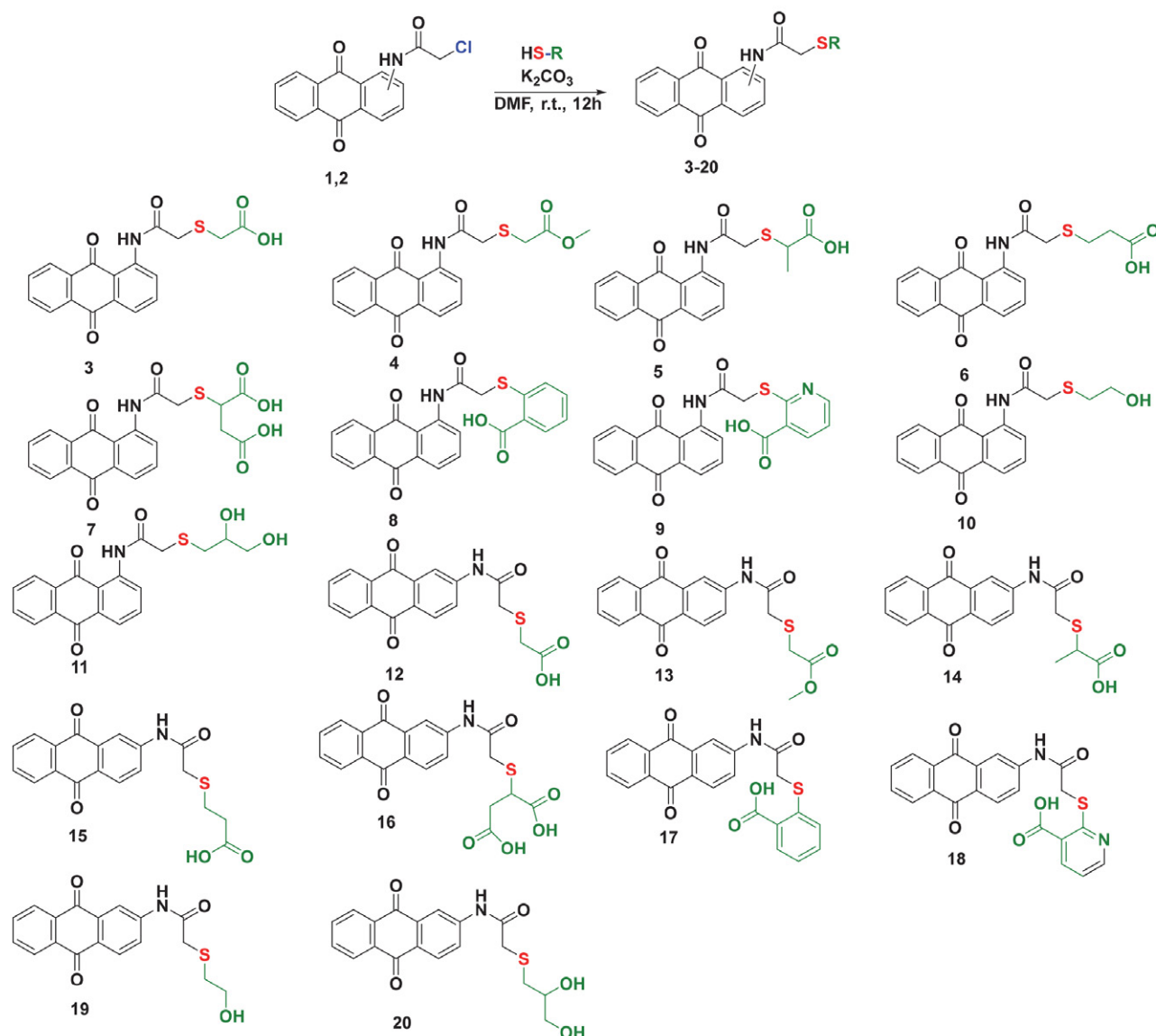
The structures of new thioether acetamides **3–20** were reliably confirmed by modern physicochemical analysis methods, namely  $^1\text{H}$  and  $^{13}\text{C}$  NMR, LC-MS, IR-Fourier spectroscopy and elemental analysis. In particular, the secondary amino group resonates at 12.41–12.62 ppm for sulfides **3–11**, and in the case of sulfides **12–20** at 10.69–10.94 ppm in the  $^1\text{H}$  NMR spectra.

In turn, the methylene group of the oxoethyl fragment of acetamide in  $^1\text{H}$  NMR observed for compounds **3–7**, **10**, **11** at 3.59–3.76 ppm, and for compounds **12–16**, **19**, **20** at 3.40–3.56 ppm. In the case of the aromatic thioether substituent of **8**, **9**, **17**, **18**, the  $\text{CH}_2$  group shifts

downfield and resonates within 3.94–4.16. In  $^{13}\text{C}$  NMR spectra, the appearance of a signal of the carbon atom of the carboxyl group at 167.88–173.84 ppm is characteristic for sulfide derivatives **4**, **6–9**, **12**, **14–18**. For sulfide derivatives **9** and **18** containing a fragment of nicotinic acid in their structures, the appearance of signals of the quaternary carbon atom of the N-C-S group of the nicotine fragment was determined at 159.59 and 160.38 ppm, respectively.

### 3. 2. Antioxidant Properties

The free-radical oxidation (FRO) research was conducted *in vitro* using a rat liver homogenate. LP and OMP as two markers of oxidative stress were used for the evaluation of antioxidant properties of the compounds.



**Scheme 1.** Synthesis of *N*-(9,10-dioxo-9,10-dihydroanthracene-1(2)-yl)-2-(*R*-thio) acetamides **3–20**

This method is based on the LP activation by ferrous ions to a level registered spectrometrically by reaction with thiobarbituric acid (TBA-active products content). The degree of OMP was determined by the amount of additional carbonyl groups formed (CG content) in the side chains of amino acids using the reaction with 2,4-diphenylhydrazine.

The results of this investigation, in particular the content of TBA-active products and CGs, found from a comparison of isomers (compounds where the substituent is introduced in position 1 or 2). Data are presented in Figures 1 and 2. All compounds were compared with control, as well as with reference antioxidant quercetin. Quercetin in the LP processes acted as a control, and in the processes of OMP it showed antioxidant properties, reducing the level of CG relative to the control by 41.5%.

The comparison antioxidant activity of isomers 3–11 and 12–20 are as follows. Compound 8 contained the residue of 2-((2-amino-2-oxoethyl)thio)benzoic acid in the position 1, showed minor antioxidant properties (8.3% content of TBA-active products) compared to the control

as presented in Figure 1. The derivative 17 increased the content of TBA-active products by 8.6%, i.e., it had prooxidant properties relative to control. The compounds 8 and 17 demonstrated antioxidant effect in OMP processes decreasing the CGs level by 15.7% and 26.4%, respectively. The compound 17 contained the residue of 2-((2-amino-2-oxoethyl)thio)benzoic acid in the position 2, decreased the level of CGs by 10.7% more than the derivative 8 in the free radical processes of protein oxidation. Therefore, 2-((2-((9,10-dioxo-9,10-dihydroanthracen-1-yl)amino)-2-oxoethyl)thio)benzoic acid 8 exhibited antioxidant properties on two FRO markers.

The compounds 10 and 19 contained 2-((2-hydroxyethyl)thio)acetamide residue in positions 1 or 2 of anthracenedione ring demonstrated similar results. In this case, derivative 10 reduced the content of TBA-active products relative to control slightly, namely by 8.7%. Compound 19 showed high prooxidant properties and significantly (by 41.0%) increased the content of TBA-active products compared to control (Fig. 1). In contrast, compound 19 showed better results on OMP processes than compound

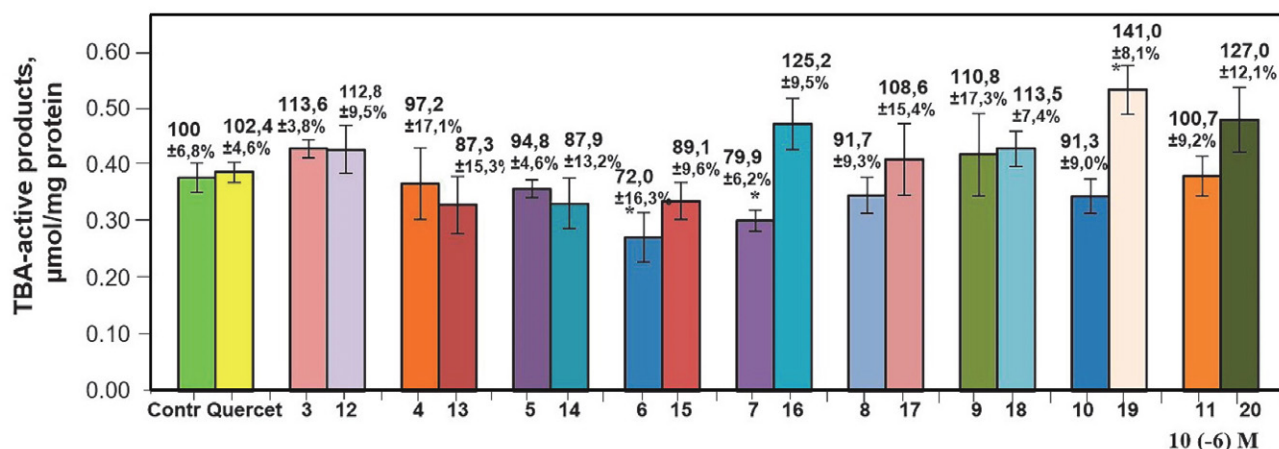


Figure 1. Influence of compounds 3–20 on amount of TBA-active products in rat liver homogenate (\*-  $p \leq 0.05$ ;  $M \pm m$ ;  $n = 5$ )

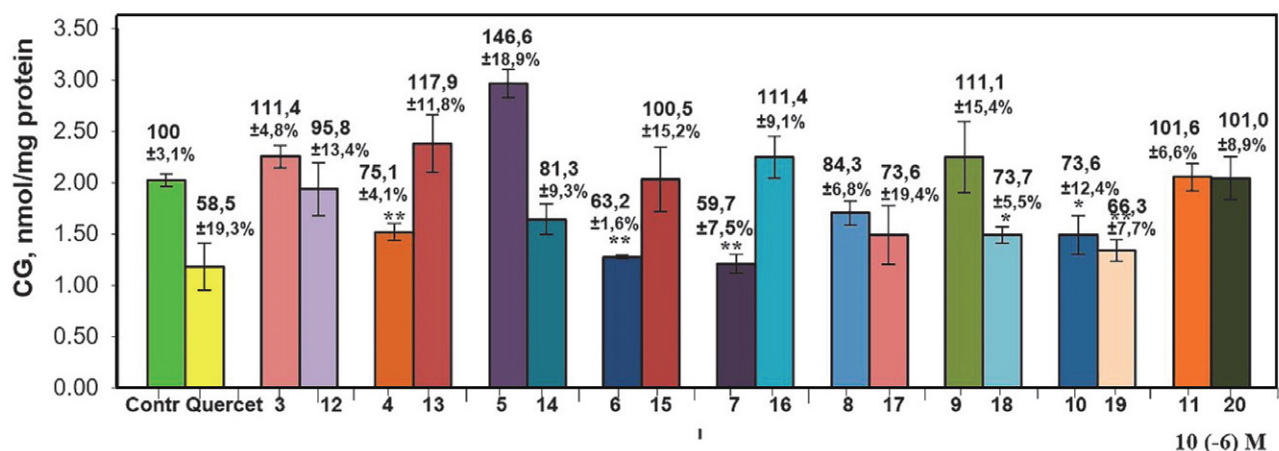


Figure 2. Influence of compounds 3–20 on amount of CGs of proteins in rat liver homogenate (\*-  $p \leq 0.05$ ; \*\*-  $p \leq 0.01$ ;  $M \pm m$ ;  $n = 5$ )

**10** and reduced the CG content by 33.7% compared to the control (Fig. 2). In turn, derivative **10** also exhibited antioxidant properties in OMP processes, reducing the level of CG proteins relative to control by 24.4%.

Moreover, compounds **6** and **15** show antioxidant activity in LP processes (Fig. 1). Derivative **6** reduces the content of TBA-active products by 28.0% relative to the control ( $p \leq 0.05$ ), whereas derivative **15** decreases the value by 10.1%. The studied compound **6** statistically significantly ( $p \leq 0.01$ ) decreases the formation of CGs in proteins in FRP of OMP processes by 37.8% relative to the control (Fig. 2). Meanwhile, the content of CGs under the action of compound **15** shows no difference to the control with a value at  $100.5 \pm 15.2\%$ .

Comparing compounds, which contain in anthracenedione nuclei the residue of succinic acid in the first (**7**) or second (**16**) position, demonstrates that compound **7** has antioxidant properties to lipids and lowers the content of TBA-active products by 21.1% (Fig. 1). Compound **16**, in contrast to compound **7**, exhibits pro-oxidant properties and increases the content of TBA-active products by 25.2% relative to control. In addition, compound **7** (Fig. 2) shows antioxidant effect in OMP processes and statistically significantly ( $p \leq 0.01$ ) decreases the level of CGs proteins by 40.3% compared to the control. In turn, 2-((2-((9,10-dioxo-9,10-dihydroanthracen-2-yl)amino)-2-oxoethyl)thio)succinic acid **16** increases the CGs content by 11.3%.

The LP study of compound **11**, which contains (dihydroxypropyl)thio)acetamide residue in the structure, has not shown antioxidant properties due to no difference in the TBA-active products content to the control (Fig. 1). Compound **20** with the ((dihydroxypropyl)thio)acetamide residue in the structure at position 2 of anthracenedione exhibits prooxidant properties and increases the content of the TBA-active product by 27.0% relative to control (Fig. 1). Compounds **11** and **20**, based on the results of the study of OMP (Fig. 2), showed that the content of protein

CGs does not differ from the control. Such contents for derivatives **11** and **20** are  $101.6 \pm 6.6\%$  and  $101.0 \pm 8.9\%$ , respectively. Thus, these compounds are neutral to the oxidation process.

In turn, compounds **3** and **12** almost equally increase the content of TBA-active products compared to the control, namely, by 13.6% and 12.8%, respectively (Fig. 1). The compound **3** in the OMP processes, as well as for LP, demonstrates a prooxidant effect due to an increase of CGs for 11.4% compared to the control (Fig. 2). In contrast, compound **12** has shown minor antioxidant properties and decreased CGs by 4.2%.

Compound **4**, due to the results of LP investigation, has the same effect as the control (Fig. 1), decreasing the level of TBA-active products only by 2.8%. Compound **13**, which has in structure the aminooxoethylthioacetate residue at the second position of anthraquinone, showed better antioxidant properties compared to its isomer **4** and reduced the content of TBA-active products relative to control by 12.8%. Furthermore, compound **4**, according to the results of OMP (Fig. 2), exhibits antioxidant properties and reduces the content of CGs by 24.9% in comparison with the control. Moreover, compound **13** shows the opposite effect due to the increasing content of CGs relative to the control by 17.9%, which indicates an increase in free radical processes in the proteins (Fig. 2).

Hence, summarizing the obtained results, the studied compounds with a substituent in the first position of anthracenedione fragment exhibit higher antioxidant properties than their isomers with a substituent in the second position. Compounds with a substitution in the first position **6**, **7**, **8** and **10** demonstrate the antioxidant properties concerning oxidative stress markers POL and OMP. Moreover, compound **6** reduces the content of TBA-active products by 28.0% and content of CGs by 36.8%, whereas derivative **7** decreases by 21.1% and 41.3%, respectively. Test compounds **4**, **10**, **17**, **19**, as well as quercetin, showed antioxidant properties only in OMP processes.

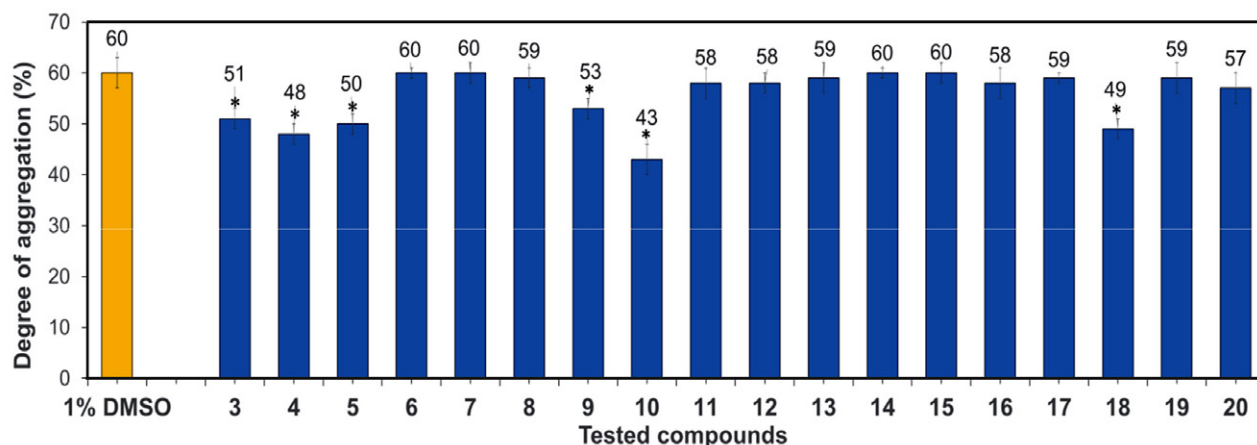


**Figure 3.** Effect of derivatives **3–20** at a concentration of 50  $\mu\text{M}$  on ADP-induced platelet aggregation in rabbit PRP ( $M \pm \text{SEM}$ ;  $n = 6$ , \*  $p \leq 0.05$  changes are statistically significant compared to the control 1% DMSO)

### 3.3. Antiplatelet Activity

Antiplatelet activity of derivatives 3–20 was studied *in vitro* using rabbit PRP. As can be seen from the results (Fig. 3), among the 20 tested compounds, only six (3, 4, 5, 9, 10, 18) showed moderate antiplatelet activity.

The most active compound, namely compound 10, inhibited ADP-induced aggregation by 28%, while the inhibitory effect of others ranged from 12% to 20%. The latter is associated with the structure of the thio fragment

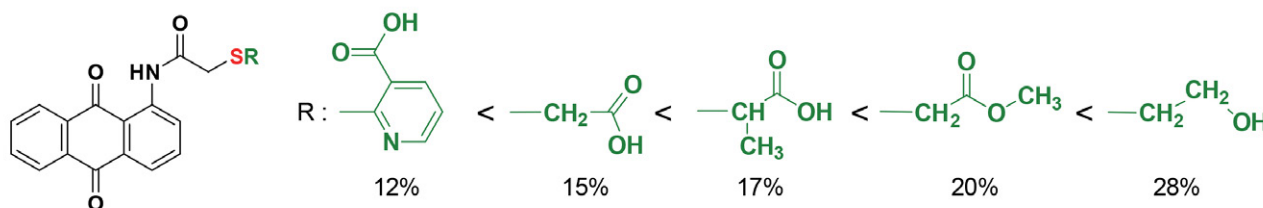


Figure 4. Correlation of substituent of the thio fragment and the inhibitory effect for five compounds 3, 4, 5, 9, 10

and the inhibitory effect is characteristic for five compounds (3, 4, 5, 9, 10), and increases in the following order of substituents (Fig. 4):

Analysis of the influence of the structure of the thio fragment on the manifestation of the antiplatelet activity of compounds 3–20 showed that anthracenedione derivatives containing this residue in the first position of the anthracenedione ring (3, 4, 5, 9, 10) can inhibit platelet aggregation. It was found that the presence of a less branched 2-((2-hydroxyethyl)thio)acetamide residue (compound 10) causes the highest percentage of the degree of inhibition. At the same time, derivatives 12–20 with a thio substituent in position 2 of the anthracenedione nucleus and compounds 6–8, 11 with branched and bulky substituents near the sulfur atom do not affect the degree of inhibition.

## 4. Conclusions

A convenient way to obtain new sulfide derivatives with a 9,10-anthracenedione ring has been proposed. It includes the interaction of 2-chloro-*N*-(9,10-dioxo-9,10-dihydroanthracen-1(2)-yl)-acetamides 1, 2 with a number of alkyl(aryl/heteroaryl)thiols at room temperature in the presence of potassium carbonate in DMF. The study of antioxidant activity in terms of lipid peroxidation and oxidative modification of proteins in rat liver homogenate *in vitro* identified compounds 6 and 7 with the best properties of radical scavenging activity in terms of the content of TBA-active products and CGs in the corresponding range 21.1–28 % and 36.8–41.3%. An *in vitro* study of the antiplatelet activity using rabbit PRP revealed derivative 10, exhibiting the highest degree of inhibition of platelet aggregation among the synthesized compounds. Sulfide

derivative 10 also demonstrated antioxidant properties in OMP processes, which manifested in lowering CGs protein level compared to control for 24.4%. The structure-activity relationships for the obtained *N*-(9,10-dioxo-9,10-dihydroanthracen-1(2)-yl)-2-(*R*-thio) acetamides were determined. The data obtained are the basis for further studies on molecular design and the search for new compounds with antioxidant and antiplatelet activity in a series of new derivatives of 9,10-anthracenedione.

## Funding

This research was funded by the Ministry of Education and Science of Ukraine, Project number: 0119U002252.

## Supplementary Data

<sup>1</sup>H and <sup>13</sup>C NMR spectra of compounds 3–20 are provided in supplementary material via the “Supplementary Content” section of this article’s webpage.

## Conflicts of Interest

The authors declare no conflict of interest.

## 5. References

1. H. Ten Cate, *Front Cardiovasc. Med.* **2021**, *8*, 637005. DOI:10.3389/fcvm.2021.637005
2. A. E. A. Dahm, *Med. Sci. (Basel)*. **2021**, *9*, 41. DOI:10.3390/medsci9020041
3. L. Gervaso, H. Dave, A. A. Khorana, *JACC CardioOncol.* **2021**, *3*, 173–190. DOI:10.1016/j.jaccao.2021.03.001
4. E. Grilz, F. Posch, S. Nopp, O. Königsbrügge, I. M. Lang, P. Klimek, S. Thurner, I. Pabinger, C. Ay, *Eur. Heart J.* **2021**, *42*, 2299–2307. DOI:10.1093/eurheartj/ehab171
5. J. Gregson, S. Kaptoge, T. Bolton, L. Pennells, P. Willeit, S. Burgess, T. Meade, *JAMA Cardiology*. **2019**, *4*, 163–173. DOI:10.1001/jamacardio.2018.4537
6. J. Hippisley-Cox, M. Patone, X. W. Mei, D. Saatci, S. Dixon, K. Khunti, *BMJ* **2021**, *374*, n1931. DOI:10.1136/bmj.n1931
7. K. Stark, S. Massberg, *Nat. Rev. Cardiol.* **2021**, *18*, 666–682. DOI:10.1038/s41569-021-00552-1



8. E. M. Page, R. A. S. Ariëns, *Thromb. Res.* **2021**, *200*, 1–8. DOI:10.1016/j.thromres.2021.01.005
9. H. Y. Lin, C. Y. Lin, M. C. Shen, *Thrombosis J.* **2021**, *19*, 43. DOI:10.1186/s12959-021-00296-5
10. C. Jerjes-Sánchez (Ed.): Mechanisms of Thrombosis. In Thrombolysis in Pulmonary Embolism, Springer, Cham, Switzerland, **2015**, pp. 1–17. DOI:10.1007/978-3-319-19707-4
11. D. Shoichiro, *Ther. Apher. Dial.* **2019**, *23*, 32–37. DOI:10.1111/1744-9987.12744
12. M. Martín-Fernández, R. Aller, M. Heredia-Rodríguez, E. Gómez-Sánchez, P. Martínez-Paz, H. Gonzalo-Benito, L. Sánchez-de Prada, Ó. Gorgojo, I. Carnicero-Frutos, E. Tamayo, Á. Tamayo-Velasco, *Redox Biol.* **2021**, *48*, 102181. DOI:10.1016/j.redox.2021.102181
13. L. Liao, M. Zhou, J. Wang, X. Xue, Y. Deng, X. Zhao, C. Peng, Y. Li, *Front Pharmacol.* **2021**, *12*, 742954. DOI:10.3389/fphar.2021.742954
14. K. Wang, T. Shang, L. Zhang, L. Zhou, C. Liu, Y. Fu, Y. Zhao, X. Li, J. Wang, *ACS Appl. Mater. Interfaces.* **2021**, *13*, 35431–35443. DOI:10.1021/acsami.1c08880
15. J. Flieger, W. Flieger, J. Baj, R. Maciejewski, *Materials (Basel)*. **2021**, *14*, 4135. DOI:10.3390/ma14154135
16. A. Varesi, S. Chirumbolo, G. Ricevuti, *Intern. Emerg. Med.* **2021**, 1–4. DOI:10.1007/s11739-021-02865-y
17. K. R. Olson, Y. Gao, K. D. Straub, *Int. J. Mol. Sci.* **2021**, *22*, 961. DOI:10.3390/ijms22020961
18. N. Q. Trung, N. M. Thong, D. H. Cuong, T. D. Manh, L. P. Hoang, N. K. Hien, P. C. Nam, D. T. Quang, A. Mechler, Q. V. Vo, *ACS Omega*, **2021**, *6*, 13391–13397. DOI:10.1021/acsomega.1c01448
19. G. Greco, E. Turrini, E. Catanzaro, C. Fimognari, *Mar. Drugs*. **2021**, *19*, 272. DOI:10.3390/md19050272
20. J. A. Duke (Ed.): Handbook of phytochemical constituents of GRAS herbs and other economic plants, CRC Press, Boca Raton, **2001**, pp. 143–144. DOI:10.1201/9780203752623
21. N. M. Storozhok, A. Drulle, I. Login, I. Dregeris, N. G. Khrapova, E. B. Burlakova, *Vopr. Med. Khim.* **1995**, *41*, 16–21.
22. G. Yen, P. Duh, D. Chuang, *Food Chem.* **2000**, *70*, 437–441. DOI:10.1016/S0308-8146(00)00108-4
23. Z. Marković, M. Filipović, N. Manojlović, A. Amić, S. Jeremić, D. Milenković, *Chem. Pap.* **2018**, *72*, 2785–2793. DOI:10.1007/s11696-018-0534-3
24. N. Liu, G. Sun, *Ind. Eng. Chem. Res.* **2011**, *50*, 5326–5333. DOI:10.1021/ie101423v
25. L. Lin, H. Du, *Spectrochim. Acta A Mol. Biomol. Spectrosc.* **2018**, *202*, 314–318. DOI:10.1016/j.saa.2018.05.058
26. Z. Marković, S. Jeremić, J. Dimitrić Marković, M. Stanojević Pirković, D. Amić, *Comput. Theor. Chem.* **2016**, *1077*, 25–31. DOI:10.1016/j.comptc.2015.10.004
27. V. Zvarych, M. Stasevych, V. Lunin, N. G. Deniz, C. Sayil, M. Ozyurek, K. Guclu, M. Vovk, V. Novikov, *Monatsh. Chem.* **2016**, *147*, 2093–2101. DOI:10.1007/s00706-016-1839-y
28. M. Stasevych, V. Zvarych, V. Lunin, N. Kopak, O. Komarovska-Porokhnyavets, N.G. Deniz, C. Sayil, M. Ozyurek, K. Guclu, M. Vovk, V. Novikov, *Monatsh. Chem.* **2018**, *149*, 1111–1119. DOI:10.1007/s00706-018-2157-3
29. A. Kaur, S. Kaur, M. Kaur, A. Mahajan, S. Bose, *World J. Pharm. Res.* **2014**, *4*, 1892–1902. DOI:10.2174/22103031113036660017
30. Z. Memariani, R. Moeini, S. Hamed, G. Narjes, S. Mozaffarpur, *J. Thromb. Thrombolysis.* **2018**, *45*, 158–179. DOI:10.1007/s11239-017-1580-3
31. A. Gouda, M. S. Amine, E. B. Pedersen, *Helv. Chim. Acta.* **2016**, *99*, 116–124. DOI:10.1002/hlca.201500207
32. V. Zvarych, M. Stasevych, V. Lunin, N. G. Deniz, C. Sayil, M. Ozyurek, K. Guclu, M. Vovk, V. Novikov, *Monatsh. Chem.* **2016**, *147*, 2093–2101. DOI:10.1007/s00706-016-1839-y
33. T. I. Halenova, I. V. Nikolaeva, M. V. Stasevych, V. I. Zvarych, V. V. Lunin, V. P. Novikov, O. M. Savchuk, *Res. J. Pharm. Biol. Chem. Sci.* **2017**, *8*, 1626–1632
34. T. Halenova, I. Nikolaeva, A. Nakonechna, V. Lubenets, *Res. Pract. Thromb. Haemost.* **2017**, *1*, 1276–1277. DOI:10.1002/rth2.12012
35. W. L. F. Armarego, C. Chai, Purification of Laboratory Chemicals, 4th ed., Elsevier, Oxford, **2003**, pp. 8–13. DOI:10.1016/B978-075067571-0/50003-X
36. M. V. Stasevych, V. I. Zvarych, V. P. Novikov, *Biointerface Res. Appl. Chem.* **2021**, *11*, 8818–8824. DOI:10.33263/BRIAC112.8818824
37. V. I. Lushchak, T. V. Bagnyukova, L. I. Luzhna, *Ukr. Biochem. J.* **2006**, *78*, 113–119.
38. G. A. Morgan, N. L. Leech, G. W. Gloeckner, K. C. Barrett, IBM SPSS for Introductory Statistics. Use and Interpretation, 4th ed., Taylor & Francis Group, New York, USA, **2012**, p. 256. DOI:10.4324/9780203127315
39. V. I. Zvarich, M. V. Stasevich, O. V. Stanko, E. Z. Komarovskaya-Porokhnyavets, V. V. Poroikov, A. V. Rudik, V. P. Novikov, *Pharm. Chem. J.* **2014**, *48*, 584–588. DOI:10.1007/s11094-014-1154-z
40. M. V. Stasevych, V. I. Zvarych, V. P. Novikov, M. V. Vovk, *Bio-interface Res. Appl. Chem.* **2021**, *11*, 7725–7734. DOI:10.33263/BRIAC111.77257734
41. V. Zvarych, M. Stasevych, V. Novikov, E. Rusanov, M. Vovk, P. Szweda, K. Grecka, S. Milewski, *Molecules.* **2019**, *24*, 4581. DOI:10.3390/molecules24244581
42. V. I. Zvarych, M. V. Stasevych, V. V. Lunin, M. V. Vovk, V. P. Novikov, *Chem. Heterocycl. Compd.* **2016**, *52*, 421–423. DOI:10.1007/s10593-016-1904-9
43. T. Strobel, Y. Schmidt, A. Linnenbrink, A. Luzhetskyy, M. Luzhetskaya, T. Taguchi, E. Brötz, T. Paululat, M. Stasevych, O. Stanko, V. Novikov, A. Bechthold, *Appl. Environ. Microbiol.* **2013**, *79*, 5224–32. DOI:10.1128/AEM.01652-13
44. M. V. Stasevich, V. I. Zvarich, V. P. Novikov, S. D. Zagorodnya, O. Yu. Povnitsa, M. A. Chaika, M. V. Nesterkina, I. A. Kravchenko, D. S. Druzhilovskiy, V. V. Poroikov, *Pharm. Chem. J.* **2020**, *53*, 905–913. DOI:10.1007/s11094-020-02098-x
45. M. Stasevych, V. Zvarych, R. Musyanovych, V. Novikov, M. Vovk, *Chem. Chem. Technol.* **2014**, *8*, 135–140. DOI:10.23939/chcht08.02.135



46. M. V. Stasevych, M. Yu. Plotnikov, M. O. Platonov, S. I. Sabat, R. Ya. Musyanovych, V. P. Novikov, *Heteroatom Chem.* **2005**, *16*, 205–211. DOI:10.1002/hc.20112

## Povzetek

S pomočjo reakcije 2-kloro-*N*-(9,10-diokso-9,10-dihidroantracen-1(2)-il)acetamidov s funkcionaliziranimi tioli v prisotnosti kalijevega karbonata v *N,N*-dimetilformamidu (DMF) pri sobni temperaturi smo izvedli sintezo serije novih *N*-(9,10-diokso-9,10-dihidroantracen-1(2)-il)-2-(*R*-tio) acetamidov. Za nove spojine smo s pomočjo *in vitro* testov na osnovi lipidne peroksidaze (LP) in oksidativne modifikacije proteinov (OMP) v homogenizatu jeter podgan določili sposobnost delovanja v vlogi lovilcev radikalov. Ugotovili smo, da spojine, ki imajo vezane substituentne na položaju 1 v antracendionskem skeletu, kažejo boljše antioksidacijske lastnosti kot njihovi izomeri s substituenti na položaju 2. Kot najbolj učinkovita lovilca radikalov sta se izkazali spojini **6** in **7**. Antioksidacijske lastnosti v OMP procesu smo določili tudi za spojino **10**; za to spojino smo izvedli tudi *in vitro* študijo delovanja proti agregaciji krvnih ploščic, kjer smo ugotovili inhibitorno delovanje na agregacijo, povzročeno z ADP.



Except when otherwise noted, articles in this journal are published under the terms and conditions of the Creative Commons Attribution 4.0 International License

Scientific paper

# A New Zn(II) Two-dimensional Coordination Polymer: Synthesis, Structure, Highly Efficient Fluorescence and DFT Study

Fen-Fang Li

Department of Chemistry and Chemical Engineering, Jinzhong University, Jinzhong, Shanxi 030600, China.

\* Corresponding author: E-mail: lffspring@126.com

Received: 03-26-2022

## Abstract

A new two-dimensional coordinate polymer,  $\{[\text{Zn}_2(\text{pbmpd})(\text{H}_2\text{O})_4] \cdot (\text{H}_2\text{O})\}_n$  ( $\text{H}_4\text{pbmpd}$  = 1,1'-(1,4-phenylenebis(methylene))bis-(1H-pyrazole-3,5-dicarboxylic acid)), has been hydrothermally synthesized and characterized by IR spectrum, elemental analysis, TGA and X-ray single-crystal/powder diffraction. Structural analyses reveal that complex **1** exhibits a two-dimensional sheet structure in the crystal lattice. In complex **1**, the carboxylic oxygen atoms and conjugated N atoms of  $\text{pbmpd}^{4-}$  bridge zinc(II) ions form indefinitely zigzag shaped one-dimensional chains through  $\pi \cdots \pi$  stacking interactions which are further connected by  $[\text{ZnO}_6]$  units to form a novel two-dimensional structure. Finally,  $\pi \cdots \pi$  stacking interactions and intermolecular hydrogen bonds assemble the two dimensional networks into a three-dimensional framework. Furthermore, the luminescent properties are also discussed. Interestingly, the solid state photoluminescence properties of the title polymer show the enhancement effect of spectrum. Density functional theory (DFT) calculations were used to support the experimental data.

**Keywords:** Zn(II) complex; crystal structure; 1,1'-(1,4- phenylenebis(methylene)) bis-(1H-pyrazole-3,5-dicarboxylic acid); fluorescence property; DFT study

## 1. Introduction

Luminescent metal–organic frameworks (LMOFs), as important functional crystalline materials, are gaining increasing attention in sensing applications during the past few years owing to their high sensitivity, short response time and their ability to be employed both in solution and the solid phase.<sup>1–3</sup> Therefore, the synthesis of LMOFs is the basis of such work. LMOFs can be synthesized quickly and conveniently through self-assembly of  $\pi$ -conjugated multidentate organic bridging ligands with  $d^{10}$  metal ions or/and lanthanide metal ions.<sup>4,5</sup> Furthermore, such ligands also possess a better selective recognition ability, higher chemical and thermal stability and so on.<sup>6,7</sup>

Polycarboxylates based pyrazole as a kind of  $\pi$ -electron rich ligand, have great benefits for the formation 2D or 3D metal–organic frameworks (MOFs), some of these, which contain  $\text{Zn}^{2+}/\text{Cd}^{2+}$  ions and/or clusters, often possessing good photoluminescence properties.<sup>8,9</sup> Furthermore, rigid multicarboxylate ligands as bridging or building blocks play crucial roles in the construction of stable coordination frameworks, but their skeleton

structures are limited. In contrast, flexible multicarboxylate ligands have remarkable advantages because their conformational freedom and flexibility can be fine-tuned by themselves to match with the coordination preference of metal ions and lower the energetic arrangement in the self-assembly process. The synthesis of coordination polymers based on flexible multicarboxylate is also influenced by the chemical and structural features of organic ligands, metal-to-ligand ratio, the coordination geometries of the metal, pH value, temperature, solvent and so on. Among these factors, the key factor is the selection of the organic ligand, which determines the topology of the synthetic architecture through its excellent coordination capabilities and versatile bridging modes. Therefore, multifarious tetracarboxylate ligands have been utilized to create desired coordination polymers with fascinating frameworks and properties, such as 5,5'-(1H-1,2,3-triazole-1,4-diyl)di-isophthalic acid,<sup>10</sup> 5,5'-(1,4-Phenylenebis(methylene) bis(oxy)di-isophthalic acid,<sup>11</sup> 1,1'-bis(3,5-dicarboxybenzyl)-4,4'-bipyridinium dichloride,<sup>12</sup> 2,3,3',4'-diphenyl ether tetracarboxylic acid.<sup>13</sup> To date, the coordination

polymers built from 1,1'-(1,4-phenylenebis(methylene))bis(1H-pyrazole-3,5-dicarboxylic acid) have rarely been explored.<sup>14, 15</sup>

Herein, we selected the ligand, 1,1'-(1,4-phenylenebis(methylene))bis(1H-pyrazole-3,5-dicarboxylic acid) ( $H_4pbmpd$ ) which the four carboxyl groups linked by two flexible  $-CH_2-$  groups and two free N atoms offer ample coordination capacities and the ability to adapt its conformation to geometrical requirements leading to producing interesting structures with amazing properties and successfully synthesized a new 2D MOF,  $\{[Zn_2(pbmpd)(H_2O)_4] \cdot (H_2O)_n\}$ . The synthesized samples were characterized by X-ray single-crystal and powder diffractions, thermal gravimetric analysis and infrared spectra. In addition, we have also discussed the photoluminescence mechanism via density functional theory (DFT) calculations.

## 2. Experimental

### 2.1. Materials and Measurements

$H_4pbmpd$  was purchased from Jinan Henghua Science & Technology Co. Ltd, China (Fig. 1). All solvents and other reagents were commercially available and were used without further purification. The IR spectrum for complex **1** was recorded in a KBr pellet in the range of 4000–400  $cm^{-1}$  on a Bruker TENSOR27 spectrometer. Element analysis was carried out using a CHNO Rapid instrument. Powder X-ray diffraction (PXRD) data were collected on a Bruker D8 Advance with Cu  $K\alpha$  radiation ( $\lambda = 1.5418 \text{ \AA}$ ). The thermogravimetric analysis (TGA) was carried out with a Dupont thermal analyser in the temperature range of 293–1073 K under an  $N_2$  atmosphere with a heating rate of 10  $K \text{ min}^{-1}$ .

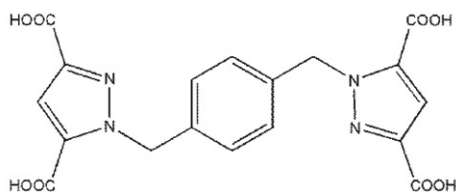


Fig. 1. 1,1'-(1,4-Phenylenebis(methylene))bis(1H-pyrazole-3,5-dicarboxylic acid,  $H_4pbmpd$ )

### 2.2. Synthesis of $\{[Zn_2(pbmpd)(H_2O)_4] \cdot (H_2O)_n\}$ (**1**)

A mixture of  $H_4pbmpd$  (33.2 mg, 0.05 mmol),  $Zn(NO_3)_2 \cdot 4H_2O$  (36.5 mg, 0.10 mmol) and a 12 mL of acetonitrile / water (2 : 10, V/V) was placed in a 15 mL of Teflon-lined stainless steel autoclave. The mixture was heated under autogenous pressure at 433 K for 72 h and then cooled to room temperature. Colourless block crystals were collected by filtration, washed with  $H_2O$ , and

dried in air. (yield: 75%, based on  $H_4pbmpd$ ). Analysis calculated for  $C_{18}H_{20}Zn_2N_4O_{13}$ : C 34.33, H 2.86, N 8.90%; found: C 34.38, H 2.81, N 8.93%. IR (KBr,  $\nu$ ,  $cm^{-1}$ , s for strong, m medium, w weak): 3416 m, 1594 s, 1534 s, 1485 s, 1431 m, 1349 s, 1289 m, 1208 w, 1131 m, 1023 s, 854 m, 794 s, 555 m.

### 2.3. Crystal Structure Determination

Diffraction data were collected using a SuperNova (Cu) X-ray Source diffractometer utilizing Cu- $K\alpha$  ( $\lambda = 1.5418 \text{ \AA}$ ) radiation at 173 K. The structure was solved by direct methods employed in the program SHELXS-2014, and refined by full-matrix leastsquares methods against  $F^2$  with SHELXL-2016.<sup>16</sup> The cell parameters were determined by SMART software. Data reduction was performed with SAINT Plus. Program SADABS was used for absorption corrections. All non-H atoms were refined anisotropically, hydrogen atoms attached to C atoms were placed geometrically and refined using a riding model approximation, with  $C-H = 0.93 \text{ \AA}$  and  $U_{iso}(H) = 1.2U_{eq}(C)$ . H atoms bonded to O were located firstly in a difference Fourier map and were refined freely. Tentative free refinements of their positional coordinates resulted in an unsatisfactory wide range of O–H and H...H (in water) distances; bond lengths were therefore restrained to 0.82 (1)  $\text{\AA}$  for O–H. The H...H (in water) distances were restrained to 1.32 (1)  $\text{\AA}$ . The O–H distances of water molecules are in the range

Table 1. Crystal data and structure refinement for Complex **1**

	<b>1</b>
Empirical formula	$C_{18}H_{20}Zn_2N_4O_{13}$
Formula weight	631.12
Temperature	173 K
Crystal system	monoclinic
Space group	$P2_1/c$
$a / \text{\AA}$	$a = 12.8594 (4)$
$b / \text{\AA}$	$b = 14.7599 (4)$
$c / \text{\AA}$	$c = 11.4301 (4)$
$\beta / (^\circ)$	$\beta = 91.303(3)$
$V / \text{\AA}^3$	2168.91 (1)
$Z$	4
Density (calculated)	1.933 $mg/m^3$
Absorption coefficient	3.477 $mm^{-1}$
$F(000)$	1280
Crystal size	$0.20 \times 0.20 \times 0.10 \text{ mm}^3$
$\theta$ range for data collection	2.7 to $26.5^\circ$
Reflections collected	8113
Independent reflections	3951 [ $R_{int} = 0.029$ ]
Completeness to $\theta = 25.50^\circ$	96.7 %
Refinement method	Full-matrix least-squares on $F^2$
Data / restraints / parameters	3951/ 0/334
Goodness-of-fit on $F^2$	1.040
Final $R$ indices [ $I > 2\sigma(I)$ ]	$R_1 = 0.0306$ , $wR_2 = 0.0819$
$R$ indices (all data)	$R_1 = 0.0389$ , $wR_2 = 0.0769$

Table 2. Selected Bond Lengths (Å) and Bond Angles (°) for Complex 1

1			
Zn(1)–O(9)	1.9886 (1)	Zn(1)–O(5)	2.0330 (1)
Zn(1)–N(1)	2.124 (2)	Zn(1)–N(3)	2.065 (2)
Zn(2)–O(3)	2.119 (2)	Zn(2)–O(4)	2.400 (2)
Zn(2)–O(10)	2.0237 (1)	Zn(2)–O(11)	2.028 (2)
Zn(1)–O(1)	2.0185 (1)	Zn(2)–O(7)	2.0815 (1)
Zn(2)–O(12)	2.0888 (1)		
O(9)–Zn(1)–O(1)	88.35 (8)	O(1)–Zn(1)–O(5)	168.77 (8)
O(9)–Zn(1)–O(5)	88.63 (8)	O(9)–Zn(1)–N(3)	111.19 (9)
O(9)–Zn(1)–N(1)	145.25 (9)	O(5)–Zn(1)–N(1)	96.65 (8)
O(1)–Zn(1)–N(1)	79.85 (8)	O(1)–Zn(1)–N(3)	109.27 (8)
O(10)–Zn(2)–O(12)	93.91 (8)	O(7)–Zn(2)–O(12)	175.82 (8)
O(11)–Zn(2)–O(12)	82.05 (8)	O(10)–Zn(2)–O(3)	141.17 (8)
O(10)–Zn(2)–O(4)	84.48 (7)	O(12)–Zn(2)–O(3)	93.05 (8)
O(7)–Zn(2)–O(4)	98.53 (7)	O(10)–Zn(2)–O(11)	104.55 (8)
O(10)–Zn(2)–O(7)	86.70 (8)	O(3)–Zn(2)–O(4)	58.05 (8)
O(5)–Zn(1)–N(3)	81.90 (8)	N(3)–Zn(1)–N(1)	103.55 (8)
O(11)–Zn(2)–O(3)	114.24 (8)	O(7)–Zn(2)–O(3)	89.04 (8)
O(11)–Zn(2)–O(4)	165.16 (8)	O(12)–Zn(2)–O(4)	85.64 (8)
O(11)–Zn(2)–O(7)	93.79 (8)		

Table 3. Hydrogen Bond Lengths (Å) and Bond Angles (°) for Complex 1

D–H...A	d(D–H)	d(H...A)	d(D...A)	∠DHA
O(13)H(13B)...O(8) <sup>v</sup>	0.82	2.04	2.848 (3)	167
O(13)–H(13A)...O(6)	0.82	1.91	2.704 (3)	162
C(13)–H(13)...O(9) <sup>vi</sup>	0.95	2.57	3.289 (3)	133
C(11)–H(11B)...O(13) <sup>vii</sup>	0.99	2.50	3.388 (3)	149
C(11)–H(11A)...O(8) <sup>v</sup>	0.99	2.32	2.974 (3)	122
C(4)–H(4B)...O(4)	0.99	2.33	2.981 (4)	123
C(2)–H(2)...O(4) <sup>i</sup>	0.95	2.30	3.246 (3)	171
O(12)–H(12B)...O(2) <sup>viii</sup>	0.82	1.96	2.746 (3)	160
O(12)–H(12A)...O(2) <sup>iii</sup>	0.82	1.91	2.715 (3)	167
O(11)–H(11D)...O(1) <sup>viii</sup>	0.82	1.94	2.735 (3)	162
O(11)–H(11C)...O(13) <sup>ix</sup>	0.82	1.90	2.690 (3)	163
O(10)–H(10B)...O(3) <sup>iii</sup>	0.82	2.15	2.949 (3)	167
O(10)–H(10A)...O(6) <sup>ix</sup>	0.82	1.85	2.654 (3)	169
O(9)–H(9B)...O(8) <sup>x</sup>	0.82	1.96	2.731 (3)	157
O(9)–H(9A)...O(7) <sup>xi</sup>	0.82	1.95	2.767 (3)	172
Cg1...Cg1 <sup>vi</sup>			4.117 (1)	
Cg1...Cg2			3.582 (1)	
C(6)–H(6)...Cg3	0.95	2.95	3.665 (3)	130
C(4)–H(4A)...Cg3 <sup>xi</sup>	0.99	2.86	3.479 (3)	124

Symmetry codes: (i)  $x, -y+1/2, z-1/2$ ; (iii)  $x, -y+1/2, z+1/2$ ; (v)  $x-1, -y+1/2, z+1/2$ ; (vi)  $-x, -y+1, -z+1$ ; (vii)  $-x, y-1/2, -z+3/2$ ; (viii)  $-x+1, y-1/2, -z+1/2$ ; (ix)  $-x+1, y-1/2, -z+3/2$ ; (x)  $-x+1, y+1/2, -z+1/2$ ; (xi)  $-x+1, -y+1, -z+1$ .

0.8199–0.8205 Å. A summary of the crystallographic data, data collection and refinement parameters for complex 1 is provided in Table 1. Selected bond lengths, bond angles and H-bonds for complex 1 are listed in Tables 2 and 3, respectively. The molecular graphics were prepared using the SHELXL-2016 and MERCURY programs.<sup>17,18</sup>

## 2. 4. Hirshfeld Surface Analysis

The Hirshfeld surface analysis<sup>19</sup> and the related 2D-fingerprint plots<sup>20</sup> were calculated using Crystal Explorer.<sup>21</sup> The CIF file of the structure 1 was imported into Crystal Explorer and high resolution Hirshfeld surfaces were mapped with the function  $d_{\text{norm}}$ . Then, the Hirshfeld surfaces were resolved into 2D-fingerprint plots, in order to quantitatively determine the nature and type of all intermolecular contacts experienced by the molecules in the crystal.

## 3. Results and Discussion

### 3. 1. IR Characterization

The peaks of FT-IR point out that the strong band around 1522 cm<sup>-1</sup> resulting from stretching vibration of carboxyl (C=O) in the free ligand is disappeared and split into two new bands at 1594 cm<sup>-1</sup> and 1534 cm<sup>-1</sup> in complex 1, which are assigned to symmetric and asymmetrical stretching vibrations of carboxyl (C=O). It suggests that the carboxyl of the ligand had been deprotonated and coordinated to the Zn(II).<sup>22</sup> Complex 1 also shows broad absorptions in the range between 3416 cm<sup>-1</sup> associated with hydrogen-bonded O–H stretching vibration.<sup>23</sup>

### 3. 2. Crystal Structure of Complex 1

The two-dimensional coordinate polymer 1 crystallizes in the  $P2_1/c$  space group of the monoclinic crystal system and shows a 2D structure. The asymmetric unit of 1 contains two independent Zn<sup>2+</sup> ions, one deprotonated pbmpd<sup>4-</sup> ligand, four coordinated water molecules

and one solvent water molecule. As depicted in Fig. 2, the Zn(1) and Zn(2) centers exhibit different coordinated environments. Zn(2) exhibits distorted hexa-coordinated environments with one monodentate oxygen atom from the pbmpd<sup>4-</sup> ligand (Zn(2)–O(7)), two chelating oxygen atoms originating from another pbmpd<sup>4-</sup> ligand (Zn(2)–O(3) and Zn(2)–O(4)) and three oxygen atoms (Zn(2)–O(10), Zn(2)–O(11) and Zn(2)–O(12)) derived from the coordinated water molecules. The Zn–O coordination distances range from 2.081 (18) to 2.398 (2) Å which are all within the normal ranges.<sup>24–26</sup> Zn(1) is penta-coordinated and displays a square pyramidal ZnN<sub>2</sub>O<sub>3</sub> geometry which is coordinated by three oxygen atoms (O(9), O(5) and O(1)) and two nitrogen atoms (N(1) and N(3)). The O(9) atom is from a terminal coordinated water molecule and O(1) and O(5) oxygen atoms are from monodentate carboxylate groups of pyrazole-carboxylate units from two different ligands. Two monodentate pyrazole nitrogen atoms (N(1) and N(3)) are derived from the two ligands. The Zn–O coordination distances range from 1.935 (7) to 2.204 (16) Å and Zn–N coordination distances range from 2.075 (4) to 2.139 (4) Å, which are also observed in reported zinc compounds.<sup>27, 28</sup> Atoms O(9), O(5), O(1) and N(1), which are nearly coplanar (the mean deviation from the common best plane is 0.147 Å), complete the square base plane, while the vertex is occupied by atom N(3) of which the distance to the square plane is 2.392 (2) Å. The selected bond lengths are listed in Table 2.

In the structure of **1**, the carboxylic oxygen atoms and conjugated N atoms bridge Zn(1) ions form an indefinitely zig-zag shaped 1D Zn(1) chains along the *c* axis through  $\pi$ – $\pi$  stacking interactions between the ring Cg1 (N(3)/N(4)/C(12)–C(14)) and the ring Cg2 (C(5)–C(10)) with the centroid distance of 3.582 (1) Å and the Zn...Zn distance is 11.43 Å (Fig. 3). Meanwhile, the Zn(1) chains are further connected by [Zn<sub>2</sub>O<sub>6</sub>] units to form a novel 2D structure (Fig. 4). The  $\pi$ – $\pi$  stacking interaction between the adjacent rings Cg1 (N(3), N(4), C(12), C(13), C(14)) and Cg1<sup>i</sup> with the centroid distance of 4.117 (1) Å, lead to a weak interconnection of these layers into a three-dimensional (3D) framework. This type of self-assembled dimers has been studied in Cd(II) complex with the similar ligand.<sup>29</sup> In addition, C(6)–H(6)...Cg3 (N(1)/N(2)/C(1)–C(3)) and C(4)–H(4A)...Cg3<sup>ii</sup> interactions (see Fig. 5), with distances of 2.86 Å and 2.95 Å respectively, are also found to stabilize the 3D network.

There are interesting strong O–H...O hydrogen bonds among the rich carboxyl molecules. Viewing along *bc* plane, inter-molecular hydrogen bonds among carboxylate from pyrazole-carboxylate and coordinated water molecules O atoms, named O(13)–H(13B)...O(8)<sup>i</sup>, O(12)–H(12B)...O(2)<sup>vii</sup>, O(13)–H(13A)...O(6), O(9)–H(9B)...O(8)<sup>viii</sup>, O(9)–H(9A)...O(7)<sup>ix</sup>, O(10)–H(10B)...O(3)<sup>vi</sup>, O(12)–H(12B)...O(2)<sup>v</sup> connect the two-dimensional coordination network into a three-dimensional framework (Fig. 6). Interatomic distances ranging from 0.2654 (3) to 2.949

(3) Å and angles within 157.4–172.4° indicated strong hydrogen bonds. Meanwhile the intra-molecular hydrogen bonds named O(13)–H(13A)...O(6) with the distance is 2.704 (3) Å is also been found to strengthen the network. The detailed hydrogen bonds are listed in Table 3.

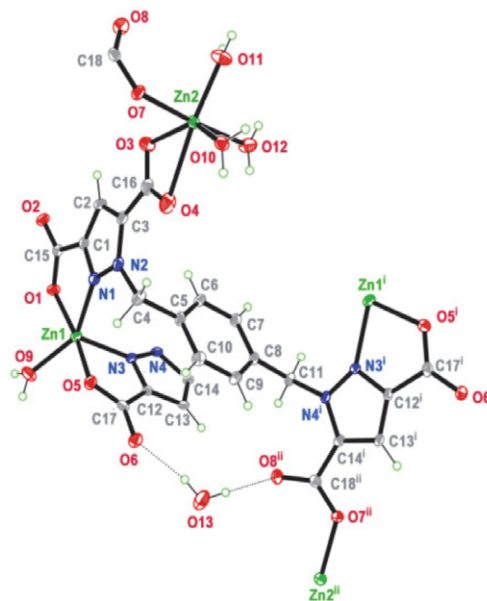


Fig. 2. The atom labels and coordination environments of the Zn(II) ions in complex **1**, with displacement ellipsoids drawn at the 30% probability level. Dashed lines represent hydrogen bonds.

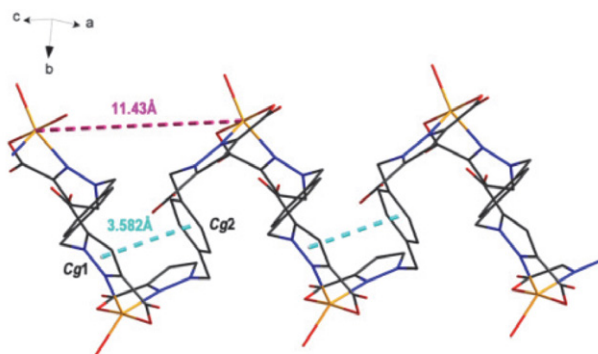


Fig. 3. The infinite one-dimensional zigzag shaped chain formed from Zn(2) atoms and pbmpd<sup>4-</sup> ligands through  $\pi$ – $\pi$  stacking interactions (blue dashed lines) along the *c* axis.

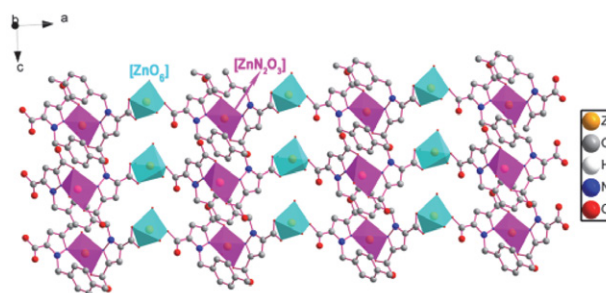


Fig. 4. The two-dimensional sheets extending in the *ac* plane formed by layers packed through with [ZnO<sub>6</sub>] and [ZnN<sub>2</sub>O<sub>3</sub>] units.



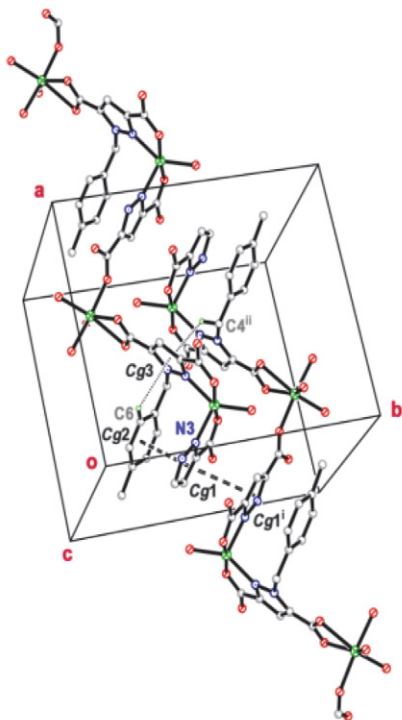


Fig. 5.  $\pi\cdots\pi$  stacking interactions (open dashed lines) and C-H $\cdots\pi$  interactions (dashed lines) present in complex 1.

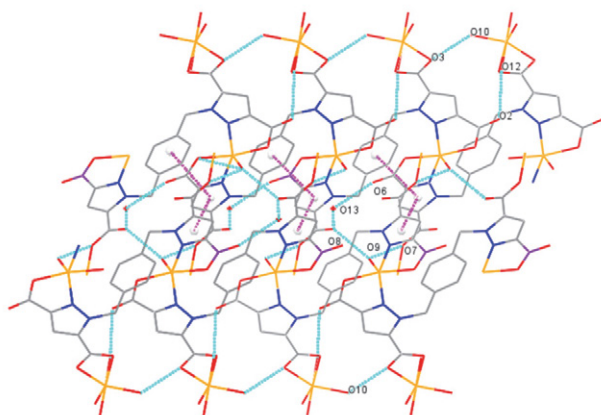


Fig. 6. The three-dimensional network through  $\pi\cdots\pi$  stacking interactions (purple lines) and inter-molecular hydrogen bonds (blue lines) viewing along  $ac$  plane. White balls represent the centroid of the rings. (Symmetry codes: (i)  $x - 1, -y + 1/2, z + 1/2$ ; (v)  $-x + 1, y - 1/2, -z + 1/2$ ; (vi)  $x, -y + 1/2, z + 1/2$ ; (vii)  $-x + 1, y - 1/2, -z + 3/2$ ; (viii)  $-x + 1, y + 1/2, -z + 1/2$ ; (ix)  $-x + 1, -y + 1, -z + 1$ .)

### 3. 3. Hirshfeld Surface Analysis

The intermolecular interactions in crystal structure **1** were quantified using Hirshfeld surface analysis and fingerprint plots (FP). The dominant intermolecular interactions are viewed as a bright red area on the  $d_{\text{norm}}$  surface. Fig. 7 illustrates samples of Hirshfeld surfaces for structure **1**. In **1**, we observe a high level of O $\cdots$ H interactions due to

the hydrogen bonds between solvents molecules and the complex. The two-dimensional fingerprint plots for complex **1** are shown in Fig. 8. The proportions of C-H $\cdots\pi$ ,  $\pi\cdots\pi$  and O-H $\cdots$ O interactions are 11.2%, 8.8% and 39.6% of the total Hirshfeld surfaces for complex **1**. It appears that in this complex rich in aromatic rings, contact characteristics of  $\pi$ -stacking or C-H/ $\pi$  interactions are less important.

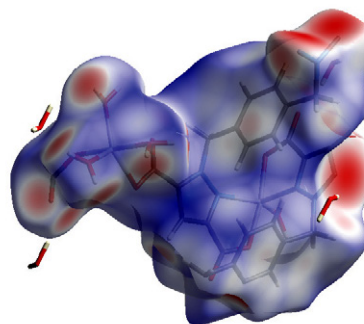


Fig. 7. Views of the Hirshfeld surfaces for **1** mapped with  $d_{\text{norm}}$ .

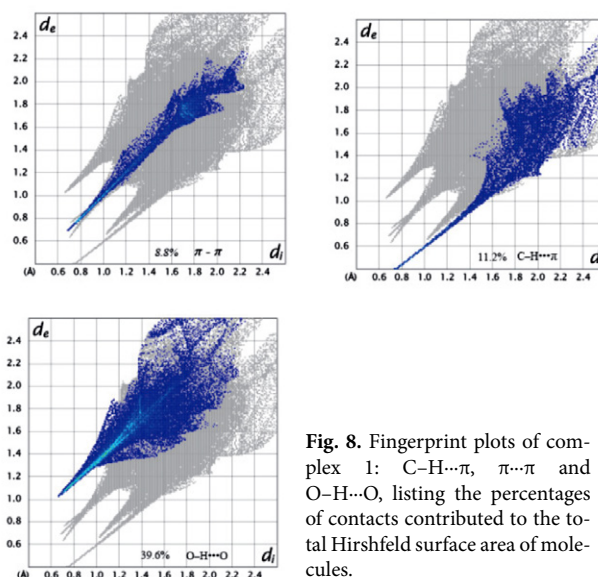


Fig. 8. Fingerprint plots of complex **1**: C-H $\cdots\pi$ ,  $\pi\cdots\pi$  and O-H $\cdots$ O, listing the percentages of contacts contributed to the total Hirshfeld surface area of molecules.

### 3. 4. PXRD and TG Analyses

To confirm that the phase of the bulk sample is pure and the crystal structure of complex **1** is truly representative of the bulk material, a powder X-ray diffraction (PXRD) experiment was carried out on a Bruker D8 Advance with Cu K $\alpha$  radiation ( $\lambda = 1.5418 \text{ \AA}$ ). The as-synthesized sample of **1** is characterized by powder X-ray diffraction (PXRD). As shown in Fig. 9a, the PXRD patterns are almost consistent with the simulated spectrum, demonstrating the high phase purity of the compounds.

As shown in Fig. 9(b), the TGA for complex **1** shows a weight loss of 12.1% (calculated 14.2%) between 293 K and 605 K, which is associated with the loss of one solvent



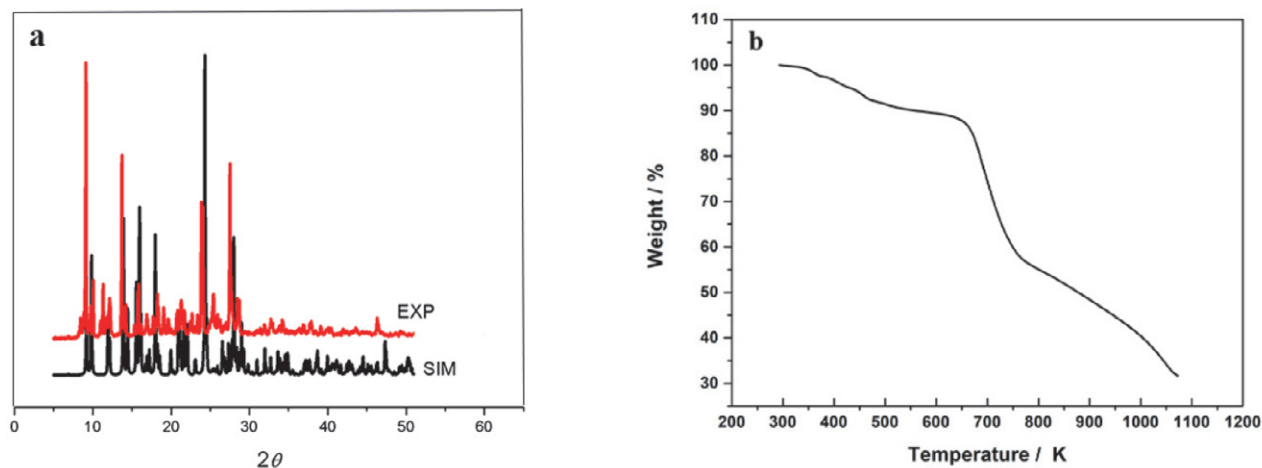


Fig. 9. (a) Comparison of the simulated and experimental PXRD patterns of complex 1. (b) Thermogravimetric analysis (TGA) curve of complex 1

water molecule and four coordinated water molecules. When the temperature is up to 646 K, the frameworks of complex 1 begin to break down gradually.

### 3. 5. Fluorescence Properties and DFT Calculation

The luminescent properties of complex 1 and free ligand were examined in the solid state at room temperature. As depicted in Fig. 10, the emission of free H<sub>4</sub>pbmpd is weak, whereas complex 1 reveals an obviously strong emission; and the maximum emission of 1 at ca. 448 nm has a blue shift compared with that of the free H<sub>4</sub>pbmpd ligand observed at  $\lambda_{em} = 495$  nm ( $\lambda_{ex} = 300$  nm). In order to obtain a better insight into the nature of the photoluminescence of complex 1, we investigated the structural, electronic and optical properties with  $S_0$  using DFT calculations at the B3LYP/6-31+G\* level of the Gaussian 09 program and  $S_1$  using TD-DFT calculations at the B3LYP/6-31+G\* level of the Gaussian 09 program.<sup>30</sup> The geometry was taken from the crystal structure. According to Kasha's rule,<sup>31</sup> the fluorescence of the compounds is only emitted from the lowest singlet excited states ( $S_1$ ) to the singlet ground state ( $S_0$ ). As depicted in Fig. 11, for complex 1, in the  $S_1$  state, the HOMO is located more on the  $\pi$  orbitals of the pyrazole-carboxylate moiety of the ligand, and the LUMO is mainly located on the  $\pi^*$  orbital of the pyrazole-phenyl moiety. Obviously, the LUMO and HOMO orbits of complex 1 are both distributed over the ligand, and their emission bands can thus be clearly assigned to the ILCTs. Meanwhile, the HOMO–LUMO energy gap of compound 1 is larger than that of the free ligand, which leads to the blue shift of the emission peak (47 nm) compared with the free H<sub>4</sub>pbmpd ligand, indicating that the HOMO–LUMO energy gap decreases to make the blue shift, as reported for other pyrazole derivat-ed polycarboxylate complexes.<sup>32</sup> The enhanced emission intensity of complex 1 may arise from the aggregation in-

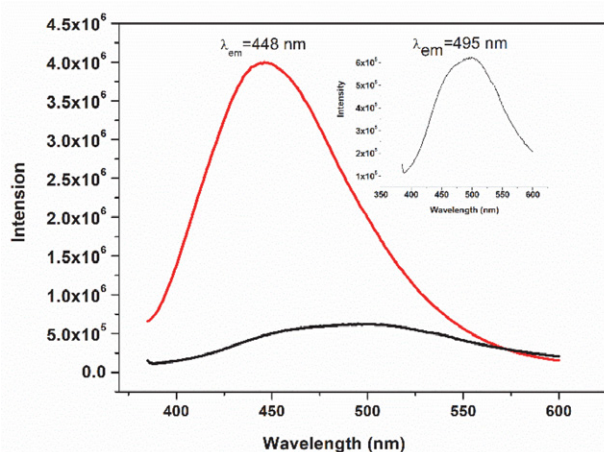


Fig. 10. Solid-state emission spectra of H<sub>4</sub>pbmpd (black) and complex 1 (red) at room temperature (inset: enlarged view of emission spectra of H<sub>4</sub>pbmpd).

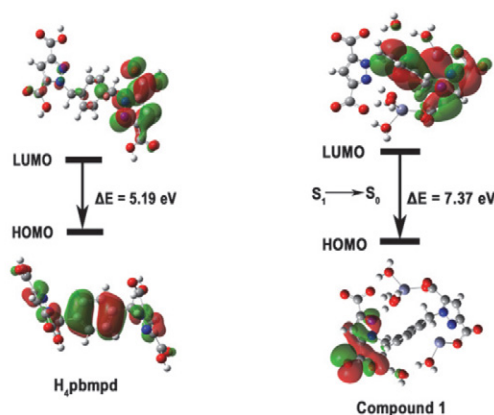


Fig. 11. The frontier MOs and the DFT calculations of H<sub>4</sub>pbmpd ligand and complex 1.

duced emission, where the coordination of the ligand and the metal ions can reduce the freedom of the ligands and their non-radiative transitions.<sup>33,34</sup>

## 4. Conclusion

A new 2D Zn(II) compound based on 1,1'-(1,4-phenylenebis(methylene))bis-(1H-pyrazole-3,5-dicarboxylic acid) has been constructed successfully. Complex **1** is consisted of two independent Zn<sup>2+</sup> ions but have different coordinated environments, one of which exhibits distorted hexa-coordinated environments, while the other displays a square pyramid ZnN<sub>2</sub>O<sub>3</sub> geometry. In complex **1**, the indefinitely zig-zag shaped 1D chains formed by the ligand pbmpd<sup>4-</sup> bridged Zn ions and [Zn<sub>2</sub>O<sub>6</sub>] units to form a 2D structure. In addition, compared to the ligand, the solid state photoluminescence properties of complex **1** show an obviously strong emission, which is assigned to the ILCTs by Density functional theory (DFT) calculations.

## Supplementary Material

CCDC 1923324 contains the supplementary crystallographic data for this paper. These data can be obtained free of charge from The Cambridge Crystallographic Data Centre via <http://www.ccdc.cam.ac.uk/conts/retrieving.html>.

## Acknowledgments

Authors appreciated the Startup Fund of Doctors of Jinzhong University. A portion of this work was performed on the Scientific Instrument Center of Shanxi University of China.

## 6. References

1. M. Pan, W. M. Liao, S.Y. Yin, S.S. Sun, C.Y. Su, *Chem Rev* **2018**, *118*, 8889–8935; DOI:10.1021/acs.chemrev.8b00222
2. H. Y. Li, S. N. Zhao, S. Q. Zang, J. Li, *Chem Soc Rev* **2020**, *49*, 6364–6401; DOI:10.1039/C9CS00778D
3. X. Y. Liu, W. P. Lustig, J. Li, *Chem. Rev* **2020**, *5*, 2671–2680; DOI:10.1021/acsenergylett.0c01148
4. Y. W. Li, J. Li, X. Y. Wan, D. F. Sheng, H. Yan, S. S. Zhang, H. Y. Ma, S. N. Wang, D. C. Li, Z. Y. Gao, J. M. Dou, D. Sun, *Inorg. Chem* **2021**, *60*, 671–681; DOI:10.1021/acs.inorgchem.0c02629
5. W. B. Liu, N. N. Li, X. Zhang, Y. Zhao, Z. Zong, R. X. Wu, J. P. Tong, C. F. Bi, F. Shao, Y. H. Fan, *Cryst. Growth Des* **2021**, *21*, 5558–5572; DOI:10.1021/acs.cgd.1c00359
6. A. Mukhopadhyay, S. Sindal, G. Savitha, J. N. Moorthy, *Inorg. Chem* **2020**, *59*, 6202–6213; DOI:10.1021/acs.inorgchem.0c00307
7. F. Y. Yi, M. L. Gu, S. C. Wang, J. Q. Zheng, L. Q. Pan, L. Han, *Inorg. Chem* **2018**, *57*, 2654–2662; DOI:10.1021/acs.inorgchem.7b03053
8. W. Q. Tong, W. N. Liu, J. G. Cheng, P. F. Zhang, G. P. Li, L. Hou, Y. Y. Wang, *Dalton Trans* **2018**, *47*, 9466–9473; DOI:10.1039/C8DT01694A
9. C. Feng, Y. H. Ma, D. Zhang, X. J. Li, H. Zhao, *Dalton Trans* **2016**, *45*, 5081–5091; DOI:10.1039/C5DT04740D
10. L. B. Sun, Y. Li, Z. Q. Liang, J. H. Yu, R. R. Xu, *Dalton Trans* **2012**, *41*, 12790–12796; DOI:10.1039/c2dt31717f
11. X. He, X. P. Lu, M. X. Li, R. E. Morris, *Cryst. Growth Des* **2013**, *13*, 1649–1654; DOI:10.1021/cg3018562
12. L. K. Li, H. Y. Li, Li Ting, L. H. Quan, J. Xu, F. A. Li, S. Q. Zang, *CrystEngComm* **2018**, *20*, 6412–6419; DOI:10.1039/C8CE01335G
13. Q. Yue, Y. Y. Wang, X. L. Hu, W. X. Guo, E. Q. Gao, *Cryst-EngComm* **2019**, *21*, 6719–6732; DOI:10.1039/C9CE01128E
14. Y. P. Xia, Y. W. Li, D. C. Li, Q. X. Yao, Y. C. Du, J. M. Dou, *Cryst-EngComm* **2015**, *17*, 2459–2463; DOI:10.1039/C5CE00162E
15. F. F. Li, M. L. Zhu, L. P. Lu, A. Wang, *Journal of Solid State Chemistry* **2020**, *290*, 121582–121590; DOI:10.1016/j.jssc.2020.121582
16. G. M. Sheldrick, SHELXS-97, Program for X-ray Crystal Structure Solution. University of Göttingen, Germany **1997**.
17. Mercury 2.3 Supplied with Cambridge Structural Database, CCDC, Cambridge, U.K. **2003–2004**.
18. L. Y. Zhang, L. P. Lu, M. L. Zhu, *Chin. J. Struct. Chem* **2018**, *37*, 427–436; DOI: 10.14102/j.cnki.0254-5861.2011-1752
19. M. A. Spackman, D. Jayatilaka, *CrystEngComm* **2009**, *11*, 19–32; DOI:10.1039/B818330A
20. M. A. Spackman, J. J. McKinnon, *CrystEngComm*, **2002**, *4*, 378–392; DOI:10.1039/B203191B
21. S. K. Wolff, D. J. Grimwood, J. J. McKinnon, M. J. Turner, D. Jayatilaka, M. A. Spackman, CrystalExplorer (Version 3.1), University of Western Australia, **2012**.
22. Q. K. Zhou, N. Y. Li, *Acta Cryst* **2017**, *C73*, 749–753; DOI:10.1107/S2053229617012189
23. G. M. Sheldrick, *Acta Crystallogr. Sect C* **2015**, *71*, 3–8; DOI:10.1107/S2053229614024218
24. Y. Y. An, L. P. Lu, M. L. Zhu, *Chin. J. Struct. Chem* **2018**, *37*, 1479–1485; DOI: 10.14102/j.cnki.0254-5861.2011-1945
25. Y. M. Zhang, S. Yuan, G. Day, X. Wang, X. Y. Yang, H. C. Zhou, *Coord. Chem. Rev* **2018**, *354*, 28–45; DOI:10.1016/j.ccr.2017.06.007
26. W. Yang, C. M. Wang, Q. Ma, X. N. Feng, H. L. Wang, J. Z. Jiang, *Cryst. Growth Des* **2013**, *13*, 4695–4704; DOI:10.1021/cg4007372
27. X. Q. Yao, G. B. Xiao, H. Xie, D. D. Qin, H. C. Ma, J. C. Liu, P. J. Yan, *CrystEngComm* **2019**, *21*, 2559–2570; DOI:10.1039/C8CE02122H
28. M. Y. Liu, H. Y. Yu, Z. L. Liu, *CrystEngComm* **2019**, *21*, 2355–2361; DOI:10.1039/C9CE00034H
29. F. F. Li, M. L. Zhu, L. P. Lu, *Acta Cryst* **2018**, *C74*, 967–973; DOI:10.1107/S2053229618010239
30. M. J. Frisch, GAUSSIAN09. Gaussian Inc., Wallingford, CT, USA **2009**.
31. M. Kasha, *Discuss. Faraday Soc* **1950**, *9*, 14–19; DOI:10.1039/df9500900014
32. B. Roy, S. Mukherjee, P. S. Mukherjee, *CrystEngComm* **2013**, *15*, 9596–9602; DOI:10.1039/c3ce41080c
33. S. D. Li, L. P. Lu, M. L. Zhu, *CrystEngComm* **2018**, *20*, 5442–5456; DOI:10.1039/C8CE00947C

34. J. J. Shen, M. X. Li, Z. X. Wang, *Cryst. Growth Des* **2014**, *14*, 2818–2830; DOI:10.1021/cg500092t

## Povzetek

Sintetizirali smo nov dvodimenzionalni koordinacijski polimer,  $\{[\text{Zn}_2(\text{pbmpd})(\text{H}_2\text{O})_4] \cdot (\text{H}_2\text{O})\}_n$  ( $\text{H}_4\text{pbmpd} = 1,1'-(1,4\text{-fenilenbis(metilen))bis-(1H-pirazol-3,5-dikarboksilna kislina)}$ ) in spojino karakterizirali z IR spektroskopijo, elementno analizo, TGA in rentgensko monokristalno/praškovo difrakcijo. Strukturna analiza je pokazala, da ima spojina **1** dvodimenzionalno plastovito strukturo. V strukturi spojine **1** karboksilatni kisikovi atomi in kojugirani N atomi iz  $\text{pbmpd}^{4+}$  povezujejo preko  $p \cdots \pi$  interakcij cinkove(II) ione v enodimenzionalne verige, ki so nadalje povezane preko  $[\text{ZnO}_6]$  enot v dvodimenzionalno strukturo. Dvodimenzionalne strukture so preko  $p \cdots \pi$  interakcij in intermolekularnih vodikovih vezi nadalje povezane v tridimenzionalno mrežo. Raziskali smo luminiscenčne lastnosti produkta, pri čemer je zanimivo, da fotoluminiscenca v trdnem stanju kaže povečanje učinka spektra. Za podporo eksperimentalnim podatkom smo uporabili izračune DFT.



Except when otherwise noted, articles in this journal are published under the terms and conditions of the Creative Commons Attribution 4.0 International License

Scientific paper

# Ternary Transition Metal Complexes with an Azo-Imine Ligand and 2,2'-Bipyridine: Characterization, Computational Calculations, and Acetylcholinesterase Inhibition Activities

Kerim Serbest,<sup>1,\*</sup> Turan Dural,<sup>1</sup> Demet Kızıl,<sup>3</sup> Mustafa Emirik,<sup>1</sup>  
Ali Zengin<sup>2</sup> and Barbaros Dinçer<sup>1</sup>

<sup>1</sup> Department of Chemistry, Recep Tayyip Erdogan University, 53100 Rize, Turkey

<sup>2</sup> Pazar Vocational School, Recep Tayyip Erdogan University, 53300 Pazar/Rize, Turkey

<sup>3</sup> Central Research Laboratory, Bursa Technical University, 16310, Bursa, Turkey

\* Corresponding author: E-mail: kerimserbest@yahoo.com

Tel.: +90 464 2234093

Received: 03-29-2022

## Abstract

New mononuclear ternary transition metal complexes:  $[M(HL)(bipy)_2]ClO_4$ , (M: Mn(II) for **1**, Ni(II) for **2**),  $[M(HL)(bipy)(ClO_4)]$ , (M: Ni(II) for **3**, Cu(II) for **4**, Zn(II) for **5**) with M(II), 2-[(hydroxyimino)methyl]-4-[-phenyldiazenyl]phenol,  $H_2L$ , and 2,2'-bipyridine were synthesized, and their structures were investigated by using various analytical, spectroscopic techniques such as elemental analysis, FTIR, UV-Vis, NMR, MALDI-TOF mass spectrometry, thermal analysis. The theoretical studies were performed by DFT techniques by using B3LYP function with 6-311++G (d, p)/LanLD2Z basis set. The electronic transitions charts of the complexes were further analyzed by TD-DFT/CAM-B3LYP method. IR and thermal analysis data verify the proposed structures. The inhibition activities of the complexes against acetylcholinesterase (AChE) extracted from *Ricania simulans* adults and nymphs were examined and all the complexes were found to be active. Among the complexes studied, the highest inhibition activity was exhibited by complex **5** with the lowest  $IC_{50}$  value ( $3.2 \pm 0.8 \mu M$ ) for AChE of adults and complex **3** with the lowest  $IC_{50}$  value ( $4.6 \pm 0.8 \mu M$ ) for AChE of nymphs.

**Keywords:** Metal complex; TDDFT; AChE inhibitor, *R. simulans*.

## 1. Introduction

Coordination compounds with the azo-imine ligands have gained significant importance related to their applications in several high technology areas such as liquid crystalline displays (LCD), optical storage, laser and ink-jet printers as well as in leather, textile and plastic industries.<sup>1–3</sup> They have attracted the attention of researchers because of their biological activities such as anti-microbial, antitumor, anticancer, anti-fungicidal.<sup>4–9</sup> Numerous azo compounds are used in pharmaceuticals and cosmetics although some of them have been reported to be toxic.<sup>1</sup> Coordination compounds have also been investigated for the treatment of Alzheimer's disease (AD), Parkinson's dis-

ease, aging, and those showing inhibitor activity of AChE promise in the use of therapeutic applications.<sup>10–12</sup> Some Co(II), Cu(II), Ni(II), Zn(II) complexes were reported as acetylcholinesterase inhibitors (AChEIs) and they also have the potential of use agricultural struggle because they are associated with excitation, tremors, and death in insects.<sup>10,13</sup>

The agricultural areas located on the coastal part of the Eastern Black Sea Region have recently been exposed to the damage caused by a different type of insect known as *Ricania simulans* (Walker, 1851). It has been seen in this region for the past 9 years, despite the motherland which is known to be China.<sup>14,15</sup> *R. simulans* is seen to be the type of pest where the population and the extended range of

which are on the increase with each passing day around this region.<sup>15,16</sup> The Ricaniidae family, which belongs to the group of hemipteran insects, is represented by 40 stripes (types) and 400 species. Although the species of this family show general propagation in tropical regions, *Ricania* species can also be seen in Palearctic regions.<sup>15,17–19</sup> It has a broad population in Japan, Southern China, Korea, Ukraine, Russia, and Georgia.<sup>15,20</sup> Included in the quarantine list due to the harm it caused in Korea where *R. simulans* was brought from Southern Asia to Russia in the 1900s and to Georgia in the 1950s and also to the Eastern Black Sea Region of Turkey in 2006 along with the young trees with eggs and with bush saplings.<sup>15</sup> Nymphs and adults of this pest that feed on vegetables, bushes, and trees without making a distinction of hosts rather harmful by absorbing the juice sap in the plant stems, leaves, and fruit. Tea gardens, which are among the most important product places of the coastline of the Eastern Black Sea Region, are under the threat of this pest, as well.<sup>15</sup>

Acetylcholinesterase (AChE, EC3.1.1.7) plays an important role in neurotransmission by hydrolyzing the neurotransmitter acetylcholine and is the target site of most insecticides. Vertebrates have both AChE and BuChE, whereas insects only have AChE.<sup>21,22</sup> With the importance of AChE in neurotransmission and insect resistance, much attention has been paid to AChE studies from both mammals and insects. Most of these studies use non-purified AChE from homogenates of body parts or the whole body.<sup>23</sup> There is no study on the inhibition of acetylcholinesterase of *R. simulans* with such complexes in the literature.

The density functional theory (DFT) is a useful tool for prediction of molecular structure, spectroscopic properties and chemical reactivity of molecular systems. Experimentally obtained spectroscopic results are supported by DFT-based theoretical calculations, which is a method frequently used recently. Since transition metal complexes

exhibit a wide variety of excited states, it remains difficult to accurately define the energy of excited states with the Time Dependent Density Functional Theory (TD-DFT). Because transition metal complexes exhibit a wide variety of excited states, it remains difficult to accurately describe the energy of excited states with the Time Dependent Density Functional Theory (TD-DFT). Common global descriptors of chemical reactivity of biologically active derivatives can be discussed using DFT methods.<sup>24–26</sup>

The study presents the synthesis, characterization, DFT calculation for the assignment of experimental IR and UV–Vis spectra and acetylcholinesterase inhibition effects of mononuclear ternary transition metal complexes (**1–5**) derived from azo-imine ligand 2-[(hydroxyimino)methyl]-4-[-phenyldiazenyl]phenol,  $H_2L$  and 2,2'-bipyridine (bipy) as co-ligand (Figure 1) on AChEs of adults and nymphs of *Ricania simulans*. Because cell extract provides the closest composition to the cell medium, *R. simulans* extracts were used in the inhibition studies. This study is expected to be a starting point and of great importance in the exploration of metal-based insecticide.

## 2. Results and Discussion

### 2.1. NMR Spectra

Zn(II) complex, **5** has no solubility in common organic solvents, low solubility just in DMSO, and so the proton NMR spectra were taken with difficulty (Figure 2). The proton NMR spectral data of the Zn(II) complex given in the experimental section was compared with the ligands, and the data clearly proved the formation of mixed ligand Zn(II) complex. Phenolic and oxime hydroxyl group protons in the ligand were observed as a singlets at 10.98 and 11.60 ppm, respectively. The oxime hydroxyl proton signal was very broadened and shifted to 11.15 ppm, while the phenolic hydroxyl proton signal disappeared. The singlet of

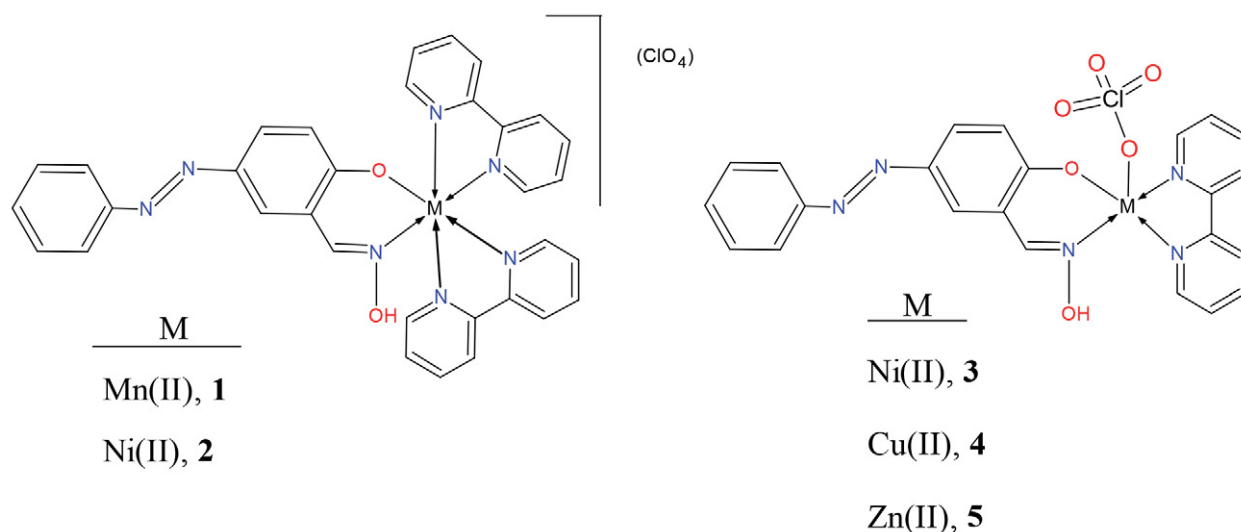


Figure 1: The proposed structures of the complexes (**1–5**) in the solid-state.

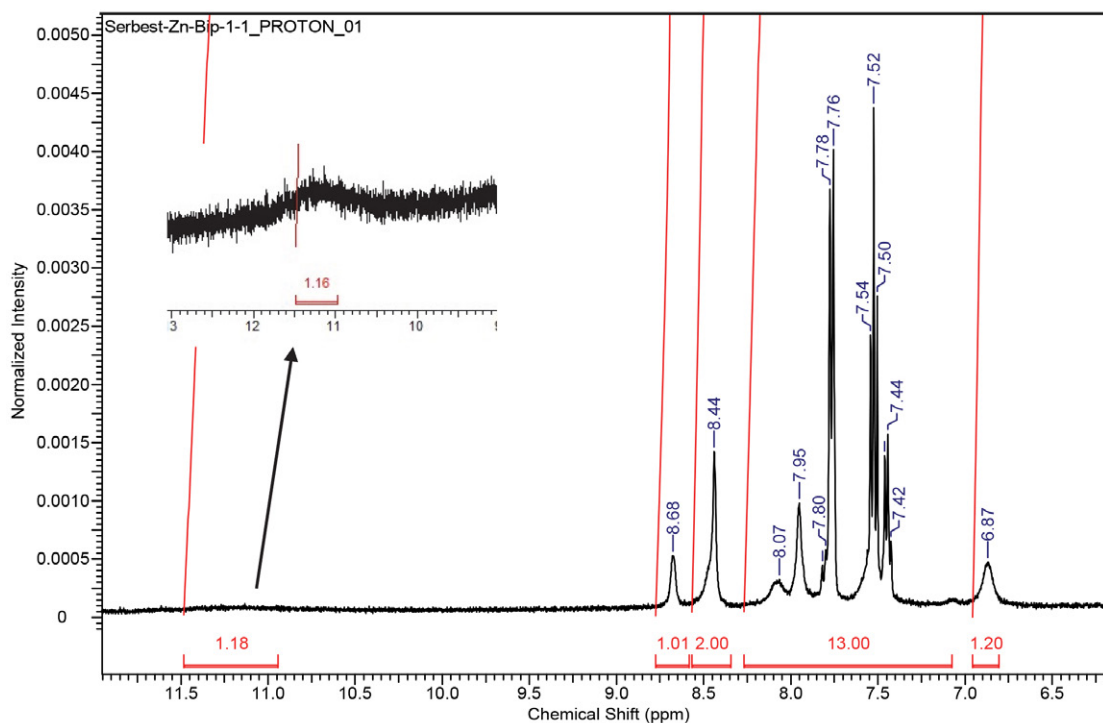


Figure 2:  $^1\text{H}$  NMR spectra of Zn(II) complex, **5** in  $\text{DMSO}-d_6$ .

imine proton was also slightly shifted to 8.44 ppm. The absence of phenolic OH proton and the low-field shift of the imine proton signal shows that the coordination of primary azo-oxime type ligand to Zn(II) ion is through the nitrogen of imine and phenolic oxygen atoms. The integrated intensities of the aromatic protons were also confirmed that Zn(II) complex contains a bipyridine molecule as co-ligand.

## 2. 2. Theoretical Calculations

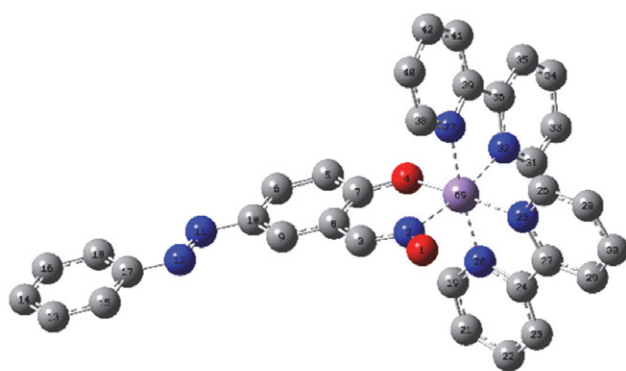
### 2. 2. 1. Molecular Structures

Geometry optimizations of the ligand and its corresponding complexes were performed using the Gaussian 09 program in the gas phase. The optimized geometry with

numbering and some of the optimized bond lengths, overlap populations, and bond orders around the metal center obtained from DFT calculations were given in Fig. 3–8.

Complexes **1**, **2**, form six-coordinated octahedral while complexes **3**, **4**, and **5** have five-coordinated distorted square-pyramidal structures.

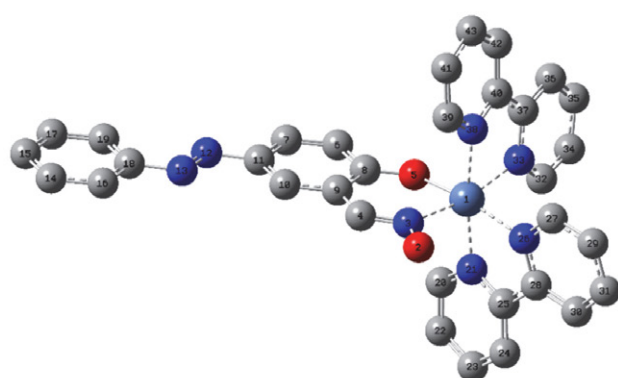
Addison, Reedijk and coworkers have proposed a geometry index for 5-coordinate transition metal complexes that can simply be calculated by taking the two largest angles around the metal center (Equation 1). The 5-coordinate index,  $\tau_5 = 1$  is for a perfect trigonal bipyramidal structure and  $\tau_5 = 0$  for a perfect square pyramidal structure.<sup>27</sup> The 5-coordinate index values of complexes **3**, **4** and **5** were found as 0.46, 0.34 and 0.17, respectively. These complexes



Bond	L	OP	BO
Mn69-N2	2.00	0.11	0.35
Mn69-O4	1.94	0.23	0.60
Mn69-N20	2.03	0.09	0.33
Mn69-N25	2.05	0.08	0.31
Mn69-N32	2.03	0.07	0.33
Mn69-N37	2.04	0.08	0.33

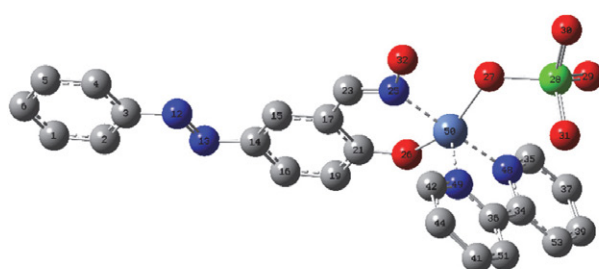
Figure 3: Optimized molecular structure of complex **1** and selected bond length in Å (L), overlap population (OP) and bond order (BO).





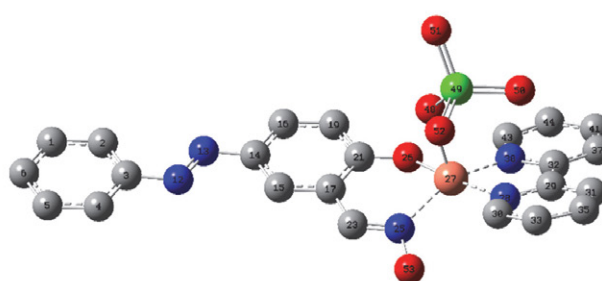
Bond	L	OP	BO
Ni1-N3	2.08	0.18	0.45
Ni1-O5	2.01	0.24	0.59
Ni1-N21	2.12	0.14	0.41
Ni1-N26	2.18	0.12	0.37
Ni1-N33	2.12	0.12	0.38
Ni1-N38	2.12	0.13	0.40

Figure 4: Optimized molecular structure of complex 2 and selected bond length in Å (L), overlap population (OP) and bond order (BO).



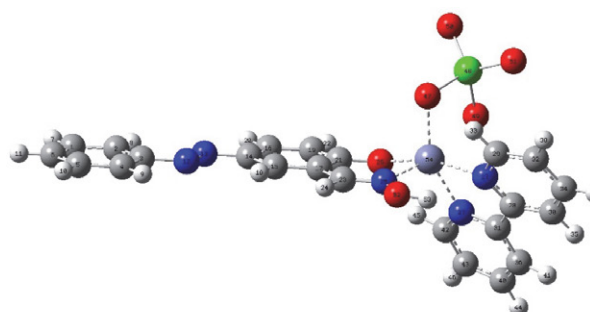
Bond	L	OP	BO
Ni50-N25	2.02	0.17	0.43
Ni50-O26	1.96	0.20	0.56
Ni50-N48	2.05	0.12	0.40
Ni50-N49	2.04	0.15	0.46
Ni50-O27	2.00	0.12	0.43

Figure 5: Optimized molecular structure of the complex 3 and selected bond length in Å (L), overlap population (OP) and bond order (BO).



Bond	L	OP	BO
Cu27-N25	2.04	0.18	0.44
Cu27-O26	1.94	0.19	0.55
Cu27-N28	2.05	0.16	0.44
Cu27-O48	2.17	0.12	0.32
Cu27-N38	2.04	0.16	0.43

Figure 6: Optimized molecular structure of the complex 4 and selected bond length in Å (L), overlap population (OP) and bond order (BO).



Bond	L	OP	BO
Zn54-N25	2.16	0.15	0.31
Zn54-O26	2.00	0.18	0.40
Zn54-N27	2.28	0.09	0.23
Zn54-N37	2.16	0.12	0.28
Zn54-O47	2.23	0.13	0.28

Figure 7: Optimized molecular structure of the complex 5 and selected bond length in Å (L), overlap population (OP) and bond order (BO).

have highly distorted coordination geometries intermediate between square-pyramidal and trigonalbipyramidal.<sup>28</sup>

$$\tau 5 = (\beta - \alpha) / 60 \quad (1)$$

**Table 1.** The two greatest valence angles around metal center for the complexes 3, 4, and 5.

Complex 3	N48-Ni50-N25	177.27	$\tau 5 = 0.46$
	O26-Ni50-O27	149.46	
Complex 4	N28-Cu27-O26	171.13	$\tau 5 = 0.34$
	N25-Cu27-N38	150.87	
Complex 5	N27-Zn54-O26	164.13	$\tau 5 = 0.17$
	O47-Zn54-N37	153.83	

The frontier orbitals' shape and the values of energies and energy gap were shown in Table 2. The energies of FMOs are important in several pharmacological and chemical fields. The electron-donating ability of a molecule is related to  $E_{HOMO}$ . The electron-accepting character of a molecule can be measured via  $E_{LUMO}$  values. The greater the  $E_{HOMO}$  is, the greater the electron donor capability, and the smaller the  $E_{LUMO}$  is the smaller the resistance to accept electrons.

The conceptual density functional theory-based descriptors can be useful to estimate the biological properties. The computed quantum chemical reactivity descriptors were illustrated in Table 3. The reactivity descriptors

including dipole moment, highest occupied molecular orbital energy ( $E_{HOMO}$ ), lowest unoccupied molecular orbital energy ( $E_{LUMO}$ ), chemical potential ( $\mu$ ), electronegativity ( $\chi$ ), hardness ( $\eta$ ), softness ( $S$ ), ionization potential ( $I$ ), electron affinity ( $A$ ), Electro-donating power ( $\omega^-$ ), electro-accepting power ( $\omega^+$ ), and net electrophilicity ( $\Delta\omega$ ) were calculated using the following equations (2–10).

$$\mu = -\chi = (E_{HOMO} + E_{LUMO})/2 \quad (2)$$

$$\eta = E_{HOMO} - E_{LUMO} \quad (3)$$

$$I = -E_{HOMO} \quad (4)$$

$$A = -E_{LUMO} \quad (5)$$

$$S = 1/2\eta \quad (6)$$

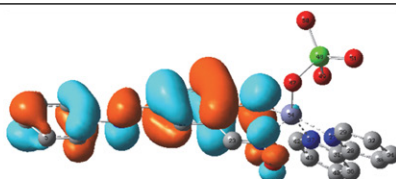
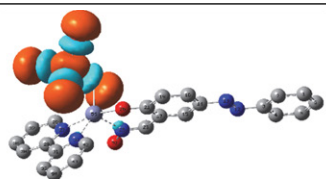
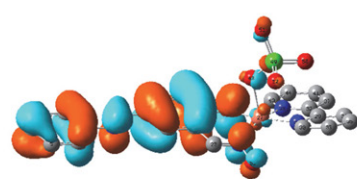
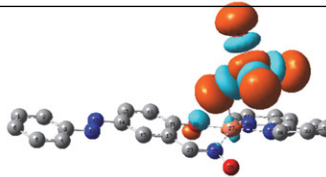
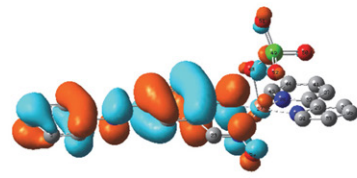
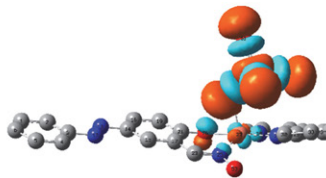
$$\omega = \mu^2/2\eta \quad (7)$$

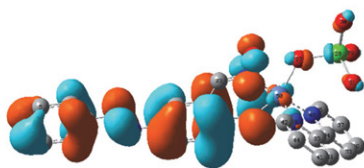
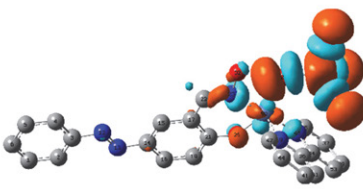
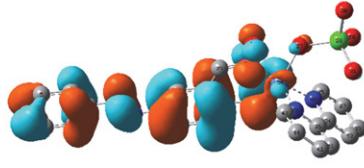
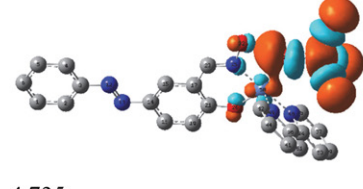
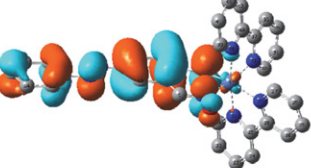
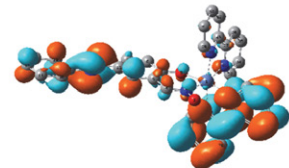
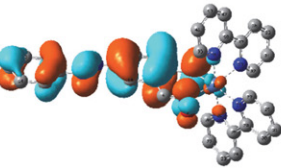
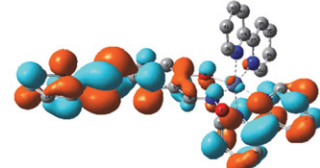
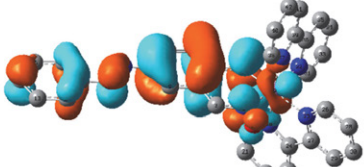
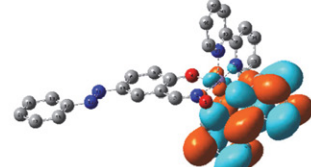
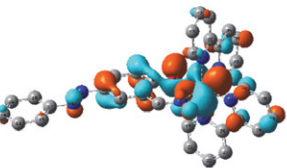
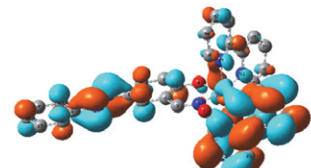
$$\omega^- = (3I + A)^2/16(I - A) \quad (8)$$

$$\omega^+ = (I + 3A)^2/16(I - A) \quad (9)$$

$$\Delta\omega = \omega^+ + \omega^- \quad (10)$$

**Table 2.** The frontier orbitals, energies, and energy gap of complexes in eV.

	HOMO (eV)	GAP	LUMO (eV)
5	 -7.059	 -3.603	
4 (Alpha)	 -6.067	 -4.312	
4 (Beta)	 -6.032	 -4.320	

	HOMO (eV)		GAP		LUMO (eV)
3 (Alpha)	 -5.908		1.089	 -4.819	
3 (Beta)	 -5.933		1.198	 -4.735	
2 (Alpha)	 -6.996		5.609	 -1.387	
2 (Beta)	 -6.954		5.57	 -1.384	
1 (Alpha)	 -6.972		5.519	 -1.453	
1 (Beta)	 -6.676		5.145	 -1.531	

The chemical reactivity increases with increasing softness and according to the calculated softness values, complex 3 is more reactive than the other complexes. It is also expected that complex 2 has more activity due to biological activity is related to increased hardness. The hard-

ness value of complex 2 (5.57) is higher than that of other complexes and indicates that this complex is more stable. It is also known that stable molecules should have lower electrophilicity values. The net electrophilicity of complex 2 is lower than that of other complexes.<sup>29,30</sup>

Table 3. The calculated quantum chemical descriptors (eV).

Comp.	HOMO	LUMO	$\mu$	$\chi$	$\eta$	I	A	S	$\omega$	$\omega^-$	$\omega^+$	$\Delta\omega$
1	-6.68	-1.53	-4.10	4.10	5.15	6.68	1.53	0.10	1.64	5.65	1.54	7.19
2	-6.95	-1.38	-4.17	4.17	5.57	6.95	1.38	0.09	1.56	5.55	1.38	6.94
3	-5.91	-4.82	-5.36	5.36	1.09	5.91	4.82	0.46	13.21	29.17	23.80	52.97
4	-6.03	-4.32	-5.18	5.18	1.71	6.03	4.32	0.29	7.82	18.34	13.17	31.51
5	-7.06	-3.60	-5.33	5.33	3.46	7.06	3.60	0.14	4.11	11.10	5.77	16.88

## 2. 2. 2. Vibrational Assignments

All the IR spectra of the compounds were obtained using the FT-ATR technique in the region of 4000–650  $\text{cm}^{-1}$ . The IR spectra of the mixed ligand complexes were compared with the starting ligands primary azo-oxime type ligand and bipyridine to determine the coordination sites that might be involved in chelation. All the vibrational signals of metal complexes (1-5) and primary ligand were calculated by using the DFT / B3LYP method to assign the experimental signals. Some selected vibrations and corresponding functional groups were summarized in Table 4.

In the IR spectrum of the azo-oxime ligand, signals of oxime protons (C=N–OH), –N=N– and C–O stretchings were observed at 3403, 1393, and 1265  $\text{cm}^{-1}$ , respectively. The primary ligand has two OH groups which are oxime and phenolic OH. The primary ligand has two OH groups which are oxime and phenolic. But, the phenolic OH signal, which is expected to appear at a lower frequency than oxime OH, could not be observed due to possible intramolecular or intermolecular hydrogen bonding. In addition to the absence of phenolic OH stretching in the IR spectrum of the complexes, the broad bands observed at approximately 3440–3190  $\text{cm}^{-1}$  were attributed to oxime OH stretchings. The intense C–O vibration of the primary ligand observed at 1265  $\text{cm}^{-1}$  was shifted to the upper wave number in the complexes (1314–1287  $\text{cm}^{-1}$ ) and the intensity was also decreased compared to the free ligand. The medium intensity imine (C=N) vibration at 1621  $\text{cm}^{-1}$  in the spectrum of the azo-oxime ligand shifted to the upper/lower wavenumber (1603–1645  $\text{cm}^{-1}$ ) and the intensity of this band increased/decreased usually in the complexes. These can be interpreted as the coordination of the metal ion to the primary ligand via the phenolic oxygen and nitrogen of imine.<sup>31,32</sup>

Free 2,2'-bipyridine has a signal at 1577  $\text{cm}^{-1}$  belonging to  $\nu(\text{C}=\text{N})$  imine group. That the signal is observed at 1544  $\text{cm}^{-1}$  for **5** and shifted to upper frequencies in the other complexes in the range of 1595–1606  $\text{cm}^{-1}$  shows that the secondary bidentate ligand is coordinated to the metal center through nitrogen atoms of imine. Several bands belonging to the C=C vibrations were observed in the range of 1575–1437  $\text{cm}^{-1}$  in the complexes. In addition, the characteristic out-of-plane C–H bending observed in 761–764  $\text{cm}^{-1}$  was attributed to the bipyridine unit. Briefly, the obtained spectral data of the complexes confirm the

coordination of the primary ligand to the central metal ion via the imine and phenolic oxygen while 2,2'-bipyridine is coordinated through the nitrogen atoms.

IR spectra present evidence of the metal-perchlorate bond in solid-state. The perchlorate anion has a tetrahedral geometry, its point group is  $T_d$ , and it has four normal vibrational modes ( $\nu_1$ – $\nu_4$ ) of the nine vibrational degrees of freedom of perchlorate, of which only two modes, the asymmetrical stretching ( $\nu_3$ , 1110  $\text{cm}^{-1}$ ) and asymmetrical bending ( $\nu_4$ , 626  $\text{cm}^{-1}$ ) are IR active.<sup>1,33</sup> But, the ATR technique does not allow us to see the lower frequencies from 650  $\text{cm}^{-1}$ . The diagnostic asymmetrical stretching band ( $\nu_3$ ) of ionic perchlorate is very broad and strong which is occasionally split. The minor shift and weak splitting of this band may be occurred because of the lattice effects as in **2**.<sup>33</sup> The Raman active symmetrical stretching band ( $\nu_1$ ) is theoretically forbidden in IR and observed as a weak band at 925–940  $\text{cm}^{-1}$ . The diagnostic asymmetrical stretching band ( $\nu_3$ ) was observed at 1107 for **1** and 1082, 1071  $\text{cm}^{-1}$  for **2** (See the supplementary file, Fig. S12, S13).<sup>34</sup>

The asymmetrical stretching band ( $\nu_3$ , 1110  $\text{cm}^{-1}$ ) of the perchlorate group splits when a coordinate bond is formed between one of its oxygen atoms and central metal ion, so the symmetry of the perchlorate is lowered to  $C_{3v}$ , and number of vibrations increases. The bands are 1115, 1085, 1071 for **3**, 1158, 1113, 1071 for **4** and 1145, 1111, 1070  $\text{cm}^{-1}$  for **5** (Fig. S14–16). The splittings confirm the monodentate coordination of the perchlorate ion in solid-state complexes (Table 3).<sup>35</sup> Based on IR data of **3**, perchlorate is coordinated monodentately. However, the conductivity data shows that complex **3**, which is compatible with the 1:1 electrolyte type, is solvolyzed in DMF.

## 2. 2. 3. UV-Vis Spectra

In order to evaluate experimental absorption bands, UV-Vis characteristics of the metal complexes were interpreted using the TDDFT/CPCM method in the implicit solvent of DMSO. The observed and predicted electronic spectra and their characters were summarized in Table 5. The calculated electronic transitions and FMO transitions that contribute to the formation of these bands are depicted in Table S1–S5. Experimentally observed bands were characterized according to contributions of molecular orbital

**Table 4.** Selected vibrational frequencies (observed and calculated, cm<sup>-1</sup>) of synthesized compounds.

Comp.		$\nu(\text{C=N-OH})$	$\nu(\text{C-H})$	$\nu(\text{C=N})$	Bipy, $\delta(\text{C-H})$	$\nu(\text{C=C})$	$\nu(\text{N=N})$	$\nu(\text{C-O})$	$\nu(\text{ClO}_4)$
<b>H<sub>2</sub>L</b>	Exp.	3403	3150–3000	1621	—	1569	1393	1265	—
	Theo.	3291(Ph), 3666	3074–2982	1654*	—	1621–1590	1514	1289	—
<b>1</b>	Exp.	— <sup>b</sup>	3100–3050	1623, 1595*	762	1519, 1468, 1439	1397	1300	1107( $\nu_3$ ); 922( $\nu_1$ )
	Theo.	3501	3113–3022	1611, 1593*	755	1545–1610	1422	1299	—
<b>2</b>	Exp.	3416 <sup>a</sup>	3150–3000	1644, 1602*	763	1575, 1494, 1472, 1440	1409	1314	1082, 1071( $\nu_3$ ); 945( $\nu_1$ )
	Theo.	3503	3095–3002	1620, 1613*	761	1458–1567	1387	1283	—
<b>3</b>	Exp.	3408 <sup>a</sup>	3100–3000	1644, 1606*	763	1548, 1476, 1440	1409	1310	1115, 1085, 1071( $\nu_1, \nu_4$ ); 933( $\nu_2$ )
	Theo.	3225	3126–3034	1632, 1620*	762	1507–1620	1412, 1420	1301	—
<b>4</b>	Exp.	3440 <sup>a</sup>	3185–3050	1645, 1602*	764	1541, 1476, 1437	1406	1313	1158, 1113, 1071( $\nu_1, \nu_4$ ); 924( $\nu_2$ )
	Theo.	3505	3146–3040	1603, 1629*	789	1508–1621	1420	1310	—
<b>5</b>	Exp.	3190 <sup>a</sup>	3100–3000	1603, 1544 *	761	1477, 1441	1405	1287	1145, 1111, 1070( $\nu_1, \nu_4$ ); 920( $\nu_2$ )
	Theo.	3499	3093–2999	1612, 1594*	761	1542–1610	1418	1326, 1339	—

(a: broad, b: not observed, Exp.: observed experimentally, Theo.: Theoretically calculated, \*: Bipy  $\nu(\text{C=N})$ )

transition and location of FMO on molecules. Since the magnetic susceptibility measurements provide information about the strength of the ligand field of the complexes

and the number of unpaired electrons, these measurements were taken into account in the spin assignment of the complexes in the DFT calculations using spin-only formula.

**Table 5.** The electronic spectral data and calculated electronic transitions of complex 1-5 and their contributions.

Comp.	$\lambda_{\text{exp.}}$ (nm) in solid	$\lambda_{\text{exp.}}$ (nm) in DMF	$\lambda_{\text{theo.}}$ (nm)	Osc. Strength	Major contributions
<b>1</b>	237	291	251	0.07	H-2(A)→L+4(A) (18%), HOMO(A)→L+4(A) (19%)
			265	0.33	H-8(A)→LUMO(A) (12%), HOMO(A)→L+5(A) (10%)
			266	0.12	H-5(A)→L+2(A) (12%)
			269	0.13	H-8(A)→LUMO(A) (14%), H-1(A)→L+4(A) (14%)
			374	0.11	H-1(A)→L+2(A) (18%)
	374	398	375	0.73	HOMO(A)→L+1(A) (38%)
			406	0.13	H-1(A)→LUMO(A) (21%), HOMO(A)→L+3(A) (18%)
			461	0.02	HOMO(B)→L+2(B) (23%)
			570	0.02	HOMO(B)→LUMO(B) (28%), HOMO(B)→L+2(B) (24%)
<b>2</b>	246	290	212	0.15	H-1(B)→L+2(B) (12%)
			218	0.19	H-7(B)→L+9(B) (32%)
			238	0.22	H-2(B)→L+3(B) (13%), H-3(A)→L+3(A) (11%)
			251	0.12	H-3(B)→LUMO(B) (17%)
			264	0.59	H-4(B)→L+2(B) (18%), H-5(A)→L+2(A) (15%)
	312	433	266	0.23	H-4(B)→L+2(B) (19%), H-8(A)→LUMO(A) (15%)
			331	0.23	HOMO(A)→L+3(A) (40%), HOMO(B)→L+3(B) (41%)
			377	1.05	HOMO(B)→LUMO(B) (35%), HOMO(A)→L+1(A) (24%)
			436	0.03	H-8(B)→L+8(B) (10%)
			447	0.02	H-9(B)→L+8(B) (27%)

3	245	362	329	0.03	H-21(A)→LUMO(A) (42%)
	311		344	0.02	H-2(A)→L+3(A) (17%), H-4(B)→L+1(B) (15%)
	379		366	0.02	H-16(B)→LUMO(B) (20%), H-1(B)→L+4(B) (13%)
			368	0.07	HOMO(B)→L+7(B) (28%), H-16(B)→LUMO(B) (15%)
			378	0.02	H-6(A)→L+1(A) (37%), HOMO(B)→L+6(B) (13%)
			381	0.03	HOMO(B)→L+6(B) (18%), HOMO(A)→L+5(A) (13%)
		429	418	0.37	HOMO(B)→L+4(B) (20%), HOMO(A)→L+2(A) (17%)
			421	0.22	HOMO(B)→L+4(B) (15%)
			480	0.16	HOMO(B)→L+2(B) (25%), HOMO(B)→L+4(B) (11%)
4	253	290	311	0.02	H-6(A)→L+5(A) (14%), H-2(A)→L+5(A) (14%)
			325	0.01	H-5(A)→L+1(A) (17%)
	372		343	0.02	H-2(A)→L+1(A) (21%)
			346	0.01	H-1(A)→L+3(A) (18%), H-2(A)→L+1(A) (14%)
		367	376	0.05	HOMO(A)→L+4(A) (63%), HOMO(A)→L+5(A) (10%)
			380	0.16	HOMO(A)→L+4(A) (24%), HOMO(B)→L+6(B) (23%)
			410	0.08	HOMO(A)→L+3(A) (73%)
			416	0.60	HOMO(A)→L+2(A) (28%), HOMO(B)→L+3(B) (29%)
		459	421	0.04	H-5(B)→L+1(B) (39%), H-4(B)→L+1(B) (15%)
			462	0.05	H-3(B)→LUMO(B) (12%), HOMO(B)→L+2(B) (43%)
			468	0.04	HOMO(A)→L+1(A) (23%), H-3(A)→LUMO(A) (13%)
			478	0.01	HOMO(B)→L+2(B) (39%)
			522	0.01	H-1(B)→L+1(B) (16%), HOMO(B)→L+1(B) (10%)
5	248		234	0.20	H-2→L+6 (24%)
		288	236	0.17	H-2→L+6 (21%), HOMO→L+7 (12%)
			250	0.09	H-3→L+3 (28%), H-10→LUMO (25%)
	292		265	0.28	H-5→L+4 (43%), H-5→L+2 (11%)
			267	0.10	H-5→L+4 (14%), H-11→LUMO (10%)
		352	314	0.03	H-6→L+1 (75%), HOMO→L+6 (10%)
	367		322	0.16	HOMO→L+6 (68%), H-6→L+1 (13%)
			368	1.09	HOMO→L+3 (87%)
			385	0.01	H-2→LUMO (71%)
			413	0.02	H-18→LUMO (33%)

The manganese(II) complex, **1** which has a distorted octahedral geometry shows three bands at 291, 398, and 461 nm in the electronic spectrum. Considering the os-

cillator powers, the first dense band consists of  $\pi \rightarrow \pi^*$  and  $d \rightarrow \pi^*$  transitions, with a predominance of  $\pi \rightarrow \pi^*$  transitions. The second band observed at 398 nm is mainly com-



posed of  $d \rightarrow n$  transitions, and attributed to metal-to-ligand charge transfer (MLCT) transition. According to the theoretical calculations, the third absorbance observed at 461 nm is attributed to  $d \rightarrow \pi^*$  transitions. The bands observed experimentally at 461 nm originate mainly in the HOMO(B)  $\rightarrow$  LUMO(B)/L+2(B) transition and can be interpreted as intra-ligand charge transfer according to the orbital character. Magnetic moment values of Mn(II) complex (**1**) were measured as 5.80 BM on the Gouy balance. Magnetic moment values measured at room temperature are compatible with  $S = 5/2$ .

The nickel(II) complex, **2** which has a distorted octahedral geometry shows two bands, at 290 and 433 nm. The first intense band is formed by the contribution of  $\pi \rightarrow \pi^*$ ,  $n \rightarrow \pi^*$  and ligand-to-metal charge transfer (LMCT) transitions, with a predominance of  $\pi \rightarrow \pi^*$  transitions. Considering the second broadband, the contribution of  $\pi \rightarrow \pi^*$  transitions is dominant. LMCT and  $d-d$  transitions were also contributed to the formation of this band. The measured magnetic moments of the synthesized Ni(II) complex, **2** are 2.89 B.M.

The distorted squarepyramid nickel(II) complex, **3** shows two absorbance bands at 362 and 429 nm. Considering the oscillatory power of the observed transitions for both bands, the contribution of  $\pi \rightarrow \pi^*$  transitions is predominant, with the contribution of  $\pi \rightarrow \pi^*$ ,  $n \rightarrow \pi^*$  and  $d \rightarrow \pi^*$  (MLCT) transitions. It can be said that the contribution of  $d \rightarrow \pi^*$  transitions is very small. The measured magnetic moments of the synthesized Ni(II) complex, **3** are 2.60 BM.

Three bands were observed in the electronic spectrum of the copper(II) complex, **4**, which has a distorted squarepyramidal geometry, at 290, 367, and 459 nm. The first dense band is attributed to  $\pi \rightarrow \pi^*$  transitions, the second band is attributed to  $\pi \rightarrow \pi^*$  and  $n \rightarrow \pi^*$  transitions, and the third band is attributed to the weighted contribution of  $\pi \rightarrow \pi^*$ ,  $n \rightarrow \pi^*$  and ligand-to-metal charge transfer transitions (LMCTs). The magnetic moments of the Cu(II) complex were measured as 2.14 BM. This observed value is consistent with the spin value of the Cu(II) ion containing an unpaired electron.

The zinc(II) complex, **5**, which has a distorted squarepyramidal geometry, two bands were observed at 288 and 352 nm in the electronic spectrum of compound **5** and attributed to  $\pi \rightarrow \pi^*$  and  $n \rightarrow \pi^*$  transitions. The Zn(II) complex is diamagnetic because the zinc ion is in the  $d^{10}$  system.

### 2. 3. Thermal Stabilities

In order to determine the metal/ligand ratio and to get information about their thermal stabilities of the ternary transition metal complexes (**1-5**) from ambient temperature to 1000 °C in the  $O_2$  atmosphere, their thermal decomposition processes were investigated by TG/DTG/DTA techniques. All the complexes studied are air-stable and have

very high thermal stability from thermal data in Table 6. The TG curves of the complexes were given in Figure 8 (see Supplementary, Fig. S1-S5 for the DTA<sub>max</sub>). The metal oxide residues in thermograms of the complexes are compatible with the proposed structures and their stoichiometry.

From the TG curve of [Mn(HL)(bipy)<sub>2</sub>] ClO<sub>4</sub>, **1** has one step decomposition stage which was observed within the temperature range of 150–507 °C and the DTA curve shows three exothermic peaks at 173, 285 and 473 °C. All of the organic moiety was removed from the structure above 507 °C and the final residue was attributed to MnO, its percentage was 10.0% (calc. 10.0%).

In case of [Ni(HL)(bipy)<sub>2</sub>] ClO<sub>4</sub>, **2**, TG curve has three exothermic decomposition steps within the range of 25–629 °C. A rapid first step decomposition was observed at 245–360 °C (with exothermic DTA peaks at 285 and 358 °C) assigned to removal HL and a bipyridine with a mass loss of 56.0% (calc. 55.9%). The exothermic second step at 360–458 °C (with exothermic DTA peaks at 410 °C) is assigned to removal ClO<sub>4</sub>-O with a mass loss of 11.6% (calc. 11.7%). The second bipyridine molecule was removed at 459–630 °C (with exothermic DTA peaks at 505 °C) with a mass loss of 22.8% (calc. 22.8%) in the third step and final residue was assigned to NiO with a mass of 8.6% (calc. 9.51%).

In case of [Ni(HL)(bipy)(ClO<sub>4</sub>)], **3**, TG curve has three step decomposition stages within the range of 25–700 °C. The endothermic dehydration of 0.5 mol adsorbed water with a mass loss of 1.6% (calc. 1.6%) was observed at 25–55 °C (DTA<sub>max</sub> at 41.2 °C) in the first step. The exothermic second step at 154–299 °C (DTA<sub>max</sub> at 291 and 305 °C) is assigned to remove a bipyridine molecule with a mass loss of 29.5 (27.7). The primary ligand, HL, and ClO<sub>4</sub>-O was removed at 299–691 °C (DTA<sub>max</sub> at 422 and 520 °C) with a mass loss of 57.6 (58.4) in the third step and final residue was assigned to NiO with a mass of 11.3% (calc. 13.5%).

In case of [Cu(HL)(bipy) (ClO<sub>4</sub>)], **4**, TG curve has three step decomposition stages within the range of 25–647 °C. The endothermic dehydration of 0.6 mol adsorbed water with a mass loss of 1.9% (calc. 1.9%) was observed at 25–56 °C (DTA<sub>max</sub> at 47 °C) in the first step. The exothermic second step at 180–342 °C (DTA<sub>max</sub> at 231 °C) is assigned to remove a bipyridine molecule with a mass loss of 27.3 (27.3). The primary ligand, HL and ClO<sub>4</sub>-O was removed at 342–647 °C (DTA<sub>max</sub> at 370, 383, and 448 °C) with a mass loss of 54.2 (56.8) in the third step, and the final residue was assigned to NiO with a mass of 16.6% (calc. 14.2%).

From the TG curve of [Zn(HL)(bipy)]ClO<sub>4</sub>, **5** has one step decomposition stage which was observed within the temperature range of 131–599 °C and the DTA curve shows four exothermic peaks at 187, 301, 368, 456 °C. All of the organic moiety was removed from the structure above 599 °C and the final residue was assigned to ZnO, its percentage was 15.70% (calc. 14.5%).

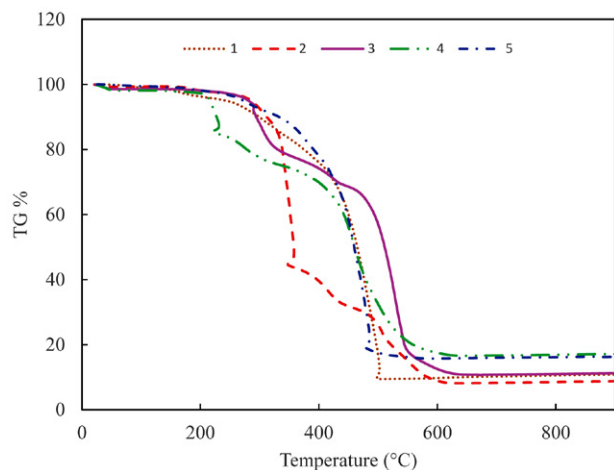


Figure 8: TG curves of the complexes (1-5).

Table 6. Thermal analysis data of the complexes.

Comp.	Decom. Step(s)	Decom. Temp., °C	DTA <sub>max</sub> , μV	Group lost, mass loss %, exp. (calc.)	Residue formula, Residue %, exp. (calc.)
1	1	150–507	173(+), 285(+), 473(+)	HL+2 bipy+ ClO <sub>4</sub> -O 90.0 (90.0)	MnO, 10.0 (10.0)
	1	245–360	285(+), 358(+)	HL+bipy 56.0 (55.9)	[Ni(bipy)] ClO <sub>4</sub> , 43.1 (44.0)
2	2	360–458	410(+)	ClO <sub>4</sub> -O 11.6 (11.7)	[Ni(bipy)]O, 31.5 (32.6)
	3	459–630	505(+)	Bipy 22.8 (22.8)	NiO, 8.6 (9.51)
	1	25–55	41.2(–)	0.5H <sub>2</sub> O, 1.6, (1.6)	[Ni(HL)(bipy)(ClO <sub>4</sub> )], 98.4 (98.4)
3	2	154–299	291(+), 305(+)	Bipy 29.5 (27.7)	[Ni(bipy)(ClO <sub>4</sub> )], 68.9 (98.4)
	3	299–691	422(+), 520(+)	HL+ ClO <sub>4</sub> -O 57.6 (58.4)	NiO, 11.3 (13.5)
	1	25–56	47(–)	0.6H <sub>2</sub> O, 1.9, (1.9)	[Ni(HL)bipy] ClO <sub>4</sub> , 98.1 (98.1)
4	2	180–342	231(+)	Bipy 27.3 (27.3)	[Cu(HL)] ClO <sub>4</sub> , 70.8 (70.8)
	3	342–647	370(+), 383(+), 448(+)	HL+ ClO <sub>4</sub> -O 54.2 (56.8)	CuO, 16.6 (14.2)
5	1	131–599	187(+), 301(+), 368(+), 456(+)	HL+ bipy+ ClO <sub>4</sub> -O 84.3 (85.5)	ZnO, 15.7 (14.5)

## 2. 4. AChE Inhibition Studies

The synthesized complexes of Mn(II), Ni(II), Cu(II), and Zn(II) with mixed ligands exhibited inhibition activity against the AChEs of adults and nymphs of *R. simulans* (Table 7). On AChE of adults of *R. simulans*, the [Zn(HL)(bipy)(OCIO<sub>3</sub>)], **5** ( $IC_{50} = 3.2 \pm 0.8 \mu M$ ) showed an inhibition effect close to edrophonium chloride ( $IC_{50} = 2.4 \pm 0.3 \mu M$ ) known as a competitive inhibitor of AChE. The [Mn(HL)(bipy)<sub>2</sub>](ClO<sub>4</sub>), **1** showed inhibition close to tacrine as an inhibitor of AChE, while

the other complexes showed better inhibition than tacrine.

Although the inhibitory effect of these complexes on the AChE of nymphs was not as much as edrophonium and tacrine, their effect on the AChE was quite high. Especially these were [Ni(HL)(bipy)(OCIO<sub>3</sub>)] (**3**) ( $IC_{50} = 4.6 \pm 0.8 \mu M$ ), [Mn(HL)(bipy)<sub>2</sub>](ClO<sub>4</sub>) (**1**) ( $IC_{50} = 5.6 \pm 1.2 \mu M$ ) and [Cu(HL)(bipy)(OCIO<sub>3</sub>)] (**4**) ( $IC_{50} = 6.4 \pm 0.7 \mu M$ ) complexes, and their inhibition concentrations were close to each other. It was observed that while [Zn(HL)(bipy)(OCIO<sub>3</sub>)] (**5**) ( $IC_{50} = 3.2 \pm 0.8 \mu M$ ) was more effective on adults, it had less effect on nymphs ( $IC_{50} = 10.1 \pm 2.4 \mu M$ ). The inhibition effect of the [Ni(HL)(bipy)<sub>2</sub>](ClO<sub>4</sub>) (**2**) complex on both stages of *R. simulans* was observed to be the same at higher concentrations than the others. As a result of inhibition studies, it was determined that the [Zn(HL)(bipy)(OCIO<sub>3</sub>)] complex was more effective

in the inhibition of AChE of the adults, and the [Ni(HL)(bipy)(OCIO<sub>3</sub>)] complex was more effective in the inhibition of AChE of the nymphs.

Although the molecular mechanism is not fully known, it is suggested that metal complexes inhibit acetylcholinesterase by binding to both catalytic active site (CAS) and peripheral anionic site (PAS) in the active site of the enzyme.<sup>36</sup> Considering the structures of the complexes, complex **1, 2** may bind CAS site while complex **3-5** may bind PAS site of the enzyme. From the results it can be speculated that metal complexes with low coordination are

more likely to bind stronger than the others to the active site of the enzyme and a higher inhibitory effect may be expected.<sup>37,38</sup>

While nymphs continue their lives in and around their hosts, they can spread to a wider area after they become adults. This implies that the sensory equipment, as well as the nervous system, must modify to accommodate the sensory requirements (such as host recognition, mate location, oviposition, aggregation, and defense) to the differences between nymphal and adult habitats. Therefore, adults are likely to have a more improved nervous system than nymphs.<sup>39</sup> In another literature, the differences in the activities of AChEs obtained from different stages of *Bactrocera dorsalis* (H.) were appraised from two perspectives. It was papered that one of them, some alterations to the protein structure occurred during the developmental stages to meet the continuously changing demands of the development of insects, the another factor, the differences in the expression level of genes encoding specific enzymes might be resulting in changes.<sup>40</sup> Because of such differences, it is normal for the AChEs from nymphs and adults of *R. simulans* to behave differently towards the inhibitors.

The inhibition effect of some copper complexes synthesized on acetylcholinesterase from *Electrophorus electricus* (eeAChE) was investigated and IC<sub>50</sub> values were determined between  $5.45 \pm 0.70$  and  $64.67 \pm 2.20$   $\mu\text{M}$ .<sup>41</sup>

The effects of [Cu(naringin)<sub>2</sub>], [Cu(naringenin)<sub>2</sub>], Cu(hesperetin)<sub>2</sub>, Cu(naringin)(2,2'-bipyridine), Cu(naringin)(phenanthroline), Cu(naringenin)(2,2'-bipyridine), Cu(hesperidin)(phenanthroline), Cu(hesperetin)(2,2'-bipyridine) and Cu(hesperetin)(phenanthroline) complexes on the activities of acetylcholinesterases obtained from human serum and electric eel were investigated. In this reported study, it was determined that the synthesized complexes have different effects on AChEs in different organisms. Also in this reported study, IC<sub>50</sub> values for huAChE were  $1.73 \pm 0.3$ ,  $0.66 \pm 0.2$ ,  $0.33 \pm 0.02$ ,  $0.012 \pm 0.002$ ,  $0.87 \pm 0.1$ ,  $0.25 \pm 0.03$ ,  $0.32 \pm 0.05$ ,  $0.33 \pm 0.05$ ,  $0.36 \pm 0.07$   $\mu\text{M}$  and IC<sub>50</sub> values for eeAChE were  $0.16 \pm 0.03$ ,  $1.41 \pm 0.4$ ,  $2.55 \pm 0.5$ ,  $0.17 \pm 0.02$ ,  $1.4 \pm 0.3$ ,  $0.46 \pm 0.2$ ,  $1.77 \pm 0.4$ ,  $0.94 \pm 0.09$ ,  $0.33 \pm 0.06$   $\mu\text{M}$ .<sup>13</sup>

**Table 7.** IC<sub>50</sub> values of acetylcholinesterase of *R. simulans* in the presence of the complexes (1-5).

Complex	IC <sub>50</sub> ( $\mu\text{M}$ ) For adults	IC <sub>50</sub> ( $\mu\text{M}$ ) For nymphs
[Mn(HL)(bipy) <sub>2</sub> ] (ClO <sub>4</sub> ), <b>1</b>	$22.0 \pm 1.8$	$5.6 \pm 1.2$
[Ni(HL)(bipy) <sub>2</sub> ] (ClO <sub>4</sub> ), <b>2</b>	$14.0 \pm 1.2$	$16.5 \pm 1.9$
[Ni(HL)(bipy)(OCIO <sub>3</sub> )], <b>3</b>	$16.0 \pm 2.1$	$4.6 \pm 0.8$
[Cu(HL)(bipy)(OCIO <sub>3</sub> )], <b>4</b>	$7.2 \pm 1.4$	$6.4 \pm 0.7$
[Zn(HL)(bipy)(OCIO <sub>3</sub> )], <b>5</b>	$3.2 \pm 0.8$	$10.1 \pm 2.4$
Edrophonium chloride	$2.4 \pm 0.3$	$0.6 \pm 0.09$
Tacrine	$18.0 \pm 1.9$	$1.2 \pm 0.4$

### 3. Conclusions

The agricultural areas located on the coastal part of the Eastern Black Sea Region have recently been exposed to the damage caused by a different type of insect known as *Ricania simulans*. The acetylcholine esterase is the target site of most insecticides. So, mixed ligand metal complexes with azo-oxime ligand and 2,2'-bipyridine as co-ligand were prepared, theoretical calculations were performed to provide information about molecular geometry, electronic structure, molecular and spectroscopic properties. Additionally, their inhibitory activities against the AChEs of adults and nymphs of *R. simulans* in this study was reported. All the complexes were found to have inhibitor activities. Interestingly, complexes **4** and **5** showed better inhibitor activity than the other complexes tested and the most active of the complex has found to be complex, **5** with IC<sub>50</sub> value of  $2.4 \pm 0.3$   $\mu\text{M}$  for adults, and complex **3** with the lowest IC<sub>50</sub> value ( $4.6 \pm 0.8$   $\mu\text{M}$ ) exhibited the most inhibition activity for nymphs. Here, it has been shown that these complexes may be used as potential metal based insecticides against *R. simulans* which has posed a big challenge to the field of agriculture.

## 4. Experimental

### 4.1. Materials and Methods

2,2'-Bipyridine (Bipy) and perchlorate salts of Mn(II), Ni(II), Cu(II), and Zn(II) were purchased from Merck. All chemical and solvents were analytical grade and used without any purification. 2-[(*E*)-(hydroxyimino) methyl]-4-[(*E*)-phenyldiazenyl]phenol, H<sub>2</sub>L was prepared according to the reported literature.<sup>9</sup>

### 4.2. Preparation of Crude Extract

About 5 g of adults or nymphs of *R. simulans* collected in July were homogenized in 20 mL phosphate buffer (pH 7.4, 0.05 M, containing 1 mM EDTA, 0.5% Triton X-100, 0.5 M NaCl) in the ice bath. The homogenates were centrifuged at 22,000xg for 30 min at 4 °C. After the supernatant was filtered via syringe filter units (pore size 0.45  $\mu\text{m}$ ). The supernatant was used as a crude extract.<sup>42</sup>

### 4.3. Measurements

Elemental analyses were measured with a LECO truspect analyzer and <sup>1</sup>H NMR spectra were measured with an Agilent Technologies 400/54 spectrometer at the Central Research Laboratory of Recep Tayyip Erdogan (RTE) University. MALDI-TOF mass spectra in a DHB matrix were recorded on a Bruker Microflex LT at the Gebze Institute of Technology for the complexes. IR spectra were recorded on a Perkin Elmer Spectrum 100 FT IR infrared spectrophotometer equipped with an ATR appa-

ratus. KBr is transparent in UV-Vis region, so solid-state electronic spectra for complexes were recorded on a SpectraMax M5 spectrophotometer in KBr discs. Magnetic susceptibility and thermogravimetric data were collected by using Sherwood MK-1 and SII 6300 TG/DTA, respectively. Molar conductivity measurements of the complexes were measured with a Hanna EC 215 conductivity meter by using 0.01 M KCl water solution as a calibrant.

#### 4. 4. Enzyme assay

The activity of AChE was determined by the spectrophotometric method using acetylthiocholine iodide (ATC) as the substrate.<sup>41</sup> The reaction mixture, in a final volume of 3 ml contained 60  $\mu\text{L}$  of 75.0 mM ATC, 60  $\mu\text{L}$  of 10.0 mM 5,5'-dithiobis(2-nitrobenzoic acid), 2.780 mL of 0.1 M potassium phosphate buffer, pH 8.0 and 100  $\mu\text{L}$  of enzyme solution. The enzymatic reaction was initiated by adding the enzyme solution to the sample cuvette. Absorbance was read after 10 min incubation at 37 °C at 412 nm. Each activity value was taken from an average of 3–5 measurements. The inhibition effect was investigated by adding different volumes of 1 mM stock inhibitor solutions to the reaction mixtures which is here the buffer volume was reduced by the volume of inhibitor solution added. One unit of AChE (EU) was defined as the amount which catalyzed the hydrolysis of 1.0  $\mu\text{M}$  of ATC per minute at room temperature, which was calculated based on an extinction coefficient of 13.6  $\text{mM}^{-1} \text{cm}^{-1}$ .<sup>42,43</sup>

The inhibition studies were performed with tacrine and edrophonium chloride, known specific inhibitors of acetylcholinesterase, and the synthesized complexes at pH 8.0 in the presence of ATC substrate. The inhibitory concentration ( $\text{IC}_{50}$ ), which inhibits the AChE activity by 50%, was determined by using the % inhibition graph drawn against the inhibitory concentration. Inhibitors and their concentration ranges were as follows: tacrine 0.1–20.0  $\mu\text{M}$ , edrophonium chloride 0.1–4.0  $\mu\text{M}$ , and the complexes 2.0–30.0  $\mu\text{M}$ . Each inhibitor was used in at least six concentrations.<sup>44</sup>

#### 4. 5. Theoretical Methodology

Quantum chemical calculations were performed to provide information about molecular geometry, electronic structure, molecular and spectroscopic properties. Fully optimized structural parameters of the ligands ( $\text{H}_2\text{L}$  and bipy) and their metal (Mn(II), Ni(II), Cu(II), Zn(II)) complexes were calculated at the DFT level (B3LYP) with basis sets 6-311++ G(d,p) for nonmetal atoms, LANL2DZ and the effective core potential (ECP) for metal atoms. Since the CAM-B3LYP method gives a better definition of the excited state transitions compared to the B3LYP function, the electronic excitations were calculated using TD-CAM-B3LYP methods and 6-311++G(2d,2p) basis set for nonmetal atoms and LANL2DZ with the effective core potential (ECP)

for metal atoms combined with a conductor-like polarizable continuum model (CPCM) in the implicit solvent of DMSO.<sup>45</sup> All calculations were done using the Gaussian 09 platform.<sup>46</sup> The optimized geometries and frontier molecular orbital (FMO) densities were visualized using the Gauss View 5 software. GAUSSSUM 3.0<sup>47</sup> to interpret the UV-Vis bands and analyze fractional contributions, and the VED-A4X<sup>48</sup> for analysis of elementary vibration modes were used.

#### 4. 6. Synthesis of the Complexes- General Procedure

Firstly, ethanolic solution of NaOH was added to the solution of the ligand,  $\text{H}_2\text{L}$  (1 mmol) in 15 mL ethyl alcohol to neutralize. To this solution was added the solution of metal(II) perchlorate ( $\text{Mn}(\text{ClO}_4)_2 \cdot 6\text{H}_2\text{O}$ ,  $\text{Ni}(\text{ClO}_4)_2 \cdot 6\text{H}_2\text{O}$ ,  $\text{Cu}(\text{ClO}_4)_2 \cdot 6\text{H}_2\text{O}$  or  $\text{Zn}(\text{ClO}_4)_2 \cdot 6\text{H}_2\text{O}$ ) (1 mmol) in 10 mL ethyl alcohol. 2,2'-bipyridine (2.0 mmol for **1** and **2**; 1.0 mmol for **3-5**) in 10 mL ethyl alcohol was added to the solution, after the solution was stirred for 30 min at room temperature. The mixture was stirred for six hours at room temperature and then allowed to stand for two days at room temperature. Solid precipitate was filtered and washed with water and ethyl alcohol, respectively. Finally, the resulting solid powders were filtered, recrystallized from a hot DMSO- $\text{H}_2\text{O}$  mixture and dried in vacuo over  $\text{CaCl}_2$ . Single crystals couldn't be obtained for X-ray diffraction studies though our great efforts.

##### *[Mn(HL)(bipy)<sub>2</sub>](ClO<sub>4</sub>)*, (**1**)

Yield 0.25 g (35%). mp 290–296 °C (dec.). Color: Brownish khaki. FT-IR ( $\text{cm}^{-1}$ ): 3100–3050  $\nu(\text{C-H})$ ; 1623, 1595  $\nu(\text{C=N})$ ; 1519, 1468, 1439  $\nu(\text{C=C-})$ ; 1397  $\nu(\text{N=N})$ ; 1300  $\nu(\text{C-O})$ ; 1141, 1107  $\nu_3(\text{ClO}_4)^-$ ; 922  $\nu_1(\text{ClO}_4)^-$ ; 762 (bipy). UV-Vis.  $\lambda_{\text{max}}$ , nm ( $\epsilon$ ,  $\text{M}^{-1} \text{cm}^{-1}$ ) in DMF: 291 (13880); 398 (8900); 461 (7300). Molar conductivity ( $\Omega^{-1} \text{cm}^2 \text{mol}^{-1}$ ) 60.  $\mu_{\text{eff}}$  B.M. (298 K): 5.80. MALDI-TOF MS ( $m/z$ ): Calc. for  $\text{C}_{33}\text{H}_{26}\text{ClN}_7\text{O}_6\text{Mn}$ : 707.0; Found: 607.9  $[\text{M}-\text{ClO}_4]^+$ . Anal. Calc.: C, 56.06; H, 3.71; N, 13.87. Found: C, 56.27; H, 3.62; N, 13.81.

##### *[Ni(HL)(bipy)<sub>2</sub>](ClO<sub>4</sub>)*, (**2**)

Yield 0.39 g (55%). mp 252–259 °C (dec.). Color: Greenish yellow. FT-IR ( $\text{cm}^{-1}$ ): 3416  $\nu(\text{OH})$ ; 1644, 1602  $\nu(\text{C=N})$ ; 1575, 1495, 1472, 1440  $\nu(\text{C=C-})$ ; 1409  $\nu(\text{N=N})$ ; 1314  $\nu(\text{C-O})$ ; 1082, 1071  $\nu_3(\text{ClO}_4)^-$ ; 945  $\nu_1(\text{ClO}_4)^-$ ; 763 (bipy). UV-Vis.  $\lambda_{\text{max}}$ , nm ( $\epsilon$ ,  $\text{M}^{-1} \text{cm}^{-1}$ ) in DMF: 290 (16420); 433 (5740). Molar conductivity ( $\Omega^{-1} \text{cm}^2 \text{mol}^{-1}$ ) 61.  $\mu_{\text{eff}}$  B.M. (298 K): 2.60. MALDI-TOF MS ( $m/z$ ): Calc. for  $\text{C}_{33}\text{H}_{26}\text{ClN}_7\text{O}_6\text{Ni}$ : 710.7; Found: 592.7  $[\text{M}-(\text{ClO}_4+\text{H}_2\text{O})]^+$ . Anal. Calc.: C, 55.77; H, 3.69; N, 13.79. Found: C, 55.54; H, 3.52; N, 13.88.

##### *[Ni(HL)(bipy)(ClO<sub>4</sub>)]*, (**3**)

Yield 0.24 g (43%). mp 248–257 °C (dec.). Color: Khaki. FT-IR ( $\text{cm}^{-1}$ ): 3408  $\nu(\text{OH})$ ; 1644, 1606  $\nu(\text{C=N})$ ;

1548, 1476, 1440  $\nu(\text{C}=\text{C})$ ; 1409  $\nu(\text{N}=\text{N})$ ; 1310  $\nu(\text{C}-\text{O})$ ; 1157, 1115, 1085, 1071  $\nu_1, \nu_4(\text{OClO}_3)^-$ ; 933  $\nu_2(\text{OClO}_3)^-$ ; 763 (bipy). UV-Vis.  $\lambda_{\text{max}}$ , nm ( $\epsilon$ ,  $\text{M}^{-1} \text{cm}^{-1}$ ) in DMF: 362 (15080); 429 (22350). Molar conductivity ( $\Omega^{-1} \text{cm}^2 \text{mol}^{-1}$ ) 82.  $\mu_{\text{eff}}$  B.M. (298 K): 1.81. MALDI-TOF MS ( $m/z$ ): Calc. for  $\text{C}_{23}\text{H}_{18}\text{ClN}_5\text{O}_6\text{Ni}$ : 554.6; Found: 453.6  $[\text{M}-\text{ClO}_4]^+$ . Anal. Calc.: C, 49.81; H, 3.27; N, 12.63. Found: C, 50.02; H, 3.33; N, 12.47.

#### $[\text{Cu}(\text{HL})(\text{bipy})(\text{ClO}_4)]$ , (4)

Yield 0.26 g (46%). mp 209–215 °C (dec.). Color: Brown. FT-IR ( $\text{cm}^{-1}$ ): 3440  $\nu(\text{OH})$ ; 1645, 1602  $\nu(\text{C}=\text{N})$ ; 1541, 1476, 1437  $\nu(\text{C}=\text{C})$ ; 1406  $\nu(\text{N}=\text{N})$ ; 1313  $\nu(\text{C}-\text{O})$ ; 1158, 1113, 1071  $\nu_1, \nu_4(\text{OClO}_3)^-$ ; 924  $\nu_2(\text{OClO}_3)^-$ ; 764 (bipy). UV-Vis.  $\lambda_{\text{max}}$ , nm ( $\epsilon$ ,  $\text{M}^{-1} \text{cm}^{-1}$ ) in DMF: 290 (19760); 367 (39130); 459 (32540). Molar conductivity ( $\Omega^{-1} \text{cm}^2 \text{mol}^{-1}$ ) 5.  $\mu_{\text{eff}}$  B.M. (298 K): 2.1. MALDI-TOF MS ( $m/z$ ): Calc. for  $\text{C}_{23}\text{H}_{18}\text{ClN}_5\text{O}_6\text{Cu}$ : 559.4; Found: 459.7  $[\text{M}-\text{ClO}_4]^+$ . Anal. Calc.: C, 49.38; H, 3.24; N, 12.52. Found: C, 49.63.74; H, 3.39 N, 12.43.

#### $[\text{Zn}(\text{HL})(\text{bipy})(\text{ClO}_4)]$ , (5)

Yield 0.16 g (29%). mp 281–289 °C (dec.). Color: Light orange. FT-IR ( $\text{cm}^{-1}$ ): 3190  $\nu(\text{OH})$ ; 1603, 1544  $\nu(\text{C}=\text{N})$ ; 1477, 1441  $\nu(\text{C}=\text{C})$ ; 1405  $\nu(\text{N}=\text{N})$ ; 1287  $\nu(\text{C}-\text{O})$ ; 1145, 1111, 1070  $\nu_1, \nu_4(\text{OClO}_3)^-$ ; 920  $\nu_2(\text{OClO}_3)^-$ ; 763 (bipy). UV-Vis.  $\lambda_{\text{max}}$ , nm ( $\epsilon$ ,  $\text{M}^{-1} \text{cm}^{-1}$ ) in DMF: 288 (22000); 352 (36270).  $^1\text{H}$  NMR  $\delta$  (400 MHz,  $\text{DMSO}-d_6$ ): 11.15 bs. (1H, OH), 8.68 s. (1H,  $\text{HC}=\text{N}$ ), 8.44 s. (2H, Ar), 8.07 s. (1H, Ar), 7.95 s. (2H, Ar), 7.77 d. (4H, Ar,  $J=8.0$  Hz), 7.52 dd. (4H, Ar,  $J=8.0$  Hz), 7.44 t. (2H, Ar,  $J=8.0$  Hz), 6.87 s. (1H, Ar). Molar conductivity ( $\Omega^{-1} \text{cm}^2 \text{mol}^{-1}$ ) 4.  $\mu_{\text{eff}}$  B.M. (298 K): dia. MALDI-TOF MS ( $m/z$ ): Calc. for  $\text{C}_{23}\text{H}_{18}\text{ClN}_5\text{O}_6\text{Zn}$ : 561.3; Found: 461.3  $[\text{M}-\text{ClO}_4]^+$ . Anal. Calc.: C, 49.22; H, 3.23; N, 12.48. Found C, 49.08; H, 3.32; N, 12.44.

### Declaration of Competing Interest

The authors declare that they have no known competing financial interests or personal relationships that could have appeared to influence the work reported in this paper.

### Acknowledgments

Part of this work was financially supported by the Research Fund of Recep Tayyip Erdogan University (Project ID:1184). The numerical calculations reported in this paper were performed at TUBITAK ULAKBIM, High Performance, and Grid Computing Center (TRUBA Resources).

## 5. References

1. K. Serbest, T. Dural, M. Emirik, A. Zengin, Ö. Faiz, *J. Mol. Struct.* **2020**, 1229, 129579. DOI:10.1016/j.molstruc.2020.129579
2. M. Sarigul, P. Deveci, M. Kose, U. Arslan, H. Türk Dagi, M. Kurtoglu, *J. Mol. Struct.* **2015**, 1096, 64–73. DOI:10.1016/j.molstruc.2015.04.043
3. M. R. Lutfur, G. Hegde, S. Kumar, C. Tschierske, V. G. Chigrinov, *Opt. Mater. (Amst)*. **2009**, 32, 176–183. DOI:10.1016/j.optmat.2009.07.006
4. W. Zafar, S. H. Sumrra, & Z. H. Chohan, *Eur. J. Med. Chem.* **2021**, 222, 113602. DOI:10.1016/j.ejmech.2021.113602
5. S. Yasmeen, S. H. Sumrra, M. S. Akram, & Z. H. Chohan, *J. Enzyme Inhib. Med. Chem.* **2017**, 32, 106–112. DOI:10.1080/14756366.2016.1238363
6. S. Rani, S. H. Sumrra, & Z. H. Chohan, *Russ. J. Gen. Chem.* **2017**, 87, 1834–1842. DOI:10.1134/S107036321708031X
7. S. H. Sumrra, M. Hanif, Z. H. Chohan *et al.* *J. Enzyme Inhib. Med. Chem.* **2016**, 31, 590–598. DOI:10.3109/14756366.2015.1050011
8. S. H. Sumrra, U. Habiba, W. Zafar, M. Imran, & Z. H. Chohan, *J. Coord. Chem.* **2020**, 73, 2838–2877. DOI:10.1080/00958972.2020.1839751
9. M. Çol Ayvaz, İ. Turan, B. Dural, S. Demir, K. Karaoglu, Y. Aliyazicioglu, K. Serbest, *TURKISH J. Chem.* **2017**, 41, 728–747. DOI:10.3906/kim-1612-53
10. M. Ikram, Saeed-Ur-Rehman, S. Rehman, R.J. Baker, C. Schulzke, *Inorganica Chim. Acta* **2012**, 390, 210–216. DOI:10.1016/j.ica.2012.04.036
11. K. Bhagat, J. V. Singh, A. Sharma, A. Kaur, N. Kumar, H.K. Gulati, A. Singh, H. Singh, P. M. S. Bedi, *J. Mol. Struct.* **2021**, 1245, 131085. DOI:10.1016/j.molstruc.2021.131085
12. I. M. Dias, H. C. S. Junior, S. C. Costa, C. M. Cardoso, A. G. B. Cruz, C. E. R. Santos, D. R. S. Candela, S. Soriano, M. M. Marques, G. B. Ferreira, G. P. Guedes, *J. Mol. Struct.* **2020**, 1205, 127564. DOI:10.1016/j.molstruc.2019.127564
13. A. L. F. Sarria, A. F. L. Vilela, B. M. Fruger, J. B. Fernandes, R. M. Carlos, M. F. das G. F. da Silva, Q. B. Cass, C. L. Cardoso, *J. Inorg. Biochem.* **2016**, 164, 141–149. DOI:10.1016/j.jinorgbio.2016.09.010
14. S.-C. Tsaur, Some Fulgoroids (Insecta: Hemiptera) Collected on Turtle Island, Taiwan. *Zool. Stud.* **2005**, 44, 1–4.
15. T. Gokturk, A. Mihli, *Ann. Agrar. Sci.* **2016**, 14, 311–314. DOI:10.1016/j.aasci.2016.09.007
16. T. Göktürk, *Artvin Çoruh Üniversitesi Orman Fakültesi Derg.* **2015**, 16, 89–93. DOI:10.17474/acuofd.44749
17. J. Nast, *Paelearctic Auchenorrhyncha (Homoptera) an Annotated Checklist*. (Polish Scientific Publishers, Warszawa, **1972**).
18. V. M. Gnezdilov, *Entomol. Rev.* **2009**, 89, 1082–1086. https://doi./10.1134/S0013873809090097
19. E. Demir, Riciania Germar, 1818 species of western palaearctic region (Hemiptera: fulgoromorpha: Ricaniidae). *Munis Entomol. Zool.* **2009**, 4, pp. 271–275.
20. J. M. Urban, J. R. Cryan, *Mol. Phylogenet. Evol.* **2007**, 42, 556–572. DOI:10.1016/j.ympev.2006.08.009
21. D. Fournier, A. Mutero, *Comp. Biochem. Physiol. Part C Pharmacol. Toxicol. Endocrinol.* **1994**, 108, 19–31. DOI:10.1016/1367-8280(94)90084-1
22. F. Li, Z. Han, *Arch. Insect Biochem. Physiol.* **2002**, 51, 37–45. DOI:10.1002/arch.10048

23. S. Keane, M. Ryan, *Insect Biochem. Mol. Biol.* **1999**, 29, 1097–1104. DOI:10.1016/S0965-1748(99)00088-0
24. S. H. Sumrra, F. Mushtaq, F. Ahmad, R. Hussain, W. Zafar, M. Imran, M. N. Zafar, *Chem. Pap.* **2022**, 76, 3705–3727. DOI:10.1007/s11696-022-02123-1
25. S. H. Sumrra, W. Zafar, H. Javed, M. Zafar, M. Z. Hussein, M. Imran, M. A. Nadeem, *BioMetals* **2021**, 34, 1329–1351. DOI:10.1007/s10534-021-00345-6
26. S. H. Sumrra, Z. Arshad, W. Zafar, *et al. R. Soc. Open Sci.* **2021**, 8, 210910. DOI:10.1098/rsos.210910
27. A. W. Addison, T. N. Rao, J. Reedijk, J. van Rijn, G. C. Verschoor, *J. Chem. Soc., Dalt. Trans.* **1984**, 1349–1356. DOI:10.1039/DT9840001349
28. M. A. Said, A. Al-unizi, M. Al-Mamary, S. Alzahrani, D. Lentz, *Inorganica Chim. Acta* **2020**, 505, 119434. DOI:10.1098/rsos.210910
29. R. V. Sakthivel, P. Sankudevan, P. Vennila, G. Venkatesh, S. Kaya, G. Serdaroğlu, *J. Mol. Struct.* **2021**, 1233, 130097. DOI:10.1016/j.molstruc.2021.130097
30. N. E. H. Bensiradj, A. Dekhira, N. Zouaghi, O. Ouamerali, *Struct. Chem.* **2020**, 31, 1493–1503. DOI:10.1007/s11224-020-01509-9
31. K. Serbest, A. Özen, Y. Ünver, M. Er, İ. Degirmencioglu, K. Sancak, *J. Mol. Struct.* **2009**, 922, 1–10. DOI:10.1016/j.molstruc.2009.02.001
32. S. H. Sumrra, W. Zafar, M. L. Asghar, F. Mushtaq, M. A. Raza, M. F. Nazar, M. A. Nadeem, M. Imran, S. Mumtaz, *J. Mol. Struct.* **2021**, 1238, 130382. DOI:10.1016/j.molstruc.2021.130382
33. N. M. N. Gowda, S. B. Naikar, G. K. N. Reddy, Perchlorate Ion Complexes. **1984**, in 255–299. DOI:10.1016/S0898-8838(08)60210-X
34. M. Ghosh, P. Biswas, U. Flörke, *Polyhedron* **2007**, 26, 3750–3762. DOI:10.1016/j.poly.2007.04.014
35. B. J. Hathaway, A. E. Underhill, *J. Chem. Soc.* **1961**, 3091–3096. DOI:10.1039/jr9610003091
36. N. A. Vyas, S. S. Bhat, A. S. Kumbhar, U. B. Sonawane *et al. Eur. J. Med. Chem.* **2014**, 75, 375–381. DOI:10.1016/j.ejmech.2014.01.052
37. A. M. Bondžić, T. D. Lazarević-Pašti, A. R. Leskovic *et al. Eur. J. Pharm. Sci.* **2020**, 151, 105376. DOI:10.1016/j.ejps.2020.105376
38. M. Junaid, N. Islam, M. K., Hossain, M. O. Ullah, M. A. Halim, *PLoS One* **2019**, 14, e0211935. DOI:10.1371/journal.pone.0211935
39. S. Piersanti, M. Rebora, G. Salerno, S. Anton, *Insects* **2020**, 11, 886. DOI:10.3390/insects11120886
40. G.-M. Shen, X.-N. Wang, W. Dou, J.-J. Wang, *Pest Manag. Sci.* **2012**, 68, 1553–1563. DOI:10.1002/ps.3340
41. V. S. Zanon, J. A. Lima, T. Cuya, F. R. S. Lima, A. C. C. da Fonseca, J. G. Gomez, R. R. Ribeiro, T. C. C. França, M. D. Vargas, *J. Inorg. Biochem.* **2019**, 191, 183–193. DOI:10.1016/j.jinorgbio.2018.11.019
42. J. Y. Son, S. Shin, K. H. Choi, I. K. Park, *Int. J. Biochem. Cell Biol.* **2002**, 34, 204–210. DOI:10.1016/S1357-2725(01)00082-6
43. G. L. Ellman, K. D. Courtney, V. Andres, R. M. Featherstone, *Biochem. Pharmacol.* **1961**, 7, 88–95. DOI:10.1016/0006-2952(61)90145-9
44. M. A. Mohamed, S. Shaaalan, A.-E.M. Ghazy, A. A. Ali, A. M. Abd-Elaziz, M. M. E. Ghanem, S. A. Abd-Elghany, *Int. J. Biol. Macromol.* **2020**, 147, 1029–1040. DOI:10.1016/j.ijbiomac.2019.10.071
45. J. Tomasi, B. Mennucci, R. Cammi, *Chem. Rev.* **2005**, 105, 2999–3094. DOI:10.1021/cr9904009
46. M. J. Frisch, G. W. Trucks, H. B. Schlegel, G. E. Scuseria, M. A. Robb, M. A., Cheeseman, J. R., Scalmani, *et al.* Gaussian 09, revision A.02. **2009**.
47. N. M. O'boyle, A. L. Tenderholt, K. M. Langner, *J. Comput. Chem.* **2008**, 29, 839–845. DOI:10.1002/jcc.20823
48. M. H. Jamroz. Vibrational Energy Distribution Analysis: VEDA 4 Program, Warsaw. **2004**.

## Povzetek

Sintetizirali smo nove enojedrne ternarne komplekse prehodnih kovin:  $[M(HL)(bipy)_2]ClO_4$ , (M: Mn(II) v spojini **1**, Ni(II) v **2**),  $[M(HL)(bipy)(ClO_4)]$ , (M: Ni(II) v spojini **3**, Cu(II) v **4**, Zn(II) v **5**) in ligandoma 2-[(hidroksiimino)metil]-4-[-fenildiazetil]fenol,  $H_2L$ , in 2,2'-bipiridin. Strukture dobljenih spojin smo preučili z različnimi analitskimi in spektroskopskimi metodami, kot so elementna analiza, FTIR, UV-Vis, NMR, MALDI-TOF masna spektrometrija in termična analiza. Teoretske raziskave smo opravili z DFT metodo in uporabo B3LYP funkcije z naborom osnov 6-311++G (d, p)/LanLD2Z. Elektronske prehode v kompleksih smo nadalje karakterizirali z metodo TD-DFT/CAM-B3LYP. IR meritve in termična analiza potrjujejo predpostavljene strukture. Inhibicijsko delovanje kompleksov smo dokazali s preiskavo učinkov na acetilholinesterazo (AChE) ekstrahirano iz odraslih primerkov in ličink *Ricania simulans*. Med preiskovanimi kompleksi ima največjo aktivnost spojina **5** z najnižjo vrednostjo  $IC_{50}$  ( $3.2 \pm 0.8 \mu M$ ) za AChE odraslih osebkov in spojina **3** z najnižjo vrednostjo  $IC_{50}$  ( $4.6 \pm 0.8 \mu M$ ) za AChE ličink.



Except when otherwise noted, articles in this journal are published under the terms and conditions of the Creative Commons Attribution 4.0 International License



# Synthesis, Antimicrobial and Molecular Docking Studies of Some New Derivatives of 2,3-Dihydroquinazolin-4(1H)-one

Karim Zahmatkesh,<sup>1</sup> Karim Akbari Dilmaghani<sup>1,\*</sup> and Yasin Sarveahrabi<sup>2</sup>

<sup>1</sup> Department of Organic Chemistry, Faculty of Chemistry, Urmia University, Urmia, 57159, Iran.

<sup>2</sup> Department of Biology, Central Tehran Branch, Islamic Azad University, Tehran, Iran.

\* Corresponding author: E-mail: k.adilmaghani@urmia.ac.ir

Tel: (+98)914-443-1392; Fax: (+98)44-357153-165

Received: 03-29-2022

## Abstract

In the present study a series of novel 2-(substituted phenyl)-3-(5-phenyl-1,3,4-thiadiazol-2-yl)-2,3-dihydroquinazolin-4(1H)-one derivatives were synthesized by refluxing isatoic anhydride, 5-phenyl-1,3,4-thiadiazol-2-amine and aromatic aldehydes in the presence of *p*-TsOH as the catalyst and in H<sub>2</sub>O as the solvent and characterized by spectroscopic data and analytical methods. Antibacterial and antifungal activity of the title compounds were evaluated against two Gram positive and two Gram negative bacterial strains and strains of fungi and compared with standard drugs, using well diffusion method minimum bactericidal/fungicidal concentration were determined. The potential  $\alpha$ -amylase and  $\alpha$ -glucosidase inhibitory activity of compounds **4a–l** were investigated *in silico* using molecular docking simulation method. Therefore, these 2,3-dihydroquinazolin-4(1H)-one derivatives may be considered as promising candidates for the development of new classes of antimicrobial and antidiabetic drugs.

**Keywords:** Isatoic anhydride, 2,3-dihydroquinazolin-4(1H)-one, antibacterial activity, antifungal activity, anti-diabetic activity.

## 1. Introduction

The 2,3-dihydroquinazolin-4(1H)-one (DHQ) is an important nitrogen-containing heterocyclic scaffold. DHQ ring system is a distinguished scaffold in drug design. DHQ in medicinal chemistry acting as an important pharmacophore has drawn much attention due to its broad spectrum of pharmaceutical activities, which include antibacterial,<sup>1,2</sup> antifungal,<sup>3–5</sup> anticancer,<sup>6–8</sup> antidiabetic,<sup>9</sup> anti-tuberculin,<sup>10</sup> anti-inflammatory,<sup>11–13</sup> cholinesterase inhibitory,<sup>14</sup> antihypertensive activities<sup>15,16</sup> and insecticidal activity<sup>17</sup>.

On the other hand, 2-amino-1,3,4-thiadiazole and its derivatives have drawn attention of many organic chemists during recent years, since many of these compounds are known to possess interesting biological properties such as antibacterial,<sup>18,19</sup> antifungal,<sup>20–22</sup> anticancer,<sup>23–25</sup> antihypertensive<sup>26,27</sup> activities. Considering the reactivity of the amine group in the derivatization process, 2-amino-1,3,4-thiadiazole moiety is a good scaffold for drug synthesis. Most of the DHQ derivatives are substituted on the carbons 2 and 3. Due to their attractive properties,

2-substituted DHQs are becoming prominent synthetic intermediates for organic chemists and pharmacologist.

Based on the above observations we report here the synthesis of a new series of 2,3-dihydroquinazolin-4(1H)-one derivatives **4a–l** with structure modifications involving incorporation of 5-phenyl-1,3,4-thiadiazol-2-amine (**3**) at position 3 and aromatic aldehydes **2a–l** at position 2 of DHQ ring system. In the present study, various aryl aldehyde groups were specifically incorporated at position 2 of the DHQ scaffold with the aim of new antibacterial, antifungal and anti diabetic drugs.

## 2. Experimental

Starting materials, solvents, and culture environments (nutrient agar/broth, Sabouraud dextrose and agar/broth) were obtained from Merck, Germany and used without any additional filtration. Microbiological tests were performed using a Memmert INC153T2T3 incubator. Melting points were determined in Philip Harris

C4954718 melting point apparatus and are uncorrected. IR spectra were recorded on a Thermo Nicolet Nexus-670 FTIR spectrophotometer, using potassium bromide pellets and the frequencies are expressed in  $\text{cm}^{-1}$ . The  $^1\text{H}$  and  $^{13}\text{C}$  NMR spectra were recorded with a Bruker Avance 400 MHz spectrometer, using TMS as the internal reference, with  $\text{DMSO}-d_6$  as the solvent. Chemical shifts are reported in parts per million (ppm). Mass spectra were obtained on a 5973 Network Mass Selective Detector instrument using electron impact ionization (EI, 70 eV). Elemental analysis was performed on FlashEA 1112 series (Thermo Finnigan) CHNS analyzer.

## 2. 1. Synthesis of 5-Phenyl-1,3,4-thiadiazol-2-amine (3)

A stirring mixture of benzoic acid (50 mmol), thiosemicarbazide (50 mmol) and phosphorus oxychloride ( $\text{POCl}_3$ ) (15 mL) was heated at  $75^\circ\text{C}$  for 1 h. After cooling to room temperature, water was added; the reaction mixture was further refluxed for 4 h. After cooling, the mixture was basified to pH 8 by the dropwise addition of 50% potassium hydroxide solution under stirring. Thus, obtained precipitate was filtered and recrystallized from ethanol.<sup>28</sup>

This compound was obtained as yellow solid in a yield 7.53 g (85%); m.p.  $225\text{--}227^\circ\text{C}$ ; IR (KBr,  $\text{cm}^{-1}$ ):  $\nu_{\text{max}}$  3267.45, 3062.96 (NH), 1629.53 (C=N), 1510.55 (strong bending NH), 664.71 (C-S);  $^1\text{H}$  NMR (500 MHz,  $\text{DMSO}-d_6$ )  $\delta$  7.42 (s, 2H, NH), 7.44–7.46 (m, 3H, ArH), 7.74 (d,  $J = 7.7$  Hz, 2H, ArH).  $^{13}\text{C}$  NMR (125 MHz,  $\text{DMSO}-d_6$ )  $\delta$  126.7 (2CH), 129.6 (2CH), 130.0, 131.4, 156.8 (C=N), 169.0 (C=N). MS  $m/z$  177.1 ( $\text{M}^+ + \text{H}$ ). Anal. Calcd for  $\text{C}_8\text{H}_7\text{N}_3\text{S}$ : C, 54.22; H, 3.98; N, 23.71; S, 18.09. Found: C, 54.23; H, 3.99; N, 23.74; S, 18.13.

## 2. 2. General Procedure for the Synthesis of Compounds 2-Substituted Phenyl-3-(5-phenyl-1,3,4-thiadiazol-2-yl)-2,3-dihydroquinazolin-4(1H)-ones 4a–l

To a round-bottom flask containing  $\text{H}_2\text{O}$  (5 mL) was added isatoic anhydride (1 mmol, 0.1631 g), relevant aldehyde (1 mmol), 1,3,4-thiadiazol-2-amine (1.1 mmol, 0.1949 g) and *p*-TsOH (our inventory was its monohydrate) (0.6 mmol, 0.1141 g). The mixture was heated under reflux for 2 hours. The precipitate was filtered and recrystallized from EtOH.<sup>29</sup> See Tables 1 and 2 and Scheme 1.

### 2-Phenyl-3-(5-Phenyl-1,3,4-thiadiazol-2-yl)-2,3-dihydroquinazolin-4(1H)-one (4a)

This compound was obtained as light brown solid in a yield 0.3113 g (81%); m.p.  $171\text{--}173^\circ\text{C}$ . IR (KBr,  $\text{cm}^{-1}$ ):  $\nu_{\text{max}}$  3364.47 (NH), 3033.20 (C-H), 1633.86 (C=O), 1500.59 (C=N), 1448.65 (strong bending NH), 1386.63 (C-N), 1180.94 (N-N), 689.71 (C-S).  $^1\text{H}$  NMR (500 MHz,  $\text{DMSO}-d_6$ )  $\delta$  6.81 (t,  $J = 7.5$  Hz, 1H, NH), 6.93 (d,  $J =$

8.2 Hz, 1H, CH), 7.32 (m, 5H, ArH), 7.41 (t,  $J = 3.8$  Hz, 1H, ArH), 7.44 (d,  $J = 0.58$  Hz, 1H, ArH), 7.55 (m, 3H, ArH), 7.82 (d,  $J = 7.9$  Hz, 1H, ArH), 7.98 (d,  $J = 6.5$  Hz, 2H, ArH), 8.34 (d,  $J = 0.2$  Hz, 1H, ArH).  $^{13}\text{C}$  NMR (125 MHz,  $\text{DMSO}-d_6$ )  $\delta$  69.0 (N-C-N), 113.2, 116.2, 118.9, 126.1 (2CH), 127.5 (2CH), 128.9, 128.9, 129.1 (2CH), 129.9 (2CH), 130.4, 131.3, 136.2, 139.8, 147.3, 158.2 (C=O), 160.9 (C=N), 164.3 (C=N). MS  $m/z$  384.2 ( $\text{M}^+ + \text{H}$ ). Anal. Calcd for  $\text{C}_{22}\text{H}_{16}\text{N}_4\text{O}_2\text{S}$ : C, 68.73; H, 4.20; N, 14.57; S, 8.34. Found: C, 68.77; H, 4.25; N, 15.02; S, 8.29.

### 2-(2-Chlorophenyl)-3-(5-phenyl-1,3,4-thiadiazol-2-yl)-2,3-dihydroquinazolin-4(1H)-one (4b)

This compound was obtained as brownish yellow solid in a yield 0.3518 g (84%); m.p.  $210\text{--}212^\circ\text{C}$ . IR (KBr,  $\text{cm}^{-1}$ ):  $\nu_{\text{max}}$  3324.17 (NH), 3056.76 (C-H), 1661.58 (C=O), 1615.33 (C=N), 1506.09 (strong bending NH), 1439.22 (C-N), 1245.53 (N-N), 748.42 (C-Cl), 685.60 (C-S).  $^1\text{H}$  NMR (500 MHz,  $\text{DMSO}-d_6$ )  $\delta$  6.86 (t,  $J = 7.6$  Hz, 1H, NH), 6.90 (d,  $J = 8.2$  Hz, 1H, CH), 7.07 (d,  $J = 7.8$  Hz, 1H, ArH), 7.20 (t,  $J = 7.7$  Hz, 1H, ArH), 7.33 (t,  $J = 7.6$  Hz, 1H, ArH), 7.41 (t,  $J = 7.8$  Hz, 1H, ArH), 7.53 (t,  $J = 3.3$  Hz, 3H, ArH), 7.57 (d,  $J = 7.9$  Hz, 1H, ArH), 7.60 (d,  $J = 3.3$  Hz, 1H, ArH), 7.93 (t,  $J = 7.4$  Hz, 3H, ArH), 8.11 (d,  $J = 4.2$  Hz, 1H, ArH).  $^{13}\text{C}$  NMR (125 MHz,  $\text{DMSO}-d_6$ )  $\delta$  67.2 (N-C-N), 112.5, 116.5, 119.1, 125.8, 127.5 (2CH), 128.1, 128.8, 129.9 (2CH), 130.3, 130.9 (2CH), 131.4 (C-Cl), 132.1, 136.3, 136.9, 146.1, 157.4 (C=O), 160.9 (C=N), 164.5 (C=N). MS  $m/z$  418.2 ( $\text{M}^+ + \text{H}$ ). Anal. Calcd for  $\text{C}_{22}\text{H}_{15}\text{ClN}_4\text{O}_2\text{S}$ : C, 63.08; H, 3.61; N, 13.38; S, 7.65. Found: C, 63.05; H, 3.62; N, 13.45; S, 7.77.

### 2-(4-Chlorophenyl)-3-(5-phenyl-1,3,4-thiadiazol-2-yl)-2,3-dihydroquinazolin-4(1H)-one (4c)

This compound was obtained as greenish yellow solid in a yield 0.3560 g (85%); m.p.  $227\text{--}229^\circ\text{C}$ . IR (KBr,  $\text{cm}^{-1}$ ):  $\nu_{\text{max}}$  3377.68 (NH), 3053.97 (C-H), 1650.19 (C=O), 1613.78 (C=N), 1488.61 (strong bending NH), 1447.76 (C-N), 1253.00 (N-N), 756.40 (C-Cl), 684.14 (C-S).  $^1\text{H}$  NMR (500 MHz,  $\text{DMSO}-d_6$ )  $\delta$  6.82 (t,  $J = 7.4$  Hz, 1H, NH), 6.94 (d,  $J = 8.2$  Hz, 1H, CH), 7.33 (d,  $J = 8.2$  Hz, 2H, ArH), 7.39 (d,  $J = 8.3$  Hz, 2H, ArH), 7.43 (d,  $J = 8.6$  Hz, 2H, ArH), 7.54 (t,  $J = 4.0$  Hz, 3H, ArH), 7.82 (d,  $J = 7.9$  Hz, 1H, ArH), 8.0 (m, 2H, ArH), 8.31 (d,  $J = 4.0$  Hz, 1H, ArH).  $^{13}\text{C}$  NMR (125 MHz,  $\text{DMSO}-d_6$ )  $\delta$  68.5 (N-C-N), 113.2, 116.3, 119.1, 127.5 (2CH), 128.1 (2CH), 129.0, 129.2 (2CH), 129.9 (2CH), 130.4, 131.3 (C-Cl), 133.6, 136.3, 138.8, 147.1, 158.1 (C=O), 160.7 (C=N), 164.4 (C=N). MS  $m/z$  418.2 ( $\text{M}^+ + \text{H}$ ). Anal. Calcd for  $\text{C}_{22}\text{H}_{15}\text{ClN}_4\text{O}_2\text{S}$ : C, 63.08; H, 3.61; N, 13.38; S, 7.65. Found: C, 63.07; H, 3.60; N, 13.41; S, 7.76.

### 2-(2-Nitrophenyl)-3-(5-phenyl-1,3,4-thiadiazol-2-yl)-2,3-dihydroquinazolin-4(1H)-one (4d)

This compound was obtained as yellow solid in a yield 0.3521 g (82%); m.p.  $199\text{--}201^\circ\text{C}$ . IR (KBr,  $\text{cm}^{-1}$ ):

$\nu_{\max}$  3356.94 (NH), 3063.28 (C–H), 1660.59 (C=O), 1615.85 (C=N), 1509.00 (strong bending NH), 1438.99 (C–N), 1509.00 and 1338.31 (NO<sub>2</sub>), 1248.33 (N–N), 687.14 (C–S). <sup>1</sup>H NMR (500 MHz, DMSO-*d*<sub>6</sub>):  $\delta$  6.88 (t, *J* = 0.5 Hz, 1H, NH), 7.27 (d, *J* = 7.4 Hz, 1H, CH), 7.41 (t, *J* = 8.08 Hz, 1H), 7.47 (d, *J* = 6.82 Hz, 1H), 7.52 (t, *J* = 1.98 Hz, 3H), 7.59 (t, *J* = 8.7 Hz, 2H, ArH), 7.92 (m, 4H, ArH), 8.02 (d, *J* = 0.8 Hz, 1H, ArH), 8.12 (d, *J* = 7.6 Hz, 1H, ArH). <sup>13</sup>C NMR (125 MHz, DMSO-*d*<sub>6</sub>)  $\delta$  65.9 (N–C–N), 112.7, 117.2, 119.6, 126.2, 126.5, 127.5 (2CH), 128.8, 129.8 (2CH), 130.2, 130.7, 131.4, 134.6, 134.8, 136.4, 146.0, 147.8 (C–NO<sub>2</sub>), 157.5 (C=O), 160.6 (C=N), 164.6 (C=N). MS *m/z* 429.1 (M<sup>+</sup> + H). Anal. Calcd for C<sub>22</sub>H<sub>15</sub>N<sub>5</sub>O<sub>3</sub>S: C, 61.53; H, 3.52; N, 16.31; S, 7.47. Found: C, 61.50; H, 3.55; N, 16.38; S, 7.41.

**2-(3-Nitrophenyl)-3-(5-phenyl-1,3,4-thiadiazol-2-yl)-2,3-dihydroquinazolin-4(1H)-one (4e)**

This compound was obtained as brownish yellow solid in a yield 0.3649 g (85%); m.p. 226–228 °C. IR (KBr, cm<sup>−1</sup>):  $\nu_{\max}$  3353.50 (NH), 3065.72 (C–H), 1659.93 (C=O), 1613.78 (C=N), 1519.31 (strong bending NH), 1444.15 (C–N), 1519.31 and 1357.73 (NO<sub>2</sub>), 1300.09 (N–N), 686.53 (C–S). <sup>1</sup>H NMR (500 MHz, DMSO-*d*<sub>6</sub>):  $\delta$  6.84 (t, *J* = 7.6 Hz, 1H, NH), 6.98 (d, *J* = 8.2 Hz, 1H, CH), 7.44 (t, *J* = 7.5 Hz, 1H, ArH), 7.56 (t, *J* = 3.5 Hz, 3H, ArH), 7.58 (d, *J* = 3.9 Hz, 1H, ArH), 7.62 (d, *J* = 8.0 Hz, 1H, ArH), 7.68 (d, *J* = 7.8 Hz, 1H, ArH), 7.85 (d, *J* = 3.3 Hz, 1H, ArH), 7.98 (m, 2H, ArH), 8.14 (d, *J* = 8.1 Hz, 1H, ArH), 8.30 (s, 1H, ArH), 8.43 (d, *J* = 4.0 Hz, 1H, ArH). <sup>13</sup>C NMR (125 MHz, DMSO-*d*<sub>6</sub>)  $\delta$  68.3 (N–C–N), 113.1, 116.4, 119.4, 121.3, 124.0, 127.5 (2CH), 129.0, 129.9 (2CH), 130.3, 130.9, 131.4, 132.4, 136.4, 142.1, 146.8, 148.5 (C–NO<sub>2</sub>), 158.0 (C=O), 160.5 (C=N), 164.6 (C=N). MS *m/z* 429.2 (M<sup>+</sup> + H). Anal. Calcd for C<sub>22</sub>H<sub>15</sub>N<sub>5</sub>O<sub>3</sub>S: C, 61.53; H, 3.52; N, 16.31; S, 7.47. Found: C, 61.55; H, 3.50; N, 16.36; S, 7.59.

**2-(4-Nitrophenyl)-3-(5-phenyl-1,3,4-thiadiazol-2-yl)-2,3-dihydroquinazolin-4(1H)-one (4f)**

This compound was obtained as light green solid in a yield 0.3606 g (84%); m.p. 190–192 °C. IR (KBr, cm<sup>−1</sup>):  $\nu_{\max}$  3371.85 (NH), 3058.92 (C–H), 1657.13 (C=O), 1609.39 (C=N), 1520.35 (strong bending NH), 1441.98 (C–N), 1490.12 and 1347.08 (NO<sub>2</sub>), 1306.95 (N–N), 693.16 (C–S). <sup>1</sup>H NMR (500 MHz, DMSO-*d*<sub>6</sub>):  $\delta$  6.85 (t, *J* = 7.6 Hz, 1H, NH), 6.96 (d, *J* = 8.3 Hz, 1H, CH), 7.44 (t, *J* = 8.0 Hz, 1H, ArH), 7.56 (m, 3H, ArH), 7.59 (m, 3H, ArH), 7.83 (t, *J* = 4.0 Hz, 1H, ArH), 7.99 (d, *J* = 3.6 Hz, 2H, ArH), 8.20 (d, *J* = 8.4 Hz, 2H, ArH), 8.41 (d, *J* = 3.7 Hz, 1H, ArH). <sup>13</sup>C NMR (125 MHz, DMSO-*d*<sub>6</sub>)  $\delta$  68.5 (N–C–N), 113.2, 116.4, 119.4, 124.4 (2CH), 127.5 (2CH), 127.6 (2CH), 129.0, 129.9 (2CH), 130.3, 131.4, 136.4, 146.8, 147.0 (C–NO<sub>2</sub>), 148.0, 158.0 (C=O), 160.5 (C=N), 164.5 (C=N). MS *m/z* 429.2 (M<sup>+</sup> + H). Anal. Calcd for C<sub>22</sub>H<sub>15</sub>N<sub>5</sub>O<sub>3</sub>S: C, 61.53; H, 3.52; N, 16.31; S, 7.47. Found: C, 61.50; H, 3.54; N, 16.30; S, 7.38.

**2-(2-Hydroxyphenyl)-3-(5-phenyl-1,3,4-thiadiazol-2-yl)-2,3-dihydroquinazolin-4(1H)-one (4g)**

This compound was obtained as green solid in a yield 0.3123 g (78%); m.p. 218–220 °C. IR (KBr, cm<sup>−1</sup>):  $\nu_{\max}$  3380.01 (NH), 3060.60 (O–H), 2946.15 (C–H), 1665.55 (C=O), 1609.81 (C=N), 1496.30 (strong bending NH), 1456.32 (C–N), 1312.71 (N–N), 1236.41 (C–O), 687.01 (C–S). <sup>1</sup>H NMR (500 MHz, DMSO-*d*<sub>6</sub>):  $\delta$  6.61 (t, *J* = 7.4 Hz, 1H, NH), 6.75 (d, *J* = 8.5 Hz, 1H, CH), 6.90 (t, *J* = 8.6 Hz, 2H, ArH), 7.12 (m, 1H, ArH), 7.35 (t, *J* = 7.8 Hz, 1H, ArH), 7.48 (d, *J* = 7.0 Hz, 2H, ArH), 7.53 (m, 2H, ArH), 7.77 (m, 2H, ArH), 7.86 (d, *J* = 8.1 Hz, 1H, ArH), 7.93 (d, *J* = 5.0 Hz, 2H, ArH), 10.23 (s, 1H, OH). <sup>13</sup>C NMR (125 MHz, DMSO-*d*<sub>6</sub>)  $\delta$  66.0 (N–C–N), 112.4, 116.1, 116.2, 118.4, 119.0, 125.4, 125.6, 127.4 (2CH), 128.7, 129.8 (2CH), 130.0, 130.4, 131.2, 135.9, 147.2, 155.2 (C–OH), 157.6 (C=O), 161.4 (C=N), 164.2 (C=N). MS *m/z* 400.2 (M<sup>+</sup> + H). Anal. Calcd for C<sub>22</sub>H<sub>16</sub>N<sub>4</sub>O<sub>2</sub>S: C, 65.99; H, 4.03; N, 13.99; S, 8.01. Found: C, 66.07; H, 4.01; N, 13.95; S, 8.25.

**2-(3-Hydroxyphenyl)-3-(5-phenyl-1,3,4-thiadiazol-2-yl)-2,3-dihydroquinazolin-4(1H)-one (4h)**

This compound was obtained as brown solid in a yield 0.3203 g (80%); m.p. 207–209 °C. IR (KBr, cm<sup>−1</sup>):  $\nu_{\max}$  3275.51 (NH), 3075.36 (O–H), 2910.10 (C–H), 1601.72 (C=O), 1505.26 (C=N), 1505.26 (strong bending NH), 1448.04 (C–N), 1379.91 (N–N), 1216.41 (C–O), 683.43 (C–S). <sup>1</sup>H NMR (500 MHz, DMSO-*d*<sub>6</sub>):  $\delta$  6.68 (t, *J* = 1.3 Hz, 1H, NH), 6.79 (d, *J* = 7.0 Hz, 1H, CH), 6.93 (m, 1H, ArH), 7.13 (t, *J* = 4.4 Hz, 3H, ArH), 7.42 (t, *J* = 8.7 Hz, 4H, ArH), 7.72 (d, *J* = 8.1 Hz, 1H, ArH), 7.83 (m, 2H, ArH), 7.99 (d, *J* = 8.1 Hz, 2H, ArH), 9.93 (s, 1H, OH). <sup>13</sup>C NMR (125 MHz, DMSO-*d*<sub>6</sub>)  $\delta$  68.9 (N–C–N), 115.4, 115.8, 116.2, 116.9, 118.8, 127.5 (2CH), 128.9, 129.9 (2CH), 130.4, 131.3, 131.6, 134.2, 136.2, 141.3, 145.9, 147.4 (C–OH), 157.9 (C=O), 164.3 (C=N), 170.0 (C=N). MS *m/z* 400.2 (M<sup>+</sup> + H). Anal. Calcd for C<sub>22</sub>H<sub>16</sub>N<sub>4</sub>O<sub>2</sub>S: C, 65.99; H, 4.03; N, 13.99; S, 8.01. Found: C, 66.02; H, 4.04; N, 14.05; S, 8.13.

**2-(4-Hydroxyphenyl)-3-(5-phenyl-1,3,4-thiadiazol-2-yl)-2,3-dihydroquinazolin-4(1H)-one (4i)**

This compound was obtained as red solid in a yield 0.3203 g (80%); m.p. 210–212 °C. IR (KBr, cm<sup>−1</sup>):  $\nu_{\max}$  3281.73 (NH), 3152.73 (O–H), 2929.54 (C–H), 1616.59 (C=O), 1582.00 (C=N), 1526.97 (strong bending NH), 1501.20 (C–N), 1299.01 (N–N), 1258.42 (C–O), 678.90 (C–S). <sup>1</sup>H NMR (500 MHz, DMSO-*d*<sub>6</sub>):  $\delta$  6.69 (m, 2H, NH, CH), 6.95 (d, *J* = 8.5 Hz, 2H, ArH), 7.13 (t, *J* = 4.0 Hz, 3H, ArH), 7.33 (t, *J* = 3.0 Hz, 1H, ArH), 7.55 (m, 2H, ArH), 7.78 (m, 2H, ArH), 7.98 (d, *J* = 7.6 Hz, 2H, ArH), 8.23 (d, *J* = 1.4 Hz, 1H, ArH), 9.80 (s, 1H, OH). <sup>13</sup>C NMR (125 MHz, DMSO-*d*<sub>6</sub>)  $\delta$  68.8 (N–C–N), 113.1, 116.2, 118.7, 126.9 (2CH), 127.5 (2CH), 128.6 (2CH), 128.9, 129.7 (2CH), 130.5, 136.1, 138.2, 146.0, 147.4, 158.0 (C–

OH), 163.8 (C=O), 164.2 (C=N), 169.3 (C=N). MS  $m/z$  400.2 ( $M^+ + H$ ). Anal. Calcd for  $C_{22}H_{16}N_4O_2S$ : C, 65.99; H, 4.03; N, 13.99; S, 8.01. Found: C, 65.90; H, 4.06; N, 13.92; S, 7.87.

### 2-(3-Methoxyphenyl)-3-(5-phenyl-1,3,4-thiadiazol-2-yl)-2,3-dihydroquinazolin-4(1H)-one (4j)

This compound was obtained as greenish yellow solid in a yield 0.3149 g (76%); m.p. 192–194 °C. IR (KBr,  $cm^{-1}$ ):  $\nu_{max}$  3259.27 (NH), 3012.24 (C–H), 1653.97 (C=O), 1615.35 (C=N), 1510.68 (strong bending NH), 1441.67 (C–N), 1295.99 (N–N), 1260.28 (C–O), 685.30 (C–S).  $^1H$  NMR (500 MHz, DMSO- $d_6$ ):  $\delta$  3.68 (s, 3H,  $CH_3$ ), 6.81 (m, 2H, NH, CH), 6.85 (d,  $J$  = 8.1 Hz, 1H, ArH), 6.94 (d,  $J$  = 9.4 Hz, 2H, ArH), 7.22 (t,  $J$  = 8.1 Hz, 1H, ArH), 7.42 (d,  $J$  = 6.5 Hz, 2H, ArH), 7.54 (m, 3H, ArH), 7.83 (d,  $J$  = 8.0 Hz, 1H, ArH), 7.98 (d,  $J$  = 6.2 Hz, 2H, ArH), 8.32 (d,  $J$  = 1.0 Hz, 1H, ArH).  $^{13}C$  NMR (125 MHz, DMSO- $d_6$ )  $\delta$  55.5 ( $CH_3$ ), 68.8 (N–C–N), 112.8, 113.2, 113.6, 116.2, 118.2, 118.9, 127.5 (2CH), 128.9, 129.8 (2CH), 130.3, 130.4, 131.3, 136.2, 141.4, 147.4, 158.2 (C–OCH $_3$ ), 159.8 (C=O), 160.9 (C=N), 164.3 (C=N). MS  $m/z$  414.2 ( $M^+ + H$ ). Anal. Calcd for  $C_{23}H_{18}N_4O_2S$ : C, 66.65; H, 4.38; N, 13.52; S, 7.73. Found: C, 66.90; H, 4.34; N, 13.83; S, 7.57.

### 2-(4-Methoxyphenyl)-3-(5-phenyl-1,3,4-thiadiazol-2-yl)-2,3-dihydroquinazolin-4(1H)-one (4k)

This compound was obtained as brownish yellow solid in a yield 0.3232 g (78%); m.p. 220–222 °C. IR (KBr,  $cm^{-1}$ ):  $\nu_{max}$  3397.48 (NH), 3057.61 (C–H), 1660.24 (C=O), 1609.56 (C=N), 1504.27 (strong bending NH), 1455.58 (C–N), 1300.42 (N–N), 1242.84 (C–O), 686.93 (C–S).  $^1H$  NMR (500 MHz, DMSO- $d_6$ ):  $\delta$  3.67 (s, 3H,  $CH_3$ ), 6.81 (m, 2H, NH, CH), 6.92 (d,  $J$  = 8.1 Hz, 2H, ArH), 7.13 (d,  $J$  = 8.0 Hz, 1H, ArH), 7.42 (m, 1H, ArH), 7.55 (m, 5H, ArH), 7.82 (d,  $J$  = 8.3 Hz, 2H, ArH), 7.98 (m, 2H, ArH).  $^{13}C$  NMR (125 MHz, DMSO- $d_6$ )  $\delta$  55.5 ( $CH_3$ ), 68.7 (N–C–N), 113.2, 114.4 (2CH), 116.2, 118.76, 127.0 (2CH), 128.6 (2CH), 128.9, 129.9 (2CH), 131.2, 131.7, 132.2, 136.2, 147.4, 158.1 (C–OCH $_3$ ), 159.7 (C=O), 160.9 (C=N), 164.2 (C=N). MS  $m/z$  414.2 ( $M^+ + H$ ). Anal. Calcd for  $C_{23}H_{18}N_4O_2S$ : C, 66.65; H, 4.38; N, 13.52; S, 7.73. Found: C, 66.73; H, 4.47; N, 13.43; S, 7.88.

### 3-(5-Phenyl-1,3,4-thiadiazol-2-yl)-2-(p-tolyl)-2,3-dihydroquinazolin-4(1H)-one (4l)

This compound was obtained as brownish yellow solid in a yield 0.2868 g (72%); m.p. 208–210 °C. IR (KBr,  $cm^{-1}$ ):  $\nu_{max}$  3373.40 (NH), 3052.07 (C–H), 1649.00 (C=O),

1613.00 (C=N), 1494.77 (strong bending NH), 1448.97 (C–N), 1290.22 (N–N), 682.73 (C–S).  $^1H$  NMR (500 MHz, DMSO- $d_6$ ):  $\delta$  2.20 (s, 3H,  $CH_3$ ), 6.80 (t,  $J$  = 8.07 Hz, 1H, NH), 6.92 (d,  $J$  = 8.2 Hz, 1H, CH), 7.11 (m, 2H, ArH), 7.14 (d,  $J$  = 7.8 Hz, 2H, ArH), 7.19 (d,  $J$  = 7.8 Hz, 2H, ArH), 7.39 (d,  $J$  = 0.3 Hz, 1H, ArH), 7.55 (m, 3H, ArH), 7.82 (d,  $J$  = 0.6 Hz, 1H, ArH), 7.97 (d,  $J$  = 6.4 Hz, 2H, ArH).  $^{13}C$  NMR (125 MHz, DMSO- $d_6$ )  $\delta$  21.0 ( $CH_3$ ), 68.9 (N–C–N), 113.2, 116.2, 126.0 (2CH), 127.5 (2CH), 128.9, 129.6 (2CH), 129.9 (2CH), 130.4, 136.2, 136.9, 138.3, 138.3 (C–CH $_3$ ), 147.4, 158.2, 160.9 (C=O), 164.2 (C=N), 169.4 (C=N). MS  $m/z$  398.2 ( $M^+ + H$ ). Anal. Calcd for  $C_{23}H_{18}N_4OS$ : C, 69.33; H, 4.55; N, 14.06; S, 8.05. Found: C, 69.63; H, 4.59; N, 14.16; S, 8.23.

## 2. 3. Antibacterial Activity (*In vitro*)

The antibacterial activity of synthesized compounds **4a–l** was evaluated against two Gram positive and two Gram negative bacteria by using the well diffusion method, minimum inhibitory concentration (MIC), and minimum bactericidal concentration (MBC). Ciprofloxacin was employed as the standard drug to compare the results. Strains of *Staphylococcus aureus* PTCC1826, *Staphylococcus epidermidis* PTCC1856, *Escherichia coli* PTCC1789, and *Pseudomonas aeruginosa* PTCC1950, were taken from the Iranian industrial microorganisms collection center (lyophilized). The bacterial cultures were developed by selective nutrient broth at 37 °C, 24 h. Nutrient broth was used for the preparation of inoculums of the bacteria and nutrient agar and broth were used for the screening method<sup>21</sup> and their results are shown in Table 3.

## 2. 4. Antifungal Activity (*In vitro*)

Also the antifungal activity of synthesized compounds **4a–l** was evaluated against two fungal strains by using the well diffusion method, minimum inhibitory concentration (MIC), and minimum fungicidal concentration (MFC). Amphotericin B was employed as the standard drug to compare the results. Strains of *Candida albicans* PTCC5027 and *Aspergillus niger* PTCC5320, were taken from the Iranian industrial microorganisms collection center. The fungal cultures were developed by selective Sabouraud dextrose broth at 37 °C and stored at 4 °C for further use. Sabouraud dextrose broth was used for the preparation of inoculums of the fungi and Sabouraud dextrose agar and broth were used for the screening method<sup>21</sup> and their results are presented in Table 4.

Table 1. Groups (X) attached to benzaldehyde

4 and 2	a	b	c	d	e	f	g	h	i	j	k	l
X	H	2-Cl	4-Cl	2-NO $_2$	3-NO $_2$	4-NO $_2$	2-OH	3-OH	4-OH	3-OCH $_3$	4-OCH $_3$	4-CH $_3$

Table 2. Structure of compounds 4a–l

4a		4g	
4b		4h	
4c		4i	
4d		4j	
4e		4k	
4f		4l	

## 2. 5. Anti-diabetic Propertises by Molecular Docking (*In silico*)

AutoDock Vina v.1.2.0 was used to perform all docking simulations. A set of new quinazolin derivatives were subjected to docking with  $\alpha$ -amylase (PDB ID: 1hny) and  $\alpha$ -glucosidase (PDB ID: 2ze0) from the protein data bank (RCSB) (<http://www.rcsb.org/pdb>). To carry out *in silico* studies, the 2D structures of the synthesized ligands **4a–l** were drawn by ChemDraw 19.1.1 and converted to ener-

gy minimized 3D structures in the pdb file format using Chem3D. By removing the heteroatoms, water molecule and cofactors, the target protein file was prepared by leaving the associated residue with protein by using Discovery Studio 4.5 Client. Preparation of target protein file AutoDockTools-1.5.6 has been done, which involves the assigning of Gasteiger charges for all the atoms of molecules converting into AD4 type. Grid box for 1hny was  $64 \times 64 \times 64$  and for 2ze0 was  $72 \times 72 \times 72$ . Docking simulations for

the compounds **4a–l** were performed against the active site of  $\alpha$ -amylase and  $\alpha$ -glucosidase, finally Discovery Studio 4.5 Client was used to visualize docking results, which are shown in Table 5 and Figure 1.

### 3. Results and Discussion

#### 3.1. Chemistry

Considering the importance of 2,3-dihydroquinazolin-4(1*H*)-ones several methods have been revealed for the synthesis of these compounds.<sup>30–32</sup> In this study compounds 2-(substituted phenyl)-3-(5-phenyl-1,3,4-thiadiazol-2-yl)-2,3-dihydroquinazolin-4(1*H*)-one **4a–l** were obtained by refluxing isatoic anhydride (**1**), 5-phenyl-1,3,4-thiadiazol-2-amine (**3**) and aromatic aldehydes **2a–l** in the presence of *p*-TsOH as the catalyst in H<sub>2</sub>O as the solvent (Scheme 1).

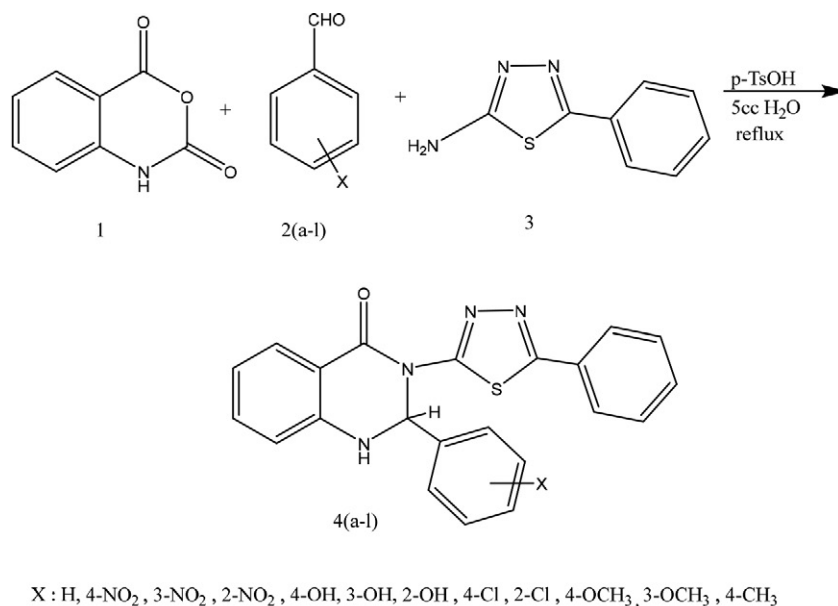
Compounds **4a–l** contain a chiral center at the carbon 2 that is formed during the reaction. Hence, these compounds are in the form of racemate. Racemates consist of an equimolar mixture of two enantiomers. About more than half of the drugs currently in use are chiral compounds and near 90% of the last ones are marketed

as racemates. Indeed, numerous studies have demonstrated that drug enantiomers may interact differently with biological macromolecules. Replacing existing racemates with unichiral drugs may result in improved safety and efficacy profile of various racemates.<sup>33,34</sup>

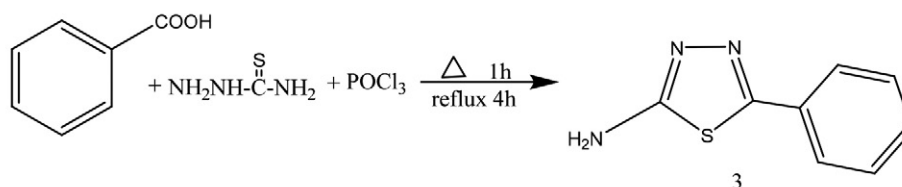
5-Phenyl-1,3,4-thiadiazol-2-amine (**3**) was obtained by refluxing benzoic acid and thiosemicarbazide in phosphorous oxychloride (Scheme 2).

Different spectroscopic data were used to confirm 2-(substituted phenyl)-3-(5-phenyl-1,3,4-thiadiazol-2-yl)-2,3-dihydroquinazolin-4(1*H*)-ones **4a–l**. All of the newly synthesized products **4a–l** were characterized by FT-IR spectroscopy, <sup>1</sup>H and <sup>13</sup>C NMR spectra, mass spectrometry and elemental analysis. In the FT-IR spectra of compounds **4a–l** the strong and sharp absorption bands due to NH and (N–CO) groups were observed at around 3379–3282 cm<sup>–1</sup> and 1655–1608 cm<sup>–1</sup>, respectively.

Also, in the <sup>1</sup>H NMR spectra, the NH proton of the 2,3-dihydroquinazolin-4(1*H*)-one ring appeared as a broad signal at 8.36–7.03 ppm and C–H proton of position 2 appeared at 5.8–6.5 ppm. The <sup>13</sup>C NMR spectra showed a signal at 171–162 ppm assigned to the N–C=O group and a signal for C–H at 66–70 ppm that confirmed the synthesis of 2,3-dihydroquinazolin-4(1*H*)-ones.



**Scheme 1.** Synthesis of 2-substituted-2,3-dihydroquinazolin-4(1*H*)-one derivatives **4a–l**



**Scheme 2.** Synthesis of 5-phenyl-1,3,4-thiadiazol-2-amine (**3**)



### 3. 2. Antibacterial Activity (*In vitro*)

As illustrated by the inhibition zone in Table 3, all tested compounds showed antibacterial activity against all Gram positive and Gram negative strains. The greatest effects of all compounds in bacteria samples were observed against *E. coli*. The best effect of the compounds against Gram positive bacteria: *S. aureus*: **4k** (IZ =  $26 \pm 0.52$ , MIC = 250, MBC = 500). *S. epidermidis*: **4j** (IZ =  $28 \pm 0.31$ , MIC = 125, MBC = 250). In this group (Gram positive bacteria), compound **4k** has the highest performance compared with ciprofloxacin than the other compounds, **4k** probably works well in penetrating the membrane of these bacteria and causes more degradation of peptidoglycans than the other synthetic structures. The best effect of the compounds against Gram negative bacteria: *E. coli*: **4l** (IZ =  $31 \pm 0.96$ , MIC = 125, MBC = 250). *P. aeruginosa*: **4i** (IZ =  $26 \pm 0.14$ , MIC = 250, MBC = 500). In this group (Gram negative bacteria), **4l** has shown the highest performance compared with ciprofloxacin than the other compounds. This compound is likely to penetrate and destroy these bacteria by destroying the inner and outer membranes. According to the results obtained from the antibacterial activity of compounds **4a–l**, it can be concluded that the synthesized compounds that have substituted phenyl groups along with thiadiazol and quinazoline **4a–l** compared to other compounds in this study, can perform well in eliminating human bacterial pathogens.

### 3. 3. Antifungal Activity (*In vitro*)

It was found that the synthesized compounds exhibited varied antifungal effects against two fungal strains (Table 4). The highest number of compounds affecting antifungal activity was observed against *C. albicans*. The best effect of the compounds against fungal specimens: *C. albicans*: **4j** (IZ =  $26 \pm 0.33$ , MIC = 250, MBC = 500) and *A. niger*: **4k** (IZ =  $21 \pm 0.66$ , MIC = 500, MBC = 1000). According to the results obtained from the antifungal activity of the compounds, it can be concluded that the synthesized compounds that have substituted phenyl groups along with thiadiazol and quinazoline **4a–l** compared with amphotericin B in this study, can perform well in eliminating human fungal pathogens.

### 3. 4. Anti-diabetic Activity (*In silico*)

In this section, it has been performed docking simulation of the newly synthesized derivatives **4a–l** binding the active site of the  $\alpha$ -amylase (PDB ID: 1hny) and  $\alpha$ -glucosidase (PDB ID: 2ze0). The docking result of the tested compounds **4c**, **4d** and **4g** showed lowest  $\Delta G_{\text{bind}}$  with  $\alpha$ -amylase by  $-10.0$  kcal/mol, and compounds **4e**, **4f** and **4i** showed lowest  $\Delta G_{\text{bind}}$ , respectively  $-10.6$ ,  $-9.5$  and  $-10.1$  with  $\alpha$ -glucosidase. The binding energies, inhibition constants and residues involved in H-bonding are presented in Table 5 and Figures 1 and 2.

Table 3. Antibacterial activity of compounds **4a–l**

Concentration of compounds: 1 mg/mL

Inhibition Zone (IZ): mm

Minimum Inhibitory Concentration (MIC): 0–1000  $\mu\text{g/mL}$

Minimum Bactericidal Concentration (MBC): 0–1000  $\mu\text{g/mL}$

$\pm$ : average three times

Cip: Ciprofloxacin

Well diameter: 9 mm

compounds	Gram positive bacteria						Gram negative bacteria					
	<i>S. aureus</i> PTCC1826			<i>S. epidermidis</i> PTCC1856			<i>E. coli</i> PTCC1789			<i>P. aeruginosa</i> PTCC1950		
	IZ	MIC	MBC	IZ	MIC	MBC	IZ	MIC	MBC	IZ	MIC	MBC
<b>4a</b>	19 $\pm$ 0.22	500	1000	21 $\pm$ 0.23	500	1000	17 $\pm$ 0.33	1000	1000	21 $\pm$ 0.02	500	1000
<b>4b</b>	21 $\pm$ 0.21	250	500	22 $\pm$ 0.26	250	500	19 $\pm$ 0.42	1000	1000	21 $\pm$ 0.21	500	1000
<b>4c</b>	17 $\pm$ 0.96	500	1000	14 $\pm$ 0.75	1000	1000	16 $\pm$ 0.78	1000	1000	20 $\pm$ 0.48	500	1000
<b>4d</b>	14 $\pm$ 0.33	1000	1000	15 $\pm$ 0.34	1000	1000	12 $\pm$ 0.92	1000	1000	16 $\pm$ 0.92	1000	1000
<b>4e</b>	16 $\pm$ 0.28	500	1000	19 $\pm$ 0.67	500	1000	14 $\pm$ 0.28	1000	1000	14 $\pm$ 0.35	1000	1000
<b>4f</b>	16 $\pm$ 0.66	500	1000	17 $\pm$ 0.33	500	1000	19 $\pm$ 0.34	1000	1000	19 $\pm$ 0.46	1000	1000
<b>4g</b>	16 $\pm$ 0.66	500	1000	16 $\pm$ 0.33	1000	1000	18 $\pm$ 0.39	1000	1000	19 $\pm$ 0.44	1000	1000
<b>4h</b>	19 $\pm$ 0.56	500	1000	22 $\pm$ 0.42	250	500	21 $\pm$ 0.37	500	1000	25 $\pm$ 0.23	500	1000
<b>4i</b>	18 $\pm$ 0.41	500	1000	19 $\pm$ 0.22	500	1000	22 $\pm$ 0.82	500	1000	<b>26<math>\pm</math>0.14</b>	<b>250</b>	<b>500</b>
<b>4j</b>	24 $\pm$ 0.76	250	500	<b>28<math>\pm</math>0.31</b>	<b>125</b>	<b>250</b>	24 $\pm$ 0.47	500	1000	21 $\pm$ 0.29	500	1000
<b>4k</b>	<b>26<math>\pm</math>0.52</b>	<b>250</b>	<b>500</b>	25 $\pm$ 0.57	250	500	26 $\pm$ 0.33	500	1000	24 $\pm$ 0.68	250	500
<b>4l</b>	24 $\pm$ 0.19	250	500	27 $\pm$ 0.29	125	250	<b>31<math>\pm</math>0.96</b>	<b>125</b>	<b>250</b>	24 $\pm$ 0.16	250	500
Cip	41 $\pm$ 0.35	15.62	31.25	46 $\pm$ 0.21	7.81	15.625	37 $\pm$ 0.33	31.25	62.50	34 $\pm$ 0.66	62.50	125

**Table 4.** Antifungal activity of compounds **4a–l**

Concentration of compounds: 1 mg/mL						
Inhibition Zone (IZ): mm						
Minimum Inhibitory Concentration (MIC): 0–1000 µg/mL						
Minimum Fungicidal Concentration (MFC): 0–1000 µg/mL						
±: average three times						
AB: Amphotericin B						
NA: No Activity						
Well diameter: 9 mm						
compounds	<i>C. albicans</i> PTCC5027			<i>A. niger</i> PTCC5320		
	IZ	MIC	MFC	IZ	MIC	MFC
<b>4a</b>	21±0.33	500	1000	17±0.66	1000	1000
<b>4b</b>	23±0.33	500	1000	20±0.66	500	1000
<b>4c</b>	20±0.33	500	1000	14±0.66	1000	1000
<b>4d</b>	14±0.33	1000	1000	11±0.66	NA	NA
<b>4e</b>	19±0.33	1000	1000	15±0.66	1000	1000
<b>4f</b>	19±0.33	1000	1000	16±0.66	1000	1000
<b>4g</b>	17±0.33	1000	1000	12±0.66	NA	NA
<b>4h</b>	21±0.33	500	1000	19±0.66	1000	1000
<b>4i</b>	20±0.33	500	1000	14±0.66	1000	1000
<b>4j</b>	<b>26±0.33</b>	<b>250</b>	<b>500</b>	20±0.66	500	1000
<b>4k</b>	25±0.33	500	1000	<b>21±0.66</b>	<b>500</b>	<b>1000</b>
<b>4l</b>	21±0.33	500	1000	19±0.66	1000	1000
<b>AB</b>	36±0.33	62.50	125	34±0.66	62.50	125

**Table 5.** Molecular docking reports for compounds **4a–l** against protein 1hny and 2ze0.

compounds	Total Energy (Kcal/mol)	$\alpha$ -amylase PDB ID: 1hny		$\alpha$ -glucosidase PDB ID: 2ze0	
		Affinity (kcal/mol)	H-Bond	Affinity (kcal/mol)	H-Bond
<b>4a</b>	11.3828	−9.6	—	−8.9	Arginine: 407
<b>4b</b>	13.3308	−9.1	—	−9.4	Arginine: 407
<b>4c</b>	11.6324	<b>−10.0</b>	Glutamic acid: 233	−9.2	Valine: 383
<b>4d</b>	−12.5194	<b>−10.0</b>	Aspartic acid: 197 Glutamic acid: 233 Histidine: 299	−9.1	Arginine: 407
<b>4e</b>	−2.1596	−9.1	—	<b>−10.6</b>	Arginine: 407 Glutamine: 167
<b>4f</b>	7.2655	−8.7	—	<b>−9.5</b>	Arginine: 197 Asparagine: 324
<b>4g</b>	7.8283	<b>−10.0</b>	Glutamic acid: 233 Aspartic acid: 300	−9.0	Arginine: 407
<b>4h</b>	9.9999	−9.1	—	−9.0	Arginine: 407
<b>4i</b>	10.1567	−9.5	—	<b>−10.1</b>	Arginine: 407 Glutamine: 167
<b>4j</b>	16.9915	−9.1	—	−9.1	Arginine: 407
<b>4k</b>	17.1349	−9.5	—	−9.0	—
<b>4l</b>	11.1987	−9.8	—	−9.3	—

## 4. Conclusion

In summary, in the present study target molecules **4a–I** were synthesized via a one-pot condensation reaction between isatoic anhydride (**1**) and 5-phenyl-1,3,4-thiadiazol-2-amine (**3**) with aromatic aldehydes **2a–I** using *p*-TsOH as the catalyst in refluxing water. The newly synthesized compounds were characterized by mass, FT-IR, <sup>1</sup>H NMR, <sup>13</sup>C NMR spectra and analytical methods. The antibacterial activities of the synthesized compounds showed that compounds **4k** against *S. aureus*, **4j** against *S. epidermidis*, **4l** against *E. coli*, and **4i** against *P. aeruginosa* have comparable inhibitory effects with the standards used. Also, the antifungal activities of the synthesized compounds showed that compounds **4j** against *C. albicans* and **4k** against *A. niger* have comparable inhibitory effects with the standards used. All compounds showed good results especially compound **4e** showed the lowest  $\Delta G_{\text{bind}}$  results (–10.6 kcal/mol) against  $\alpha$ -glucosidase and compounds **4c** and **4g** showed the lowest  $\Delta G_{\text{bind}}$  results (–10.0 kcal/mol) against  $\alpha$ -amylase.

## Acknowledgments

The authors are grateful to Urmia University for providing a fellowship for the present work.

## Supplementary Data

Copies of IR, <sup>1</sup>H NMR, <sup>13</sup>C NMR and MS spectra of compounds **4a–I** are provided in supplementary material via the “Supplementary Content” section of this article’s webpage.

## 6. References

1. J. Zhang, J. Zhao, L. Wang, J. Liu, D. Ren, Y. Ma, *Tetrahedron*, **2016**, 72, 936–943. DOI:10.1016/j.tet.2015.12.055
2. K. F. Sina, A. Yahyazadeh, N. Mahmoodi, *Lett. Org. Chem.* **2021**, 18, 176–182. DOI:10.2174/1570178617999200706010203
3. K. Hemalatha, G. Madhumitha, L. Ravi, V. Gopiesh Khanna, N. Abdullah Al-Dhabi, M. Valan Arasu, *J. Photochem. Photobiol. B: Biology* **2016**, 161, 71–79. DOI:10.1016/j.jphotobiol.2016.05.005
4. V. Jatav, S. Kashaw, P. Mishra, *Med. Chem. Res.* **2008**, 17, 2–7, 169–18. DOI:10.1007/s00044-007-9047-2
5. R. Appani, B. Bhukya, K. Gangarapu, *Scientifica* 2016, Volume 2016, Article ID 1249201. DOI:10.1155/2016/1249201
6. M. R. Mohareb, A. P. Halim, *Acta Chim. Slov.* **2018**, 65, 554–568. DOI:10.17344/acs.2017.4146
7. S. Poorirani, S. Sadeghian-Rizi, Gh. Khodarahmi, M. R. Khajouei, F. Hassanzadeh, *Res. Pharm. Sci.* **2018**, 13, 450–459. DOI:10.4103/1735-5362.236838
8. R. M. Mohareb, R. A. Ibrahim, A. M. Elmetwally, M. S. Gamaan, *Acta Chim. Slov.* **2022**, 69, 13–29. DOI:10.17344/acs.2021.6733
9. A. Barmak, K. Niknam, Gh. Mohebbi, *ACS Omega*, **2019**, 4, 19, 18087–18099. DOI:10.1021/acsomega.9b01906
10. N. Nagaladinne, A. A. Hindusta, D. Nayakanti, *Indian J. Pharm. Sci.* **2020**, 82, 984–995. DOI:10.36468/pharmaceutical-sciences.730
11. N. Krasovska, V. Stavitskiy, I. Nosulenko, O. Karpenko, O. Voskoboinik, S. Kovalenko, *Acta Chim. Slov.* **2021**, 68, 395–403. DOI:10.17344/acs.2020.6440
12. A. A. Abdel-Aziz, L. A. Abou-Zeid, K. E. H. ElTahir, M. A. Mohamed, M. A. Abu El-Enin, A. S. El-Azab, *Bioorg. Med. Chem.* 2016, 15, 24, 3818–3828. DOI:10.1016/j.bmc.2016.06.026
13. K. Hemalatha, G. Madhumitha, C. S. Vasavi, P. Munusami, *J. Photochem. Photobiol. B: Biology* **2015**, 143, 139–147. DOI:10.1016/j.jphotobiol.2014.12.028
14. M. Sarfraz, N. Sultana, U. Rashid, M. S. Akram, A. Sadiq, M. I. Tariq, *Bioorg. Chem.* 2017, 70, 237–244. DOI:10.1016/j.bioorg.2017.01.004
15. N. Irshad, A. Khan, Alamgeer, S. Khan, M. Sh. Iqbal, *Biomed. Pharmacother.* 2021, 139, 111567. DOI:10.1016/j.biopha.2021.111567
16. S. Mahgoub, M. K. El-Sayed, M. F. El-Shehry, S. M. Awad, Y. E. Mansour, S. S. Fatahala, *Bioorg. Chem.* 2021, 116, 105272. DOI:10.1016/j.bioorg.2021.105272
17. Y. Zhou, Q. Feng, F. Dia, Q. Liu, D. Wang, Y. Chen, L. Xiong, H. Song, Y. Lia, Zh. Lia, *Bioorg. Med. Chem.* **2013**, 21, 4968–4975. DOI:10.1016/j.bmc.2013.06.060
18. H. Tahtaci, H. Karacık, A. Ece, M. Er, M. Gül Şeker, *Mol. Inf.* 2017, 36, 1700083. DOI:10.1002/minf.201700083
19. Ch. Kamoutsis, M. Fesatidou, A. Petrou, A. Geronikaki, V. Poroikov, M. Ivanov, M. Sokovic, P. Mladenka, *Antibiotics* 2021, 10, 804. DOI:10.3390/antibiotics10070804
20. M. Er, A. M. Abounakhla, H. Tahtaci, A. H. Bawah, S. S. Çınaroğlu, A. Onaran, A. Ece, *Chem. Cent. J.* 2018, 12, 121. DOI:10.1186/s13065-018-0485-3
21. A. A. Radwan, F. K. Alanazi, M. H. Al-Agamy, *Braz. J. Pharm. Sci.* 2017, 53. DOI: 10.1590/s2175-97902017000115239
22. A. C. Karaburun, U. A. Çevik, D. Osmaniye, B. N. Sağlık, B. K. Çavuşoğlu, S. Levent, Y. Özkay, A. S. Koparal, M. Behçet, Z. A. Kaplancıklı, *Molecules* 2018, 23, 3129. DOI:10.3390/molecules23123129
23. S. M. Gomha, M. M. Edrees, Z. A. Muhammad, A. A. El-Reedy, *Drug. Des. Devel. Ther.* 2018, 12, 1511–1523. DOI:10.2147/DDDT.S165276
24. R. Kumar, S. Bua, S. Ram, S. Del Prete, C. Capasso, C. T. Supuran, P. K. Sharma, *Bioorg. Med. Chem.* 2017, 25, 1286–1293. DOI:10.1016/j.bmc.2016.12.047
25. A. Aliabadi, A. M. Farani; S. Roodabeh, F. Ahmadi, *Iran. J. Pharm. Res.* 2017, 16, 165–172. PMID: 28496472.
26. Y. Xiao, S. Sun, J. T. Yu; J. Cheng, *Synlett* 2019, 30, 2041–2050. DOI:10.1055/s-0037-1611905
27. W. A. M. A. El-Enany; S. M. Gomha, A. K El-Ziaty, W. Hussein, M. M. Abdulla, Sh. A. Hassan, H. A. Sallam, R. S. Ali, *Synth. Commun.* 2019, 50, 85–96. DOI:10.1080/00397911.2019.1683207

28. Sh. G. Alegaon, K. R. Alagawadi, *Med. Chem. Res.* 2012, 21, 816–824. DOI:10.1007/s00044-011-9598-0
29. M. Baghbanzadeh, P. Salehi, M. Dabiri, G. Kozehgary, *Synthesis* 2006, 2, 344–348. DOI:10.1055/s-2005-924766
30. N. Ramesh, M. G. Rao, R. Valara, V. U. Rao, B. H. Babu, *Med. Chem. Res.* 2016, 25, 1945–1951. DOI:10.1007/s00044-016-1630-y
31. P. Sivaguru, K. Parameswaran, M. Kiruthiga, P. Vadivel, A. Lalitha, *J. Iran. Chem. Soc.* 2015, 12, 95–100. DOI:10.1007/s13738-014-0459-x
32. X. Wu, S. Oschatz, A. Block, A. Spannenberg, P. Langer, *Org. Biomol. Chem.* 2014, 12, 1865–1870. DOI:10.1039/c3ob42434k
33. K. M. Rentsch, *J. Biochem. Biophys. Meth.* 2002, 54, 1–9. DOI:10.1016/S0165-022X(02)00124-0
34. J. McConalhy, M. J. Owens, *J. Clin. Psychiatry – Primary Care Companion* 2003, 5, 70–73. 10.4088/PCC.v05n0202

## Povzetek

V tej študiji predstavljamo serijo novih 2-(substituiranih fenil)-3-(5-fenil-1,3,4-tiadiazol-2-il)-2,3-dihidrokinazolin-4(1*H*)-onskih derivatov, ki smo jih pripravili s pomočjo refluktiranja izatojskega anhidrida, 5-fenil-1,3,4-tiadiazol-2-amina in aromatskih aldehydov v prisotnosti *p*-TsOH kot katalizatorja in v H<sub>2</sub>O kot topilu. Spojine smo karakterizirali s pomočjo spektroskopskih in analitskih metod. Določili smo antibakterijsko aktivnost proti dvema Gram pozitivnima in dvema Gram negativnima bakterijama ter aktivnost proti glivam; v vseh primerih smo izvedli tudi primerjavo s standardnimi učinkovinami. Z uporabo metode difuzije smo določili minimalno baktericidno oz. fungicidno koncentracijo. Morebitno inhibitorno aktivnost spojin **4a–l** za  $\alpha$ -amilazo in  $\alpha$ -glukozidazo smo raziskovali *in silico* s pomočjo metode molekulskega sidranja. Ugotovili smo, da so pripravljene 2,3-dihidrokinazolin-4(1*H*)-onski derivati obetavni kandidati za nadaljnji razvoj novih razredov učinkovin, ki bodo imele delovanje proti mikrobom in diabetesu.



Except when otherwise noted, articles in this journal are published under the terms and conditions of the Creative Commons Attribution 4.0 International License

Scientific paper

# Synthesis, Crystal Structures and Urease Inhibition of Mononuclear Copper(II) and Nickel(II) Complexes with Schiff Base Ligands

Jian Jiang,<sup>1,\*</sup> Peng Liang,<sup>2</sup> Huiyuan Yu<sup>3</sup> and Zhonglu You<sup>3</sup><sup>1</sup> College of Chemical Engineering and Machinery, Eastern Liaoning University, Dandong 118003, P. R. China<sup>2</sup> School of Engineering and Technology, Eastern Liaoning University, Dandong 118003, P. R. China<sup>3</sup> Department of Chemistry and Chemical Engineering, Liaoning Normal University, Dalian 116029, P. R. China

\* Corresponding author: E-mail: jiangjiandd2012@126.com

Received: 03-30-2022

## Abstract

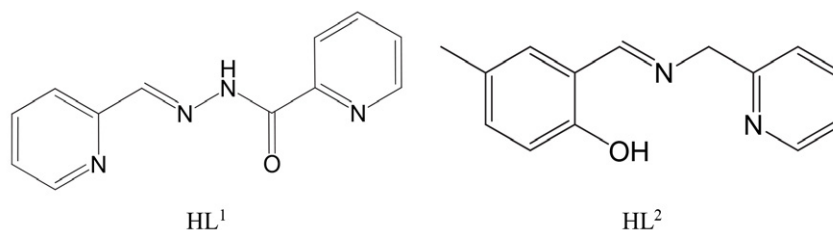
Three mononuclear copper(II) and nickel(II) complexes,  $[\text{Cu}(\text{L}^1)(\text{NCS})(\text{CH}_3\text{OH})]$  (**1**),  $[\text{Cu}(\text{L}^2)(\text{NCS})]$  (**2**) and  $[\text{Ni}(\text{L}^2)(\text{N}_3)]$  (**3**), where  $\text{L}^1$  and  $\text{L}^2$  are the monoanionic forms of the Schiff bases  $\text{N}'$ -(pyridin-2-ylmethylene)picolinohydrazide ( $\text{HL}^1$ ) and 4-methyl-2-(((pyridin-2-ylmethyl)imino)methyl)phenol ( $\text{HL}^2$ ), have been prepared and characterized by elemental analysis, IR and UV-Vis spectroscopy, as well as single crystal X-ray diffraction studies. The Cu atom in complex **1** is in a square pyramidal coordination, with the three N atoms of the ligand L and the N atom of the thiocyanate ligand in the basal plane, and with the methanol O atom at the apical position. The Cu and Ni atoms in complexes **2** and **3** are in square planar coordination, with the three donor atoms of the Schiff base ligands and the terminal N atoms of thiocyanate and azide ligands. Complexes **1** and **2** inhibit the *Jack bean* urease with  $\text{IC}_{50}$  value of  $0.33 \pm 0.12$  and  $0.39 \pm 0.10 \mu\text{mol L}^{-1}$ , respectively. Molecular docking study was performed to investigate the interaction between the complexes and the enzyme.

**Keywords:** Schiff base; Copper complex; Nickel complex; Crystal structure; Urease inhibition

## 1. Introduction

Urease is a nickel-containing enzyme, which widely be found in bacteria, fungi, algae, plants, and even in soil. The enzyme catalyzes the hydrolysis of urea to produce  $\text{NH}_3$  with the rate  $10^{14}$  times faster than that without urease. This process leads to a significant increase in pH of soil, and damage the plants.<sup>1</sup> In human being and animals, urease plays a vital role in peptic ulceration, urinary catheter incrustation, kidney stone, pyelonephritis, urolithiasis, hepatic encephalopathy and arthritis.<sup>2</sup> Thus, the control of side effects of the urease is a hot topic in science. Urease inhibitors have been proved to be the best way to control the activity of urease. A variety of urease inhibitors have been reported, including inorganic metal salts,<sup>3</sup> hydroxamic acid derivatives, triazoles, semicarbazones, Schiff bases, urea derivatives, oxadiazole, *etc.*<sup>4</sup> However, most of them were prevented from application because of their low inhibition efficiency.<sup>5</sup> Inorganic urease inhibitors such as the nitrate and chloride salts of copper, have ef-

fective activities. However, they are harmful to both soil and living organisms.<sup>6</sup> Recent reports indicated that some Schiff base copper(II) complexes have good urease inhibitory activities.<sup>7</sup> Khan and co-workers reported that some hydrazones have potential urease inhibitory activity. The diacyl hydrazide group ( $-\text{NH}-\text{N}=\text{CH}-$ ) in the compounds serves as stabilizing agent in the active site and prevent the binding of substrate. In addition to stabilize the inhibitors, the  $-\text{NH}$  group of diacyl hydrazide was involved making strong hydrogen bonds with amino acid Arg439 and Ala636 of the urease.<sup>8</sup> Considering that copper and nickel complexes with Schiff bases have a wide range of biological applications,<sup>9</sup> in the present work, three mononuclear copper(II) and nickel(II) complexes,  $[\text{Cu}(\text{L}^1)(\text{NCS})(\text{CH}_3\text{OH})]$  (**1**),  $[\text{Cu}(\text{L}^2)(\text{NCS})]$  (**2**) and  $[\text{Ni}(\text{L}^2)(\text{N}_3)]$  (**3**), where  $\text{L}^1$  and  $\text{L}^2$  are the monoanionic forms of the Schiff bases  $\text{N}'$ -(pyridin-2-ylmethylene)picolinohydrazide ( $\text{HL}^1$ , Scheme 1) and 4-methyl-2-(((pyridin-2-ylmethyl)imino)methyl)phenol ( $\text{HL}^2$ , Scheme 1) are presented.



Scheme 1. The Schiff base ligands.

## 2. Experimental

### 2. 1. Materials and Measurements

2-Pyridinecarboxaldehyde, 2-picolinyl hydrazide, 5-methylsalicylaldehyde, 2-aminomethylpyridine, copper acetate, copper nitrate, nickel nitrate, ammonium thiocyanate, sodium azide and solvents with AR grade were purchased from Xiya Chemicals Co. Ltd. (China). Elemental analyses for C, H and N were performed on a Perkin-Elmer 240C elemental analyzer. IR spectra were recorded on a Jasco FT/IR-4000 spectrometer as KBr pellets in the 4000–400  $\text{cm}^{-1}$  region. Electronic spectra were recorded on a Lambda 35 spectrophotometer.  $^1\text{H}$  and  $^{13}\text{C}$  NMR were recorded on a Bruker 300 MHz instrument. Single crystal X-ray diffraction was carried out on a Bruker SMART 1000 CCD diffractometer.

### 2. 2. Synthesis of *N*'-(Pyridin-2-ylmethylene)picolinohydrazide (HL<sup>1</sup>)

2-Pyridinecarboxaldehyde (1.1 g, 0.010 mol) and 2-picolinyl hydrazide (1.4 g, 0.010 mol) were mixed in methanol (50 mL). The mixture was stirred at 25 °C for 30 min to give colorless solution. Then the solvent was evaporated to give gummy product, which was re-crystallized from ethanol to give yellow crystalline product of HL<sup>1</sup>. Yield: 1.8 g (80%). M.p. 172–173 °C. Anal. Calc. for  $\text{C}_{12}\text{H}_{10}\text{N}_4\text{O}$  (%): C, 63.71; H, 4.46; N, 24.76. Found (%): C, 63.53; H, 4.60; N, 24.63. IR data ( $\text{cm}^{-1}$ ): 3290w (NH), 1698s (C=O), 1647m (C=N).  $^1\text{H}$  NMR (300 MHz,  $\text{CDCl}_3$ ):  $\delta$  11.18 (s, 1H, NH), 8.89 (d, 1H, PyH), 8.72 (d, 1H, PyH), 8.35 (d, 1H, PyH), 7.90 (t, 1H, PyH), 7.88 (d, 1H, PyH), 7.81 (m, 2H, PyH), 7.62 (m, 1H, PyH), 7.28 (s, 1H, CH=N).  $^{13}\text{C}$  NMR (75 MHz,  $\text{CDCl}_3$ ):  $\delta$  159.79, 152.14, 151.80, 149.56, 148.31, 147.70, 137.14, 136.56, 126.46, 125.98, 122.54, 121.02.

### 2. 3. Synthesis of 4-Methyl-2-(((pyridin-2-ylmethyl)imino)methyl)phenol (HL<sup>2</sup>)

2-Pyridinecarboxaldehyde (1.1 g, 0.010 mol) and 2-aminomethylpyridine (1.1 g, 0.010 mol) were mixed in methanol (50 mL). The mixture was stirred at 25 °C for 30 min to give colorless solution. Then the solvent was evaporated to give gummy product, which was re-crystallized from ethanol to give yellow crystalline product of

HL<sup>2</sup>. Yield: 1.9 g (84%). M.p. 155–156 °C. Anal. Calc. for  $\text{C}_{14}\text{H}_{14}\text{N}_2\text{O}$  (%): C, 74.31; H, 6.24; N, 12.38. Found (%): C, 74.45; H, 6.32; N, 12.23. IR data ( $\text{cm}^{-1}$ ): 3378w (OH), 1638m (C=N).  $^1\text{H}$  NMR (300 MHz,  $\text{CDCl}_3$ ):  $\delta$  10.32 (s, 1H, OH), 8.72 (s, 1H, CH=N), 8.43 (d, 1H, PyH), 7.71 (t, 1H, PyH), 7.52 (s, 1H, PyH), 7.27 (t, 1H, PyH), 7.15–7.10 (m, 2H, PyH), 6.83 (d, 1H, PyH), 5.21 (s, 2H,  $\text{CH}_2$ ), 2.32 (s, 3H,  $\text{CH}_3$ ).  $^{13}\text{C}$  NMR (75 MHz,  $\text{CDCl}_3$ ):  $\delta$  161.23, 159.31, 158.27, 148.46, 137.87, 133.53, 132.02, 130.55, 123.72, 121.55, 120.63, 115.91, 64.83, 21.72.

### 2. 4. Synthesis of Methanol-isothiocyanato-*N*'-(pyridin-2-ylmethylene)picolinohydrazido)copper(II) (1)

HL<sup>1</sup> (0.023 g, 0.10 mmol), copper nitrate trihydrate (0.024 g, 0.10 mmol) and ammonium thiocyanate (0.0076 g, 0.10 mmol) were mixed in methanol (30 mL). The mixture was stirred at ambient temperature for 30 min to give blue solution. The solvent was slowly evaporated to give single crystals. Yield: 0.013 g (34%). Anal. Calc. for  $\text{C}_{14}\text{H}_{13}\text{CuN}_5\text{O}_2\text{S}$  (%): C, 44.38; H, 3.46; N, 18.48. Found (%): C, 44.53; H, 3.55; N, 18.37. IR data ( $\text{cm}^{-1}$ ): 3438w (OH), 2081s (NCS), 1645s (C=O), 1598s (C=N), 1560s, 1475w, 1386m, 1332w, 1289w, 1251w, 1167m, 1082m, 1040m, 760w, 688w, 579w, 511w, 472w. UV–Vis data (methanol,  $\lambda/\text{nm}$  ( $\epsilon/\text{M}^{-1}\text{cm}^{-1}$ )): 215 (17,565), 255 (11,450), 367 (13,270).

### 2. 5. Synthesis of Isothiocyanato-(4-methyl-2-(((pyridin-2-ylmethyl)imino)methyl)phenolato)copper(II) (2)

Complex 2 was prepared by following the same method as described in section 2.4 for complex 1, but with HL<sup>1</sup> replaced by HL<sup>2</sup> (0.023 g, 0.10 mmol). Yield: 0.016 g (46%). Anal. Calc. for  $\text{C}_{15}\text{H}_{13}\text{CuN}_3\text{OS}$  (%): C, 51.94; H, 3.78; N, 12.11. Found (%): C, 51.77; H, 3.86; N, 11.98. IR data ( $\text{cm}^{-1}$ ): 2078s (NCS), 1629s (C=N), 1528w, 1461m, 1417w, 1385m, 1318w, 1276w, 1215m, 1160m, 1121w, 1071w, 1052m, 842m, 802w, 761m, 709w, 608w, 561w, 525w, 475w. UV–Vis data (methanol,  $\lambda/\text{nm}$  ( $\epsilon/\text{M}^{-1}\text{cm}^{-1}$ )): 223 (19,675), 246 (17,630), 272 (15,352), 385 (4,533).

### 2. 6. Synthesis of Azido-(4-methyl-2-(((pyridin-2-ylmethyl)imino)methyl)phenolato)nickel(II) (3)



Complex **3** was prepared by the same method as described for complex **2**, but with ammonium thiocyanate replaced by sodium azide (0.0065 g, 0.10 mmol), and with copper nitrate trihydrate replaced by nickel nitrate hexahydrate (0.029 g, 0.10 mmol). Yield: 0.019 g (58%). Anal. Calc. for  $C_{14}H_{13}N_5NiO$  (%): C, 51.58; H, 4.02; N, 21.48. Found (%): C, 51.39; H, 3.92; N, 21.37. IR data ( $cm^{-1}$ ): 2041s ( $N_3$ ), 1627s ( $C=N$ ), 1530w, 1471m, 1449w, 1387m, 1318w, 1279w, 1222m, 1168m, 1140w, 1118w, 1074m, 1054m, 983w, 822m, 763m, 709w, 610w, 560w, 533w, 464w. UV–Vis data (methanol,  $\lambda/nm$  ( $\epsilon/M^{-1} cm^{-1}$ )): 223 (18,720), 242 (17,315), 283 (8,120), 383 (6,350).

## 2. 7. X-ray Diffraction

Diffraction intensities for the complexes were collected at 298(2) K using a Bruker SMART 1000 CCD area-detector diffractometer with MoK $\alpha$  radiation ( $\lambda = 0.71073$  Å). The collected data were reduced with the SAINT,<sup>10</sup> and multi-scan absorption correction was performed using the SADABS.<sup>11</sup> The structures were solved by direct method and refined against  $F^2$  by full-matrix least-squares method using the SHELXL package.<sup>12</sup> All of the non-hydrogen atoms were refined anisotropically. Hydrogen atoms were placed in calculated positions and constrained to ride on

their parent atoms. The crystallographic data for the complexes are summarized in Table 1.

## 2. 8. Urease Inhibitory Activity Assay

The measurement of urease inhibitory activity was carried out according to the literature method.<sup>13</sup> The assay mixture containing 75  $\mu L$  of *Jack bean* urease and 75  $\mu L$  of tested compounds with various concentrations (dissolved in DMSO) was preincubated for 15 min on a 96-well assay plate. Acetohydroxamic acid was used as a reference. Then 75  $\mu L$  of phosphate buffer at pH 6.8 containing phenol red (0.18 mmol  $L^{-1}$ ) and urea (400 mmol  $L^{-1}$ ) were added and incubated at 25 °C. The reaction time required for enough ammonium carbonate to form to raise the pH of the phosphate buffer from 6.8 to 7.7 was measured by a micro-plate reader (560 nm) with the end-point being determined by the color change of phenol-red indicator.

## 2. 6. Molecular Docking Study

Molecular docking study of the molecules of complexes **1** and **2** into the 3D X-ray structure of the *Jack bean* urease was carried out by using the AutoDock 4.0 software as implemented through the graphical user interface Au-

Table 1. Crystal data for the complexes

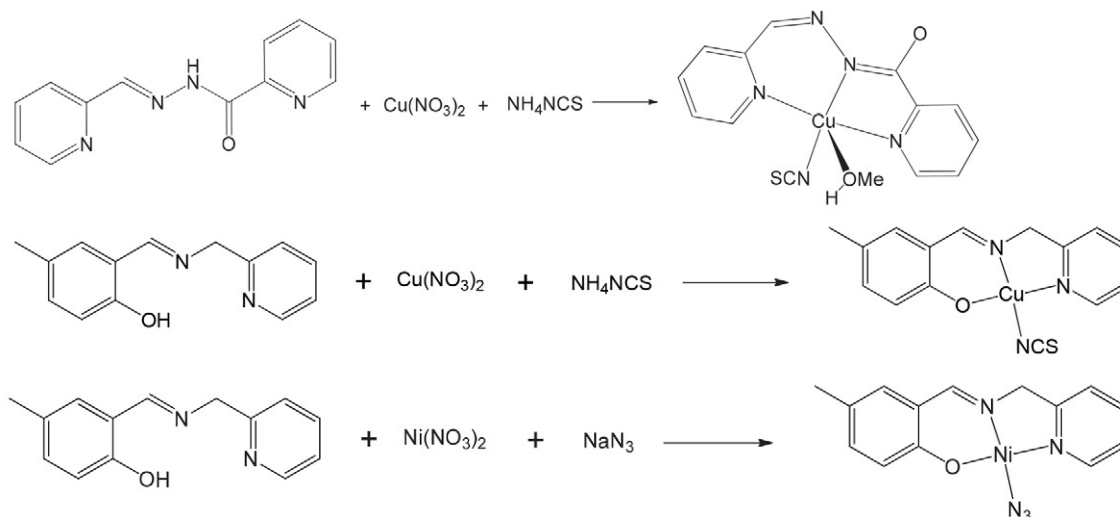
	1	2	3
Chemical Formula	$C_{14}H_{13}CuN_5O_2S$	$C_{15}H_{13}CuN_3OS$	$C_{14}H_{13}N_5NiO$
Fw	378.89	346.88	326.00
$T$ (K)	298(2)	298(2)	298(2)
$\lambda$ (Mo K $\alpha$ ) (Å)	0.71073	0.71073	0.71073
Crystal system	Triclinic	Monoclinic	Triclinic
Space group	$P-1$	$P2_1/n$	$P-1$
$a$ (Å)	7.0645(10)	6.9831(12)	7.3030(11)
$b$ (Å)	10.6425(14)	15.342(1)	9.0155(10)
$c$ (Å)	11.4005(16)	13.333(1)	10.5740(12)
$\alpha$ (°)	69.749(2)	90	88.622(1)
$\beta$ (°)	75.837(2)	91.873(1)	77.044(1)
$\gamma$ (°)	85.187(2)	90	85.605(1)
$V$ (Å <sup>3</sup> )	779.71(19)	1427.7(3)	676.5(2)
$Z$	2	4	2
$\mu$ (Mo K $\alpha$ ) ( $cm^{-1}$ )	1.550	1.677	1.601
$D_c$ ( $g cm^{-3}$ )	1.614	1.614	1.601
Reflections	4179	8002	3662
Unique reflections	2885	2639	2307
Observed reflections [ $I^3 2s(I)$ ]	2354	1418	1939
Parameters	212	191	191
Restraints	3	0	0
Goodness of fit on $F^2$	1.030	0.984	1.054
$R_{int}$	0.0166	0.1392	0.0195
$R_1$ [ $I^3 2s(I)$ ]	0.0474	0.0767	0.0347
$wR_2$ [ $I^3 2s(I)$ ]	0.1106	0.1278	0.0765
$R_1$ (all data)	0.0625	0.1538	0.0461
$wR_2$ (all data)	0.1194	0.1490	0.0820
$\Delta\rho_{max}/\Delta\rho_{min}$ , $e \text{ Å}^{-3}$	1.074/−0.320	0.437/−0.380	0.393/−0.288

toDockTools (ADT 1.5.2). In the docking, grid box size of  $40 \times 50 \times 58 \text{ \AA}^3$  for the complex points in  $x$ ,  $y$ , and  $z$  directions was built, the maps were centered on the original ligand molecule in the catalytic site of the protein. A grid spacing of  $0.375 \text{ \AA}$  and a distance-dependent function of the dielectric constant were used for the calculation of the energetic map. 100 runs were generated by using Lamarckian genetic algorithm searches. Default settings were used with an initial population of 50 randomly placed individuals, a maximum number of  $2.5 \times 10^6$  energy evaluations, and a maximum number of  $2.7 \times 10^4$  generations. A mutation rate of 0.02 and a crossover rate of 0.8 were chosen. The results of the most favorable free energy of binding were selected as the resultant complex structures.

### 3. Results and Discussion

#### 3.1. Chemistry

The Schiff bases HL<sup>1</sup> and HL<sup>2</sup> were readily prepared by the condensation reaction of equimolar quantities of 2-pyridinecarboxaldehyde with 2-picolinyl hydrazide, and 5-methylsalicylaldehyde with 2-aminomethylpyridine, respectively, in methanol. The copper complexes **1** and **2** were prepared by the reaction of equimolar quantities of the Schiff bases, copper nitrate and ammonium thiocyanate in methanol. To study the influence of the anions of copper salts on the structures of the complexes, we tried to use copper acetate in the syntheses, yet, the same structures as those prepared with copper nitrate have been obtained. The nickel complex **3** was prepared by the reaction of equimolar quantities of the Schiff base, nickel nitrate and sodium azide in methanol. The complexes are soluble in methanol, ethanol, acetonitrile, DMSO and DMF. Single crystals were obtained by slow evaporation of the methanolic solution of the complexes. The free Schiff bases and the complexes are stable in air at  $25^\circ\text{C}$ .



Scheme 3. The synthetic procedure for the complexes.

#### 3.2. Structure Description of Complex 1

The molecular structure of the complex is shown in Fig. 1. Selected bond lengths and angles are given in Table 2. The Cu atom is five-coordinated in a square pyramidal geometry, with the three nitrogen atoms (N1, N3, N4) of the Schiff base ligand L and the thiocyanate nitrogen atom (N5) defining the basal plane, and with the methanol oxygen atom (O2) occupying the apical position. The distortion of the square pyramidal coordination can be observed by the bond angles around the Cu center. The *cis* and *trans* angles in the basal plane are  $82.31(14)$ – $94.32(15)^\circ$  and  $168.66(13)$ – $174.99(16)^\circ$ , respectively. The bond angles among the apical and basal donor atoms are  $89.22(14)$ – $96.05(11)^\circ$ . The Cu–N bond lengths related to the Schiff base ligand are  $1.938(3)$ – $2.033(3) \text{ \AA}$ , and the Cu–N bond length related to the thiocyanate ligand is  $1.964(4) \text{ \AA}$ , which are comparable to the copper(II) complexes with similar ligands.<sup>14</sup> The apical bond length of Cu1–O2 is

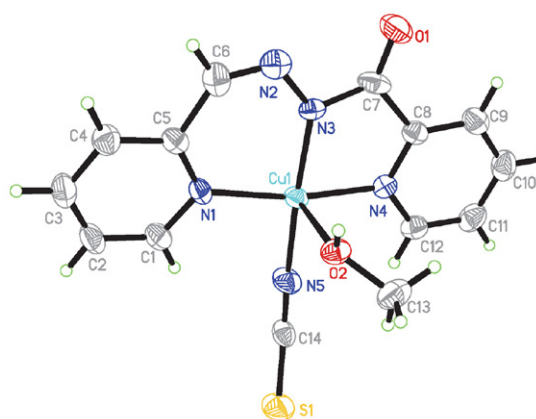


Fig. 1. A perspective view of the molecular structure of complex **1** with the atom labeling scheme. Thermal ellipsoids are drawn at the 30% probability level.

longer than the basal bonds, which is not uncommon for methanol coordinated complexes.<sup>15</sup>

In the crystal structure of the complex, two adjacent molecules are linked through intermolecular O–H...N and O–H...O hydrogen bonds (Table 3), to form a dimer. The dimers are linked through intermolecular C–H...O hydrogen bonds (Table 3), to form ladder like chains along the *b* axis (Fig. 2). Moreover, there are  $\pi$ ... $\pi$  interactions among the molecules (Table 4).

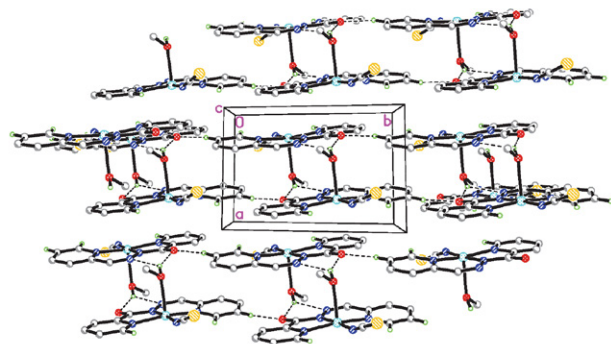


Fig. 2. Molecular packing diagram of complex 1, viewed along the *c* axis. Hydrogen bonds are shown as dashed lines.

Table 2. Selected bond lengths (Å) and angles (°) for the complexes

1			
Cu1–N1	2.033(3)	Cu1–N3	1.938(3)
Cu1–N4	2.033(3)	Cu1–N5	1.964(4)
Cu1–O2	2.365(3)		
N3–Cu1–N5	174.99(16)	N3–Cu1–N1	90.05(14)
N5–Cu1–N1	94.32(15)	N3–Cu1–N4	82.31(14)
N5–Cu1–N4	93.00(15)	N1–Cu1–N4	168.66(13)
N3–Cu1–O2	92.76(12)	N5–Cu1–O2	89.22(14)
N1–Cu1–O2	96.05(11)	N4–Cu1–O2	92.69(12)
2			
Cu1–O1	1.895(4)	Cu1–N1	2.004(5)
Cu1–N2	1.921(5)	Cu1–N3	1.936(6)
O1–Cu1–N2	93.73(19)	O1–Cu1–N3	89.7(2)
N2–Cu1–N3	176.4(2)	O1–Cu1–N1	176.10(19)
N2–Cu1–N1	82.4(2)	N3–Cu1–N1	94.2(2)
3			
Ni1–O1	1.831(2)	Ni1–N1	1.842(2)
Ni1–N2	1.908(2)	Ni1–N3	1.909(3)
O1–Ni1–N1	94.84(10)	O1–Ni1–N2	178.74(9)
N1–Ni1–N2	84.92(10)	O1–Ni1–N3	88.10(11)
N1–Ni1–N3	176.74(11)	N2–Ni1–N3	92.18(12)

### 3. 3. Structure Description of Complexes 2 and 3

The molecular structures of complexes 2 and 3 are shown in Figs. 3 and 4, respectively. Selected bond lengths and angles are given in Table 2. Both the complexes are of distorted square planar geometry. The Cu and Ni atoms

are coordinated by the phenolate O, imino N and pyridine N atoms of the Schiff base ligands, and the N atoms of thiocyanate (for 2) and azide (for 3) ligands. The distortion of the square planar coordination can be observed by the bond angles around the metal centers. The *cis* and *trans* angles are 82.4(2)–94.2(2)° and 176.1(2)–176.4(2)° for 2, and 84.9(1)–94.8(1)° and 176.7(1)–178.7(1)° for 3, respectively. The Cu–O and Cu–N bond lengths in complex 2 are longer than the Ni–O and Ni–N bond lengths in complex 3, which are in accordance with the bond values observed in similar copper(II) and nickel(II) complexes with Schiff base ligands.<sup>14,16</sup>

In the crystal structure of complex 2, the molecules are stacked with  $\pi$ ... $\pi$  interactions (Table 4, Fig. 5). In the crystal structure of complex 3, two adjacent molecules are linked through intermolecular C–H...N hydrogen bonds (Table 3), to form a dimer (Fig. 6). Moreover, there are  $\pi$ ... $\pi$  interactions among the molecules (Table 4).

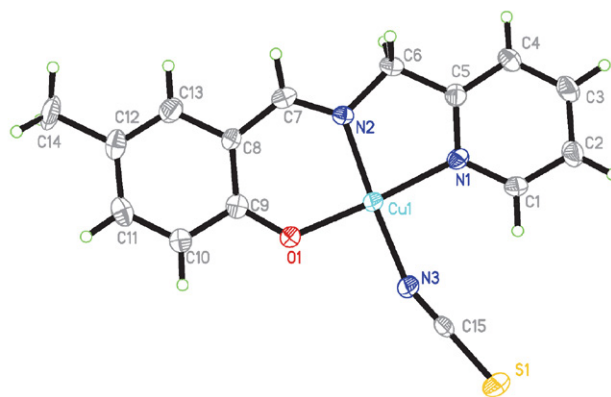


Fig. 3. A perspective view of the molecular structure of complex 2 with the atom labeling scheme. Thermal ellipsoids are drawn at the 30% probability level.

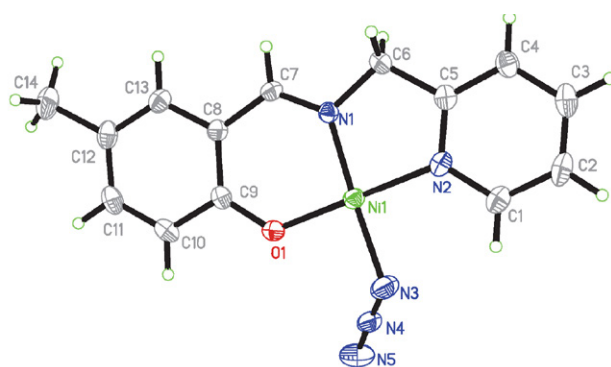
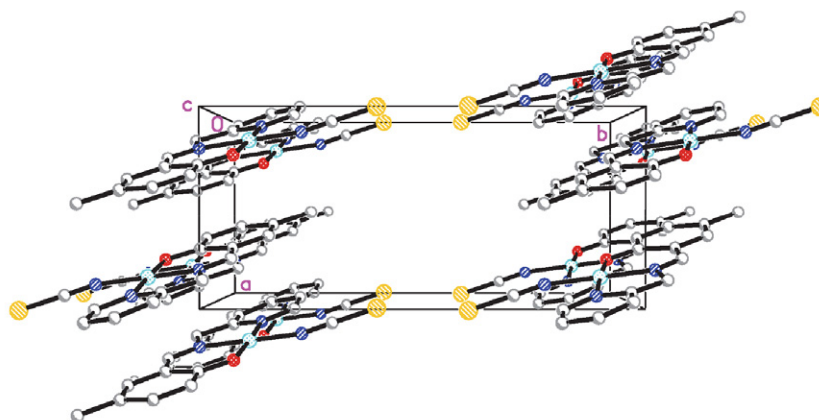
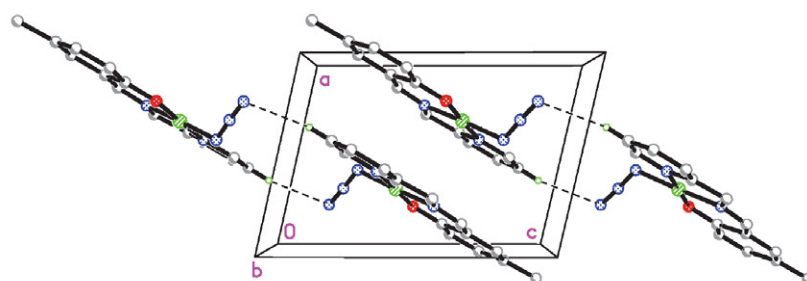


Fig. 4. A perspective view of the molecular structure of complex 3 with the atom labeling scheme. Thermal ellipsoids are drawn at the 30% probability level.

### 3. 4. IR Spectra

The infrared spectra of the free Schiff bases and the complexes were recorded in the region of 4000–400

Fig. 5. Molecular packing diagram of complex 2, viewed along the *c* axis.Fig. 6. Molecular packing diagram of complex 3, viewed along the *b* axis. Hydrogen bonds are shown as dashed lines.**Table 3.** Hydrogen bond distances (Å) and bond angles (°) for complexes 1 and 3

<i>D</i> – <i>H</i> ... <i>A</i>	<i>d</i> ( <i>D</i> – <i>H</i> )	<i>d</i> ( <i>H</i> ... <i>A</i> )	<i>d</i> ( <i>D</i> ... <i>A</i> )	Angle ( <i>D</i> – <i>H</i> ... <i>A</i> )
<b>1</b>				
O2–H2...N2 <sup>i</sup>	0.86(1)	2.40(3)	3.038(5)	132(3)
O2–H2...O1 <sup>i</sup>	0.86(1)	2.09(2)	2.852(5)	148(3)
C2–H2A...O1	0.93	2.48(2)	3.399(5)	170(3)
<b>3</b>				
C2–H2...N5 <sup>ii</sup>	0.93	2.62(3)	3.510(5)	161(4)

Symmetry codes: (i) 1 – *x*, 1 – *y*, 1 – *z*; (ii) 1 – *x*, 1 – *y*, – *z*.

cm<sup>–1</sup> using KBr pellets. There is a weak and sharp band at 3290 cm<sup>–1</sup> in the spectrum of HL<sup>1</sup>, which is assigned to the NH vibration. The broad and weak bands at 3378–3438 cm<sup>–1</sup> of HL<sup>2</sup> and complex 1 can be assigned to the OH vibrations. The bands at 1647 cm<sup>–1</sup> for HL<sup>1</sup> and 1645 cm<sup>–1</sup> for complex 1 are due to the azomethine group,  $\mu(\text{C}=\text{N})$ .<sup>17</sup> They are almost in the same frequency, indicates that the imine N atom is not participate in coordination. The intense band for the C=O group is observed at 1698 cm<sup>–1</sup> for HL<sup>1</sup>. The absence of the band in the spectrum of complex 1 indicates that the C=O group turned to other form. The bands at 1638 cm<sup>–1</sup> for HL<sup>2</sup> and 1627–1629 cm<sup>–1</sup> for complexes 2 and 3 are due to the azomethine group.<sup>17</sup> The shift to lower frequencies

**Table 4.**  $\pi$ ... $\pi$  interactions of the complexes

<i>Cg</i> ... <i>Cg</i>	distance (Å)	<i>Cg</i> ... <i>Cg</i>	distance (Å)
<b>1</b>			
<i>Cg</i> 1... <i>Cg</i> 1 <sup>iii</sup>	3.448(5)	<i>Cg</i> 1... <i>Cg</i> 2 <sup>iii</sup>	3.818(5)
<i>Cg</i> 1... <i>Cg</i> 2 <sup>i</sup>	4.445(5)	<i>Cg</i> 1... <i>Cg</i> 3 <sup>iii</sup>	4.645(5)
<i>Cg</i> 2... <i>Cg</i> 2 <sup>i</sup>	4.938(5)	<i>Cg</i> 2... <i>Cg</i> 3 <sup>iii</sup>	3.636(5)
<i>Cg</i> 4... <i>Cg</i> 4 <sup>i</sup>	3.935(5)	<i>Cg</i> 4... <i>Cg</i> 3 <sup>iii</sup>	4.651(5)
<b>2</b>			
<i>Cg</i> 5... <i>Cg</i> 6 <sup>i</sup>	3.794(4)	<i>Cg</i> 1... <i>Cg</i> 2 <sup>iv</sup>	4.967(4)
<i>Cg</i> 5... <i>Cg</i> 8 <sup>i</sup>	3.507(4)	<i>Cg</i> 1... <i>Cg</i> 4 <sup>iv</sup>	3.569(4)
<i>Cg</i> 6... <i>Cg</i> 6 <sup>i</sup>	3.389(4)	<i>Cg</i> 2... <i>Cg</i> 2 <sup>iv</sup>	3.612(4)
<i>Cg</i> 6... <i>Cg</i> 8 <sup>i</sup>	4.610(4)	<i>Cg</i> 2... <i>Cg</i> 4 <sup>iv</sup>	3.601(4)
<i>Cg</i> 7... <i>Cg</i> 8 <sup>i</sup>	3.721(4)	<i>Cg</i> 3... <i>Cg</i> 4 <sup>iv</sup>	4.823(4)
<b>3</b>			
<i>Cg</i> 9... <i>Cg</i> 9 <sup>i</sup>	3.982(4)	<i>Cg</i> 1... <i>Cg</i> 2 <sup>iii</sup>	4.006(4)
<i>Cg</i> 9... <i>Cg</i> 10 <sup>i</sup>	3.558(4)	<i>Cg</i> 1... <i>Cg</i> 4 <sup>iii</sup>	3.563(4)
<i>Cg</i> 9... <i>Cg</i> 12 <sup>i</sup>	4.776(4)	<i>Cg</i> 2... <i>Cg</i> 2 <sup>iii</sup>	3.479(4)
<i>Cg</i> 10... <i>Cg</i> 10 <sup>i</sup>	4.624(4)	<i>Cg</i> 2... <i>Cg</i> 3 <sup>i</sup>	3.781(4)
<i>Cg</i> 10... <i>Cg</i> 12 <sup>iii</sup>	4.530(4)	<i>Cg</i> 3... <i>Cg</i> 4 <sup>iii</sup>	3.799(4)
<i>Cg</i> 11... <i>Cg</i> 12 <sup>i</sup>	3.638(4)		

Symmetry codes: iii: – *x*, 1 – *y*, 1 – *z*; iv: 2 – *x*, 1 – *y*, 1 – *z*. *Cg*1, *Cg*2, *Cg*3 and *Cg*4 are the centroids of Cu1–N3–C7–C8–N4, Cu1–N1–C5–C6–N2–N3, N4–C8–C9–C10–C11–C12 and N1–C1–C2–C3–C4–C5 in complex 1, respectively. *Cg*5, *Cg*6, *Cg*7 and *Cg*8 are the centroids of Cu1–N1–C5–C6–N2, Cu1–O1–C9–C8–C7–N2, N1–C1–C2–C3–C4–C5 and C8–C9–C10–C11–C12–C13 in complex 2, respectively. *Cg*9, *Cg*10, *Cg*11 and *Cg*12 are the centroids of Ni1–N1–C6–C5–N2, Ni1–O1–C9–C8–C7–N1, N2–C1–C2–C3–C4–C5 and C8–C9–C10–C11–C12–C13 in complex 3, respectively.



in the spectra of the complexes indicates that the imine N atoms form coordination bonds with the metal atoms. The typical absorption for the thiocyanate ligands in complexes **1** and **2** is observed at 2078–2081  $\text{cm}^{-1}$ .<sup>18</sup> The typical absorption for the azide ligand in complex **3** is observed at 2041  $\text{cm}^{-1}$ .<sup>19</sup>

### 3. 5. Urease Inhibitory Activity

Complexes **1** and **2** have excellent inhibitory activity on the *Jack bean* urease, with  $\text{IC}_{50}$  values of  $0.33 \pm 0.27$  and  $0.39 \pm 0.10 \mu\text{mol L}^{-1}$ , respectively, whereas the free Schiff bases HL<sup>1</sup> and HL<sup>2</sup>, and the nickel complex **3** have weak activity ( $> 50 \mu\text{mol L}^{-1}$ ). The reported copper complexes have shown better activity than the reference drug acetohydroxamic acid ( $\text{IC}_{50} = 28.5 \pm 2.7 \mu\text{mol L}^{-1}$ ) and the copper nitrate ( $\text{IC}_{50} = 8.6 \pm 1.5 \mu\text{mol L}^{-1}$ ). The two copper complexes have better activity against urease than the copper(II) complex with the Schiff base ligand *N,N'*-bis(4-fluorosalicylidene)-1,2-diaminopropane ( $\text{IC}_{50} = 2.1\text{--}3.4 \mu\text{mol L}^{-1}$ ),<sup>20</sup> and the copper(II) complex with

the reduced Schiff base ligand 2,2'-((propane-1,3-diylbis(azanediyl))bis(methylene)diphenol ( $\text{IC}_{50} = 1.6 \mu\text{mol L}^{-1}$ ).<sup>21</sup>

### 3. 6. Molecular Docking Study on Complexes 1 and 2

Molecular docking study was performed to inspect the binding effects between the molecules of complexes **1** and **2** with the *Jack bean* urease. The binding models of the complexes with the urease are depicted in Figs. 7 and 8. The results indicate that the complex molecules fit well with the active site of the urease. The interactions of the complex molecules with the urease have been established in a variety of conformations because of the flexibility of the molecules and the amino acid residues of the urease. The binding energy is  $-5.78 \text{ kcal/mol}$  for **1** and  $-5.78 \text{ kcal/mol}$  for **2**. It is lower than the binding energy of the AHA inhibited model ( $-5.01 \text{ kcal/mol}$ ). The negative values reveal that the complex molecules combine well with the center of the urease.

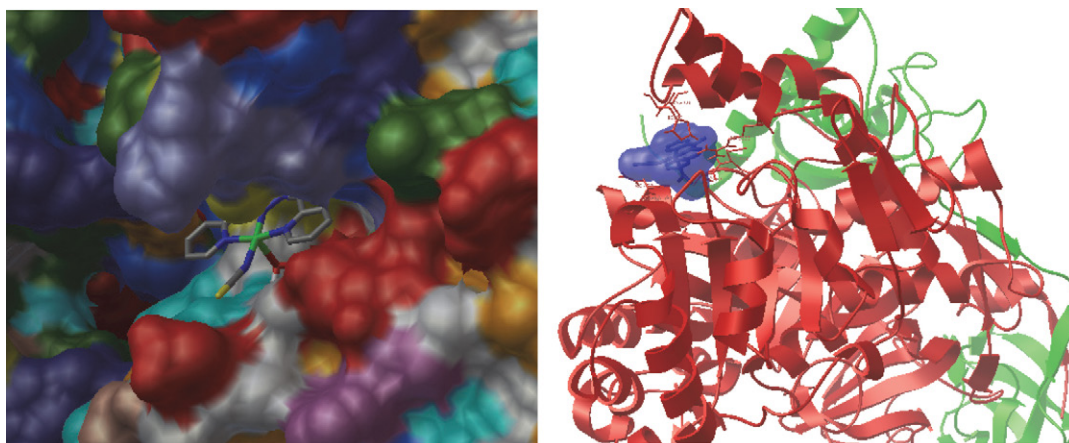


Fig. 7. Binding mode of the molecule of complex **1** with *Jack bean* urease. Left: The enzyme is shown as surface, and the complex is shown as sticks. Right: The enzyme is shown as ribbons, and the complex is shown as a filling model.

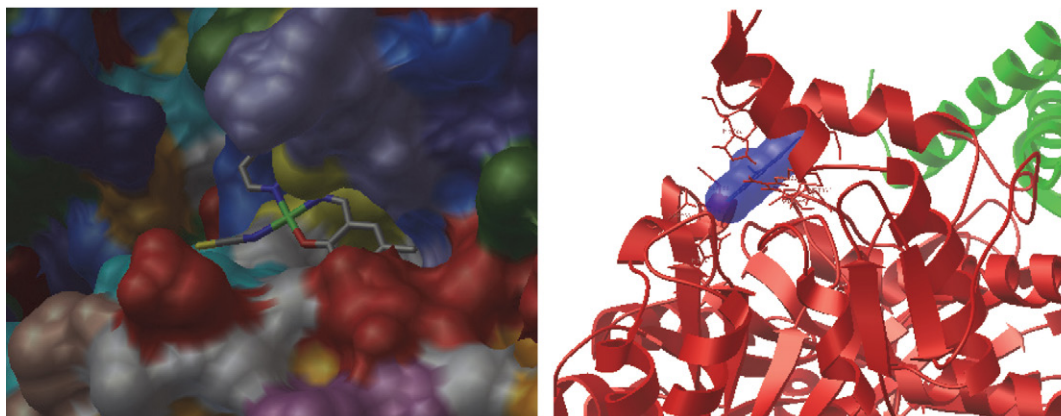


Fig. 8. Binding mode of the molecule of complex **2** with *Jack bean* urease. Left: The enzyme is shown as surface, and the complex is shown as sticks. Right: The enzyme is shown as ribbons, and the complex is shown as a filling model.

## 4. Conclusion

In summary, the present paper intends to report the syntheses, crystal structures and urease inhibition activity of three mononuclear copper(II) and nickel(II) complexes with the tridentate Schiff base ligands *N'*-(pyridin-2-yl-methylene)picolinohydrazide and 4-methyl-2-((pyridin-2-ylmethyl)imino)methylphenol. Both the copper complexes have shown effective inhibitory activity on *Jack bean* urease.

## Appendix A. Supplementary material

CCDC 2160252 (1), 2163190 (2) and 2163191 (3) contain the supplementary crystallographic data for this article. These data can be obtained free of charge at <http://www.ccdc.cam.ac.uk/const/retrieving.html> or from the Cambridge Crystallographic Data Centre (CCDC), 12 Union Road, Cambridge CB2 1EZ, UK; Fax: +44(0)1223-336033 or E-mail: [deposit@ccdc.cam.ac.uk](mailto:deposit@ccdc.cam.ac.uk).

## 5. References

- (a) A. Ray, C. Nkwonta, P. Forrestal, M. Danaher, K. Richards, T. O'Callaghan, S. Hogan, E. Cummins, *Rev. Environ. Health* **2021**, 36, 477–491; DOI:10.1515/reveh-2020-0088  
(b) T. Lan, Y. X. Huang, X. Song, O. P. Deng, W. Zhou, L. Luo, X. Y. Tang, J. Zeng, G.D. Chen, X. S. Gao, *Environ. Pollut.* **2021**, 293, 118499; DOI:10.1016/j.envpol.2021.118499  
(c) M. P. Byrne, J. T. Tobin, P. J. Forrestal, M. Danaher, C. G. Nkwonta, K. Richards, E. Cummins, S.A. Hogan, T. F. O'Callaghan, *Sustainability* **2020**, 12, 6018. DOI:10.3390/su12156018
- (a) A.T. Fiori-Duarte, R.P. Rodrigues, R.R. Kitagawa, D.F. Kawano, *Curr. Med. Chem.* **2020**, 27, 3967–3982; DOI:10.2174/0929867326666190301143549  
(b) M. Taha, N. H. Ismail, S. Imran, A. Wadood, F. Rahim, M. Riaz, *J. Bioorg. Med. Chem.* **2015**, 23, 7211–7218. DOI:10.1016/j.bmc.2015.10.017
- (a) G. I. Perez-Perez, C. B. Gower, M. J. Blaser, *Infect. Immun.* **1994**, 62, 299–302. DOI:10.1128/iai.62.1.299-302.1994
- (a) R. Mamidala, S. R. S. Bhimathati, A. Vemn, *Bioorg. Chem.* **2021**, 114, 105010; DOI:10.1016/j.bioorg.2021.105010  
(b) S. Iqbal, A. Khan, R. Nazir, S. Kiran, S. Perveen, K. M. Khan, M.I. Choudhary, *Med. Chem.* **2020**, 16, 244–255; DOI:10.2174/1573406415666190415163309  
(c) S. Daud, O.U.R. Abid, A. Sardar, B.A. Shah, M. Rafiq, A. Wadood, M. Ghufuran, W. Rehman, Zain-ul-Wahab, F. Iftikhar, R. Sultana, H. Daud, B. Niaz, *Med. Chem. Res.* **2022**, 31, 316–336; DOI:10.1007/s00044-021-02814-6  
(d) M. Talebi, E. Hamidian, F. Niasari-Naslaji, S. Rahmani, F. S. Hosseini, S. Boumi, M. N. Montazer, M. Asadi, M. Amanlou, *Med. Chem. Res.* **2021**, 30, 1220–1229; DOI:10.1007/s00044-021-02727-4  
(e) M. A. S. Aslam, S. Mahmood, M. Shahid, A. Saeed, J. Iqbal, *Eur. J. Med. Chem.* **2011**, 46, 5473–5479; DOI:10.1016/j.ejmech.2011.09.009  
(f) E. Menteşe, M. Emirlik, B.B. Sökmen, *Bioorg. Chem.* **2019**, 86, 151–158. DOI:10.1016/j.bioorg.2019.01.061
- (a) Z.-J. Chen, Y.-N. Chen, C.-N. Xu, S.-S. Zhao, Q.-Y. Cao, S.-S. Qian, J. Qin, H.-L. Zhu, *J. Mol. Struct.* **2016**, 1117, 293–299; DOI:10.1016/j.molstruc.2016.03.084  
(b) Z.-P. Xiao, Z.-Y. Peng, J.-J. Dong, R.-C. Deng, X.-D. Wang, H. Ouyang, P. Yang, J. He, Y.-F. Wang, M. Zhu, X.-C. Peng, W.-X. Peng, H.-L. Zhu, *Eur. J. Med. Chem.* **2013**, 68, 212–221.
- (a) B. Krajewska, *J. Mol. Catal. B: Enzym.* **2009**, 59, 9–21; DOI:10.1016/j.molcatb.2009.01.003  
(b) L. Habala, F. Devínsky, A.E. Egger, *J. Coord. Chem.* **2018**, 71, 907–940. DOI:10.1080/00958972.2018.1458228
- (a) H. Pervez, M. Ahmad, S. Zaib, M. Yaqub, M. M. Naseer, J. Iqbal, *MedChemComm* **2016**, 7, 914–923; DOI:10.1039/C5MD00529A  
(b) H. Pervez, N. Khan, J. Iqbal, S. Zaib, M. Yaqub, M. M. Naseer, *Acta Chim. Slov.* **2018**, 65, 108–118; DOI:10.17344/acsi.2017.3649  
(c) H. Zhao, X.-R. Liu, X. Wang, J. Hu, Y.-J. Cai, Q.-A. Peng, *Acta Chim. Slov.* **2021**, 68, 804–810; DOI:10.17344/acsi.2021.6781  
(d) S. Han, Y. Wang, *Acta Chim. Slov.* **2021**, 68, 961–969. DOI:10.17344/acsi.2021.6965
- (a) M. Ahmed, M. Imran, M. Muddassar, R. Hussain, M.U. Khan, S. Ahmad, M.Y. Mehboob, S. Ashfaq, *J. Mol. Struct.* **2020**, 1220, 128740; DOI:10.1016/j.molstruc.2020.128740  
(b) F. Naz, Kanwal, M. Latif, U. Salar, K.M. Khan, M. al-Rashida, I. Ali, B. Ali, M. Taha, S. Perveen, *Bioorg. Chem.* **2020**, 105, 104365. DOI:10.1016/j.bioorg.2020.104365
- (a) S. Hosny, G.A. Gouda, S.M. Abu-El-Wafa, *Appl. Organomet. Chem.* **2022**, e6627;  
(b) N. Biswas, S. Saha, B.K. Biswas, M. Chowdhury, A. Rahman, V. Junghare, S. Mohapatra, S. Hazra, E. Zangrando, R.R. Choudhury, *J. Coord. Chem.* **2021**, 74, 1482–1504; DOI:10.1080/00958972.2021.1913128  
(c) W.-G. Zhang, J.-H. Liang, *Acta Chim. Slov.* **2021**, 68, 921–929; DOI:10.17344/acsi.2021.6902  
(d) C. Liu, *Acta Chim. Slov.* **2021**, 68, 983–989; DOI:10.1515/dzph-2020-0068  
(e) Y. Yuan, X.-K. Lu, G.-Q. Zhou, X.-Y. Qiu, *Acta Chim. Slov.* **2021**, 68, 1008–1015; DOI:10.17344/acsi.2021.7070  
(f) J.-L. Hou, H.-Y. Wu, C.-B. Sun, Y. Bi, W. Chen, *Acta Chim. Slov.* **2020**, 67, 860–865. DOI:10.17344/acsi.2020.5824
- Bruker, SMART and SAINT, Bruker AXS Inc., Madison, **2002**.
- G. M. Sheldrick. SADABS, University of Göttingen, Germany, **1996**.
- G. M. Sheldrick, *Acta Crystallogr.* **2015**, C71, 3–8.
- W.-J. Mao, P.-C. Lv, L. Shi, H.-Q. Li, H.-L. Zhu, *Bioorg. Med. Chem.* **2009**, 17, 7531–7536. DOI:10.1016/j.bmc.2009.09.018
- (a) C. J. Matthews, K. Avery, Z. Xu, L.K. Thompson, L. Zhao, D. O. Miller, K. Biradha, K. Poirier, M.J. Zaworotko, C. Wilson, A. E. Goeta, J. A. K. Howard, *Inorg. Chem.* **1999**, 38, 5266–5276; DOI:10.1021/ic990598f



- (b) L. N. Dawe, T. S. M. Abedin, T. L. Kelly, L. K. Thompson, D. O. Miller, L. Zhao, C. Wilson, M. A. Leech, J. A. K. Howard, *J. Mater. Chem.* **2006**, *16*, 2645–2659. DOI:10.1039/B602595A
15. (a) R. Vafazadeh, R. Esteghamat-Panah, A.C. Willis, A.F. Hill, *Polyhedron* **2012**, *48*, 51–57; DOI:10.1016/j.poly.2012.08.057  
(b) H. Hosseini-Monfared, E. Pousaneh, S. Sadighian, S.W. Ng, *Z. Anorg. Allg. Chem.* **2013**, *639*, 435–442. DOI:10.1002/zaac.201200395
16. (a) H.S. Jena, J. Subramanian, V. Manivannan, *Inorg. Chim. Acta* **2011**, *365*, 177–182. DOI:10.1016/j.ica.2010.09.007
17. (a) C. Liu, *Acta Chim. Slov.* **2022**, *69*, 157–166; DOI:10.17344/acsi.2022.7176  
(b) H.-Y. Liu, X. Gan, J.-Y. Ding, Z.-T. Li, Q. Chen, *Acta Chim. Slov.* **2021**, *68*, 693–699. DOI:10.17344/acsi.2021.6716
18. (a) L.-W. Xue, X. Fu, G.-Q. Zhao, Q.-B. Liu, *Acta Chim. Slov.* **2021**, *68*, 17–24; DOI:10.17344/acsi.2020.5817  
(b) F.-M. Wang, L.-J. Li, G.-W. Zang, T.-T. Deng, Z.-L. You, *Acta Chim. Slov.* **2020**, *67*, 1155–1162. DOI:10.17344/acsi.2020.6056
19. (a) S.-F. Yu, X.-Y. Qiu, S.-J. Liu, *Acta Chim. Slov.* **2020**, *67*, 1301–1308; DOI:10.17344/acsi.2020.6321  
(b) G.-P. Cheng, L.-W. Xue, C.-X. Zhang, *Acta Chim. Slov.* **2017**, *64*, 261–265. DOI:10.17344/acsi.2016.3036
20. Y. Y. Luo, J. Q. Wang, B. T. Zhang, Y. X. Guan, T. Yang, X. Y. Li, L. Y. Xu, J. Wang, Z. L. You, *J. Coord. Chem.* **2020**, *73*, 1765–1777. DOI:10.1080/00958972.2020.1795645
21. M. M. Duan, Y. M. Li, L. Y. Xu, H. L. Yang, F.W. Luo, Y. X. Guan, B. T. Zhang, C. L. Jing, Z.L. You, *Inorg. Chem. Commun.* **2019**, *100*, 27–31. DOI:10.1016/j.inoche.2018.12.009

## Povzetek

Sintetizirali smo tri enojedrne komplekse bakra(II) in niklja(II),  $[\text{Cu}(\text{L}^1)(\text{NCS})(\text{CH}_3\text{OH})]$  (**1**),  $[\text{Cu}(\text{L}^2)(\text{NCS})]$  (**2**) in  $[\text{Ni}(\text{L}^2)(\text{N}_3)]$  (**3**), kjer sta  $\text{L}^1$  in  $\text{L}^2$  monoanionski obliki Schiffovih baz  $\text{N}^2$ -(piridin-2-ilmetilen)pikolinohidrazida ( $\text{HL}^1$ ) in 4-metil-2-(((piridin-2-ilmetil)imino)metil)fenola ( $\text{HL}^2$ ), ter jih okarakterizirali z elementno analizo, IR in UV-Vis spektroskopijo ter monokristalno rentgensko analizo. Atom Cu je v kompleksu **1** kvadratno piramidalno koordiniran s tremi N atomi liganda L in N atomom tiocianatnega liganda v ekvatorialnem položaju ter z O atomom metanola v apikalnem položaju. Atoma Cu in Ni sta v kompleksih **2** in **3** kvadratno planarno koordinirana s tremi donorskimi atomi ligandov Schiffove baze in terminalnimi N atomi tiocianatnih in azidnih ligandov. Kompleksa **1** in **2** zavirata ureazo stročnice *Canavalia ensiformis* z vrednostjo  $\text{IC}_{50}$   $0,33 \pm 0,12$  oziroma  $0,39 \pm 0,10 \mu\text{mol L}^{-1}$ . Za preučitev interakcij med kompleksi in encimom je bila izvedena študija molekularnega dockinga.



Except when otherwise noted, articles in this journal are published under the terms and conditions of the Creative Commons Attribution 4.0 International License

# Electroanalytical Determination of Ziram by Differential Pulse Voltammetry with Reduced Graphene Oxide/Gold Nanoparticles Modified Glassy Carbon Electrode

Nazife Aslan,<sup>1\*</sup> Sema Bilge Ocak<sup>2</sup> and Uğur Gökmen<sup>3</sup>

<sup>1</sup> Ankara Hacı Bayram Veli University, Polatlı Science and Arts Faculty, Department of Chemistry, 06900 Ankara, Turkey

<sup>2</sup> Gazi University, Graduate School of Natural and Applied Sciences, 06560 Ankara, Turkey

<sup>3</sup> Gazi University, Faculty of Technology Metallurgical and Materials Engineering, 06500 Ankara, Turkey

\* Corresponding author: E-mail: nazife.aslan@hbv.edu.tr

Received: 04-04-2022

## Abstract

The preparation of gold nanoparticles-reduced graphene oxide-based sensor materials for the determination of zinc(II) dimethyldithiocarbamate (ziram) is described in this paper. The graphene oxide (GO) was synthesized using a modified Hummer's method. A composite sensor consisting of gold nanoparticles (AuNPs) and reduced graphene oxide (RGO) was electrochemically fabricated on a glassy carbon electrode. The nanocomposite was evaluated utilizing scanning electron microscopy (SEM). Cyclic voltammetry was used to illuminate the modified sensor's electrochemical properties at each stage of the modification. The suggested sensor was demonstrated good analytical performance to determine ziram pesticide in water and peach juice, including a very low detection limit, a large linear range, and a low RSD.

**Keywords:** Reduced graphene oxide; ziram; nanomaterials; sensors

## 1. Introduction

Materials having sizes or properties ranging from 1 to 100 nm in one or more dimensions are called nanomaterials. Superior thermal, mechanical, electrical, and biological properties not available in conventional materials are the important characteristics of these materials.<sup>1</sup>

The combination of these distinctive properties with their remarkable recognition abilities has resulted in improved performance. Apart from their high mechanical strength and low weight, nanomaterials' surface features, including area, roughness, energetics, and electron distributions, are primarily the result of their unique properties. It is obvious that nanomaterials, which has applications such as providing clean drinking water, improving air quality, developing new energy sources and at the same time removing dangerous and toxic substances from our environment, will help create a sustainable environment.<sup>2</sup>

Graphene is one of the most important nanomaterials, with a wide range of applications that are expanding.<sup>3,4</sup> It is made up of sp<sup>2</sup> bonded carbon atoms with a single atom thickness, as is well known. As a result of these

characteristics, it exhibits remarkable electron transport capability and catalytic behavior for particular chemicals. Overall, due to its high specific surface area, low cost, ease of processing and safety, and superior electrical conductivity, it can play a vital role in increasing the performance of sensors.<sup>5,6</sup> With its potential application areas, it is one of the most investigated materials nowadays.<sup>7</sup> Graphene, on the other hand, is hydrophobic and does not form stable dispersions in polar solvents.<sup>8</sup> This severely limits its use in sensor development. An effective method for overcoming this problem is in situ chemical or electrochemical reduction of highly hydrophilic graphene oxide (GO) to produce graphene.<sup>9</sup> The electrochemical reduction method is commonly used because it is a green process that does not require a strong chemical reducing agent.<sup>10</sup>

Metal nanoparticles (NP) have qualities that are determined by their size and form. Chemical and biosensors, catalyst synthesis, electronic device component preparation, imaging systems, medical and environmental applications all use a variety of metal NPs in various sizes, forms, and morphologies.<sup>11,12</sup> Among them gold nanoparticles (AuNPs) have been received great interests as sensor

devices due to its high selectivity, sensitivity, biocompatibility and excellent chemical stability. Especially, the introduction of AuNPs into modified electrodes has obvious advantages in improving the sensor performances.<sup>13,14</sup> It has been stated in the literature that sensors made with reduced graphene oxide (RGO)-metal nanocomposites superior qualities such as sensitivity, lower detection limits, and faster electron transfer kinetics.<sup>15,16</sup> RGO has hydroxyl (-OH) and carboxylate (-COOH) groups in its structure, which allows it to interact with metal nanoparticles to create a metal nanoparticle-graphene based electrochemical sensor.<sup>17,18</sup> Therefore, AuNPs/RGO have recently been used in electrochemical sensors for pesticide and other organic and inorganic pollutant detection.<sup>19–24</sup>

Pesticides are widely employed as agrochemicals to enhance agricultural production by controlling or killing insects, pests, and fungi. Uncontrolled pesticide use, on the other hand, could endanger public health.<sup>25,26</sup> Ziram is a dithiocarbamate (DTC) fungicide that is commonly used to control moulds, black spot, rot, and blight, as well as to maintain the quality of fruits and vegetables throughout transit and storage. Ziram residues, on the other hand, can cause major health problems, such as headaches and nausea, as well as cancer. It's also linked to skin allergies, asthma, Parkinson's disease risk, and inflammation of the eyes and respiratory tract.<sup>27–32</sup>

Several analytical instruments, such as high-performance liquid chromatography followed by atomic absorption spectrometry (HPLC-AAS),<sup>33</sup> liquid chromatography-mass spectrometry (LC-MS/MS),<sup>34</sup> and gas chromatography-mass spectrometry (GC-MS),<sup>35</sup> gas chromatography-electron capture detector (GC-ECD),<sup>36</sup> inductively coupled plasma mass spectrometry<sup>37</sup> are widely used in monitoring environmental contaminants such as ziram in agricultural products. Electrochemical detection<sup>38–43</sup> and immunoassays<sup>44</sup> are some of the other rapid methods for detecting trace compounds that have been proposed. Because of their numerous advantages, such as rapid response, a wide dynamic range, portability, ease of modification, and low cost, electrochemical sensors are a viable and rapid instrument for detecting pesticide residues in food and environmental samples.

The goal of this research was to explore if composites of reduced graphene oxide and gold nanoparticles might be employed as an electrochemical sensor material for low-concentration voltammetry-based pesticide residue monitoring. A glassy carbon electrode (GCE) modified with RGO and AuNPs was used to create and measure a new voltammetric sensor for the determination of ziram. The results indicated that the AuNPs/RGO-modified glassy carbon electrode could provide a quick and easy platform for ziram detection with high sensitivity, fast response, and wide detection range. So far, only a few electrochemical methods for the detection of ziram using nanocomposite sensors have been published, and real sample applications in foods are extremely limited.<sup>45,46</sup> As a result, it is critical

to develop new methods that will serve as an alternative to existing analysis methods.

Using a scanning electron microscope, the surface specimens of the produced RGO/AuNPs/GCE were examined. For AuNPs electrodeposition and ziram determination, cyclic voltammetry (CV) and differential pulse voltammetry (DPV) were utilized. Furthermore, limit of detection, limit of quantification, linearity, repeatability, reproducibility and pH of the sensor were investigated in detail. The RGO/AuNPs/GCE has been successfully used as electrochemical sensor to determining of ziram fungicide in peach juice and tap water samples.

## 2. Experimental

### 2.1. Reagents

Graphite (Alfa Aesar, <20  $\mu\text{m}$ ),  $\text{HAuCl}_4 \cdot \text{H}_2\text{O}$  99.995%, zinc(II) dimethyldithiocarbamate (99.9%),  $\text{K}_3[\text{Fe}(\text{CN})_6]$ ,  $\text{K}_4[\text{Fe}(\text{CN})_6]$ , hydrogen peroxide, boric acid, o-phosphoric acid and sulfuric acid were provided by Sigma Aldrich; Merck supplied sodium nitrate ( $\text{NaNO}_3$ ), potassium permanganate ( $\text{KMnO}_4$ ), sodium hydroxide, sodium acetate, hydrochloric acid, sodium dihydrogenphosphate. $2\text{H}_2\text{O}$ , sodium monohydrogenphosphate. $7\text{H}_2\text{O}$  and potassium chloride. The Britton Robinson (BR) buffer solution and all other solutions were made with ultrapure water. All experiments were carried out at room temperature. All sensor applications were performed in BR buffer with a pH of 8.0 and 100 mM KCl as a supporting electrolyte.

### 2.2. Instrumentation

The CH Instruments 660B model Ivium potentiostat/galvanostat Electrochemical Analyzer (Ivium Technologies, Netherlands) was used for all electrochemical experiments. A triple electrode system was used in the experiments, including an Ag/AgCl reference electrode, a glassy carbon working electrode, and a Pt wire counter electrode.

Carl Zeiss AG's EVO<sup>®</sup> 50 Series was used to capture scanning electron microscopic (SEM) pictures. An ORION Model 720A pH/ion meter and a combined glass electrode were used to obtain the pH readings. The pH-meter was calibrated with commercial pH 4.0; 7.0 and 10.0 buffer solutions prior to the measurements. When not in use, the glass electrode was immersed in deionized water.

### 2.3. Graphene Oxide Synthesis

Graphene oxide is synthesized from graphite powder using a modified Hummer process.<sup>47</sup> 5 g graphite powder, 2.5 g sodium nitrate ( $\text{NaNO}_3$ ), and 115 mL 96.4% sulfuric acid ( $\text{H}_2\text{SO}_4$ ) were mixed in the first step of the synthesis process. In an ice bath, the entire mixture was agitated for

1 hour and, 15 g potassium permanganate ( $\text{KMnO}_4$ ) was gently added to the mixture. The temperature was kept below 5 °C for the permanganate addition. The solution was taken out of the ice bath and stirred for 2 hours until it turned dark green.

The temperature of the mixture was kept between 35–40 °C during these procedures. 500 mL deionized water was gently added to the mixture in the second step of the synthesis process, and stirring was continued for 1 hour. To remove excess  $\text{KMnO}_4$ , 8.4 mL of hydrogen peroxide ( $\text{H}_2\text{O}_2$ , 35.7%) was gently dropped and stirred for 10 minutes. The exothermic process happened, and the temperature was allowed to fall to room temperature.

Following a 10-minute centrifugation at 5000 rpm, 10 mL hydrochloric acid and 30 mL deionized water were added. After that, the supernatant was decanted, and the remaining residue was rewashed three times with an HCl/deionized water mixture until pH 7 was achieved. As a result, the prepared GO was vacuum-dried overnight at 50 °C for 24 hours.

## 2. 4. Characterization of Graphene Oxide

Graphene oxide nanostructures were investigated using a Zeiss Evo 60 EP model Scanning Electron Microscope (SEM) with magnifications of 2500 X and accelerating voltages of 15 kV.

## 2. 5. RGO/AuNPs/GCE Nanocomposite Sensor Fabrication

The non-modified GCE (nGCE) was polished manually with  $\text{Al}_2\text{O}_3$  suspension (0.3 m, ATM GMBH, Germany), rinsed with deionized water, and sonicated in ethanol and double-distilled water for 5 minutes, respectively.

GO was dispersed into sodium acetate buffer by stirring at room temperature, and the resultant liquid was ultrasonicated for 4 hours, providing a homogeneous black dispersion containing 1 mg  $\text{mL}^{-1}$  GO.

The buffer solution of sodium acetate serves as both a buffer and an intercalant. The intercalation of sodium ions inhibits restacking of the electrochemically reduced graphene sheets, resulting in a larger electrochemically active surface area for the RGO modified electrode. The electrode was cleaned with deionized water after electrochemical reduction and placed in a 50°C oven for 15 minutes to thoroughly evaporate the solvent and increase RGO molecule adherence to the electrode surface.

The GO dispersion was then dropped 5  $\mu\text{L}$  onto a pre-cleaned GCE and let to dry at room temperature. The GO/GCE was placed in an electrochemical cell containing an acetate buffer solution (pH = 5) and 50 cyclic voltammetric scans between (+0.4) V and (–0.4) V were done at a scan rate of 0.050 V/s. As a result, the GO treated GCE was electrochemically reduced to RGO and dried in the open air for 10 minutes. RGO/GCE was then immersed

in a 3 mmol  $\text{L}^{-1}$   $\text{HAuClO}_4 \cdot \text{H}_2\text{O}$  solution prepared in 0.01 mol  $\text{L}^{-1}$   $\text{Na}_2\text{SO}_4$  and 0.01 mol  $\text{L}^{-1}$   $\text{H}_2\text{SO}_4$  solution in the measurement cell. To electrodeposit Au nanoparticles (AuNPs) on the RGO/GCE, 20 consecutive cycles in the potential range of 0.2 to +1.0 V at a scan rate of 0.050 V  $\text{s}^{-1}$  were utilized. The modified sensor was labeled RGO/GCE/AuNPs, dried, and used as an electrochemical sensor. When it wasn't in use, the sensor was kept at room temperature.

## 2. 6. Electrochemical Measurements

Appropriate volumes of supporting electrolyte (KCl) and pesticide standard solution were added to the electrochemical cell with a total volume of 5.0 mL in the cyclic voltammetry and differential pulse voltammetry methods used in this study. To record the background signals, voltammogram of the supporting electrolyte was obtained before adding the pesticide solution to be examined. At a scanning rate of 0.050 V  $\text{s}^{-1}$ , cyclic voltammetric measurements were taken. According to the potential signaled by the pesticides, the most appropriate potential range was employed in both methods. Cyclic voltammograms of the GCE and modified electrode were acquired by scanning the potential between 0.80 V and +1.00 V vs. Ag/AgCl at a scan rate of 0.050 V  $\text{s}^{-1}$ . All other voltammetric measurements were performed in a BR buffer solution at room temperature ( $25 \pm 1$  °C) (0.04 mol  $\text{L}^{-1}$ , pH 8.0)

## 2. 7. Optimization of the Experimental Conditions for Ziram

To create a highly sensitive method with a low detection limit, it's crucial to identify the most effective experimental conditions. On bare and modified GCE, the effect of scan rate, pH, and supporting electrolyte on the voltammetric response of ziram was examined. The sensitivity of the assay was shown by putting the constructed sensor to the test with real samples.

## 2. 8. Real Sample Application of the Sensor

Tap water and peach juice samples were analyzed using the spiking approach to determine the applicability of the RGO/AuNPs/GCE sensor.

Tap water samples were taken from our laboratory and spiked with a certain amount of standard ziram solution. To maintain a homogeneous mixture, it was agitated for 3 hours in an ultrasonic bath. This solution was added to electrochemical cells containing 100 mM KCl in Britton-Robinson (BR) buffer solution (0.04 mol  $\text{L}^{-1}$ , pH 8.0) in quantities of 250  $\mu\text{L}$ , 500  $\mu\text{L}$ , and 1500  $\mu\text{L}$ . The DPV method was used to analyze the samples.

Peach juice was also tested to the method's application. Peaches were picked from a farmer's garden that practices organic farming and avoids using pesticides. The

peach juice obtained by squeezing the fruit was filtered through the filter paper and the pulp was removed. In 25 mL of peach juice, a known amount of 1.01 mM ziram stock solution was added. To get a homogenous mixture, it was sonicated for 2–3 hours in an ultrasonic bath. 25 mL acetone was added to the mixture before it was transferred to centrifuge tubes. The organic phase was filtered via a Buchner funnel using Whatman filter paper (No.4) after centrifugation at 4000 rpm for 10 minutes. To remove the solvent, the filtrate was transferred to a 250 mL rotating vacuum evaporator vessel. After the solvent had evaporated, the residue was dissolved in acetone to yield a total volume of 5.0 mL. The blank sample was made by following the identical steps as the peach juice sample that did not contain ziram.

### 3. Results and Discussion

#### 3.1. Characterization of Graphene Oxide

SEM image of the prepared GO is presented Figure 1. From the SEM image it is evident that GO has a multiple lamellar layer structure and it is possible to distinguish the edges of individual sheets. The layers are stacked one above the other and also show wrinkled areas, which could be attributed to intrinsic and extrinsic factors such as thermal fluctuation, defects, and functionalization. The wrinkled structure of the GO can increase the effective surface area and thus provide a good platform for bonding the AuNPs.

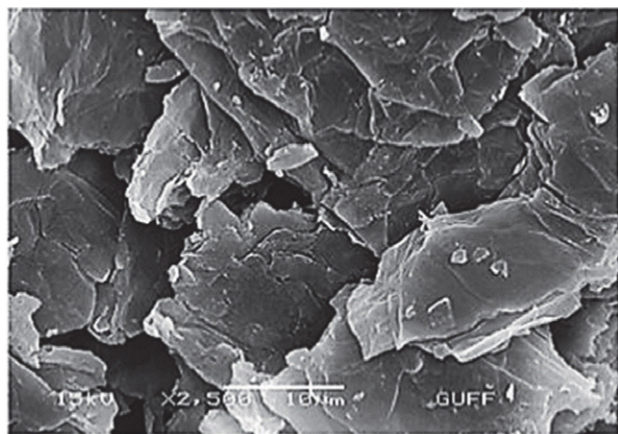


Figure 1. SEM images of synthesized graphene oxide.

#### 3.2. Optimization of RGO/AuNPs Sensor Fabrication

The electropolymerization cycles were investigated to achieve the best responses for ziram determination. Effect of GO concentration on sensor response was investigated

using 0.5 mg mL<sup>-1</sup>; 1.0 mg mL<sup>-1</sup>; 1.5 mg mL<sup>-1</sup>; and 2.0 mg mL<sup>-1</sup>. The highest current response was observed with the electrode prepared with 1.0 mg mL<sup>-1</sup> GO and this value was selected as the optimum GO concentration (Fig. 2). GO concentration higher than 1.0 mg mL<sup>-1</sup> did not increase the sensor response. The results could be attributed to the thicker RGO layer, which restricted electrical conductivity.

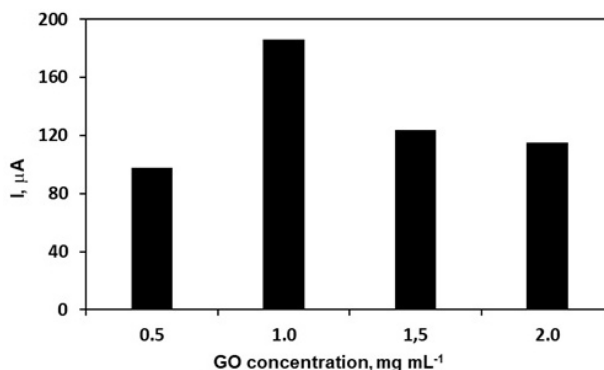


Figure 2. Effect of GO concentration on the response of the RGO/GCE.

Fig. 3 shows the cyclic voltammogram of electrochemical reduction peak of graphene oxide at  $-1.14$  V. Electrons act as a reducing agent, causing RGO to occur on the GCE surface. Wang et al. reported the electrochemical reduction mechanism of graphene oxide with two assumptions.<sup>48</sup> The reduction of newly formed hydrogen atoms produced near the electrode surface during the water electrolysis process was one of the expectations. The following reaction takes place during water electrolysis.

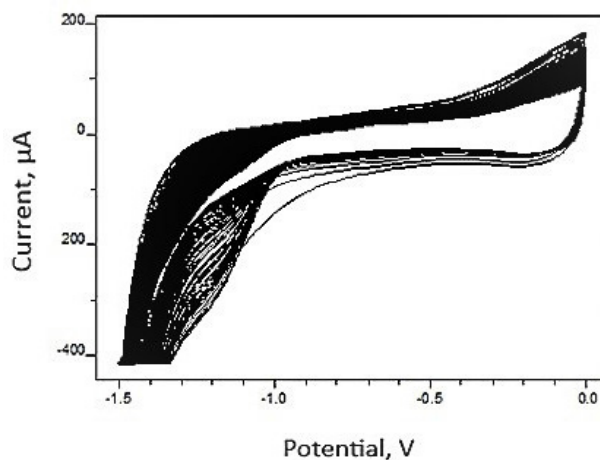
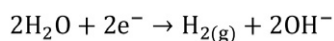
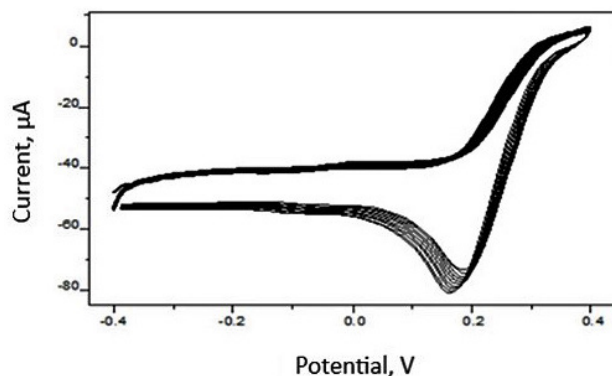


Figure 3. CV of electrochemical reduction of 1.0 mg mL<sup>-1</sup> graphene oxide on GCE surface in acetate buffer solution (pH = 5) at the scan rate of 0.050 V s<sup>-1</sup> in the potential range of  $(-1.2) - (2.2)$  V.

Hydrogen gas produced at the edges of graphene oxide can also contribute to the reduction process of graphene oxide.

During the electrochemical reduction process, a cathodic peak was observed due to the formation of reduced graphene oxide. The continuous deposition of conducting reduced graphene oxide on the electrode surface was evidenced by the linear increase in peak current with consecutive cycles. The current intensity stabilized after approximately 15–20 cycles and the electrochemically active surface area reached its maximum value. Then, the RGO/GCE was washed with ultrapure water. According to the literature, gold nanoparticles were successfully deposited on the RGO/GCE surface.<sup>49</sup>



**Figure 4.** Repetitive cyclic voltammogram of RGO/GCE in 0.01 mol L<sup>-1</sup> H<sub>2</sub>SO<sub>4</sub> solution containing 3 mmol L<sup>-1</sup> HAuClO<sub>4</sub> and 0.01 mol L<sup>-1</sup> Na<sub>2</sub>SO<sub>4</sub> at a scan rate of 0.050 V s<sup>-1</sup> in the potential range of (–0.4) – (0.4) V.

### 3. 3. Electrochemical Characterization of RGO/AuNPs/GCE Nanocomposite

The cyclic voltammogram (CV) of the [Fe(CN)<sub>6</sub>]<sup>3-/4-</sup> redox probe is a useful method for investigating the characteristics of surface-modified electrodes. For this, electrochemical characteristics of the modified and unmodified sensors were investigated in 100 mM KCl containing 5.0 mM of [Fe(CN)<sub>6</sub>]<sup>3-/4-</sup> ions. Figure 5 shows the CVs recorded for GCE, RGO/GCE, and AuNPs/RGO/GCE. In these three voltammograms, reversible peaks of [Fe(CN)<sub>6</sub>]<sup>3-/4-</sup> were observed. Although all voltammograms showed a pair of redox peaks corresponding to Fe<sup>3+</sup>/Fe<sup>2+</sup>, the current intensity varied.

Because of the RGO's large surface area and great conductivity, it was observed that peak currents increased slightly once the GCE surface was modified with RGO. When the surface was modified with gold nanoparticles, the peak currents were significantly increased compared to the currents obtained with GCE and RGO/GCE. These changes can be interpreted as that AuNPs assisting electron transfer between the redox probe and the electrode.

This finding supports the idea that combining the two nanomaterials, RGO and AuNPs, increased the electrode's sensitivity by raising the current intensity or enhance the current due to electro catalytic effect and large surface area.<sup>50</sup>

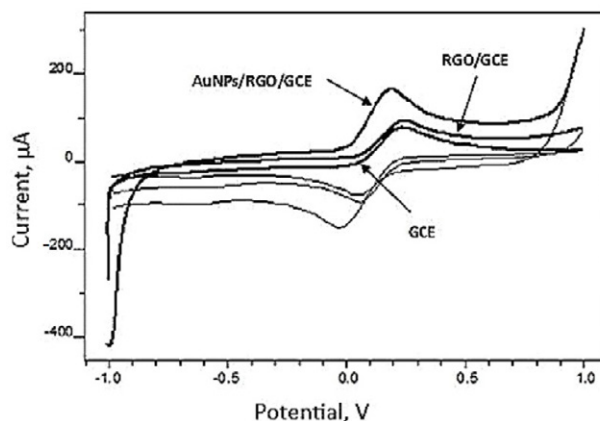


**Figure 5.** Cyclic voltammograms of GCE, RGO/GCE and AuNPs/RGO/GCE in 5.0 mM [Fe(CN)<sub>6</sub>]<sup>3-/4-</sup> containing 100 mM KCl.

### 3. 4. Electrochemical Performance of the Sensors

In 0.04 mol L<sup>-1</sup> BR buffer solution (pH 8.0), the CV responses of the bare GCE, RGO/GCE, and AuNPs/RGO/GCE sensors to  $1.50 \times 10^{-3}$  mol L<sup>-1</sup> ziram were individually examined. Figure 6 depicts a comparison of voltammograms obtained using GCE, RGO/GCE, and AuNPs/RGO/GCE sensors under the same experimental conditions. The anodic peak current of ziram was investigated using the CV results. Because of the distribution of AuNPs on the electrode surface, the current measured at AuNPs modified RGO/GCE was significantly higher than the current measured at RGO/GCE and bare GCE. As a result of their distinctive properties, the simultaneous presence of RGO and AuNPs improved the sensitivity of ziram detection. A synergic effect of their combination was demonstrated as a result of a larger surface area and increased conductivity.

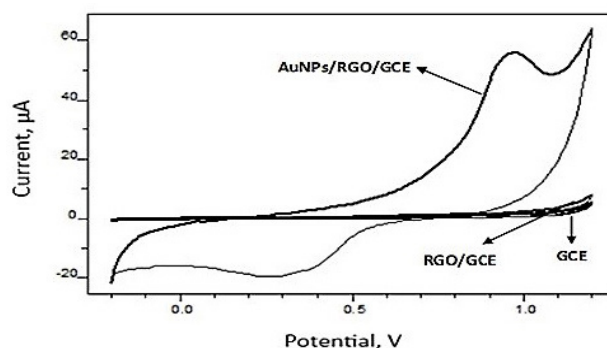


**Figure 6.** The cyclic voltammograms of  $1.50 \times 10^{-3}$  mol L<sup>-1</sup> ziram in BR buffer solution with pH 8.0 at scan rate 0.050 v s<sup>-1</sup>, for the bare GCE, RGO/GCE and AuNPs/RGO/GCE.



### 3. 5. Optimization of Experimental Conditions

The pH of the supporting solution has critical importance in obtaining good analytical performance for a developed sensor. Therefore, the effect of pH was investigated for ziram in  $0.04 \text{ mol L}^{-1}$  BR buffer solutions. This study was carried out at  $1.52 \times 10^{-3} \text{ mol L}^{-1}$  constant ziram concentration over the pH range from 5.0 to 10.0. The variation of peak currents and peak potentials of the voltammograms recorded for the ziram oxidation were given in Table 1. The current response of the AuNPs/RGO/GCE sensor increased with the pH increasing from 5.0 to 8.0 and then gradually decreased from 8.0 to 10.0 (Fig. 7). As seen from the Figure, at pH 5.0 AuNPs/RGO/GCE sensor showed small anodic peak at around 0.72 V. But increase of pH value causes increase of peak currents up to pH 8.0. Only a fluctuation was observed for the peak potential at pH 7.0. The voltammetric response was pH sensitive and maximum peak current was appeared at pH 8.01. As a result, BR buffer solution at pH 8.01 was chosen for the following work. The ziram's oxidation peak potential shifted to less negative values ranging from 8.0 to 10.0, indicating proton transfer participation in the electrode reaction.

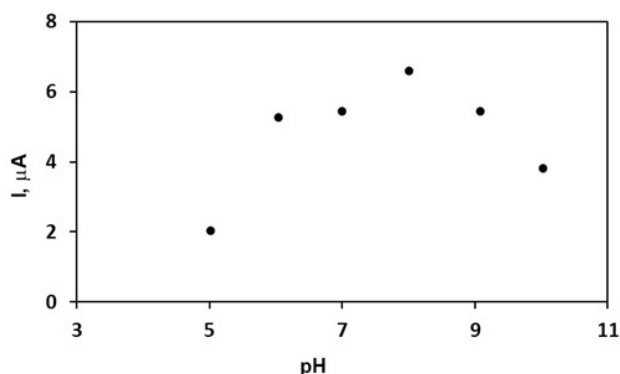


Figure 7. Effect of pH of ziram solutions on the current intensity of AuNPs/RGO/GCE

Table 1. Variation of peak potential and peak current of  $1.52 \times 10^{-3} \text{ mol L}^{-1}$  ziram solution at a scan rate of  $0.050 \text{ V s}^{-1}$  and different pH in  $0.04 \text{ mol L}^{-1}$  BR buffer solutions.

pH	Peak current (μA)	Peak potential (V)
5.01	2.027	0.722
6.04	5.256	0.744
7.00	5.445	0.676
8.01	6.605	0.710
9.08	5.430	0.652
10.03	3.815	0.648

The scan rate is an important parameter to evaluate the electrochemical behaviour, adsorption and diffusion properties of ziram on the electrode surface. Therefore,

the effect of scan rate on the oxidation peak current of  $1.0 \times 10^{-4} \text{ mol L}^{-1}$  ziram was studied. The variation of the peak current of ziram versus the square root of the scan rate was plotted (Figure 8). It has been observed that with the scan rate increasing, the anodic peak current increased. In the  $0.050\text{--}0.300 \text{ V s}^{-1}$  range, there was good linearity between the square root of scan rate and peak current. The linear regression equation was  $(\mu\text{A}) = 0.2783 (\mu\text{A s})^{0.0785} (\mu\text{A})$  with correlation coefficient 0.9919. The correlation coefficient is very close to 1.0, indicating that the oxidation process is controlled by diffusion.<sup>51,52</sup>

In addition, it was observed that logarithm of peak current changed linearly with the logarithm of scan rate and slope value for this linear line is 0.6346. For ideal diffusion-controlled the slope is between 0.5 and 1.0.<sup>53</sup>

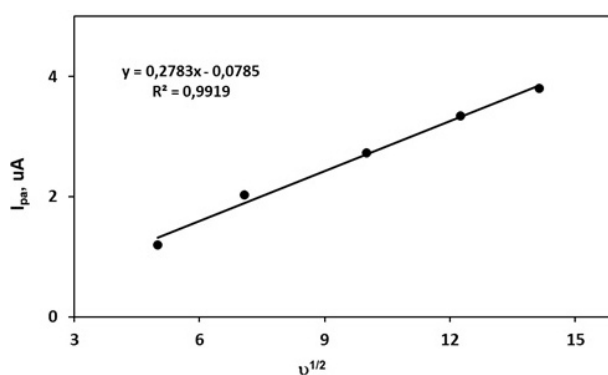


Figure 8. Variation of anodic peak current ( $I_{pa}$ ) versus the square root of scan rate ( $v^{1/2}$ )

### 3. 6. Analytical Performance Parameters of the Sensor

The correlation between ziram concentrations and anodic peak currents was examined utilizing the DPV method in BR buffer solution (pH 8.0) with the AuNPs/RGO/GCE composite sensor under optimized experimental conditions. The calibration graph was shown in Fig. 9. Over the range of  $1.50 \times 10^{-5} \text{ mol L}^{-1}$  to  $1.63 \times 10^{-7} \text{ mol L}^{-1}$ , the peak current increases linearly with the increasing ziram concentration. The linearity between the anodic peak current and the ziram concentration is shown in the following equation;

$$I_{pa}(\mu\text{A}) = 2 \times 10^7 \cdot C_{\text{ziram}}(\mu\text{M}) + 5.5336 \quad (1)$$

$$(R^2 = 0.9996)$$

The linear range of the calibration curve is  $1.50 \times 10^{-5} \text{ mol L}^{-1}$  to  $1.63 \times 10^{-7} \text{ mol L}^{-1}$  with the LOD values of  $1.19 \times 10^{-7} \text{ mol L}^{-1}$  for ziram. The formulas  $(3 \times s/m)$  and  $(10 \times s/m)$  were used to calculate the method's limit of detection (LOD) and limit of quantification (LOQ).<sup>54</sup> Where  $s$  denotes the measurement's standard deviation and  $m$  denotes the calibration curve's slope (or the sensitivity).

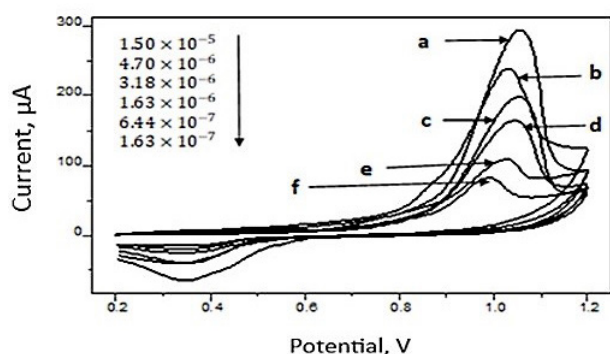


**Figure 9.** The calibration voltammograms at different concentrations of ziram in BR buffer (pH 8) at AuNPs/RGO/GCE by DPV (a)  $1.50 \times 10^{-5}$ ; (b)  $4.70 \times 10^{-6}$ ; (c)  $3.18 \times 10^{-6}$ ; (d)  $1.63 \times 10^{-6}$ ; (e)  $6.44 \times 10^{-7}$ ; (f)  $1.63 \times 10^{-7}$  mol L<sup>-1</sup>.

LOD value satisfies the MRLs established by the The Codex Alimentarius Commission (CAC), for stone fruits ( $7.0 \text{ mg kg}^{-1}$ ).<sup>55</sup> Particular pesticide limit levels have also been set at  $0.1 \text{ µg L}^{-1}$  by the European Union. This value was decided as the LOD for all pesticides found in drinking water. That means the method is sensitive enough and the developed sensor can be used with high reliability in detecting the maximum allowable residue level of ziram in fresh fruits and water. All validation and regression parameters are tabulated in Table 2.

**Table 2.** Analytical performance of the RGO/AuNPs/GCE sensor for ziram.

Parameters	Value
Linear working range, mol L <sup>-1</sup>	$1.50 \times 10^{-5} - 1.63 \times 10^{-7}$
LOD (mol L <sup>-1</sup> )	$1.19 \times 10^{-7}$
LOQ (mol L <sup>-1</sup> )	$7.80 \times 10^{-7}$
Calibration equation	$I_{pa} (\text{µA}) = 2 \times 10^{-7} c_{\text{ziram}} (\text{µM}) + 5.5336$
Regression coefficient (R <sup>2</sup> )	0.9996
Selectivity (µA/µM)	$2 \times 10^7$
Intercept	5.5336
Reproducibility (RSD, %)	2.35
Repeatability (RSD, %)	4.12

### 3. 7. Reproducibility and Repeatability

To demonstrate the reproducibility of the RGO/AuNPs/GCE sensor, 3 modified electrodes were prepared under the same composition. Under optimized experimental conditions, repeated DPV measurements ( $n = 5$ ) from a solution that contains  $5.0 \times 10^{-4} \text{ mol L}^{-1}$  ziram were used to identify the peak current for each electrode. The anodic peak currents for ziram had a relative standard deviation (RSD) of 2.35% (Table 2). This implies that the electrode has a high level of repeatability. Multiple DPV

measurements ( $n = 5$ ) were used to assess the sensor's repeatability, giving RSD value of 4.12% (Table 2).

### 3. 8. Real Sample Analysis

The analytical applicability of the prepared sensor was performed with tap water and peach juice. The recovery of the method was evaluated by spiking tap water and peach juice samples with ziram at low, middle and high concentration levels of the calibration graph. Calculated recovery values and added ziram concentrations are given in Table 3 and Table 4.

The obtained recovery values were between 96.4 and 107.6%. These results show that the developed electrochemical sensor can effectively be applied with high sensitivity and selectivity for ziram determination in two different matrices.

**Table 3.** Recovery results obtained by standard addition method in tap water sample using RGO/AuNPs/GCE sensor.

No	Added ziram, (mg L <sup>-1</sup> )	Found ziram, (mg L <sup>-1</sup> )	Recovery, %	RSD, %	Relative error, %
1	0.56	0.54 ( $\pm 0.02$ )	96.4 ( $\pm 2.73$ )	2.83	-3.6
2	1.68	1.64 ( $\pm 0.02$ )	97.6 ( $\pm 1.19$ )	1.22	-2.4
3	2.50	2.69 ( $\pm 0.04$ )	107.6 ( $\pm 1.67$ )	1.55	7.6

\* The average of three measurements is used for each value. RSD, Relative Standard Deviation

**Table 4.** Recovery values obtained by standard addition method in peach juice using RGO/AuNPs/GCE sensor.

No	Added ziram, (mg L <sup>-1</sup> )	Found ziram, (mg L <sup>-1</sup> )	Recovery, %	RSD, %	Relative error, %
1	0.62	0.65 ( $\pm 0.03$ )	104.8 ( $\pm 4.3$ )	4.07	4.84
2	1.86	1.83 ( $\pm 0.03$ )	98.8 ( $\pm 1.6$ )	1.64	-1.61
3	2.48	2.37 ( $\pm 0.04$ )	95.3 ( $\pm 1.6$ )	1.71	-4.70

\* The average of three measurements is used for each value. RSD, Relative Standard Deviation

## 4. Conclusion

A sensitive electrochemical sensor for the rapid detection of ziram was successfully constructed by modifying AuNPs improved RGO on GCE. Using cyclic voltammetry and differential pulse voltammetry, the electrochemical behaviour and real sample applicability of RGO/AuNPs/GCE were examined. The proposed electrochemical method was validated and the constructed sensor was proven to have good sensitivity and selectivity, as well as a low detection limit. Furthermore, the method has been used

to accurately determine the ziram in spiked tap water and peach juice. The created RGO/AuNPs/GCE sensor is effective and promising due to its relatively simple modification method and disposable feature, as well as its potential to be used for direct measurements in water and peach juice. The findings of this study add to the analytical methodologies for ziram determination that have been used thus far.

### Data available on request from the authors

The data that support the findings of this study are available from the corresponding author, [Aslan, N.], upon reasonable request.

Nazife Aslan <http://orcid.org/0000-0002-2622-5908>

### Declaration of competing interest

The authors declare that they have no known competing financial interests or personal relationships that could have appeared to influence the work reported in this article.

The authors also declare that they have no conflict of interest with suggested reviewers.

### Acknowledgements

The authors express their gratitude for the support from Gazi University with Grand Numbers BAP- 65/2020-03.

## 5. References

1. T. A. Saleh, V. K. Gupta, *Nanomaterial and Polymer Membranes* **2016**, 83–133; DOI:10.1016/B978-0-12-804703-3.00004-8
2. M. H. Mahnashi, A. M. Mahmoud, A. Az, K. Alhazzani, S. A. Alanazi, M. M. Alanazi, M. M. El-Wakil, *Microchemical Journal* **2021**, 164, 106020–106025; DOI:10.1016/j.microc.2021.106020
3. O. Arjmand, M. Ardjmand, A. M. Amani, M. H. Eikani, *Acta Chim. Slov.* **2020**, 67, 496–506; DOI:10.17344/acs.2019.5513
4. V. Vukojević, S. Djurdjica, M. Ognjanović, M. Fabián, A. Samphaod, K. Kalcher, D. M. Stanković, *Journal of Electroanalytical Chemistry* **2018**, 823, 610–616; DOI:10.1016/j.jelechem.2018.07.013
5. P. K. Kalambate, B. J. Sanghavi, S. P. Karna, A. K. Srivastava, *Sens. Actuators B* **2015**, 213, 285–294; DOI:10.1016/j.snb.2015.02.090
6. X. Ye, Y. Du, D. Lu, C. Wang, *Anal. Chim. Acta* **2013**, 779, 22–34; DOI:10.1016/j.aca.2013.03.061
7. R. Sengupta, M. Bhattacharya, S. Bandyopadhyay, A. K. Bhowmick, *Prog. Polym. Sci.* **2011**, 36(5), 638–670; DOI:10.1016/j.progpolymsci.2010.11.003
8. P. J. Wessely, U. Schwalke, *Appl. Surf. Sci.* **2014**, 291, 83–86; DOI:10.1016/j.apsusc.2013.09.142
9. S. F. Pei, H. M. Cheng, *Carbon* **2012**, 50(9), 3210–3228; DOI:10.1016/j.carbon.2011.11.010
10. S. L. Yang, S. L. Luo, C. B. Liu, W. Z. Wei, *Colloid Surface B* **2012**, 96, 75–79; DOI:10.1016/j.colsurfb.2012.03.007
11. V. Stanković, S. Đurđić, M. Ognjanović, J. Mutić, K. Kalcher, D. M. Stanković, *Journal of Electroanalytical Chemistry* **2020**, 876, 114487–114493; DOI:10.1016/j.jelechem.2020.114487
12. A. M. Mahmoud, M. M. El-Wakil, M. H. Mahnashi, M. F. B. Ali, S. A. Alkahtani, *Microchimica Acta* **2019**, 186, 617–624. DOI:10.1007/s00604-019-3647-7
13. Y. Liu, G. Gao, J. Hu and X. Z., *Int. J. Electrochem. Sci.* **2018**, 13, 11853–11866; DOI:10.20964/2018.12.05
14. Y. Zhou, M. Ma, H. He, Z. Cai, N. Gao, C. He, G. Chang, X. Wang, Y. He, *Biosensors and Bioelectronics* **2019**, 146, 111751; DOI:10.1016/j.bios.2019.111751
15. R. Wang, Z. Wu, C. Chen, Z. Qin, H. Zhu, Guo. Wang, C. Wu, W. Dong, W. Fan and J. Wang, *Chem. Commun.* **2013** 49, 8250–8252; DOI:10.20964/2018.12.05
16. Y. Liu, G. Gao, J. Hu, X. Zou, *Int. J. Electrochem. Sci.*, **2018**, 13, 11853 – 11866; DOI:10.20964/2018.12.05
17. E. Er, H. Çelikkan, N. Erk, M. Levent Aksu, *Electrochim Acta* **2015**, 157, 252–257; DOI:10.1016/j.electacta.2015.01.020
18. P. Sharma, G. Darabdhara, T.M. Reddt, A. Borah, P. Bezboruah, P. Gogoi, N. Hussain, P. Sengupta, M.R. Das, *Catal. Commun.* **2013**, 40, 139–144; DOI:10.1016/j.catcom.2013.06.021
19. P. Dong, B. Jiang, J. Zheng, *Anal. Methods*, **2019**, 11, 2428–2434; DOI:10.1039/C9AY00549H
20. B. Jiang, P. Dong, J. Zheng, *Talanta* **2018**, 183, 114–121; DOI:10.1016/j.talanta.2018.02.016
21. J. Lu, Y. Sun, G.I.N. Waterhouse, Z. Xu, *Adv. Polym. Technol.* **2018**, 37, 3629–3638; DOI:10.1002/adv.22147
22. M-S. Tsai, C-J. Lua, P-G. Sub, *Materials Chemistry and Physics* **2018**, 215, 293–298; DOI:10.1016/j.matchemphys.2018.05.058
23. Y. Gao, X. Wu, H. Wang, W. Lu and M. Guo, *Analyst* **2018**, 143, 297–303; DOI:10.1039/C7AN01706E
24. M.H. Ghanbaria, A. Khoshrooc, H. Sobatid, M.R. Ganjalie, M. Rahimi-Nasrabadi, F. Ahmadi, *Microchemical Journal* **2019**, 147, 198–206; DOI:10.1016/j.microc.2019.03.016
25. F. Gendi, D-W. Sun, H. Pu, Q. Wei, *Talanta* **2019**, 195(1), 841–849; DOI:10.1016/j.talanta.2018.11.114
26. A. Hussain, H. Pu, D-W. Sun, *Food Chemistry* **2020**, 317, 126429; DOI:10.1016/j.foodchem.2020.126429
27. P. Fanjul-Bolado, R. Fogel, J. Limson, C. Purcarea, A. Vasilescu, *Biosensors* **2021**, 11(1), 12–37. DOI:10.3390/bios11010012
28. C. A. Martin, K. M. Myers, A. Chen, N. T. Martin, A. Barajas, D. E. Krantz, *Experimental Neurology* **2016**, 275(1), 232–241; DOI:10.1016/j.expneurol.2015.09.017
29. A. Scheyer, C. Graeff, S. Morv, *Chemosphere* **2005**, 58, 1517–1524; DOI:10.1016/j.chemosphere.2004.10.013
30. K. Wang, D-W. Sun, H. Pu, Q. Wei, *Food Chem.* **2020**, 310, 125923; DOI:10.1016/j.foodchem.2019.125923
31. USEPA, Code of Federal Regulations: Part 180-Tolerances and Exemptions for Pesticide Chemical Residues in Food **2014**, 24 (Available at <https://www.ecfr.gov/cgi-bin/text-idx?>)

32. C. A. Martin, K. M. Myers, A. Chen, N. T. Martin, A. Barajas, D. E. Krantz, *Exp. Neurol.* **2016**, 275, 232–241; DOI:10.1016/j.expneurol.2015.09.017
33. J. Al-Alam, L. Bom, A. Chbani, Z. Fajloun, M. Millet, *J. Chromatogr. Sci.* **2017**, 55(4), 429–435; DOI:10.3390/polym11091449
34. B. Schmidt, H. B. Christensen, A. Petersen, J. J. Sloth, M. E. Food Additives & Contaminants: Part A **2013**, 30(7), 1287–1298. DOI:10.1080/19440049.2013.801083
35. Y. Nolvachai, C. Kulsing, P. J. Marriott, *Crit. Rev. Environ. Sci. Technol.* **2015**, 45(19), 2135–2173; DOI:10.1080/10643389.2015.1010431
36. J. Chen, F. Fu, S. Wu, J. Wang, Z. Wang, *J. Sep. Sci.* **2017**, 40(19), 3898–3904; DOI:10.1002/jssc.201700455
37. L. M. Silva, D. De Souza, *Electrochimica Acta* **2017**, 224, 541–550; DOI:10.1016/j.electacta.2016.11.133
38. D. Amorello, S. Orecchio, *Microchemical Journal* **2013**, 110, 334–339; DOI:10.1016/j.microc.2013.05.002
39. P. Qiu, Y. N. Ni, *Chin. Chem. Lett.* **2008**, 19(11), 1337–1340; DOI:10.1016/j.cclet.2008.07.013
40. D. M. Stanković, K. Kalcher, *Sens. Actuators B* **2016**, 233, 144–147; DOI:10.1016/j.snb.2016.04.069
41. L. Janíková-Bandžuchová, R. Šelešová, K. Schwarzová-Pecková, J. Chýlková, *Electrochimica Acta* **2015**, 154, 421–429; DOI:10.1016/j.electacta.2014.12.064
42. A. Vasilescu, A. M. Titoiu, C. Purcarea, G. Necula-Petrareanu, Romanian OSIM Patent Application No. A/00587, 13 August **2018**
43. R. Šelešová, K. Schwarzová-Pecková, R. Sokolová, K. Krejčová, P. Martinková-Kelišková, *Electrochimica Acta* **2015**, 381(10), 138260; DOI:10.1016/j.electacta.2021.138260
44. N. S. Khan, D. Pradhan, S. Choudhary, P. Saxena, N. K. Poddar, A. K. Jain, *Journal of Analytical Science and Technology* **2021**, 12–32. DOI:10.1186/s40543-021-00282-6
45. L. G. Shaidarova, G. K. Budnikov, S. A. Zaripova, *J. Anal. Chem.* **2001**, 56(8), 748–753. DOI:10.1023/A:1016741828696
46. S. Wyantuti, R. Tjokronegoro, S. Rochani, *Proceeding of The International Seminar on Chemistry* **2008**, 374–376.
47. N. I. Zaabaa, K. L. Fooa, U. Hashimad, S. J. Tanbc, W. W. Liu, C. H. Voona, *Solvent Influence* **2017**, 8, 469–477; DOI:10.1016/j.proeng.2017.04.118
48. Y. Xu, H. Bai, G. Lu, C. Li, G. Shi, *J. Am. Chem. Soc.* **2008**, 130(18), 5856–5857. DOI:10.1021/ja800745y
49. X. Wang, I. Kholmanov, H. Chou, S. R. Rodney, *ACS Nano* **2015**, 9(9), 87378743; DOI:10.1021/acsnano.5b03814
50. J. Wang, *Analytical Electrochemistry*, Wiley-VCH, New York 2000
51. I. H. Taşdemir, M. A. Akay, N. Erk, E. Kılıç, *Electroanalysis* **2010**, 22(17–18), 2101–2109. DOI:10.1002/elan.201000100
52. Y. Jiang, D. Shengyuan, L. Janping, J. Huangxian, G. Sundaram, *Biosens. Bioelectron.* **2011**, 29(1), 159–166; DOI:10.1016/j.bios.2011.08.011
53. D. Caschera, F. Federici, D. Zane, F. Focanti, A. Curulli, G. Padeletti, *J. Nanopart. Res.* **2009**, 11, 1925–1936; DOI:10.1007/s11051-008-9547-0
54. M. H. Mahnashi, A.M. Mahmoud, S.A. Alkahtani, R. Ali, M. M. El-Wakil, *Anal. Bioanal. Chem.* **2020**, 412, 355–364; DOI:10.1007/s00216-019-02245-8
55. Food and Agriculture Organization of the United Nations (FAO). [www.fao.org/fao-who-codexalimentarius/codex-texts/dbs/pestres/pesticide-detail](http://www.fao.org/fao-who-codexalimentarius/codex-texts/dbs/pestres/pesticide-detail). (accessed December 22, **2021**).

## Povzetek

V tem prispevku je opisana priprava senzorskih materialov na osnovi reduciranega grafenovega oksida z nanodelci zlata za določanje cinkovega(II)dimetilditiokarbamata (zirama). Grafenov oksid (GO) je bil sintetiziran po modificirani Hummerjevi metodi. Kompozitni senzor, sestavljen iz nanodelcev zlata (AuNP) in reduciranega grafenovega oksida (RGO), je bil elektrokemično izdelan na elektrodi iz steklenega ogljika. Nanokompozit je bil ovrednoten z uporabo vrstične elektronske mikroskopije (SEM). Ciklična voltometrija je bila uporabljena za prikaz elektrokemičnih lastnosti modificiranega senzorja na vsaki stopnji modifikacije. Predlagani senzor je pokazal dobro analitično zmogljivost za določanje pesticida ziram v vodi in breskovem soku, vključno z zelo nizko mejo zaznave, velikim linearnim razponom in nizkim RSD.



Except when otherwise noted, articles in this journal are published under the terms and conditions of the Creative Commons Attribution 4.0 International License

Scientific paper

# Electronic Structures and Reactivities of COVID-19 Drugs: A DFT Study

Seyda Aydogdu and Arzu Hatipoglu\*

Department of Chemistry, Yildiz Technical University, 34220, Istanbul, Turkey

\* Corresponding author: E-mail: hatiparzu@yahoo.com

Received: 04-06-2022

## Abstract

These days, the world is facing the threat of pandemic Coronavirus Disease 2019 (COVID-19). Although a vaccine has been found to combat the pandemic, it is essential to find drugs for an effective treatment method against this disease as soon as possible. In this study, electronic and thermodynamic properties, molecular electrostatic potential (MEP) analysis, and frontier molecular orbitals (FMOs) of nine different covid drugs were studied with Density Functional Theory (DFT). In addition, the relationship between the electronic structures of these drugs and their biological effectiveness was examined. All parameters were computed at the B3LYP/6-311++g(d,p) level. The Solvent effect was evaluated using conductor-like polarizable continuum model (CPCM) as the solvation model. It was observed that electrophilic indexes were important to understand the efficiencies of these drugs in COVID-19 disease. Paxlovid, hydroxyquinone, and nitazoxanide were found as the most thermodynamically stable molecules. Thermodynamic parameters also demonstrated that these drugs were more stable in the aqueous media. Global descriptors and the reactivity of these drugs were found to be related. Nitazoxanide molecule exhibited the highest dipole moment. The high dipole moments of drugs can cause hydrophilic interactions that increase their effectiveness in an aqueous solution.

**Keywords:** COVID-19; SARS-COV-2; Global descriptors; DFT; Solvent effect.

## 1. Introduction

The Covid-19 outbreak is an important threat to public health nowadays. Many people died, and this pandemic caused a significant economic crisis and panic. During the last few decades,  $\beta$  class of coronaviruses led to mortality diseases like SARS and MERS.<sup>1</sup> In December 2019, in Wuhan, China, an outbreak of the new type of Coronavirus Disease (COVID-19) caused a global health and economic crisis. This virus is coronavirus 2 (SARS-COV-2), a type of  $\beta$  coronavirus.<sup>2</sup> Its common symptoms are shortness of breath, fatigue, fever, cough, and flue. In some more severe cases, COVID-19 infection leads to organ failure and even death.<sup>3</sup> The mortality rate of COVID-19 is approximately 6.8%, which is smaller than the mortality rate of SARS (10%) and MERS (36%). Despite the smaller mortality rate compared to SARS and MERS, the higher contagious property of COVID-19 and the unpredictability of disease progression worsened the situation and resulted in more deaths worldwide.<sup>1,4,5</sup> To date (January 31, 2022), WHO reported that there were 223 countries and territories that suffered from coronavirus with 364,191,494 confirmed cases and death number of 5,631,457 people.<sup>6</sup> Although a

vaccine has been found for COVID-19, it is essential to have appropriate drugs that are effective, inexpensive, and easily available for treatment. Therefore, more information is urgently needed on effective drug therapy and possible therapeutics used to combat the COVID-19 pandemic.

It is very difficult to develop a new antiviral drug against COVID-19 and meet the urgent need for treatment. Drug discovery is expensive and time-consuming, a process that takes at least 15 years for a newly designed drug to reach patients from the laboratory.<sup>7,8</sup> These are the limiting factors for control and prevention of this global pandemic.

After analyzing the genome of SARS-COV-2, it is understood that the spike S protein of the virus effectively binds to the human angiotensin-converting enzyme 2 receptors. Once it enters a human cell, it releases immediately and replicates itself.<sup>9,10</sup> Based on this information, many known possible therapeutics have been tested preclinically and clinically so far, but few of them have been proven effective against this disease such as chloroquine, hydroxychloroquine, favipiravir and so on.<sup>11</sup> Remdisevir and chloroquine can be used effectively to cure COVID-19.<sup>12</sup> The

combination of favipiravir with different antiviral agents has been studied for the treatment of COVID-19 and it has been found that the combination of antivirals is an appropriate treatment.<sup>13,14</sup> Nowadays, COVID-19 vaccines are used to prevent the disease. It is also known that at least 54.4% of the world's population receives a dose of vaccine<sup>15</sup>, but drug treatment is still needed to prevent the pandemic.

Computational methods can be a good alternative for studying in such emergency and difficult situations. In comparison to experimental methods, computational ones, are not expensive or time-consuming.<sup>16</sup> There are some studies in the literature by using computational methods related to COVID-19. Molecular docking for inhibition of M<sup>Pro</sup>, 3CL<sup>Pro</sup>, E proteins, and RdRp enzymes against SARS-COV-2 with drugs such as chloroquine, hydroxychloroquine, favipiravir, umifenovir, paxlovid, galidesivir, ribavirin, molnupiravir, and remdesivir have been investigated.<sup>17–28</sup> Electronic and optoelectronic properties of hydroxychloroquine, chloroquine, azithromycin, and favipiravir were investigated by the DFT method to understand the possible drug delivery system.<sup>29–31</sup> Although many studies have been conducted on the pharmacological properties of COVID-19 drugs, there is still lack of information about the effect of the electronic properties of these molecules on their physicochemical properties and reactivities. Therefore, it is crucial to examine the electronic properties of COVID-19 drugs to better understand their biological effectiveness. As mutations occur in the SARS-COV-2 protein, the need to determine the properties of COVID-19 drugs with rapid and effective methods has become more urgent than ever.

The purpose of this study is to calculate the electronic and thermodynamic properties of already used and newly proposed COVID-19 drugs. DFT method is applied for all calculations. In this respect, some chemical descriptors such as hardness ( $\eta$ ), electrophilic index ( $\omega$ ), chemical potential ( $\mu$ ), softness ( $S$ ) and frontier orbital energies, and thermodynamic parameters (such as enthalpy, Gibbs free energy, and entropy) are evaluated. Hydroxychloroquine, chloroquine, nitazoxanide, favipiravir, galidesivir, ribavirin, fluvoxamine, molnupiravir and paxlovid are selected as model drugs owing to the differences in their electronic structures. And, their efficiencies are investigated against COVID-19.

## 2. Computational Details

All the calculations were carried out with Density Functional Theory (DFT) method with Gaussian 09 program.<sup>32</sup> The drug molecules were optimized using Becke's three parameter functional which combines Becke and HF exchange with the Lee-Yang-Parr correlation term at B3LYP/6-311++g(d,p) level.<sup>33</sup> Frequency analysis, calculated at the same level of theory, indicated that the opti-

mized structures were at the stationary points corresponding to local minima without any imaginary frequency. The structural visualizations of the drugs were prepared by using the GaussView 5.0 software.<sup>34</sup> Since blood itself is a water-based system, the Conductor-Like Polarizable Continuum Method (CPCM) was used to compute the effect of water on the properties of drugs. The solvent was water with the dielectric constant value  $\epsilon = 78.3$ .<sup>35</sup> Thermodynamic parameters were obtained by frequency analysis and solvation energies were also calculated. The energies were corrected by including zero-point vibrational energy (ZPVE) at the B3LYP/6-311++G(d,p) level.

Quantum chemical descriptors were calculated within the conceptual framework of the DFT to determine the reactivity of drugs. The reactivity of molecules can be predicted with global descriptors, which are determined by perturbations related to the change in the number of electrons. Some of the global descriptors studied in this paper are chemical potential ( $\mu$ ), hardness ( $\eta$ ), electrophilic index ( $\omega$ ), and softness ( $S$ ). Hardness, softness, and chemical potential were calculated by Koopman's theorem. According to this theorem ionization potential and electron affinity of a system are equal to the negative value of the energy of the highest occupied molecular orbital ( $E_{\text{HOMO}}$ ) and the energy of the lowest unoccupied molecular orbital ( $E_{\text{LUMO}}$ ). By using the Koopman's theorem these global reactivity descriptors are defined as<sup>36–38</sup>,

$$\mu = \frac{E_{\text{LUMO}} + E_{\text{HOMO}}}{2}, \quad (1)$$

$$\eta = \frac{E_{\text{LUMO}} - E_{\text{HOMO}}}{2}, \quad (2)$$

$$\omega = \frac{\mu^2}{2\eta}, \quad (3)$$

$$S = \frac{1}{2\eta}, \quad (4)$$

## 3. Results and Discussion

### 3.1. Energies and Global Descriptors

The structures of nine studied COVID-19 drugs, hydroxychloroquine, chloroquine, nitazoxanide, favipiravir, galidesivir, ribavirin, fluvoxamine, molnupiravir, and paxlovid, are shown in Figure 1 and optimized geometries of drugs are given in Figure 2. Some of these drugs are functionalized derivatives of the classic heteroaromatic rings, such as quinoline (hydroxychloroquine and chloroquine as molecules 1, 2), thiazolide (nitazoxanide as molecule 3), pyrazine (favipiravir as molecule 4). Others are nucleoside-based heterocyclic molecules, similar to the adenosine base of galidesivir (molecule 5) and the guanosine base of ribavirin (molecule 6). The newly proposed alter-



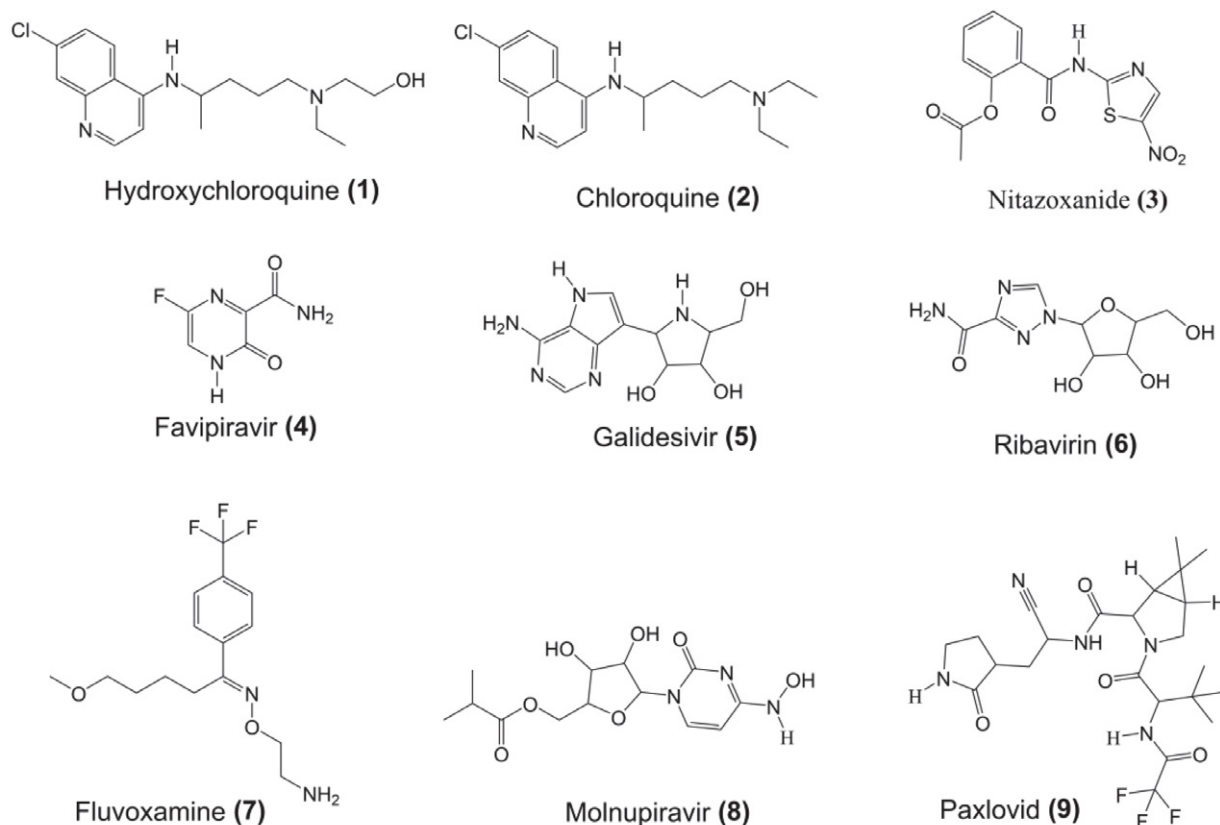


Figure 1. Structures of drug molecules

native drugs are fluvoxamine (molecule 7), a selective serotonin reuptake inhibitor (SSRI), ribonucleoside antiviral prodrug molnupiravir (molecule 8), and nitrile warhead paxlovid (molecule 9).

The calculated  $E_{\text{HOMO}}$ ,  $E_{\text{LUMO}}$ ,  $\Delta E$ , hardness ( $\eta$ ), chemical potential ( $\mu$ ), electrophilic index ( $\omega$ ), softness ( $S$ ) and dipole moments ( $D$ ) are listed in Table 1 for gas and aqueous media. The hardness is a good descriptor for chemical stability and reactivity and it is related to the energy gap. Hard molecules have large band gap energies. As seen in Table 1 the hardest molecules are 6 and 9, the least hard is 3. Molecules 5, 6, 7, 8, and 9, which contain electronegative atoms such as -OH and -F in their molecular structure, are those with highest hardness. Molecules 1, 2 and 3, which have fewer electronegative atoms in their molecular structure, are those with low hardness compared to the others. Molecule 3, which contains one sulfur atom in the ring in its structure, has the lowest hardness. The hardness of molecules increases in order of  $6 > 9 > 7 > 5 > 8 > 4 > 1 > 2 > 3$ . Softness is the opposite of hardness, and possesses a similar relation. The chemical potential ( $\mu$ ) is the measure of escaping tendency of electrons. The chemical potential also shows almost the same trend with hardness except for molecules 4, 5, and 8.

The electron accepting ability of a molecule is related to its electrophilicity index value. The electrophilic index

value of molecules is in order  $4 > 3 > 1 > 6 > 2 > 8 > 7 > 9 > 5$ . Molecules with an electrophilic index value higher than 1.5 eV have an electrophilic character.<sup>37</sup> As seen in Table 1, the electrophilic index value of all drug molecules is greater than 1.5 eV. Therefore, it can be inferred that all the studied molecules have an electrophilic character. It is known that the cysteine moieties of proteins are nucleophilic. So, it is advantageous to have an electrophilic agent for the treatment of COVID-19.<sup>39</sup> In general, all drugs have in common the ability to accept electrons, which may increase the interaction of drugs with the SARS-COV-2 virus.

The in vitro half-maximal effective concentration ( $EC_{50}$ ) values for SARS-COV-2 virus in Vero E6 values are given in Figure 3. As can be seen in the figure, the molecules with the highest  $EC_{50}$  values are 6, 9, and 4, respectively. These drugs are less efficient than the others. Molecule 9, Paxlovid, is the new drug which Pfizer has developed for COVID-19 and has just been approved for use. Molecule 6, Ribavirin is in a class of antiviral medications, and molecule 4, Favipiravir, is the more efficient drug for COVID-19 disease.<sup>40</sup> Favipiravir, as an antiviral drug, has been authorized for treating COVID-19 in several countries, under emergency provisions. There is a relationship between the  $EC_{50}$  values of the molecules and their global descriptors. Drugs with high  $EC_{50}$  values have high hardness and lower chemical potential values. Although there

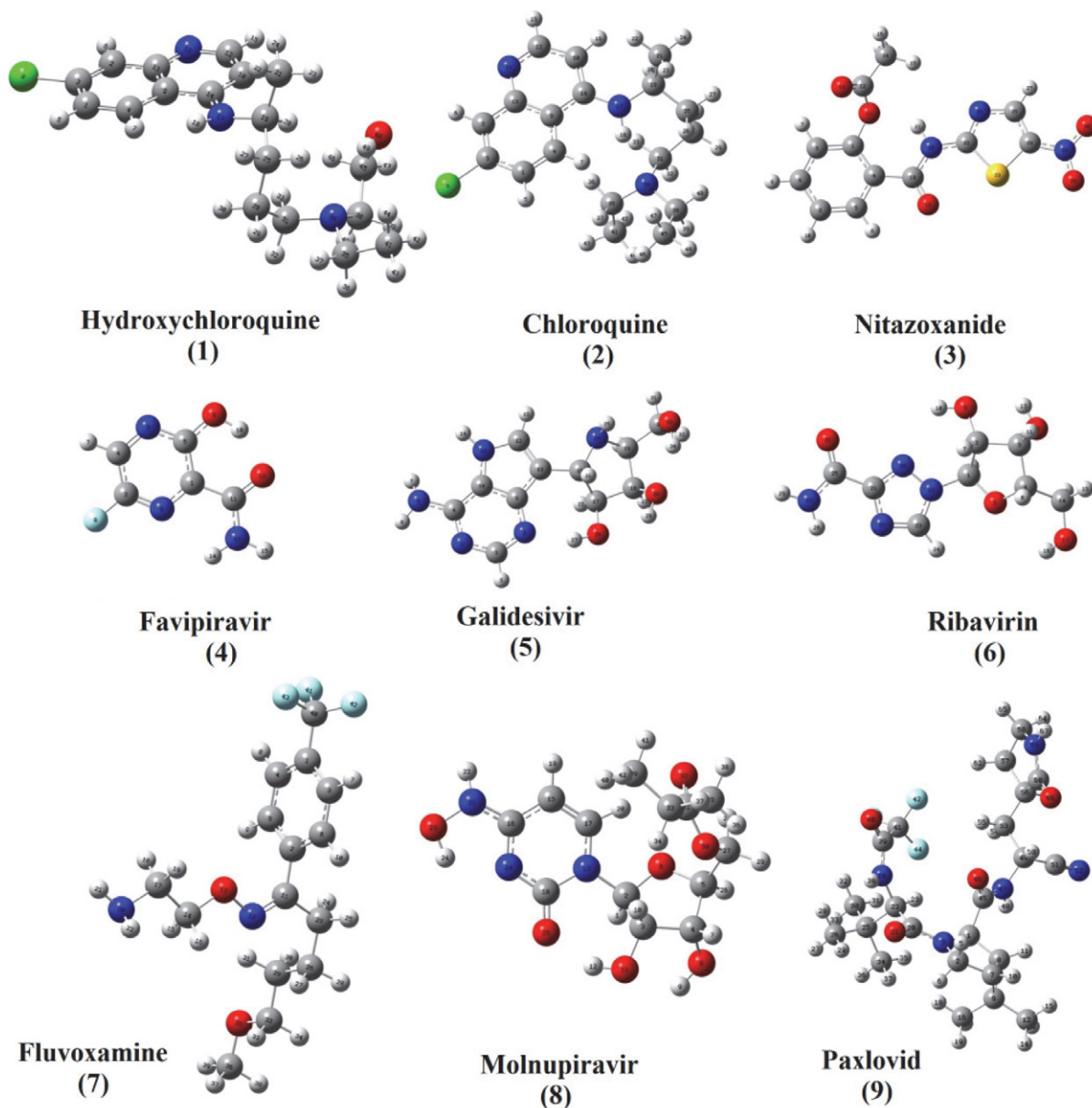


Figure 2. Optimized geometries of drug molecules

are not enough experimental studies on the efficacy of these drugs for COVID-19, the relationship between the global descriptors of these drugs and their  $EC_{50}$  values can be used to select the effective drug candidates.

The dipole moment is an important factor affecting the solubility of a drug. The solubility and polarity of the drug must be balanced to optimize the drug efficacy.<sup>3</sup> In biological systems, a high dipole moment value is a desirable property for drug delivery.<sup>16</sup> Dipole moments of drug molecules increase in the aqueous medium because of the hydrogen bonds. It means that the solubility of these drugs in an aqueous medium may be enhanced with the increase of polarity. The dipole moments of the molecules (1-9) are around 3.04–26.10 Debye in the aqueous

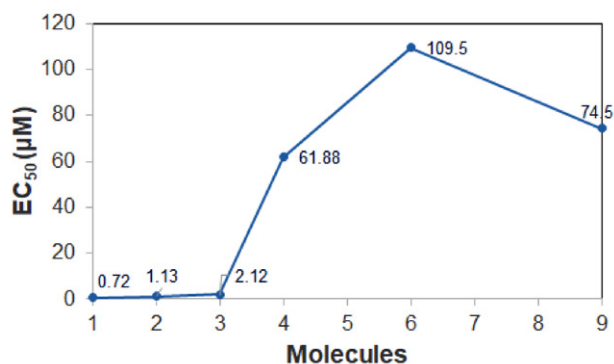


Figure 3. In vitro half-maximal effective concentration ( $EC_{50}$ ) of drugs

**Table 1.** Global descriptors: hardness ( $\eta$ ), chemical potential ( $\mu$ ), electrophilic index ( $\omega$ ), softness ( $S$ ), frontier orbitals energies ( $E_{\text{HOMO}}$ ,  $E_{\text{LUMO}}$ ) and dipole moments ( $D$ ) of drugs, (values in italic apply to the gas phase)

	$E_{\text{HOMO}}$ eV	$E_{\text{LUMO}}$ eV	$\Delta E$ eV	$\eta$ eV	$S$ eV	$\mu$ eV	$\omega$ eV	$D$ Debye
1	-6.05	-1.71	4.34	2.17	0.23	-3.88	3.46	9.29
	-5.99	-1.59	4.40	2.20	0.23	-3.62	3.27	6.90
2	-5.94	-1.65	4.29	2.15	0.23	-3.80	3.36	9.26
	-5.81	-1.44	4.37	2.18	0.23	-3.62	3.01	6.99
3	-3.81	-2.00	1.81	0.91	0.55	-2.91	4.66	26.10
	-3.07	-0.82	2.25	1.12	0.44	-1.94	1.68	14.58
4	-7.31	-2.73	4.58	2.29	0.22	-5.02	5.50	4.31
	-7.37	-2.85	4.52	2.26	0.22	-5.11	5.77	3.24
5	-6.35	-1.20	5.15	2.57	0.19	-3.77	2.77	8.63
	-6.37	-1.31	5.05	2.53	0.20	-3.84	2.92	6.70
6	-7.75	-1.51	6.25	3.12	0.16	-4.63	3.43	3.04
	-7.45	-1.44	6.03	3.02	0.17	-4.46	3.30	2.08
7	-6.94	-1.41	5.53	2.77	0.18	-4.18	3.15	4.19
	-6.83	-1.64	5.19	2.60	0.19	-4.23	3.45	5.20
8	-6.66	-1.54	5.12	2.56	0.20	-4.10	3.29	6.41
	-6.71	-1.66	5.05	2.53	0.20	-4.19	3.47	5.20
9	-7.14	-1.13	6.01	3.00	0.17	-4.13	2.85	8.71
	-7.15	-0.94	6.22	3.11	0.16	-4.04	2.63	5.58

medium and 2.08–14.58 Debye in the gas phase. Among the calculated drug molecules the largest dipole moment value is found for molecule 3. This large dipole moment value can allow high polarity in some regions of the drug

and hydrophilic interactions in the solvent that increases its activity. Dipole moments **1,2,5** and **9** are greater than those of **4,6,7** and **8**. Hence, **1,2,5** and **9** are more polarized and may show more hydrophilic properties. This

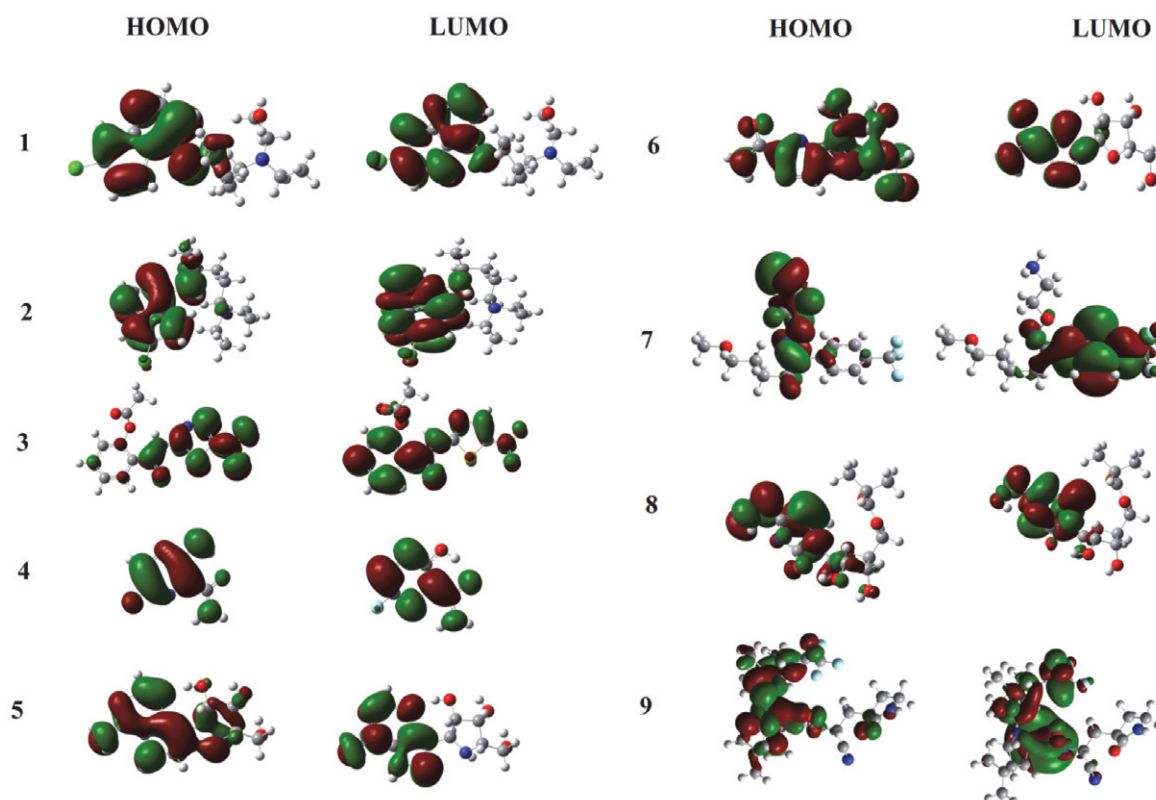


**Figure 4** Frontier molecular orbitals of drug molecules

feature can turn these drugs into active molecules in an aqueous media.

### 3. 2. Frontier Molecular Orbitals Analysis

Frontier Molecular Orbitals (FMOs) are important parameters used to understand the distribution of electrophilic regions of molecules and their chemical interaction parts with other molecules.<sup>41,42</sup> The chemical reactivity of a molecule can be determined by using the energy gap value of frontier orbitals ( $\Delta E$ ). A small energy gap indicates a more reactive molecule. As seen in Table 1, molecule 3 has the smallest  $\Delta E$  values in both phases. Thus, this molecule is the most reactive one. The electron-withdrawing  $-\text{NO}_2$  group in 3, can disrupt the distribution of the  $\pi$  electron

system, which leads to deteriorated molecular backbone conjugation, thus decreasing the chemical stability of the molecule. Molecule 6 is the least reactive molecule with the highest energy gap value of 6.25 eV.

The FMOs of all studied drug molecules are given in Figure 4. As can be seen from the Figure, the HOMO orbitals are  $\pi$ -bonding molecular orbitals. HOMO and LUMO orbitals are mainly distributed on the quinoline ring of the molecule for 1 and 2. While HOMO of molecule 3 is distributed on the functionalized part of the thiazolidine ring, LUMO is distorted all through the molecule. The HOMO orbital is  $\pi$  bonding type and the LUMO orbital is  $\pi^*$  antibonding type for molecule 4 and they are mainly distributed all through the molecule. For molecules 5 and 6, the electron distribution of the HOMO or-

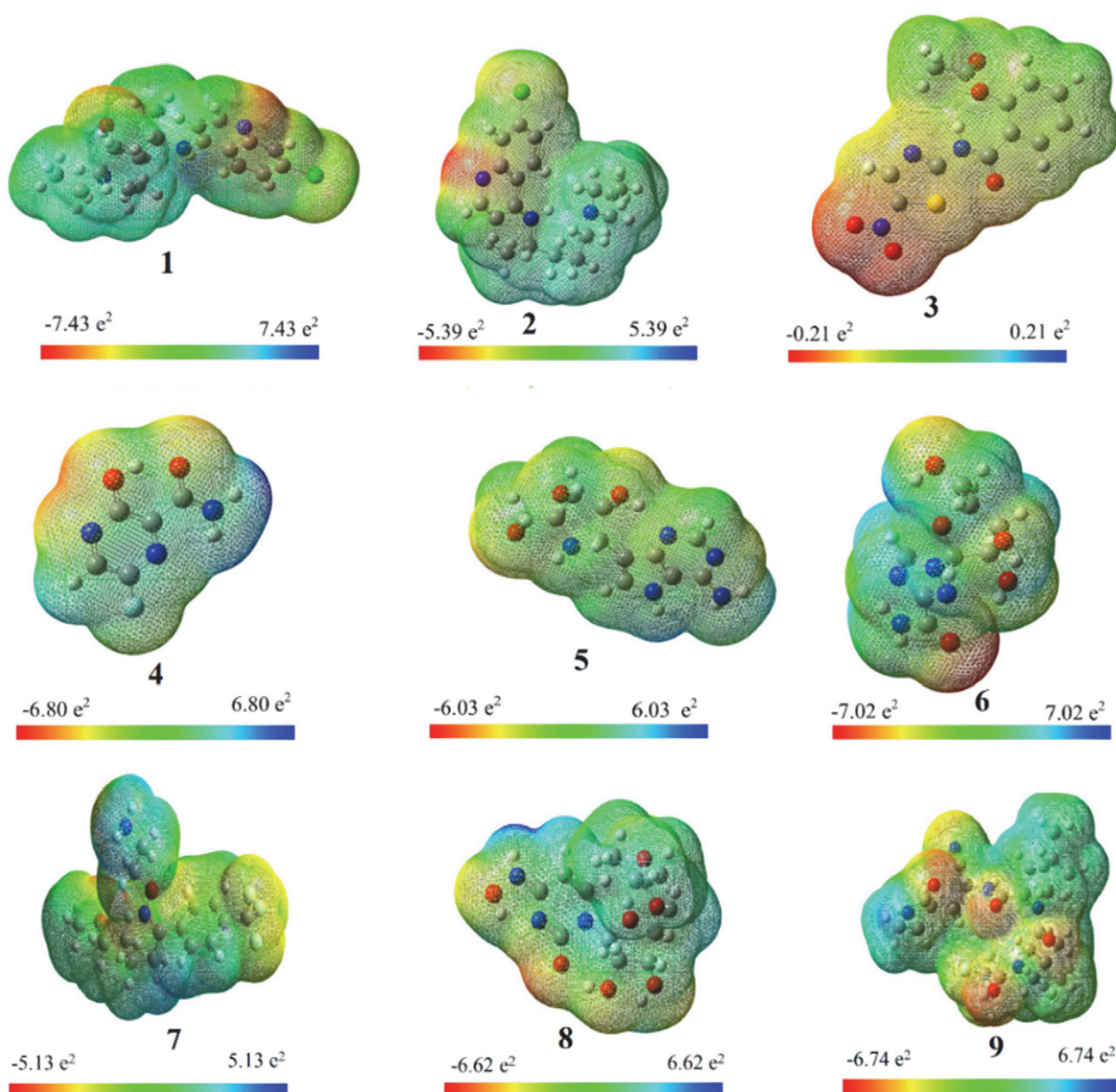


Figure 5. Molecular Electrostatic Potential Plots of molecules



bital is delocalized almost throughout the molecule, while the LUMO orbital is found in its two fused aromatic rings in molecule **5** and at the 1,2,4-triazole portion in molecule **6**. HOMO is distributed on the etheric part and LUMO is on the benzene trifluoro acetamide part of molecule **7**. The HOMO and LUMO orbitals of the antiviral prodrug **8** are distributed over the heterocyclic rings of the molecule. The boundary orbitals electron cloud is mainly on the pyrrolidine ring and isobutyl portion of molecule **9**. In the study of Macchiagodena et.al., these parts of molecule **9** were found to approach to the SARS-COV-2 6LU7 protein.<sup>22</sup> Thus, according to FMOs, these sites are predicted as the active sites for the probable chemical interactions.

### 3. 3 MEP Surfaces

Molecular Electrostatic Potential (MEP) surfaces are the three-dimensional visualization of the charge distribution of atoms on a molecule.<sup>43</sup> Such surfaces supply information about electronic distribution of molecules, their nucleophilic and electrophilic attack parts, and formation of possible hydrogen bonds.<sup>44</sup> In these surfaces, the red color shows the more negative potential of the molecule whereas the blue color shows the more positive potential. The green color represents the neutral part of the molecule with almost zero charge.<sup>45</sup>

MEP surfaces of the molecules **1–9** are shown in Figure 5. For all molecules, at least one hydrogen bonding region is detected. Thus, hydrogen bonding stabilizations decrease the energy values of the molecules with the aqueous media.

As seen in Figure 5, the electron distributions of **1** and **2** are almost the same, but they differ in the number of hydroxyl groups. Since molecule **1** has more hydroxyl groups, its negative regions are dominant. Thereby, it is more effective against SARS-COV-2 than that of molecule **2**.<sup>11,19,30</sup> Molecule **3** has more red areas than the others, and they are mainly concentrated on the  $-\text{NO}_2$  group, which removes the electron density from the molecule's  $\pi$  system and makes the molecule less electrophilic. The electrophilic region of molecule **4** is on the hydroxyl group while the hydrogen atoms of the amino group are the nucleophilic part. But the fluorine atom in **4** has no effect on the electronic behavior of the pyrazine ring. In molecule **5**, the ribose ring has a higher electron density due to the electron-donating hydroxyl groups, while the electron-positive areas are hydrogens bonding to the nitrogen atom. In molecule **6**, the most negative region belongs to the oxygen atom of the carbonyl group, and the positive potential region belongs to the hydrogen atoms. For molecule **7**, the electrophilic regions are etheric oxygen and fluorine atoms. In molecule **8**, the blue color distribution is in the hydrogen atoms of the amine group. Due to the electron withdrawal properties of fluorine atoms, this region in molecule **9** can cause electron localization.

### 3. 4. Thermodynamic Properties

The solvation-free energies of the studied drug molecules are calculated using their Gibbs free energy change values between the solvent phase and the gas phase (Figure 6). As depicted from the figure, all the molecules' solvation-free energies are negative, indicating their spontaneous solubility in water. This result is in accordance with the increased dipole moment values in the aqueous medium. The solvation energies of the molecules vary between  $(-6.83) - (-53.99)$  kcal mol<sup>-1</sup>. As noticed in Figure 6, the solvation free energies of all molecules, are quite similar except of molecule **3**. Since molecule **3** has less electronegative atoms in its structure, it differs from the others. Molecules **1** and **2**, **4**, and **7** are structurally very similar. Therefore their solvation-free energies are also close to each other, for **1** and **2** they are  $-8.66$ ,  $-6.83$  kcal mol<sup>-1</sup> and for **4** and **7**  $-8.15$ ,  $-9.14$  kcal mol<sup>-1</sup> respectively. For molecules **5**, **6**, **8**, **9** solvation-free energies are found as  $-14.48$ ,  $-13.81$ ,  $-16.31$  and  $-18.72$  kcal mol<sup>-1</sup>, respectively.

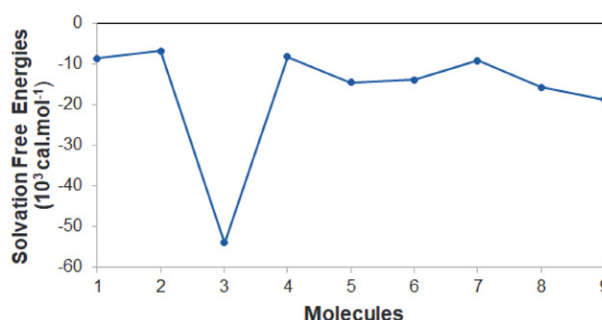


Figure 6. Solvation-free energies of drugs

Thermodynamic parameters of the studied drug molecules have been calculated at 298.15 K. The calculated total energies (E), enthalpy ( $\Delta H$ ), entropy (S), Gibbs free energy ( $\Delta G$ ) with ZPE correction for water and gas phases are listed in Table 2. As can be seen from the table, the molecules with the lowest energies are **9**, **3**, and **1**, while the molecules with the highest energies are **4**, **6**, and **5**. The most thermodynamically stable molecules are found as **9**, **3**, and **1** due to their enthalpy and Gibbs free energy values (Table 2). The thermal stabilities of all molecules are higher in the aqueous medium. Since the thermal stability of drug molecules is necessary for drug durability, it can be inferred from the results that all molecules are more stable in an aqueous medium.<sup>46</sup>

### 3. 5. The Effect of Electronic Structure on Biological Effectiveness

A drug binding efficiency to an active point of an enzyme or a protein is related to its electronic structure.<sup>47</sup> Therefore, the electronic properties of drugs are important

**Table 2.** Calculated energies and thermodynamic parameters of drugs. ZPE, E,  $\Delta H$ ,  $\Delta G$  (in cal.mol<sup>-1</sup>), S (in cal mol<sup>-1</sup> K<sup>-1</sup>)

	1	2	3	4	5	6	7	8	9
<b>Aqueous medium</b>									
ZPE .10 <sup>6</sup>	0.26	0.26	0.13	0.06	0.18	0.14	0.22	0.21	0.34
E .10 <sup>6</sup>	-879.21	-832.00	-879.41	-381.27	-582.10	-569.30	-717.64	-751.54	-1110.63
$\Delta H$ .10 <sup>6</sup>	-879.20	-831.99	-879.40	-381.26	-582.09	-569.30	-717.63	-751.52	-1110.61
$\Delta G$ .10 <sup>6</sup>	-879.25	-832.03	-879.44	-381.30	-582.13	-569.33	-717.68	-751.57	-1110.67
S	163.53	160.47	146.88	92.70	132.54	127.72	176.80	165.37	220.36
<b>Gas</b>									
ZPE .10 <sup>6</sup>	0.26	0.26	0.13	0.06	0.18	0.14	0.22	0.21	0.35
E .10 <sup>6</sup>	-879.21	-831.99	-879.32	-381.26	-582.09	-569.29	-717.64	-751.52	-1110.61
$\Delta H$ .10 <sup>6</sup>	-879.19	-831.98	-879.31	-381.26	-582.08	-569.28	-717.62	-751.50	-1110.58
$\Delta G$ .10 <sup>6</sup>	-879.21	-832.03	-879.35	-381.28	-582.12	-569.32	-717.68	-751.55	-1110.65
S	169.13	159.39	148.30	92.02	128.92	130.39	177.00	162.18	232.45

for predicting their biological activity. In Figure 3, the in vitro half-maximal effective concentration (EC<sub>50</sub>) values of molecules are shown for the studied molecules except for **5**, **7**, and **8**.<sup>7,12,48</sup>

According to the results of experimental biological studies, it was understood that quinoline derivative drugs **1** and **2** in Vero E6 were more active for the SARS-COV-2 virus.<sup>7</sup> Because the unpaired electrons of the nitrogen atom in the quinoline ring and the availability of suitable sites for the hydrogen bond affect the activities of these types of drugs positively.<sup>49,50</sup> The reason why the EC<sub>50</sub> value of **1** is less than that of **2** may be due to the hydrogen bonding of the hydroxyl group in its structure. Molecule **3** may be an important molecule to treat COVID-19 due to the presence of sulfur atom in its structure, which may change the amino acid residue of the target compound by disulfide bond formation. In addition, the sulfur atom may be important for the formation of a hydrogen bond.<sup>51</sup> However, the electron-withdrawing feature of the -NO<sub>2</sub> group in the structure of **3** reduces the electron conjugation, resulting in a higher EC<sub>50</sub> value than for **1** and **2**. The lone pair electrons, halogen atom, and electron conjugation of the heterocyclic ring make molecule **4** more effective than molecule **6** against COVID-19 disease. It is known that halogen atoms increase the electron density of the rings for  $\pi$ -stacking interactions as well as halogen bonding.<sup>44</sup> It is understood from the results of the Saul et al. study<sup>8</sup> that **1** and **2** are more effective against COVID-19 than **4**. The decreased electronegativity of the halogen atom in drugs **1** and **2** can increase the electron density of the quinoline ring, which may lead to the interaction of these molecules with the target site of SARS-COV-2. Although molecule **6** has a lower conjugate electron cloud in its structure, its highest hydrogen bonding ability causes an easier to attach to the target site in comparison to the other molecules. The trifluoroacetamide moiety of molecule **9** is the potential site for hydrogen bond interactions with the amino acid of the spike protein. The halogen-type hydrogen bonding ability and electron-withdrawing substituents are key fac-

tors governing the biological effectiveness. Based on all these results, we can say that the structural modification of drugs has a significant effect on the electronic structure of drugs. Therefore, a complete characterization of the electronic properties of drugs is important to understand their biological activities.

## 4. Conclusions

The fight against COVID-19 can be achieved with both vaccine prevention and drug treatment. Electronic behavior of drugs may point out their effectiveness against genetic variants of SARS-COV-2. In this study, electronic and thermodynamic properties, and quantum chemical descriptors of nine drugs are calculated. The results can be summarized as follows;

- Drug molecules containing electronegative atoms such as -OH and halogen atoms have higher hardness. Molecule **6** (ribavirin) is found as the hardest molecule.
- Electrophilic character of drug molecules may increase their interaction with SARS-COV-2.
- Paxlovid (**9**), nitazoxanide (**3**), and hydroxychloroquine (**1**) are found as the most thermodynamically stable drug molecules. All the studied molecules are thermodynamically more stable in an aqueous medium.
- The trifluoroacetamide in molecule **9** may be the appropriate site for binding to the amino acid of the spike protein.
- Structures of drugs have a significant effect on their electronic properties. Accordingly, their biological activities may also differ.
- The frontier molecular orbitals and MEP surfaces allow the prediction of reactive and possible interaction sites of drug molecules. Nucleophilic attacks may take place to the quinoline ring, two fused heterocyclic ring of **1** and **2**, 1,2,4-triazole



parts of **6**, and pyrrolidine ring, isobutyl part of the **9**.

In summary, quantum chemical descriptors and electronic properties can be used as suitable parameters to evaluate the efficacy of drugs to treat COVID-19.

## Acknowledgements

The authors express their thanks to Yildiz Technical University. Project No. 2012-01-02-KAP02

## 5. References

1. A. Hazafa, F. Abbas, S. Bano, M. Farman, N. Jahan, M. Mumtaz, H. Naeem, M. Naeem, S. Sadiqa, I. ul-Haq, K. ur-Rahman, *Drug Metab Rev*, **2020**, 52 (3), 408–424. DOI:10.1080/03602532.2020.1770782
2. D. L. McKee, S. Laufer, C. Naujokat, U. Stange, A. Sternberg, *Pharmacol Res*, **2020**, 157, 104859–104868. DOI:10.1016/j.phrs.2020.104859
3. V. V. Kouznetsov, *Eur J Med Chem*, **2020** 203 (112647), 1–10.
4. C. Ma, Y. Chen, Y. Hu, B. Hurst, M.T. Marty, M.D. Sacco, T. Szeto, B. Tarbet, J. A. Townsend, J. Wang, X. Zhang, *Cell Res*, **2020**, 30, 678–692. DOI:10.1038/s41422-020-0356-z
5. J. Shio-Shin, L. Ping-Ing, H. Po-Ren, *J Microbiol Immunol Infect*, **2020**, 53, 436–443.
6. WHO (2021), Official Updates – Coronavirus Disease 2020 , Coronavirus disease (COVID-19) pandemic website, <https://www.who.int/emergencies/diseases/novel-coronavirus-2019> accessed time 31.01.2022
7. J. Zhe, L. Hai-Bo, L. Jing-Yi, J. Lu, F. Rang, J. Zi-Li, *Eur J Pharmacol*, **2020**, 883, 173326–173333.
8. S. Saul, S. Einav, *ACS Infect. Dis* **2020**, 6, 2304–2318. DOI:10.1021/acsinfecdis.0c00343
9. P. M. Mitrasinovic, *Acta Chim. Slov.* 2020, 67, 949–956 DOI:10.17344/acsi.2020.6009
10. B. Furlani, K. Kouter, D. Rozman, A. V. Paska, *Acta Chim. Slov.* 2021, 68, 268–278 DOI:10.17344/acsi.2021.6691
11. P. Chibber, A. S. Haq, I. Ahmed, N. I. Andrabi, G. Singh, *Eur J Pharmacol*, **2020**, 883, 173372–173387. DOI:10.1016/j.ejphar.2020.173372
12. M. Wang, R. Cao, Z. Hu, J. Liu, Z. Shi, G. Xiao, M. Xu, X. Yang, L. Zhang, W. Zhong, *Cell Res*, **2020**, 30, 269–271. DOI:10.1038/s41422-020-0282-0
13. E. A. Coomes, H. Haghbayan, *J Antimicrob Chemother*, **2020**, 75, 2013–2014. DOI:10.1093/jac/dkaa171
14. H. Koba, K. Kasahara, H. Kimura, T. Kaneda, T. Ueda, T. Yoneda, *Clin Case Rep* **2020**, 00, 1–6.
15. WHO Coronavirus disease (COVID-19): Vaccines <https://ourworldindata.org/covid-vaccinations> (accessed time 27.12.2021)
16. S. G. Novir, M.R. Aram, *Chem Phys Lett*, **2020**, 757 (137869), 1–10. DOI:10.1016/j.cplett.2020.137869
17. N. Al-Masoudi, R.S. Elias, B. Saeed, *Biointerface Res Appl Chem*, **2020**, 10 (5), 6444–6459 DOI:10.33263/BRIAC105.64446459
18. L. I. Hage-Melim, M.P. Barcelosb, L.C. Correia, H.B. de Lima, N. K. S. de Oliveiraa, C. H. T. de Paula da Silva, L. B. Federico, V. C. C. Franciscoa, I. A. G. Francischini, S. Q. Gomes, *Life Sci*, **2020**, 256 (117963), 1–13. DOI:10.1016/j.lfs.2020.117963
19. D. Gentile, V. Fucchi, P.M. Furneri, A. Rescifica, *Int J Mol Sci*, **2020**, 21 (5856), 2–16. DOI:10.3390/ijms21165856
20. B. Ahmad, M. Batool, Q. Ain, M. S.Kim, S. Choi, Exploring the Binding Mechanism of PF-07321332 SARS-CoV-2-Protease Inhibitor through Molecular Dynamics and Binding Free Energy Simulations *Int. J. Mol. Sci.*, **2021**, 22, 2–13. DOI:10.3390/ijms22179124
21. M. Pavan, G. Bolcato, D. Bassani, M. Sturlese, *J Enzyme Inhib*, **2021**, 36 (1), 1646–1650. DOI:10.1080/14756366.2021.1954919
22. M. Macchiagodena, M. Pagliai, P. Procacci, *J. Mol. Graph.* **2022**, 110, 108042–108051. DOI:10.1016/j.jmkgm.2021.108042
23. M. Jukič, K. Kores, D. Janežič, U. Bren, *Front. Chem.* **2021**, 9, 757826. DOI:10.3389/fchem.2021.757826
24. M. Jukic, D. Janežic, U. Bren, *Int. J. Mol. Sci.* **2021**, 22, 11143. DOI:10.3390/ijms222011143
25. M. Jukic, D. Janežic, U. Bren, *Molecules* **2020**, 25, 5808. DOI:10.3390/molecules25245808
26. M. Jukic, B. Škrlj, G. Tomšič, S. Pleško, C. Podlipnik, U. Bren, *Molecules*, 2021, 26, 3003. DOI:10.3390/molecules26103003
27. A. V. Sharov, T. M. Burkhanova, T. T. Tok, M. G. Babashkina, D. A. Safin, *Int. J. Mol. Sci.* 2022, 23, 1508. DOI:10.3390/ijms23031508
28. T. da S. Arouche, A. F. Reis, A. Y. Martins, J. F. S. Costa, R. N. C. Junior, A. M. J. C. Neto, J. Nanosci. *Nanotechnol.*, 2020, 20, 7311–7323. DOI:10.1166/jnn.2020.18955
29. Ö. Alver, C. Parlak, P. Ramasami, Y. Umar, *Main Group Met Chem*, **2019**, 42, 143–149. DOI:10.1515/mgmc-2019-0016
30. G. W. Ejub, C. Fonkem, J. M. B. Ndjaka, L. P. Ndukum, T. Nya, Y. Tadjouteu Assatse, R. A. Yossa Kamsi, *Heliyon*, **2020**, 6 (04647), 1–11. DOI:10.1016/j.heliyon.2020.e04647
31. T. A. Altalhi, K. Alswat, W. F. Alsanie, A. Aldalbahi, H. S. El-Sheshtawy, M. M. Ibrahim, *J Mol Struct*, **2021**, 1228, 129459–129468. DOI:10.1016/j.molstruc.2020.129459
32. M. J. Frisch, C. Adamo, A.J. Austin, et al. **2009** Gaussian 09 Revision B.01. Gaussian Inc., Wallingford
33. L. Rhyman, H. H. Abdallah, Y. S. Choong, P. Kharkar, C. Parlak, P. Ramasami, M. Tursun, *Phys Sci Rev*, **2018**, 20170198, 1–10.
34. R. Dennington, T. Keith, J. Millam GaussView, Version 5, Semichem Inc., Shawnee Mission, KS, **2009**
35. J. Foresman, E. Frish Exploring chemistry. **1996** Gaussian Inc, Pittsburg
36. P. Geerlings, F. De Proft, W. Langenaeker, *Chem Rev*, **2003**, 103, 1793–1874. DOI:10.1021/cr990029p
37. L. R. Domingo, P. Perez, *Org Biomol Chem*, **2011**, 9, 7168–7175. DOI:10.1039/c1ob05856h
38. C. Soriano-Correa, C. Barrientos-Salcedo, R. O. Esquivel, A. Raya, *Chem Phys* **2014**, 438, 48–59. DOI:10.1016/j.chemphys.2014.04.012
39. S. Ray, A. S. Murkin, *Biochemistry*, **2019**, 58, 5234–5244.

- DOI:10.1021/acs.biochem.9b00293
40. L. Chih-Chia, C. Mei-Yu, L. Wan-Shin, C. Yuh-Lih, J. Chin Med Assoc, **2020**, 83 (6), 534–536.
  41. G. W. Ejuh, J. M. B. Ndjaka, Y. T. Assatse, C. Fonkem, R. A. Y. Kamsi, P. L. Ndukum, F. T. Nya, Opt Quantum Electron, **2020**, 52, 498, 1–22. DOI:10.1007/s11082-020-02617-w
  42. L. H. M. Huziar, N. J. Olvera-Maturana, C. H. Rios-Reyes, J. Robles, J. A. Rodriguez, Open Chem, **2015**, 13, 52–60.
  43. N. Sepay, U. C. Halder, A. A. Hoque, R. Mondal, M. Muddasir, N. Sepay, Struct Chem, **2020**, 31, 1831–1840. DOI:10.1007/s11224-020-01537-5
  44. A. Sagaama, S. Antonia Brandan, T. B. Issa, N. Issaoui, Heliyon, **2020**, 6 (e04640) 1–29. DOI:10.1016/j.heliyon.2020.e04640
  45. J. S. Al- Otaibi, Spectrochim Acta A, **2020**, 235 (118333), 1–5. DOI:10.1016/j.saa.2020.118333
  46. H. Nikoofard, F. Faridbod, M. Sargolzaei, Acta Chim Slov, **2017**, 64, 842–848. DOI:10.17344/acs.2017.3357
  47. S. M. LaPointe, D. F. A. Weaver, Curr Comput Aided Drug Des, **2007**, 3 (4), 290–296. DOI:10.2174/157340907782799390
  48. J. Xu, H. Li, P. Y. Shi, J. Zhou, Broad Spectrum Antiviral Agent Niclosamide and Its Therapeutic Potential, ACS Infect Dis, **2020**, 6, 909–915. DOI:10.1021/acsinfecdis.0c00052
  49. A. Ghaleb, A. Aouidate, M. Aarjane, H. Anane, H. B. El Ayouchia S. E. Stiriba, J Biomol Struct Dyn, **2020**, 17, 1–11.
  50. M. Hagar, H. A. Ahmed, G. Aljohani, O. A. Alhaddad, Int J Mol Sci, **2020**, 21 (3922), 1–13. DOI:10.3390/ijms21113922
  51. S. Sheikh, K. H. Gowd, A. K. K. Reddy, J Sulfur Chem, **2020**, 42 (1), 1–12. DOI:10.1080/17415993.2020.1817457

## Povzetek

Te dni se svet sooča z grožnjo pandemije koronavirusne bolezni 2019 (COVID-19). Čeprav je bilo najdeno cepivo za boj proti tej pandemični bolezni, je nujno, da čim prej poiščemo tudi zdravila za učinkovito metodo njenega zdravljenja. V tej študiji smo raziskali elektronske in termodinamične lastnosti in mejne molekularne orbitale (FMO) devetih različnih covidnih zdravil s teorijo gostotnega funkcionala (DFT) in z analizo molekularnega elektrostatskega potenciala (EMP). Poleg tega smo preučili povezavo med elektronskimi strukturami teh zdravil in njihovo biološko učinkovitost. Vse parametre smo izračunali na ravni B3LYP/6-311+g(d,p). Vpliv topila smo ovrednotili z uporabo modela polarizirajočega kontinuuma (CPCM) kot modela solvatacije. Opazili smo, da so za razumevanje učinkovitosti teh zdravil pri bolezni COVID-19 pomembni elektrofilni indeksi. Paxlovid, hidroksikinon in nitazoksanid so se izkazali za najbolj termodinamično stabilne molekule. Termodinamični parametri so tudi pokazali, da so bila ta zdravila stabilnejša v vodnih medijih. Ugotovili smo, da so globalni deskriptorji in reaktivnost teh zdravil povezani. Molekula nitazoksanida je imela največji dipolni moment. Visoki dipolni momenti zdravil lahko povzročijo hidrofilne interakcije, ki povečujejo njihovo učinkovitost v vodni raztopini.



Except when otherwise noted, articles in this journal are published under the terms and conditions of the Creative Commons Attribution 4.0 International License

Scientific paper

# Industrial Wastewater as a Source of External Organic Carbon for the Biological Nutrient Removal

Bibiána Kožárová\*, Ronald Zakhar, Zuzana Imreová, Hana Hanuljaková,  
Ines Karlovská and Miloslav Drtil

Department of Environmental Engineering, Faculty of Chemical and Food Technology, Slovak University of Technology,  
Radlinského 9, 812 37 Bratislava, Slovak Republic

\* Corresponding author: E-mail: b.kozarova@gmail.com,  
+421907 478 032

Received: 04-10-2022

## Abstract

Addition of external organic carbon source for denitrification is generally used in wastewater treatment plants (WWTPs) to intensify nitrogen removal processes. The aim of the laboratory survey was to measure the composition of concentrated industrial wastewater, determine the possibilities of its use as an external denitrification substrate, and assess its overall impact on WWTP. The obtained results demonstrate that the analysed industrial wastewater is biodegradable, and can be used as a denitrification substrate without special adaptation of biomass. The denitrification rates with tested wastewater were in the range of 1.6 to 1.9 mg<sub>N</sub>/g-h. Negative influence of long-term dosing of industrial wastewater on activated sludge were not confirmed. The effect of imported wastewater on WWTP must be assessed comprehensively, including the impact of heavy metals from wastewater on the sludge quality. The instructions on how to calculate this balance are provided in the article.

**Keywords:** Biodegradability of industrial wastewater, biological wastewater treatment, heavy metals in sludge, denitrification rate, semicontinuous bioreactors

## 1. Introduction

Over the years, considerable effort has been made to advance and optimize the technologies for effective biological nitrogen removal at wastewater treatment plants (WWTPs).<sup>1,2</sup> Heterotrophic denitrification is an efficient process in which, through microbiological activity, a reduction of nitrates and nitrites to nitrogen gas occurs.<sup>3</sup> It has a unique place in the biological removal of nitrogen from wastewater. This is because during the denitrification, nitrogen passes from water into the air. Anoxic zones without dissolved oxygen, in which the redox potential values are in the range of approximately –50 mV to 50 mV for calomel electrode and approximately 150 mV to 250 mV for standard hydrogen electrode, are necessary for this process.<sup>4</sup> Denitrification is most often used in wastewater treatment, where the sources of electrons for nitrogen reduction are organic compounds.<sup>5</sup> The process takes place even in the absence of exogenous organic carbon (C<sub>org</sub>) but its rate is significantly lower. In this case, bacteria use their internal organic compounds as a source of electrons (endogenous process).

In many WWTPs, the absence of readily biodegradable organic substrate in the wastewater is a limiting factor for successful removal of higher nitrogen concentrations. This occurs mainly due to the long sewerage networks in which organic compounds are anaerobically decomposed, while nitrogen remains in the wastewater. Groundwater leakage into the sewer system<sup>6</sup> can also be a contributor of excess nitrogen in the wastewater, although this problem is not commonly reported. In the groundwater of the Slovak Republic, there is NO<sub>3</sub><sup>–</sup> usually present at dozens mg/l.<sup>7</sup> The average groundwater infiltration into the damaged pipes is 36.85% of the total wastewater volume.<sup>8</sup> If the leakage of the groundwater into sewerage is too high, then this nitrogen source is certainly interesting. Increased nitrogen input into wastewater can be also a consequence of the changes in eating habits of a population. While in the Slovak standard<sup>9</sup> nitrogen production is reported at the level of 11 g/d per capita, Pitter<sup>4</sup> already stated the production at 12 g/d per capita and it is possible to find in the literature the production up to 14 g/d per capita.<sup>10</sup>

In the case of insufficient concentrations of C<sub>org</sub> in the wastewater, or too short retention time of wastewater

under anoxic conditions at WWTP, a possible solution is the dosing of suitable external organic substrate into the denitrification reactor (to increase the denitrification rate).<sup>11</sup>

Composition of organic compounds has a strong effect on the presence of denitrifying microorganisms and thus on denitrification efficiency. Available external sources of  $C_{org}$  are alcohols, especially methanol (cost-effective, although it requires some adaptation of biomass and increased demands on operational safety because it is toxic and explosive) or ethanol (does not require such adaptation of biomass but is more expensive).<sup>4</sup> Organic acids (mainly acetic acid) also require less problematic adaptation because the biomass at the WWTP recognizes them (they are formed by acidogenesis and acetogenesis in the sewerage system), but they are also more expensive. Another option is saccharides (e.g., glucose, amyloid, sucrose).<sup>12</sup> The use of alternative  $C_{org}$  sources such as concentrated wastewater from industries are an interesting option.<sup>13,14</sup> In any case, these wastewaters must be treated, and therefore their import to WWTPs, where they increase the efficiency of denitrification, will bring double benefits. The usability of wastewater from the agro-food industry (e.g., milk bottling industries, potato processing industries, wastewater from winery industries) is commonly reported<sup>15</sup>, however other industries also produce external organic substrates.

The specific denitrification rates reported in  $mg_N/g\cdot h$  vary considerably – mostly from tenths up to 20  $mg_N/g\cdot h$  (referred to g of dry solids).<sup>12,16–22</sup> For activated sludge adapted to sewage, acetate is reported as the substrate with the highest denitrification rates. Denitrification rates are affected by test conditions. The optimal reaction temperatures were 15–35 °C in which complete denitrification was achieved and nitrite accumulation was observed at 10 °C indicating the incomplete denitrification at low temperature.<sup>23</sup> Temperature change from 10 °C to 20 °C exerted a more significant positive effect on both the specific denitrification and carbon consumption rates than a further temperature increase from 20 °C to 30 °C.<sup>24</sup> The denitrification rate is also positively related to the pH value. At lower pH values, the nitrogen oxidoreductases were progressively inhibited in such way, that the overall rate of denitrification decreased and  $N_2O$  produced increased.<sup>25</sup> The process was stable in the neutral pH range and the highest denitrification rates were obtained at the pH values from 7.1 till 7.8.<sup>26</sup> In Cao et al.<sup>27</sup> maximum denitrification rates were measured at pH of 6.6–7.5 with inhibited denitrification at pH increased to 8.5 and 9.2.

The values of the rates also depend on the composition of the biomass during the tests, adaptation, and sludge retention time (SRT) (the higher the SRT values, the higher the increase in volumetric rates, but the specific rates related to the unit amount of biomass may also decrease).<sup>11</sup> If denitrification rates are measured in batch kinetic tests, then the test conditions are different from those in the activated sludge reactor. In the batch test, there is

a substrate concentration gradient (i.e., at the beginning of the test there are high substrate concentrations, and they only gradually decrease). According to the so-called Monod kinetics, the substrate removal rate decreases with decreasing substrate concentration.<sup>28,29</sup> When assessing denitrification rates, it is also necessary to consider whether the organic substrate is single- or multicomponent. According to Henze et al.<sup>29</sup> and Phillips et al.<sup>30</sup>, the denitrification rates achieved in batch kinetic tests are divided into 3 parts. In the first phase of the tests, the rate is the highest because an easily degradable organic substrate enters the denitrification; in the second phase of the test, the rate is slower because high molecular weight and insoluble organic compounds requiring hydrolysis are denitrified; and finally in the third phase, the rate is the lowest because only endogenous denitrification takes place. The rates calculated according to the recommendations of the technical standards<sup>9,11</sup> are on the level of 0.5–3  $mg_N/g\cdot h$ . Such rates are observed also at real WWTPs<sup>31</sup>. According to Henze et al.<sup>5</sup> the denitrification rates valid for temperatures 10–20 °C are 0.1–0.2  $mg_N/g\cdot h$  for endogenous denitrification, 0.6–2  $mg_N/g\cdot h$  for raw wastewater, and 1–9  $mg_N/g\cdot h$  for methanol and acetate. In summary, denitrification rates measured with a given substrate above 1  $mg_N/g\cdot h$  can be considered a positive result.

Organic matter is an essential factor for microbial growth and development. In addition to the biodegradability, price and storage options<sup>12</sup>, choice of external organic substrate is influenced also by the following factors: the highest possible chemical oxygen demand ( $COD_{Cr}$ ) and specific  $COD_{Cr}$  expressed in  $mg\ COD_{Cr}/mg$  substrate; efficiency at which the bacteria are able to use it; toxicity of intermediates or substrate itself; composition stability (with the best possible homogeneity)<sup>4,5</sup>. The next factors are the lowest possible portion of nitrogen in the substrate; the highest possible portion of compounds in the substrate entering the denitrification reaction; low portion of compounds entering the assimilation reaction associated with the growth of new biomass; and the lowest possible ratio of high molecular weight and undissolved compounds.<sup>4,5,11</sup>

The objectives of this study were to analytically determine the content of components present in industrial wastewater with a high COD concentration, monitor its impact on the biological stage of WWTPs, and to present the possibilities of using concentrated industrial wastewater as an external source for the denitrification (e.g., at municipal WWTPs with the lack of denitrification capacity, where the accelerating of denitrification could help to achieve the legal requirements on treated wastewater and to reduce the payment of fees for discharged nitrogen).<sup>32,33</sup>

## 2. Materials and Methods

The analysed parameters, their abbreviations, respective symbols, and the method of determination are

shown in Table 1. All analyses were performed according to standard procedures.<sup>34</sup>

Activated sludge for denitrification and respirometry tests was cultivated in three long-term semicontinuous lab-scale bioreactors<sup>35</sup> (designated  $R_1$ ,  $R_2$ , and  $R_3$ ) with a total volume of 1 litre placed on magnetic stirrers. Mixing and aeration of the activated sludge in models  $R_1$ ,  $R_2$ , and  $R_3$  were set up in the following way: 5 hours after the addition of the substrate mixing (i.e., denitrification) followed by 17 hours aeration (i.e., nitrification and oxidation of residual organic compounds with  $O_2$ ), and 2 hours sedimentation and draw off effluent and dosing of the substrate. The volumetric load expressed in kg  $COD_{Cr}$  was maintained at  $0.88 \text{ kg/m}^3 \cdot \text{d}$ . The hydraulic retention time was 1.8 days and the set SRT was 15 days. Reactors were operated at the laboratory temperature  $27\text{--}30^\circ\text{C}$  (experiments performed during summer months). Such temperatures were higher than typical municipal wastewater temperatures in Slovakia (approx.  $10^\circ\text{C}$  during winter and  $20\text{--}25^\circ\text{C}$  during summer<sup>8</sup>). However, these differences were neglected, because biological heterotrophic processes (like denitrification) are not significantly influenced by temperature. In addition, the main aim of the research was not to measure absolute values of denitrification rates but to evaluate biodegradability under anoxic conditions from the differences between endogenous, exogenous and total rates.

The substrate was dosed every 24 hours. Substrate for the reactor  $R_1$  (i.e., reference reactor) contained glucose, peptone, and starch. The substrate consisting of glucose, peptone, starch, and industrial wastewater was dosed into reactor  $R_2$  in a ratio of 1:1 (mg  $COD_{Cr, \text{glucose} + \text{peptone} + \text{starch}}$  : mg  $COD_{Cr, \text{industrial wastewater}}$ ). Only the industrial wastewater was dosed into reactor  $R_3$ . Total concentration of  $COD_{Cr}$  in each substrate was  $1,600 \text{ mg/l}$ . Nutrients (N and P) were dosed in the form of  $NH_4Cl$  and  $KH_2PO_4$ . The concentrations of TKN ( $N-NH_4 + N_{org}$ ) were at the level of  $55 \text{ mg/l}$  and  $P-PO_4$  at the level of  $12 \text{ mg/l}$ . To ensure the supply of micronutrients for activated sludge, reject water from dewatering of digested sludge at real municipal WWTP was added ( $30 \text{ ml}_{\text{reject water}}/\text{l}_{\text{of substrate}}$ ). The pH was adjusted with a sodium hydro-carbonate solution to 7.

Denitrification tests were performed on the 0, 7<sup>th</sup>, and 22<sup>nd</sup> day of operation of the laboratory reactors  $R_1$ ,  $R_2$ , and  $R_3$ . 22 days represent 1.5 times the value of SRT;

within 22 days the original activated sludge (inoculum) with SRT of 15 days is completely replaced. For more complicated substrates, due to slower adaptation and slower growing biomass, it is possible to recommend higher SRTs and longer duration of experiments.<sup>35</sup> In this research, the 3 week duration of the experiments was also set according to the requirements of the industrial wastewater producer.

Before the denitrification test, activated sludge was taken from the reactors  $R_1$ ,  $R_2$ ,  $R_3$  (taken as an excess sludge), diluted to a concentration of  $1 \text{ g/l}$  and poured into biochemical oxygen demand (BOD) bottles  $D_1$ ,  $D_2$ , and  $D_3$ . After a 2-hour aeration to remove residual degradable organic compounds, aeration was replaced by a slow stirring and the tested substrate was added. Initial  $N-NO_3$  concentration in all 3 bottles was  $30 \text{ mg/l}$ . Organic exogenous substrate wasn't added to the bottle  $D_1$  (this denitrification test was comparative and only endogenous denitrification was performed). Organic substrate was added to the BOD bottles  $D_2$  and  $D_3$  to allow comparison of endogenous and total denitrification rates. If total respiration rates in bottles  $D_2$  and  $D_3$  were higher than the endogenous rate in  $D_1$ , the organic substrate was degradable and usable in denitrification. Glucose was added to bottle  $D_2$  in the ratio  $COD_{Cr} : N-NO_3 = 15 \text{ mg/mg}$  ( $COD_{Cr} = 450 \text{ mg/l}$ ). Organic substrate was added excessively with the aim to eliminate denitrification rate limitation. The tested industrial wastewater was added to bottle  $D_3$ , also in the ratio of  $COD_{Cr} : N-NO_3 = 15 \text{ mg/mg}$ . By comparing the rates in bottles  $D_2$  and  $D_3$ , denitrification with industrial wastewater and a standard biodegradable compound was assessed. At the same time, nutrients N and P were added to bottles  $D_2$  and  $D_3$  to avoid limiting the denitrification by their absence.

During the tests, changes in pH were also monitored and their values were continuously adjusted to the neutral range of  $6.8\text{--}7.3$  (with a diluted acid or alkali). During denitrification in a closed reactor, the pH can rise, but also fall slightly.<sup>36</sup> Except for the decrease in  $N-NO_3$ , the decrease in  $COD_{Cr}$  and the possible formation of  $N-NO_2$  as an intermediate product of incomplete denitrification were also monitored. Tests lasted for 24 hours and the samples for analysis were taken in 3 hour intervals (during the first 9 hours, 4 samples, including taking sample at time 0); the last sample was taken after 24 hours (the significance of

**Table 1.** Analysed parameters, their abbreviations (symbols), and the method of determination.

Gravimetric methods	Spectrophotometric methods	Atomic absorption spectrometry
total solids (TS) total	chemical oxygen demand ( $COD_{Cr}$ )	cadmium (Cd)
suspended solids (TSS)	ammonium nitrogen ( $N-NH_4$ )	chromium (Cr)
volatile solids (VS) activated	total Kjeldahl nitrogen (TKN)	copper (Cu)
sludge concentration (Xc)	nitrite nitrogen ( $N-NO_2$ )	nickel (Ni)
sludge volume index (SVI)	nitrate nitrogen ( $N-NO_3$ )	lead (Pb)
	phosphate phosphorus ( $P-PO_4$ )	zinc (Zn)

Note: Spectrophotometer HACH DR5000 and atomic absorption spectrometer ContrAA 700 Analytik Jena were used

this sample was only a control). Denitrification rates and organic substrate consumption were evaluated according to the decline in  $\text{N-NO}_3$  and  $\text{COD}_{\text{Cr}}$  concentrations. For the first 9 hours of the test, the denitrification rate was not limited by the absence of organic substrate and the decline in concentrations was linear. The specific denitrification rates in  $\text{mg}_\text{N}/\text{g}\cdot\text{h}$  could thus be calculated from the slope of decrease of the concentrations divided by time and sludge concentration. The principle of such batch denitrification tests with further details is given in Bodík et al.<sup>35</sup>

Respirometric determination of biomass activity from individual reactors  $R_1$ ,  $R_2$ , and  $R_3$  was also performed by measuring oxygen consumption rates<sup>34,37</sup> and comparing endogenous ( $r_{\text{X,ox,en}}$ ), total ( $r_{\text{X,ox,t}}$ ), and substrate (exogenous) respiration rates ( $r_{\text{X,ox}}$ ) in 300 ml closed BOD bottles. The tests of anoxic biomass activity from denitrification tests were thus supplemented with information about oxic activity.

Respirometric measurements were performed on days 0 and 22. On day 0, only one respirometric measurement was performed, with the exogenous substrate glucose. The aim was to obtain information about the activity of the sludge before the addition of industrial wastewater. On day 22, three respirometric measurements with activated sludge from reactors  $R_1$ ,  $R_2$ , and  $R_3$  were performed to assess changes in oxic activity in all 3 reactors (especially in reactors  $R_2$  and  $R_3$ , where the biomass was exposed for 22 days to industrial wastewater). Before the respirometric tests, sludge taken as excess sludge from reactors  $R_1$ ,  $R_2$ , and  $R_3$  was aerated for 2 hours to remove residual exogenous organic compounds. The biomass was diluted to 1 g/l and the allylthiourea (10 mg/l) was added to suppress oxygen consumption by nitrification. For the first 5 minutes,  $r_{\text{X,ox,en}}$  was measured and then, for  $r_{\text{X,ox,t}}$  measurements, the following exogenous substrates were injected into the system: on day 0, glucose was added to the sludge; on day 22, glucose was used for the biomass from reactor  $R_1$ , glucose and industrial wastewater in the ratio  $\text{COD}_{\text{Cr}} = 1:1$  for biomass from reactor  $R_2$  and only industrial wastewater for biomass from reactor  $R_3$ . The concentration of exogenous  $\text{COD}_{\text{Cr}}$  in the BOD bottles after substrate dosing in all three cases was 17 mg/l. Respirograms were created by evaluating the respirometric measurements from which

the respiration rates  $r_{\text{X,ox,en}}$ ,  $r_{\text{X,ox,t}}$ ,  $r_{\text{X,ox}}$  in  $\text{mg}_{\text{O}_2}/\text{g}\cdot\text{h}$ , and substrate consumption rate  $r_{\text{X}}$  in  $\text{mg}_{\text{CHSKCr}}/\text{g}\cdot\text{h}$  were calculated according to Bodík et al.<sup>35,37</sup>

### 3. Results and Discussion

The sample of industrial wastewater (from the automotive industry) was partially turbid, grey in colour, and had a faint odour in concentrated form. The tested sample had concentrations of  $\text{COD}_{\text{Cr}} = 40.3$  g/l,  $\text{BOD}_5 : \text{COD}_{\text{Cr}} = 0.37$ ,  $\text{BOD}_5 = 14.8$  g/l (measured with unadapted inoculum),  $\text{N-NH}_4 = 16$  mg/l,  $\text{N-NO}_3 = 11$  mg/l,  $\text{P-PO}_4 = 21$  mg/l,  $\text{TS (105 }^\circ\text{C)} = 41.5$  g/l,  $\text{TSS (105 }^\circ\text{C)} = 2.1$  g/l,  $\text{VS (550 }^\circ\text{C)} = 68\%$ , and  $\text{pH } 6.2$ . Solvents based on glycol are the main fraction in the wastewater (the detailed composition of organic compounds is confidential; request of the producer). The concentration of heavy metals is in Table 2, focusing on the metals included in the Act on the application of sewage sludge to soil no. 188/2003<sup>38</sup>, as there is an assumption that the metals present in the wastewater will be adsorbed into activated sludge and can thus influence its treatment and handling. According to their toxicity and bioaccumulation tendency, high concentrations of metals in sewage sludge can be also obstacle to its reuse.<sup>39,40</sup> The other metals listed in the Act of Slovak Republic (no. 188/2003)<sup>38</sup> (As, Hg) were not determined; their occurrence in industrial wastewater according to its producer can be neglected. Table 2 also shows the real concentrations of metals in sludge from Slovak municipal WWTPs (average values valid for Slovak WWTPs according to Kozáková et al.<sup>41</sup>). These concentrations were used in the calculations to assess the acceptable amount of industrial wastewater imported to the WWTP as an external denitrification substrate.

Results of the denitrification tests are shown in Fig. 1. Day 0 assays inform about immediate response of non-adapted biomass to the addition of industrial wastewater (i.e., biomass that has been previously fed only with glucose, peptone, and starch). Subsequently, these tests were repeated on days 7 and 22 to see how the characteristics and parameters of biomass change after long-term exposure to industrial wastewater. The comparison of values

**Table 2.** The concentrations of heavy metals in industrial wastewater, real concentrations of metals in sludge from Slovak WWTP<sup>41</sup>, and limit concentrations of metals in sludge from WWTP applied to soil.<sup>38</sup>

Parameter	Industrial wastewater (mg/l)	Real concentrations of metals in sludge (mg/kg sludge dry matter)	Limit concentrations of metals in sludge (mg/kg sludge dry matter)
Cd	≤ 0.1	0.8	10
Cr	0.4	41	1,000
Cu	0.2	168	1,000
Ni	1.8	25	300
Pb	≤ 0.1	38	750
Zn	38.1	979	2,500



measured on day 0 ( $r_{X,D,endo} = 0.27 \text{ mg}_N/\text{g}\cdot\text{h}$ ;  $r_{X,D,total,industrial \text{ wastewater}} = 1.6 \text{ mg}_N/\text{g}\cdot\text{h}$ ) shows the immediate biological degradation of organic substances and no need for special adaptation of the biomass. Denitrification tests performed on day 7 and 22 show that industrial wastewater remains degradable for denitrification purposes even after long-term exposure (rates  $r_{X,D,endo} = 0.17 \text{ mg}_N/\text{g}\cdot\text{h}$  vs.  $r_{X,D,total,industrial \text{ wastewater}} = 1.9 \text{ mg}_N/\text{g}\cdot\text{h}$  and  $r_{X,D,endo} = 0.25 \text{ mg}_N/\text{g}\cdot\text{h}$  vs.  $r_{X,D,total,industrial \text{ wastewater}} = 1.6 \text{ mg}_N/\text{g}\cdot\text{h}$ ). Industrial wastewater did not deactivate the biomass. Denitrification rates measured with industrial wastewater were lower than the rates measured with glucose as a standard organic substrate ( $r_{X,D,total,industrial \text{ wastewater}} = 1.6\text{--}1.9 \text{ mg}_N/\text{g}\cdot\text{h}$  vs.  $r_{X,D,total,glucose} = 3.1\text{--}4.7 \text{ mg}_N/\text{g}\cdot\text{h}$ ). Nevertheless, industrial wastewater can be used as external organic substrate for denitrification at WWTP. The intermediate  $\text{N-NO}_2$  and its undissociated form  $\text{HNO}_2$  were not accumulated in any of the denitrification tests with industrial wastewater. The  $\text{COD}_{Cr} : \text{N-NO}_3$  ratio (ratio of  $\text{mg COD}_{Cr}$  in industrial wastewater consumed in denitrification of  $1 \text{ mg N-NO}_3$ ) was 9. According to stoichiometry of denitrification reaction involving both dissimilation and assimilation, standard ratios are in the range of 5–7 (consumption of  $\text{COD}_{Cr}$  calculated for the reduction of  $\text{N-NO}_3$  to  $\text{N}_2$  is  $2.86 \text{ mg}_{\text{COD}}/\text{mg}_N$ ; the next  $\text{COD}_{Cr}$  is consumed for a growth of new biomass, which depends on the bacteria involved in denitrification and which can not be stoichiometrically calculated).<sup>4,11</sup>

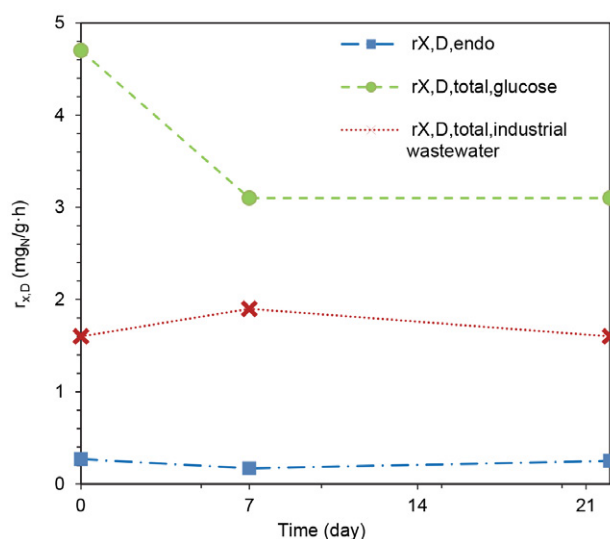


**Figure 1.** Rates of endogenous denitrification  $r_{X,D,endo}$  (test  $D_1$ ), total denitrification  $r_{X,D,total,glucose}$  with glucose as organic substrate (test  $D_2$ ), and total denitrification  $r_{X,D,total,industrial \text{ wastewater}}$  with industrial wastewater as organic substrate (test  $D_3$ ).

The long-term impact of industrial wastewater on activated sludge and biomass adaptation was also evaluated from the concentrations of  $\text{N-NH}_4$  and  $\text{COD}_{Cr}$  in the effluent of models  $R_1$ ,  $R_2$ , and  $R_3$ . These indicators were

used to monitor the influence on the nitrification and the concentration of residual and non-biodegradable organic matter from industrial wastewater (Table 3). At the same time, the values of volatile suspended solids (VSS) (as a share of organic matter in activated sludge) and sludge volume index (SVI) were evaluated (Table 3). All these parameters are important for WWTP as they influence a possible deterioration of the effluent from the WWTP, where industrial wastewater would be considered as an external denitrification substrate. Nitrification was efficient throughout the whole experiment, as confirmed by  $\text{N-NH}_4$  concentrations in the effluents from all 3 models (differences of 1.9 to  $3.7 \text{ mg/l}$  can be neglected). An important parameter in terms of fees for treated wastewater<sup>33</sup> is the residual  $\text{COD}_{Cr}$ . If the industrial wastewater contains hardly or non-biodegradable organic compounds, it is necessary to quantify the possible increase of  $\text{COD}_{Cr}$  concentration in the effluent from the WWTP. The increase of  $\text{COD}_{Cr}$  concentration occurred in models  $R_2$  and  $R_3$  with dosed industrial wastewater, where the average concentration increased from  $59 \text{ mg/l}$  to  $129$  and  $145 \text{ mg/l}$ . If we balance the average values of  $\text{COD}_{Cr}$  from industrial wastewater in the influent to models  $R_2$  and  $R_3$  ( $800 \text{ mg/l}$  in model  $R_2$  and  $1,600 \text{ mg/l}$  in model  $R_3$ ) and  $\text{COD}_{Cr}$  increase in the effluent from these models, the impact is as follows:

- In model  $R_2$ , every  $100 \text{ mg/l}$  of  $\text{COD}_{Cr}$  from industrial wastewater added to the activated sludge reactor increased the concentration of effluent  $\text{COD}_{Cr}$  by  $8.8 \text{ mg/l}$  (calculated as  $(129 \text{ mg/l} - 59 \text{ mg/l}) / 800 \text{ mg/l} \cdot 100 \text{ mg/l}$ )
- In model  $R_3$ , every  $100 \text{ mg/l}$  of  $\text{COD}_{Cr}$  of liquid waste added to the activated sludge reactor increased the concentration of effluent  $\text{COD}_{Cr}$  by  $5.4 \text{ mg/l}$  (calculated as  $(145 \text{ mg/l} - 59 \text{ mg/l}) / 1,600 \text{ mg/l} \cdot 100 \text{ mg/l}$ )
- If we assume that for denitrification of  $10 \text{ mg/l N-NO}_3$  it is necessary to add industrial wastewater with  $\text{COD}_{Cr}$  of  $90 \text{ mg/l}$  (ratio  $\text{COD}_{Cr} : \text{N-NO}_3 = 9$  measured in denitrification tests  $D_3$ ), then reduction of  $10 \text{ mg/l N-NO}_3$  in the effluent from WWTP is connected with  $\text{COD}_{Cr}$  increase  $4.9\text{--}7.9 \text{ mg/l}$  ( $5.4 \text{ mg/l} \cdot 90 \text{ mg/l} / 100 \text{ mg/l}$ ;  $8.8 \text{ mg/l} \cdot 90 \text{ mg/l} / 100 \text{ mg/l}$ ).

**Table 3.** Average effluent concentrations and their range for reference model  $R_1$ , model  $R_2$  with glucose and industrial wastewater, and model  $R_3$  with only industrial wastewater dosing.

Parameter	$R_1$	$R_2$	$R_3$
$\text{N-NH}_4$ (mg/l)	1.9 0.2–6	3.5 0.4–6	3.7 1.6–5.3
$\text{COD}_{Cr}$ (mg/l)	59 49–97	129 87–169	145 61–167
VSS (%)	79 81–82	75 71–86	75 70–82
SVI (ml/g)	52 45–60	48 43–49	51 45–64

Table 4. Results of respirometric measurements.

Respirometric rates	Typical values according to Bodík et al. <sup>35</sup>	Day 0 <sup>a)</sup>	Day 22 <sup>b)</sup>		
			(Model R <sub>1</sub> )	(Model R <sub>2</sub> )	(Model R <sub>3</sub> )
$r_{X,ox,en}$ (mgO <sub>2</sub> /g·h)	1–10	3	4	3	4
$r_{X,ox}$ (mgO <sub>2</sub> /g·h)	10–100	20	22	22	20
$r_{X,max}$ (mgCOD/g·h)	30–200	71	68	65	61

<sup>a</sup> Reference measurement with glucose as an exogenous substrate; measured with biomass used as a common inoculum for models R<sub>1</sub>, R<sub>2</sub>, and R<sub>3</sub>

<sup>b</sup> Exogenous substrates: glucose for activated sludge from model R<sub>1</sub>, glucose + industrial wastewater (1:1) for activated sludge from model R<sub>2</sub>, industrial wastewater for activated sludge from model R<sub>3</sub>

The impact of industrial wastewater on biomass was also monitored using the parameters VSS and SVI. The differences between models R<sub>1</sub>, R<sub>2</sub>, and R<sub>3</sub> are insignificant (negligible accumulation of inorganic compounds and activated sludge retained the formation of compact flocs with good sedimentation properties).

Results from respirometric measurements obtained during testing industrial wastewater are shown in Table 4. The results confirm that oxic respiration activity (i.e., ability to remove glucose as a reference substrate and industrial wastewater) has changed minimally during the operation of models R<sub>1</sub>, R<sub>2</sub>, and R<sub>3</sub>. The main conclusion is that industrial wastewater was not toxic to the biomass. The measured respiration rates in Table 4 are also compared with the recommended rates and even though they are at the lower end of the typical values from literature<sup>35</sup>, they are still acceptable and do not affect the previous statement.

In the case of additional industrial wastewater to the denitrification reactor, it is also important to assess how many m<sup>3</sup> can be imported to the WWTP so that the permitted concentration limits of heavy metals in sludge are not exceeded. Heavy metals in the wastewater are at the WWTP mostly adsorbed into the primary and activated sludge, and subsequently, remain in the digested sludge removed from the WWTP. The legislation defines these concentrations for cases where the sludge from WWTP is applied to the soil.<sup>38</sup> Application to the soil, either directly or as a compost from composting plants, is currently still the most common method of sludge management in Slovakia.<sup>41</sup> The following calculation shows an example of how to evaluate such balance for specific heavy metals and specific WWTP. The calculation assumes Cr in industrial wastewater, import of wastewater to WWTP with a capacity of approximately 10,000 inhabitants, inflow of 150 l/d per capita, specific production of sludge dry matter of 40 g/d per capita<sup>9,11</sup>, and concentrations of metal according to Table 2:

- WWTP inflow = 10,000 inhabitants · 150 l/d = 1,500 m<sup>3</sup>/d
- Daily sludge production = 10,000 inhabitants · 40 g/d = 400 kg/d

- Limit concentration of Cr in sewage sludge defined by Slovak legislation = 1,000 mg/kg
- Average background concentration of Cr in sludge at Slovak WWTPs: 41 mg/kg
- Capacity of sludge to adsorb Cr (the limit concentration defined by legislation is not to exceeded) = 1,000 mg/kg – 41 mg/kg = 959 mg/kg
- Possibility to import Cr in industrial wastewater to the WWTP = 400 kg/d · 959 mg/kg = 383,600 mg/d = 3.84 kg/d
- Concentration of Cr in industrial wastewater = 0.4 mg/l
- Volume of industrial wastewater with 383,600 mg/d of Cr = 383,600 mg/d / 0.4 mg/l = 959,000 l/d = 959 m<sup>3</sup>/d
- Conclusion of the example calculation for Cr: at a WWTP with a capacity of 10,000 inhabitants, 959 m<sup>3</sup>/d of industrial wastewater can be imported as an external denitrification substrate and the Cr concentration in sludge will not exceed the limit of 1,000 mg/kg. This consideration includes simplification that Cr from industrial wastewater is completely absorbed to the sludge. The volume of industrial water (959 m<sup>3</sup>/d) represents 64% of the WWTP inflow (1,500 m<sup>3</sup>/d).

The percentage of industrial wastewater imported to the WWTP with a capacity of 10,000 inhabitants calculated for other heavy metals from Table 2 are given in Table 5.

Table 5. The percentage of industrial wastewater to the WWTP (with a capacity of 10,000 inhabitants) for selected heavy metals.

Heavy metal	Volume of liquid waste (m <sup>3</sup> /d)	Percentage of liquid waste according to WWTP inflow (%)
Cr	959	64
Cd	36.8	2
Cu	1,664	111
Ni	61.1	4
Pb	2,835	189
Zn	15.9	1

According to these balances, Zn represents the worst case since it reduces the percentage of daily imported

volume of industrial wastewater to only 1% (15.9 m<sup>3</sup>/d). However, this amount of industrial wastewater is still interesting. It represents approximately 424 mg/l COD<sub>Cr</sub> and this concentration has a potential to denitrify 47 mg/l N-NO<sub>3</sub> (COD<sub>Cr</sub> of industrial wastewater = 40.3 g/l; ratio COD<sub>Cr</sub> : N-NO<sub>3</sub> = 9).

## 4. Conclusion

The main results emerging from the testing of industrial wastewater as a possible external denitrification substrate imported to the municipal WWTP to increase the rate and efficiency of denitrification are as follows:

- Industrial wastewater is biodegradable, also for non-adapted biomass
- Denitrification resulted in nitrogen gas production without accumulation of intermediate products
- The denitrification rates with industrial wastewater as an external substrate were in the range of 1.6 to 1.9 mg<sub>N</sub>/g.h. Addition of this substrate improves denitrification efficiency
- Negative impact of long-term dosing of industrial wastewater on activated sludge was not confirmed
- Partial increase of COD<sub>Cr</sub> concentration in the effluent from activated sludge reactor was measured (small amount of organic compounds in industrial wastewater was non-biodegradable). The addition of industrial wastewater with COD<sub>Cr</sub> concentration of 100 mg/l increased the COD<sub>Cr</sub> concentration in the WWTP effluent by 5–9 mg/l. This problem can be regulated by the amount of industrial wastewater applied into the denitrification reactor.
- The impact of the imported industrial wastewater as an external denitrification substrate for WWTP must be assessed comprehensively, including details such as the accumulation of heavy metals from the wastewater in the activated sludge. The instructions on how to calculate this balance are provided in the article.

## 5. References

1. T. Kurbus, J. Vrtovšek, M. Roš, *Acta Chim. Slov.* **2008**, 55, 474–479.
2. M. Roš, J. Vrtovšek, *Acta Chim. Slov.* **2004**, 51, 779–785.
3. J. Vrtovšek, M. Roš, *Acta Chim. Slov.* **2006**, 53, 396–400.
4. P. Pitter, *Hydrochemistry*, 5<sup>th</sup> Edition, VŠCHT, Praha, **2015**.
5. M. Henze, P. Harremoës, J. La Cour Jansen, E. Arvin, *Wastewater Treatment – Biological and Chemical Processes*. 2<sup>nd</sup> Edition, Springer Verlag, Berlin, **1997**. DOI:10.1007/978-3-662-22605-6
6. O. Kracht, W. Gujer, *Water Sci. Technol.* **2005**, 52 (3), 209–218. DOI:10.2166/wst.2005.0078
7. SHMÚ, Evaluation of Groundwater Quality in Slovakia – year 2019, [https://www.shmu.sk/File/Hydrologia/Monitoring\\_PzV/Monitoring\\_kvality\\_PzV/KvPzV\\_2019/KvPzV\\_2019\\_hodnotenie.pdf](https://www.shmu.sk/File/Hydrologia/Monitoring_PzV/Monitoring_kvality_PzV/KvPzV_2019/KvPzV_2019_hodnotenie.pdf), (assessed: February 23, 2022)
8. L. Bekerová, P. Belica, M. Dubcová, P. Hucko, *Vodohospodársky spravodajca*. **2021**, 64 (9–10), 27–31.
9. Slovak Technical Standard 75 6401, Sewage Treatment Plants for More Than 500 Population Equivalents, **1999**.
10. Chan A. Andersson, N. Johansson, M. Christensson, *Water Pract. Technol.* **2014**, 9 (2), 215–224. DOI:10.2166/wpt.2014.025
11. M. Drtil, M. Hutňan, Technological Project. Slovak Chemical Library FCHPT STU in Bratislava. 1<sup>st</sup> Edition, **2013**.
12. M. Pečenka, J. Svojtka, M. Koller, J. Wanner, Optimalisation of Denitrification by Means of External Substrate Dosing. Proceedings of the IWA Specialized Conference: Nutrient Management in Wastewater Treatment Processes and Recycle Streams, Krakow (PL), **1995**, pp. 1041–1045.
13. A. Mahmoud, R. A. Hamza, E. Elbeshbishy, *Sci. Total Environ.* **2022**, 816, 151578. DOI:10.1016/j.scitotenv.2021.151578
14. S. Lee, T. Moon, S. Park, M. Choi, Ch. Kim, *Korean J. Chem. Eng.* **2013**, 30, 1911–1917. DOI:10.1007/s11814-013-0131-7
15. A. De Lucas, L. Rodríguez, J. Villaseñor, F. J. Fernández, *Water Res.* **2005**, 39 (15), 3715–3726. DOI:10.1016/j.watres.2005.06.024
16. F. Morgan-Sagastume, J. L. Nielsen, P. H. Nielsen, *FEMS Microbiol. Ecol.* **2008**, 66 (2), 447–461. DOI:10.1111/j.1574-6941.2008.00571.x
17. C. Cherchi, A. Onnis-Hayden, I. El-Shawabkeh, A. Z. Gu, *Water Environ. Res.* **2009**, 81 (8), 788–799. DOI:10.2175/106143009X12465435982610
18. M. Swinarski, J. Makinia, K. Czerwionka, M. Chrzanowska, J. Drewnowski, *Water Environ. Res.* **2009**, 81 (9), 896–906. DOI:10.2175/106143009X407438
19. N. F. Y. Tam, Y. S. Wong, G. Leung, *Water Sci. Technol.* **1992**, 26 (5–6), 1047–1055. DOI:10.2166/wst.1992.0546
20. S. Hallin, M. Pell, *Water Res.* **1998**, 32, 13–18. DOI:10.1016/S0043-1354(97)00199-1
21. A. Onnis-Hayden, D. Dair, Ch. Johnson, A. Schramm, A. Z. Gu, *Proceedings of the Water Environment Federation*. **2007**, 3099–3119. DOI:10.2175/193864707787973789
22. P. Cyplik, W. Juzwa, R. Marecik, J. Powierska-Czarny, A. Piotrowska-Cyplik, J. Czarny, A. Drożdżyńska, Ł. Chrzanowski, *Chemosphere*. **2013**, 93 (11), 2823–2831. DOI:10.1016/j.chemosphere.2013.09.083
23. R. Liao, Y. Miao, J. Li, Y. Li, Z. Wang, J. Du, Y. Li, A. Li, H. Shen, *RSC Adv.* **2018**, 8, 42087–42094. DOI:10.1039/C8RA08256A
24. P. Elefsiniotis, D. Li, *Biochem. Eng. J.* **2006**, 28 (2), 148–155. DOI:10.1016/j.bej.2005.10.004
25. R. Knowles, *Microbiol. Rev.* **1982**, 46 (1), 43–70. DOI:10.1128/mr.46.1.43-70.1982
26. L. Foglar, D. Gašparac, *Desalin. Water Treat.* **2013**, 51 (37–39), 7157–7165. DOI:10.1080/19443994.2013.792162
27. X. Cao, D. Qian, X. Meng, *Environ Technol.* **2013**, 34 (1–4), 45–51. DOI:10.1080/09593330.2012.679700
28. J. Wanner, *Activated Sludge Bulking and Foaming Control*, CRC Press, **1995**.

29. M. Henze, M. C. M. van Loosdrecht, G. A. Ekama, D. Brdjanovic, *Biological Wastewater Treatment: Principles, modelling and design*. IWA Publishing, **2008**. DOI:10.2166/9781780401867
30. H. M. Phillips, J. L. Barnard, C. Debarbadillo, A. R. Shaw, M. T. Steichen, C. Wallis-Lage, *Proceedings of the Water Environment Federation*, **2009**, 252–276. DOI:10.2175/193864709793901301
31. M. Drtil, I. Bodík, S. Vlčková, D. Kolníková, R. Brezina, P. Levársky, J. Tichý, Z. Imreová, M. Švorcová, *SOVAK*. **2018**, 3, 12–16.
32. Slovak Government Regulation no. 269/2010 Coll. Requirements for the Achievement of Good Water Status.
33. Slovak Government Regulation no. 755/2004 Coll. which Establishes the Amount of Unregulated Payments, Fees and Details Related to Charging for Water Use.
34. R. Baird, L. Bridgewater, *Standard Methods for the Examination of Water and Wastewater*. 23<sup>rd</sup> Edition, American Public Health Association, Washington, D.C., **2017**.
35. I. Bodík, O. Čížmarová, J. Derco, M. Drtil, M. Hutňan, Z. Imreová, T. Mackuľák, M. Vrabel, R. Zakhar, *Laboratory Exercises II – Environmental Technologies*. STU, Bratislava. Faculty of Chemical and Food Technology. Slovak Chemical Library FCHPT STU in Bratislava, **2021**.
36. M. Drtil, P. Németh, K. Kucman, I. Bodík, V. Kašperek, *Water Res.* **1995**, 29 (5), 1353–1360. DOI:10.1016/0043-1354(94)00228-Y
37. S. Čech, J. Chudoba, P. Grau, *Water Sci. Technol.* **1985**, 17 (2–3), 259–272. DOI:10.2166/wst.1985.0135
38. Act of the Slovak Republic no. 188/2003 Coll. on the Application of Sewage Sludge and Bottom Sediments into the Land.
39. K. Cer Kerčmar, M. Zupančič, P. Bukovec, *Acta Chim. Slov.* **2008**, 55, 1023–1029.
40. S. M. Mousavi, S. A. Hashemi, A. Babapoor, A. Savardashtaki, H. Esmaeili, Y. Rahnama, F. Mojoudi, S. Bahrani, S. Jahandideh, M. Asadi, *Acta Chim. Slov.* **2019**, 66, 865–873. DOI:10.17344/acsi.2019.4984
41. K. Kozáková, L. Sumegová, I. Balážová Pijáková, *Vodohospodársky spravodajca*. **2018**, 61 (1–2), 32–34.

## Povzetek

Dodatek zunanjšega vira organskega ogljika za denitrifikacijo se običajno uporablja v čistilnih napravah odpadnih vod za namen intenziviranja procesov odstranjevanja dušika. Cilj laboratorijske raziskave je bil izmeriti sestavo koncentrirane industrijske odpadne vode, ugotoviti možnosti njene uporabe kot zunanjšega substrata za denitrifikacijo in oceniti njen celoten vpliv na čistilno napravo. Dobljeni rezultati kažejo, da je analizirana industrijska odpadna voda biološko razgradljiva in se lahko uporablja kot denitrifikacijski substrat brez posebne prilagoditve biomase. Stopnje denitrifikacije pri testirani odpadni vodi so bile v območju od 1,6 do 1,9 mg N/g·h. Negativni vpliv dolgotrajnega doziranja industrijske odpadne vode na aktivno blato ni bil potrjen. Vpliv uvožene odpadne vode na čistilno napravo je treba oceniti celovito, vključno z vplivom težkih kovin iz odpadne vode na kakovost blata, kar je navedeno tudi v tej raziskavi.



Except when otherwise noted, articles in this journal are published under the terms and conditions of the Creative Commons Attribution 4.0 International License

Scientific paper

# Environmentally Friendly Extraction of Bioactive Compounds from *Rosa canina* L. fruits Using Deep Eutectic Solvent (DES) as Green Extraction Media

Hyrije Koraqi,<sup>1,2,\*</sup> Bujar Qazimi,<sup>1</sup> Cengiz Česko<sup>2</sup>  
and Anka Trajkovska Petkoska<sup>3</sup>

<sup>1</sup> Faculty of Pharmacy, UBT-Higher Education Institution, St. Rexhep Krasniqi No.56, 10000 Pristina, Kosovo

<sup>2</sup> Faculty of Food Science and Biotechnology, UBT-Higher Education Institution, St. Rexhep Krasniqi No.56, 10000 Pristina, Kosovo

<sup>3</sup> Faculty of Technology and Technical Sciences, St. Clement of Ohrid University of Bitola, Dimitar Vlahov, 1400 Veles, Republic of North Macedonia

\* Corresponding author: E-mail: hyrie.koraqi@ubt-uni.net  
Phone: +383 38 541 400 Fax: +383 38 542 138

Received: 04-28-2022

## Abstract

In this study, the green extraction of bioactive compounds from Rosehip (*Rosa canina* L.) fruits and their antioxidant activity were investigated. An ultrasound-assisted extraction combined with deep eutectic solvents (DES) was used for this purpose. Deep eutectic solvents based on citric acid were specially designed. Namely, hydrogen bond donor (HBD) such as glycerol and ethylene glycol as well as hydrogen bond acceptor (HBA) like citric acid were used. After choosing the best option of DES, for extraction of the bioactive ingredients, optimal extraction conditions of the ultrasonic-assisted extraction have been optimized through Box-Behnken design of response surface methodology (RSM). Total phenolics content (TPC), total anthocyanins content (TAA), and antioxidant activity against 2,2-diphenyl-1-picrylhydrazyl (DPPH) have been found as 103.37 mg GAE/g DW in DES2, 92.23 mg GAE/g DW in DES1, 3.25mg C3G/100g-DW in DES2, 1.31 mg C3G/100g-DW in DES1, and 101.85% inhibition in DES2, 94.32%. The results of this study showed that this method is a competitive sustainable, green, and effective extraction of bioactive compounds from Rosehip (*Rosa canina* L.) fruits.

**Keywords:** *Rosa canina* L. fruits, deep eutectic solvent, Green extraction, Antioxidant activity, Experimental design

## 1. Introduction

*Rosa canina* L, which is also known as Rosehip, is a member of the Rosaceae family and the genus *Rosa* which comprises nearly 200 species that are naturally distributed almost in many countries such as Europe, Asia, the Middle East, and North America.<sup>1–3</sup> In Kosovo, *Rosa canina* L. fruits are found in all areas of the country and are traditionally used for food or medical purposes. Functional foods and food supplements, such as herbal food supplements and nutraceuticals, that help protect humans against oxidative stress and a variety of diseases have piqued attention all over the world. *Rosa canina* L. fruits are high in phenolic compounds, which operate as

natural antioxidants; flavonoids, anthocyanins, and high vitamin C content; vitamins A, B1, B2, B6, D, E, and K; organic acids, such as citric acid, malic acid, carotenoids, sugars, mineral elements, and fibers.<sup>4–6</sup> *Rosa canina* L. is a remarkable fruit that is a rich source of biologically active compounds with pharmacological features. Moreover, it is used for a wide variety of purposes like protection of health and therapy for flu, infections, protect the kidneys from oxidative stress, possesses an antidiabetic, antimicrobial, inflammatory diseases, and chronic pains. *Rosa canina* L. fruits have anti-ulcer and anti-aging properties. Chemoprevention, antioxidant, antimutagenic, and anticarcinogenic properties are also known.<sup>7,8</sup> Due to the above-mentioned properties, *Rosa canina* L. fruits

are commonly used in the food, pharmaceutical, and cosmetic industries. Namely, it could be, used as food and drink such as tea, marmalades, jellies, and jams. However, it has recently been utilized as an ingredient in probiotic drinks, yogurts, and health supplements.<sup>4</sup> In the scientific literature, there is still lack of information on phenolic compounds, flavonoids and the antioxidant activity of *Rosa canina* L. fruits. Novel applications are given in a very limited number of studies mainly on the extraction of phenolic compounds and antioxidant activity based on solid-liquid extraction with traditional organic solvents (methanol, ethanol, acetone, ethyl acetate, etc.) and water/organic solvent mixtures have been used to extract the bioactive components from *Rosa canina* L. fruits. Organic solvents, on the other hand, have several disadvantages, such as toxicity, volatility, non-degradability, and flammability. They are also very expensive, but their use in the extraction process poses potential dangers to both human health and the environment.<sup>9,10</sup> From the point of view of green chemistry several studies have been conducted to overcome these issues by replacing conventional organic solvents with deep eutectic solvents (DES) as a new generation of eco-friendly solvents.<sup>11–13</sup> Therefore, recently ionic liquids have been developed and entitled as deep eutectic solvents (DES). DES are designable solvents formed by molecular interactions, especially hydrogen bonds.<sup>14</sup> DES can be formed by mixing two or three inexpensive materials such as organic acids, polyols, sugars, amines, and quaternary ammonium salts.<sup>15</sup> Ultrasound-assisted extraction (UAE) is a novel extraction method known for being very efficient and environmentally friendly. The frequency of the ultrasonic bath has a significant effect on the extraction process while the ultrasound irritation helps to reduce reaction time and increase mass transfer during this operation. In addition, the ultrasound allows greater penetration of the solvent into the food matrix, which increases the contact surface area between solid and liquid phases.<sup>16</sup> In the current study, DES containing hydrogen bond donors (polyol) and hydrogen bond acceptor (organic acid) has been synthesized and used for determination total phenolic content, total flavonoid content, anthocyanin content, from *Rosa canina* L. fruits and their antioxidant activity using UAE. After the determination of the best designed DES, the UAE experiments were designed by Box-Behnken design (BBD) along with response surface methodology (RSM). In this context, our study has overcome the issues related to conventional organic solvents and replace them with DES as a new generation of eco-friendly solvents. To the best of our knowledge, there is no any report on the green extraction of antioxidant phenolic compounds from *Rosa canina* L. fruits using the combination of UAE-DES. Therefore, the main objectives of this study are (i) to evaluate the most effective solvent to extract phenolic compounds from *Rosa canina* L. fruits, (ii) to screen significant extraction variables in

UAE-DES using a Box-Behnken design (BBD) along with response surface methodology (RSM), and (iii) to quantify the phenolic compounds and antioxidant activity of the *Rosa canina* L. extract at optimum conditions.

## 2. Materials and methods

### 2.1. Plant Material

*Rosa canina* L. fruits were collected during September 2021 from the spontaneous flora of the central part of Kosovo. Rosehips were washed several times with tap water and dried at room temperature. The fruits were immediately transferred to the laboratory in polyethylene bags and stored at  $-4^{\circ}\text{C}$  until analysis.

### 2.2. Chemical Materials

All chemicals used in experiments were analytical grade. Ethanol was provided from Alkaloid (Skopje, North Macedonia). Folin–Ciocalteu reagent, citric acid, glycerol, ethylene glycol, sodium carbonate, and gallic acid were purchased from Sigma–Aldrich (Germany).

### 2.2. Extract Preparation

Ultrasound-assisted extraction was conducted in a digital ultrasonic bath at  $25^{\circ}\text{C}$ . Rosehip fruits (500 mg) and solvent were sealed in an Erlenmeyer flask and placed into the digital ultrasonic bath. The extract was centrifuged at  $5000\times g$  for 25 min. After centrifugation, the supernatant was filtered through a  $0.45\ \mu\text{m}$  syringe and stored at  $-4^{\circ}\text{C}$  until analysis.

### 2.3. Preparation of Deep Eutectic Solvent-DES

A hydrogen bond acceptor (HBA) and a hydrogen bond donor (HBD) were dried at  $45^{\circ}\text{C}$  for 24 h before use. Before were mixed along with heating at  $80^{\circ}\text{C}$  by a magnetic stirrer. When a homogeneous liquid was observed, the acidity of the liquids was measured by a pH meter. The appropriate molar ratio of the used solvents, was weight and it is listed in table 1. The prepared DES compositions were stored in a desiccator to prevent moisture absorption until further analysis.

**Table 1.** Components and their properties used in the design of DES for the UAE of *Rosa canina* L. fruits

DES/No.	HBA	Chemical formula	HBD	Chemical formula	pH
DES 1	Citric acid	$\text{C}_6\text{H}_8\text{O}_7$	Glycerol	$\text{C}_3\text{H}_8\text{O}_3$	1.5
DES 2	Citric acid	$\text{C}_6\text{H}_8\text{O}_7$	Ethylene glycol	$\text{C}_2\text{H}_6\text{O}_2$	1.0



## 2. 4. Experimental Designs

### 2. 4. 1. Screening of Solvents

In the initial screening of the extraction efficiencies of the solvents, the *Rosa canina* L. fruits samples (500 mg) were mixed with the selected solvents (5 mL). Other parameters were kept constant in accordance with the concept that one factor at a time approach will be changed. The extraction of phenolic compounds was conducted at 40 °C for 30 min with an ultrasound amplitude of 20%. The supernatant phase was collected after centrifugation at 10,000xg for 10 min. The extracts were stored at –4 °C under dark conditions.

it can be calculated according to equation 1:

$$\text{Antioxidant activity \% inhibition of DPPH} = [(A_{\text{control}} - A_{\text{sample}}) / A_{\text{control}}] \times 100 \quad (1)$$

$A_{\text{control}}$  represents the absorbance of the diluted DPPH solution, and  $A_{\text{sample}}$  represents the absorbance of the sample.

### 2. 6. Statistical Analysis

The differences among extraction solvents were determined using analysis of variance (ANOVA), followed by Duncan tests (SPSS 22 package program for Windows,

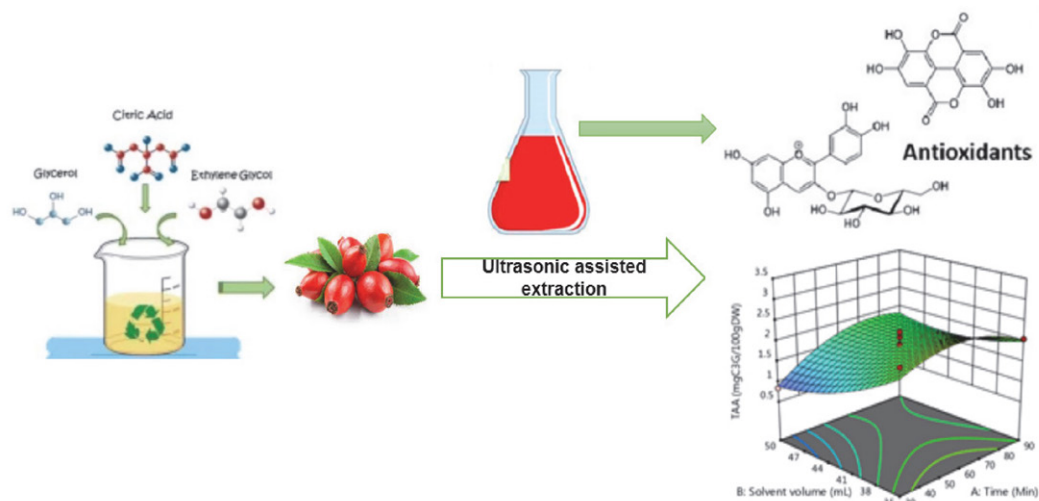


Figure 1. Experimental design for extraction bioactive compounds from *Rosa canina* L. fruits

### 2. 5. Determination of bioactive properties and antioxidant activity (TPC, TAA, DPPH)

Total phenolics content (TPC) was determined by Folin Ciocalteu Reagent spectrophotometrically at 765 nm using the method of Singleton et al. (1999),<sup>17</sup> with some modifications reported by Koraqi and Lluga-Rizani (2022)<sup>18</sup>. The results are presented as mg gallic acid (mg GAE/g DW) equivalent per gram *Rosa canina* L. fruits sample. Total anthocyanin analysis (TAA) was conducted by the pH differential method reported by Lee et al. (2005)<sup>19</sup> with some modifications.<sup>20</sup> TAA is based on the measurement of the absorbance of the anthocyanins, which depends on the pH alteration (pH = 1.0 and pH = 4.5). The wavelength was 530 and 657 nm. As for Total anthocyanin content, is presented as mg cyaniding-3-glucoside (mg C3G/g DW) equivalent per gram *Rosa canina* L. fruits. Regarding antioxidant activity against a free radical, the 2,2-diphenyl-1-picrylhydrazyl (DPPH) test was applied at 517 nm.<sup>21</sup> Inhibition power of the extracts towards DPPH radical is stated as a percentage (% inhibition) and

Chicago, IL, USA). Statistical significance was defined at a 95% confidence level. Design Expert v13.0 trial software (Stat-Ease, USA) was used for the construction of experimental designs (BBD and RSA), regression analysis of experimental data, and plotting of 3D response surface graphs. ANOVA test was used to assess the statistical significance of the regression coefficient by F-test at 95% confidence level. The adequacy of the fitted polynomial model was expressed by the coefficient of determination ( $R^2$ ) and lack of fit test.

## 3. Results and Discussion

### 3. 1. Comparison of the Deep Eutectic Solvent (DES)

Citric acid-based DES has been synthesized with polyol HBD such as glycerol and ethylene glycol. Figure 2 shows that the superior yield for all dependent variables (DPPH, TPC, and TAA) has been gained by the citric acid/

ethylene glycol combination. Hrnčič et al. (2019)<sup>22</sup> extracted *Rosa canina* L. fruits with conventional solvents (methanol solution-MeOH and water), where TPC and DPPH changed between 8.13 mg GAE/g extract and 9.01% DPPH Inhibition, respectively. Our results for TPC were 13 times better, whilst our phenolic quantity was almost twice compared to those of the previous studies. Su et al. (2007)<sup>23</sup> also reported a lower value of TPC than 5.09 mg GAE/g in 50% acetone extract and 2.57 mg GAE/g in 80% methanolic extract. Furthermore, Fascella et al. (2019)<sup>24</sup> declared a lower value of TPC (6784.5 mg GAE/100 g DW), but a similar values with our results for TAA (3.86 mg CGE/100g DW) and antioxidant activity DPPH IC<sub>50</sub> (80.8%) against DPPH radical when they extracted *Rosa canina* L. fruits with traditional extraction method through the water. IC<sub>50</sub> values in the DPPH assay correspond to lower antioxidant activity, and vice versa.<sup>24</sup> Lower value of TPC in ethanolic extract (40%–70% EtOH) has been reported by Ilbay et al. (2013)<sup>16</sup> as well, 47.23 mg GAE/g DW in optimal conditions (40% EtOH, at 50 °C, time 81.23 min.). Bozhuyuk et al. (2021)<sup>25</sup> reported similar results for extraction with conventional solvents as TPC (390–532 mg GAE/100g DW; and TAA 3.62–7.81 mg/kg) extracted from *Rosa canina* L. fruits. Our findings for TPC were higher in comparison with these studies. Most of these findings are reported in Table 2. Even though both of the DES mixtures surpassed the conventional solvents reported in the literature, citric acid/ethylene glycol formulation was shown as a better one mainly due to its viscosity.<sup>26</sup> Since ethylene glycol is a less viscous liquid than glycerol, therefore its mixture with citric acid has been shown better in terms diffusion into the plant matrix.<sup>27</sup> After the success of the citric acid/ethylene glycol, a statistical experimental design study was performed. In order to achieve a clearer liquid, water addition into the DES system showed as a good addition for rising polarity of the system.<sup>27</sup> Hence, the water content in the DES has been chosen as a process variable for the ultrasonic-assisted extraction of *Rosa canina* L. fruits (Table 3).

### 3. 2. Box-Behnken Design and Modeling of Ultrasonic-Assisted Extraction

After the success of the citric acid/ethylene glycol, a statistical experimental design study was performed. In order to achieve a clearer and more fluid liquid, water addition into the DES system is a must in addition to rising

polarity.<sup>27</sup> Hence, the water content in the DES has been chosen as a process variable for the UAE of *Rosa canina* L. fruits (Table 3). Table 4 gives the content of TPC, TAA, and DPPH obtained by UAE under several process conditions. Table 5 summarizes the statistical outcome of the current system depending on the ANOVA test of BBD through RSM. The final equation in terms of coded factors for TPC (Response 1) is given as equation 2:

$$\text{TPC} = 96.23 - 1.32A + 2.52B - 0.6162C + 1.04AB - 0.9666AC + 5.02BC + 4.69A^2 + 1.96B^2 + 1.32C^2 \quad (2)$$

Table 3. Operation parameters of the UAE of *Rosa canina* L. fruits

Independent parameter	Unit	Symbol	Levels with the codes		
			–1	0	+1
Time	Min	A	30	60	90
Solvent volume	mL	B	35	42.5	50
Water content	%, v/v	C	10	30	50

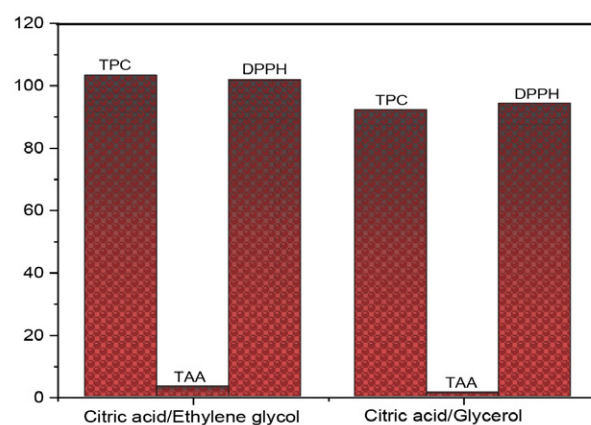


Figure 2. Comparative results of the selected DES on the performance of UAE of *Rosa canina* L. fruits

F 5.32 and p-value 0.0192 for the model are indications of the significance of the model. Regarding process parameters, if the p-value is less than 0.05 ( $p < 0.05$ ), it means that the terms of the model are significant. Time of UAE was the most influential parameter, followed by sol-

Table 2. Extraction of bioactive compounds from *Rosa canina* L. fruits reported in scientific literature

Plant material	Solvents	Extraction method	Reference
<i>Rosa canina</i> L.	40% EtOH	Ultrasonic-assisted extraction	16
<i>Rosa canina</i> L.	Methanol, MeOH-water	Maceration, Soxhlet extraction	22
<i>Rosa canina</i> L.	80% MeOH, 50% acetone	Conventional	23
<i>Rosa canina</i> L.	Water	Traditional extraction	24
<i>Rosa canina</i> L.	Acetone, water, acetic acid	Conventional	25

vent quantity ( $p < 0.05$ ). Effects of interactions between the variables were also found statistically important ( $p < 0.05$ ). According to the ANOVA test,  $R^2$  was found as 0.9702, whilst adjusted- $R^2$  was 0.9086. That means that there is a convincing relationship between the experimental and calculated data as seen in Figure 3. The quadratic polynomial model derived from the BBD of RSM for TAA (response 2) is given in Equation 3:

$$\begin{aligned} \text{TAA} = & 1.90 - 0.107A + 0.4213B - \\ & 0.0013C + 0.1950AB + 0.0650AC - 0.1675BC - \\ & 0.2593A^2 + 0.1833B^2 + 0.4482C^2 \end{aligned} \quad (3)$$

Similarly, the model was statistically significant to represent the experimental data based on the F and p values (Table 4). The most influential parameter was solvent volume (v/v) of DES ( $p < 0.05$ ). However, water addition into the DES solution was not a statistically significant process parameter depending on the ANOVA test results ( $p > 0.05$ ). A satisfactory relationship was also observed between the experimental and calculated data for response 2 (Figure 3), where  $R^2$  and adjusted- $R^2$  were 0.9649 and 0.9198, respectively. The second-order equation in terms of coded factors for response 3 is given in Equation 4:

$$\begin{aligned} \text{DPPH} = & 100.17 + 1.32A + 0.7940B - 1.41C - \\ & 1.69AB - 2.05AC - 0.8030BC - 0.3196A^2 - \\ & 0.8954B^2 + 1.86C^2 \end{aligned} \quad (4)$$

The equation derived for DPPH was statistically important for making estimations about the response for given levels of each factor as seen in Table 4. Time of UAE was

the most effective independent factor, followed by solvent volume ( $p < 0.05$ ). Unexpectedly, the amount of water in the extractant system was not a statistically effective process parameter ( $p > 0.05$ ). As already seen in Figures 3 and 4, there is a convincing relationship between the actual and estimated results. Depending on the ANOVA findings,  $R^2$  was found as 0.9780, whereas adjusted- $R^2$  was 0.9326.

### 3. 3. Effect of Process Parameters on Ultrasonic-Assisted Extraction of *Rosa Canina* L. Fruits

Figures 3 presents three-dimensional (3D) surfaces for UAE of *Rosa canina* L. fruits. As seen in Figure 3, the time of UAE has a predominant effect on the phenolics extraction of the current plant material. Increasing the time leads to enhancement in the TPC extraction, where there had been quick cell breakage based on the rise in temperature. Regarding the solvent amount to extract the plant, there was a slight effect such as increasing the yield. Since the current DES is not too viscous, the water addition had a mild effect on the enhancement of the TPC extraction.

Actually, time did not have a profound impact on the TAA yield as seen in the Figures 3 and 4 as it is presented that water content rise in the extractant system favors the TAA extraction due to the decline in surface tension and viscosity as well as an increase in polarity. In respect of DPPH, we observed similar inclinations towards the process parameters of UAE of *Rosa canina* L. fruits. This finding is in a good agreement with the correlation ( $r = 0.879$ ) between the total phenolics and antioxidant activity of *Rosa canina* L. fruits. In the matter of TAA, its relationship

**Table 4.** Effects of operation factors on the responses of *Rosa canina* L. fruits extract obtained by UAE

Run	Factor 1 A: Time (Min)	Factor 2 B: Solvent volume (mL)	Factor 3 C: Water content (%, v/v)	Response 1 TPC (mg GAE/gDW)	Response 2 TAA mgC3G/100gDW)	Response 3 DPPH (inhibition %)
1	60	35	50	90.66±0.01	2.5±0.02	102.77±0.01
2	60	42.5	30	98.44±0.03	3.25±0.03	95.01±0.01
3	30	50	30	106.72±0.03	2.41±0.02	101.65±0.02
4	90	50	30	105.64±0.02	2.46±0.02	101.15±0.03
5	60	42.5	30	95.66±0.01	1.53±0.01	101.61±0.03
6	30	35	30	102.21±0.02	1.57±0.01	93.36±0.04
7	60	50	50	104.19±0.03	2.62±0.02	99.43±0.02
8	60	42.5	30	95.61±0.04	1.8±0.01	103.66±0.02
9	30	42.5	10	101.49±0.01	2.23±0.02	101.24±0.01
10	30	42.5	50	105.12±0.03	2.03±0.03	99.77±0.03
11	60	42.5	30	92.94±0.04	1.92±0.03	97.03±0.01
12	90	35	30	96.96±0.04	0.84±0.01	99.62±0.01
13	90	42.5	50	101.06±0.02	2.07±0.01	98.07±0.02
14	90	42.5	10	101.29±0.01	2.01±0.02	107.75±0.01
15	60	50	10	98.32±0.02	2.89±0.02	101.10±0.02
16	60	35	10	104.86±0.02	2.10±0.01	101.23±0.01
17	60	42.5	30	98.50±0.01	0.98±0.01	103.51±0.03

Data are given as the mean ( $n = 3$ ) ± standard deviation.

**Table 5.** Analysis of variance test for the Box-Behnken design for the UAE for TPC, TAA and %DPPH

Source	Sum of squares	Df	Mean square	F-value	p-value
TPC Model	302.04	9	33.56	5.32	0.0192
A-Time	13.97	1	13.97	2.22	0.0102
B-Solvent volume	50.95	1	50.95	8.08	0.0249
C-Water content	3.04	1	3.04	0.4817	0.5100
AB	4.34	1	4.34	0.6886	0.4340
AC	3.74	1	3.74	0.5928	0.4665
BC	100.72	1	100.72	15.97	0.0052
A <sup>2</sup>	92.65	1	92.65	14.69	0.0064
B <sup>2</sup>	16.17	1	16.17	2.57	0.1533
C <sup>2</sup>	7.32	1	7.32	1.16	0.3169
Residual	44.13	7	6.30		
Lack of fit	22.59	3	7.53	1.40	0.3658
Pure error	21.55	4	5.39		
Cor total	346.17	16			
TAA Model	3.03	9	0.3370	0.7472	0.0257
A-Time	0.0925	1	0.0925	0.2050	0.6644
B-Solvent volume	1.42	1	1.42	3.15	0.0493
C-Water content	0.0000	1	0.0000	0.0000	0.0259
AB	0.1521	1	0.1521	0.3373	0.5796
AC	0.0169	1	0.0169	0.0375	0.8520
BC	0.1122	1	0.1122	0.2489	0.6332
A <sup>2</sup>	0.2830	1	0.2830	0.6275	0.4543
B <sup>2</sup>	0.1414	1	0.1414	0.3135	0.5930
C <sup>2</sup>	0.8460	1	0.8460	1.88	0.2131
Residual	3.16	7	0.4510		
Lack of fit	0.3407	3	0.1136		
Pure error	2.82	4	0.7040	0.1613	0.9171
Cor total	6.19	16			
DPPH Model	83.39	9	9.27	0.6531	0.0299
A-Time	13.98	1	13.98	0.9852	0.3540
B-Solvent volume	5.04	1	5.04	0.3555	0.0298
C-Water content	15.91	1	15.91	1.12	0.0348
AB	11.42	1	11.42	0.8051	0.3994
AC	16.86	1	16.86	1.19	0.3117
BC	2.58	1	2.58	0.1818	0.6826
A <sup>2</sup>	0.4300	1	0.4300	0.0303	0.8667
B <sup>2</sup>	3.38	1	3.38	0.2379	0.6406
C <sup>2</sup>	14.61	1	14.61	1.03	0.3439
Residual	99.30	7	14.19		
Lack of fit	37.36	3	12.45	0.8044	0.5532
Pure error	61.93	4	15.48		
Cor total	182.68	16			

( $r = 0.003$ ) with the antioxidant effect against DPPH radical (% Inhibition) has been found to be extremely weak.

## 4. Conclusions

This study revealed an efficient and sustainable approach for the extraction of antioxidant phenolic compounds from *Rosa canina* L. fruits. In the extraction process, the combination of green solvents-DES and ultrasound-assisted extraction was evaluated and optimized

using experimental design approaches including one variable at a time, solvent volume, and water content (v/v). Two different deep eutectic solvents have been prepared using glycerol and ethylene glycol (hydrogen bond donor) and citric acid (hydrogen bond acceptor). Citric acid/ethylene glycol mixture has produced the most efficient *Rosa canina* L. fruits extract through ultrasonic-assisted extraction. The correlation ( $r > 0.99$ ) between the phenolics and the anthocyanin contents in *Rosa canina* L. fruits indicates that anthocyanins contribute to the most to the phenolic in the plant. On the other hand, the proposed second-order

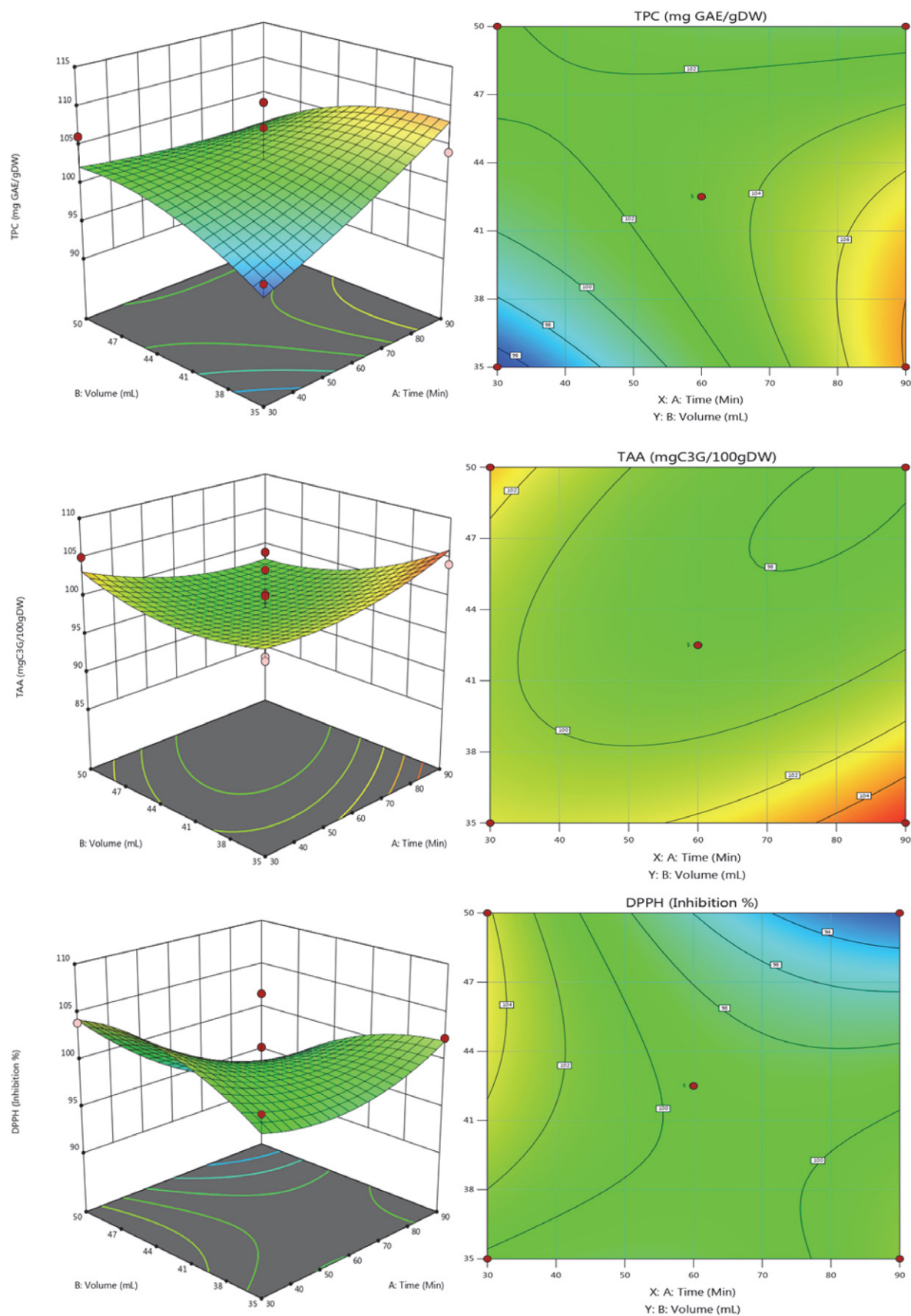
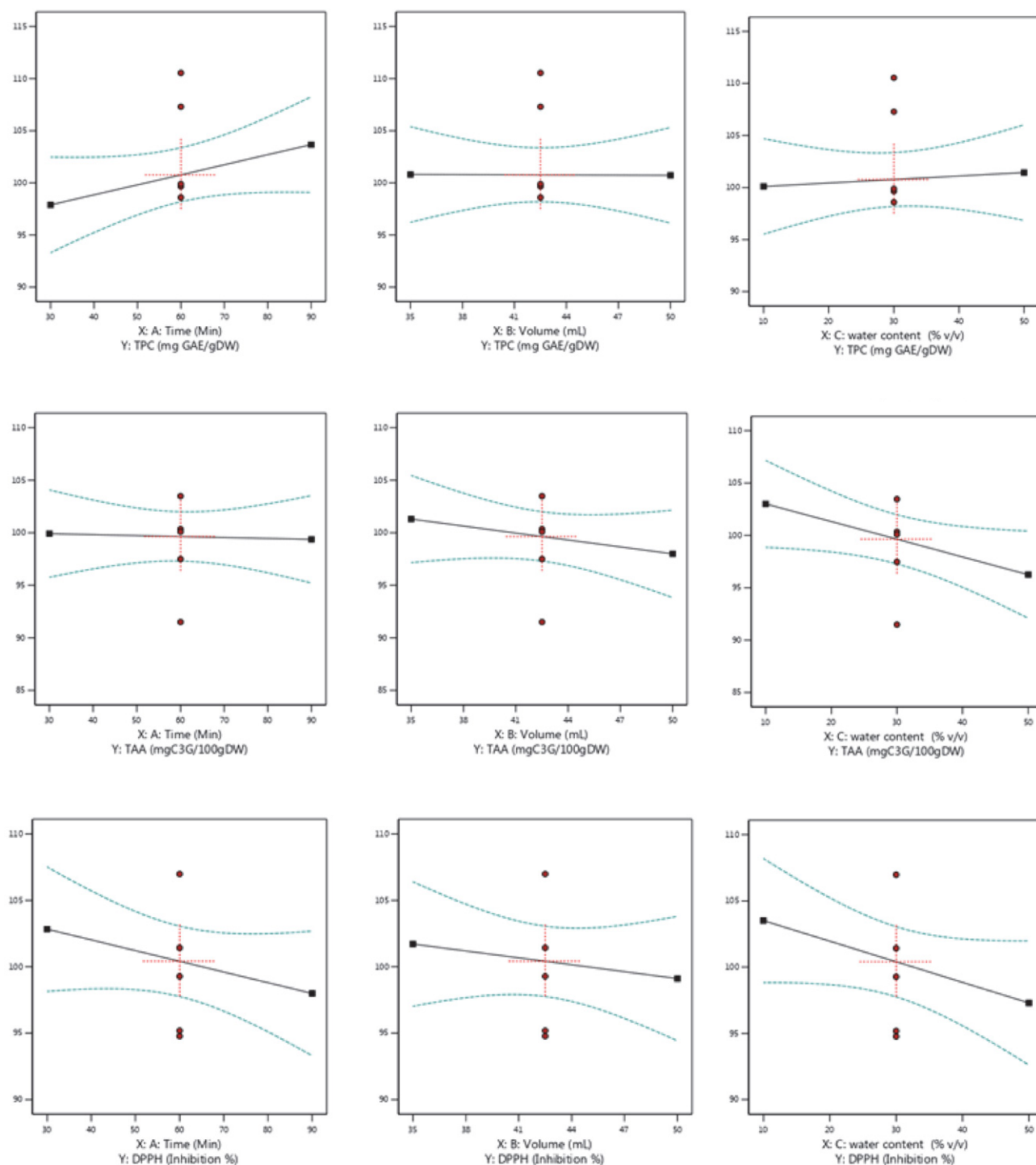


Figure 3. A 2D contour plots and 3D response surface of TPC, TAA, and DPPH as a function of time (min) and solvent volume (mL)





**Figure 4.** The effect of DES extraction parameters (time, solvent volume, water content) on TPC, TAA, and DPPH

models of the Box-Behnken design have been decided to be satisfactory depending on the statistical indicators such as  $p < 0.05$ ,  $R^2 > 0.96$  and adjusted  $R^2 > 0.91$ . We could optimize the bioactive ingredients in the *Rosa canina* L. fruits extract obtained by ultrasonic-assisted extraction as an efficient, economically and applicable approach. On

the other hand, the results of this study can be utilized for further applications of antioxidant phenolic compounds from *Rosa canina* L. fruits in the food, cosmetical, and pharmaceutical industries as well as this study could help in using the same approach for extraction of the bioactive compounds from other plants.



## 5. References

1. G. Angelov, S.S. Boyadzhieva, S.S. Georgieva, *Cent. Eur. J. Chem.*, **2014**, *12*, 502–508. DOI:10.2478/s11532-013-0395-0
2. C. Moldovan, M. Babotă, A. Mocan, L. Menghini, S. Cesa, A. Gavan, C. Sisea, C.D. Vodnar, I.M. Dias, C. Pereira, I.C.F.R. Ferreira, G. Crișana, L. Barros, *Food & Function*, **2021**, *12*, 3939. DOI:10.1039/D0FO02783A
3. A. Bhave, V. Schulzova, H. Chmelarova, L. Mrnka, J. Hajslova, *Journal of food and drug analysis*, **2017**, *25*, 681–690. DOI:10.1016/j.jfda.2016.12.019
4. N. Demir, O. Yildiz, M. Alpaslan, A. A. Hayaloglu, *LWT - Food Science and Technology*, **2014**, *57*, 126–133. DOI:10.1016/j.lwt.2013.12.038
5. S. Alp, S. Ercisli, T. Jurikova, O. Cakir, S. Gozlekci, *Not Bot Horti Agrobo.*, **2016**, *44*, 472–476. DOI:10.15835/nbha44210432
6. N. Koczka, E. Stefanovits-Bányai, A. Ombódi, *Medicines*, **2018**, *5*, 84. DOI:10.3390/medicines5030084
7. M. Polumackanycz, M. Kaszuba, A. Konopacka, U. Marzec-Wróblewska, M. Wesolowski, K. Waleron, A. Bucinski, A. Viapiana, *Molecules*, **2020**, *25*, 5272. DOI:10.3390/molecules25225272
8. M. Liaudanskas, I. Noreikiene, K. Zymone, R. Juodyte, V. Žvikas, V. Janulis, *Antioxidants*, **2021**, *10*, 545. DOI:10.3390/antiox10040545
9. J. C. Clarke, W. C. Tu, O. Levers, A. Bröhl, P. J. Hallett, *Chem. Rev.*, **2018**, *118*, 2, 747–800. DOI:10.1021/acs.chemrev.7b00571
10. B. Tang, H. Zhang, K. H. Row, *Journal of Separation Science*, **2015**, *38*, 1053–1064. DOI:10.1002/jssc.201401347
11. B. Ozturk, C. Parkinson, M. Gonzalez-Miquel, *Separation and Purification Technology*, **2018**, *206*, 1–13. DOI:10.1016/j.seppur.2018.05.052
12. X. Wang, Y. Wu, J. Li, A. Wang, G. Li, X. Ren, W. Yin, *Industrial Crops & Products*, **2020**, *151*, 112442. DOI:10.1016/j.indcrop.2020.112442
13. L. Wu, Z. Chen, S. Li, L. Wang, J. Zhang, *Separation and Purification Technology*, **2021**, *262*, 118339. DOI:10.1016/j.seppur.2021.118339
14. J. M. Silva, E. Silva, R. L. Reis, A. R. C. Duarte, *Sustainable Chemistry and Pharmacy*, **2019**, *14*, 100192. DOI:10.1016/j.scp.2019.100192
15. E. L. Smith, A. P. Abbott, K. S. Ryder, *Chemical Reviews*, **2014**, *114*(21), 11060–11082. DOI:10.1021/cr300162p
16. Z. Ilbay, S. S. ahin, S. I. Kirbaslar, *J Sci Food Agric.*, **2013**, *93*, 2804–2809. DOI:10.1002/jsfa.6104
17. V. L. Singleton, R. Orthofer, R.M. Lamuela-Raventos, *Methods in Enzymology*, **1999**, *299*, 152–178. DOI:10.1016/S0076-6879(99)99017-11
18. H. Koraqi and K. Llugar-Rizani, *Agriculture and Forestry*, **2022**, *68*, 1, 159–171. DOI:10.17707/AgricultForest.68.1.09
19. J. Lee, R. W. Durst, R. E. Wrolstad, *Journal of AOAC INTERNATIONAL*, **2005**, *88*, 5, 1269–1278. DOI:10.1093/jaoac/88.5.1269
20. M. M. Giusti and R. E. Wrolstad, *Current Protocols in Food Analytical Chemistry*, **2001**, F1.2.1–F1.2.13. DOI:10.1002/0471142913.faf0102s00
21. S. Şahin S. and R. Şamli, *Ultrasonics Sonochemistry*, **2013**, *20*, 595–602. DOI:10.1016/j.ultsonch.2012.07.029
22. K. M. Hrnčič, D. Cör, P. Kotnik, Ž. Knez, *Acta Chim. Slov.*, **2019**, *66*, 751–761. DOI:10.17344/acsi.2019.5253
23. L. Su, J. Yin, D. Charles, K. Zhou, J. Moore, L. Yu, *Food Chemistry*, **2007**, *100*, 990–997. DOI:10.1016/j.foodchem.2005.10.058
24. G. Fascella, F. D'Angiolillo, M. M. Mammano, M. Amenta, V. F. Romeo, P. Rapisarda, G. Ballistreri, *Food Chemistry*, **2019**, *289*, 56–64. DOI:10.1016/j.foodchem.2019.02.127
25. M. R. Bozhuyuk, S. Ercisli, N. Karatas, H. Ekiert, H. O. Elan-sary, A. Szopa, *Sustainability*, **2021**, *13*, 14, 8060. DOI:10.3390/su13148060
26. L. Duan, L. L. Dou, L. Guo, P. Li, E. H. Liu, *ACS Sustainable Chem. Eng.*, **2016**, *4*, 2405–2411. DOI:10.1021/acssuschemeng.6b00091
27. E. Kurtulbaş, G. A. Pekel, M. Bilgin, P. D. Makris, S. Şahin, *Biomass Conv. Bioref.*, **2022**, *12*, 351–360. DOI:10.1007/s13399-020-00606-3

## Povzetek

V tej študiji je bila raziskana zelena ekstrakcija bioaktivnih spojin iz plodov šipka (*Rosa canina* L.) in njihovo antioksidativno delovanje. V ta namen je bila uporabljena ultrazvočna ekstrakcija v kombinaciji z globokimi evtektičnimi topili (DES). Posebej zasnovana so bila globoka evtektična topila na osnovi citronske kisline. Uporabljeni so bili donorji vodikove vezi (HBD), kot sta glicerol in etilen glikol, ter akceptor vodikove vezi (HBA), kot je citronska kislina. Po izboru najboljše možnosti DES za ekstrakcijo bioaktivnih sestavin so bili optimalni pogoji ultrazvočne ekstrakcije optimizirani s pomočjo Box-Behnkenovega oblikovanja metodologije odzivne površine (RSM). Skupna vsebnost fenolov (TPC), skupna vsebnost antocianinov (TAA) in antioksidativna aktivnost proti 2,2-difenil-1-pikrilhidrazilu (DPPH) je bila ugotovljena kot 103,37 mg GAE/g DW v DES2, 92,23 mg GAE/g DW v DES1, 3,25 mg C3G/100 g-DW v DES2, 1,31 mg C3G/100 g-DW v DES1 in 101,85 % inhibicija v DES2, 94,32 %. Rezultati študije so pokazali, da je predstavljena ekstrakcija bioaktivnih spojin iz plodov šipka (*Rosa canina* L.) konkurenčno trajnostna, zelena in učinkovita.



Except when otherwise noted, articles in this journal are published under the terms and conditions of the Creative Commons Attribution 4.0 International License

# Syntheses, Characterization and Crystal Structures of Dicyanamide Bridged Polynuclear Copper(II) and Zinc(II) Complexes with Urease Inhibitory Activity

Li Zhang,<sup>1</sup> Yuqing Gu,<sup>1</sup> Xinhui Feng,<sup>1</sup> Ting Yang,<sup>2</sup> Xiaoyan Li,<sup>3</sup> Jing Wang<sup>1</sup> and Zhonglu You<sup>1,\*</sup>

<sup>1</sup> Department of Chemistry, Liaoning Normal University, Dalian 116029, P. R. China

<sup>2</sup> Dalian Institute of Chemical Physics, Chinese Academy of Sciences, Dalian 116023, P.R. China

<sup>3</sup> Zibo Vocational Institute, Zibo 255314, P.R. China

\* Corresponding author: E-mail: youzhonglu@126.com  
Tel.: +8641182156989

Received: 05-16-2022

## Abstract

A pair of structurally similar dicyanamide bridged copper(II) and zinc(II) complexes  $[\text{CuL}(\text{dca})]_n$  (1) and  $[\text{ZnL}(\text{dca})]_n$  (2), were prepared from the fluorine containing Schiff base 5-fluoro-2-(((2-hydroxyethyl)imino)methyl)phenol (HL). The compounds were characterized by physico-chemical methods. Structures of the complexes were confirmed by single crystal X-ray diffraction. The Cu atom in complex 1 is in square pyramidal coordination, whereas the Zn atom in complex 2 is in trigonal bipyramidal coordination. The copper complex has effective *Jack bean* urease inhibitory activity, with  $\text{IC}_{50}$  value of  $0.14 \pm 0.12 \mu\text{mol L}^{-1}$ .

**Keywords:** Schiff base; copper and zinc complexes; crystal structure; urease inhibition

## 1. Introduction

Schiff bases derived from salicylaldehyde and its analogues with various primary amines represent indispensable ligands in coordination chemistry because of their diversified coordination modes with a large number of inorganic salts.<sup>1</sup> Schiff bases as interesting chemotherapeutic agents have received considerable attention in recent years. Schiff base complexes have interesting pharmaceutical applications such as antifungal, antitumor, antibacterial and bio-modeling techniques.<sup>2</sup>

Urease (amidohydrolase; EC 3.5.1.5) is a nickel-containing enzyme that catalyzes the hydrolysis of urea to  $\text{NH}_3$  and  $\text{CO}_2$ . The catalyzed reaction rate is about  $10^{14}$  times faster than the uncatalyzed. Urease enzyme is widely found in fungi, bacteria and plants.<sup>3</sup> The high efficiency of urease increased the hydrolysis of urea into  $\text{NH}_3$ , which leads to severe toxicity in air and disgusting economic damages.<sup>4</sup> In human, urease may produce several health concerns including hepatic coma, pyelonephritis, gastric and peptic ulcer.<sup>5</sup> In recent years, various kinds of

urease inhibitors such as dithiobisacetamides, thioureas, thiosemicarbazides, hydroxamic acids are reported in the fields of medicine.<sup>6</sup> However, most of them are not applicable due to the low efficiency and side effects. Therefore, it is of great interest to explore new urease inhibitors. Some Schiff bases have been reported to have urease inhibitory activities.<sup>7</sup> Our research group has pioneered the work on urease inhibitors with complexes derived from Schiff bases, and found that some copper, nickel, and zinc complexes have effective activities.<sup>8</sup> Schiff bases with halide groups are reported to have enhanced urease inhibitory activity.<sup>9</sup> Xiao and coworkers reported that the introduction of fluorine atom in the hydroxamic acid compounds can increase their urease inhibitory activities.<sup>10</sup> In addition, dicyanamide anion is an interesting ligand in coordination chemistry, which can lead to the formation of metal complexes with versatile structures.<sup>11</sup> In order to construct new structures of dicyanamide bridged complexes, and explore new urease inhibitors, two copper(II) and zinc(II) complexes,  $[\text{CuL}(\text{dca})]_n$  (1) and  $[\text{ZnL}(\text{dca})]_n$  (2), were prepared from

the fluorine containing Schiff base 5-fluoro-2-(((2-hydroxyethyl)imino)methyl)phenol (HL).

## 2. Experimental

### 2.1. Materials and Measurements

4-Fluorosalicylaldehyde and 2-aminoethanol were purchased from TCI Inc. (Japan). Other reagents and solvents were obtained from Xiya Reagent Company of China. *Jack bean* urease was purchased from Sigma-Aldrich. Elemental analyses were performed on a Perkin-Elmer 240C elemental analyzer. IR spectra were recorded on a Jasco FT/IR-4000 spectrometer as KBr pellets in the 4000–400  $\text{cm}^{-1}$  region. UV-Vis spectra were recorded on a Perkin-Elmer Lambda 900 spectrometer. Conductivity measurements were performed using a Metrohm 712 conductometer at 25 °C. The urease inhibitory activity was measured on a Bio-Tek Synergy HT microplate reader. Single crystal structures were determined by Bruker D8 Venture single crystal diffraction.

### 2.2. Synthesis of HL and the Complexes

#### 2.2.1. 5-Fluoro-2-(((2-hydroxyethyl)imino)methyl)phenol (HL)

4-Fluorosalicylaldehyde (0.010 mol, 1.4 g) and 2-aminoethanol (0.010 mol, 0.61 g) were mixed in methanol (30 mL). The mixture was stirred for 30 min at reflux. The solvent was evaporated by distillation to give yellow solid, which was recrystallized from ethanol to give yellow crystalline product. The product was washed three times with cold ethanol and dried in air. Yield: 1.5 g (82%). Characteristic IR data (KBr,  $\text{cm}^{-1}$ ): 3372 (OH), 1635 (C=N). UV-Vis data (methanol,  $\lambda/\text{nm}$ ): 230, 335. Anal. Calcd for  $\text{C}_9\text{H}_{10}\text{FNO}_2$ : C, 59.01; H, 5.50; N, 7.65. Found: C, 58.87; H, 5.58; N, 7.73%.

#### 2.2.2. *catena*-( $\mu_2$ -Dicyanamide)(5-fluoro-2-(((2-hydroxyethyl)imino)methyl)phenolate)copper(II) (1)

The Schiff base HL (1.0 mmol, 0.18 g) was dissolved in methanol (20 mL), to which was added dropwise  $\text{Cu}(\text{NO}_3)_2 \cdot 3\text{H}_2\text{O}$  (1.0 mmol, 0.24 g) and  $\text{NaN}(\text{CN})_2$  (1.0 mmol, 0.089 g) dissolved in methanol (20 mL). The mixture was stirred for 20 min at room temperature. The filtrate was kept in air for a few days, to form deep blue crystals suitable for single crystal X-ray diffraction. The isolated crystals were washed three times with cold methanol and dried in air. Yield: 0.17 g (55%). Characteristic IR data (KBr,  $\text{cm}^{-1}$ ): 3438 (OH), 2304, 2243, 2175 ( $\text{N}(\text{CN})_2$ ), 1648 (C=N). UV-Vis data (methanol,  $\lambda/\text{nm}$ ): 270, 352. Anal. Calcd for  $\text{C}_{11}\text{H}_9\text{CuFN}_4\text{O}_2$ : C, 42.38; H, 2.91; N, 17.97. Found: C, 42.51; H, 3.02; N, 17.83%.  $\Lambda_{\text{M}}$  ( $10^{-3} \text{ mol L}^{-1}$  in methanol): 35  $\Omega^{-1} \text{ cm}^2 \text{ mol}^{-1}$ .

#### 2.2.3. *catena*-( $\mu_2$ -Dicyanamide)(5-fluoro-2-(((2-hydroxyethyl)imino)methyl)phenolate)zinc(II) (2)

The zinc complex was prepared with the same method as described for the copper complex, but with  $\text{Cu}(\text{NO}_3)_2 \cdot 3\text{H}_2\text{O}$  replaced with  $\text{Zn}(\text{NO}_3)_2 \cdot 6\text{H}_2\text{O}$  (1.0 mmol, 0.30 g). Colorless block shaped crystals suitable for single crystal X-ray diffraction were obtained after 5 days. Yield: 0.20 g (64%). Characteristic IR data (KBr,  $\text{cm}^{-1}$ ): 3420 (OH), 2341, 2273, 2199 ( $\text{N}(\text{CN})_2$ ), 1643 (C=N). UV-Vis data (methanol,  $\lambda/\text{nm}$ ): 272, 345. Anal. Calcd for  $\text{C}_{11}\text{H}_9\text{FN}_4\text{O}_2\text{Zn}$ : C, 42.13; H, 2.89; N, 17.87. Found: C, 42.02; H, 2.97; N, 17.75%.  $\Lambda_{\text{M}}$  ( $10^{-3} \text{ mol L}^{-1}$  in methanol): 28  $\Omega^{-1} \text{ cm}^2 \text{ mol}^{-1}$ .

### 2.3. X-ray Crystallography

Diffraction intensities for the complexes were collected at 298(2) K using a Bruker D8 Venture diffractometer with MoK $\alpha$  radiation ( $\lambda = 0.71073 \text{ \AA}$ ). The collected data were reduced with SAINT,<sup>12</sup> and multi-scan absorption correction was performed using SADABS.<sup>13</sup> Structures of the complexes were solved by direct methods and refined against  $F^2$  by full-matrix least-squares method using SHELXTL.<sup>14</sup> All of the non-hydrogen atoms were refined anisotropically. The hydroxyl H atoms of the Schiff base ligands in the complexes were located from difference Fourier maps and refined isotropically, with O–H distances restrained to 0.85(1)  $\text{\AA}$ . The remaining hydrogen atoms were placed in calculated positions and constrained to ride on their parent atoms. Crystallographic data for the complexes are summarized in Table 1.

Table 1 Crystal data for the complexes

	1	2
Formula	$\text{C}_{11}\text{H}_9\text{CuFN}_4\text{O}_2$	$\text{C}_{11}\text{H}_9\text{FN}_4\text{O}_2\text{Zn}$
FW	311.76	313.59
Crystal system	Monoclinic	Monoclinic
Space group	$P2_1/c$	$P2_1/n$
<i>a</i> ( $\text{\AA}$ )	7.6028(11)	7.5125(9)
<i>b</i> ( $\text{\AA}$ )	15.340(2)	10.8296(12)
<i>c</i> ( $\text{\AA}$ )	10.6785(15)	16.1164(19)
$\alpha$ ( $^\circ$ )	90	90
$\beta$ ( $^\circ$ )	91.869(2)	94.623(2)
$\gamma$ ( $^\circ$ )	90	90
<i>V</i> ( $\text{\AA}^3$ )	1244.7(3)	1306.9(3)
<i>Z</i>	4	4
<i>T</i> (K)	298(2)	298(2)
$\mu$ (MoK $\alpha$ ) ( $\text{cm}^{-1}$ )	1.770	1.894
Reflections/parameters	7343/175	6740/175
Unique reflections	2321	2425
Observed reflections	2055	2016
[ $I > 2\sigma(I)$ ]		
Restraints	1	1
Goodness of fit on $F^2$	1.059	1.051
$R_1$ , $wR_2$ [ $I > 2\sigma(I)$ ]	0.0356, 0.0952	0.0309, 0.0826
$R_1$ , $wR_2$ (all data)	0.0405, 0.0985	0.0393, 0.0870

## 2. 4. Urease Inhibitory Activity Assay

The measurement of urease inhibitory activity was carried out according to the literature method.<sup>15</sup> The compounds (0.100 mmol) and the reference drug acetohydroxamic acid, as well as copper and zinc perchlorate were first dissolved by 5.0 mL DMSO, then diluted to 1.0 L by distilled water. The assay mixture containing 75  $\mu$ L of *Jack bean* urease and 75  $\mu$ L of tested compounds with various concentrations (100  $\mu$ mol L<sup>-1</sup>, 50  $\mu$ mol L<sup>-1</sup>, 25  $\mu$ mol L<sup>-1</sup>, 12.5  $\mu$ mol L<sup>-1</sup>, 6.25  $\mu$ mol L<sup>-1</sup>, 3.12  $\mu$ mol L<sup>-1</sup>, 1.56  $\mu$ mol L<sup>-1</sup>, 0.78  $\mu$ mol L<sup>-1</sup>) pre-incubated for 15 min on a 96-well assay plate. Then 75  $\mu$ L of phosphate buffer at pH 6.8 containing phenol red (0.18 mmol L<sup>-1</sup>) and urea (400 mmol L<sup>-1</sup>) were added and incubated at room temperature. The reaction time required for enough ammonium carbonate to form to raise the pH phosphate buffer from 6.8 to 7.7 was measured by micro-plate reader (560 nm) with end-point being determined by the color change of phenol-red indicator.

## 3. Results and Discussion

### 3. 1. Chemistry

The Schiff base HL was facile synthesized from 4-fluorosalicylaldehyde with 2-aminoethanol in methanol. The complexes **1** and **2** (Scheme 1) were synthesized according to the similar method from the Schiff base, sodium dicyanamide with copper nitrate and zinc nitrate, respectively, in methanol. If copper or zinc nitrate was replaced with chloride or bromide salt, the same structures for the complexes can be obtained. Molar conductivities of the complexes in methanol are within the normal values 20–40  $\Omega^{-1}$  cm<sup>2</sup> mol<sup>-1</sup>, indicate their non-electrolytic nature.<sup>16</sup>

### 3. 2. Structure Description of the Complexes

#### Complex 1

Molecular structure of the polymeric copper complex **1** is shown in Figure 1. Selected bond lengths and

angles are given in Table 2. The smallest repeat unit of the complex contains [CuL(N(CN)<sub>2</sub>)], which is bridged by dicyanamide ligands to form one dimensional chain structure. The Cu atom is in square pyramidal geometry, with the phenolate oxygen (O1), imino nitrogen (N1) and hydroxyl oxygen (O2) atoms of the Schiff base ligand, and the N2 atom of the dicyanamide ligand located at the basal plane, and with the N4A (symmetry code for A:  $-1 + x, y, z$ ) atom of the symmetry related dicyanamide ligand located at the apical position. The Cu atom deviates from the least-squares plane defined by the four basal donor atoms by 0.250(1) Å. The coordination geometry can be defined as distorted square pyramid because the structural index  $\tau$  value is 0.30.<sup>17</sup> The bond lengths of the Cu–O (1.9271(19)–2.035(2) Å) and Cu–N (1.937(2)–1.977(2) Å) in the basal plane of the complex are comparable to those observed in the copper(II) complexes with Schiff base ligands.<sup>18</sup>

In the crystal structure of complex **1**, the [CuL] units are linked by dicyanamide ligands, to form one dimensional chain structure along the *a* axis. The chains are

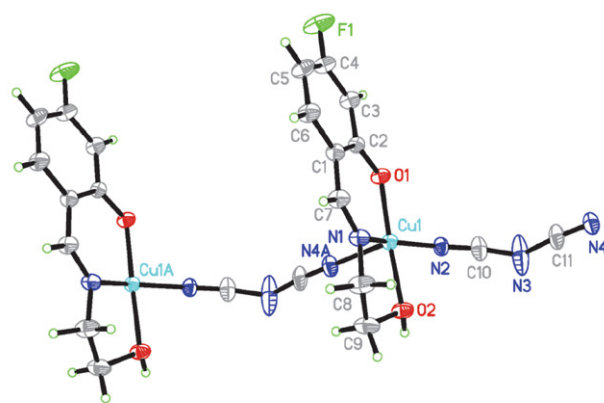
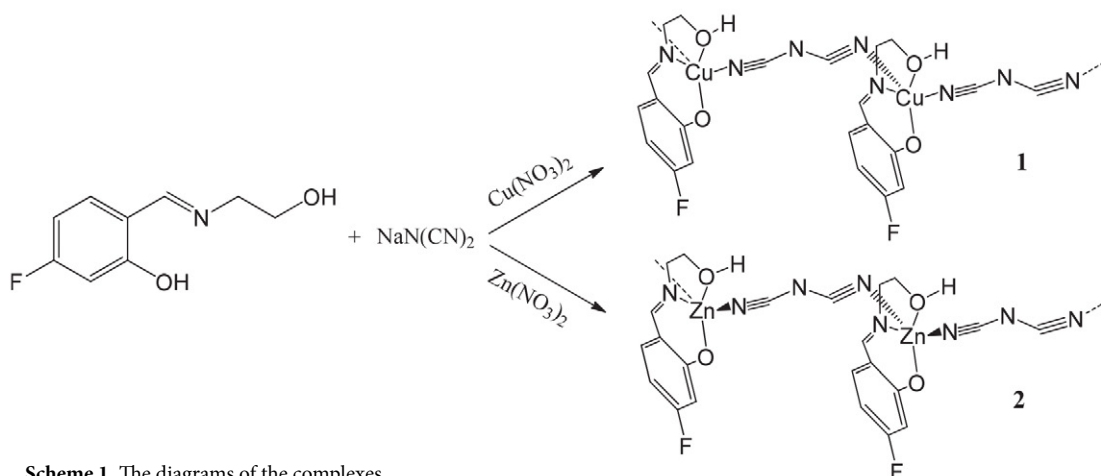


**Figure 1.** Molecular structure of **1**, showing the atom-numbering scheme. Displacement ellipsoids for non-hydrogen atoms are drawn at 30% probability level. Atoms labeled with the suffix A are related to the symmetry operation  $-1 + x, y, z$ .



**Scheme 1.** The diagrams of the complexes.



further linked through intermolecular hydrogen bonds of O–H...O hydrogen bonds ( $O2-H2 = 0.85(1)$  Å,  $H2...O1^i = 1.90(1)$  Å,  $O2...O1^i = 2.734(3)$  Å,  $O2-H2...O1^i = 170(4)^\circ$ , symmetry code for  $i$ :  $\frac{1}{2} - x, -\frac{1}{2} + y, \frac{1}{2} - z$ ), to form two-dimensional network along the  $ac$  plane (Figures 2 and 3).

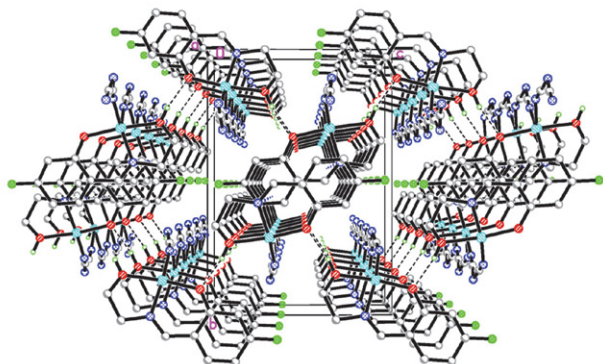


**Figure 2.** Molecular packing diagram of **1**, viewed along the  $a$  axis. Hydrogen bonds are shown as dashed lines.

**Table 2** Selected bond lengths (Å) and angles ( $^\circ$ ) for the complexes

	<b>1</b>	<b>2</b>
M1–N1	1.937(2)	2.002(2)
M1–N2	1.977(2)	2.016(2)
M1–O1	1.927(2)	1.988(2)
M1–O2	2.035(2)	2.246(2)
M1–N4A	2.249(3)	1.993(2)
O1–M1–N1	93.95(9)	92.26(8)
O1–M1–N2	92.28(9)	96.06(10)
N1–M1–N2	155.31(11)	120.66(10)
O1–M1–O2	173.23(8)	169.53(8)
N1–M1–O2	81.51(9)	77.28(9)
N2–M1–O2	89.87(10)	89.21(10)
O1–M1–N4A	95.48(10)	98.15(10)
N1–M1–N4A	101.08(11)	128.85(9)
N2–M1–N4A	102.06(10)	107.86(10)
O2–M1–N4A	90.34(10)	88.78(10)

M = Cu for **1**, Zn for **2**.

## Complex 2

Molecular structure of the polymeric zinc complex **2** is shown in Figure 4. The smallest repeat unit of the complex contains  $[ZnL(N(CN)_2)_2]$ , which is bridged by dicyanamide ligands to form one dimensional chain structure. The Zn atom is in trigonal bipyramidal geometry, with the imino nitrogen (N1) atom of the Schiff base ligand, and two nitrogen (N2 and N4A, symmetry code for A:  $-1 + x, y, z$ ) atoms from two dicyanamide ligands located at the equatorial plane, and with the phenolate oxygen (O1) and hydroxyl oxygen (O2) atoms of the Schiff base ligand located at the axial positions. The Zn atom deviates from the

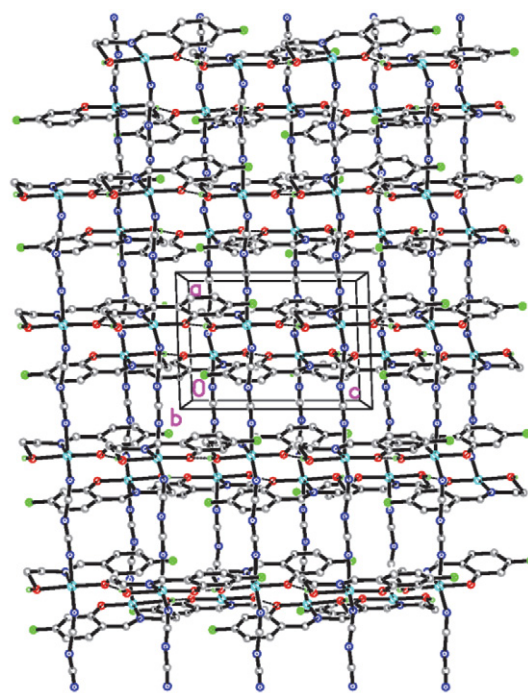


**Figure 3.** Molecular packing diagram of **1**, viewed along the  $b$  axis. Hydrogen bonds are shown as dashed lines.

least-squares plane defined by the three equatorial donor atoms by  $0.187(1)$  Å. The coordination geometry can be defined as distorted trigonal bipyramid because the structural index  $\tau$  value is 0.68.<sup>17</sup> The bond lengths of the Zn–O ( $1.988(2)$ – $2.247(2)$  Å) and Zn–N ( $1.993(2)$ – $2.016(2)$  Å) of the complex are comparable to those observed in the zinc(II) complexes with Schiff base ligands.<sup>19</sup>

In the crystal structure of complex **1**, the  $[ZnL]$  units are linked by dicyanamide ligands, to form one dimensional chain structure along the  $a$  axis. The chains are

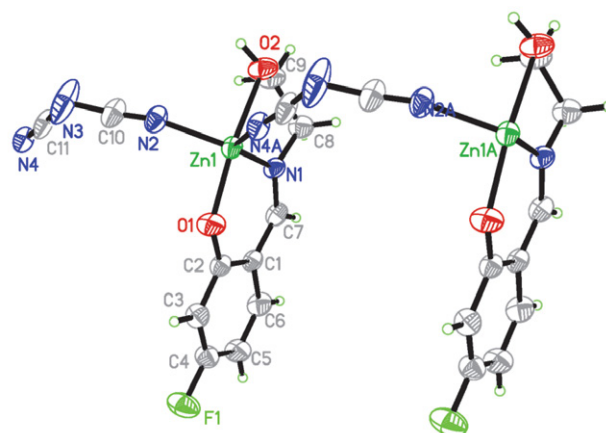


**Figure 4.** Molecular structure of **2**, showing the atom-numbering scheme. Displacement ellipsoids for non-hydrogen atoms are drawn at 30% probability level. Atoms labeled with the suffix A are related to the symmetry operation  $-1 + x, y, z$ .

further linked through intermolecular hydrogen bonds of O–H...O hydrogen bonds ( $O2-H2 = 0.85(1) \text{ \AA}$ ,  $H2...O1^i = 1.91(1) \text{ \AA}$ ,  $O2...O1^i = 2.714(3) \text{ \AA}$ ,  $O2-H2...O1^i = 161(4)^\circ$ , symmetry code for  $i$ :  $-x, -1-y, -z$ ) along the  $b$  axis, to form two-dimensional network along the  $ab$  plane (Figures 5 and 6).

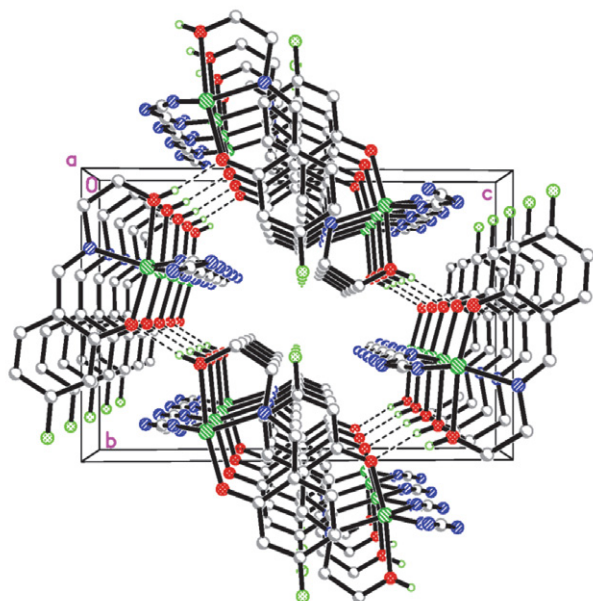


**Figure 5.** Molecular packing diagram of **2**, viewed along the  $a$  axis. Hydrogen bonds are shown as dashed lines.

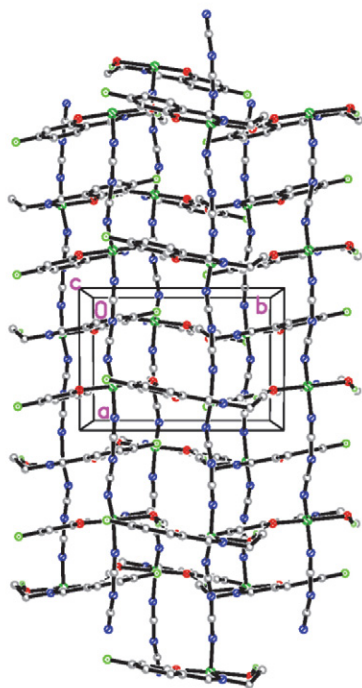


**Figure 6.** Molecular packing diagram of **2**, viewed along the  $c$  axis. Hydrogen bonds are shown as dashed lines.

### 3. 3. IR and UV-Vis Spectra

The weak bands centered at  $3438$  and  $3420 \text{ cm}^{-1}$  in complexes **1** and **2**, respectively, are assigned to  $\nu(O-H)$ . The intense absorption bands at  $2304$ ,  $2243$  and  $2175 \text{ cm}^{-1}$  in **1**, and  $2341$ ,  $2273$  and  $2199 \text{ cm}^{-1}$  in **2**, are assigned to the stretching vibrations of dicyanamide ligands.<sup>20</sup> Strong absorptions at  $1648 \text{ cm}^{-1}$  in **1** and  $1643 \text{ cm}^{-1}$  in **2** are assigned to azomethine groups,  $\nu(C=N)$ .<sup>20b</sup> The phenolic  $\nu(Ar-O)$  appear at  $1288 \text{ cm}^{-1}$  in **1** and  $1301 \text{ cm}^{-1}$  in **2**. The weak bands in the range of  $400\text{--}600 \text{ cm}^{-1}$  for the complexes can be assigned to  $\nu(M-O)$ .<sup>21</sup>

The electronic spectra of the complexes were determined with methanol as solvent. The spectra of the complexes reveal intense absorption bands at  $270\text{--}272 \text{ nm}$  are assigned to  $n\text{--}\pi^*$  transition of the azomethine groups. The bands observed at  $340\text{--}360 \text{ nm}$  in the spectra of the complexes are assigned to ligand to metal charge transfer transitions.<sup>22</sup>

### 3. 4. Urease Inhibitory Activity Assay

The results of the inhibition assays against the urease for the synthetic compounds are listed in Table 3. The copper complex has good inhibitory activity on urease with  $IC_{50}$  value of  $0.14 \pm 0.12 \text{ }\mu\text{mol L}^{-1}$ , whereas the zinc complex has no activity. The copper complex show better activity than the reference drug acetohydroxamic acid ( $IC_{50} = 37.2 \pm 4.0 \text{ }\mu\text{mol L}^{-1}$ ). Both the copper and zinc complexes have better activities than copper and zinc perchlorate. Thus, the copper complex would be a potential urease inhibitor that deserves further study on the treatment of diseases like hepatic coma, pyelonephritis, gastric and peptic ulcer, as well as on the application in the nitrogen containing fertilizer.

**Table 3** Inhibition of urease by the tested materials

Tested materials	Percentage Inhibition rate <sup>#</sup>	$IC_{50}$ ( $\mu\text{mol L}^{-1}$ )
HL	–	> 100
<b>1</b>	$99 \pm 2.1$	$0.14 \pm 0.12$
<b>2</b>	$33 \pm 1.8$	$3.4 \pm 1.6$
Copper perchlorate	$87.5 \pm 2.6$	$8.8 \pm 1.4$
Zinc perchlorate	–	> 100
Acetohydroxamic acid	$85.5 \pm 3.9$	$28.1 \pm 3.6$

<sup>#</sup> The concentration of the tested material is  $100 \text{ }\mu\text{mol L}^{-1}$ .

– indicates no activity.

## 4. Conclusion

This work reports the syntheses, characterization and crystal structures of two new dicyanamide bridged copper and zinc complexes with fluorine containing Schiff base 5-fluoro-2-(((2-hydroxyethyl)imino)methyl)phenol.



The copper complex has effective urease inhibitory activity. The results indicated that the copper complex can be further optimized and developed as a prospective lead urease inhibitor.

## Supplementary data

CCDC 2170031 (1) and 2170032 (2) contain the supplementary crystallographic data for this paper. These data can be obtained free of charge via <http://www.ccdc.cam.ac.uk/conts/retrieving.html>, or from the Cambridge Crystallographic Data Centre, 12 Union Road, Cambridge CB2 1EZ, UK; fax: (+44) 1223-336-033; or e-mail: [deposit@ccdc.cam.ac.uk](mailto:deposit@ccdc.cam.ac.uk).

## Acknowledgments

This work was financially supported by the Education Office of Liaoning Province (Project No. LJKZ0984).

## 5. References

- (a) H. Kargar, P. Forootan, M. Fallah-Mehrjardi, R. Behjatmanesh-Ardakani, H. A. Rudbari, K. S. Munawar, M. Ashfaq, M. N. Tahir, *Inorg. Chim. Acta* **2021**, 523, 120414; DOI:10.1016/j.ica.2021.120414
- (b) S. H. Sumrra, W. Zafar, S. A. Malik, K. Mahmood, S. S. Shafqat, S. Arif, *Acta Chim. Slov.* **2022**, 69, 200–216; DOI:10.17344/acsi.2022.7182
- (c) Y. Yuan, X.-K. Lu, G.-Q. Zhou, X.-Y. Qiu, *Acta Chim. Slov.* **2021**, 68, 1008–1015. DOI:10.17344/acsi.2021.7070
- (a) S. U. Parsekar, K. Paliwal, P. Haldar, P. K. S. Antharjanam, M. Kumar, *ACS Omega* **2022**, 7, 2881–2896; DOI:10.1021/acsomega.1c05750
- (b) H. Kargar, M. Fallah-Mehrjardi, M. Ashfaq, K. S. Munawar, M. N. Tahir, R. Behjatmanesh-Ardakani, H. A. Rudbari, A. A. Ardakani, S. Sedighi-Khavidak, *J. Coord. Chem.* **2021**, 74, 2720–2740; DOI:10.1080/00958972.2021.1990271
- (c) L.-W. Xue, X. Fu, G.-Q. Zhao, Q.-B. Li, *Acta Chim. Slov.* **2021**, 68, 17–24. DOI:10.17344/acsi.2020.5817
- (a) G. Mohiuddin, K. M. Khan, U. Salar, Kanwal, M. A. Lodhi, A. Wadood, M. Riaz, S. Perveen, *Bioorg. Chem.* **2019**, 83, 29–46; DOI:10.1016/j.bioorg.2018.10.021
- (b) W.-Q. Song, M.-L. Liu, S.-Y. Li, Z.-P. Xiao, *Curr. Top. Med. Chem.* **2022**, 22, 95–107; DOI:10.2174/1568026621666211129095441
- (c) Q. Liu, W.-W. Ni, Z. Li, C.-F. Bai, D.-D. Tan, C.-J. Pu, D. Zhou, Q.-P. Tian, N. Luo, K.-L. Tan, L. Dai, Y. Yan, Y. Pei, X.-H. Li, Z.-P. Xiao, H.-L. Zhu, *Eur. J. Pharm. Sci.* **2018**, 121, 293–300. DOI:10.1016/j.ejps.2018.05.029
- (a) F. S. Carlos, R. J. Kunde, R. O. de Sousa, C. Weinert, A. D. Ulguim, F. Viero, I. Rossi, M. P. Buchain, C. L. Boechat, F. A. D. Camargo, *Nutr. Cycl. Agroecosys.* **2022**. DOI:10.1007/s10705-022-10203-7
- (b) T. Lan, X. Q. He, Q. Wang, O. P. Deng, W. Zhou, L. Luo, G. D. Chen, J. Zeng, S. Yuan, M. Zeng, H. H. Xiao, X. S. Gao, *Appl. Soil Ecol.* **2022**, 174, 104412; DOI:10.1016/j.apsoil.2022.104412
- (c) L. A. R. Ferreira, S. R. Silva, O. T. Kolln, *Inter. J. Plant Prod.* **2022**. DOI:10.1007/s42106-022-00191-7
- (a) Q. Liu, W.-K. Shi, S.-Z. Ren, W.-W. Ni, W.-Y. Li, H.-M. Chen, P. Liu, J. Yuan, X.-S. He, J.-J. Liu, P. Cao, P.-Z. Yang, Z.-P. Xiao, H.-L. Zhu, *Eur. J. Med. Chem.* **2018**, 156, 126–136; DOI:10.1016/j.ejmech.2018.06.065
- (b) W.-W. Ni, Q. Liu, S.-Z. Ren, W.-Y. Li, L.-L. Yi, H. Jing, L.-X. Sheng, Q. Wan, P.-F. Zhong, H.-L. Fang, H. Ouyang, Z.-P. Xiao, H.-L. Zhu, *Bioorg. Med. Chem.* **2018**, 26, 4145–4152; DOI:10.1016/j.bmc.2018.07.003
- (c) W.-K. Shi, R.-C. Deng, P.-F. Wang, Q.-Q. Yue, Q. Liu, K.-L. Ding, M.-H. Yang, H.-Y. Zhang, S.-H. Gong, M. Deng, W.-R. Liu, Q.-J. Feng, Z.-P. Xiao, H.-L. Zhu, *Bioorg. Med. Chem.* **2016**, 24, 4519–4527; DOI:10.1016/j.bmc.2016.07.052
- (d) A. F. Uberti, N. Callai-Silva, M. V. C. Grahl, A. R. Piovesan, E. G. Nachtigall, C. R. G. Furini, C. R. Carlini, *Inter. J. Mol. Sci.* **2022**, 23, 3091. DOI:10.3390/ijms23063091
- (a) M.-L. Liu, W.-Y. Li, H.-L. Fang, Y.-X. Ye, S.-Y. Li, W.-Q. Song, Z.-P. Xiao, H. Ouyang, H.-L. Zhu, *ChemMedChem* **2022**, 17, e202100618; DOI:10.2174/1573406416999200818152440
- (b) W.-W. Ni, H.-L. Fang, Y.-X. Ye, W.-Y. Li, L. Liu, Z.-J. Fu, Dawalamu, W.-Y. Zhu, K. Li, F. Li, X. Zou, H. Ouyang, Z.-P. Xiao, H.-L. Zhu, *Med. Chem.* **2021**, 17, 1046–1059; DOI:10.2174/1573406416999200818152440
- (c) W.-Y. Li, W.-W. Ni, Y.-X. Ye, H.-L. Fang, X.-M. Pan, J.-L. He, T.-L. Zhou, J. Yi, S.-S. Liu, M. Zhou, Z.-P. Xiao, H.-L. Zhu, *J. Enzyme Inhib. Med. Chem.* **2020**, 35, 404–413; DOI:10.1080/14756366.2019.1706503
- (d) W.-W. Ni, H.-L. Fang, Y.-X. Ye, W.-Y. Li, C.-P. Yuan, D.-D. Li, S.-J. Mao, S.-E. Li, Q.-H. Zhu, H. Ouyang, Z.-P. Xiao, H.-L. Zhu, *Future Med. Chem.* **2020**, 12, 1633–1645; DOI:10.4155/fmc-2020-0048
- (e) Z.-P. Xiao, W.-K. Shi, P.-F. Wang, W. Wei, X.-T. Zeng, J.-R. Zhang, N. Zhu, M. Peng, B. Peng, X.-Y. Lin, H. Ouyang, X.-C. Peng, G.-C. Wang, H.-L. Zhu, *Bioorg. Med. Chem.* **2015**, 23, 4508–4513; DOI:10.1016/j.bmc.2015.06.014
- (f) T.-R. Wang, Q.-C. Zhou, J.-L. Ren, M.-J. Zhu, R.-M. Xie, G.-H. Sheng, *J. Struct. Chem.* **2018**, 59, 1674–1677; DOI:10.1134/S0022476618070211
- (g) Y. Wang, *J. Struct. Chem.* **2021**, 62, 1667–1677; DOI:10.1134/S0022476621110020
- (h) X.-F. Chen, C.-F. Wang, S. Kong, C. Li, X. Zhou, C.-Y. Zhang, G.-H. Sheng, H.-L. Zhu, *J. Struct. Chem.* **2017**, 58, 797–803. DOI:10.1134/S0022476617040229
- (a) S. Han, Y. Wang, *Acta Chim. Slov.* **2021**, 68, 961–969; DOI:10.17344/acsi.2021.6965
- (b) A. Barakat, S. M. Soliman, M. Ali, A. Elmaghany, A. M. Al-Majid, S. Yousuf, Z. Ul-Haq, M. I. Choudhary, A. El-Faham, *Inorg. Chim. Acta* **2020**, 503, 119405; DOI:10.1016/j.ica.2019.119405
- (c) M. Ikram, S. Rehman, M. N. Akhtar, F. Subhan, S. Aslam, *Pharm. Chem. J.* **2020**, 54, 469–477. DOI:10.1007/s11094-020-02224-9

8. (a) J. Q. Wang, Y. Y. Luo, Y. X. Zhang, Y. Chen, F. Gao, Y. Ma, D. M. Xian, Z. L. You, *J. Coord. Chem.* **2021**, 74, 1028–1038; DOI:10.1080/00958972.2020.1861603
- (b) F. Niu, K. X. Yan, L. H. Pang, D. Qu, X. L. Zhao, Z. L. You, *Inorg. Chim. Acta* **2015**, 435, 299–304; DOI:10.1016/j.ica.2015.07.014
- (c) Z. L. You, M. Y. Liu, C. F. Wang, G. H. Sheng, X. L. Zhao, D. Qu, F. Niu, *RSC Advances* **2016**, 6, 16679–16690; DOI:10.1039/C6RA00500D
- (d) C. L. Jing, C. F. Wang, K. Yan, K. D. Zhao, G. H. Sheng, D. Qu, F. Niu, H. L. Zhu, Z. L. You, *Bioorg. Med. Chem.* **2016**, 24, 270–276; DOI:10.1016/j.bmc.2015.12.013
- (e) M. M. Duan, Y. M. Li, L. Y. Xu, H. L. Yang, F. W. Luo, Y. X. Guan, B. T. Zhang, C. L. Jing, Z. L. You, *Inorg. Chem. Commun.* **2019**, 100, 27–31; DOI:10.1016/j.inoche.2018.12.009
- (f) Y. M. Li, L. Y. Xu, M. M. Duan, B. T. Zhang, Y. H. Wang, Y. X. Guan, J. H. Wu, C. L. Jing, Z. L. You, *Polyhedron* **2019**, 166, 146–152; DOI:10.1016/j.poly.2019.03.051
- (g) Z.-L. You, D.-H. Shi, J.-C. Zhang, Y.-P. Ma, C. Wang, K. Li, *Inorg. Chim. Acta* **2011**, 384, 54–61. DOI:10.1016/j.ica.2011.11.039
9. Y. Luo, J. Wang, B. Zhang, Y. Guan, T. Yang, X. Li, L. Xu, J. Wang, Z. You, *J. Coord. Chem.* **2020**, 73, 1765–1777. DOI:10.1080/00958972.2020.1795645
10. Z.-P. Xiao, Z.-Y. Peng, J.-J. Dong, R.-C. Deng, X.-D. Wang, H. Ouyang, P. Yang, J. He, Y.-F. Wang, M. Zhu, X.-C. Peng, W.-X. Peng, H.-L. Zhu, *Eur. J. Med. Chem.* **2013**, 68, 212–221. DOI:10.1016/j.ejmech.2013.07.047
11. (a) H. Ogawa, K. Mori, K. Murashima, S. Karasawa, N. Koga, *Inorg. Chem.* **2016**, 55, 717–728; DOI:10.1021/acs.inorgchem.5b02159
- (b) J. Zhang, A.-H. Li, B.-L. Liu, R.-J. Tao, *Inorg. Chem. Commun.* **2013**, 35, 333–336; DOI:10.1016/j.inoche.2013.07.010
- (c) D. Mal, R. Sen, C. Adhikary, Y. Miyashita, K. I. Okamoto, A. Bhattacharjee, P. Gutlich, S. Koner, *J. Coord. Chem.* **2008**, 61, 3486–3492. DOI:10.1080/00958970802072773
12. Bruker, SMART and SAINT, Bruker AXS Inc., Madison, **2002**.
13. G. M. Sheldrick, SADABS, University of Göttingen, Germany, **1996**.
14. G. M. Sheldrick, *Acta Crystallogr.* **2015**, C71, 3–8.
15. W.-J. Mao, P.-C. Lv, L. Shi, H.-Q. Li, H.-L. Zhu, *Bioorg. Med. Chem.* **2009**, 17, 7531–7536. DOI:10.1016/j.bmc.2009.09.018
16. W. J. Geary, *Coord. Chem. Rev.* **1971**, 7, 81–122. DOI:10.1016/S0010-8545(00)80009-0
17. A. W. Addison, T. N. Rao, J. Reedijk, J. van Rijn, G. C. Verschoor, *J. Chem. Soc. Dalton Trans.* **1984**, 1349–1356. DOI:10.1039/DT9840001349
18. (a) M. Maiti, D. Sadhukhan, S. Thakurta, S. Roy, G. Pilet, R. J. Butcher, A. Nonat, L. J. Charbonniere, S. Mitra, *Inorg. Chem.* **2012**, 51, 12176–12187; DOI:10.1021/ic3012958
- (b) G. Marinescu, A. M. Madalan, S. Shova, M. Andruh, *J. Coord. Chem.* **2012**, 65, 1539–1547. DOI:10.1080/00958972.2012.675435
19. (a) D. Mal, R. Sen, C. Adhikary, Y. Miyashita, K.-I. Okamoto, A. Bhattacharjee, P. Gutlich, S. Koner, *J. Coord. Chem.* **2008**, 61, 3486–3492; DOI:10.1080/00958970802072773
- (b) R. Karmakar, C. R. Choudhury, D. L. Hughes, G. P. A. Yap, M. S. El Fallah, C. Desplanches, J.-P. Sutter, S. Mitra, *Inorg. Chim. Acta* **2006**, 359, 1184–1192. DOI:10.1016/j.ica.2005.09.013
20. (a) A. Ray, G. Pilet, C. J. Gomez-Garcia, S. Mitra, *Polyhedron* **2009**, 28, 511–520; DOI:10.1016/j.poly.2008.11.054
- (b) G. Marinescu, A. M. Madalan, S. Shova, M. Andruh, *J. Coord. Chem.* **2012**, 65, 1539–1547. DOI:10.1080/00958972.2012.675435
21. S. Basak, S. Sen, S. Banerjee, S. Mitra, G. Rosair, M. T. Garland Rodriguez, *Polyhedron* **2007**, 26, 5104–5112. DOI:10.1016/j.poly.2007.07.025
22. A. Ray, D. Sadhukhan, G. M. Rosair, C. J. Gomez-Garcia, S. Mitra, *Polyhedron* **2009**, 28, 3542–3550. DOI:10.1016/j.poly.2009.07.017

## Povzetek

Sintetizirali smo dva strukturno sorodna bakrova(II) in cinkova(II) kompleksa z dicianamidnim mostovnim ligandom, [CuL(dca)]<sub>n</sub> (**1**) in [ZnL(dca)]<sub>n</sub> (**2**), z vezavo fluor vsebujoče Schiffove baze 5-fluoro-2-(((2-hidroksietil)imino)metil) fenol (HL). Spojini smo okarakterizirali s fizikalno-kemijskimi metodami. Strukturi kompleksov smo določili z monokristalno rentgensko difrakcijo. V kompleksu **1** je atom Cu koordiniran kvadratno piramidalno, medtem ko je atom Zn v kompleksu **2** koordiniran trigonalno bipiramidalno. Bakrov kompleks učinkovito zavira ureazo stročnice *Canavalia ensiformis* z vrednostjo IC<sub>50</sub> 0,14 ± 0,12 μmol L<sup>-1</sup>.



Except when otherwise noted, articles in this journal are published under the terms and conditions of the Creative Commons Attribution 4.0 International License

Scientific paper

# Phosphate Ion Removal from Synthetic and Real Wastewater Using $\text{MnFe}_2\text{O}_4$ Nanoparticles: A Reusable Adsorbent

Widodo Brontowiyono,<sup>1</sup> Indrajit Patra,<sup>2</sup> Shaymaa Abed Hussein,<sup>3</sup> Alimuddin,<sup>4</sup> Ahmed B. Mahdi,<sup>5</sup> Samar Emad Izzat,<sup>6</sup> Dhuha Mohsin Al-Dhalemi,<sup>7,\*</sup> Ahmed Kareem Obaid Aldulaim,<sup>8</sup> Rosario Mireya Romero Parra,<sup>9</sup> Luis Andres Barboza Arenas<sup>10</sup> and Yasser Fakri Mustafa<sup>11</sup>

<sup>1</sup> Department of Environmental Engineering and Centre for Environmental Studies, Islamic University of Indonesia, Yogyakarta-55589, Indonesia

<sup>2</sup> NIT Durgapur, West Bengal, India

<sup>3</sup> Al-Manara College for Medical Sciences, Maysan, Iraq

<sup>4</sup> Physical Sciences Section, School of Sciences, Maulana Azad National Urdu University, Hyderabad-500032, Telangana, India

<sup>5</sup> Anesthesia Techniques Department, Al-Mustaqbal University College, Babylon, Iraq

<sup>6</sup> Pharmacy Department, Al-Nisour University College, Baghdad, Iraq

<sup>7</sup> Altoosi University College, Najaf, Iraq

<sup>8</sup> Department of Pharmacy, Al-Zahrawi University College, Karbala, Iraq

<sup>9</sup> Universidad Continental, Lima, Perú

<sup>10</sup> Universidad Tecnológica del Perú, Perú

<sup>11</sup> Department of Pharmaceutical Chemistry, College of Pharmacy, University of Mosul, Mosul-41001, Iraq

\* Corresponding author: E-mail: [\\_dhuha14@yahoo.com](mailto:_dhuha14@yahoo.com)

Received: 06-29-2022

## Abstract

The purpose of this study was to eliminate phosphate (P) from wastewater using  $\text{MnFe}_2\text{O}_4$  nanoparticles. BET, TGA/DTG, FTIR, SEM, TEM, VSM, XRD and EDX/Map analyses were used to determine the  $\text{MnFe}_2\text{O}_4$  surface properties. The specific surface area of the adsorbent was  $196.56 \text{ m}^2/\text{g}$  and VSM analysis showed that the adsorbent has a ferromagnetic property. The maximum P sorption efficiency using  $\text{MnFe}_2\text{O}_4$  (98.52%) was achieved at pH 6, temperature of  $55^\circ\text{C}$ , P concentration of  $10 \text{ mg/L}$ , time of 60 min, and sorbent dosage of  $2.5 \text{ g/L}$ , which is a significant value. Also, the thermodynamic study indicated that the P sorption process is spontaneous and endothermic. Moreover, the utmost sorption capacity of P using  $\text{MnFe}_2\text{O}_4$  was  $39.48 \text{ mg/g}$ . Besides,  $\text{MnFe}_2\text{O}_4$  can be used for up to 6 reuse cycles with high sorption efficiency (>91%). Also,  $\text{MnFe}_2\text{O}_4$  was able to remove phosphate, COD, and  $\text{BOD}_5$  from municipal wastewater with considerable removal efficiencies of 82.7%, 75.8%, and 77.3%, respectively.

**Keywords:** Sorption,  $\text{MnFe}_2\text{O}_4$  nanoparticles, phosphate, wastewater

## 1. Introduction

Water pollution is a serious problem that can harm any living thing.<sup>1–2</sup> Among different contaminants, phosphate (P) ion pollution is one of the most important environmental issues worldwide. The presence of P at high concentrations in natural water has adverse impacts on

water ecology.<sup>3</sup> By increasing the concentration of P in water, algae and other aquatic plants grow and reduce the level of dissolved oxygen and eliminate photosynthesis in water.<sup>4</sup> Detergents and chemical fertilizers are the largest source of P ions. Domestic effluents and running water from fields where phosphate fertilizers are used release large amounts of P ions into natural waters. According to

the EPA, the maximum allowable level and the limit of P ion release in the environment are reported to be 0.1 ppm and less than 0.05 ppm, respectively.<sup>5</sup> Also, the allowable limit of P ions in drinking water is 0.2 ppm and the standard for discharge of phosphate ions into surface water is 6 ppm. The concentration of P in urban, rural, and agricultural wastewaters is very high (between 15–2000 ppm).<sup>5,6</sup> P has a critical role as an essential matter for plant growth in the soil as well as a limiting element in the algae growth and eutrophication phenomenon in water. A concentration of 0.005–0.05 mg/L is required to cause the eutrophication phenomenon.<sup>7</sup> This phenomenon leads to the abundant growth of aquatic plants, the growth of algae, and the imbalance of organisms in water resources. P in surface waters and effluents are commonly found chemically in the form of organic phosphates (such as detergents) and mineral phosphates (polyphosphates and orthophosphates). Organic polyphosphates and phosphates are converted to orthophosphates after hydrolysis and biodegradation.<sup>8</sup>

There are various procedures for wastewater treatment, including reverse osmosis, membrane technology, chemical deposition, ion exchange, nanofiltration, coagulation, and sorption process. Most of the physical processes such as reverse osmosis have high operating costs.<sup>9–11</sup> Among these processes, the sorption process is a suitable method to eliminate P ions, because this process is economical, simple, reversible, low-cost, high selectivity, and high operating speed.<sup>12</sup> P ions are insoluble in water and can be easily sorbed on the sorbent surface. Many adsorbents have been recently utilized for eliminating P ions, including  $\text{Fe}_3\text{O}_4$ ,<sup>13</sup> magnetic/clay,<sup>14</sup> chitosan,<sup>15</sup> goethite nanoparticles,<sup>16</sup> aluminum hydroxide modified palygorskite nano-composites,<sup>17</sup> zirconium oxide,<sup>18</sup> sludge derived biochar,<sup>19</sup> and iron/biochar.<sup>20</sup> Magnetic particles have received much attention for elimination of pollutants from sewage due to their simple synthesis, excellent surface area, and considerable removal efficiency of contaminants.<sup>21</sup>  $\text{MFe}_2\text{O}_4$  ( $\text{M} = \text{Co}, \text{Mn}, \text{Cu}, \text{Zn}, \text{Mg}$ ) with the structure of cubic spinel or  $\text{MO} \cdot \text{Fe}_2\text{O}_3$  shows an important group of iron oxides in which  $\text{Fe}^{3+}$  and  $\text{M}^{2+}$  occupy quadrilateral or octahedral sites.  $\text{MFe}_2\text{O}_4$  magnetic configurations can be engineered by controlling the chemical features of  $\text{M}^{2+}$  to produce a wide range of magnetic features.<sup>22</sup> Iron-manganese oxide spinel with  $\text{MnFe}_2\text{O}_4$  structure is an example of metal oxides, which has high thermal and mechanical stability.  $\text{MnFe}_2\text{O}_4$  spinel nanocrystalline can be synthesized by various procedures such as microwave, hydrothermal, and chemical co-precipitation processes. One of the main advantages of  $\text{MnFe}_2\text{O}_4$  is its simple synthesis, which distinguishes it from other adsorbents.<sup>21</sup> To control the size of  $\text{MFe}_2\text{O}_4$  in the chemical coprecipitation method, pH and temperature adjustment is essential.<sup>22</sup> Nanoadsorbents have properties such as high sorption capacity, excellent performance even at low concentration levels and low cost. Also, they are able to be reused in several cycles with-

out major loss in performance.<sup>23</sup> Due to these properties,  $\text{MnFe}_2\text{O}_4$  nanoparticles were used in this research.

The purpose of this work was to eliminate P ions using  $\text{MnFe}_2\text{O}_4$  nanoparticles.  $\text{MnFe}_2\text{O}_4$  was utilized for the first time for removing phosphate. The nanoadsorbent was synthesized by the chemical co-precipitation method and analyzed by various devices like SEM, BET, TEM, FTIR, XRD, TGA-DTG, VSM, and EDX/Map. Also, the impact of various factors was studied on the P ions removal and the best operating conditions were identified. Moreover, kinetic, isotherm, and thermodynamic behaviors of P ion sorption were studied using  $\text{MnFe}_2\text{O}_4$  nanoparticles.

## 2. Chemicals and Procedures

### 2.1. Chemicals and Devices

In this study, several chemicals were utilized to synthesize  $\text{MnFe}_2\text{O}_4$  nanoparticles as well as P ions stock solution, including  $\text{KH}_2\text{PO}_4$  (purity = 99%, Sandia Co., China),  $\text{MnCl}_2$  with a purity of 97%,  $\text{NaOH}$  with a purity of 99%, acetone with a purity of 99%,  $(\text{NH}_4)_6\text{MO}_7\text{O}_{24}$  with a purity of 99%,  $\text{HCl}$  with a purity of 37%,  $\text{H}_4\text{NO}_3\text{V}$  with a purity of 99% (Merck Co., Germany), and  $\text{FeCl}_3 \cdot 6\text{H}_2\text{O}$  (purity = 99%, Sigma Aldrich Co.).

Also, digital scale (FX 300 I model), magnetic stirrer (HPMT 700 model), magnet, oven (DZF-6020 model), pH meter (RPB1000 model) and UV-vis spectrophotometer (Shimadzu 1700 model, Japan) were utilized to weigh materials, heating and mixing, separation of nanoparticles from the solution, drying the sorbent, regulating the sample pH, determining the residual concentration of P ions in the solution, respectively.

### 2.2. Preparing Phosphate Stock Solution and $\text{MnFe}_2\text{O}_4$ Synthesis

$\text{KH}_2\text{PO}_4$  salt was employed to prepare the P stock solution. For this purpose, 4.39 g of  $\text{KH}_2\text{PO}_4$  was added to one liter of distilled water and stirred to dissolve completely in water. Different concentrations of 10, 20, 30, 50, 70, and 100 ppm were prepared by diluting the initial stock solution.

$\text{MnFe}_2\text{O}_4$  magnetic nanoparticles were synthesized by the chemical co-precipitation approach at 80 °C. For this purpose, 0.1 mol of  $\text{MnCl}_2$  and 0.2 mol of  $\text{FeCl}_3 \cdot 6\text{H}_2\text{O}$  were dissolved in 100 mL of distilled water and stirred at 80 °C for 20 min by a magnetic stirrer. Next,  $\text{NaOH}$  (3 molar) was added to the suspension dropwise to regulate the solution pH at 11. The mixture was stirred for 3 h. After that, the solution color changed to black, indicating the synthesis of  $\text{MnFe}_2\text{O}_4$  nanoparticles. The formed nanoparticles were separated from the mixture by a magnet and washed with distilled water and acetone ( $\text{C}_3\text{H}_6\text{O}$ ) to neutralize (pH = 7). Afterwards,  $\text{MnFe}_2\text{O}_4$  nanoparticles were placed in an oven at 100 °C for 1 day to dry. The

above-mentioned nanoparticles were ground with a mortar and used as a sorbent.<sup>24</sup>

Several analyses were utilized for identifying the features of  $\text{MnFe}_2\text{O}_4$  before and after the process, including BET (JW-DA, China) for measuring the specific surface area, SEM (TESCAN, Czech Republic) for identifying the sorbent morphology, TEM (CM120, The Netherlands) for investigating the particle distribution, EDX/Map (TESCAN, Czech Republic) for specifying the percentage of elements, FTIR (Alpha, BRUKER, Germany) for determining functional groups, XRD (D6792, The Netherlands) for determining the crystalline phases, VSM (7404, LAKE SHORE, USA) for identifying the magnetic strength of the sorbent, and TGA/DTG (PYRIS, PERKIN ELMER, USA) for specifying the thermal stability of the sorbent.

### 2. 3. Quantitative Determination of P

To produce a suitable reagent for measuring phosphate ions, 12.5 g of  $(\text{NH}_4)_6\text{MO}_7\text{O}_{24}$  was dissolved in 150 mL of distilled water (solution A). In another balloon, 0.625 g of ammonium metavanadate ( $\text{H}_4\text{NO}_3\text{V}$ ) was dissolved in 150 mL of distilled water and gently heated (solution B). The solution B was added to solution A and stirred for 5 min. Then, 165 mL of HCl was added to the solution A+B and its volume was raised to 500 mL by distilled water. This solution was then used as the reagent. The colorimetric method was used to measure P ions by the reagent. To measure residual P ions after the sorption process,  $\text{MnFe}_2\text{O}_4$  was separated from the solution using a magnet. Then, 10 ml of the solution containing P ions was mixed with 0.5 ml of the reagent solution. Finally, the concentration of P ions was measured by a UV-vis spectrophotometer device (Shimadzu 1700 model, Japan) at a wavelength of 361 nm.

### 2. 4. Sorption Tests

The P ion sorption tests were performed using  $\text{MnFe}_2\text{O}_4$  nanoparticles as a batch process. The impact of effective factors such as pH (2–11), adsorbent dosage (0.5–4 g/L), time (5–13 min), temperature (25–55 °C), and P ion concentration (10–100 ppm) was studied to remove P ions. For optimization of pH, various solutions were synthesized in different pHs and P ion concentration of 20 mg/L. Then, 2 g/L of  $\text{MnFe}_2\text{O}_4$  was added to the phosphate solutions. Then, the solutions were stirred at 25 °C with a mixing rate of 500 rpm. After 60 min, the remaining concentration of P ion was measured. Also, to investigate the impact of P ion concentration on the sorption efficiency, several experiments were done at various concentrations of P ion (10–100 ppm), pH of 6, the adsorbent dosage of 2.5 g/L, temperature of 55 °C, mixing rate of 500 rpm, and contact time of 60 min. The sorption capacity ( $q_e$ ) and sorption efficiency (R) were measured using Equations 1 and 2.

$$q_e = \frac{C_i - C_e \times V}{W} \quad (1)$$

$$R(\%) = \frac{C_i - C_e}{C_i} \times 100 \quad (2)$$

In mentioned equations,  $C_i$ ,  $C_e$ ,  $W$ , and  $V$  are the P initial concentration, the P remaining concentration (ppm), the adsorbent amount (g/L), and the sample volume (L), respectively.<sup>25</sup>

### 2. 5. Kinetic, Isotherm, and Thermodynamic Behaviors

There are 3 steps in the sorption of contaminants using a sorbent, which can affect the sorption kinetics, including 1) transfer of contaminants from the solution to the adsorbent surface, 2) penetration of contaminants into the pores inside the adsorbent, and 3) sorption of contaminants on the adsorbent inner surface.<sup>26</sup> In this research, pseudo-first order (PFO) and pseudo-second order (PSO) kinetics were employed to investigate P ions sorption. To this end, several experiments were done at different concentrations of P ions (10–100 ppm) and different contact times (5–130 min). Other factors like pH of 6, mixing rate of 500 rpm, the adsorbent dosage of 2.5 g/L, and temperature of 55 °C were considered constant. Equations 3 and 4 describe the PFO and PSO models, respectively:

$$\ln(q_e - q_t) = \ln q_e - K_1 t \quad (3)$$

$$\frac{t}{q_t} = \frac{1}{K_2 q_e^2} + \frac{t}{q_e} \quad (4)$$

In these models,  $q_e$  (mg/g),  $q_t$  (mg/g),  $K_1$  ( $\text{min}^{-1}$ ) and  $K_2$  (g/mg.min) are the sorption capacity at equilibrium time, sorption capacity at time  $t$ , the PFO kinetic model constant and the PSO kinetic model constant, respectively.<sup>27,28</sup>

Also, sorption isotherms describe the distribution of contaminant molecules on the adsorbent surface. The most important models are the Langmuir, Dubinnin-Radushkevich (D-R) and Freundlich. The Langmuir theory is used for monolayer sorption on a homogeneous surface with an infinite number of identical sites. In this theory, it is assumed that the adsorbent sites are saturated after monolayer sorption. This model is defined below.<sup>29</sup>

$$\frac{C_e}{q_e} = \frac{C_e}{q_{\max}} + \frac{1}{K_L q_{\max}} \quad (5)$$

In this model,  $C_e$  (mg/L),  $q_{\max}$  (mg/g) and  $K_L$  (L/mg) are the P ion equilibrium concentration, the sorption capacity at equilibrium time, and the Langmuir constant, respectively.

Another isotherm model (Freundlich) describes the sorption process on a heterogeneous surface. The follow-

ing relationship defines the Freundlich model:

$$\ln q_e = \ln K_f + \frac{1}{n} \ln C_e \quad (6)$$

Where,  $K_f$  (mg/g(L/mg)<sup>1/n</sup>) and  $n$  are the Freundlich constants. Also,  $n$  indicates whether the sorption process is desirable or not.<sup>30,31</sup>

Moreover, the D-R model is another important isotherm and assumes that the sorption energy on the surface is homogeneous. The D-R linear model is defined below:

$$\ln q_e = \ln q_m - \beta \varepsilon^2 \quad (7)$$

Where,  $q_m$  (mol/g),  $\beta$  (mol<sup>2</sup>/J<sup>2</sup>), and  $\varepsilon$  are the theory saturation capacity, the mean sorption free energy, and Polanyi potential, respectively. The Polanyi potential is calculated from Equation 8:

$$\varepsilon = RT \ln \left( 1 + \frac{1}{C_e} \right) \quad (8)$$

Also, the following relationship describes the type of the sorption process:

$$E = \frac{1}{\sqrt{2\beta}} \quad (9)$$

For  $E$  between 8–16 kJ/mol and lower than 8 kJ/mol, the sorption process will be chemical and physical, respectively.<sup>32</sup>

Also, thermodynamic parameters like Gibbs free energy changes ( $\Delta G^\circ$ ), entropy changes ( $\Delta S^\circ$ ), and enthalpy changes ( $\Delta H^\circ$ ) are employed to determine the nature of the sorption process. Using these parameters, it can be determined whether the sorption process is endothermic or exothermic.<sup>27</sup>

$$\Delta G^\circ = \Delta H^\circ - T\Delta S^\circ = -RT \ln K_d \quad (10)$$

$$\ln(K_d) = \frac{\Delta S^\circ}{R} - \frac{\Delta H^\circ}{RT} \quad (11)$$

$$K_d = \frac{q_e}{C_e} \quad (12)$$

In these relationships,  $K_d$  is the equilibrium constant.

Negative values of  $\Delta G^\circ$  in various temperatures indicate the spontaneous nature of the sorption process. For  $-80 \text{ kJ/mol} < \Delta G^\circ < 0$  and  $-400 \text{ kJ/mol} < \Delta G^\circ < -80 \text{ kJ/mol}$ , the sorption process will be physical and chemical, respectively.<sup>33</sup> Also, positive values of  $\Delta H^\circ$  indicate that the sorption process is endothermic and vice versa. Moreover, positive values of  $\Delta S^\circ$  indicate an increase in the solid-solute surface disorder during the sorption process, and its negative values display a decrease in irregularity in the sorption process.<sup>27</sup> For investigating the thermodynamic behavior of P ion sorption using  $\text{MnFe}_2\text{O}_4$  nanoparticles, several tests were performed in various temperatures (25–55 °C), pH of 6, mixing rate of 500 rpm, nanoparticles dos-

age of 2 g/L, P ion concentration of 20 mg/L and contact time of 60 min.

## 2. 6. Desorption Experiments and Reusability of the Adsorbent

To investigate the desorption process, the sorption of P ions was done in optimal conditions using  $\text{MnFe}_2\text{O}_4$  nanoparticles. Next,  $\text{MnFe}_2\text{O}_4$  was separated from the solution and dried. Then,  $\text{MnFe}_2\text{O}_4$  was added to 50 ml of  $\text{H}_2\text{SO}_4$  solution in various concentrations (1–5 mol/liter) and stirred for 2 h. Next, the adsorbent was separated from the solutions and the concentration of residual P ions was measured. After that, the optimal concentration of  $\text{H}_2\text{SO}_4$  was obtained to have the highest efficiency. Next, to study the desorption capability and reusability of the adsorbent in eight cycles,  $\text{H}_2\text{SO}_4$  solution was used at the optimal concentration (4 molar). The desorption percentage of P ions was calculated as follows:

$$\text{Desorption}(\%) = \left( \frac{q_1}{q_2} \right) \times 100 \quad (13)$$

Where  $q_1$  and  $q_2$  are the desorption capacity (mg/g) and the sorption capacity (mg/g) of P ions, respectively.<sup>34</sup>

## 3. Results and Discussion

### 3. 1. Characteristics of $\text{MnFe}_2\text{O}_4$

For determining the surface features of  $\text{MnFe}_2\text{O}_4$  nanoparticles such as specific surface area and pore size, BET analysis was used. According to Table 1, the specific surface area, pores volume and average pore size of  $\text{MnFe}_2\text{O}_4$  were 196.56 m<sup>2</sup>/g, 0.366 cm<sup>3</sup>/g, and 74.49 °A, respectively. The adsorbent pore size shows that  $\text{MnFe}_2\text{O}_4$  is mesoporous. Also, the high specific surface area of the adsorbent shows that contaminants can be adsorbed on the  $\text{MnFe}_2\text{O}_4$  surface. According to previous studies, the specific surface area of  $\text{CoFe}_2\text{O}_4$ ,  $\text{ZnFe}_2\text{O}_4$ ,<sup>35</sup>  $\text{MgFe}_2\text{O}_4$ ,<sup>36</sup>  $\text{Fe}_2\text{O}_3$  and  $\text{Fe}_3\text{O}_4$ <sup>37</sup> were 71.56, 120.1, 35.2, 150 and 130 m<sup>2</sup>/g, respectively, which are lower than our study.

**Table 1.** Surface features of  $\text{MnFe}_2\text{O}_4$  nanoparticles by BET analysis

BET specific surface area	196.56 m <sup>2</sup> /g
Langmuir specific surface area	m <sup>2</sup> /g 273.21
Pore volume	cm <sup>3</sup> /g 0.366
BJH pore volume	cm <sup>3</sup> /g 0.392
Mean pore size	74.49 °A
BJH average width of absorption pores	74.44 °A
BJH average width of desorption pores	67.14 °A

SEM, EDAX, and Mapping analyses were used to determine the morphology of  $\text{MnFe}_2\text{O}_4$  nanoparticles, distribution of elements, active sites on the adsorbent sur-



face, and elemental compositions before and after the P ion sorption process, as shown in Figure 1. SEM image for  $\text{MnFe}_2\text{O}_4$  nanoparticles shows that there are many holes and bumps, which are effective in the phosphate ion sorption (Figure 1 (a)). Also, EDAX and Mapping analyses for  $\text{MnFe}_2\text{O}_4$  nanoparticles indicate several elements such as Fe (46.87%), O (28.5%), and Mn (24.63%) in its surface, which confirm the correct synthesis of  $\text{MnFe}_2\text{O}_4$  nanoparticles (Figure 1 (b and c)). After sorption of P ions, many changes were observed on the  $\text{MnFe}_2\text{O}_4$  surface, which can be due to the sorption of P ions (Figure 1 (d)). Also, EDAX analysis showed that the percentage of elements has been changed. According to Figure 1 (f), the percentages of Fe, O, and Mn were changed to 46.1%, 22.58%, and 30.6%, respectively. Moreover, 0.73% of P was seen after the P ion sorption.

TEM analysis was also employed to determine the morphology and particle size of  $\text{MnFe}_2\text{O}_4$  nanoparticles (Figure 2). The outcomes show that the particle size of  $\text{MnFe}_2\text{O}_4$  is smaller than 50 nm. The particles in the  $\text{MnFe}_2\text{O}_4$  structure have spherical and cubic morphologies with fine size distribution. A similar morphology was observed by Cabrera et al.<sup>38</sup>

Figure 3 indicates FTIR analysis for  $\text{MnFe}_2\text{O}_4$  nanoparticles. For  $\text{MnFe}_2\text{O}_4$  nanoparticles before sorption, a wide peak was seen at  $3363\text{ cm}^{-1}$ , which can be attributed to the stretching vibration of hydroxyl group

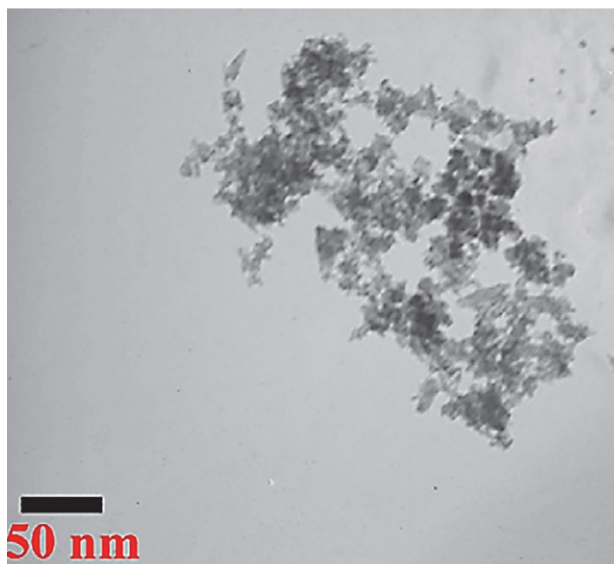


Figure 2. TEM image for  $\text{MnFe}_2\text{O}_4$  nanoparticles

(-OH). Also, another absorption peak was seen at  $586\text{ cm}^{-1}$ , which shows the spinel ferrite crystal structure of  $\text{MnFe}_2\text{O}_4$ . Also, the absorption peak at  $586\text{ cm}^{-1}$  shows intrinsic stretching vibrations of metals at tetrahedral sites.<sup>39</sup> Moreover, two peaks were observed at  $1624\text{ cm}^{-1}$  and  $964\text{ cm}^{-1}$ , which indicate C = C and C-O vibrations,

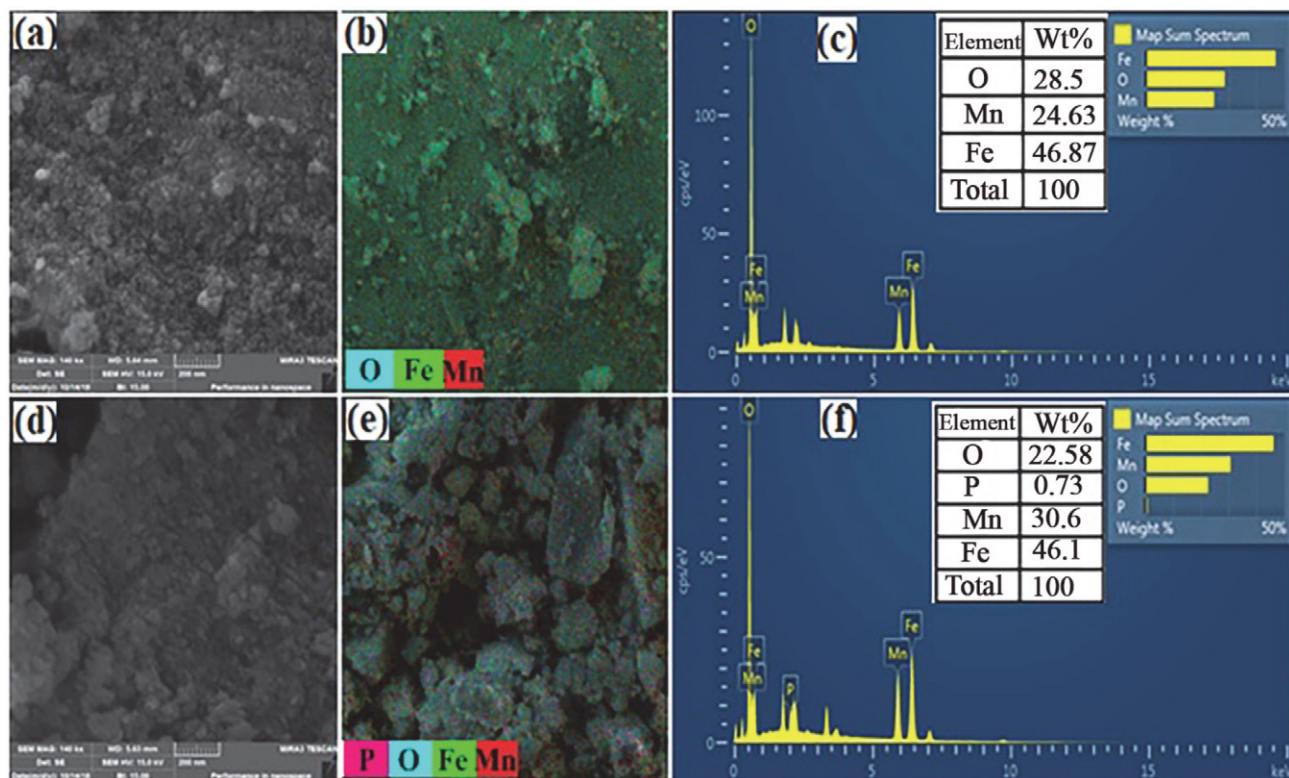
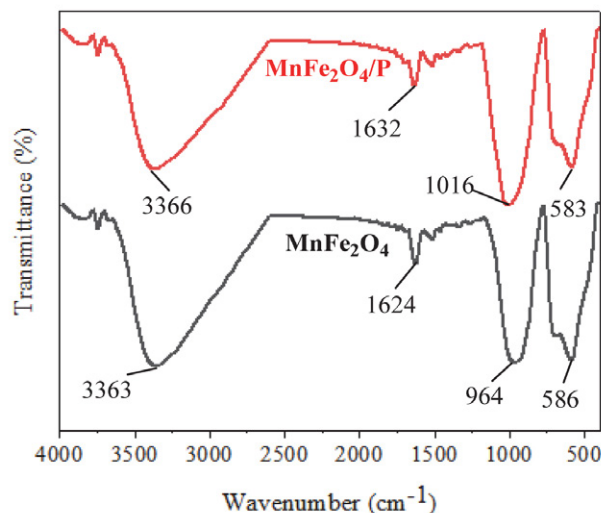


Figure 1. SEM, Mapping, and EDAX analysis for  $\text{MnFe}_2\text{O}_4$  nanoparticles before sorption (a-c) and after sorption of P ions (d-f)

respectively.<sup>24</sup> After sorption of P, the range of absorption peaks in the  $\text{MnFe}_2\text{O}_4$  structure was slightly changed, which can be due to the interaction of functional groups and phosphate ions. To this end, functional groups of -OH, C = C, C-C, and Fe-O in the  $\text{MnFe}_2\text{O}_4$  structure were shifted to 3366, 1632, 1016, and 583  $\text{cm}^{-1}$ , respectively.<sup>40–42</sup>



**Figure 3.** FTIR results for  $\text{MnFe}_2\text{O}_4$  nanoparticles before and after sorption of P ions

Moreover, XRD analysis for determining the crystalline phases in the  $\text{MnFe}_2\text{O}_4$  structure is demonstrated in Figure 4. Several peaks with various intensities were observed at 18.04°, 29.6°, and 35.02°, which are attributed to the crystalline phases of (111), (220), and (311), respectively. Also, other peaks were observed at 42.42°, 56.62°, and 61.74°, which are attributed to the crystalline phases of (400), (422), and (440), respectively. These crystalline phases correspond to the card number 0449-075-01.<sup>24,38</sup> The peak at 35.02° is attributed to the spinel structure of Mn ferrite, which has been confirmed by Cabrera et al.<sup>38</sup>

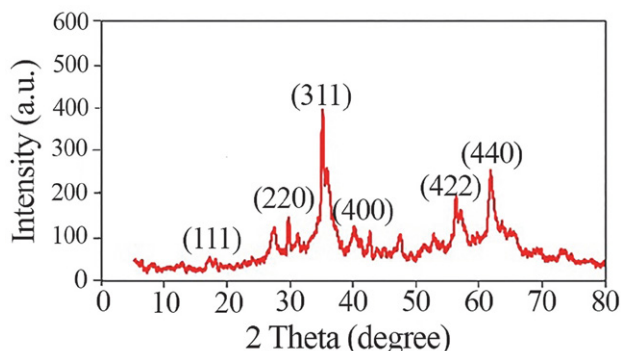


**Figure 4.** XRD results for  $\text{MnFe}_2\text{O}_4$  nanoparticles

Furthermore, VSM analysis was used to measure the magnetic strength of  $\text{MnFe}_2\text{O}_4$  nanoparticles (Figure 5). According to the results, magnetic saturation, coercive force, and magnetic resonance of  $\text{MnFe}_2\text{O}_4$  nanoparticles were 6.377 emu/g, 230 Oe, and 2.245 emu/g, respectively. The amount of magnetic saturation and the resulting figure shows that  $\text{MnFe}_2\text{O}_4$  nanoparticles have ferromagnetic properties and can be separated from the aqueous media by a magnet (1 Tesla).<sup>43</sup>

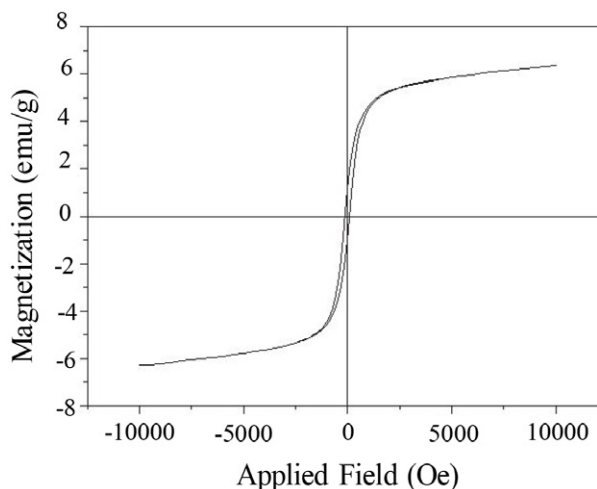


**Figure 5.** Magnetic behavior of  $\text{MnFe}_2\text{O}_4$  nanoparticles

Eventually, the thermal stability of  $\text{MnFe}_2\text{O}_4$  nanoparticles was investigated by TGA-DTG analysis (Figure 6). In the temperature range of 50–300 °C,  $\text{MnFe}_2\text{O}_4$  nanoparticles lost 5% by weight, which can be due to the evaporation of moisture from its surface.<sup>44</sup> By increasing temperature from 300 to 900 °C,  $\text{MnFe}_2\text{O}_4$  nanoparticles had the highest weight loss (8 wt.%), which is due to the structural degradation and dehydroxylation of  $\text{MnFe}_2\text{O}_4$  nanoparticles.<sup>45</sup> Also, its weight loss in the temperature range of 900–1000 °C was about 2% by weight. Generally,  $\text{MnFe}_2\text{O}_4$  nanoparticles showed a weight loss of 15 wt.%.

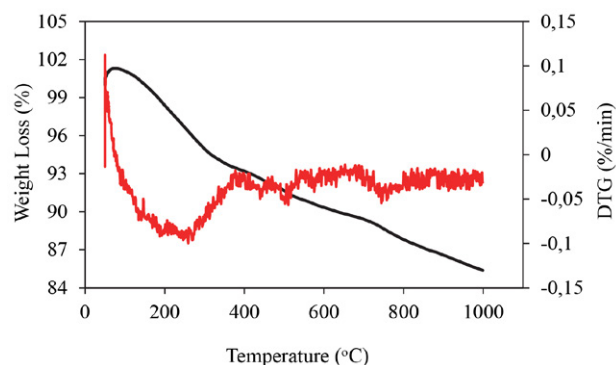


**Figure 6.** TGA-DTG analysis for thermal stability of  $\text{MnFe}_2\text{O}_4$  nanoparticles

### 3. 2. Effective Factors on the P Ion Removal

The solution pH is a key factor in the sorption process and can affect the surface properties of the adsorbent. Also, pH causes the release of various forms of ions in the solution.<sup>46</sup> Figure 7 shows the impact of pH at different temperatures on the uptake of P ions. Depending on the solution pH, phosphate species are present in water and seawater as  $\text{H}_3\text{PO}_4$ ,  $\text{H}_2\text{PO}_4^-$ ,  $\text{HPO}_4^{2-}$ , and  $\text{PO}_4^{3-}$  ions. The pH value of municipal effluent normally is in the range of 6.5–7.3, and  $\text{H}_2\text{PO}_4^-$  species is the major species of phosphate.<sup>47</sup> At  $\text{pH} > 2$ ,  $\text{H}_3\text{PO}_4$  is the predominant species of P ion in solution, which is due to the absence of electrostatic forces. By increasing the pH from 2 to 6,  $\text{H}_2\text{PO}_4^-$  and  $\text{HPO}_4^{2-}$  are the main species in the solution, which have a strong attraction to the  $\text{MnFe}_2\text{O}_4$  adsorbent, enhancing removal efficiency. At  $\text{pH} > 6$ , the sorption efficiency decreases because the solution contains large amounts of  $\text{H}_2\text{PO}_4^-$  and  $\text{PO}_4^{3-}$  species, and these ions compete fiercely with  $\text{OH}^-$  ions to sit on the active sites of the adsorbent.<sup>20</sup> Therefore, the highest removal efficiency (96.56%) was obtained at pH 6.

Also, the impact of temperature on the P ion sorption is shown in Figure 7. The tests were performed at the adsorbent dosage of 2 g/L, P ion concentration of 20 mg/L, mixing rate of 500 rpm, time of 60 min, and pH of 6. As shown, the sorption efficiency of P ions enhances from 86.83% to 96.56% with raising the temperature from 25 to 55 °C, respectively, demonstrating that the sorption of P ions using  $\text{MnFe}_2\text{O}_4$  nanoparticles is endothermic.<sup>20</sup> Therefore, the optimal temperature for removing P ions using  $\text{MnFe}_2\text{O}_4$  nanoparticles was 55 °C.

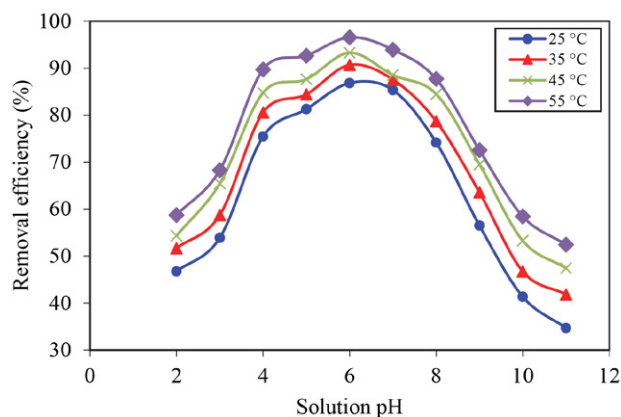


**Figure 7.** Impact of pH at different temperatures on the P ion sorption using  $\text{MnFe}_2\text{O}_4$  nanoparticles (contact time = 60 min, mixing rate = 500 rpm, pH = 6, P ion concentration = 20 mg/L and adsorbent dosage = 2 g/L)

The initial concentration of P ions in the solution plays an important role as the driving force overcoming the resistance due to the mass transfer between the liquid and solid phases. The impact of phosphate ion concentration at different contact times on the P ion sorption using

$\text{MnFe}_2\text{O}_4$  nanoparticles is indicated in Figure 8. As shown, the removal efficiency of P ions decreases from 97.43% to 87.54% with increasing P ion concentration from 10 to 100 mg/L, respectively, which is due to the greater accessibility of active sites at low P ion concentrations. At a constant adsorbent dose, the ratio of active sites to P ions decreases with increasing P ion concentration, resulting in a decrease in the interaction between P ions and sorption sites.<sup>48,49</sup> Therefore, the highest removal efficiency of P ions (97.43%) was obtained at a concentration of 10 mg/L.

Also, the contact time is a key factor for understanding the equilibrium sorption rate by the adsorbent. The time-dependent sorption provides the sorption rate in which contaminants can be adsorbed on the adsorbent surface.<sup>50</sup> Figure 8 presents the impact of contact time on the P ion sorption efficiency. As shown, the contact time has an impressive impact on the sorption process, so that with increasing time from 5 to 60 min, the P ion sorption efficiency increases from 46.26% to 97.43%, respectively. With increasing contact time, P ions in the solution have a greater chance of being located on  $\text{MnFe}_2\text{O}_4$  sorption sites. However, the removal efficiency decreases at higher contact times, which may be due to the saturation of  $\text{MnFe}_2\text{O}_4$  sorption sites.<sup>51</sup> It can be assumed that the sorption process of P ions using  $\text{MnFe}_2\text{O}_4$  mainly follows intraparticle diffusion and sorption complex mechanisms. Previous researchers have also found the same trend for sorption of other ions.<sup>52</sup> Therefore, 60 min was considered as the optimal contact time.

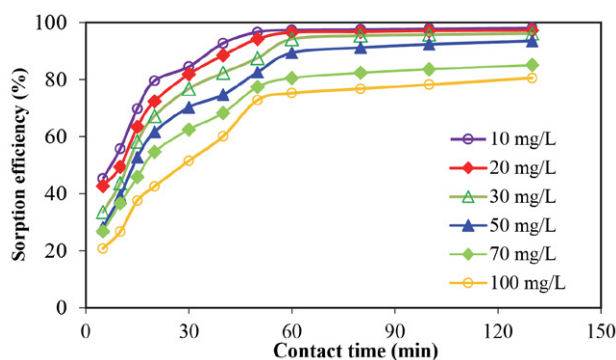


**Figure 8.** Impact of contact time in various concentrations of P ion on the removal efficiency (Conditions: pH = 6, mixing rate = 500 rpm, adsorbent dosage = 2 g/L, and temperature = 55 °C)

Adsorbent dosage is another critical factor in the P ion sorption efficiency because it directly affects the economics of the process. The removal efficiency and sorption capacity of P ions using  $\text{MnFe}_2\text{O}_4$  nanoparticles in various concentrations of  $\text{MnFe}_2\text{O}_4$  (0.5–4 g/L) are illustrated in Figure 9. It is observed that the P ion removal efficiency increases with increasing  $\text{MnFe}_2\text{O}_4$  concentration from 0.5 to 2.5 g/L, which is due to an increase in sorption sites. At adsorbent dosage  $> 2.5$  g/L, no significant change in removal efficiency was observed because almost all P ions



are adsorbed by the adsorbent and the  $\text{MnFe}_2\text{O}_4$  sorption sites are saturated. Also, the sorption capacity of P ions decreases with increasing  $\text{MnFe}_2\text{O}_4$  concentration. P ions in solution aggregate at high adsorbent dosages, which leads to saturation of the adsorbent surface and thus reduces the sorption capacity.<sup>53–55</sup> According to the results, the utmost sorption capacity of P ions using  $\text{MnFe}_2\text{O}_4$  nanoparticles was attained as 9.172 mg/g. Also, the utmost sorption efficiency (98.52%) was obtained at the adsorbent dosage of 2.5 g/L.

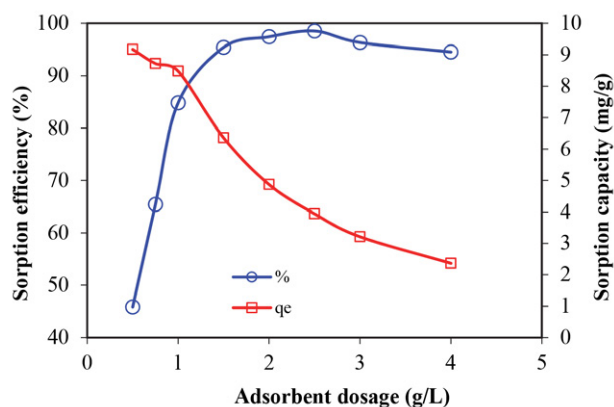


**Figure 9.** Impact of  $\text{MnFe}_2\text{O}_4$  dose on sorption efficiency and sorption capacity of P ions (Conditions: pH = 6, mixing rate = 500 rpm, P ion concentration = 10 ppm, contact time = 60 min, and temperature = 55 °C)

### 3. 3. Sorption Isotherms

The Langmuir, D-R, and Freundlich models were used to study the sorption isotherms of P ions using  $\text{MnFe}_2\text{O}_4$  nanoparticles (Figure 10 and Table 2). To this end, several experiments were performed in various P ion concentrations (10–100 ppm). According to the results, the correlation coefficient ( $R^2$ ) for the Freundlich model (0.978) was higher than the Langmuir (0.973) and D-R (0.814) models, indicating that the Freundlich isotherm model can better describe the P ion sorption process. Also, sorption of P ions occurs in multilayers on the heterogeneous surfaces of  $\text{MnFe}_2\text{O}_4$  nanoparticles. Moreover, the  $R^2$  value for the D-R model was small, indicating that the D-R model is not fitted well with the experimental data. The highest sorption capacity of P ions by the Langmuir model was 39.84 mg/g, which is an acceptable amount. The Langmuir separation factor  $R_L$  was also between 0 and 1, indicating that the P ions sorption process is favorable. Besides, the value of  $n$  in the Freundlich model was greater than 1, showing that the P ions sorption process using  $\text{MnFe}_2\text{O}_4$  nanoparticles is physical. Using the D-R model, the mean free energy ( $E$ ) was obtained as 2.331 KJ/mol, which is less than 8 KJ/mol, and shows that the P ion sorption using  $\text{MnFe}_2\text{O}_4$  nanoparticles is physical. The maximum sorption capacity by the D-R model was

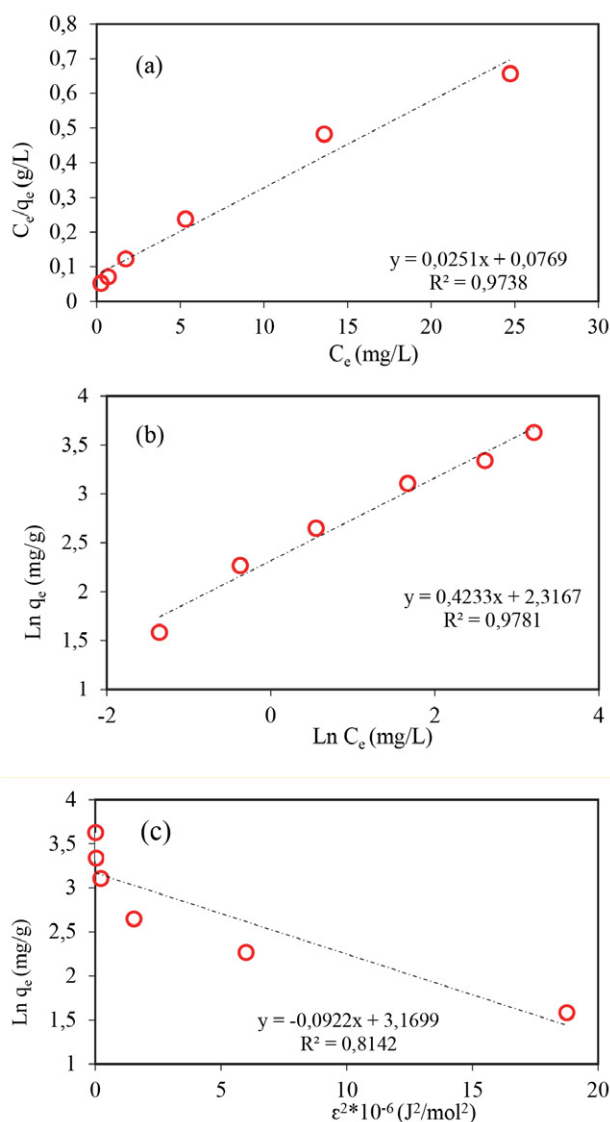


**Figure 10.** Sorption isotherms of P ions using the Langmuir (a), Freundlich (b) and D-R (c) models (Conditions: pH = 6,  $\text{MnFe}_2\text{O}_4$  dose = 2 g/L, temperature = 55 °C, time = 60 min, mixing rate = 500 rpm)

23.805 mg/g, which is less than the value obtained by the Langmuir model. Also, the Langmuir ( $K_L$ ) and Freundlich ( $K_f$ ) model constants were 0.326 L/g and 10.142 mg/g.(L/mg)<sup>1/n</sup>, respectively.

The maximum sorption capacity of P ions using  $\text{MnFe}_2\text{O}_4$  nanoparticles was compared with previous works, as reported in Table 3. As reported, Silica/2-methyl-1-naphthylamine composite with the maximum sorption capacity of 159.12 mg/g<sup>56</sup> and bentonite/magnesium hydroxide with the maximum sorption capacity of 4.3 mg/g<sup>57</sup> showed the highest and lowest sorption capacities. Also, the adsorbent used in this work ( $\text{MnFe}_2\text{O}_4$  nanoparticles) with an utmost sorption capacity of 39.84 mg/g showed a suitable sorption capacity compared to other adsorbents.

**Table 2.** Parameters of P ions sorption isotherms using  $\text{MnFe}_2\text{O}_4$  nanoparticles

Model	Factor	Value
Langmuir	$q_m(\text{mg/g})$	39.84
	$K_L(\text{L/mg})$	0.326
	$R^2$	0.973
	$R_L$	0.029–0.234
Freundlich	$n$	2.362
	$K_f(\text{mg/g}(\text{L/mg})^{1/n})$	10.142
	$R^2$	0.978
D-R	$E(\text{KJ/mol})$	2.331
	$q_m(\text{mg/g})$	23.805
	$\beta \times 10^{+6}(\text{mol}^2/\text{J}^2)$	0.092
	$R^2$	0.814

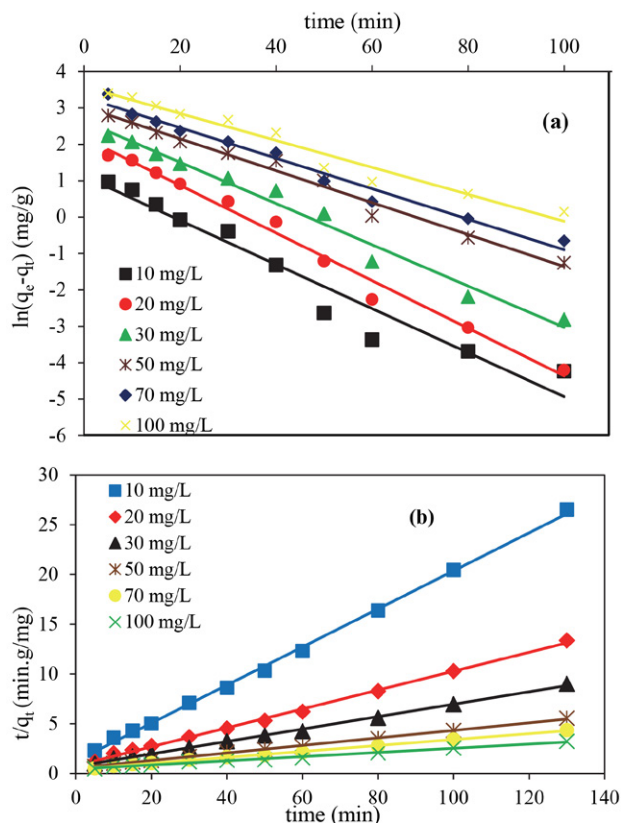
**Table 3.** Comparing the maximum sorption capacity of P ions using various adsorbents

Reference	$q_{\max}(\text{mg/g})$	Adsorbent
11	52.1	cross-linked chitosan
12	13	acicular goethite nanoparticles
13	16.86	aluminum hydroxide/ palygorskite nano-composite
56	159.12	Silica/2-methyl-1-naphthylamine composite
57	4.3	Carboxymethyl cellulose/Fe
58	57.8	Magnetite
58	66.6	Ferrihydrite
58	50.5	Goethite
59	6.722	Chitosan
60	8.21	iron oxide
61	36	Fe-Mn binary oxide
Present study	39.84	$\text{MnFe}_2\text{O}_4$

### 3. 4. Sorption Kinetics

Kinetic models determine the sorption mechanisms. They also determine whether the sorption process follows the PFO or PSO kinetic models. The PFO and PSO models were used to study the kinetic behavior of

the P ions sorption using  $\text{MnFe}_2\text{O}_4$  nanoparticles. To this end, several experiments were performed at various P ion concentrations from 10 ppm to 100 ppm and different contact times from 5 min to 130 min. The results of sorption kinetics are provided in Figure 11 and Table 4. As reported, the amount of  $q_{e,\text{cal}}$  in different concentrations of P ions (10, 20, 30, 50, 70, and 100 ppm) for the PFO model were calculated as 3.063, 8.864, 14.042, 20.753, 27.01, and 36.205 mg/g, respectively, while these values for the PSO model were 5.23, 10.548, 16.025, 26.455, 33.67, and 47.46

**Figure 11.** Sorption kinetics of P ions using  $\text{MnFe}_2\text{O}_4$  nanoparticles in different concentrations of P ion (10–100 ppm) and different contact times (5–130 min), including the PFO model (a) and PSO model (b) (Other conditions: adsorbent dosage = 2 g/L, temperature = 55 °C, mixing rate = 500 rpm and pH = 6)**Table 4.** Sorption kinetics of P ions using  $\text{MnFe}_2\text{O}_4$  nanoparticles

Kinetic model	Parameter	P ion concentration					
		10 ppm	20 ppm	30 ppm	50 ppm	70 ppm	100 ppm
PFO	$R^2$	0.9441	0.9887	0.9878	0.985	0.9779	0.9638
	$K_1(\text{min}^{-1})$	0.0605	0.0654	0.0567	0.0439	0.0419	0.037
	$q_{e,\text{cal}}(\text{mg/g})$	3.063	8.864	14.042	20.753	27.01	36.205
	$q_{e,\text{exp}}(\text{mg/g})$	4.906	9.726	14.427	23.38	29.792	40.28
PSO	$R^2$	0.9985	0.9978	0.9978	0.9979	0.9977	0.992
	$K_2(\text{g/mg} \cdot \text{min})$	0.029	0.011	0.005	0.002	0.002	0.0009
	$q_{e,\text{cal}}(\text{mg/g})$	5.23	10.548	16.025	26.455	33.67	47.46
	$q_{e,\text{exp}}(\text{mg/g})$	4.906	9.726	14.427	23.38	29.792	40.28

mg/g, respectively, which indicates that the amounts of  $q_{e,cal}$  for the PSO model are larger than that of the PFO model at all P ion concentrations. Also, the PFO kinetic constant ( $K_1$ ) in these concentrations were obtained as 0.0605, 0.0654, 0.0567, 0.0439, 0.0419, and 0.037  $\text{min}^{-1}$ , respectively. The kinetic study shows that the PSO model has more ability to describe the kinetic behavior of P ion sorption due to higher  $R^2$  values ( $R^2 > 0.99$ ) in different concentrations of P ions compared to the PFO model with  $R^2$  between 0.94–0.98. Moreover, the kinetic constant of the PSO model ( $K_2$ ) is smaller than  $K_1$  in different concentrations of P ion.<sup>19</sup>

### 3. 5. Thermodynamic Study of P Ion Sorption

The thermodynamic parameters are calculated through the plot of  $\ln K_d$  against  $1/T$ , as shown in Figure 12. The thermodynamic constants are also reported in Table 5. As given, negative values of  $\Delta G^\circ$  in various temperatures ( $-2.954$  kJ/mol at  $25^\circ\text{C}$  and  $-7.205$  kJ/mol at  $55^\circ\text{C}$ ) show that the P ion sorption process is spontaneous. Also, the  $\Delta G^\circ$  values are between 0 to  $-20$  kJ/mol, indicating that the P ion sorption process using  $\text{MnFe}_2\text{O}_4$  nanoparticles is physical. Moreover,  $\Delta H^\circ$  was a positive value ( $38.024$  kJ/mol), indicating that the P ion sorption process is endothermic, which confirms the results of the impact of temperature on the sorption process. Furthermore,  $\Delta S^\circ$  was a positive value ( $136.848$  J/mol K), showing that irregularities between the solid (adsorbent) and liquid (solution) phases increase during the P ion sorption process using  $\text{MnFe}_2\text{O}_4$  nanoparticles.<sup>62</sup>

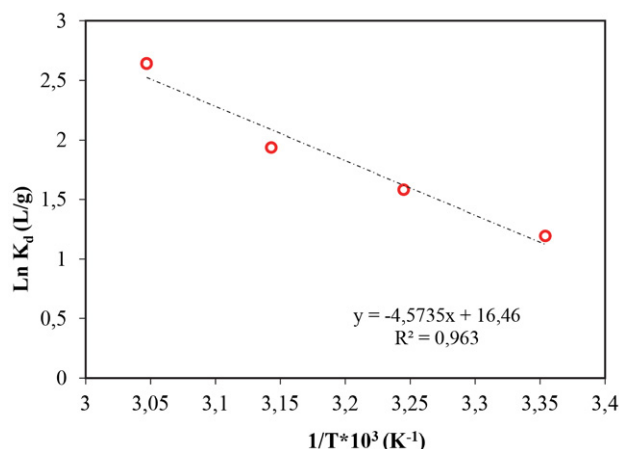


**Figure 12.** The thermodynamic behavior of P ion sorption using  $\text{MnFe}_2\text{O}_4$  nanoparticles (Conditions: mixing rate = 500 rpm, pH = 6,  $\text{MnFe}_2\text{O}_4$  dose = 2 g/L, P ion concentration = 10 mg/L, and contact time = 60 min)

### 3. 6. Reusability of $\text{MnFe}_2\text{O}_4$

The reusability of the adsorbent in different cycles is very important for its industrial applications due to the

**Table 5.** Thermodynamic parameters for P ion sorption using  $\text{MnFe}_2\text{O}_4$  nanoparticles

Temperature ( $^\circ\text{C}$ )	$\Delta G^\circ$ (kJ/mol)	$\Delta H^\circ$ (kJ/mol)	$\Delta S^\circ$ (J/mol K)
25	-2.954	38.024	136.848
35	-4.053		
45	-5.123		
55	-7.205		

cost-effectiveness of the process.<sup>63,64</sup> After examining the sorption efficiency of  $\text{MnFe}_2\text{O}_4$  nanoparticles in the removal of P ions from an aqueous solution, the reusability of  $\text{MnFe}_2\text{O}_4$  nanoparticles was studied in eight reuse cycles to assess its industrial utilization potential (Figure 13). The solution containing  $\text{H}_2\text{SO}_4$  was used to study the reusability of  $\text{MnFe}_2\text{O}_4$ . Figure 13 (a) shows the impact of  $\text{H}_2\text{SO}_4$  concentration on the P ion sorption using  $\text{MnFe}_2\text{O}_4$  nanoparticles. According to the results, the desorption efficiency of P ions increases with increasing  $\text{H}_2\text{SO}_4$  concentration. However, no significant change was seen in the P ion desorption efficiency at  $\text{H}_2\text{SO}_4$  concentration above 4 mol/liter. Therefore, the  $\text{H}_2\text{SO}_4$  concentration of 4 mol/liter was considered the optimum value to study the reusability of  $\text{MnFe}_2\text{O}_4$  nanoparticles. According to Figure 13 (b),  $\text{MnFe}_2\text{O}_4$  nanoparticles were able to remove P ions

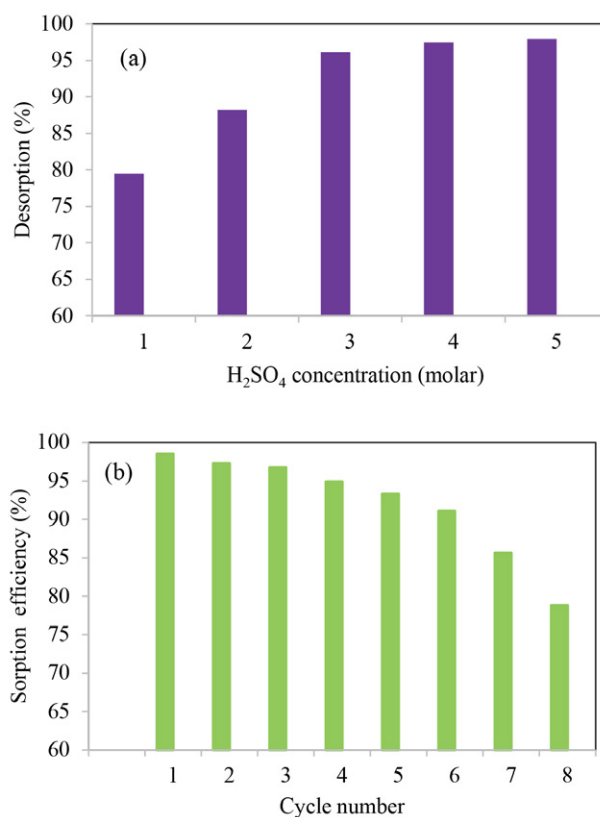


**Figure 13.** Desorption efficiency (a) and reusability (b) of  $\text{MnFe}_2\text{O}_4$  nanoparticles for removal of P ions from aqueous solution



from an aqueous solution with a sorption efficiency above 91% after six cycles. However, the sorption efficiency of P ions in the 7<sup>th</sup> and 8<sup>th</sup> cycles were 85.6 and 78.8%, respectively, which are not suitable sorption efficiencies. Therefore, MnFe<sub>2</sub>O<sub>4</sub> nanoparticles can be used for up to 6 reuse cycles, which is significant reusability.

### 3. 7. Treatment of Wastewater Using MnFe<sub>2</sub>O<sub>4</sub> Nanoparticles

MnFe<sub>2</sub>O<sub>4</sub> nanoparticles were used to treat urban wastewater and the physical properties of the wastewater before and after treatment are reported in Table 6. As shown, the initial values of COD, BOD<sub>5</sub>, pH, and phosphate ions before sorption were 310 ppm, 185 ppm, 9.5, and 22 ppm, respectively. After adding MnFe<sub>2</sub>O<sub>4</sub> nanoparticles to the wastewater, the values of COD, BOD<sub>5</sub>, pH, and phosphate ions were changed to 75 ppm, 42 ppm, 9, and 3.8 ppm, respectively. The results show that the concentration of phosphate ions has been reduced by 82.7%, which is a proper amount. Also, the removal efficiency of COD and BOD<sub>5</sub> using MnFe<sub>2</sub>O<sub>4</sub> was 75.8% and 77.3%, respectively.

**Table 6.** The concentration of contaminants in urban wastewater before and after adding MnFe<sub>2</sub>O<sub>4</sub> nanoparticles

Parameter	Initial value	After treatment	Removal percentage (%)
Phosphate (ppm)	22	3.8	82.7
COD (ppm)	310	75	75.8
BOD <sub>5</sub> (ppm)	185	42	77.3
pH	9.5	9	–

## 4. Conclusion

The presence of P at high concentrations in water has adverse impacts on water ecology and causes eutrophication. Therefore, the concentration of P in water must be reduced. In this study, the sorption capability of MnFe<sub>2</sub>O<sub>4</sub> nanoparticles was investigated in the removal of P ions from synthetic and real wastewater. The physical and structural properties of the aforementioned adsorbent were studied by several analyses such as TEM, SEM, EDAX, Mapping, XRD, VSM, FTIR, BET, and TGA. According to these analyses, MnFe<sub>2</sub>O<sub>4</sub> nanoparticles have a highly porous structure with many active sites, which can be effective in the sorption process. The sorption study indicated that the highest sorption efficiency of P ions was obtained as 98.52%, which was achieved at pH of 6, mixing rate of 500 rpm, MnFe<sub>2</sub>O<sub>4</sub> dosage of 2.5 g/L, P ion concentration of 10 ppm, temperature of 55 °C and contact time of 60 min. Also, the maximum sorption capacity obtained by the Langmuir model was 39.84 mg/g, which is an acceptable amount compared to other adsorbents for

P removal. Moreover, the isotherm and kinetic studies showed that the P ion sorption process using MnFe<sub>2</sub>O<sub>4</sub> follows the Freundlich and PSO models. Therefore, heterogeneous surfaces of the adsorbent are very important in the P ion sorption process. Furthermore, the D-R and Freundlich isotherm models show that the P ion sorption process using MnFe<sub>2</sub>O<sub>4</sub> is physical. The thermodynamic factors like  $\Delta G^\circ$ ,  $\Delta S^\circ$ , and  $\Delta H^\circ$  displayed that the sorption of P ions using MnFe<sub>2</sub>O<sub>4</sub> nanoparticles is spontaneous and endothermic. Besides, MnFe<sub>2</sub>O<sub>4</sub> nanoparticles can be reused for up to 6 cycles with high sorption efficiency. Also, MnFe<sub>2</sub>O<sub>4</sub> nanoparticles were able to remove COD, BOD<sub>5</sub> and P ions from municipal wastewater with high removal efficiency (>75%). In general, MnFe<sub>2</sub>O<sub>4</sub> nanoparticles are recommended for industrial wastewater treatment.

## Conflict of Interests Statement

No conflict of interests is declared by the authors.

## 5. References

1. L. Dai, Z. Wang, T. Guo, L. Hu, Y. Chen, C. Chen, G. Yu, L. Q. Ma, J. Chen. *Chemosphere* **2022**, 293, 133576. DOI:10.1016/j.chemosphere.2022.133576
2. W. Liu, J. Zheng, X. Ou, X. Liu, Y. Song, C. Tian, W. Rong, Z. Shi, Z. Dang, Z. Lin. *Environ. Sci. Technol.* **2018**, 52, 13336–13342. DOI:10.1021/acs.est.8b02213
3. Q. Guan, G. Zeng, J. Song, C. Liu, Z. Wang, S. Wu. *J. Environ. Manage.* **2021**, 293, 112961. DOI:10.1016/j.jenvman.2021.112961
4. M. R. Awual, A. Jyo, S. A. El-Safty, M. Tamada, N. Seko. *J. Hazard Mater.* **2011**, 188, 164–171. DOI:10.1016/j.jhazmat.2011.01.092
5. X. Liu, L. Zhang. *Powder Technol.* **2015**, 277, 112–119. DOI:10.1016/j.powtec.2015.02.055
6. M. El Bouraie, A. A. Masoud. *Appl. Clay Sci.* **2017**, 140, 157–164. DOI:10.1016/j.clay.2017.01.021
7. O. Axinte, I. Volf, L. Bulgariu. *Environ. Eng. Manage. J.* **2017**, 16, 625–631. DOI:10.30638/eemj.2017.064
8. C. E. Boyd. Phosphorus. In: *Water Quality*. Springer, Cham. **2015**. DOI:10.1007/978-3-319-17446-4\_12
9. I. W. Almanassra, V. Kochkodan, G. McKay, M. A. Atieh, T. Al-Ansari. *J. Environ. Manage.* **2021**, 287, 112245. DOI:10.1016/j.jenvman.2021.112245
10. L. Zhang, L. Wang, Y. Zhang, D. Wang, J. Guo, M. Zhang, Y. Li. *Environ. Res.* **2022**, 206, 112629. DOI:10.1016/j.envres.2021.112629
11. W. Liu, J. Li, J. Zheng, Y. Song, Z. Shi, Z. Lin, L. Chai. *Environ. Sci. Technol.* **2020**, 54, 11971–11979. DOI:10.1021/acs.est.0c01855
12. I. S. Bădescu, D. Bulgariu, I. Ahmad, L. Bulgariu. *J. Environ. Manage.* **2018**, 224, 288–297. DOI:10.1016/j.jenvman.2018.07.066
13. S. Y. Yoon, C. G. Lee, J. J. H. Park, S. B. Kim, S. H. Lee, J. W.

- Choi. *Chem. Eng. J.* **2014**, *236*, 341–347. DOI:10.1016/j.cej.2013.09.053
14. J. Chen, L. G. Yan, H. Q. Yu, S. Li, L. L. Qin, G. Q. Liu, Y. F. Li, B. Du. *Chem. Eng. J.* **2016**, *287*, 162–172. DOI:10.1016/j.cej.2015.11.028
15. M. H. Mahaninia, L. D. Wilson. *J. Colloid Interface Sci.* **2017**, *485*, 201–212. DOI:10.1016/j.jcis.2016.09.031
16. R. F. Moreira, S. Vandresen, D. B. Luiz, H. J. José, G. L. Puma. *J. Environ. Chem. Eng.* **2017**, *5*, 652–659. DOI:10.1016/j.jece.2016.12.018
17. M. Pan, X. Lin, J. Xie, X. Huang. *RSC Adv.* **2017**, *7*, 4492–4500. DOI:10.1039/C6RA26802A
18. K. Qin, F. Li, S. Xu, T. Wang, C. Liu. *Chem. Eng. J.* **2017**, *322*, 275–280. DOI:10.1016/j.cej.2017.04.046
19. S. Saadat, E. Raei, N. Talebbeydokhti. *J. Environ. Manage.* **2018**, *225*, 75–83. DOI:10.1016/j.jenvman.2018.07.037
20. Q. Yang, X. Wang, W. Luo, J. Sun, Q. Xu, F. Chen, J. Zhao, S. Wang, F. Yao, D. Wang, X. Li. *Bioresour. Technol.* **2018**, *247*, 537–544. DOI:10.1016/j.biortech.2017.09.136
21. T. Shanmugavel, S. G. Raj, G. R. Kumar, G. Rajarajan. *Phys. Procedia* **2014**, *54*, 159–163. DOI:10.1016/j.phpro.2014.10.053
22. S. Sun, H. Zeng, D. B. Robinson, S. Raoux, P. M. Rice, S. X. Wang, G. Li. *J. Am. Chem. Soc.* **2004**, *126*, 273–279. DOI:10.1021/ja0380852
23. M. R. Awual, A. M. Asiri, M. M. Rahman, N. H. Alharthi. *Chem. Eng. J.* **2019**, *363*, 64–72. DOI:10.1016/j.cej.2019.01.125
24. M. Ghobadi, M. Gharabaghi, H. Abdollahi, Z. Boroumand, M. Moradian. *J. Hazard. Mater.* **2018**, *351*, 308–316. DOI:10.1016/j.jhazmat.2018.03.011
25. M. R. Awual, T. Yaita, S. Suzuki, H. Shiwaku. *J. Hazard. Mater.* **2015**, *291*, 111–119. DOI:10.1016/j.jhazmat.2015.02.066
26. M. H. Dehghani, D. Sanaei, I. Ali, A. Bhatnagar. *J. Mol. Liq.* **2016**, *215*, 671–679. DOI:10.1016/j.molliq.2015.12.057
27. İ. Şentürk, M. Alzein. *Acta Chim. Slov.* **2020**, *67*, 55–69. DOI:10.17344/acsi.2019.5195
28. D. Ge, H. Yuan, J. Xiao, N. Zhu. *Sci. Total Environ.* **2019**, *679*, 298–306. DOI:10.1016/j.scitotenv.2019.05.060
29. M. R. Awual, M. M. Hasan, A. Islam, M. M. Rahman, A. M. Asiri, M. A. Khaleque, M. C. Sheikh. *J. Clean. Prod.* **2019**, *228*, 778–785. DOI:10.1016/j.jclepro.2019.04.280
30. A. Syafiuddin, S. Salmiati, J. Jonbi, M. A. Fulazzaky. *J. Environ. Manage.* **2018**, *218*, 59–70. DOI:10.1016/j.jenvman.2018.03.066
31. B. Bai, D. Rao, T. Chang, Z. Guo. *J. Hydrol.* **2019**, *578*, 124080. DOI:10.1016/j.jhydrol.2019.124080
32. J. Mittal, A. Mariyam, F. Sakina, R. T. Baker, A. K. Sharma, A. Mittal. *J. Clean. Prod.* **2021**, *321*, 129060. DOI:10.1016/j.jclepro.2021.129060
33. R. A. Rashid, A. H. Jawad, M. A. M. Ishak, N. N. Kasim. *Desalination. Water Treat.* **2016**, *57*, 27226–27236. DOI:10.1080/19443994.2016.1167630
34. N. El Messaoudi, M. El Khomri, Z. Goodarzvand Chegini, N. Chlif, A. Dbik, S. Bentahar, M. Iqbal, A. Jada, A. Lacherai. *Int. J. Environ. Anal. Chem.* **2021**. DOI:10.1080/03067319.2021.1912338
35. R. Ramadan, N. Shehata. *DESALIN. WATER TREAT.* **2021**, *227*, 370–383. DOI:10.5004/dwt.2021.27248
36. A. Doi, M. Nishibori, K. Obata, T. Suzuki, K. Shimanoe, S. Matsushima. *J. Ceram. Soc. JAPAN* **2016**, *124*, 777–780. DOI:10.2109/jcersj2.16042
37. S. Lavrynenko, A. G. Mamalis, D. Sofronov, A. Odnovolova, V. Starikov. *Mater Sci Forum* **2018**, *915*, 116–120. DOI:10.4028/www.scientific.net/MSF.915.116
38. L. I. Cabrera, Á. Somoza, J. F. Marco, C. J. Serna, M. Puerto Morales. *J. Nanopart. Res.* **2012**, *14*, 1–14. DOI:10.1007/s11051-012-0873-x
39. R. S. Yadav, I. Kuřitka, J. Vilcakova, T. Jamatia, M. Machovsky, D. Skoda, P. Urbánek, M. Masař, M. Urbánek, L. Kalina, J. Havlica. *Ultrason. Sonochem.* **2020**, *61*, 104839. DOI:10.1016/j.ultsonch.2019.104839
40. R. Liu, L. Chi, X. Wang, Y. Wang, Y. Sui, T. Xie, H. Arandiyán. *Chem. Eng. J.* **2019**, *357*, 159–168. DOI:10.1016/j.cej.2018.09.122
41. L. Zhang, Y. Xu, H. Liu, Y. Li, S. You, J. Zhao, J. Zhang. *J. Water Process Eng.* **2021**, *44*, 102368. DOI:10.1016/j.jwpe.2021.102368
42. Y. Zhang, Z. Pan, J. Yang, J. Chen, K. Chen, K. Yan, X. Meng, X. Zhang, M. He. *Powder Technol.* **2022**, *399*, 117193. DOI:10.1016/j.powtec.2022.117193
43. K. Mensah, H. Mahmoud, M. Fujii, H. Shokry. *J. Water Process Eng.* **2022**, *45*, 102512. DOI:10.1016/j.jwpe.2021.102512
44. C. Cannas, A. Falqui, A. N. N. A. Musinu, D. Peddis, G. Piccaluga. *J. Nanopart. Res.* **2006**, *8*, 255–267. DOI:10.1007/s11051-005-9028-7
45. M. Artus, S. Ammar, L. Sicard, J. Y. Piquemal, F. Herbst, M. J. Vaulay, F. Fiévet, V. Richard. *Chem. Mater.* **2008**, *20*, 4861–4872. DOI:10.1021/cm702464e
46. D. Gugala-Fekner. *Acta Chim. Slov.* **2018**, *65*, 119–126. DOI:10.17344/acsi.2017.3652
47. M. R. Awual, M. A. Shenashen, A. Jyo, H. Shiwaku, T. Yaita. *J. Ind. Eng. Chem.* **2014**, *20*, 2840–2847. DOI:10.1016/j.jiec.2013.11.016
48. C. Shi, Z. Wu, F. Yang, Y. Tang. *Solid State Sci.* **2021**, *119*, 106702. DOI:10.1016/j.solidstatesciences.2021.106702
49. H. Liu, T. Chen, X. Zou, Q. Xie, C. Qing, D. Chen, R. L. Frost. *Chem. Eng. J.* **2013**, *234*, 80–87. DOI:10.1016/j.cej.2013.08.061
50. M. R. Awual, M. M. Hasan, A. M. Asiri, M. M. Rahman. *Compos. B Eng.* **2019**, *171*, 294–301. DOI:10.1016/j.compositesb.2019.05.078
51. D. Xu, J. Liu, T. Ma, X. Zhao, H. Ma, J. Li. *Environ. Technol. Innov.* **2022**, *26*, 102264. DOI:10.1016/j.eti.2021.102264
52. R. M. Kamel, A. Shahat, W. H. Hegazy, E. M. Khodier, M. R. Awual. *J. Mol. Liq.* **2019**, *285*, 20–26. DOI:10.1016/j.molliq.2019.04.060
53. U. Fegade, G. Jethave, K. Y. Su, W. R. Huang, R. J. Wu. *J. Environ. Chem. Eng.* **2018**, *6*, 1918–1925. DOI:10.1016/j.jece.2018.02.040
54. L. R. Bonetto, F. Ferrarini, C. De Marco, J. S. Crespo, R. Guégan, M. Giovanela. *J. Water Process Eng.* **2015**, *6*, 11–20. DOI:10.1016/j.jwpe.2015.02.006

55. W. Liu, F. Huang, Y. Liao, J. Zhang, G. Ren, Z. Zhuang, J. Zhen, Z. Lin, C. Wang. *Angew. Chem.* **2008**, *120*, 5701–5704. DOI:10.1002/ange.200800172
56. M. R. Awual. *J. Clean. Prod.* **2019**, *228*, 1311–1319. DOI:10.1016/j.jclepro.2019.04.325
57. L. T. Eberhardt, S. H. Min, J. S. Han. *Bioresour. Technol.* **2006**, *97*, 2371–2376. DOI:10.1016/j.biortech.2005.10.040
58. Z. Ajmal, A. Muhmood, M. Usman, S. Kizito, J. Lu, R. Dong, S. Wu. *J. Colloid Interface Sci.* **2018**, *528*, 145–155. DOI:10.1016/j.jcis.2018.05.084
59. X. Cui, H. Li, Z. Yao, Y. Shen, Z. He, X. Yang, H. Y. Ng, C. H. Wang. *J. Clean. Prod.* **2019**, *207*, 846–856. DOI:10.1016/j.jclepro.2018.10.027
60. L. Zeng, X. Li, J. Li. *Water Res.* **2004**, *38*, 1318–1326. DOI:10.1016/j.watres.2003.12.009
61. G. Zhang, H. Liu, R. Liu, J. Qu. *J. Colloid Interface Sci.* **2009**, *335*, 168–174. DOI:10.1016/j.jcis.2009.03.019
62. X. Lin, K. Lu, A. K. Hardison, Z. Liu, X. Xu, D. Gao, J. Gong, W. S. Gardner. *Ecol. Indic.* **2021**, *126*, 107639. DOI:10.1016/j.ecolind.2021.107639
63. M. R. Awual, A. Jyo. *Desalination* **2011**, *281*, 111–117. DOI:10.1016/j.desal.2011.07.047
64. X. Tian, R. Yang, T. Chen, Y. Cao, H. Deng, M. Zhang, X. Jiang. *J. Hazard. Mater.* **2022**, *426*, 128121. DOI:10.1016/j.jhazmat.2021.128121

## Povzetek

Namen te raziskave je odstraniti fosfat (P) iz odpadne vode z uporabo nanodelcev  $\text{MnFe}_2\text{O}_4$ . Za določitev površinskih lastnosti  $\text{MnFe}_2\text{O}_4$  so bile uporabljene analize BET, TGA/DTG, FTIR, SEM, TEM, VSM, XRD in EDX/Map. Specifična površina adsorbenta je bila  $196,56 \text{ m}^2/\text{g}$ , analiza VSM pa je pokazala, da ima adsorbent feromagnetne lastnosti. Največja učinkovitost sorpcije P z uporabo  $\text{MnFe}_2\text{O}_4$  (98,52 %) je bila dosežena pri pH 6, temperaturi  $55^\circ\text{C}$ , koncentraciji P  $10 \text{ mg/L}$ , času 60 min in odmerku sorbenta  $2,5 \text{ g/L}$ , kar je pomembna vrednost. Poleg tega je termodinamična študija pokazala, da je proces sorpcije P spontan in endotermičen. Največja sorpcijska kapaciteta P z uporabo  $\text{MnFe}_2\text{O}_4$  je bila  $39,48 \text{ mg/g}$ .  $\text{MnFe}_2\text{O}_4$  se lahko uporablja za do 6 ciklov ponovne uporabe z visoko sorpcijsko učinkovitostjo (>91 %). Poleg tega je  $\text{MnFe}_2\text{O}_4$  odstranil fosfat, KPK in BPK5 iz komunalne odpadne vode s precejšnjo učinkovitostjo odstranjevanja, in sicer 82,7 %, 75,8 % in 77,3 %.



Except when otherwise noted, articles in this journal are published under the terms and conditions of the Creative Commons Attribution 4.0 International License

# Syntheses, Structures and Insulin-Like Activity of Two Oxidovanadium(V) Complexes with Similar Nicotinothrazone Ligands

Gao-Qi Zhou, Xiao-Yang Qiu\*, Shu-Juan Liu, Chu-Yi Wang

College of Science & Technology, Ningbo University, Ningbo 315315, P. R. China

\* Corresponding author: E-mail: xiaoyang\_qiu@126.com

Received: 06-05-2022

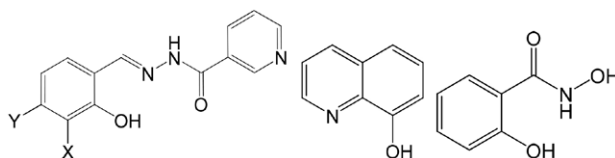
## Abstract

Two new oxidovanadium(V) complexes,  $[\text{VOL}^1(\text{HQ})]$  (1) and  $[\text{VOL}^2(\text{SAH})]$  (2), were prepared by the reaction of  $[\text{VO}(\text{acac})_2]$  (where acac = acetylacetonate) with  $N'$ -(3-ethoxy-2-hydroxybenzylidene)nicotinothrazone ( $\text{H}_2\text{L}^1$ ) and 8-hydroxyquinoline (HHQ), and  $N'$ -(2-hydroxy-4-methoxybenzylidene)nicotinothrazone ( $\text{H}_2\text{L}^2$ ) and salicylhydroxamic acid (HSAH), respectively, in methanol. Crystal and molecular structures of the complexes were determined by elemental analysis, infrared spectroscopy and single crystal X-ray diffraction. The V atoms in both complexes are in octahedral coordination. Thermal stability of the complexes was studied. Both complexes can decrease the blood glucose level in alloxan-diabetic mice, but the blood glucose level in the treated normal mice was not altered.

**Keywords:** Nicotinothrazone ligand; oxovanadium complex; crystal structure; thermal property; insulin-like activity

## 1. Introduction

It was reported that inorganic vanadium salts exhibited insulin-like activity at 40 years ago.<sup>1</sup> Interestingly, a pharmacological advantage of the vanadium salts is that it can be orally administered with long-term insulin-like activity *in vivo*.<sup>1b,2</sup> However, inorganic vanadium salts are considered as less active and more toxic when compared with vanadium complexes with various types of ligands.<sup>3</sup> Thus, a number of vanadium complexes have been prepared to improve the stability and membrane permeability of the vanadyl cation or decrease the toxicity of the vanadate anion.<sup>4</sup> Metal complexes with nicotinothrazone ligands have received particular attention in biological and medicinal chemistry.<sup>5</sup> 8-Hydroxyquinoline (HHQ) and salicylhydroxamic acid (HSAH) are widely known bidentate ligands in coordination chemistry.<sup>6</sup> However, only two HQ coordinated oxovanadium complexes and one SAH coordinated oxidovanadium complex with thrazone ligands have been reported so far.<sup>7</sup> In the present paper, two new oxovanadium(V) complexes with thrazone and HQ or SAH ligands,  $[\text{VOL}^1(\text{HQ})]$  (1) and  $[\text{VOL}^2(\text{SAH})]$  (2) ( $\text{H}_2\text{L}^1 = N'$ -(3-ethoxy-2-hydroxybenzylidene)nicotinothrazone,  $\text{H}_2\text{L}^2 = N'$ -(2-hydroxy-4-methoxybenzylidene)nicotinothrazone; Scheme 1), have been presented.



**Scheme 1.** The thrazone, HHQ and HSAH ligands.  $\text{H}_2\text{L}^1$ : X = OEt, Y = H;  $\text{H}_2\text{L}^2$ : X = H, Y = OMe.

## 2. Experimental

### 2.1. Materials and Measurements

Commercially available 3-ethoxysalicylaldehyde, 4-methoxysalicylaldehyde and nicotinothrazone were purchased from Sigma-Aldrich and used without further purification. Other solvents and reagents were made in China and used as received.  $\text{H}_2\text{L}^1$  and  $\text{H}_2\text{L}^2$  were prepared according to the literature method.<sup>8</sup> C, H and N elemental analyses were performed with a Perkin-Elmer elemental analyser. Infrared spectra were recorded on a Nicolet AVATAR 360 spectrometer as KBr pellets in the (4000–400)  $\text{cm}^{-1}$  region. Thermal stability analysis was performed on a Perkin-Elmer Pyris Diamond TG-DTA thermal analyses system. Molar conductivity data were determined with a DDS-11A conductometer.

## 2. 2. Synthesis of [VOL<sup>1</sup>(HQ)] (1)

A methanolic solution (10 mL) of [VO(acac)<sub>2</sub>] (0.1 mmol, 26.5 mg) was added to a methanolic solution (10 mL) of H<sub>2</sub>L<sup>1</sup> (0.1 mmol, 28.5 mg) and HHQ (0.1 mmol, 14.5 mg) with stirring. The mixture was stirred for 30 min at room temperature to give a deep brown solution. The resulting solution was allowed to stand in air for a few days. Brown block-shaped crystals suitable for X-ray single crystal diffraction were formed at the bottom of the vessel. The isolated products were washed three times with cold ethanol, and dried in air. The yield was 55%. Anal. calc. for C<sub>24</sub>H<sub>19</sub>N<sub>4</sub>O<sub>5</sub>V: C, 58.31; H, 3.87; N, 11.33; found: C, 58.12; H, 3.78; N, 11.46%.

## 2. 3. Synthesis of [VOL<sup>2</sup>(SAH)] (2)

This complex was prepared according to the same method as that described for **1**, with H<sub>2</sub>L<sup>1</sup> replaced by H<sub>2</sub>L<sup>2</sup> (0.1 mmol, 27.1 mg), and HHQ replaced by HSAH (0.1 mmol, 15.3 mg). The yield was 63%. Anal. calc. for C<sub>21</sub>H<sub>17</sub>N<sub>4</sub>O<sub>7</sub>V: C, 51.65; H, 3.51; N, 11.47; found: C, 51.56; H, 3.62; N, 11.38%.

## 2. 4. X-Ray Crystallography

Diffraction intensities for the complexes were collected at 298(2) K using a Bruker D8 VENTURE PHOTON diffractometer with MoK $\alpha$  radiation ( $\lambda$  =

0.71073 Å). The collected data were reduced using the SAINT program,<sup>9</sup> and multi-scan absorption corrections were performed using the SADABS program.<sup>10</sup> The structures were solved by direct methods and refined against  $F^2$  by full-matrix least-squares methods using the SHELXTL.<sup>11</sup> All of the non-hydrogen atoms were refined anisotropically. The amino hydrogen atom in complex **2** was located from a difference Fourier map and refined isotropically, with N–H distance restrained to 0.90(1) Å. The remaining hydrogen atoms were placed in idealized positions and constrained to ride on their parent atoms. The crystallographic data for the complexes are summarized in Table 1.

## 2. 5. Glucose-Lowering Assay

Male Kunming mice, weighing about 25–30 g, were obtained from Experimental Animal Center, Shandong Lukang Pharmaceutical Co., Ltd of China, and maintained on a light/dark cycle. All animals were allowed free access to food and water. Temperature and relative humidity were maintained at 25 °C and 50%. Mice were acclimatized for a week prior to induction of diabetes. Diabetes was induced by a single intra-peritoneal injection of freshly prepared alloxan (200 mg kg<sup>-1</sup> body weight) in 0.9% saline. The control mice were injected with an equal volume of vehicle. After a week, blood was collected from the tail vein and serum samples were analyzed for blood glucose. Animals showing fasting (12 h) blood glucose higher than 11.1 mmol L<sup>-1</sup> were considered to be diabetic and used for the study.

The experimental animals were randomly divided into 8 groups with 4 mice each according to the blood glucose. Group 1, normal control group: normal mice treated with 0.5% carboxymethyl cellulose (CMC). Groups 2 and 3, treated normal groups: normal mice treated with 20 mg V kg<sup>-1</sup> complexes. Group 4, diabetic control group: alloxan diabetic mice treated with 0.5% CMC. Groups 5–8, treated diabetic groups: alloxan diabetic mice treated with the complexes at doses of 10 and 20 mg V kg<sup>-1</sup> intragastric administration. The complexes were administered as suspensions in 0.5% CMC. The substances were administered intragastrically once a day at the volume of 10 mL kg<sup>-1</sup> for 2 weeks.

## 3. Results and Discussion

### 3. 1. General

Replacement of two acetylacetonate ligands of [VO(acac)<sub>2</sub>] by hydrazone and 8-hydroxyquinoline or salicylhydroxamate ligands in methanol resulted in the formation of two structurally similar complexes. The complexes are soluble in DMF, DMSO, methanol, ethanol, and acetonitrile. Molar conductance of complexes **1** and **2** at the concentration of 10<sup>-4</sup> mol L<sup>-1</sup> are 16 Ω<sup>-1</sup> cm<sup>2</sup> mol<sup>-1</sup>

**Table 1.** Crystallographic data and refinement parameters for the complexes

Parameter	Value	
	1	2
Chemical formula	C <sub>24</sub> H <sub>19</sub> N <sub>4</sub> O <sub>5</sub> V	C <sub>21</sub> H <sub>17</sub> N <sub>4</sub> O <sub>7</sub> V
Formula weight	494.4	488.3
Crystal system	Monoclinic	Monoclinic
Space group	<i>P</i> 2 <sub>1</sub> / <i>n</i>	<i>P</i> 2 <sub>1</sub> / <i>n</i>
Unit cell parameters		
<i>a</i> / Å	9.0157(5)	11.0094(8)
<i>b</i> / Å	11.4002(6)	17.7842(12)
<i>c</i> / Å	21.6406(11)	12.6825(10)
$\beta$ / °	97.130(2)	101.446(2)
<i>V</i> / Å <sup>3</sup>	2207.0(2)	2433.8(3)
<i>Z</i>	4	4
<i>D</i> <sub>calc</sub> / g cm <sup>-3</sup>	1.488	1.333
<i>T</i> / K	298(2)	298(2)
$\mu$ / mm <sup>-1</sup>	0.495	0.453
<i>F</i> (000)	1016	1000
Unique reflections	4095	4526
Observed reflections [ <i>I</i> > 2σ( <i>I</i> )]	3380	3562
Parameters	308	303
Restraints	0	1
<i>R</i> <sub>1</sub> , <i>wR</i> <sub>2</sub> [ <i>I</i> > 2σ( <i>I</i> )]	0.0377, 0.0943	0.0621, 0.2062
<i>R</i> <sub>1</sub> , <i>wR</i> <sub>2</sub> (all data)	0.0503, 0.1021	0.0797, 0.2229
Goodness of fit on <i>F</i> <sup>2</sup>	1.041	1.105

and  $23 \Omega^{-1} \text{ cm}^2 \text{ mol}^{-1}$ , respectively, indicating they are non-electrolytes.<sup>12</sup>

### 3. 2. Crystal Structure Description of the Complexes

The molecular structures and atom numbering schemes of complexes **1** and **2** are shown in Figures 1 and 2, respectively. Selected bond lengths and angles are given in Table 2. The V atoms in the complexes are in

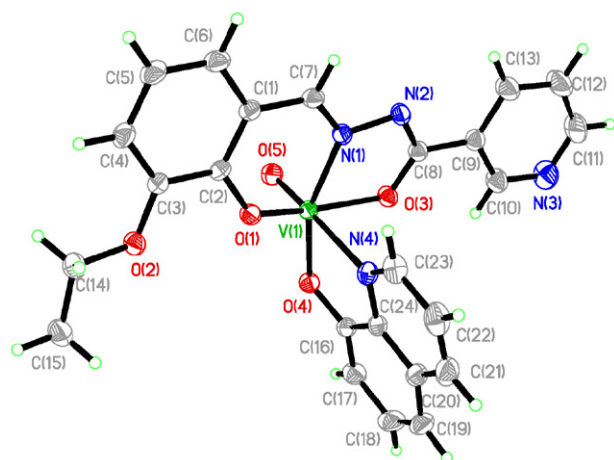


**Figure 1.** ORTEP plot of the molecular structure of complex **1**. Displacement ellipsoids of non-hydrogen atoms are drawn at the 30% probability level.

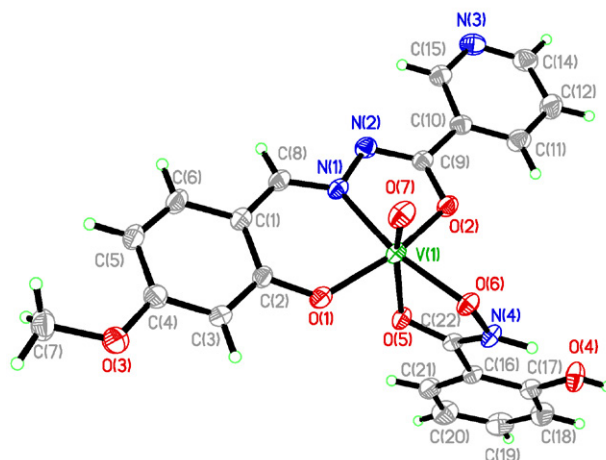


**Figure 2.** ORTEP plot of the molecular structure of complex **2**. Displacement ellipsoids of non-hydrogen atoms are drawn at the 30% probability level.

**Table 2.** Selected bond distances (Å) and angles (°) for the complexes.

<b>1</b>			
V(1)–O(1)	1.8606(14)	V(1)–O(3)	1.0619(15)
V(1)–O(4)	1.8501(14)	V(1)–O(5)	1.5862(16)
V(1)–N(1)	2.0777(17)	V(1)–N(4)	2.3416(18)
O(5)–V(1)–O(4)	99.57(7)	O(5)–V(1)–O(1)	99.77(8)
O(4)–V(1)–O(1)	107.28(6)	O(5)–V(1)–O(3)	99.01(8)
O(4)–V(1)–O(3)	88.15(6)	O(1)–V(1)–O(3)	153.21(7)
O(5)–V(1)–N(1)	96.70(7)	O(4)–V(1)–N(1)	158.03(7)
O(1)–V(1)–N(1)	84.23(6)	O(3)–V(1)–N(1)	74.74(6)
O(5)–V(1)–N(4)	175.26(7)	O(4)–V(1)–N(4)	75.87(6)
O(1)–V(1)–N(4)	82.99(6)	O(3)–V(1)–N(4)	79.70(6)
N(1)–V(1)–N(4)	87.39(7)		
<b>2</b>			
V(1)–O(1)	1.855(3)	V(1)–O(2)	1.947(3)
V(1)–O(5)	2.218(3)	V(1)–O(6)	1.885(3)
V(1)–O(7)	1.585(3)	V(1)–N(1)	2.084(3)
O(7)–V(1)–O(1)	99.53(14)	O(7)–V(1)–O(6)	92.80(13)
O(1)–V(1)–O(6)	110.89(12)	O(7)–V(1)–O(2)	102.68(14)
O(1)–V(1)–O(2)	149.95(13)	O(6)–V(1)–O(2)	88.08(11)
O(7)–V(1)–N(1)	94.18(14)	O(1)–V(1)–N(1)	84.21(12)
O(6)–V(1)–N(1)	162.05(12)	O(2)–V(1)–N(1)	74.26(11)
O(7)–V(1)–O(5)	166.78(13)	O(1)–V(1)–O(5)	81.35(11)
O(6)–V(1)–O(5)	74.73(10)	O(2)–V(1)–O(5)	81.60(10)
N(1)–V(1)–O(5)	99.02(11)		



the other coordinate bonds, yet, it is not uncommon for such complexes.<sup>13</sup> The bond lengths in both complexes are comparable to each other, and also similar to those observed in the mononuclear oxidovanadium(V) complexes with octahedral coordination.<sup>13</sup> The angular distortion in the octahedral environment around V comes from the five- and six-membered chelate rings taken by the nicotinothiazone ligands. For the same reason, the *trans* angles significantly deviate from the ideal values of 180°. Distortion of the octahedral coordination can be observed from the coordinate bond angles, ranging from 74.74(6)° to 107.28(6)° for the perpendicular angles, and from 153.21(7)° to 175.26(7)° for the diagonal angles for **1**, and from 74.26(11)° to 110.89(12)° for the perpendicular angles, and from 149.95(13)° to 162.05(12)° for the diagonal angles for **2**. The displacement of the V atoms from the equatorial plane is 0.30 Å for **1** and 0.23 Å for **2**. The dihedral angles between the benzene ring and the pyridine ring of the hydrazone ligands are 6.2(3)° in **1** and 6.3(5)° in **2**. In the crystal structure of **2**, the adjacent two complex molecules are linked by O–H...N hydrogen bonds [O(4)–H(4A)...N(3)<sup>i</sup>: O(4)–H(4A) = 0.82 Å, H(4A)...N(3)<sup>i</sup> = 1.92 Å, O(4)...N(3)<sup>i</sup> = 2.736(4) Å, O(4)–H(4A)...N(3)<sup>i</sup> = 172°; symmetry code: i)  $-\frac{1}{2} + x, 1\frac{1}{2} - y, \frac{1}{2} + z$ ], to form a dimer. The dimers are further linked by N–H...O hydrogen bonds [N(4)–H(4)...O(6)<sup>ii</sup>: N(4)–H(4) = 0.90(1) Å, H(4)...O(6)<sup>ii</sup> = 2.14(4) Å, N(4)...O(6)<sup>ii</sup> = 2.838(4) Å; symmetry code: ii)  $1 - x, 2 - y, 1 - z$ ], to form one dimensional chain.

### 3. 3. IR Spectra

Complexes **1** and **2** exhibit typical bands at 963 cm<sup>-1</sup> and 975 cm<sup>-1</sup>, respectively, assigned to the V=O vibration.<sup>14</sup> The bands due to  $\nu_{C=O}$  were absent in the complexes, but new C–O stretches appeared at 1266 cm<sup>-1</sup> for **1** and 1250 cm<sup>-1</sup> for **2**. This suggests occurrence of keto-imine tautomerization of the ligands during complexation. The intense  $\nu_{C=N}$  absorptions are observed at 1602 cm<sup>-1</sup> for **1** and **2**.<sup>15</sup> The weak peaks in the low wave numbers in the region (400–650) cm<sup>-1</sup> may be attributed to V–O and V–N bonds in the complexes.

### 3. 4. Thermal Property

Differential thermal (DT) and thermal gravimetric analyses (TGA) were conducted to examine the stability of the complexes (Figures 3 and 4). For **1**, the complex decomposed from 170 °C to 490 °C, corresponding to the loss of the nicotinothiazone and HQ ligands and the formation of V<sub>2</sub>O<sub>5</sub>. The total observed weight loss of 82.7% is close to the calculated value of 81.6%. For **2**, the complex decomposed from 170 °C to 510 °C, corresponding to the loss of the nicotinothiazone and SAH ligands and the formation of V<sub>2</sub>O<sub>5</sub>. The total observed weight loss of 82.3% is close to the calculated value of 81.4%.

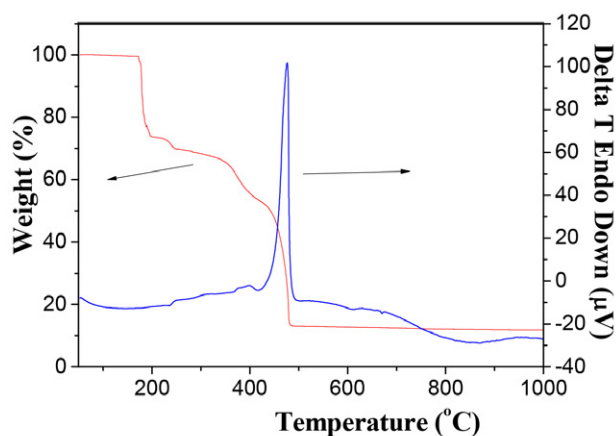


Figure 3. DT-TGA curves of complex **1**.

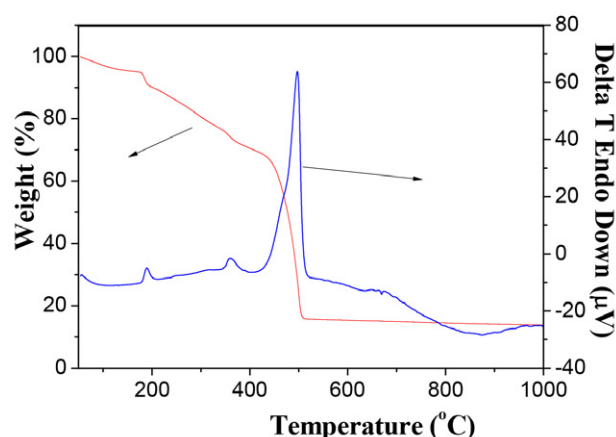


Figure 4. DT-TGA curves of complex **2**.

### 3. 5. Insulin-Like Activity of the Complexes

The results are listed in Table 3, which showed that both complexes had blood glucose-lowering effect at doses of 10.0 and 20.0 mg V kg<sup>-1</sup>. Both complexes can decrease the blood glucose level in alloxan-diabetic mice, whereas the blood glucose level in the treated normal mice (20.0 mg V kg<sup>-1</sup> by intragastric administration for 2 weeks) was not altered as compared with the untreated normal mice. The alloxan-diabetic mice exhibited significant hyperglycemia. After 2-week administration with the complexes, the blood glucose level was decreased compared with the diabetic control group. The glucose-lowering effect of both complexes is similar to each other. VOSO<sub>4</sub> was also assayed as comparison, and showed similar activities as compared to the complexes.

## 4. Conclusion

Two new mononuclear oxidovanadium(V) complexes derived from mixed ligands *N*-(3-ethoxy-2-

Table 4 Effects of the complexes on blood glucose levels of mice

Group	Dose (mg V kg <sup>-1</sup> ) <sup>a</sup>	Blood glucose (mmol L <sup>-1</sup> )			
		0	7 d	14 d	21 d
normal mice	CMC	5.8±0.5	5.9±0.7	5.9±0.9	5.8±0.8
normal mice + 1	20.00	5.7±0.8	5.8±1.0	5.9±1.1	5.9±0.8
normal mice + 2	20.00	5.7±0.6	5.9±0.7	5.8±0.9	5.8±1.3
normal mice + VOSO <sub>4</sub>	20.00	5.6±0.5	5.7±0.4	5.8±0.8	5.7±0.9
alloxan mice	CMC	16.7±1.5	16.0±1.2	15.7±1.4	15.5±1.5
alloxan mice + 1	20.00	8.2±1.3	6.2±1.5	6.1±1.3	6.4±1.3
alloxan mice + 1	10.00	9.3±1.5	6.7±1.1	6.9±1.2	7.0±1.4
alloxan mice + 2	20.00	7.8±1.4	6.1±1.2	6.2±1.4	6.0±1.1
alloxan mice + 2	10.00	9.7±1.2	6.6±1.3	6.5±1.0	6.3±1.3
alloxan mice + VOSO <sub>4</sub>	20.00	8.3±1.1	6.4±0.8	6.3±0.5	6.2±1.0
alloxan mice + VOSO <sub>4</sub>	10.00	9.5±1.0	6.8±1.1	6.7±0.9	6.1±0.7

<sup>a</sup> Data were expressed as mean±standard deviations.

hydroxybenzylidene)nicotinohydrazide and 8-hydroxy-quinoline, and *N*'-(2-hydroxy-4-methoxybenzylidene)nicotinohydrazide and salicylhydroxamic acid, respectively, were prepared and structurally characterized. The V atoms are in octahedral coordination. Thermal stability of the complexes was studied. The bioassay indicated that both complexes have effective insulin-like activity on alloxan-diabetic mice, which deserve further study.

### Supplementary Data

CCDC 979511 (1) and 979512 (2) contain the supplementary crystallographic data for the complexes. These data can be obtained free of charge via <http://www.ccdc.cam.ac.uk/conts/retrieving.html>, or from the Cambridge Crystallographic Data Center, 12 Union Road, Cambridge CB2 1EZ, UK; fax: (+44)1223-336-033; or e-mail: [deposit@ccdc.cam.ac.uk](mailto:deposit@ccdc.cam.ac.uk).

### Acknowledgments

This work was financially supported by Ningbo Public Welfare Funds (Project Nos. 202002N3056 and 2021S142).

## 5. References

- (a) Y. Shechter, S. J. D. Karlsh. *Nature* **1980**, 284, 556–558; DOI:10.1038/284556a0  
(b) C. E. Heyliger, A. G. Tahiliani, J. H. McNeill. *Science* **1985**, 227, 1474–1477. DOI:10.1126/science.3156405
- J. Meyerovitch, Z. Farfel, J. Sack, Y. Shechter. *J. Biol. Chem.* **1987**, 262, 6658–6662. DOI:10.1016/S0021-9258(18)48292-0
- (a) M. Haratake, M. Fukunaga, M. Ono, M. Nakayama. *J. Biol. Inorg. Chem.* **2005**, 10, 250–258; DOI:10.1007/s00775-005-0634-8  
(b) S. Guo, N. Sun, Y. Ding, A. Li, Y. Jiang, W. Zhai, Z. Li, D. Qu, Z. You. *Z. Anorg. Allg. Chem.* **2018**, 644, 1172–1176. DOI:10.1002/zaac.201800060
- (a) K. H. Thompson, J. H. McNeill, C. Orvig. *Chem. Rev.* **1999**, 99, 2561–2571; DOI:10.1021/cr980427c  
(b) I. Goldwaster, D. Gefel, E. Gershonov, M. Fridkin, Y. Shechter. *J. Inorg. Biochem.* **2000**, 80, 21–25; DOI:10.1016/S0162-0134(00)00035-0  
(c) M. Melchior, S. J. Rettig, B. D. Liboiron, K. H. Thompson, V. G. Yuen, J. H. McNeill, C. Orvig. *Inorg. Chem.* **2001**, 40, 4686–4690; DOI:10.1021/ic000984t  
(d) J. Szklarzewicz, A. Jurowska, M. Hodorowicz, G. Kazez, M. Gluch-Lutwin, J. Sapa. *Inorg. Chim. Acta* **2021**, 516, 120135; DOI:10.1016/j.ica.2020.120135  
(e) T. Kolesa-Dobravc, K. Maejima, Y. Yoshikawa, A. Meden, H. Yasui, F. Perdih. *New J. Chem.* **2018**, 42, 3619–3632; DOI:10.1039/C7NJ04189F  
(f) L. Y. Xu, Y. M. Li, M. M. Duan, Y. X. Li, M. X. Han, J. H. Wu, Y. H. Wang, K. X. Dong, Z. L. You. *Polyhedron* **2019**, 165, 138–142. DOI:10.1016/j.poly.2019.03.016
- (a) M. F. Wang, Z. Y. Yang, Y. Li, H. G. Li. *J. Coord. Chem.* **2011**, 64, 2974–2983; DOI:10.1080/00958972.2011.610102  
(b) A. El-Dissouky, O. Al-Fulaij, M. K. Awad, S. Rizk. *J. Coord. Chem.* **2010**, 63, 330–345; DOI:10.1080/00958970903366959  
(c) K. M. Ibrahim, I. M. Gabr, R. R. Zaky. *J. Coord. Chem.* **2009**, 62, 1100–1111; DOI:10.1080/00958970802464616  
(d) A. S. El-Tabl, F. A. El-Saied, A. N. Al-Hakimi. *J. Coord. Chem.* **2008**, 61, 2380–2401. DOI:10.1080/00958970801914041
- (a) A. F. A. Peacock, S. Parsons, P. J. Sadler. *J. Am. Chem. Soc.* **2007**, 129, 3348–3357; DOI:10.1021/ja068335p  
(b) T. Birk, J. Bendix. *Inorg. Chem.* **2003**, 42, 7608–7615; DOI:10.1021/ic034777f  
(c) H. M. Colquhoun, D. J. Williams, Z. X. Zhu. *J. Am. Chem. Soc.* **2002**, 124, 13346–13347; DOI:10.1021/ja027851m  
(d) T. Tekeste, H. Vahrenkamp. *Inorg. Chim. Acta* **2007**, 360, 1523–1528; DOI:10.1016/j.ica.2006.08.013  
(e) T. K. Si, S. Chakraborty, A. K. Mukherjee, M. G. B. Drew, R. Bhattacharyya. *Polyhedron* **2008**, 27, 2233–2242.

- DOI:10.1016/j.poly.2008.03.031
7. (a) Z.-P. Deng, S. Gao, H. Zhao, L.-H. Huo. *Chinese J. Inorg. Chem.* **2007**, 23, 173–176;  
(b) T. Ghosh, B. Mondal, T. Ghosh, M. Sutradhar, G. Mukherjee, M. G. B. Drew. *Inorg. Chim. Acta* **2007**, 360, 1753–1761; DOI:10.1016/j.ica.2006.10.003  
(c) S. Gao, Z.-Q. Weng, S.-X. Liu. *Polyhedron* **1998**, 17, 3595–3606. DOI:10.1016/S0277-5387(98)00154-5
  8. (a) V. S. Sergienko, V. L. Abramenko, L. K. Minacheva, M. A. Poraikoshits, V. G. Sakharova. *Russ. J. Coord. Chem.* **1993**, 19, 28–37;  
(b) J. C. Cui, H. D. Yin, Y. L. Qiao. *Acta Crystallogr.* **2007**, E63, o2633.
  9. Bruker, SMART and SAINT. Bruker AXS Inc., Madison, Wisconsin, USA, 2002.
  10. G. M. Sheldrick. SADABS. *Program for Empirical Absorption Correction of Area Detector*, University of Göttingen, Germany, 1996.
  11. G. M. Sheldrick. SHELXTL V5.1 *Software Reference Manual*, Bruker AXS, Inc., Madison, Wisconsin, USA, 1998.
  12. W. J. Geary. *Coord. Chem. Rev.* **1971**, 7, 81–122. DOI:10.1016/S0010-8545(00)80009-0
  13. (a) Q. W. Yang, P. Wang, Y. Lei. *Acta Chim. Slov.* **2020**, 67, 927–933; DOI:10.17344/acsi.2020.5932  
(b) Q.-A. Peng, X.-P. Tan, Y.-D. Wang, S.-H. Wang, Y.-X. Jiang, Y.-M. Cui. *Acta Chim. Slov.* **2020**, 67, 644–650; DOI:10.17344/acsi.2019.5650  
(c) G.-X. He, L.-W. Xue, Q.-L. Peng, P.-P. Wang, H.-J. Zhang. *Acta Chim. Slov.* **2019**, 66, 570–575; DOI:10.17344/acsi.2018.4868  
(d) H.-Y. Qian. *Acta Chim. Slov.* **2019**, 66, 995–1001; DOI:10.4149/neo\_2019\_190112N36  
(e) K.-H. Yang. *Acta Chim. Slov.* **2014**, 61, 629–636.
  14. (a) C.-L. Zhang, X.-Y. Qiu, S.-J. Liu. *J. Coord. Chem.* **2019**, 72, 3248–3257; DOI:10.1080/00958972.2019.1690647  
(b) H.-Y. Liu, Y.-S. Yin, L.-J. Yang, X.-L. Zou, Y.-F. Ye. *Acta Chim. Slov.* **2020**, 67, 130–136; DOI:10.17344/acsi.2019.5286  
(c) Y.-J. Cai, Y.-Y. Wu, F. Pan, Q.-A. Peng, Y.-M. Cui. *Acta Chim. Slov.* **2020**, 67, 896–903; DOI:10.17344/acsi.2020.5895  
(d) M. Liang, N. Sun, D.-H. Zou. *Acta Chim. Slov.* **2018**, 65, 964–969. DOI:10.17344/acsi.2018.4625
  15. (a) J.-X. Lei, J. Wang, Y. Huo, Z. L. You. *Acta Chim. Slov.* **2016**, 63, 670–677;  
(b) L.-W. Xue, Y.-J. Han, X.-Q. Luo. *Acta Chim. Slov.* **2019**, 66, 622–628; DOI:10.17344/acsi.2019.5039  
(c) Y. Lei. *Acta Chim. Slov.* **2022**, 69, 235–242. DOI:10.17344/acsi.2022.7296

## Povzetek

Z reakcijo  $[\text{VO}(\text{acac})_2]$  (acac = acetilacetonat) z  $N^{\circ}$ -(3-etoksi-2-hidroksibenziliden)nikotinohidrazidom ( $\text{H}_2\text{L}^1$ ) in 8-hidroksikinolinom (HHQ) ter z  $N^{\circ}$ -(2-hidroksi-4-metoksibenziliden)nikotinohidrazidom ( $\text{H}_2\text{L}^2$ ) in salicilhidroksamsko kislino (HSAH) v metanolu smo pripravili dva nova oksidovanadijeva(V) kompleksa  $[\text{VOL}^1(\text{HQ})]$  (**1**) in  $[\text{VOL}^2(\text{SAH})]$  (**2**). Kristalno in molekulsko strukturo kompleksov smo določili z elementno analizo, infrardečo spektroskopijo in monokristalno rentgensko difrakcijo. Atomi vanadija v obeh kompleksih so v oktaedrični koordinaciji. Proučevali smo termično stabilnost kompleksov. Oba kompleksa lahko zmanjšata raven glukoze v krvi pri aloksan-diabetičnih miših, vendar se raven glukoze v krvi pri zdravljenih normalnih miših ni spremenila.



Except when otherwise noted, articles in this journal are published under the terms and conditions of the Creative Commons Attribution 4.0 International License

# Antiproliferative and Antiprostata Cancer Activities of Heterocyclic Compounds Derived from Cyclohexane-1,4-dione

Nadia Y. Megally Abdo<sup>1</sup> and Rafat Milad Mohareb<sup>\*,2</sup>

<sup>1</sup> Department of Chemistry, Faculty of Science, Cairo University, Giza, Egypt

<sup>2</sup> Chemistry Department, Faculty of Education, Alexandria University, 21526 Alexandria, Egypt

\* Corresponding author: E-mail: raafat-mohareb@cu.edu.eg

Received: 04-13-2021

## Abstract

2-Amino-6-oxo-4,5,6,7-tetrahydrobenzo[*b*]thiophene-3-carbonitrile (**3**) was prepared from the reaction of cyclohexane-1,4-dione with elemental sulfur and malononitrile in 1,4-dioxane and triethylamine as catalyst. The latter compound reacted with triethyl orthoformate and either malononitrile or ethyl cyanoacetate in 1,4-dioxane in the presence of triethylamine to produce 4*H*-thieno[2,3-*f*]chromene derivatives **10a,b**. In addition, fused pyran and pyridine derivatives were synthesized starting from compound **3**. The cytotoxicities of the synthesized compounds were studied using the six cancer cell lines together with c-Met kinase and PC-3 cell line. The most active compounds were tested against five tyrosine kinases and Pim-1 kinase, most of which showed strong inhibition, encouraging further work.

**Keywords:** Cyclohexan-1,4-dione; thiophene; thiazole; cytotoxicity; tyrosine inhibitions

## 1. Introduction

Sulfur-containing heterocyclic compounds have attracted much attention in recent years because of their great medicinal and pharmaceutical importance.<sup>1,2</sup> Benzo[*b*]thiophene derivatives are one type of such sulfur-containing heterocyclic compounds and are good candidates for anticancer applications.<sup>3–7</sup> In addition, benzo[*b*]thiophene derivatives exhibit numerous other pharmacological effects, including antitumor agents,<sup>8</sup> anti-inflammatory agents,<sup>9,10</sup> antimicrobial agents,<sup>11,12</sup> anti-leishmanial agents,<sup>13,14</sup> antioxidants,<sup>15</sup> anti-anxiety agents, serotonin antagonists, and antiarrhythmic agents.<sup>16</sup> In addition, the combination of benzo[*b*]thiophene with other heterocyclic rings such as thiazole, thiophene, pyran, or pyridine rings increases the biological significance of such compound series.<sup>17–20</sup> Recently, our research group focused on benzo[*b*]thiophene derivatives by performing further heterocyclization reactions and then investigating their anticancer activities; in particular, some compounds showed inhibition of kinase and Pim-1.<sup>21–25</sup> In extension of this work, in this manuscript we show the synthesis of 2-amino-6-hydroxy-4,7-dihydrobenzo[*b*]thiophene-3-carbonitrile (**3**) starting from cyclohexane-1,4-dione, followed by further heterocycli-

zation to prepare compounds whose antiproliferative activities and kinase inhibitions were investigated.

## 2. Experimental

### 2. 1. General

<sup>13</sup>C NMR and <sup>1</sup>H NMR spectra were recorded using a Bruker DPX300 instrument in DMSO with TMS as the internal standard for protons and solvent signals as the internal standard for carbon spectra. Chemical shift values are given in  $\delta$  (ppm). Mass spectra were checked using EIMS (Shimadzu) and ESI-esquire 3000 from Bruker Daltonics. Elemental analyzes were performed using the Microanalytical Data Unit at Cairo University. All reactions were monitored by TLC on 2  $\times$  5 cm, 0.25 mm thick, precoated silica gel 60 F254 plates (Merck).

#### 2. 1. 1. Synthesis of 2-amino-6-oxo-4,5,6,7-tetrahydrobenzo[*b*]thiophene-3-carbonitrile (**3**)

To a solution of cyclohexane-1,4-dione (**1**) (1.2 g, 0.01 mol) in 1,4-dioxane (30 mL) with triethylamine (0.50 mL) was added malononitrile (0.66 g, 0.01 mol) and ele-

mental sulfur (0.32 g, 0.01 mol). The reaction mixture was heated at reflux for 1 h, and the product was filtered and dried.

Light brown crystals from 1,4-dioxane, yield: 75%; m.p.: 160–163 °C; IR (KBr)  $\nu_{\max}$  (cm<sup>-1</sup>): 3422–3236 (OH, NH<sub>2</sub>), 2966 (CH aliphatic), 2196 (CN), 1706 (CO), 1624 (C=C); <sup>1</sup>H NMR (300 MHz, DMSO-*d*<sub>6</sub>)  $\delta$  2.65 (d, 2H, *J* = 6.7 Hz, CH<sub>2</sub>-CH=C), 3.39 (s, 2H, D<sub>2</sub>O exchangeable, NH<sub>2</sub>), 5.54 (s, 2H, CH<sub>2</sub>), 6.82 (t, 1H, *J* = 6.7 Hz, CH<sub>2</sub>-CH=C), 9.97 (s, 1H, OH, D<sub>2</sub>O exchangeable); <sup>13</sup>C NMR (75 MHz, DMSO-*d*<sub>6</sub>)  $\delta$  22.6 (CH<sub>2</sub>-CH=C), 50.3 (CH<sub>2</sub>), 66.3 (CH<sub>2</sub>-CH=C), 116.2 (CN), 118.4, 121.7, 128.9, 134.0 (thiophene C), 161.8 (CO); EIMS (m/z, %): 192 [M<sup>+</sup>, 20]. Anal. Calcd. for C<sub>9</sub>H<sub>8</sub>N<sub>2</sub>OS: C, 56.23; H, 4.19; N, 14.57; S, 16.68. Found: C, 55.94; H, 4.08; N, 14.39; S, 16.30.

## 2. 1. 2. Synthesis of 2-amino-7-benzylidene-6-hydroxy-4,7-dihydrobenzo[*b*]thiophene-3-carbonitrile (5)

Benzaldehyde (4) (1.06 g, 0.01 mol) was added to a solution of compound 3 (1.92 g, 0.01 mol) in 1,4-dioxane (30 mL) containing piperidine (0.50 mL) and heated for 1 h at reflux. The reaction mixture was cooled and poured into cold water containing a few drops of hydrochloric acid. The precipitated solid was filtered off, washed and dried.

Red crystals from 1,4-dioxane, yield: 76%; m.p.: 180–182 °C; IR (KBr)  $\nu_{\max}$  (cm<sup>-1</sup>): 3428–3231 (OH, NH<sub>2</sub>), 2923 (CH aliphatic), 2201 (CN), 1625 (C=C); <sup>1</sup>H NMR (300 MHz, DMSO-*d*<sub>6</sub>)  $\delta$  2.89 (d, 2H, *J* = 4.6 Hz, CH<sub>2</sub>-CH=C), 3.44 (s, 2H, D<sub>2</sub>O exchangeable, NH<sub>2</sub>), 7.21 (t, 1H, *J* = 4.6 Hz, CH<sub>2</sub>-CH=C), 7.49–7.93 (m, 6H, C<sub>6</sub>H<sub>5</sub> and C=CH-C<sub>6</sub>H<sub>5</sub>), 10.01 (s, 1H, OH, D<sub>2</sub>O exchangeable); <sup>13</sup>C NMR (75 MHz, DMSO-*d*<sub>6</sub>)  $\delta$  22.2 (CH<sub>2</sub>-CH=C), 66.3 (CH<sub>2</sub>-CH=C), 77.2, 114.5 (C=C), 116.2 (CN), 119.8, 120.4, 126.2, 128.4, 129.5, 131.2, 133.4, 134.5, 154.5 (C<sub>6</sub>H<sub>5</sub>, thiophene C); EIMS (m/z, %): 280 [M<sup>+</sup>, 32]. Anal. Calcd. for C<sub>16</sub>H<sub>12</sub>N<sub>2</sub>OS: C, 68.55; H, 4.31; N, 9.99; S, 11.44. Found: C, 68.60; H, 4.29; N, 10.29; S, 11.09.

## 2. 1. 3. Synthesis of 2-amino-6-hydroxy-7-(2-hydroxybenzylidene)-4,7-dihydrobenzo[*b*]thiophene-3-carbonitrile (7)

A solution of compound 3 (1.92 g, 0.01 mol) in 1,4-dioxane (30 mL) containing piperidine (0.50 mL) was refluxed with salicylaldehyde (6) (1.22 g, 0.01 mol) for 1 h, the precipitated solid was filtered and dried after addition of cold water containing a few drops of hydrochloric acid.

Reddish brown crystals from 1,4-dioxane, yield: 77%; m.p.: 190–192 °C; IR (KBr)  $\nu_{\max}$  (cm<sup>-1</sup>): 3423–3231 (OH-NH<sub>2</sub>), 2925 (CH aliphatic), 2210 (CN), 1605 (C=C); <sup>1</sup>H NMR (300 MHz, DMSO-*d*<sub>6</sub>)  $\delta$  2.99 (d, 2H, CH<sub>2</sub>-CH=C), 3.32 (s, 2H, D<sub>2</sub>O exchangeable, NH<sub>2</sub>), 6.95 (m, 2H, 2 CH=C), 7.40–7.78 (m, 4H, C<sub>6</sub>H<sub>4</sub>), 10.25, 11.26 (2s, 2H, D<sub>2</sub>O exchangeable, 2OH); <sup>13</sup>C NMR (75 MHz,

DMSO-*d*<sub>6</sub>)  $\delta$  20.8 (CH<sub>2</sub>-CH=C), 66.9 (CH<sub>2</sub>-CH=C), 77.9, 118.9 (C=C), 116.5 (CN), 120.2, 125.9, 127.9, 128.8, 129.6, 131.1, 133.6, 134.2, 146.7 (C<sub>6</sub>H<sub>4</sub>, thiophene C); EIMS (m/z, %): 296 [M<sup>+</sup>, 51]. Anal. Calcd. for C<sub>16</sub>H<sub>12</sub>N<sub>2</sub>O<sub>2</sub>S: C, 64.85; H, 4.08; N, 9.45; S, 10.82. Found: C, 64.60; H, 4.29; N, 9.79; S, 10.58.

## 2. 1. 4. Synthesis of 4H-thieno[2,3-*f*]chromene derivatives 10a,b

Triethyl orthoformate (8) (1.48 mL, 0.01 mol) and either molononitrile (2) (0.66 g, 0.01 mol) or ethyl cyanoacetate (9) (1.13 mL, 0.01 mol) were added to a solution of compound 3 (1.92 g, 0.01 mol) in 1,4-dioxane (30 mL) with triethylamine (0.50 mL). The reaction mixture was heated at reflux for 2 h, cooled, and neutralized with cold water containing a few drops of hydrochloric acid; the precipitated product was filtered off and dried.

## 2,7-Diamino-4H-thieno[2,3-*f*]chromene-3,8-dicarbonitrile (10a)

Light brown crystals from 1,4-dioxane, yield: 47%; m.p.: >300 °C; IR (KBr)  $\nu_{\max}$  (cm<sup>-1</sup>): 3424–3228 (2NH<sub>2</sub>), 2924 (CH aliphatic), 2215, 2201 (2CN), 1626 (C=C); <sup>1</sup>H NMR (300 MHz, DMSO-*d*<sub>6</sub>)  $\delta$  3.39 (s, 2H, D<sub>2</sub>O exchangeable, NH<sub>2</sub>), 7.09–7.54 (m, 4H, pyran H-4 and Ar-H), 7.91 (s, 2H, D<sub>2</sub>O exchangeable, NH<sub>2</sub>); <sup>13</sup>C NMR (75 MHz, DMSO-*d*<sub>6</sub>)  $\delta$  77.1 (pyran C-4), 116.5, 117.3 (2CN), 114.7, 118.9, 120.2, 125.9, 127.9, 128.8, 131.1, 133.6, 134.2, 136.7 (Ar-C, pyran, thiophene); EIMS (m/z, %): 268 [M<sup>+</sup>, 44]. Anal. Calcd. For C<sub>13</sub>H<sub>8</sub>N<sub>4</sub>OS: C, 58.20; H, 3.01; N, 20.88; S, 11.95. Found: C, 58.50; H, 3.39; N, 20.62; S, 11.69.

## Ethyl 2,7-diamino-3-cyano-4H-thieno[2,3-*f*]chromene-8-carboxylate (10b)

Pale brown crystals from 1,4-dioxane, yield: 62%; m.p.: >300 °C; IR (KBr)  $\nu_{\max}$  (cm<sup>-1</sup>): 3423–3211 (2NH<sub>2</sub>), 2923 (CH aliphatic), 2201 (CN), 1706 (CO), 1621 (C=C); <sup>1</sup>H NMR (300 MHz, DMSO-*d*<sub>6</sub>)  $\delta$  1.16 (t, 3H, *J* = 7.21 Hz, OCH<sub>2</sub>CH<sub>3</sub>), 3.41 (s, 2H, D<sub>2</sub>O exchangeable, NH<sub>2</sub>), 4.20 (q, 2H, *J* = 7.21 Hz, OCH<sub>2</sub>CH<sub>3</sub>), 7.26–7.61 (m, 4H, pyran H-4 and Ar-H), 7.83 (s, 2H, D<sub>2</sub>O exchangeable, NH<sub>2</sub>); <sup>13</sup>C NMR (75 MHz, DMSO-*d*<sub>6</sub>)  $\delta$  88.5 (OCH<sub>2</sub>CH<sub>3</sub>), 45.5 (OCH<sub>2</sub>CH<sub>3</sub>), 77.4 (pyran C-4), 116.2 (CN), 115.6, 118.3, 120.8, 121.9, 122.3, 128.1, 130.3, 132.0, 133.4, 147.4 (Ar-C, pyran, thiophene), 162.6 (CO); EIMS (m/z, %): 315 [M<sup>+</sup>, 56]. Anal. Calcd. for C<sub>15</sub>H<sub>13</sub>N<sub>3</sub>O<sub>3</sub>S: C, 57.13; H, 4.16; N, 13.33; S, 10.17. Found: C, 57.40; H, 4.39; N, 13.62; S, 10.49.

## 2. 1. 5. Synthesis of *N'*-(2-amino-3-cyano-4,7-dihydrobenzo[*b*]thiophen-6-yl)-2-cyanoacetohydrazide (12)

To a solution of compound 3 (1.92 g, 0.01 mol) in 1,4-dioxane (30 mL) was added cyanoacetylhydrazine (11) (0.99 g, 0.01 mol) and the reaction mixture was heated un-

der reflux for 3 h and the resulting precipitate was collected by filtration after cooling.

Pale brown crystals from 1,4-dioxane, yield: 41%; m.p.: >300 °C; IR (KBr)  $\nu_{\max}$  (cm<sup>-1</sup>): 3418–3205 (NH<sub>2</sub>, 2NH), 2923 (CH aliphatic), 2210, 2197 (2CN), 1698 (CO), 1621 (C=C); <sup>1</sup>H NMR (300 MHz, DMSO-*d*<sub>6</sub>)  $\delta$  2.71 (d, 2H, *J* = 6.8 Hz,  $\text{CH}_2\text{-CH=}$ ), 3.37 (s, 2H, D<sub>2</sub>O exchangeable, NH<sub>2</sub>), 3.76 (s, 2H, CO- $\text{CH}_2\text{-CN}$ ), 5.54 (s, 2H, CH<sub>2</sub>), 6.83 (t, 1H, *J* = 6.8 Hz, CH<sub>2</sub>- $\text{CH=}$ ), 8.13, 9.93 (2s, 2H, D<sub>2</sub>O exchangeable, 2NH); <sup>13</sup>C NMR (75 MHz, DMSO-*d*<sub>6</sub>)  $\delta$  35.8 (CH<sub>2</sub>), 66.3 (CH<sub>2</sub>), 77.4, 118.5 (C=C), 98.9 (CO- $\text{CH}_2\text{-CN}$ ), 115.7, 116.2 (2CN), 129.9, 133.3, 136.6, 154.7 (thiophene C), 162.6 (CO);  $\delta$  EIMS (m/z, %): 273 [M<sup>+</sup>, 24]. Anal. Calcd. for C<sub>12</sub>H<sub>11</sub>N<sub>5</sub>OS: C, 52.73; H, 4.06; N, 25.62; S, 11.73. Found: C, 52.50; H, 4.39; N, 25.82; S, 11.69.

## 2. 1. 6. Synthesis of ethyl 2,7-diamino-3,8-dicyano-9-hydroxy-4,5-dihydronaphtho[1,2-*b*]thiophene-6-carboxylate (13)

A solution of compound 3 (1.92 g, 0.01 mol) (30 mL) and ethyl cyanoacetate (9) (1.13 mL, 0.01 mol) in 1,4-dioxane was heated at reflux with triethylamine (0.50 mL) for 3 hours. The solid formed was filtered off and dried after neutralizing the reaction mixture with cold water containing a few drops of hydrochloric acid.

Pale brown crystals from 1,4-dioxane, yield: 46%; m.p.: >300 °C; IR (KBr)  $\nu_{\max}$  (cm<sup>-1</sup>): 3521–3209 (OH, 2NH<sub>2</sub>), 2928 (CH aliphatic), 2208, 2199 (2CN), 1704 (CO), 1624 (C=C); <sup>1</sup>H NMR (300 MHz, DMSO-*d*<sub>6</sub>)  $\delta$  1.20 (t, 3H, *J* = 6.90 Hz, OCH<sub>2</sub>CH<sub>3</sub>), 2.65 (m, 4H, CH<sub>2</sub>-CH<sub>2</sub>), 3.36 (s, 2H, D<sub>2</sub>O exchangeable, NH<sub>2</sub>), 4.19 (q, 2H, *J* = 6.90 Hz, OCH<sub>2</sub>CH<sub>3</sub>), 7.84 (s, 2H, D<sub>2</sub>O exchangeable, NH<sub>2</sub>), 9.91 (s, 1H, D<sub>2</sub>O exchangeable, OH); <sup>13</sup>C NMR (75 MHz, DMSO-*d*<sub>6</sub>)  $\delta$  18.5 (OCH<sub>2</sub>CH<sub>3</sub>), 46.9 (OCH<sub>2</sub>CH<sub>3</sub>), 56.0, 67.3 (CH<sub>2</sub>-CH<sub>2</sub>), 115.5, 116.2 (2CN), 118.1, 119.7, 120.7, 122.5, 128.4, 129.3, 132.2, 133.3, 152.4 (Ph, thiophene C), 162.6 (CO); EIMS (m/z, %): 354 [M<sup>+</sup>, 52]. Anal. Calcd. for C<sub>17</sub>H<sub>14</sub>N<sub>4</sub>O<sub>3</sub>S: C, 57.62; H, 3.98; N, 15.81; S, 9.05. Found: C, 57.50; H, 3.87; N, 15.53; S, 8.84.

## 2. 1. 7. Synthesis of 4,7-dihydrobenzo[*b*]thiophene derivatives 15a,b

A cold solution (0–5 °C) of compound 3 (1.92 g, 0.01 mol) in ethanol (30 mL) containing sodium acetate (2.5 g) was added to a cold solution of either benzenediazonium chloride (14a) (0.01 mol) or 4-methylbenzenediazonium chloride (14b) (0.01 mol) [prepared by adding sodium nitrite solution (0.7 g, 0.01 mol in 10 mL water) to a cold solution of either aniline oil (0.93 g, 0.01 mol) or 4-methylaniline (1.07 g, 0.01 mol) in concentrated hydrochloric acid (8 mL, 18%) with constant stirring]. The whole mixture was kept at room temperature for 1 hour and the resulting product was collected by filtration.

## 2-Amino-6-hydroxy-7-(2-phenylhydrazono)-4,7-dihydrobenzo[*b*]thiophene-3-carbonitrile (15a)

Black crystals from ethanol, yield: 81%; m.p.: >300 °C; IR (KBr)  $\nu_{\max}$  (cm<sup>-1</sup>): 3518–3214 (OH, NH<sub>2</sub>, NH), 2924 (CH aliphatic), 2199 (CN), 1625 (C=C); <sup>1</sup>H NMR (300 MHz, DMSO-*d*<sub>6</sub>)  $\delta$  2.79 (d, 2H, CH<sub>2</sub>), 3.44 (s, 2H, D<sub>2</sub>O exchangeable, NH<sub>2</sub>), 7.17–7.63 (m, 6H, C<sub>6</sub>H<sub>5</sub> and CH=C), 7.94 (s, 1H, D<sub>2</sub>O exchangeable, NH), 9.01 (s, 1H, D<sub>2</sub>O exchangeable, OH); <sup>13</sup>C NMR (75 MHz, DMSO-*d*<sub>6</sub>)  $\delta$  20.8 (CH<sub>2</sub>), 67.2, 115.2 (CH=C), 116.4 (CN), 119.4, 121.7, 126.1, 128.4, 128.9, 132.1, 133.4, 137.1 (C<sub>6</sub>H<sub>5</sub> and thiophene), 182.8 (C=N); EIMS (m/z, %): 296 [M<sup>+</sup>, 61]. Anal. Calcd. for C<sub>15</sub>H<sub>12</sub>N<sub>4</sub>OS: C, 60.79; H, 4.08; N, 18.91; S, 10.82. Found: C, 60.49; H, 3.87; N, 18.53; S, 10.54.

## 2-Amino-6-hydroxy-7-(2-(*p*-tolyl)hydrazono)-4,7-dihydrobenzo[*b*]thiophene-3-carbonitrile (15b)

Dark brown crystals from ethanol, yield: 84%; m.p.: >300 °C; IR (KBr)  $\nu_{\max}$  (cm<sup>-1</sup>): 3524–3226 (OH, NH<sub>2</sub>, NH), 2922 (CH aliphatic), 2200 (CN), 1626 (C=C); <sup>1</sup>H NMR (300 MHz, DMSO-*d*<sub>6</sub>)  $\delta$  2.27 (s, 3H, CH<sub>3</sub>),  $\delta$  3.05 (d, 2H, CH<sub>2</sub>), 3.40 (s, 2H, D<sub>2</sub>O exchangeable, NH<sub>2</sub>), 7.17–7.59 (m, 5H, C<sub>6</sub>H<sub>4</sub> and CH=C), 7.92 (s, 1H, D<sub>2</sub>O exchangeable, NH), 9.21 (s, 1H, D<sub>2</sub>O exchangeable, OH); <sup>13</sup>C NMR (75 MHz, DMSO-*d*<sub>6</sub>)  $\delta$  16.5 (CH<sub>3</sub>), 20.8 (CH<sub>2</sub>), 66.5, 114.6 (CH=C), 117.4 (CN), 119.4, 121.7, 125.5, 128.2, 130.8, 132.7, 133.5, 137.0 (C<sub>6</sub>H<sub>5</sub> and thiophene), 184.1 (C=N); EIMS (m/z, %): 310 [M<sup>+</sup>, 57]. Anal. Calcd. for C<sub>16</sub>H<sub>14</sub>N<sub>4</sub>OS: C, 61.92; H, 4.55; N, 18.05; S, 10.33. Found: C, 62.20; H, 4.24; N, 18.37; S, 10.41.

## 2. 1. 8. Synthesis of dihydrobenzo[*b*]thiophene derivatives 19 and 20

A solution of compound 3 (1.92 g, 0.01 mol) in dimethylformamide (30 mL) and phenyl isothiocyanate (16) (1.35 mL, 0.01 mol) was cooled overnight in the presence of potassium hydroxide (0.5 g). To the reaction mixture either  $\alpha$ -chloroacetone (18a) (0.92 mL, 0.01 mol) or ethyl chloroacetate (18b) (1.22 mL, 0.01 mol) was added and allowed to stand overnight. The synthesized product was obtained by neutralizing the reaction mixture with a solution of cold water and a few drops of hydrochloric acid, filtered and dried.

## 2-Amino-6-hydroxy-7-(4-methyl-3-phenylthiazol-2(3*H*)-ylidene)-4,7-dihydrobenzo[*b*]thiophene-3-carbonitrile (19)

Dark brown crystals from ethanol, yield: 79%; m.p.: 182 °C; IR (KBr)  $\nu_{\max}$  (cm<sup>-1</sup>): 3518–3220 (OH, NH<sub>2</sub>), 2924 (CH aliphatic), 2188 (CN), 1629 (C=C); <sup>1</sup>H NMR (300 MHz, DMSO-*d*<sub>6</sub>)  $\delta$  2.56 (s, 3H, CH<sub>3</sub>), 2.72 (d, 2H, *J* = 4.5 Hz, CH<sub>2</sub>), 3.30 (s, 2H, D<sub>2</sub>O exchangeable, NH<sub>2</sub>), 7.06 (t, 1H, *J* = 4.5 Hz, CH), 7.09–7.61 (m, 6H, C<sub>6</sub>H<sub>5</sub> and thiazole H-5), 10.07 (s, 1H, D<sub>2</sub>O exchangeable, OH); <sup>13</sup>C NMR (75 MHz, DMSO-*d*<sub>6</sub>)  $\delta$  22.5 (CH<sub>3</sub>), 34.3 (CH<sub>2</sub>),



74.2, 118.1 (CH=C), 116.1 (CN), 121.7, 123.6, 124.4, 125.7, 127.8, 128.4, 128.7, 129.2, 129.4, 137.5, 139.4, 153.2 (C<sub>6</sub>H<sub>5</sub>, thiazole, thiophene); EIMS (m/z, %): 365 [M<sup>+</sup>, 24]. Anal. Calcd. for C<sub>19</sub>H<sub>15</sub>N<sub>3</sub>O<sub>2</sub>S<sub>2</sub>: C, 62.44; H, 4.14; N, 11.50; S, 17.55. Found: C, 62.59; H, 4.50; N, 11.22; S, 17.31.

**Ethyl 2-(((2-amino-3-cyano-6-oxo-5,6-dihydrobenzo[b]thiophen-7(4H)-ylidene)(phenyl-amino)methyl)thio)acetate (20)**

Dark brown crystals from ethanol, yield: 78%; m.p.: 150 °C; IR (KBr)  $\nu_{\max}$  (cm<sup>-1</sup>): 3518–3220 (OH, NH<sub>2</sub>, NH), 2929 (CH aliphatic), 2127 (CN), 1722 (CO), 1635 (C=C); <sup>1</sup>H NMR (300 MHz, DMSO-*d*<sub>6</sub>)  $\delta$  1.19 (t, 3H, *J* = 7.1 Hz, OCH<sub>2</sub>CH<sub>3</sub>), 2.72 (d, 2H, CH<sub>2</sub>), 3.06 (s, 2H, CH<sub>2</sub>), 3.30 (s, 2H, D<sub>2</sub>O exchangeable, NH<sub>2</sub>), 4.15 (q, 2H, *J* = 7.1 Hz, OCH<sub>2</sub>CH<sub>3</sub>), 7.06–7.72 (m, 6H, C<sub>6</sub>H<sub>5</sub> and CH), 8.96 (s, 1H, D<sub>2</sub>O exchangeable, NH), 10.07 (s, 1H, D<sub>2</sub>O exchangeable, OH); <sup>13</sup>C NMR (75 MHz, DMSO-*d*<sub>6</sub>)  $\delta$  13.9 (OCH<sub>2</sub>CH<sub>3</sub>), 28.7 (CH<sub>2</sub>), 45.5 (OCH<sub>2</sub>CH<sub>3</sub>), 50.1 (CH<sub>2</sub>), 72.4, 118.7 (CH=C), 116.1 (CN), 121.2, 121.7, 123.6, 124.4, 125.7, 127.8, 128.7, 130.4, 137.5, 139.4 (C=C, C<sub>6</sub>H<sub>5</sub>, thiophene C), 163.2 (CO); EIMS (m/z, %): 413 [M<sup>+</sup>, 24]. Anal. Calcd. for C<sub>20</sub>H<sub>19</sub>N<sub>3</sub>O<sub>3</sub>S<sub>2</sub>: C, 58.09; H, 4.63; N, 10.16; S, 15.51. Found: C, 58.36; H, 4.50; N, 10.22; S, 15.31.

**2. 1. 9. Synthesis of ethyl 2-amino-3-cyano-8-(phenylamino)-4,5-dihydrobenzo[1,2-*b*:5,6-*c'*]dithiophene-6-carboxylate (21)**

Compound **20** (4.13 g, 0.01 mol) was heated in a solution of 1,4-dioxane containing triethylamine (0.50 mL) for 2 h under reflux. The resulting solution was neutralized with an ice water solution containing a few drops of hydrochloric acid to give the synthesized solid, which was filtered and dried.

Brown crystals from ethanol, yield: 78%; m.p.: 225 °C; IR (KBr)  $\nu_{\max}$  (cm<sup>-1</sup>): 3418–3220 (NH<sub>2</sub>, NH), 2924 (CH aliphatic), 2199 (CN), 1722 (CO), 1633 (C=C); <sup>1</sup>H NMR (300 MHz, DMSO-*d*<sub>6</sub>)  $\delta$  1.19 (t, 3H, *J* = 7.2 Hz, OCH<sub>2</sub>CH<sub>3</sub>), 3.06 (m, 4H, CH<sub>2</sub>-CH<sub>2</sub>), 3.30 (s, 2H, D<sub>2</sub>O exchangeable, NH<sub>2</sub>), 4.15 (q, 2H, *J* = 7.2 Hz, OCH<sub>2</sub>CH<sub>3</sub>), 7.26–7.79 (m, 5H, C<sub>6</sub>H<sub>5</sub>), 8.96 (s, 1H, D<sub>2</sub>O exchangeable, NH); <sup>13</sup>C NMR (75 MHz, DMSO-*d*<sub>6</sub>)  $\delta$  14.3 (OCH<sub>2</sub>CH<sub>3</sub>), 45.5 (OCH<sub>2</sub>CH<sub>3</sub>), 61.5, 62.9 (CH<sub>2</sub>-CH<sub>2</sub>), 116.1 (CN), 118.0, 121.7, 128.8, 129.2, 129.9, 130.5, 131.6, 132.4, 133.0, 134.7, 136.4, 140.0 (C<sub>6</sub>H<sub>5</sub>, thiophene) 161.5 (CO); EIMS (m/z, %): 395 [M<sup>+</sup>, 24]. Anal. Calcd. for C<sub>20</sub>H<sub>17</sub>N<sub>3</sub>O<sub>2</sub>S<sub>2</sub>: C, 60.74; H, 4.33; N, 10.62; S, 16.22. Found: C, 60.49; H, 4.21; N, 10.82; S, 15.93.

**2. 1. 10. Synthesis of 5,9-dihydro-4H-thieno[2,3-*f*]chromene derivatives 23a-f**

A mixture of compound **3** (1.92 g, 0.01 mol), either malononitrile (**2**) (0.66 g, 0.01 mol) or ethyl cyanoacetate

(**9**) (1.13, 0.01 mol) and either benzaldehyde (**4**) (1.06 g, 0.01 mol), 4-chlorobenzaldehyde (**22a**) (1.4 g, 0.01 mol) or 4-methoxybenzaldehyde (**22b**) (1.36 g, 0.01 mol) in 1,4-dioxane (40 mL) and triethylamine (0.5 mL) was heated under reflux for 3 h and the precipitated product was kept under reflux. The precipitated product was recovered by adding cold water and a few drops of hydrochloric acid to the resulting mixture, filtered and dried.

**2,7-Diamino-9-phenyl-5,9-dihydro-4H-thieno[2,3-*f*]chromene-3,8-dicarbonitrile (23a)**

Reddish brown crystals from ethanol, yield: 40%; m.p.: 230 °C; IR (KBr)  $\nu_{\max}$  (cm<sup>-1</sup>): 3422–3210 (2NH<sub>2</sub>), 2924 (CH aliphatic), 2227, 2198 (2CN), 1625 (C=C); <sup>1</sup>H NMR (300 MHz, DMSO-*d*<sub>6</sub>)  $\delta$  3.09 (m, 4H, CH<sub>2</sub>-CH<sub>2</sub>), 3.34 (s, 2H, D<sub>2</sub>O exchangeable, NH<sub>2</sub>), 7.24–7.96 (m, 6H, pyran H-4 and C<sub>6</sub>H<sub>5</sub>), 8.54 (s, 2H, D<sub>2</sub>O exchangeable, NH<sub>2</sub>); <sup>13</sup>C NMR (75 MHz, DMSO-*d*<sub>6</sub>)  $\delta$  62.1, 65.3 (CH<sub>2</sub>-CH<sub>2</sub>), 76.5 (pyran C-4), 115.6, 116.6 (2CN), 118.4, 119.3, 122.6, 123.6, 128.9, 129.5, 129.9, 130.1, 131.9, 132.5, 133.7, 154.4 (C<sub>6</sub>H<sub>5</sub>, pyran, thiophene C); EIMS (m/z, %): 346 [M<sup>+</sup>, 34]. Anal. Calcd. for C<sub>19</sub>H<sub>14</sub>N<sub>4</sub>OS: C, 65.88; H, 4.07; N, 16.17; S, 9.26. Found: C, 65.59; H, 3.88; N, 16.32; S, 9.09.

**2,7-Diamino-9-(4-chlorophenyl)-5,9-dihydro-4H-thieno[2,3-*f*]chromene-3,8-dicarbonitrile (23b)**

Red crystals from ethanol, yield: 77%; m.p.: 160 °C; IR (KBr)  $\nu_{\max}$  (cm<sup>-1</sup>): 3421–3206 (2NH<sub>2</sub>), 2959 (CH aliphatic), 2225, 2195 (2CN), 1621 (C=C); <sup>1</sup>H NMR (300 MHz, DMSO-*d*<sub>6</sub>)  $\delta$  3.09 (m, 4H, CH<sub>2</sub>-CH<sub>2</sub>), 3.40 (s, 2H, D<sub>2</sub>O exchangeable, NH<sub>2</sub>), 7.26 (s, 1H, pyran H-4), 7.40–7.97 (m, 4H, C<sub>6</sub>H<sub>4</sub>), 8.53 (s, 2H, D<sub>2</sub>O exchangeable, NH<sub>2</sub>); <sup>13</sup>C NMR (75 MHz, DMSO-*d*<sub>6</sub>)  $\delta$  63.2, 65.3 (CH<sub>2</sub>-CH<sub>2</sub>), 76.8 (pyran C-4), 115.9, 116.2 (2CN), 118.4, 119.1, 120.3, 121.9, 123.9, 129.4, 129.8, 130.7, 131.4, 132.5, 133.1, 148.1 (C<sub>6</sub>H<sub>4</sub>, pyran, thiophene C); EIMS (m/z, %): 380 [M<sup>+</sup>, 45]. Anal. Calcd. for C<sub>19</sub>H<sub>13</sub>ClN<sub>4</sub>OS: C, 59.92; H, 3.44; N, 14.71; S, 8.42. Found: C, 59.95; H, 3.24; N, 14.56; S, 8.73.

**2,7-Diamino-9-(4-methoxyphenyl)-5,9-dihydro-4H-thieno[2,3-*f*]chromene-3,8-dicarbonitrile (23c)**

Reddish brown crystals from ethanol, yield: 82%; m.p.: 120 °C; IR (KBr)  $\nu_{\max}$  (cm<sup>-1</sup>): 3418–3220 (2NH<sub>2</sub>), 2924 (CH aliphatic), 2214, 2199 (2CN), 1633 (C=C); <sup>1</sup>H NMR (300 MHz, DMSO-*d*<sub>6</sub>)  $\delta$  3.06 (m, 4H, CH<sub>2</sub>-CH<sub>2</sub>), 3.36 (s, 2H, D<sub>2</sub>O exchangeable, NH<sub>2</sub>), 3.88 (s, 3H, OCH<sub>3</sub>), 7.11–7.20 (m, 3H, pyran H-4 and Ar-H), 7.85–7.99 (m, 2H, Ar-H), 8.38 (s, 2H, D<sub>2</sub>O exchangeable, NH<sub>2</sub>); <sup>13</sup>C NMR (75 MHz, DMSO-*d*<sub>6</sub>)  $\delta$  55.0 (OCH<sub>3</sub>), 62.9, 66.3 (CH<sub>2</sub>-CH<sub>2</sub>), 77.3 (pyran C-4), 115.8, 116.8 (2CN), 114.0, 114.8, 119.4, 122.1, 124.0, 129.6, 129.7, 130.5, 131.7, 132.7, 133.3, 157.2 (C<sub>6</sub>H<sub>4</sub>, pyran, thiophene C); EIMS (m/z, %): 376 [M<sup>+</sup>, 56]. Anal. Calcd. for C<sub>20</sub>H<sub>16</sub>N<sub>4</sub>O<sub>2</sub>S: C, 63.81; H, 4.28; N, 14.88; S, 8.52. Found: C, 63.69; H, 3.90; N, 14.60; S, 8.82.

**Ethyl 2,7-diamino-3-cyano-9-phenyl-5,9-dihydro-4H-thieno[2,3-f]chromene-8-carboxylate (23d)**

Brown crystals from acetic acid, yield: 83%; m.p.: 161 °C; IR (KBr)  $\nu_{\max}$  (cm<sup>-1</sup>): 3425–3211 (2NH<sub>2</sub>), 2933 (CH aliphatic), 2198 (CN), 1733 (CO), 1612 (C=C); <sup>1</sup>H NMR (300 MHz, DMSO-*d*<sub>6</sub>)  $\delta$  1.07 (t, 3H, *J* = 7.2 Hz, OCH<sub>2</sub>CH<sub>3</sub>), 3.17 (m, 4H, CH<sub>2</sub>-CH<sub>2</sub>), 3.39 (s, 2H, D<sub>2</sub>O exchangeable, NH<sub>2</sub>), 4.18 (q, 2H, *J* = 7.2 Hz, OCH<sub>2</sub>CH<sub>3</sub>), 7.08 (s, 1H, pyran H-4), 7.25–7.62 (m, 5H, C<sub>6</sub>H<sub>5</sub>), 8.23 (s, 2H, D<sub>2</sub>O exchangeable, NH<sub>2</sub>); <sup>13</sup>C NMR (75 MHz, DMSO-*d*<sub>6</sub>)  $\delta$  13.5 (OCH<sub>2</sub>CH<sub>3</sub>), 44.4 (OCH<sub>2</sub>CH<sub>3</sub>), 61.9, 65.1 (CH<sub>2</sub>-CH<sub>2</sub>), 97.9 (pyran C-4), 116.5 (CN), 121.7, 122.9, 123.7, 124.7, 127.9, 129.2, 130.9, 131.4, 133.8, 138.9, 147.5, 155.3 (C<sub>6</sub>H<sub>5</sub>, pyran, thiophene C), 163.1 (CO); EIMS (*m/z*, %): 393 [M<sup>+</sup>, 32]. Anal. Calcd. for C<sub>21</sub>H<sub>19</sub>N<sub>3</sub>O<sub>3</sub>S: C, 64.10; H, 4.87; N, 10.68; S, 8.15. Found: C, 64.39; H, 4.60; N, 10.90; S, 8.31.

**Ethyl 2,7-diamino-9-(4-chlorophenyl)-3-cyano-5,9-dihydro-4H-thieno[2,3-f]chromene-8-carboxylate (23e)**

Brown crystals from ethanol, yield: 79%; m.p.: 102 °C; IR (KBr)  $\nu_{\max}$  (cm<sup>-1</sup>): 3423–3221 (2NH<sub>2</sub>), 2921 (CH aliphatic), 2194 (CN), 1721 (CO), 1608 (C=C); <sup>1</sup>H NMR (300 MHz, DMSO-*d*<sub>6</sub>)  $\delta$  1.31 (t, 3H, *J* = 6.9 Hz, OCH<sub>2</sub>CH<sub>3</sub>), 2.95 (m, 4H, CH<sub>2</sub>-CH<sub>2</sub>), 3.38 (s, 2H, D<sub>2</sub>O exchangeable, NH<sub>2</sub>), 4.31 (q, 2H, *J* = 6.9 Hz, OCH<sub>2</sub>CH<sub>3</sub>), 7.15 (s, 1H, pyran H-4), 7.66–8.07 (m, 4H, C<sub>6</sub>H<sub>4</sub>), 8.40 (s, 2H, D<sub>2</sub>O exchangeable, NH<sub>2</sub>); <sup>13</sup>C NMR (75 MHz, DMSO-*d*<sub>6</sub>)  $\delta$  14.1 (OCH<sub>2</sub>CH<sub>3</sub>), 55.4 (OCH<sub>2</sub>CH<sub>3</sub>), 62.4, 66.3 (CH<sub>2</sub>-CH<sub>2</sub>), 96.5 (pyran C-4), 116.0 (CN), 117.9, 121.8, 122.9, 124.1, 128.7, 129.6, 130.5, 131.9, 133.1, 137.9, 147.4, 154.9 (C<sub>6</sub>H<sub>4</sub>, pyran, thiophene C), 163.9 (CO); EIMS (*m/z*, %): 427 [M<sup>+</sup>, 41]. Anal. Calcd. for C<sub>21</sub>H<sub>18</sub>ClN<sub>3</sub>O<sub>3</sub>S: C, 58.94; H, 4.24; N, 9.82; S, 7.49. Found: C, 59.09; H, 4.50; N, 10.02; S, 7.31.

**Ethyl 2,7-diamino-3-cyano-9-(4-methoxyphenyl)-5,9-dihydro-4H-thieno[2,3-f]chromene-8-carboxylate (23f)**

Reddish brown crystals from ethanol, yield: 68%; m.p.: 89 °C; IR (KBr)  $\nu_{\max}$  (cm<sup>-1</sup>): 3413–3212 (2NH<sub>2</sub>), 2915 (CH aliphatic), 2205 (CN), 1714 (CO), 1621 (C=C); <sup>1</sup>H NMR (300 MHz, DMSO-*d*<sub>6</sub>)  $\delta$  1.30 (t, 3H, *J* = 7.2 Hz, OCH<sub>2</sub>CH<sub>3</sub>), 2.91 (m, 4H, CH<sub>2</sub>-CH<sub>2</sub>), 3.33 (s, 2H, D<sub>2</sub>O exchangeable, NH<sub>2</sub>), 3.86 (s, 3H, OCH<sub>3</sub>), 4.29 (q, 2H, *J* = 7.2 Hz, OCH<sub>2</sub>CH<sub>3</sub>), 7.09–7.17 (m, 3H, pyran H-4 and Ar-H), 7.81–8.10 (m, 2H, Ar-H), 8.31 (s, 2H, D<sub>2</sub>O exchangeable, NH<sub>2</sub>); <sup>13</sup>C NMR (75 MHz, DMSO-*d*<sub>6</sub>)  $\delta$  13.9 (OCH<sub>2</sub>CH<sub>3</sub>), 55.1 (OCH<sub>3</sub>), 55.9 (OCH<sub>2</sub>CH<sub>3</sub>), 62.7, 66.3 (CH<sub>2</sub>-CH<sub>2</sub>), 98.5 (pyran C-4), 116.1 (CN), 114.8, 121.2, 122.6, 123.9, 128.1, 129.4, 130.7, 131.7, 133.4, 138.7, 147.8, 154.3 (C<sub>6</sub>H<sub>4</sub>, pyran, thiophene C), 163.5 (CO); EIMS (*m/z*, %): 423 [M<sup>+</sup>, 54]. Anal. Calcd. for C<sub>22</sub>H<sub>21</sub>N<sub>3</sub>O<sub>4</sub>S: C, 62.40; H, 5.00; N, 9.92; S, 7.57. Found: C, 62.70; H, 4.72; N, 9.92; S, 7.81.

**2. 1. 11. Synthesis of 4,5,6,9-tetrahydrothieno [2,3-f]quinoline derivatives 24a-f.**

A mixture of compound 3 (1.92 g, 0.01 mol), either

malononitrile (2) (0.66 g, 0.01 mol) or ethyl cyanoacetate (9) (1.13, 0.01 mol) and either benzaldehyde (4) (1.06 g, 0.01 mol), 4-chlorobenzaldehyde (22a) (1.4 g, 0.01 mol), or 4-methoxybenzaldehyde (22b) (1.36 g, 0.01 mol) in 1,4-dioxane (40 mL) containing ammonium acetate (0.5 g) was heated for 3–5 h under reflux. The obtained solution was neutralized by adding a few drops of hydrochloric acid and cold water. The product was precipitated, filtered off, washed with water and dried.

**2,7-Diamino-9-phenyl-4,5,6,9-tetrahydrothieno[2,3-f]quinoline-3,8-dicarbonitrile (24a)**

Crimson red crystals from ethanol, yield: 72%; m.p.: 110 °C; IR (KBr)  $\nu_{\max}$  (cm<sup>-1</sup>): 3424–3208 (2NH<sub>2</sub>, NH), 2919 (CH aliphatic), 2214, 2194 (2CN), 1620 (C=C); <sup>1</sup>H NMR (300 MHz, DMSO-*d*<sub>6</sub>)  $\delta$  2.81 (m, 4H, CH<sub>2</sub>-CH<sub>2</sub>), 3.42 (s, 2H, D<sub>2</sub>O exchangeable, NH<sub>2</sub>), 7.10 (s, 1H, pyridine H-4), 7.26–8.07 (m, 5H, C<sub>6</sub>H<sub>5</sub>), 8.54 (s, 2H, D<sub>2</sub>O exchangeable, NH<sub>2</sub>), 10.01 (s, 1H, D<sub>2</sub>O exchangeable, NH); <sup>13</sup>C NMR (75 MHz, DMSO-*d*<sub>6</sub>)  $\delta$  60.4, 64.5 (CH<sub>2</sub>-CH<sub>2</sub>), 76.1 (pyridine C-4), 116.1, 116.6 (2CN), 114.7, 115.5, 121.4, 124.8, 129.3, 132.5, 133.8, 135.7, 138.2, 139.3, 148.3, 154.3 (C<sub>6</sub>H<sub>5</sub>, pyridine, thiophene C); EIMS (*m/z*, %): 345 [M<sup>+</sup>, 34]. Anal. Calcd. for C<sub>19</sub>H<sub>15</sub>N<sub>5</sub>S: C, 66.07; H, 4.38; N, 20.27; S, 9.28. Found: C, 66.18; H, 4.50; N, 20.23; S, 8.98.

**2,7-Diamino-9-(4-chlorophenyl)-4,5,6,9-tetrahydrothieno[2,3-f]quinoline-3,8-dicarbonitrile (24b)**

Brick red crystals from ethanol, yield: 89%; m.p.: 140 °C; IR (KBr)  $\nu_{\max}$  (cm<sup>-1</sup>): 3424–3209 (2NH<sub>2</sub>, NH), 2920 (CH aliphatic), 2221, 2197 (2CN), 1622 (C=C); <sup>1</sup>H NMR (300 MHz, DMSO-*d*<sub>6</sub>)  $\delta$  2.94 (m, 4H, CH<sub>2</sub>-CH<sub>2</sub>), 3.36 (s, 2H, D<sub>2</sub>O exchangeable, NH<sub>2</sub>), 7.22 (s, 1H, pyridine H-4), 7.63–8.05 (m, 4H, C<sub>6</sub>H<sub>4</sub>), 8.54 (s, 2H, D<sub>2</sub>O exchangeable, NH<sub>2</sub>), 10.03 (s, 1H, D<sub>2</sub>O exchangeable, NH); <sup>13</sup>C NMR (75 MHz, DMSO-*d*<sub>6</sub>)  $\delta$  60.3, 65.6 (CH<sub>2</sub>-CH<sub>2</sub>), 76.3 (pyridine C-4), 116.2, 117.1 (2CN), 114.3, 115.5, 123.9, 125.6, 129.7, 131.9, 133.7, 134.9, 137.9, 139.2, 147.3, 154.9 (C<sub>6</sub>H<sub>4</sub>, pyridine, thiophene); EIMS (*m/z*, %): 379 [M<sup>+</sup>, 64]. Anal. Calcd. for C<sub>19</sub>H<sub>14</sub>ClN<sub>5</sub>S: C, 60.07; H, 3.71; N, 18.44; S, 8.44. Found: C, 60.12; H, 3.49; N, 18.29; S, 8.54.

**2,7-Diamino-9-(4-methoxyphenyl)-4,5,6,9-tetrahydrothieno[2,3-f]quinoline-3,8-dicarbonitrile (24c)**

Orange crystals from ethanol, yield: 77%; m.p.: 117 °C; IR (KBr)  $\nu_{\max}$  (cm<sup>-1</sup>): 3421–3207 (2NH<sub>2</sub>, NH), 2925 (CH aliphatic), 2217, 2193 (2CN), 1614 (C=C); <sup>1</sup>H NMR (300 MHz, DMSO-*d*<sub>6</sub>)  $\delta$  2.83 (m, 4H, CH<sub>2</sub>-CH<sub>2</sub>), 3.32 (s, 2H, D<sub>2</sub>O exchangeable, NH<sub>2</sub>), 3.88 (s, 3H, OCH<sub>3</sub>), 7.12–7.20 (m, 3H, pyridine H-4 and Ar-H), 7.96–8.10 (m, 2H, Ar-H), 8.38 (s, 2H, D<sub>2</sub>O exchangeable, NH<sub>2</sub>), 9.98 (s, 1H, D<sub>2</sub>O exchangeable, NH); <sup>13</sup>C NMR (75 MHz, DMSO-*d*<sub>6</sub>)  $\delta$  55.8 (OCH<sub>3</sub>), 62.6, 66.1 (CH<sub>2</sub>-CH<sub>2</sub>), 76.8 (pyridine C-4), 116.4, 116.9 (2CN), 114.7, 115.1, 124.0, 128.4, 129.7, 132.1, 133.3, 135.1, 138.6, 139.7, 147.8, 157.3 (C<sub>6</sub>H<sub>4</sub>, pyridine, thiophene C); EIMS (*m/z*, %): 375 [M<sup>+</sup>, 49]. Anal.

Calcd. for  $C_{20}H_{17}N_5OS$ : C, 63.98; H, 4.56; N, 18.65; S, 8.54. Found: C, 64.29; H, 4.80; N, 18.42; S, 8.31.

**Ethyl 2,7-diamino-3-cyano-9-phenyl-4,5,6,9-tetrahydrothieno[2,3-*f*]quinoline-8-carboxylate (24d)**

Pale brown crystals from acetic acid, yield: 69%; m.p.: 145 °C; IR (KBr)  $\nu_{\max}$  ( $\text{cm}^{-1}$ ): 3419–3207 (2NH<sub>2</sub>, NH), 2981 (CH aliphatic), 2196 (CN), 1719 (CO), 1606 (C=C); <sup>1</sup>H NMR (300 MHz, DMSO-*d*<sub>6</sub>)  $\delta$  1.30 (t, 3H, *J* = 6.3 Hz, OCH<sub>2</sub>CH<sub>3</sub>), 2.78 (m, 4H, CH<sub>2</sub>-CH<sub>2</sub>), 3.42 (s, 2H, D<sub>2</sub>O exchangeable, NH<sub>2</sub>), 4.33 (q, 2H, *J* = 6.3 Hz, OCH<sub>2</sub>CH<sub>3</sub>), 7.14 (s, 1H, pyridine H-4), 7.56–8.06 (m, 5H, C<sub>6</sub>H<sub>5</sub>), 8.39 (s, 2H, D<sub>2</sub>O exchangeable, NH<sub>2</sub>), 9.83 (s, 1H, D<sub>2</sub>O exchangeable, NH); <sup>13</sup>C NMR (75 MHz, DMSO-*d*<sub>6</sub>)  $\delta$  14.1 (OCH<sub>2</sub>CH<sub>3</sub>), 55.3 (OCH<sub>2</sub>CH<sub>3</sub>), 61.3, 63.5 (CH<sub>2</sub>-CH<sub>2</sub>), 98.1 (pyridine C-4), 116.6 (CN), 115.7, 121.0, 123.4, 124.3, 127.9, 130.9, 133.7, 135.8, 137.1, 139.8, 147.3, 154.7 (C<sub>6</sub>H<sub>5</sub>, pyridine, thiophene C), 163.1 (CO); EIMS (*m/z*, %): 392 [*M*<sup>+</sup>, 34]. Anal. Calcd. for  $C_{21}H_{20}N_4O_2S$ : C, 64.27; H, 5.14; N, 14.28; S, 8.17. Found: C, 64.50; H, 4.92; N, 14.56; S, 8.44.

**Ethyl 2,7-diamino-9-(4-chlorophenyl)-3-cyano-4,5,6,9-tetrahydrothieno[2,3-*f*]quinoline-8-carboxylate (24e)**

Reddish brown crystals from ethanol, yield: 77%; m.p.: 98–100 °C; IR (KBr)  $\nu_{\max}$  ( $\text{cm}^{-1}$ ): 3422–3209 (2NH<sub>2</sub>, NH), 2978 (CH aliphatic), 2198 (CN), 1720 (CO), 1610 (C=C); <sup>1</sup>H NMR (300 MHz, DMSO-*d*<sub>6</sub>)  $\delta$  1.28 (t, 3H, *J*

= 6.93 Hz, OCH<sub>2</sub>CH<sub>3</sub>), 2.84 (m, 4H, CH<sub>2</sub>-CH<sub>2</sub>), 3.36 (s, 2H, D<sub>2</sub>O exchangeable, NH<sub>2</sub>), 4.31 (q, 2H, *J* = 6.93 Hz, OCH<sub>2</sub>CH<sub>3</sub>), 7.15 (s, 1H, pyridine H-4), 7.44–8.07 (m, 4H, C<sub>6</sub>H<sub>4</sub>), 8.40 (s, 2H, D<sub>2</sub>O exchangeable, NH<sub>2</sub>), 10.01 (s, 1H, D<sub>2</sub>O exchangeable, NH); <sup>13</sup>C NMR (75 MHz, DMSO-*d*<sub>6</sub>)  $\delta$  14.5 (OCH<sub>2</sub>CH<sub>3</sub>), 55.1 (OCH<sub>2</sub>CH<sub>3</sub>), 61.7, 63.4 (CH<sub>2</sub>-CH<sub>2</sub>), 97.6 (pyridine C-4), 116.4 (CN), 115.2, 121.6, 123.5, 124.5, 128.1, 131.6, 133.2, 135.6, 137.4, 139.8, 147.5, 154.7 (C<sub>6</sub>H<sub>4</sub>, pyridine, thiophene C), 163.8 (CO); EIMS (*m/z*, %): 426 [*M*<sup>+</sup>, 66]. Anal. Calcd. for  $C_{21}H_{19}ClN_4O_2S$ : C, 59.08; H, 4.49; N, 13.12; S, 7.51. Found: C, 59.30; H, 4.41; N, 13.45; S, 7.81.

**Ethyl 2,7-diamino-3-cyano-9-(4-methoxyphenyl)-4,5,6,9-tetrahydrothieno[2,3-*f*]quinoline-8-carboxylate (24f)**

Brown crystals from ethanol, yield: 89%; m.p.: 87 °C; IR (KBr)  $\nu_{\max}$  ( $\text{cm}^{-1}$ ): 3417–3212 (2NH<sub>2</sub>, NH), 2984 (CH aliphatic), 2203 (CN), 1716 (CO), 1625 (C=C); <sup>1</sup>H NMR (300 MHz, DMSO-*d*<sub>6</sub>)  $\delta$  1.29 (t, 3H, *J* = 6.82 Hz, OCH<sub>2</sub>CH<sub>3</sub>), 2.68 (m, 4H, CH<sub>2</sub>-CH<sub>2</sub>), 3.34 (s, 2H, D<sub>2</sub>O exchangeable, NH<sub>2</sub>), 3.87 (s, 3H, OCH<sub>3</sub>), 4.31 (q, 2H, *J* = 6.82 Hz, OCH<sub>2</sub>CH<sub>3</sub>), 7.08–7.22 (m, 3H, pyridine H-4 and Ar-H), 8.01–8.04 (m, 2H, Ar-H), 8.30 (s, 2H, D<sub>2</sub>O exchangeable, NH<sub>2</sub>), 9.91 (s, 1H, D<sub>2</sub>O exchangeable, NH); <sup>13</sup>C NMR (75 MHz, DMSO-*d*<sub>6</sub>)  $\delta$  13.9 (OCH<sub>2</sub>CH<sub>3</sub>), 50.1 (OCH<sub>3</sub>), 55.6 (OCH<sub>2</sub>CH<sub>3</sub>), 62.0, 66.3 (CH<sub>2</sub>-CH<sub>2</sub>), 98.4 (pyridine C-4), 116.1 (CN), 115.9, 121.3, 123.8, 124.7, 127.9, 131.2,

**Table 1.** *In vitro* growth inhibitory effects IC<sub>50</sub> ± SEM (μM) of the newly synthesized compounds against cancer cell lines.

Compound No	IC <sub>50</sub> ± SEM (μM)					
	A549	H460	HT29	MKN-45	U87MG	SMMC-7721
3	6.29 ± 1.63	5.59 ± 2.35	4.29 ± 2.61	6.77 ± 2.37	7.18 ± 2.57	5.82 ± 1.31
5	6.27 ± 1.80	8.61 ± 2.29	4.36 ± 1.59	3.38 ± 1.62	5.80 ± 1.08	2.49 ± 0.68
7	3.18 ± 1.63	0.42 ± 0.30	1.52 ± 0.23	4.61 ± 2.51	2.63 ± 1.38	1.79 ± 0.83
10a	8.53 ± 2.36	8.29 ± 2.13	8.34 ± 3.70	8.39 ± 2.42	9.68 ± 3.37	8.27 ± 2.91
10b	1.22 ± 0.87	0.52 ± 0.32	0.73 ± 0.48	1.49 ± 0.41	2.46 ± 0.83	1.32 ± 0.42
12	0.24 ± 0.15	0.32 ± 0.22	0.34 ± 0.09	0.42 ± 0.33	0.24 ± 0.19	0.26 ± 0.14
13	4.26 ± 2.12	3.14 ± 1.39	8.14 ± 3.52	6.91 ± 2.42	3.62 ± 1.47	4.73 ± 2.68
15a	3.25 ± 1.08	2.18 ± 0.07	2.68 ± 1.17	2.69 ± 0.98	2.80 ± 1.32	5.54 ± 2.38
15b	4.65 ± 1.36	5.43 ± 2.25	1.39 ± 0.89	1.82 ± 0.96	2.34 ± 0.29	1.80 ± 0.28
19	1.23 ± 0.39	1.44 ± 0.83	2.31 ± 0.67	1.35 ± 0.68	0.89 ± 0.46	1.25 ± 0.59
20	3.12 ± 1.68	4.29 ± 2.39	5.27 ± 3.54	3.18 ± 1.26	4.31 ± 2.82	3.27 ± 1.57
21	1.02 ± 0.95	1.28 ± 0.79	1.08 ± 2.80	2.28 ± 1.23	1.67 ± 0.85	1.62 ± 0.63
23a	1.32 ± 0.88	1.43 ± 0.87	1.74 ± 0.69	1.52 ± 0.83	0.89 ± 0.35	1.63 ± 0.69
23b	0.27 ± 0.18	0.39 ± 0.19	0.62 ± 0.35	0.82 ± 0.63	0.72 ± 0.53	1.29 ± 0.83
23c	7.26 ± 2.58	3.18 ± 2.31	6.68 ± 2.40	5.62 ± 3.42	4.71 ± 1.26	6.80 ± 2.26
23d	8.53 ± 3.57	5.72 ± 3.86	6.48 ± 2.68	7.38 ± 1.87	4.69 ± 2.41	6.50 ± 2.81
23e	0.28 ± 0.15	0.32 ± 0.14	0.36 ± 0.15	0.19 ± 0.06	0.38 ± 0.15	0.17 ± 0.08
23f	4.53 ± 2.51	6.48 ± 2.63	6.59 ± 1.42	6.29 ± 1.38	6.75 ± 2.69	6.58 ± 2.80
24a	4.59 ± 2.26	5.53 ± 2.70	6.31 ± 2.29	6.50 ± 2.63	8.53 ± 2.72	6.32 ± 2.42
24b	0.40 ± 0.33	0.23 ± 0.18	0.52 ± 0.23	0.41 ± 0.25	0.26 ± 0.19	0.25 ± 0.08
24c	3.34 ± 1.24	4.67 ± 1.50	2.80 ± 0.77	2.53 ± 1.19	3.35 ± 1.64	4.49 ± 2.06
24d	6.40 ± 2.58	6.94 ± 2.39	6.29 ± 2.43	6.58 ± 2.30	5.68 ± 2.39	6.55 ± 1.90
24e	1.27 ± 0.53	0.82 ± 0.57	0.83 ± 0.82	1.72 ± 0.94	0.79 ± 0.26	0.59 ± 0.24
24f	0.48 ± 0.26	0.56 ± 0.32	0.42 ± 0.35	0.67 ± 0.40	0.29 ± 1.85	0.69 ± 0.42
Foretinib	0.08 ± 0.01	0.18 ± 0.03	0.15 ± 0.023	0.03 ± 0.0055	0.90 ± 0.13	0.44 ± 0.062

133.4, 135.1, 137.6, 139.4, 147.8, 154.3 (C<sub>6</sub>H<sub>4</sub>, pyridine, thiophene C), 163.4 (CO); EIMS (m/z, %): 422 [M<sup>+</sup>, 33]. Anal. Calcd. for C<sub>22</sub>H<sub>22</sub>N<sub>4</sub>O<sub>3</sub>S: C, 62.54; H, 5.25; N, 13.26; S, 7.59. Found: C, 62.77; H, 5.52; N, 13.09; S, 7.31.

## 2. 2. Biology Section

### Materials

ATP (adenosine triphosphate) is used in this biology section. DMSO (dimethyl sulfoxide), MgCl<sub>2</sub> (magnesium chloride) were purchased from Sigma. Receptor tyrosine kinases c-Kit, Flt-3, VEGFR-2, EGFR, and PDGFR were purchased from Carina Biosciences (Kobe, Japan).

### 2. 2. 1. Cell proliferation test

The antiproliferative activities of the newly synthesized compounds (Table 1) were evaluated against the five c-Met-dependent cancer cell lines (A549, HT -29, MKN-45, U87MG, and SMMC-7721) and one c-Met-independent cancer cell line (H460) with foretinib as a positive control using the standard MTT assay *in vitro*.<sup>26</sup> The experimental procedure was applied according to the previously reported work.<sup>27–29</sup>

### *In vitro* cell experiments

All compounds were tested for their cytotoxicity in the six cancer cell lines using the MTT method. The results, expressed as IC<sub>50</sub> (average of at least three independent experiments), were summarized in Table 1. The data presented in Table 1 show that the tested compounds exhibited moderate to strong cytotoxicity against the six cancer cell lines in the single-digit LM range. Compounds **12**, **19**, **23a**, **23b**, **23e**, **24b**, **24e**, and **24f** exhibited higher cytotoxicity against U87MG than foretinib (the positive control).

### 2. 2. 2. Structure Activity Relationship

Table 1 shows the inhibitory effect of the new compounds on cancer cell lines A549, H460, HT -29, MKN-45, U87MG, and SMMC-7721. There are many compounds that showed high inhibitory values, such as **10b**, **12**, **23b**, **23e**, **24b**, **24e**, and **24f**. In addition, some compounds showed moderate inhibition, such as **7**, **20**, **21**, **23a**, and **24c**. The analysis of Table 1 shows that the substituted groups and the type of heterocyclic ring have a great influence on the inhibitions. Thiophene derivatives **3** and **5** had little inhibitory effect on the cancer cell lines tested. In contrast, fused derivative **7** showed moderate inhibition. Surprisingly, 4*H*-thieno[2,3-*f*]chromene derivatives **10a** and **10b** showed low inhibitory values, while compound **10a** (Y = COOEt) showed high inhibitory values, which was attributed to the presence of the COOEt group. Hydrazide-hydrazone derivative **12** showed strong inhibition against the tested cancer cell lines, while compounds **13**

and **15a,b** showed moderate inhibition. In addition, compounds **19** and **21** showed moderate inhibition, with compound **19** exhibiting high inhibition against the U87MG cell line with an IC<sub>50</sub> of 0.89M. For thieno[2,3-*f*]chromene derivatives **23a-f**, the different substituents played the major role in the inhibitions of the compounds. Compound **23a** (X = CN, Y = H) showed moderate inhibitions, while compounds **23b** (X = CN, Y = Cl) and **23e** (X = COOEt, Y = Cl) showed the strongest inhibitions against the tested cancer cell lines. In contrast, compounds **23c**, **23d**, and **23f** showed lower inhibitory activity. Interestingly, compounds **24a-f**, **24b**, **24e**, and **24f** showed the highest inhibitory values among the six compounds, as the high inhibitory values of compounds **24b** and **24e** were due to the electronegative Cl group. Compound **24f** showed high inhibition values despite the electron-donating OCH<sub>3</sub> group, while the inhibition values of compounds **24a**, **24c**, and **24d** decreased.

### 2. 2. 3. HTRF Kinase Assay

The c-Met kinase activity of the newly synthesized compounds was assayed using a homogeneous time-resolved fluorescence (HTRF) assay (Table 2), as reported previously.<sup>30</sup> In addition, the maximally active compounds **7**, **10a**, **10b**, **13**, **15a**, **21**, **24a**, **24b**, **24c**, **24d**, and **24e** were extra assayed using the same screening method for the five tyrosine kinases (c-Kit, Flt-3, VEGFR-2, EGFR, and PDGFR) (Table 3). The experimental technique and chemicals used were based on reported work.<sup>31</sup>

### Enzymatic *in vitro* tests

All freshly prepared benzo[*b*]thiophene derivatives were evaluated for their inhibitory activity against c-Met enzyme<sup>32</sup> in a homogeneous time-resolved fluorescence (HTRF) assay, with foretinib serving as a positive control. The antiproliferative activity of all newly synthesized compounds against the human prostate cancer cell line PC-3 was calculated by MTT assay<sup>33,34</sup> using SGI-1776 as the reference drug. The results, reported as IC<sub>50</sub> (average of at least three independent experiments) for both HTRF and antiproliferative activity, are shown in Table 2. Most of the compounds tested showed potent antiproliferative activity with IC<sub>50</sub> values of less than 30 mM. In most cases, the heterocycles were associated with the benzothiophene moiety, and variations in substituents had a marked effect on antiproliferative activity. The most potent compounds against c-Met kinase were compounds **7**, **10b**, **13**, **15a**, **21**, **24b**, **24c**, **24d**, and **24e**. It is very surprising that compounds **10b**, **13**, **15a**, **24b**, **24c**, **24d** and **24e** showed stronger inhibition than the reference drug foretinib (IC<sub>50</sub> 1.16 mM). On the other hand, screening with the prostate cancer cell line PC-3 showed that compounds **10b**, **23c**, **23e**, **24a**, **24b** and **24d** had the highest inhibition values. All tested compounds showed higher inhibition than the reference drug SGI-1776, except compounds **3**, **10a**, **15b** and **23f**.

**Table 2.** c-Met enzymatic activity of the newly synthesized compounds.

Compound No	IC <sub>50</sub> (nM) c-Met	IC <sub>50</sub> (nM) PC-3
3	4.65 ± 1.42	6.56 ± 1.38
5	10.23 ± 3.58	2.16 ± 1.13
7	1.18 ± 0.69	2.51 ± 0.34
10a	1.64 ± 0.89	6.42 ± 2.51
10b	0.33 ± 0.16	0.28 ± 0.16
12	4.38 ± 1.64	3.58 ± 1.24
13	0.48 ± 0.15	2.48 ± 1.20
15a	0.32 ± 0.20	4.26 ± 1.42
15b	13.62 ± 4.53	8.37 ± 2.63
19	4.116 ± 5.41	8.57 ± 2.46
20	6.34 ± 2.62	2.17 ± 1.15
21	1.27 ± 0.71	2.08 ± 0.85
23a	8.32 ± 2.74	2.36 ± 1.27
23b	18.27 ± 4.58	2.39 ± 0.83
23c	5.82 ± 1.29	0.92 ± 0.32
23d	18.29 ± 4.70	1.06 ± 0.73
23e	2.41 ± 1.04	0.83 ± 0.41
23f	6.24 ± 2.38	8.41 ± 2.49
24a	2.08 ± 0.87	0.96 ± 0.42
24b	0.08 ± 0.03	0.16 ± 0.04
24c	0.32 ± 0.26	1.03 ± 0.69
24d	0.22 ± 0.08	0.59 ± 0.08
24e	0.06 ± 0.004	1.15 ± 0.72
24f	5.31 ± 2.62	4.33 ± 1.36
	<b>Foretinib</b>	<b>SGI-1776</b>
	1.16 ± 0.17	4.86 ± 0.16

## 2. 2. 4. Inhibition of Tyrosine Kinases (Enzyme IC<sub>50</sub> (nM))

The five tyrosine kinases c-Kit, Flt-3, VEGFR-2, EGFR, and PDGFR were used using sorafenib as the reference drug to test the inhibitions of the selected compounds. The selection of the compounds was based on their high inhibitory activity against the six cancer cell lines. Table 2 shows that compounds **7**, **10a**, **10b**, **13**, **15a**, **21**, **24a**, **24b**, **24c**, **24d**, and **24e** had the highest inhibitory values. The data in Table 3 show that compounds **10a**, **13**, **24b**, and **24a** had the highest inhibitory activity among the compounds tested.

Table 3 showed that compounds **10a**, **10b**, **24b**, **24c**, and **24e** inhibit the investigated tyrosine kinases most strongly, whereas compounds **7**, **21**, **24a**, and **24d** show only slight inhibition.

## 2. 2. 5. Inhibition of Selected Anti-Pim-1 Kinase Compounds

In addition, compounds **10b**, **12**, **19**, **21**, **23a**, **23b**, **23e**, **24b**, **24e**, and **24f** were selected to investigate their inhibitory effects on Pim-1 kinase (Table 4). Based on their IC<sub>50</sub> values in a range of 10 concentrations, these

**Table 3.** Inhibition of tyrosine kinases (Enzyme IC<sub>50</sub> (nM)) by compounds **7**, **10a**, **10b**, **13**, **15a**, **21**, **24a**, **24b**, **24c**, **24d** and **24e**.

Compound	c-Kit	Flt-3	VEGFR-2	EGFR	PDGFR
7	4.16	2.68	3.19	2.57	0.83
10a	0.43	0.29	0.61	0.39	0.71
10b	0.24	1.29	2.42	1.29	2.06
13	1.03	0.48	1.18	0.49	0.25
15a	1.69	1.22	0.63	0.52	0.69
21	2.72	4.53	5.62	3.41	1.58
24a	3.62	2.95	2.80	2.45	3.68
24b	0.36	0.42	0.53	0.29	0.31
24c	0.48	0.61	0.58	1.22	0.72
24d	1.08	2.40	2.35	3.06	2.69
24e	0.22	0.36	0.18	0.49	0.31
Foretinib	0.19	0.17	0.20	0.13	0.26

compounds showed strong inhibition against both c-Met kinase and the cancer cell lines tested. The most active compounds were **10b**, **23a**, **23e**, **24b**, and **24f**, with IC<sub>50</sub> values of 0.29, 0.036, 0.26, 0.43, and 0.31 mM, respectively.

**Table 4.** The inhibitions of compounds **10b**, **12**, **19**, **21**, **23a**, **23b**, **23e**, **24b**, **24e** and **24f** toward Pim-1 kinase.

Compound	Inhibition ratio at 10 μM	IC <sub>50</sub> (μM)
10b	94	0.29
12	30	> 10
19	24	> 10
21	30	> 10
23a	96	0.036
23b	26	> 10
23e	95	0.26
24b	88	0.43
24e	28	> 10
24f	89	0.31
SGI-1776	–	0.048

## 3. Results and Discussion

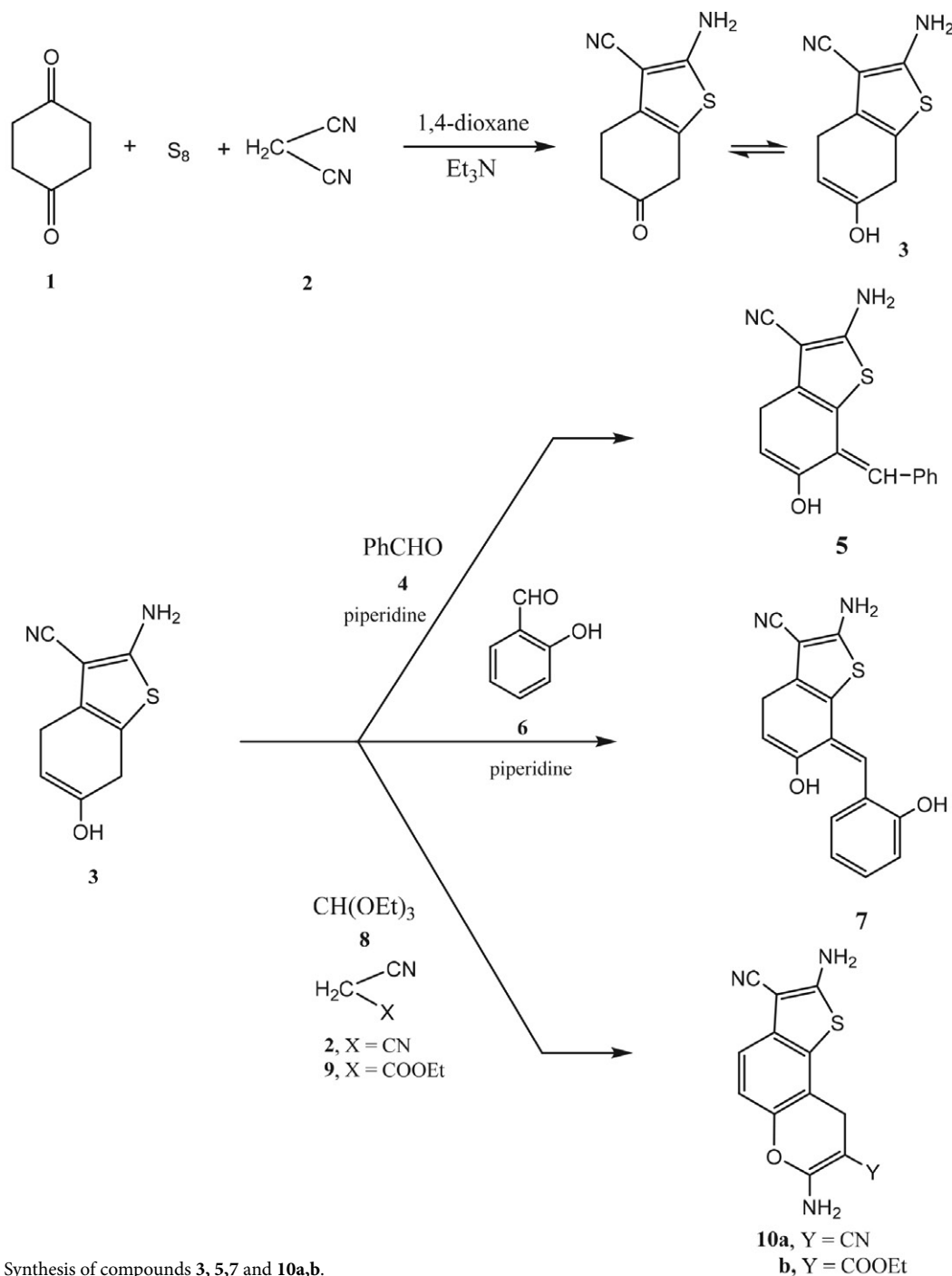
### 3. 1. Chemistry

In recent years, our research group has carried out numerous heterocyclic reactions with cyclohexanedione derivatives.<sup>35–37</sup> The aim of these reactions was the synthesis of thiophene derivatives by Gewald's thiophene method,<sup>38–41</sup> and the synthesis of hydrazide-hydrazone derivatives.<sup>42,43</sup> The prepared compounds showed interesting results as anticancer agents. As a continuation of our work here, we demonstrated the heterocyclization of cyclohexane-1,4-dione and then studied its biological evaluation. The reaction sequences for the synthesis of the final compounds **3** to **24a–f** are shown in Schemes 1–4. The chemical structures of the new compounds were secured by spectral data (IR, <sup>1</sup>H and <sup>13</sup>C NMR, MS). Cyclohexane-1,4-dione

was subjected to Gewald's thiophene synthesis by reacting it with elemental sulfur and malononitrile (**2**) in 1,4-dioxane with triethylamine under reflux to give 2-amino-6-oxo-4,5,6,7-tetrahydrobenzo[*b*]thiophene-3-carbonitrile (**3**). The spectral data showed that compound **3** was present in both the keto and enol tautomeric structures. The presence of a broad signal at  $\nu$  3422  $\text{cm}^{-1}$  confirmed the presence of the OH group along with the appearance of a signal at  $\nu$  1706  $\text{cm}^{-1}$  due to the presence of the CO group in the IR spectrum. In addition, the  $^1\text{H}$  NMR spectrum showed the appearance of a doublet and a triplet at

$\delta$  2.65 and 6.82 ppm for the  $\text{CH}_2\text{--CH=C}$  protons besides a singlet at  $\delta$  5.54 ppm for the  $\text{CH}_2$  group between OH and the  $\text{sp}^2$  carbon and two singlet at  $\delta$  3.39 and 9.97 ppm ( $\text{D}_2\text{O}$  interchangeable) corresponding to the  $\text{NH}_2$  and OH groups, respectively. In addition, the  $^{13}\text{C}$  NMR spectrum showed signals at  $\delta$  22.6 ( $\text{CH}_2\text{--CH=C}$ ), 50.3 ( $\text{CH}_2$ ), 66.3 ( $\text{CH}_2\text{--CH=C}$ ), 116.2 (CN), 118.4, 121.7, 128.9, 134.0 (thiophene C), and 161.8 (CO).

Compound **3** was the major starting compound for various heterocyclization reactions because it contains an active methylene moiety between the OH group and the



Schema 1: Synthesis of compounds **3**, **5**, **7** and **10a,b**.

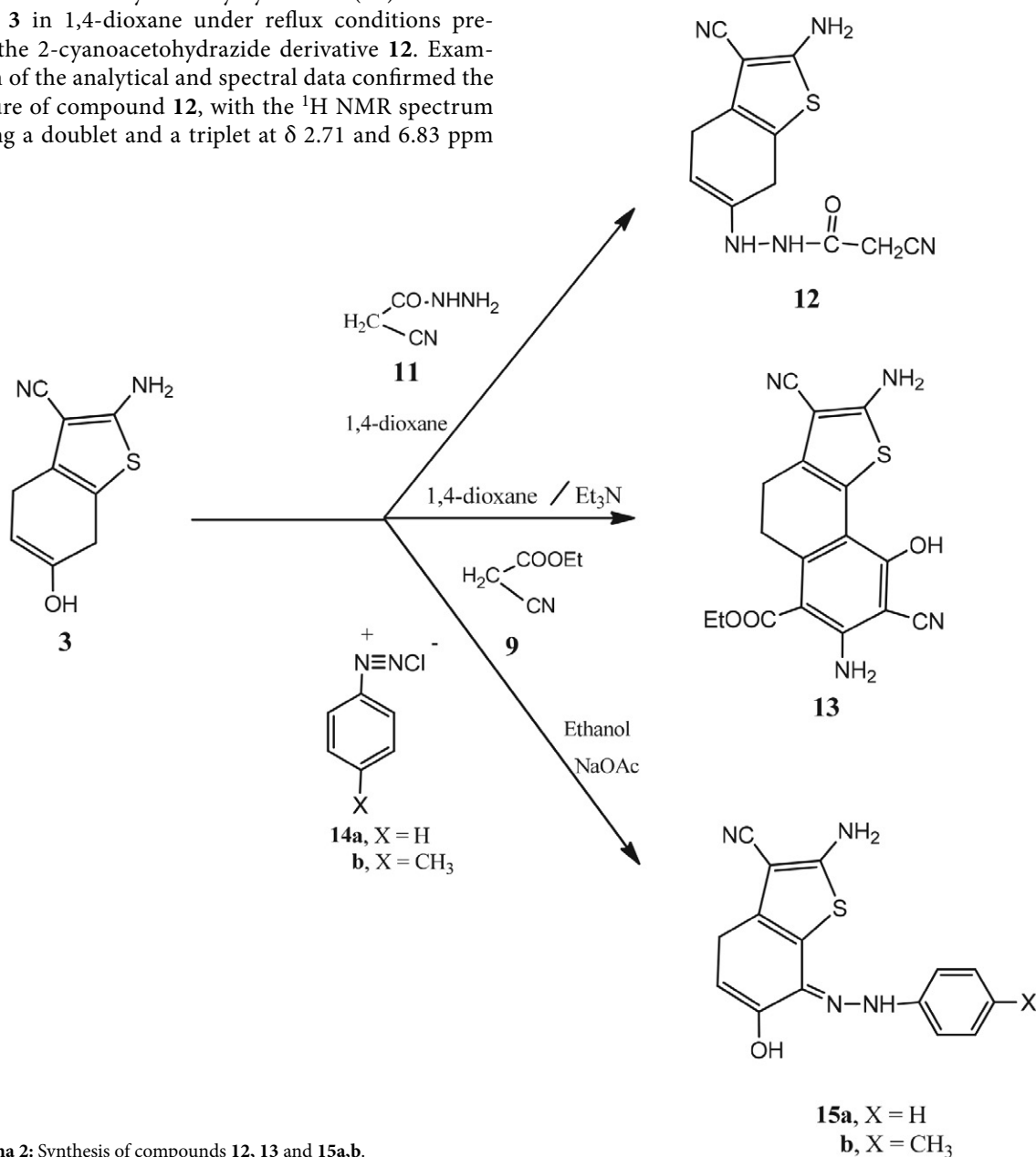


sp<sup>2</sup> carbon. For example, compound **3** reacted with benzaldehyde in 1,4-dioxane containing a catalytic amount of piperidine to give the arylidene derivative **5**. Similarly, the reaction of compound **3** with salicylaldehyde (**6**) formed the 2-hydroxybenzylidene derivative **7**.

The synthesis, reactions, and biological activities of 4*H*-pyran-containing molecules have been extensively studied. In addition, 4*H*-pyran derivatives are also an essential component of some pharmaceutical agents and natural products.<sup>44–46</sup> This inspired us to synthesize 4*H*-pyran derivatives via the multicomponent reaction of compound **3**. Thus, compound **3** was subjected to a multicomponent reaction with ethyl orthoformate and either malononitrile (**2**) or ethyl cyanoacetate (**9**) to give 4*H*-pyran derivatives **10a** and **10b**, respectively (Scheme 1).

Addition of cyanoacetylhydrazine (**11**) to compound **3** in 1,4-dioxane under reflux conditions prepared the 2-cyanoacetohydrazide derivative **12**. Examination of the analytical and spectral data confirmed the structure of compound **12**, with the <sup>1</sup>H NMR spectrum showing a doublet and a triplet at δ 2.71 and 6.83 ppm

confirming the presence of CH<sub>2</sub>–CH=C protons, in addition to two singlet at δ 3.76 and 5.54 ppm for the protons CO–CH<sub>2</sub>–CN and CH<sub>2</sub>, respectively. In addition to the presence of three singlet (D<sub>2</sub>O exchangeable) at δ 3.37, 8.13 and 9.93 ppm for NH<sub>2</sub> and two NH groups, respectively. The <sup>13</sup>C NMR spectrum showed signals at δ 35.8 (CH<sub>2</sub>–CH=C), 66.3 (CH<sub>2</sub>), 77.4, 118.5 (CH<sub>2</sub>–CH=C), 98.9 (CO–CH<sub>2</sub>–CN), 115.7, 116.2 (2CN), 129.9, 133.3, 136.6, 154.7 (thiophene C), 162.6 (CO). In addition, ethyl cyanoacetate (**9**) reacted with compound **3** in 1,4-dioxane containing a catalytic amount of triethylamine to produce the dihydronaphtho[1,2-*b*]thiophene derivative **13**. The study of analytical and spectral data confirmed the proposed structure of compound **13** as mentioned in the experimental section. On the other



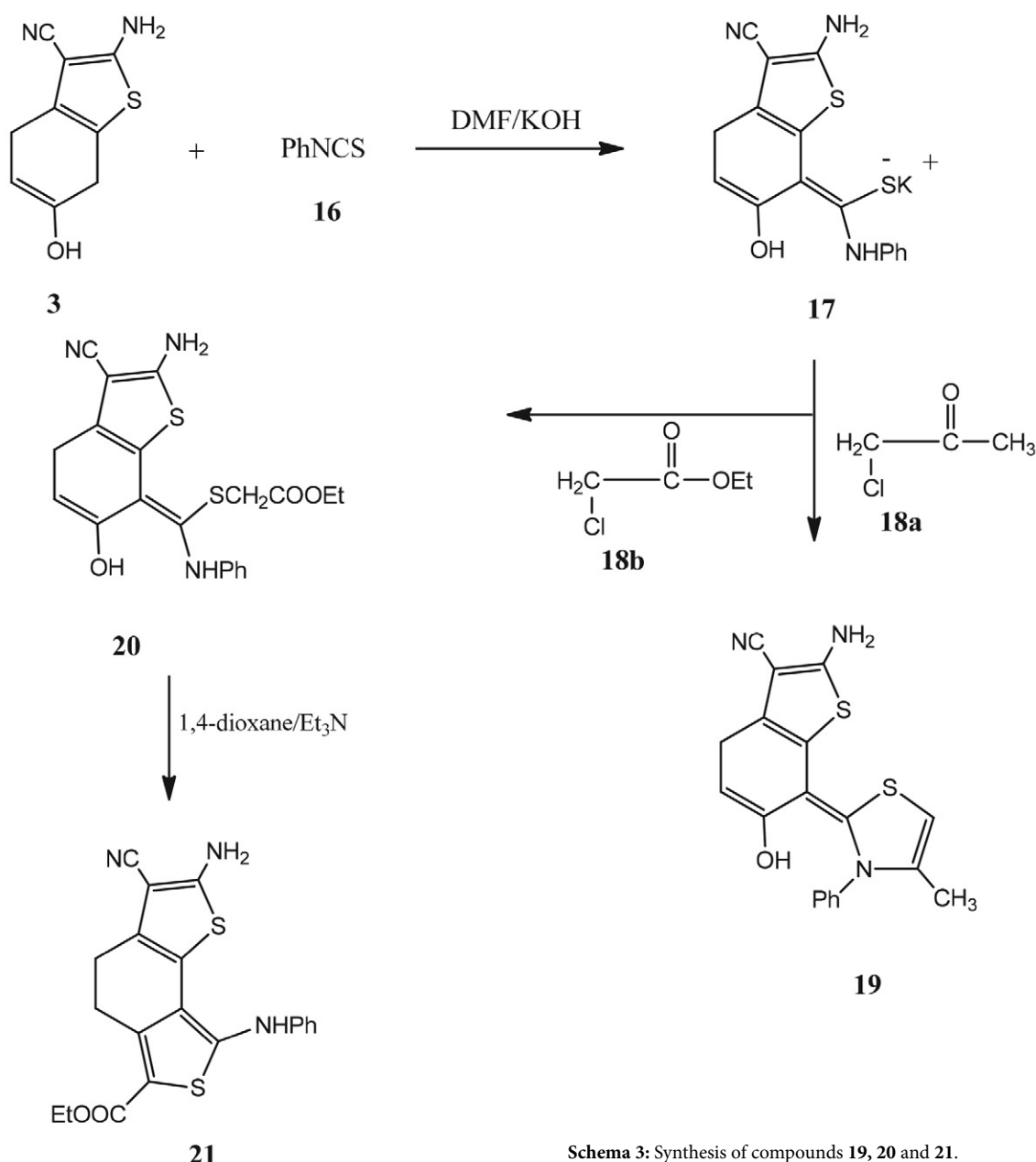
Scheme 2: Synthesis of compounds **12**, **13** and **15a,b**.

hand, compound **3** reacted with either benzenediazonium chloride or p-tolylbenzenediazonium chloride in ethanol solution containing sodium acetate at 0–5 °C to give the corresponding arylhydrazone derivatives **15a** and **15b**, respectively (Scheme 2).

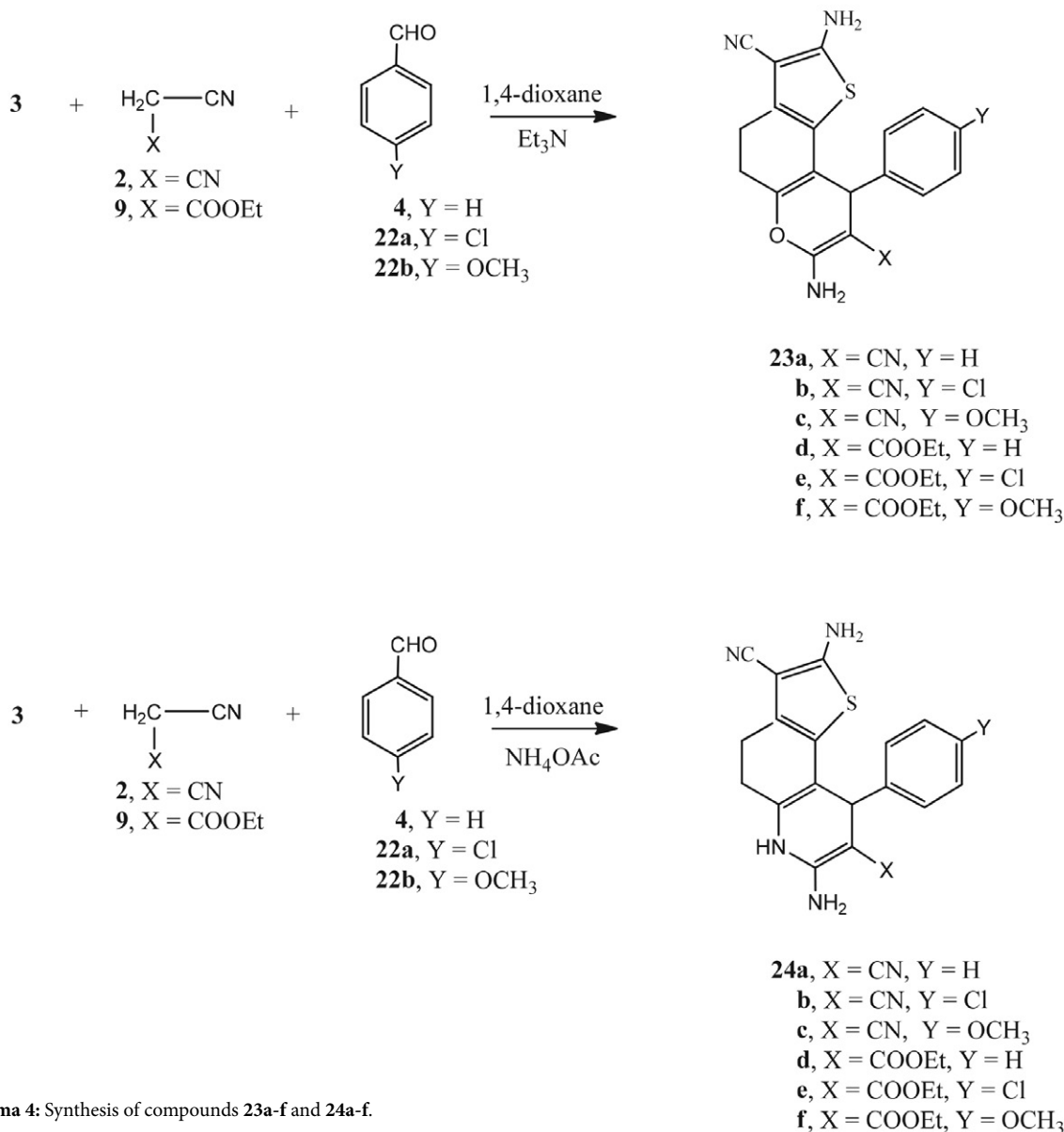
Continuing our previous work on the synthesis of thiophene or thiazole derivatives using phenyl isothiocyanate in basic dimethylformamide and subsequent heterocyclization of the intermediate potassium salt by  $\alpha$ -haloketones,<sup>47,48</sup> in this work we have demonstrated such reactions with the aim of preparing heterocyclic compounds with predicted biological activity. For example, the reaction of compound **3** with phenyl isothiocyanate and potassium hydroxide in dimethylformamide gave the potassium salt intermediate **17**, followed by the addition of  $\alpha$ -chloro-

acetone (**18a**) to the intermediate **17**, giving the thiazole derivative **19**. However, reaction with ethyl  $\alpha$ -chloroacetate (**18b**) surprisingly gave the thioether derivative **20**. Heating of compound **20** in 1,4-dioxane with a catalytic amount of triethylamine gave the condensed dithiophene derivative **21** (Scheme 3). The structures of compounds **19**, **20**, and **21** were confirmed by the data reported in the experimental section.

Moreover, the multicomponent reaction of compound **3** with either malononitrile or ethyl cyanoacetate and either benzaldehyde, 4-chlorobenzaldehyde, or 4-methoxybenzaldehyde in 1,4-dioxane in the presence of trimethylamine as catalyst gave the 4*H*-thieno[2,3-*f*]chromene derivatives **23a-f**. Similarly, reaction of compound **3** with malononitrile or ethyl cyanoacetate and either benzal-



Scheme 3: Synthesis of compounds **19**, **20** and **21**.



**Schema 4:** Synthesis of compounds **23a-f** and **24a-f**.

hyde, 4-chlorobenzaldehyde or 4-methoxybenzaldehyde in 1,4-dioxane with ammonium acetate gave the 4,5,6,9-tetrahydrothieno[2,3-*f*]quinoline derivatives **24a-f**. The structure of compounds **23a-f** and **24a-f** (Scheme 4) was determined based on the study of their spectral data and elemental analyzes (see Experimental section).

## 4. Conclusion

The benzo[*b*]thiophene derivative was the major starting compound for several heterocyclization reactions. All new compounds were tested on the six cancer cell lines. In addition, the *c*-Met kinase activity of all compounds was calculated, and the most active compounds were tested against five other tyrosine kinases. In addition, compounds **10b**, **12**, **20**, **21**, **23a**, **23b**, **23e**, **24b**, **24e**, and

**24f** were selected to investigate their inhibitory effect on Pim-1 kinase, as these compounds showed a large inhibitory effect on *c*-Met kinase and the cancer cell lines studied. The results obtained in this work will stimulate further work in the future.

### Human and Animal Rights

No Animals/Humans were used for studies that are basis of this research.

### Consent for Publication

This work is consent for publication through the Journal formats.

### Conflict of Interest

The authors declare no conflict of interest, financial or otherwise.

## 5. References

1. M. Garcia-Valverde, T. Torroba, *Molecules*, **2005**, *10*, 318–320. DOI:10.3390/10020318
2. S. Pathania, R. K. Narang, R. K. Rawal, *Eur. J. Med. Chem.*, **2019**, *180*, 486–508. DOI:10.1016/j.ejmech.2019.07.043
3. S. Archana, P. Pathania, A. Chawla, *Bioorg. Chem.*, **2020**, *101*, 104026–104044. DOI:10.1016/j.bioorg.2020.104026
4. M. S. Al-Said, M. S. Bashandy, S. I. Al-Qasoumi, M. M. Ghorab, *Eur. J. Med. Chem.*, **2011**, *46*, 137–141. DOI:10.1016/j.ejmech.2010.10.024
5. S. Xue, H. Guo, M. Liu, J. Jin, D. Ju, Z. Liu, Z. Li, *Eur. J. Med. Chem.*, **2015**, *96*, 151–161. DOI:10.1016/j.ejmech.2015.04.016
6. R. S. Keri, K. Chand, S. Budagumpi, S. B. Somappa, S. A. Patil, B. MallannaNagaraja, *Eur. J. Med. Chem.*, **2017**, *138*, 1002–1033. DOI:10.1016/j.ejmech.2017.07.038
7. B. Rosada, A. Bekier, J. Cytarska, W. Płaziński, O. Zavyalova, A. Sikora, K. Dzitko, K. Z. Łączkowski, *Eur. J. Med. Chem.*, **2019**, *184*, 111765. DOI:10.1016/j.ejmech.2019.111765
8. R. M. Mohareb, W. W. Wardkhan, N. S. Abbas, *AntiCancer Agent Med. Chem.*, **2019**, *19*, 1737–1753. DOI:10.2174/1871520619666190402153429
9. C. K. Khatri, K. S. Indalkar, C. R. Patil, S. N. Goyal, G. U. Caturbhuj, *Bioorg. Med. Chem. Lett.*, **2017**, *27*, 1721–1726. DOI:10.1016/j.bmcl.2017.02.076
10. K. M. Khan, Z. Nullah, M. A. Lodhi, S. Jalil, M. I. Choudhary, *J. Enzyme Inhib. Med. Chem.*, **2006**, *21*, 139–143. DOI:10.1080/14756360500480418
11. M. Arora, J. Sravanan, S. Mohan, S. Bhattacharjee, *Int. J. Pharm. Pharm. Sci.*, **2013**, *5*, 315–319.
12. S. D. Rao, S. Rasheed, T. S. K. Basha, N. C. Raju, K. Naresh, *Der. Pharm. Chem.*, **2013**, *5*, 61–74.
13. R. M. Mohareb, A. A. Fahmy, *Eur. Chem. Bull.*, **2013**, *2*, 545–553. DOI: 10.17628/ECB.2013.2.545.545.
14. K. A. Rodrigues, C. N. Dias, P. L. Nêris, J. C. Rocha, M. T. Scotti, L. Scotti, S. R. Mascarenhas, R. C. Veras, I. A. Medeiros, T. S. Keesen, T. B. Oliveira, M. C. Lima, T. L. Balliano, T. M. Aquino, R. O. Moura, M. F. J. Junior, M. R. Oliveira, *Eur. J. Med. Chem.*, **2015**, *106*, 1–14. DOI:10.1016/j.ejmech.2015.10.011
15. M. A. Gouda, H. F. Eldien, M. M. Girges, M. A. Berghot, *Med. Chem.*, **2013**, *2*, 2228–2232. DOI:10.1248/cpb.c17-00582
16. A. E. Amr, M. H. Sherif, M. G. Assy, M. A. Al-Omar, I. Ragab, *Eur. J. Med. Chem.*, **2010**, *45*, 5935–5942. DOI:10.1016/j.ejmech.2010.09.059
17. M. A. Gouda, M. A. Berghot, G. E. Abd El-Ghani, A. M. Khalil, *Eur. J. Med. Chem.*, **2010**, *45*, 1338–1345. DOI:10.1016/j.ejmech.2009.12.020
18. K. El-Sharkawy, H. M. El-Sehrawi, R. A. Ibrahim, *Int. J. Org. Chem.*, **2012**, *2*, 126–134. DOI:10.4236/ijoc.2012.22020
19. R. M. Mohareb, J. Schatz, *Bioorg. Med. Chem.*, **2011**, *19*, 2707–2713. DOI:10.1016/j.bmc.2011.02.051
20. R. M. Mohareb, M. H. Mohamed, *Heteroatom Chem.*, **2001**, *12*, 518–527. DOI:10.1002/hc.1079
21. R. M. Mohareb, N. Y. Megally, F. O. Al-farouk, *Acta Chim. Slov.*, **2017**, *64*, 117–128. DOI:10.17344/acsi.2016.2920
22. R. M. Mohareb, N. Y. Megally, K. A. EL-Sharkawy, *AntiCancer Agent Med. Chem.*, **2018**, *18*, 1736–1749. DOI:10.2174/1871520618666180604091358
23. N. Y. Abdo, R. M. Mohareb, P. A. Halim, *Bioorg. Chem.*, **2020**, *97*, 103667–103677. DOI:10.1016/j.bioorg.2020.103667
24. N. Y. Abdo, R. M. Mohareb, W. N. Al-darkazali, *AntiCancer Agent Med. Chem.*, **2020**, *20*, 335–345. DOI:10.2174/1871520619666190730103425
25. R. M. Mohareb, N. Y. Megally Abdo, W. N. Al-darkazali, *Lett. Drug Des. Discov.*, **2020**, *17*, 597–609. DOI:10.2174/1570180816666190618115128
26. S. Li, Y. Zhao, K. Wang, Y. Gao, J. Han, B. Cui, P. Gong, *Bioorg. Med. Chem.*, **2013**, *21*, 2843–2855. DOI:10.1016/j.bmc.2013.04.013
27. L. Liu, A. Siegmund, N. Xi, P. Kaplan-Lefko, K. Rex, A. Chen, J. Lin, J. Moriguchi, L. Berry, L. Y. Huang, Y. Teffera, Y. J. Yang, Y. H. Zhang, S. F. Bellon, M. Lee, R. Shimanovich, A. Bak, C. Dominguez, M. H. Norman, J. C. Harmange, I. Dus-sault, T. S. Kim, *J. Med. Chem.*, **2008**, *51*, 3688–3691. DOI:10.1021/jm800401t
28. M. L. Peach, N. Tan, N. Tan, S. J. Choyke, A. Giubellino, G. Athauda, T. R. Burke, M. C. Nicklaus, D. P. Bottaro, *J. Med. Chem.*, **2009**, *52*, 943–951. DOI:10.1021/jm800791f
29. F. D. Bacco, P. Luraghi, E. Medico, G. Reato, F. Girolami, T. Perera, P. Gabriele, P. M. Comoglio, C. Boccaccio, *J. Natl. Cancer Inst.*, **2011**, *103*, 645–661. DOI:10.1093/jnci/djr093
30. W. Zhu, W. Wang, S. Xu, J. Wang, Q. Tang, C. Wu, Y. Zhao, P. Zheng, *Bioorg. Med. Chem.*, **2016**, *24*, 1749–1756. DOI:10.1016/j.bmc.2016.02.046
31. J. Liu, M. Nie, Y. Wang, J. Hu, F. Zhang, Y. Gao, Y. Liu, P. Gong, *Eur. J. Med. Chem.*, **2016**, *123*, 431–446. DOI:10.1016/j.ejmech.2016.07.059
32. Z. Zhang, J. C. Lee, L. Li, V. Olivas, V. Au, T. LaFramboise, M. Abdel-Rahman, X. Wang, A. D. Levine, J. K. Rho, Y. J. Choi, C. M. Choi, S. W. Kim, S. J. Jang, Y. S. Park, W. S. Kim, D. H. Lee, J. S. Lee, V. A. Miller, M. Arcila, M. Ladanyi, P. Moonsamy, C. Sawyers, T. J. Boggon, P. C. Ma, C. Costa, M. Taron, R. Rosell, B. Halmos, T. G. Bivona, *Nat. Genet.*, **2012**, *44*, 852–860. DOI:10.1038/ng.2330
33. T. Nakagawa, O. Tohyama, A. Yamaguchi, T. Matsushima, K. Takahashi, S. Funasaka, S. Shirotori, M. Asada, *Cancer Sci.*, **2010**, *101*, 210–215. DOI:10.1111/j.1349-7006.2009.01343.x
34. R. Tiedt, E. Degenkolbe, P. Furet, B. A. Appleton, S. Wagner, J. Schoepfer, E. Buck, D. A. Ruddy, J. E. Monahan, M. D. Jones, J. Blank, D. Haasen, P. Drueckes, M. Wartmann, C. McCarthy, W. R. Sellers, F. Hofmann, *Cancer Res.*, **2011**, *71*, 5255–5264. DOI:10.1158/0008-5472.CAN-10-4433
35. R. M. Mohareb, R. A. Ibrahim, E. S. Alwan, *Acta Chim. Slov.*, **2021**, *68*, 51–64. DOI:10.17344/acsi.2020.6090
36. A. E. M. Abdallah, R. M. Mohareb, M. H. E. Helal, G. J. Mo-feed, *Acta Chim. Slov.*, **2021**, *68*, 604–616. DOI:10.17344/acsi.2020.6446
37. R. M. Mohareb, R. A. Ibrahim, A. M. Elmetwally, M. S. Gamaan, *Acta Chim. Slov.*, **2022**, *69*, 13–29. DOI: 10.17344/acsi.2021.6733.

38. B. P. McKibben, C. H. Cartwright, A. L. Castelhana, *Tetrahedron Lett.*, **1999**, 40, 5471–5474. DOI:10.1016/S0040-4039(99)01108-9
39. K. Wang, D. Kim, A. Dömling, *J. Comb. Chem.* **2010**, 12, 111–118. DOI:10.1021/cc9001586
40. R. Mishra, K. K. Jha, S. Kumar, I. Tomer, *Der Pharma Chemica*, **2011**, 3, 38–54.
41. R. M. Mohareb, Y. R. Milad, A. Ali Masoud, *Acta Chim. Slov.*, **2021**, 68, 72–87. DOI:10.17344/acsi.2020.6182
42. R. M. Mohareb, F. Al-Omran, *Steroids*, **2012**, 77, 1551–1559. DOI:10.1016/j.steroids.2012.09.007
43. M. Bingul, S. Ercan, M. Boga, *J. Mol. Struct.*, **2020**, 1213, 128202. DOI:10.1016/j.molstruc.2020.128202
44. L. F. Tietza, U. Beyfuss, *Angew. Chem. Int. Ed. Engl.*, **1993**, 32, 131–163. DOI:10.1002/anie.199301312
45. R. W. Armstrong, A. P. Combs, P. A. Tempest, S. D. Brown, T. A. Keating, *Acc. Chem. Res.* **1996**, 29, 123–143. DOI:10.1021/ar9502083
46. A. Domling, I. Ugi, *Angew. Chem. Int. Ed.*, **2000**, 39, 3168–3210. DOI:10.1002/1521-3773(20000915)39:18<3168::AID-ANIE3168>3.0.CO;2-U
47. R. M. Mohareb, D. H. Fleita, O. K. Sakka, *Molecules*, **2010**, 16, 16–27. DOI:10.3390/molecules16010016
48. R. M. Mohareb, N. Y. Megally Abdo, M. S. Gamaan, *J. Heterocycl. Chem.*, **2020**, 57, 2512–2527. DOI:10.1002/jhet.3966

## Povzetek

V prispevku je opisana priprava 2-amino-6-okso-4,5,6,7-tetrahidrobenzo[*b*]tiofen-3-karbonitril (**3**) z reakcijo cikloheksan-1,4-diona z elementarnim žveplom in malononitrilom v 1,4-dioksanu in s trietilaminom kot katalizatorjem. Iz pripravljene spojine so z reakcijo s trietil ortoformatom in malononitrilom ali etil cianoacetatom v 1,4-dioksanu kot topilu, v prisotnosti trietilamina, nastali 4*H*-tieno[2,3-*f*]kromenski derivati **10a,b**. Poleg teh so iz spojine **3** pripravili tudi kondenzirane piranske in piridinske derivate. Citotoksičnost sintetiziranih spojin so preučevali na šestih rakavih celičnih linijah skupaj s c-Met kinazo in PC-3 celično linijo. Najbolj aktivne spojine so bile dodatno testirane na petih tirozin kinazah in Pim-1 kinazi. Večina testiranih spojin je pokazala močno inhibicijo, kar je dobra spodbuda za nadaljnje delo.



Except when otherwise noted, articles in this journal are published under the terms and conditions of the Creative Commons Attribution 4.0 International License

# Superparamagnetic Tragacanth Coated $\text{Fe}_3\text{O}_4@\text{SiO}_2$ Nanoparticles for the Loading and Delivery of Metformin

Fereshte Farajian<sup>1</sup> and Payman Hashemi<sup>1,\*</sup>

Department of Chemistry, Faculty of Science, Lorestan University, Khoramabad, I.R. Iran

\* Corresponding author: E-mail: Hashemi.p@lu.ac.ir

Phone: +986633120611

Received: 10-27-2021

## Abstract

A novel superparamagnetic nano-composite of  $\text{Fe}_3\text{O}_4@\text{SiO}_2$  coated by tragacanth gum (TG) as a natural product has been prepared. The obtained  $\text{SiO}_2@\text{Fe}_3\text{O}_4@\text{TG}$  nanoparticles were characterized by Fourier transform infrared spectroscopy, energy dispersive X-ray analysis, scanning electron microscopy and dynamic light scattering analyzer. The magnetic nano-composite was applied for the loading and delivery of metformin, an oral diabetes medicine. The conditions for the loading of the drug were optimized by a central composite design optimization method. The maximum loading efficiency of the sorbent for metformin was obtained at pH 7 and its maximum *in-vitro* release was achieved at pH 1.6, using a phosphate-buffered saline medium. The loading capacity of the sorbent was dependent on the initial metformin concentration and exceeded to 19.6 mg/g in a 200 mg/L solution. A study of the adsorption isotherms for the drug indicated the best fitting into the Langmuir and Freundlich isotherms at the low and high metformin concentrations, respectively. The results indicated that the prepared  $\text{Fe}_3\text{O}_4@\text{SiO}_2@\text{TG}$  adsorbent, as a non-toxic and low-cost sorbent, was quite appropriate for drug delivery applications.

**Keywords:** Tragacanth; Hydrogel adsorbent; Magnetic nanoparticles; Metformin

## 1. Introduction

In recent years, the interest for the use of nanoparticles (NPs), especially magnetic NPs, for analytical purposes and in drug delivery applications has been increased. The major properties of magnetic NPs include easy separation by an external magnetic field, simple syntheses, high surface area, high firmness, reusability and biocompatibility.<sup>1,2</sup> The superparamagnetic iron oxide core increases the binding capacity of NPs and enables them to replace the centrifugation step with magnetic separation. It also simplifies the application of NPs in immune assay.<sup>3</sup> The oxidation potential of iron NPs is high and it is frequently necessary to coat their surfaces by mineral or organic compounds.<sup>4</sup>  $\text{SiO}_2$  is one of the materials used for coating ferrite NPs as it is non-toxic, water-dispersible, and environmentally friendly.<sup>5</sup> Coating of magnetic NPs with biopolymers is also desirable as they can increase the adsorption capacity and selectivity of the NPs for numerous applications.<sup>6–9</sup>

Hydrogels are materials with swellable polymeric networks storing a great quantity of water. The potential to absorb water is due to the presence of polar and hydro-

philic groups in the polymer network. The durability of hydrogels, on the other hand, is affected by crosslinking. Both artificial and natural polymers have been employed for the production of hydrogels. However, the natural polymeric hydrogels have several advantages such as high capacity of water absorption, low expense, long operation life, low toxicity, and high gel stability.<sup>10</sup>

Tragacanth gum (TG) is a natural adhesive mixture of polysaccharides obtained from the plant of *Astragalus* sp. It is a biosorbent and porous hydrogel material that is a non-toxic, abundant, low-cost and biocompatible biopolymer.<sup>8,9,11</sup> TG can be modified by various functional groups such as carboxylic acid, primary and secondary hydroxyl groups and epoxy groups which would enhance its selectivity and provide favourable adsorption conditions.<sup>11–13</sup> The molecular structure of TG is shown in Figure 1. TG has been used in many applications such as wound covering,<sup>14</sup> drug delivery,<sup>15</sup> natural antibacterial<sup>16</sup> and dispersing and thickening agent.<sup>17</sup> TG is a biodegradable, biocompatible, inodorous, flavorless, osteogenic, and resistant biopolymer upon a wide pH range.<sup>18,19</sup> However, the pure TG alone has some weaknesses and hence, it is



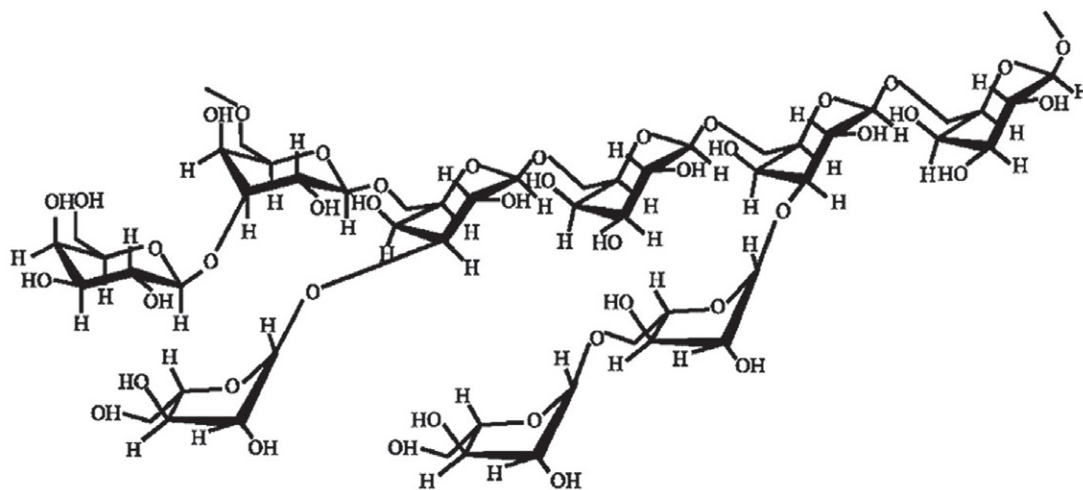


Figure 1. The chemical structure of TG.

frequently strengthened with either organic or inorganic materials such as clays,<sup>20</sup> carbon nanotubes<sup>21</sup> methacrylate polymers,<sup>12,13</sup> and metal nanoparticles.<sup>22</sup>

The goal of the current study is to describe a novel synthesis of  $\text{Fe}_3\text{O}_4@\text{SiO}_2@\text{TG}$  nanocomposite with an easy method as a magnetic adsorbent with biocompatibility, low toxicity, and low cost. The  $\text{SiO}_2$  shell is anticipated to increase the resistance of the nanoparticles in acidic conditions and TG is a non-toxic drug delivery platform. The synthesized adsorbents would be studied for the loading and delivery of metformin as an oral diabetes medicine. In addition to the study of the adsorption mechanisms, multivariate methods are used for optimization of the loading conditions

## 2. Experimental Section

### 2.1. Chemical and Apparatus

All applied chemicals were of analytical reagent grade and were used as received. Sodium hydroxide, ammonia solution 25%, tetraethyl orthosilicate (TEOS), ferric chloride ( $\text{FeCl}_3 \cdot 6\text{H}_2\text{O}$ ), ferrous chloride ( $\text{FeCl}_2 \cdot 4\text{H}_2\text{O}$ ) and ethanol were obtained from Merck chemical company.

A stock solution (1000 mg/g) of metformin was prepared by dissolving required quantity of the drug in methanol. Further dilutions were made by deionized water and prepared daily prior to use. Saline phosphate buffer solution (0.15 mol/L) was prepared by dissolving 0.8 g NaCl, 0.2 g KCl, 1.44 g  $\text{Na}_2\text{HPO}_4$  and 0.24 g  $\text{KH}_2\text{PO}_4$  in 1000 mL of distilled water. This solution was used for buffering test samples after adjustment of its pH (typically on 7.0). TG was obtained from local shops with the best quality and the pieces with transparent color were used for experiments. All solutions were prepared with deionized water.

All the spectrophotometric measurements of metformin were accomplished at its  $\lambda_{\text{max}}$  (232 nm) by a Shimadzu UV-1650PC UV-Vis spectrophotometer (Japan).

A pair of quartz cells (Esquartz, model Q124) were used for the measurements.

For the measurement of the hydrodynamic sizes and zeta potential values of  $\text{Fe}_3\text{O}_4@\text{SiO}_2$  and  $\text{Fe}_3\text{O}_4@\text{SiO}_2@\text{GT}$  particles as-prepared, a zeta potential and dynamic light scattering (DLS) analyzer, SZ-100 - HORIBA (Japan) was used. The particles were diluted with 20% ethanol in deionized water (pH 7).

### 2.2. Synthesis of $\text{Fe}_3\text{O}_4$ NPs

For the preparation of  $\text{Fe}_3\text{O}_4$  NPs an ordinary chemical co-precipitation method was applied.<sup>23</sup> In brief, 50 mL of 0.001 mol/L equimolar mixture of  $\text{FeCl}_3 \cdot 6\text{H}_2\text{O}$ , and  $\text{FeCl}_2 \cdot 4\text{H}_2\text{O}$  was prepared in deionized water. The mixture of the iron salts was sonicated for 15 min at room temperature. The mixture was then transferred to a round bottom two neck flask and heated to 80 °C under reflux in argon atmosphere. Then, 5 mL of concentrated ammonium hydroxide (25% w/w) was slowly added to it during 30 min. A color change from yellowish to black was observed in the mixture that was further heated to 90 °C for 1.5 h under the argon atmosphere. Next, the prepared  $\text{Fe}_3\text{O}_4$  nanoparticles were washed several times with deionized water after being separated by a permanent magnet.

Finally, the obtained  $\text{Fe}_3\text{O}_4$  NPs were re-suspended in 100 mL of deionized water. The obtained NPs were stable in this form up to two months.

### 2.3. Synthesis of $\text{Fe}_3\text{O}_4@\text{SiO}_2$ NPs

Since hydrophobic  $\text{Fe}_3\text{O}_4$  nanoparticles are unstable, they are usually coated by a silica shell.<sup>3</sup> For silanization of the magnetic NPs a typical Stöber method was used. For this purpose, 1.5 g of  $\text{Fe}_3\text{O}_4$  NPs were added to a solution of 16 mL distilled water, 80 mL ethanol and 2 mL 25% ammonia. The composition was then dispersed for 15 min in an ultrasonic bath. After that, 1.0 mL of tetraethyl

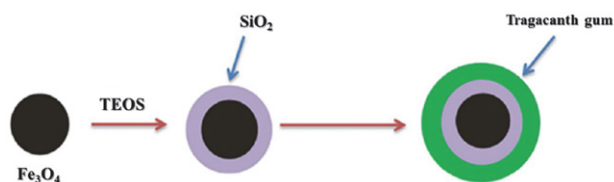


**Figure 2.** Schematic illustration of the procedure used for the synthesis of  $\text{Fe}_3\text{O}_4@\text{SiO}_2@\text{TG}$  NPs.

orthosilicate (TEOS) was added dropwise to the solution containing the NPs. The suspension was shaken on a shaker-bath for 24 h at room temperature. Eventually, the NPs were gathered by a permanent magnet and rinsed several times by distilled water.

## 2. 4. Coating of $\text{Fe}_3\text{O}_4@\text{SiO}_2$ NPs with TG

For the coating of the silanized magnetite NPs with TG, 0.02 g of TG powder was dissolved in 10 mL distilled water at 70 °C in a glass beaker. Subsequently, 1.5 g of  $\text{Fe}_3\text{O}_4@\text{SiO}_2$  NPs were added to the solution under stirring at 1200 rpm and the solution was shaken for 4 h in room temperature. Finally, the  $\text{Fe}_3\text{O}_4@\text{SiO}_2@\text{TG}$  NPs were washed by distilled water several times and the magnetic NPs were separated by a magnet (Figure 2) and stored in 20% ethanol.

## 2. 5. Central Composite Design (CCD) Optimization

A CCD method was used for the optimization of sample volume, adsorbent mass, pH and contact time. For each factor a low and high level was defined based on the results of some primary trials. For each of the four studied factors, five levels were suggested by the Minitab software as shown in Table 1.

The recovery or adsorption efficiency for the drug was regarded as the response or independent function for the optimization. The initiation of the design and statistical analyses of the results were performed using Minitab 16 software.

A drug concentration of 20 mg/L with the pH adjusted by a phosphate buffered saline solution (0.15 mol/L) was used during the optimization. After addition of the adsorbent, the mixture was shaken in a thermostated water

bath for a preset time and the  $\text{Fe}_3\text{O}_4@\text{SiO}_2@\text{TG}$  particles were collected using a permanent magnet. The quantity of adsorbed metformin was computed by the absorbance measurements at 232 nm before and after the adsorption. Standard solutions of metformin in the range of 1 to 20 mg/L were utilized for the calibration.

## 2. 6 Calculation of the Adsorption Capacity

Adsorption capacity of the adsorbent was calculated in mg/g, by its loading with different metformin concentrations. This was done by adding 5 mg of the adsorbent to 1 mL of the drug solutions at pH 7. The residual amount of the drug in solution was calculated by absorption measurements at 232 nm using the UV/Vis spectrophotometer. The adsorption capacity was then calculated from equation 1:

$$q = [(C_o - C_t) \cdot V] / m \quad (1)$$

In this equation,  $q$  is the amount of analyte adsorbed or adsorption capacity (mg/g) of the adsorbent,  $C_o$  is the metformin concentration before addition of the sorbent and  $C_t$  represents its equilibrium concentration (mg/L),  $V$  represents the volume of the solution (L) and  $m$  is the adsorbent mass (g).

## 3. Results and Discussion

### 3. 1. Characterization of the NPs

In the introductory experiments,  $\text{Fe}_3\text{O}_4$ ,  $\text{Fe}_3\text{O}_4@\text{SiO}_2$  and  $\text{Fe}_3\text{O}_4@\text{SiO}_2@\text{TG}$  magnetic NPs were prepared and characterized by Fourier transform infrared spectroscopy (FT-IR), energy dispersive X-ray analysis (EDX), scanning electron microscopy (SEM) and dynamic light scattering (DLS) analyzer. Figure 3 shows the FT-IR spectra of the NPs. In the FT-IR spectrum of  $\text{Fe}_3\text{O}_4$  NPs (Figure 3a), the peak that appeared at wavenumber  $584\text{ cm}^{-1}$  is related to stretching vibrations of Fe-O. The bands in the range of  $1200\text{--}1000\text{ cm}^{-1}$  in (Figure 3b and 3c) belong to the Si-O covalent bond vibrations and confirms the coating of silica on nanoparticles. In the FT-IR spectra associated with  $\text{Fe}_3\text{O}_4@\text{SiO}_2@\text{TG}$  magnetic NPs (Figure 3c), other major vibrational peak in  $3712\text{ cm}^{-1}$  is related to stretching vibration of C-H. This band is a proof of the fixation of TG layer on  $\text{Fe}_3\text{O}_4@\text{SiO}_2$  magnetic NPs.

**Table 1.** The studied parameters and suggested levels in the CCD optimization.

Factor	Abbreviation	Factors' levels				
		$-\alpha$	Low	0	High	$+\alpha$
pH	pH	2	3.5	5	6.5	8
Contact time (min)	Time	20	30	40	50	60
Temperature (°C)	T	25	30	35	40	45
Sample volume (mL)	$V_s$	1	3	5	7	9

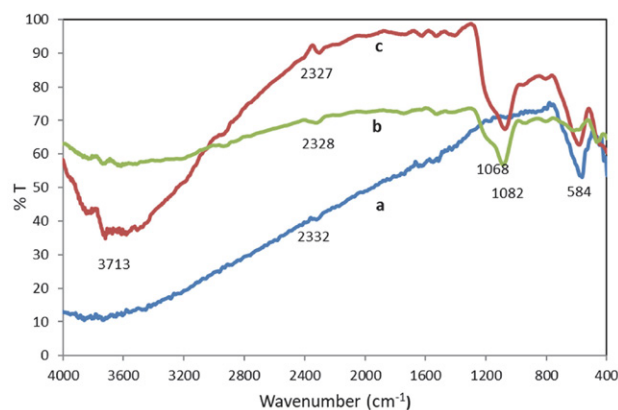


**Figure 3.** FT-IR spectra of  $\text{Fe}_3\text{O}_4$  (a),  $\text{Fe}_3\text{O}_4@\text{SiO}_2$  (b) and  $\text{Fe}_3\text{O}_4@\text{SiO}_2@\text{TG}$  (c) nanoparticles.

The dimension and morphology of  $\text{Fe}_3\text{O}_4$ ,  $\text{Fe}_3\text{O}_4@\text{SiO}_2$  and  $\text{Fe}_3\text{O}_4@\text{SiO}_2@\text{TG}$  nanoparticles were evaluated by SEM. Figure 4 shows the spherical morphology and narrow size spreading of the NPs with an average size of 50–70 nm for  $\text{Fe}_3\text{O}_4@\text{SiO}_2@\text{TG}$ . Energy dispersive X-ray (EDX) analysis was used for the elemental mappings and distribution of the prepared  $\text{Fe}_3\text{O}_4@\text{SiO}_2$  and  $\text{Fe}_3\text{O}_4@\text{SiO}_2@\text{TG}$  nanoparticles. Based on the EDX results, C, N, O, Si and Fe were recognized in the study of  $\text{Fe}_3\text{O}_4@\text{SiO}_2@\text{TG}$  nanoparticles and as expected, the quantity of carbon in the  $\text{Fe}_3\text{O}_4@\text{SiO}_2@\text{TG}$  nanoparticles was more than that of  $\text{Fe}_3\text{O}_4@\text{SiO}_2$  due to the presence of TG in the former. The results apparently confirm covering of the nanoparticles by TG.

Zeta potential study of  $\text{Fe}_3\text{O}_4@\text{SiO}_2$  and GT coated adsorbents indicated a  $-26.6$  mV potential for the  $\text{Fe}_3\text{O}_4@\text{SiO}_2$  and  $-23$  mV for the  $\text{Fe}_3\text{O}_4@\text{SiO}_2@\text{GT}$  adsorbent. This indicates that coating of the adsorbent with GT only slightly reduces the negative charge of it. The DLS results indicated that the hydrodynamic sizes of the adsorbents

are increased to 191 and 253 nm, respectively. It also showed some swelling of the  $\text{SiO}_2$  and TG shells in solution that confirms a biocompatible coating for the incorporation of the drug.<sup>24</sup>

### 3. 2. Effect of pH on Adsorption

One of the important parameters in analyzing adsorption systems is pH, that influences both the chemistry of the sample and the adsorbent binding sites.<sup>25</sup> In the present study, the efficacy of pH on the adsorption or loading the drug was investigated in a range of  $\text{pH} = 2\text{--}11$  with an primary drug concentration of 20 mg/L and using 50 mg of the adsorbent in a mixing time of 30 min (Figure 5). As shown in the figure, by increasing pH from 2 to 7, the adsorption efficiency increases, so that at pH 7, the highest loading is obtained. At higher pH values, a moderate decrease in the efficiency is observed. Alteration of pH can change the surface charge of magnetic NPs.<sup>26</sup> More negative surface charges are expected at a higher pH that is more suitable for the extraction of metformin. This

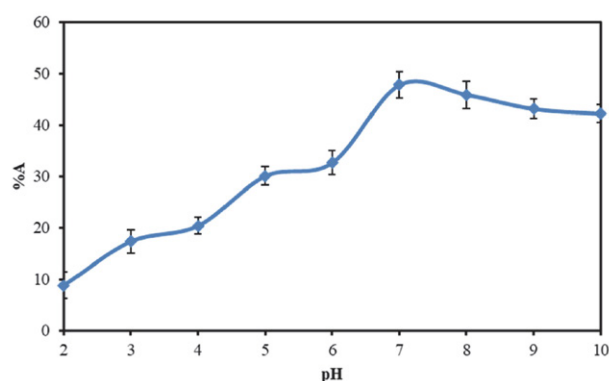


**Figure 5.** Effect of pH on the adsorption of metformin on the  $\text{Fe}_3\text{O}_4@\text{SiO}_2@\text{TG}$  NPs. Sample volume, 5 mL; adsorbent mass, 50 mg; drug concentration, 20 mg/L; mixing time, 30 min; temperature, 25 °C.

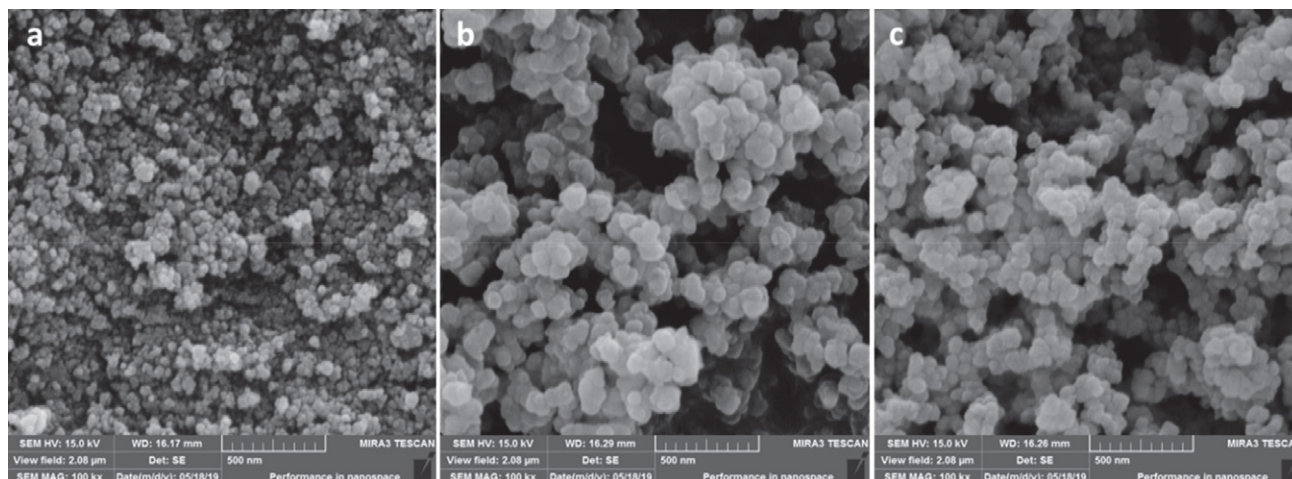


**Figure 4.** SEM images of  $\text{Fe}_3\text{O}_4$  (a),  $\text{Fe}_3\text{O}_4@\text{SiO}_2$  (b) and  $\text{Fe}_3\text{O}_4@\text{SiO}_2@\text{GT}$  (c) MNPs.

is supported by the increase in the adsorption efficiency up to pH 7 in Figure 5.

### 3. 3. Optimization of the Adsorption Conditions

A central composite design (CCD) method was used for the optimization of the loading of metformin on the adsorbent. CCD is one of the most usual multifunctional optimization techniques. In this process, two low and high levels are defined for each factor with the addition of at least one center point and some axial or star points. With this pattern, the approximation of both linear and quadratic effects are possible.<sup>27</sup> For a reasonable estimation of the experimental error, replicate analyses are performed on the center points.<sup>28</sup>

Four factors of pH, temperature (T), volume of sample ( $V_s$ ) and contact time (Time) were studied and optimized by the CCD model. The five levels designed for

**Table 2.** Conditions of the performed tests and their related adsorption efficiency attained by the experiments in the CCD optimization.

Run order	pH	$V_s$ (mL)	Time (min)	T (°C)	Adsorption (%)
1	10	3	50	30	45.8
2	8	7	50	30	44.9
3	9	9	40	35	31.7
4	9	5	40	35	44.6
5	9	5	40	35	55.1
6	9	5	60	35	44.5
7	8	3	30	30	75.6
8	8	3	50	30	68.9
9	8	3	30	40	60.0
10	9	5	40	25	44.1
11	9	5	40	35	44.9
12	10	3	50	40	61.4
13	11	5	40	35	57.3
14	8	7	30	30	47.9
15	10	3	30	30	63.8
16	10	3	30	40	63.8
17	9	1	40	35	79.0
18	10	7	30	40	36.4
19	10	7	30	30	41.8
20	9	5	40	35	51.5
21	9	5	40	35	59.2
22	9	5	40	35	48.3
23	9	5	40	35	56.6
24	8	7	30	40	36.0
25	8	7	50	40	38.0
26	7	5	40	35	31.7
27	10	7	50	40	61.3
28	8	3	50	40	67.0
29	9	5	40	45	58.9
30	10	7	50	30	44.7
31	9	5	20	35	44.6

each factor is shown in Table 1. The levels of the factors in 31 planned experiments by the model and the received response values for each experiment is shown in Table 2. Optimization of the studied factors were accomplished using a response surface model. Some three-dimensional response plots are shown in Figure 6 to demonstrate how the response variable changes with variation of a pair of factors while all other factors stay constant.

As shown in Figure 6a, at a high pH, an increase in adsorption is observed with time, while at a lower pH, such effect is not considerable which indicates the rapid adsorption of metformin on the adsorbent. Figure 6b demonstrates the interaction between pH and temperature (T); at a low temperature, adsorption is decreased by increasing the pH but at a higher temperature, it is slightly increased. In Figure 6c it is shown that at a low sample volume, adsorption efficiency is increased by time, while an opposite effect is observed at a higher sample volume. The same or even more remarkable effect is detected for the dual effect of pH and sample volume (not shown in the figure).

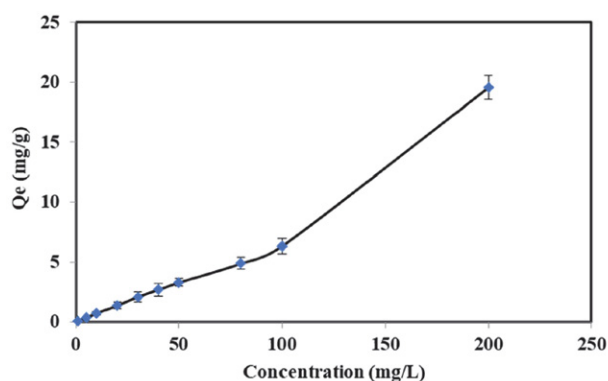


**Figure 6.** Three-dimensional surface plots in CCD optimization procedure. (a) Effects of pH and contact time, (b) Effects of pH and temperature (T), (c) Effects of contact time and volume of sample ( $V_s$ ).

Table 3 displays the results of the data analysis by the CCD model for the discrete and combined effects and second order interactions of the studied variables. Based on the t-test results, the most considerable variable is the sample volume with a large negative effect on the adsorption efficiency. The other factors are statistically negligible with the order of  $\text{pH} > T > \text{Time}$ . The squared terms of the factors are also negligible but the  $\text{pH} \times T$  and  $\text{Time} \times T$  interactions may be considered notable at a 90% confidence level.

The anticipated optimized conditions suggested by the model for the whole data were as follows:  $\text{pH} = 7$ , temperature = 25 °C, volume of sample = 1.0 mL, and contact time = 20 min. By execution of 6 replicated analyses in the optimum conditions, an adsorption efficiency of  $83.27(\pm 6.45)\%$  was obtained for metformin.



**Table 3.** Effects of the factors, coded coefficients (Coef), standard errors (SE) of the coefficients, t-values and p-values of the variables obtained by the CCD model.

Term	Effect	Coef	SE Coef	T-Value	P-Value
Constant		51.46	2.89	17.81	0.000
pH	2.66	1.33	1.56	0.85	0.407
Time	0.54	0.27	1.56	0.17	0.864
T	1.68	0.84	1.56	0.54	0.599
Vs	−20.82	−10.41	1.56	−6.67	0.000
pH×pH	−1.94	−0.97	1.43	−0.68	0.507
Time×Time	−1.92	−0.96	1.43	−0.67	0.512
T×T	1.56	0.78	1.43	0.54	0.594
Vs×Vs	3.48	1.74	1.43	1.22	0.241
pH×Time	1.01	0.51	1.91	0.26	0.795
pH×T	7.89	3.94	1.91	2.06	0.056
pH×Vs	6.76	3.38	1.91	1.77	0.096
Time×T	7.04	3.52	1.91	1.84	0.084
Time×Vs	5.86	2.93	1.91	1.53	0.145
T×Vs	−0.71	−0.36	1.91	−0.19	0.854

### 3. 4. Adsorption Capacity

The adsorption capacity of the  $\text{Fe}_3\text{O}_4@\text{SiO}_2@\text{TG}$  adsorbent or its maximum metformin loading was associated with the primary concentration of the drug in the sample. The capacity was calculated by suspending variant amounts of the adsorbent in a buffered solution of the analyte, under the optimum conditions. The effect of primary concentration of metformin on the adsorption capacity is shown in Figure 7. The adsorption capacity of the nano-composite increased with increasing the primary concentration of metformin. The maximum capacity obtained for 200 mg/L of metformin was 19.6 mg/g.

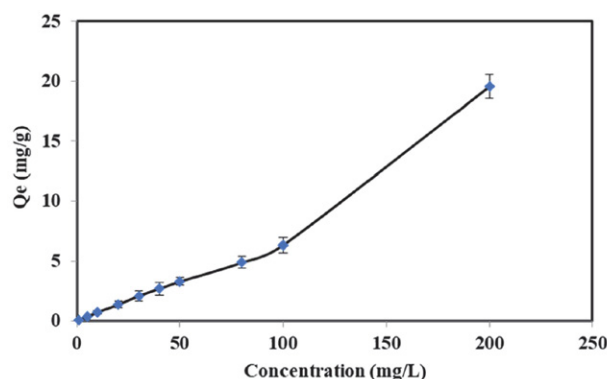


**Figure 7.** The adsorption capacity of NPs as a function of the initial concentration of metformin under the optimized conditions; pH, 7; T, 25 °C; t, 20 min; sample volume, 1.0 mL; adsorbent mass, 40 mg; number of replicates, 3.

### 3. 5. Study of the Adsorption Isotherms

The mechanism of interaction of metformin with the adsorbent was examined by studying the adsorption

isotherms in batch experiments. For the analysis of the experimental data, two adsorption models of Langmuir and Freundlich were used. The Langmuir adsorption isotherm relates the monolayer adsorption of a species onto the adsorbent superficial with some well-defined sites. According to this model, the plot of  $C_e/q$ , in which  $C_e$  is the equilibrium concentration of the analyte in solution and  $q$  is the balanced adsorption capacity of the sorbent, versus  $C_e$  should be linear. The Freundlich isotherm is not restricted to the formation of a monolayer and is related to the reversible adsorption. Accordingly, a linear plot is attained for plotting  $\log q$  versus  $\log C_e$ .<sup>29</sup>

Figure 8a and 8b are the corresponding plots of the Langmuir and Freundlich models, respectively. Regarding  $R^2$  as an indication of the desirable fit of experimental data, the Langmuir adsorption is more appropriate at lower than 5.8 mg/L  $C_e$  values suggesting the monolayer adsorption of metformin at low metformin concentrations. At higher  $C_e$  values, however, the Freundlich adsorption,

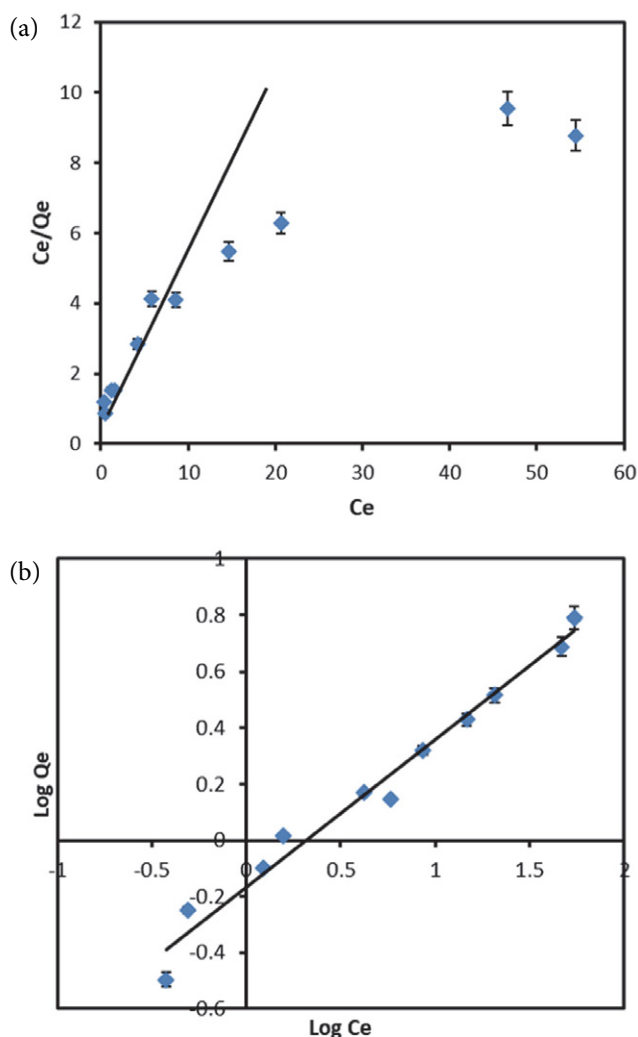


**Figure 8.** a The Langmuir adsorption isotherm and b The Freundlich adsorption isotherm for the results shown in Figure 7.

with an  $R^2$  value of 0.9772, is more appropriate than the Langmuir adsorption indicating the possibility of multi-layer adsorption mechanism in this region. The values of  $b$  (Langmuir constant),  $q_m$  (maximum one-layer adsorption capacity),  $k_F$  and  $n$  (Freundlich constants) were computed to be 1.36 L/mg, 1.81 mg/g, 0.68, and 1.91, respectively.<sup>29</sup> The Freundlich constant  $n$  is higher than one, representing the appropriate conditions for the adsorption.<sup>26</sup>

### 3. 6. Evaluation of Drug Release

The influence of contact time on the desorption or the release rate of metformin from the prepared adsorbent was studied in a range from 5 to 50 min. Metformin was first loaded on the adsorbent at the optimized conditions (pH 7, volume of sample 1.0 mL,  $T$  25 °C, and contact time 20 min). The desorption was accomplished using phosphate buffered saline at three different pH values of 1.6, 3.0, and 7.3. The low pH values were selected as the region with minimum adsorption of metformin (see Figure 5). The release at pH 7.3 was also studied because this is the pH of the human body.

The corresponding results are shown in Figure 9. The maximum drug desorption or delivery was obtained within 10 to 30 min by changing the pH from 1.6 to 3.0 and a maximum delivery of 85% was obtained at pH 3.0. It is also seen that at the body pH of 7.3 some 38% delivery is observed which may be useful when the drug is used for intravenous injections.

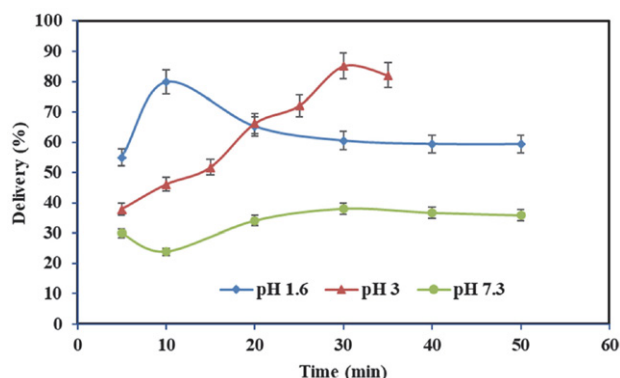


**Figure 9.** Metformin desorption (delivery) from the loaded  $\text{Fe}_3\text{O}_4@ \text{SiO}_2@ \text{TG}$  NPs in pH 1.6, 3.0 and 7.3. Number of replicates: 3.

## 4. Conclusions

Coating of  $\text{Fe}_3\text{O}_4@ \text{SiO}_2$  magnetic NPs by TG as a natural hydrogel was successfully carried out using a simple modifying process. Characterization of the prepared NPs by FT-IR, EDX and SEM corroborated the structure and the relatively uniform sizes of the prepared NPs. The results demonstrated that the synthesized  $\text{Fe}_3\text{O}_4@ \text{SiO}_2@ \text{TG}$  nanocomposite is a suitable carrier for the loading and

releasing of metformin, as it is non-toxic, highly porous, low cost, and biocompatible.

The modified nanocomposite established a high efficiency for metformin adsorption with a loading capacity up to 19.6 mg/g in a short time. The adsorption on the prepared NPs fitted into Langmuir isotherm at low concentrations of metformin while it was best fitted into Freundlich isotherm in a higher concentration area. Maximum desorption of the medicine happened in pH of 1.6 to 3.0 within 10 to 30 min. The results indicated the potential use of the  $\text{Fe}_3\text{O}_4@ \text{SiO}_2@ \text{TG}$  adsorbent as an inorganic-organic hybrid for the loading and delivery of metformin and possibly for the removal of pharmaceutical residues in the environment.

## 5. References

1. A. A. Alqadami, M. Naushad, M. A. Abdalla, T. Ahamad, Z. A. AlOthman, S. M. Alshehri, A. A. Ghfar, *Journal of Cleaner Production* **2017**, 156, 426–436. DOI:10.1016/j.jclepro.2017.04.085
2. A. A. Alqadami, M. Naushad, M. A. Abdalla, M. R. Khan, Z. A. AlOthman, *Journal of Chemical & Engineering Data* **2016**, 61, 3806–3813. DOI:10.1021/acs.jced.6b00446
3. K. Hemmati, A. Masoumi, M. Ghaemy, *Carbohydrate polymers* **2016**, 136, 630–640. DOI:10.1016/j.carbpol.2015.09.006
4. C. Singh, A. Goyal, S. Bansal, S. Singhal, *Materials Research Bulletin* **2017**, 85, 109–120. DOI:10.1016/j.materresbull.2016.09.010
5. M. Coşkun, M. Korkmaz, *Journal of nanoparticle research* **2014**, 16, 2316. DOI:10.1007/s11051-014-2316-3
6. S. Hanif, A. Shahzad, *Journal of nanoparticle research* **2014**, 16, 2429. DOI:10.1007/s11051-014-2429-8
7. A. Mittal, R. Ahmad, I. Hasan, *Desalination and Water Treatment* **2016**, 57, 19820–19833. DOI:10.1080/19443994.2015.1104726
8. S. Nasirimoghaddam, S. Zeinali, S. Sabbaghi, *Journal of Industrial and Engineering Chemistry* **2015**, 27, 79–87. DOI:10.1016/j.jiec.2014.12.020
9. S. Sadeghi, F. A. Rad, A. Z. Moghaddam, *Materials Science and Engineering: C* **2014**, 45, 136–145. DOI:10.1016/j.msec.2014.08.063
10. E. M. Ahmed, *Journal of advanced research* **2015**, 6, 105–121. DOI:10.1016/j.jare.2013.07.006
11. R. Sahraei, Z. S. Pour, M. Ghaemy, *Journal of cleaner production* **2017**, 142, 2973–2984. DOI:10.1016/j.jclepro.2016.10.170
12. K. Hemmati, A. Masoumi, M. Ghaemy, *Polymer* **2015**, 59, 49–56. DOI:10.1016/j.polymer.2014.12.050
13. K. Hemmati, A. Masoumi, M. Ghaemy, *RSC advances* **2015**, 5, 85310–85318. DOI:10.1039/C5RA14356J
14. B. Singh, L. Varshney, S. Francis, *Radiation Physics and Chemistry* **2017**, 135, 94–105. DOI:10.1016/j.radphyschem.2017.01.044
15. B. Singh, V. Sharma, *Carbohydrate polymers* **2017**, 157, 185–195. DOI:10.1016/j.carbpol.2016.09.086



16. M. Nasiri, M. Barzegar, M. A. Sahari, M. Niakousari, *Food Hydrocolloids* **2017**, *72*, 202–209. DOI:10.1016/j.foodhyd.2017.05.045
17. A. Komeilyfard, M. Fazel, H. Akhavan, A. Mousakhani Ganjeh, *Journal of texture studies* **2017**, *48*, 114–123. DOI:10.1111/jtxs.12216
18. R. Sahraei, M. Ghaemy, *Carbohydrate polymers* **2017**, *157*, 823–833. DOI:10.1016/j.carbpol.2016.10.059
19. S. Kulanthavel, S. R. VS, T. Agarwal, S. Pradhan, K. Pal, S. Giri, T. K. Maiti, I. Banerjee, *Journal of Materials Chemistry B* **2017**, *5*, 4177–4189. DOI:10.1039/C7TB00390K
20. S. Pirsai, F. Mohtarami, S. Kalantari, *Chemical Review and Letters* **2020**, *3*, 98–103.
21. S. Mallakpour, F. Tabesh, *International Journal of Biological Macromolecules* **2021**, *166*, 722–729. DOI:10.1016/j.ijbiomac.2020.10.229
22. A. Bahrami, R. R. Mokarram, M. S. Khiabani, B. Ghanbarzadeh, R. Salehi, *International journal of biological macromolecules* **2019**, *129*, 1103–1112. DOI:10.1016/j.ijbiomac.2018.09.045
23. M. Faraji, Y. Yamini, E. Tahmasebi, A. Saleh, F. Nourmohammadian, *Journal of the Iranian Chemical Society* **2010**, *7*, S130–S144. DOI:10.1007/BF03246192
24. J. Szűcsóvá, A. Zeleňáková, O. Kapusta, A. Berkutova, V. Zeleňák, in *Book Influence of silica coating on magnetic properties and Zeta potential of Fe<sub>3</sub>O<sub>4</sub>@ mSiO<sub>2</sub> core-shell for drug delivery systems*, ed., ed. by Editor, AIP Publishing LLC, City, **2018**, Vol. 1996, Chap. Chapter, pp. 020047. DOI:10.1063/1.5048899
25. Z. L. Yaneva, N. V. Georgieva, *International Review of Chemical Engineering* **2012**, *4*, 127–146.
26. K. Ahalya, N. Suriyanarayanan, S. Sangeetha, *Materials science in semiconductor processing* **2014**, *27*, 672–681. DOI:10.1016/j.mssp.2014.08.009
27. M. A. Bezerra, R. E. Santelli, E. P. Oliveira, L. S. Villar, L. A. Escalera, *Talanta* **2008**, *76*, 965–977. DOI:10.1016/j.talanta.2008.05.019
28. F. N. Serenjah, P. Hashemi, M. Safdarian, Z. Kheirollahi, *Journal of the Iranian Chemical Society* **2014**, *11*, 733–739. DOI:10.1007/s13738-013-0346-x
29. F. G. Adivi, P. Hashemi, A. D. Tehrani, *Polymer Bulletin* **2019**, *76*, 1239–1256. DOI:10.1007/s00289-018-2418-7

## Povzetek

Pripravili smo nov superparamagnetni nanokompozitni material iz Fe<sub>3</sub>O<sub>4</sub>@SiO<sub>2</sub>, prevlečen s tragakantovim gumijem (TG) kot naravnim proizvodom. Pridobljene SiO<sub>2</sub>@Fe<sub>3</sub>O<sub>4</sub>@TG nanodelce smo okarakterizirali z infrardečo spektroskopijo s Fourierjevo transformacijo, energijsko-disperzno rentgensko žarkovno analizo, vrstično elektronsko mikroskopijo in dinamično analizo svetlobnega sipanja. Magnetni nanokompozitni material smo uporabili za vezavo in sproščanje metformina, oralne učinkovine proti diabetesu. Pogoje za vezavo učinkovine smo optimizirali s pomočjo metode faktor-skega načrta. Največjo vezavno učinkovitost sorbenta za metformin smo dobili pri pH 7, maksimalno *in-vitro* sproščanje v salinem mediju s fosfatnim pufrom pa pri pH 1,6. Vezavna kapaciteta sorbenta je bila odvisna od začetne koncentracije metformina in je dosegla 19,6 mg/g v raztopini s koncentracijo 200 mg/L. Študij adsorpcijskih izoterm za učinkovino je pokazal najboljše prileganje Langmuirjevi izotermi pri nizkih koncentracijah in Freundlichovi izotermi pri visokih koncentracijah metformina. Rezultati dokazujejo, da je pridobljeni Fe<sub>3</sub>O<sub>4</sub>@SiO<sub>2</sub>@TG adsorbent, ki je nestrupen in cenen, povsem primeren za uporabo pri dostavi zdravilnih učinkovin.



Except when otherwise noted, articles in this journal are published under the terms and conditions of the Creative Commons Attribution 4.0 International License

Scientific paper

# Investigation of Biological and Prooxidant Activity of Zinc Oxide Nanoclusters and Nanoparticles

Iliana A. Ivanova,<sup>1</sup> Elitsa L. Pavlova,<sup>2</sup> Aneliya S. Kostadinova,<sup>3</sup>  
Radostina D. Toshkovska,<sup>1,4</sup> Lyubomira D. Yocheva,<sup>5</sup> Kh El-Sayed,<sup>6,7</sup>  
Mohamed A. Hassan,<sup>6,7</sup> Heba El-Sayed El-Zorkany<sup>6,7</sup> and Hisham A. Elshoky<sup>6,7,8\*</sup>

<sup>1</sup> Dept. Microbiology, Faculty of Biology, Sofia University Saint Kliment Ohridski, 8 Dragan Tsankov Blvd, 1164 Sofia, Bulgaria

<sup>2</sup> Faculty of Physics, Sofia University "St. Kliment Ohridski", 5 James Bourchier Blvd., 1164 Sofia, Bulgaria

<sup>3</sup> Institute of biophysics and biomedical engineering, Bulgarian academy of science, Akad. Georgi Bonchev 21str, Sofia 1113, Bulgaria

<sup>4</sup> Institute of Organic Chemistry with Center of Phytochemistry, 9 Acad. G. Bonchev Str, Sofia

<sup>5</sup> Faculty of Medicine, 1 Kozyak Str, 1407, Sofia, Bulgaria

<sup>6</sup> Nanotechnology and Advanced Materials Central Lab, Agricultural Research Center, Giza, Egypt

<sup>7</sup> Regional Center for Food and Feed, Agricultural Research Center, Giza, Egypt.

<sup>8</sup> Tumor Biology Research Program, Department of Research, Children's Cancer Hospital Egypt 57357, P.O Box 11441, 1 Seket Al-Emam Street, Cairo, Egypt

\* Corresponding author: E-mail: heshamalshoky@sci.cu.edu.eg; heshamalshoky@gmail.com

Received: 12-13-2021

## Abstract

Zinc oxide (ZnO) nanomaterials offer some promising antibacterial effects. In this study, a new form of ZnO is synthesized, named ZnO nanocluster bars (NCs). Herein, ZnO NCs, ZnO nanoparticles (NPs), ZnO coated with silica (ZnO-SiO<sub>A</sub>, ZnO-SiO<sub>B</sub>), and SiO<sub>2</sub> NPs were prepared, characterized, and their antimicrobial and prooxidant activity were tested. The prooxidant activity of all nanomaterials was studied according to free-radical oxidation reactions (pH 7.4 and pH 8.5) in chemiluminescent model systems. Each form of new synthesized ZnO nanomaterials exhibited a unique behavior that varied from mild to strong prooxidant properties in the Fenton's system. ZnO NPs and ZnO NCs showed strong antibacterial effects, ZnO-SiO<sub>A</sub> NPs did not show any antibacterial activity representing biocompatibility. All tested NMs also underwent oxidation by H<sub>2</sub>O<sub>2</sub>. ZnO NCs and ZnO NPs exhibited strong oxidation at pH 8.5 in the O<sub>2</sub><sup>-</sup> generating system. While, SiO<sub>2</sub>, ZnO-SiO<sub>A</sub> and ZnO-SiO<sub>B</sub> possessed pronounced 60–80% antioxidant effects, SiO<sub>2</sub> NPs acted as a definitive prooxidant which was not observed in other tests. ZnO NCs are strongly oxidized, assuming that ZnO NCs provide a slower release of ZnO, which leads to having a stronger effect on bacterial strains. Thus, ZnO NCs are an important antibacterial agent that could be an emergent replacement of traditional antibiotics.

**Keywords:** ZnO; nanoclusters; nanocomposites; antimicrobial activity; ROS; chemiluminescence.

## 1. Introduction

Multi-drug resistant (MDR) bacteria have become an important problem because of the extensive use of antibiotics, which are often applied without proper medical indications. The inappropriate selection and switch between antimicrobial alternates cause "selection pressure." All

of this causes MDR bacteria. Consequently, while many studies have focused on identifying new effective bactericidal materials, new alternative strategies for combating bacterial resistance remain under investigation.<sup>1–4</sup>

Nanotechnology introduces a special solution to the MDR bacteria. Several nanomaterials (NMs) have been used in antibacterial treatments, antibacterial vaccines,

antibiotic delivery carriers, and antibacterial coatings for implantable devices and medicinal materials to prevent infection and promote infection wound healing to help control bacterial infections. They are applied in microbial diagnostic systems too.<sup>5</sup>

ZnO is known for its anti-inflammatory, astringent, and soothing effects.<sup>6,7</sup> Therefore, ZnO has been used in cosmetics, including sunscreens, toothpaste, and shampoos, after the nineteenth century.<sup>8</sup> Furthermore, the US Food and Drug Administration (FDA) has classified ZnO as “Generally Recognized as Safe” (GRAS) because of its non-toxic properties. Zn is used as a food additive too.<sup>9,10</sup> Recently, ZnO NMs have attracted considerable attention because of their antimicrobial activity. ZnO NMs’ superiority in fighting microbial resistance is attributed to their nonspecific activity, small particle size, high surface area, low cost, and efficiency against various bacteria with low toxicity to human cells.<sup>11</sup>

Unfortunately, we have limited knowledge of NMs’ mechanisms of action against bacteria. The suggested mechanisms include oxidative stress induction, metal ion release, and non-oxidative mechanisms.<sup>5,12,13</sup> The bacterial destruction by ZnO NMs is believed to follow two pathways: binding to cell membranes, consequently disrupting their potential and integrity and inducing generation of reactive oxygen species (ROS).<sup>5</sup> ZnO NMs are mutagens albeit weak ones.<sup>14</sup>

Many studies attempted to investigate and use ZnO nanoparticles in different applications.<sup>15,16</sup> Smaller ZnO nanoparticles usually show higher cellular inhibition activity. Furthermore, surface modification of ZnO NMs can affect their properties that may change or improve their antimicrobial activity.<sup>17</sup>

While the generation of ROS is important for antibacterial activity of ZnO NMs, it is necessary to investigate the kinetics of free radical generation, affected by ZnO NMs.<sup>18,19</sup> The chemiluminescent assay is a convenient method for such studies. It can be used to monitor the dynamics of free radical reactions and to determine their prooxidant/antioxidant activity. The chemiluminescent technique is advantageous because of its accuracy, sensitivity, high speed, and relatively low cost; moreover, it requires a small sample volume. Many physical and chemical probes, such as luminol and lucigenin, can be used to enhance chemiluminescence. These reactions are accompanied by emission in the range of 480–580 nm; hence, they can be harnessed to assess the quantum yield of generated free radicals.<sup>20–22</sup>

We synthesized a completely new form of ZnO nanoaggregates in this study called ZnO nanocluster bars (ZnO NCs). Their prooxidant and antimicrobial effects were evaluated compared with different forms of ZnO NMs as spherical ZnO NPs with/without silica coating. Furthermore, the prooxidant activity of all NMs was examined as free radical oxidation reactions at pH 7.4 and pH 8.5 in chemiluminescent model systems.

## 2. Experimental

### 2. 1. Materials

The materials used in this study were purchased with high purity; zinc acetate dihydrate (99.5%, Merck, Germany), 2-propanol (99.9%, Sigma-Aldrich), sodium hydroxide (99.5%, Sigma-Aldrich), tetraethyl orthosilicate (TEOS, 98%, Sigma-Aldrich), iron sulphate (P. A.) (Merck, Germany), ammonia solution (25%, Sigma-Aldrich), phenazine methosulfate (PhMS) (N-methyldibenzopyrazine methyl sulfate salt) (P. A.) (Merck, Germany), hydrogen peroxide (30%) (Boron, Bulgaria), disodium hydrogen phosphate (P. A.) (Boron, Bulgaria), citric acid (P. A.) (Boron, Bulgaria), lucigenin (bis-N-methylacridinium nitrate) (P. A.) (Aldrich, USA),  $\beta$ -nicotinamide adenine dinucleotide, reduced form (P. A.) (NAD.H, Boehringer, Germany) and dimethyl sulfoxide (P. A.) (DMSO, Aldrich, USA). All chemicals were used as-purchased without further purification.

### 2. 2. Preparation of ZnO Nanocluster Bars (ZnO NCs)

A solvothermal process prepared the ZnO nanocluster bars as follows; 1 g of zinc acetate was ultrasonically dispersed in 80 mL of 2-propanol in a 150 mL beaker for 30 min at room temperature. Then, 2 g of oxalic acid was added followed by another 30 min of ultrasonication. To complete the hydrothermal preparation process, the mixture was poured from the beaker in a Teflon-based stainless steel autoclave and placed in the oven for 24 h at 180 °C. Subsequently, the prepared NPs were washed three times with DI-H<sub>2</sub>O and ethanol by centrifugation (4500 rpm at 10 °C for 30 min.), the same step was repeated for DI-H<sub>2</sub>O and ethanol three times until the whole quantity is washed. The precipitate was dried in an oven at 180 °C for 8 h. Then, the powder was calcined in a muffle oven at 400 °C for 2 h.

### 2. 3. Preparation of ZnO Nanoparticles (ZnO NPs)

ZnO nanoparticles were obtained using a modified method as described by G. Simonelli et. al.<sup>23–25</sup> Briefly, a 46.5 mM of zinc acetate dihydrate was prepared by dissolving 2.195 g in 20 mL of 2-propanol at 50 °C and then the volume was increased to 210 mL by 2-propanol. Note that 0.8 g of sodium hydroxide in 40 mL solution (35 mL 2-propanol + 5 mL DI-H<sub>2</sub>O) was added under continuous stirring in an ice bath. Then, the solution was stirred at 60 °C for 2 h, and the temperature was measured and followed up to ensure that it did not rise over that because this influenced the particle sizes. Subsequently, the preparation vessel was kept stable at room temperature for three days for additional aging. Then, the sample was repeatedly centrifuged at

7000 rpm/15 min till all other chemical residuals were completely removed. The precipitate was dried in the oven at 180 °C for 8 h. Then, the powder was calcined in a muffle oven at 400 °C for 2 h. Characterization measurements were performed using DLS, zeta potential, XRD and TEM.

## 2. 4. Preparation of Silica Capped ZnO NPs (ZnO-SiO NPs<sub>A, B</sub>)

ZnO NPs were dispersed in water as per Bartczak's protocol with modification.<sup>18,26</sup> In an ultrasonic bath, 0.5 g of ZnO NPs in 100 mL of 2-propanol was sonicated for 15 min at room temperature. The pH of the ZnO NP solution was increased to 10 by the dropwise addition of 1 M ammonium hydroxide solution and monitoring the change using a pH meter. Next, 100 mL of 2% TEOS in DI-H<sub>2</sub>O was added, and the suspension was sonicated for 1 h at room temperature. NPs then reacted overnight at 60 °C with stirring before purification from excess by-products and organic solvent residues by triple centrifugation (13000 rpm, 15 min at room temperature) with the same approach mentioned for ZnO NC preparation. (ZnO-SiO<sub>A</sub>) NPs were then dried in a hot air oven at 80 °C overnight. For the second form of SiO<sub>2</sub> capped ZnO NPs (ZnO-SiO<sub>B</sub>), the same procedure was performed but without pH adjustment of the ZnO solution.

## 2. 5. Preparation of Silica Nanoparticles (SiO<sub>2</sub> NPs)

In brief, 300 mL of DI-H<sub>2</sub>O was added to 300 mL ethanol and stirred for 10 min at room temperature. Then, 45 mL of TEOS were added and sonicated for 20 min. The dropwise additions of 1 M ammonium hydroxide solution were made until pH 10 was reached, and the reaction was stirred overnight. Next, the SiO<sub>2</sub> NPs were washed well with DI-H<sub>2</sub>O using centrifugation at 10000 rpm for 15 min, using the same procedure as before, until ammonia odor disappears and pH becomes neutral. The precipitate was dried in the oven at 45 °C overnight; finally, the yield was ground to obtain a fine silica powder.<sup>26</sup>

## 2. 6. Characterization of the Prepared Nanoparticles

A transmission electron microscope (TEM, Tecnai G20, FEI, Netherlands) was used for imaging the nano-materials that were prepared. The bright field imaging was employed at an accelerating voltage of 200 kV using a lanthanum hexaboride (LaB<sub>6</sub>) electron source gun, and the Eagle CCD camera was used to acquire and collect transmitted electron images with an image resolution (4K x 4K). Before imaging, the aqueous suspensions of prepared nanoparticles were prepared in an ultrasonicator (SB-120DTN, Taiwan) for 10 min, and then particles were

deposited from a dilute aqueous suspension onto a 200 mesh-carbon coated copper grid placed on filter paper and left for drying at room temperature as a common method for preparing TEM samples.

However, powder X-ray diffraction (XRD – X'Pert PRO, PANalytical, The Netherlands) was used to reveal the crystal structure of the prepared NMs. XRD operated at 45 kV and 30 mA using X-ray source “Cu K $\alpha$  radiation” ( $\lambda = 1.5404 \text{ \AA}$ ). The step time and step sizes were 0.5 s/step and 0.02 degree/step, respectively, in the range of 4° – 80° (2 $\theta$ ). Peaks matching and analysis were performed using high score plus software.

Particle size distribution analysis and zeta potentials of the prepared materials were measured using Zetasizer Nano S, Malvern Instruments, UK, to evaluate hydrodynamic size and surface charge. These measurements were performed in aqueous solutions after NMs were dispersed in deionized water using an ultrasonicator for 15 minutes to obtain stable suspensions. A portion of suspension was transferred in 10 mm x 10 mm cuvette (DTS1070) to measure particle size and zeta potential.

## 2. 7. Microorganisms

The antimicrobial activity was tested against Gram-positive *Bacillus cereus* NBIMCC1095, *Staphylococcus epidermidis* ATCC 12228 bacteria, and Gram-negative *Escherichia coli* BL21DE3 bacteria. All bacteria purchased from National Bank for Industrial Microorganisms and Cell Cultures (NBIMCC, Bulgaria) were grown in nutrient broth (NB Conda, Spain) at 37 °C and 180 rpm (shaker Rotomax, incubator ED053, Germany) for 24 h with two sub-cultivations. Microbial density of cultures in an exponential phase of 0.5–0.6 was determined according to McFarland.

## 2. 8. Antimicrobial Activity

Antibacterial influence of each type of prepared NMs was investigated using spot-diffusion in agar. Briefly, 100  $\mu\text{L}$  of each bacterial suspension was homogeneously spread on nutrient agar plates. 10  $\mu\text{L}$  drops of investigated material were put on inoculated solid medium. Plates were left for 2 h at 4–6 °C to afford diffusion of dispersions and cultured for 24 h, and then 48 h at 37 °C. The diameters of sterile zones were measured in mm.<sup>27,28</sup>

## 2. 9. Chemiluminescent Assay

The chemiluminescent method was applied to study effect of NMs on the kinetics of free-radical oxidation reactions using activated chemiluminescence and the probe lucigenin.<sup>29</sup>

The higher acidity of medium favors radical formation reactions and enables the achievement of reliable differences. Two different pH systems were investigated –



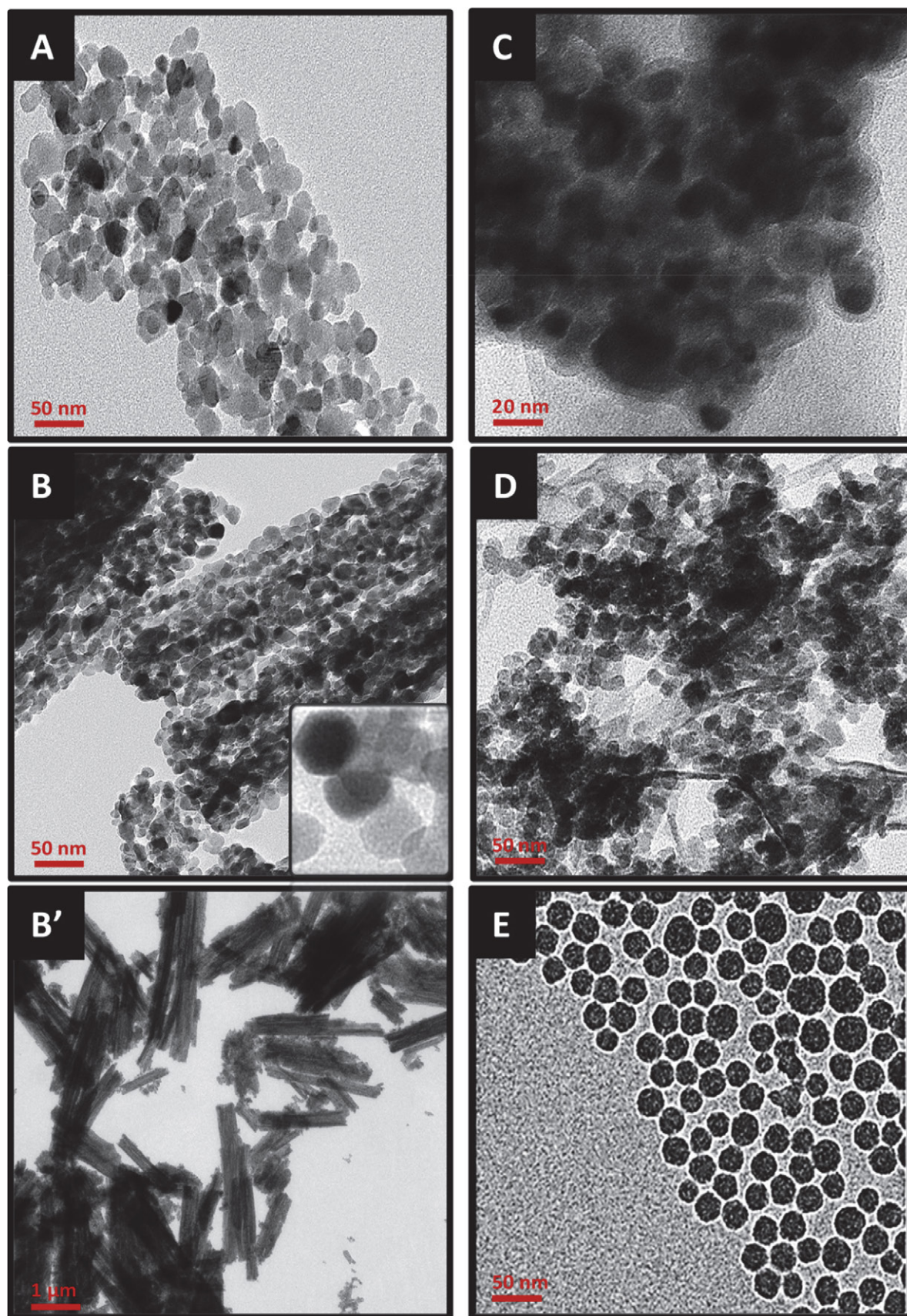


**Figure 1:** TEM images of (A) ZnO-NPs, (B and B') different magnifications of ZnO nanocluster bars, (C) ZnO-SiO<sub>A</sub>, (D) ZnO-SiO<sub>B</sub>, and (E) SiO<sub>2</sub> NPs, respectively.

pH 7.4 and pH 8.5, physiological and alkaline. Three *ex vivo* model systems were implemented in buffers and here described briefly.<sup>22</sup> First system, generating hydroxyl radicals ( $\cdot\text{OH}$ ) system, it contains 0.2 mol of sodium hydrogen phosphate buffer, with the appropriate pH, Fenton's reagent [ $\text{FeSO}_4$  ( $5.10^{-4}$  mol) –  $\text{H}_2\text{O}_2$  (1.5%), lucigenin ( $10^{-4}$  mol)] and NMs.

The second system contains the oxidant hydrogen peroxide ( $\text{H}_2\text{O}_2$ ): 0.2 mol sodium hydrogen phosphate buffer, with appropriate pH,  $\text{H}_2\text{O}_2$  (1.5%), the chemiluminescent probe lucigenin ( $10^{-4}$  mol), and NMs. The third system is for the generation of superoxide radicals ( $\text{O}_2^{\cdot-}$ ) through the reaction NAD.H-PhMS. It contains 0.2 mol of sodium hydrogen phosphate buffer with the specific pH, NAD.H ( $10^{-4}$  mol), phenazine-metasulfate ( $10^{-6}$  mol), lucigenin ( $10^{-4}$  mol) and NMs. The control samples do not contain any NMs. The reactions are monitored for 3 minutes every 3 seconds; the maximum peak for each curve was obtained.

## 2. 10. Statistics

All experiments were performed in triple reproducible measurements; statistical analysis was implemented using Origin 8.5 and Microsoft Office Excel 2010. To measure the strength of the relationship between tested variables, correlation coefficients ( $r$ ) between the sensitivity of the selected bacterial strains toward the antimicrobial effect of ZnO NPs, ZnO NCs, ZnO- $\text{SiO}_A$ , and ZnO- $\text{SiO}_B$  NMs tested by spot diffusion and chemiluminescent assays are calculated.

## 3. Results and Discussion

### 3. 1. Characterization

#### Transmission electron microscopy (TEM) imaging

Fig. 1 shows the TEM micrographs of ZnO NMs and  $\text{SiO}_2$  NPs. TEM images (Fig. 1A, B, and B') demonstrated that ZnO NPs and ZnO NCs agglomerated to certain extent. The average diameter size, measured using TEM-TIA software, of the prepared ZnO-NPs (Fig. 1A, B) and  $\text{SiO}_2$  NPs (Fig. 1E) was between 22.9–38.1 and 19–25 nm. The ZnO NCs agglomerated in NCs with a length of 2–3  $\mu\text{m}$  and a width between 200 and 350 nm. The image of ZnO NCs comprised small ZnO NPs with an average particle size of 14.3–21.5 nm. However, ZnO- $\text{SiO}_2$  NPs demonstrated two different morphological forms. Fig. 1C shows a homogeneous sphere capped ZnO- $\text{SiO}_A$  NPs with an average diameter of  $\sim 20 \pm 3$  nm, and the silica layer surrounding the ZnO NPs with an estimated layer thickness of  $4 \pm 0.5$  nm. However, ZnO- $\text{SiO}_B$  show in Fig. 1D with less homogeneity in particle size and additional aggregation than ZnO- $\text{SiO}_A$  with an average particle size of  $13.4 \pm 3$  nm for ZnO cores and  $3.5 \pm 0.7$  nm for  $\text{SiO}_2$  cap. Fig. 1E shows well-dispersed and homogeneous spherical  $\text{SiO}_2$  NPs with an average  $38 \pm 3$  nm diameter. The change in the shape depends on the method of preparation, which causes the  $\text{SiO}_2$  NPs to appear to be in a good and homogeneous shape.

#### X-ray diffraction (XRD) analysis

Fig. 2(a–e) shows the XRD patterns for ZnO NPs-, ZnO NCs-, and  $\text{SiO}_2$ -coated ZnO and  $\text{SiO}_2$ . All the dif-

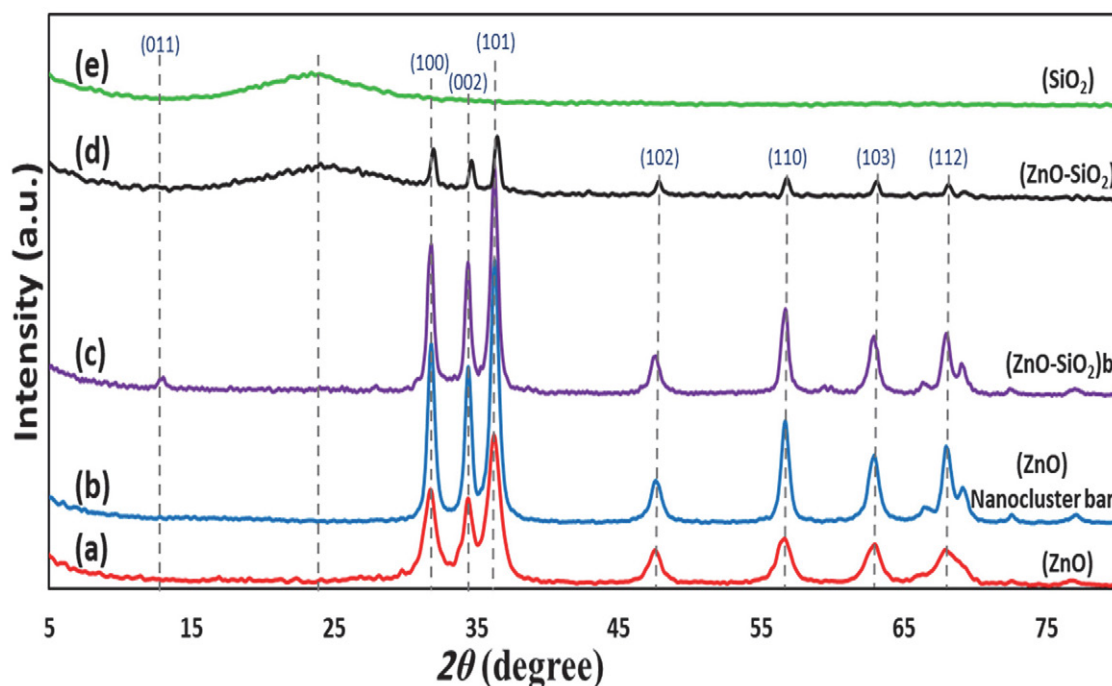


Figure 2: XRD patterns of (a) ZnO NPs, (b) ZnO NC bars, (c) ZnO- $\text{SiO}_{2A}$ , (d) ZnO- $\text{SiO}_{2B}$ , and (e)  $\text{SiO}_2$  NPs, respectively.



fraction peaks of ZnO-containing materials are fitted to the hexagonal (wurtzite) ZnO structure (JCPDS no. 01–080–3002) with lattice parameters ( $a = b = 3.25$  Å,  $c = 5.21$  Å), and a space group  $P6_3mc$ . The primary peaks of ZnO appeared at diffraction angles of  $2\theta$ : 31.8°, 34.4°, 36.2°, 47.5°, 56.6°, 62.8°, and 67.9° for ZnO NPs and ZnO NCs. While the SiO<sub>2</sub>-coated ZnO NPs present a combination of SiO<sub>2</sub> peaks at  $2\theta = 23.2^\circ$  and ZnO diffraction peaks with a slight peak shifting (Fig. 2c). This may indicate a complete formation of SiO<sub>2</sub>-coated ZnO nanostructure. Furthermore, Figure 2d shows the diffraction peaks of pure SiO<sub>2</sub> with a broad distinguished peak at  $23.2^\circ$ , which is well-matched with the JCPDS card (no. 01–077–9207). All XRD patterns show highly pure materials with no contamination.

### Particles size distribution analysis and zeta-potential measurements

Table 1 shows the particle size distributions and zeta potential measurements for ZnO NPs, ZnO NCs, SiO<sub>2</sub>-coated ZnO (A&B), and SiO<sub>2</sub> NPs. The average hy-

drodynamic diameter of ZnO, SiO<sub>2</sub>-coated ZnO (A&B), and SiO<sub>2</sub> NPs is  $46.0 \pm 4.9$ ,  $49.3 \pm 8.4$ ,  $48.5 \pm 6.7$ , and  $68.7 \pm 9.4$  nm, respectively, which demonstrates a homogeneous size distribution. Increasing hydrodynamic diameters for SiO<sub>2</sub>-coated ZnO (A&B) rather than ZnO NPs appear from the shell layer of SiO<sub>2</sub> on the core particles of ZnO. However, the results shown from ZnO NCs are  $1968 \pm 237$  nm because of intensive agglomerations of ZnO nanoparticles suspended in an aqueous solution. However, the zeta potential measurements show a negative charge on the prepared NMs except SiO<sub>2</sub>-coated ZnO (B), which was prepared without adjusting the pH. The pH of the preparation medium plays an important role in the surface charge and zeta potential results. As the pH increased, the surface tendency of the prepared materials to carry more negative charges increased.

### The antimicrobial activity

The antimicrobial effect of NMs was determined using the spot diffusion test. Most of the nanoparticles possess a contact killing effect that could not be demonstrat-

**Table 1:** The particles size distributions and zeta potential measurements of ZnO NPs, ZnO NCs, and SiO<sub>2</sub>-coated ZnO (A&B) and SiO<sub>2</sub>

	ZnO	ZnO cluster	ZnO-SiO <sub>A</sub>	ZnO-SiO <sub>B</sub>	SiO <sub>2</sub>
<b>Particle size diameter (nm)</b>	$46.0 \pm 4.9$	$1968 \pm 237$	$49.3 \pm 8.4$	$48.5 \pm 6.7$	$68.7 \pm 9.4$
<b>Zeta-Potential (mV)</b>	$-16.5 \pm 5.4$	$-11.37 \pm 2.7$	$-21.78 \pm 6.3$	$19.3 \pm 4.2$	$-27.2$

**Table 2.** Inhibition zones (mm) of the tested bacteria

Nanoparticles	Nanoparticles Concentration (mg/mL)	Tested microorganisms* Inhibition zones (mm)		
		<i>E. coli</i> (BL21DE)	<i>B. cereus</i> (NBIMCC1095)	<i>S. epidermidis</i> (ATCC 12228)
ZnO NPs	3	$10 \pm 0.5$	$6 \pm 0.5$	$13 \pm 0.5$
	1.5	$10 \pm 0.5$	0	$10 \pm 0.5$
	0.5	0	0	0
	0.25	0	0	0
ZnO NCs	3	$10 \pm 0.5$	$9.5 \pm 0.5$	$15 \pm 0.5$
	1.5	0	$8 \pm 0.5$	$8 \pm 0.5$
	0.5	0	$5 \pm 0.5$	0
	0.25	0	$4 \pm 0.5$	0
ZnO-SiO <sub>A</sub>	3	0	0	0
	1.5	0	0	0
	0.5	0	0	0
	0.25	0	0	0
ZnO-SiO <sub>B</sub>	3	$10 \pm 0.5$	$10 \pm 0.5$	$15 \pm 0.5$
	1.5	0	$8 \pm 0.5$	$7 \pm 0.5$
	0.5	0	0	0
	0.25	0	0	0
SiO <sub>2</sub>	3	0	0	0
	1.5	0	0	0
	0.5	0	0	0
	0.25	0	0	0

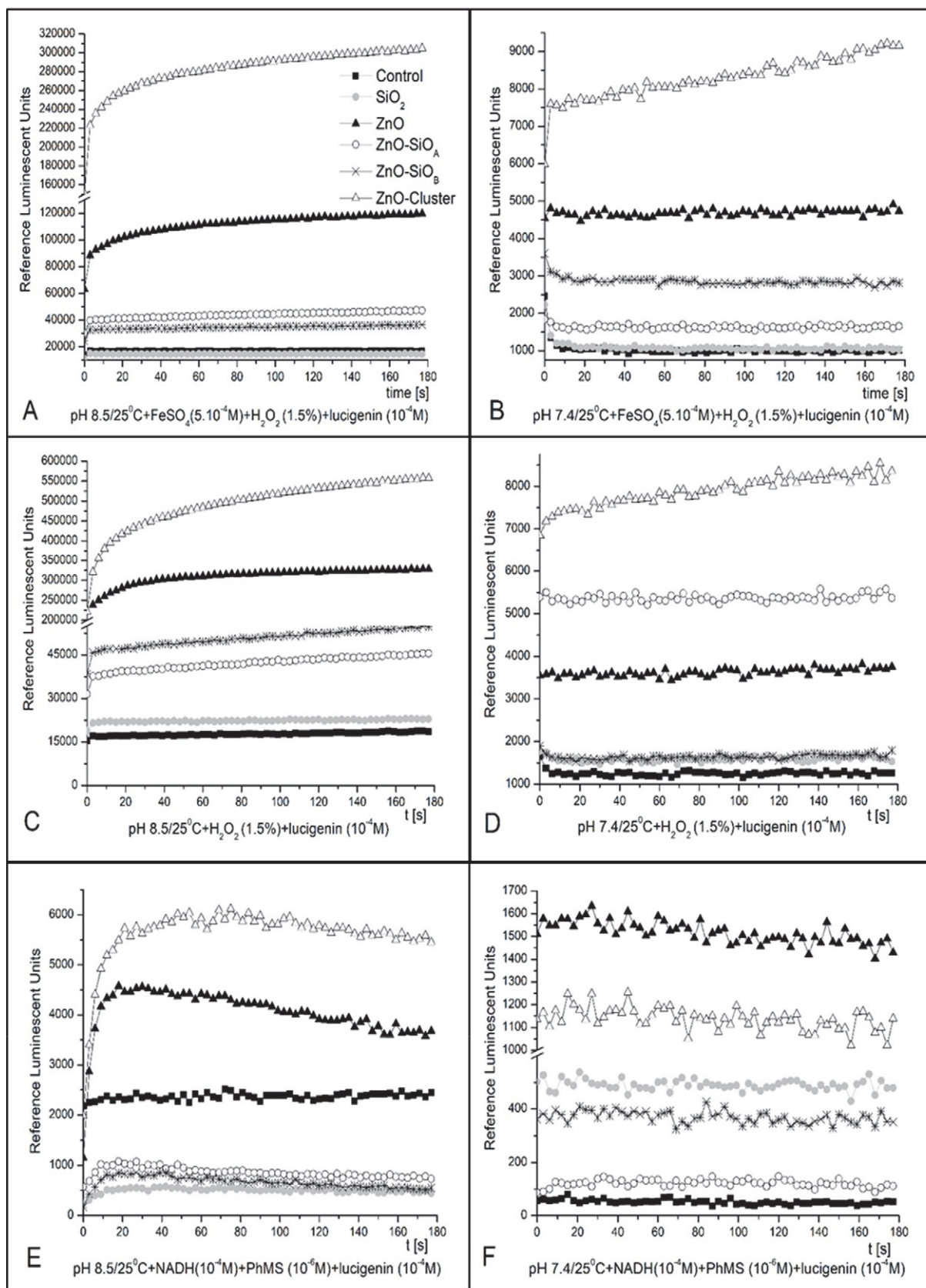


**Figure 3.** Chemiluminescence induced in the Fenton's system (system I: A, B), by H<sub>2</sub>O<sub>2</sub> (system II: C, D) and O<sub>2</sub><sup>-</sup> radicals (system III: E, F) in seconds, at pH 8.5 and 7.4 in the presence/absence of NMs.

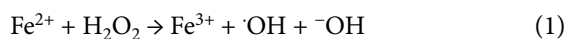
ed if nanomaterials are dropped on paper disks or in agar wells, because of impossible agar diffusion or diminishing of the nanoparticle–bacteria interaction.<sup>27</sup>

From the results, it is obvious that the SiO<sub>2</sub> NPs and ZnO-SiO<sub>A</sub> were completely safe at concentrations up to 3 mg/mL; however, all other tested materials showed bactericidal effects at a higher concentration than 3 mg/mL. All tested bacteria show high sensitivity against ZnO NPs at 3 mg/mL, while only *E. coli* and *S. epidermidis* were inhibited at 1.5 mg/mL. While, lower concentrations of ZnO NPs were safe on all the tested bacteria. Furthermore, ZnO-SiO<sub>A</sub> was completely safe on bacteria at all concentrations; however, ZnO-SiO<sub>B</sub> showed higher toxicity compared to the naked silica particles. ZnO NCs have shown the largest sterile zones at the diffusion test and demonstrated the strongest antibacterial effect if used in concentrations of 3 mg/mL or less. As shown in Table 2, the most sensitive of all three tested bacteria were *Bacillus cereus* compared to *E. coli* and *S. epidermidis*.

ZnO NMs, and many metal oxide nanoparticles, possess bactericidal properties because of the generation of ROS. The chemiluminescent method was used to trace the concentration and kinetics of ROS generation by determining the quantum yields of these reactions in the 480–580 nm range. Three chemiluminescent model systems were applied.

#### • System I

The interaction between Fe<sup>2+</sup> ions and H<sub>2</sub>O<sub>2</sub> produces highly reactive, short-living ·OH radicals. Generally, the resulting chemiluminescent emission is considerably higher than that from other mixtures.



At pH 8.5 the control chemiluminescence signal in this system reaches 17006 reference luminescent units (RLU) in the interaction between the reagents, the so-called fast flash, and usually decreases with time (Fig. 3A). The sample containing SiO<sub>2</sub> NPs follows this kinetics but with slightly lower values, representing the same levels and is not susceptible to oxidation by ROS. All other NMs

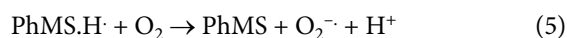
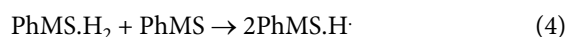
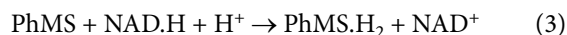
exhibit mild to strong prooxidant properties. ZnO NPs intensify the luminescent signal seven times, ZnO-SiO<sub>A</sub> almost three times, ZnO-SiO<sub>B</sub> more than two times, and most pronounced oxidation is registered with ZnO NCs 18 times. All kinetics is smooth, with no obvious peaks (Fig. 3A). At physiological pH 7.4 (Fig. 3B), almost the same effects are registered but at considerably lower levels; at this pH, ZnO-SiO<sub>A</sub> and ZnO-SiO<sub>B</sub> change places but maintain a mild prooxidant activity. Strong prooxidant activities exhibit the ZnO NCs almost four times and ZnO NPs and ZnO-SiO<sub>B</sub> NMs two times or less intensification of the signal.

#### • System II

In this system, hydrogen peroxide serves as both an oxidizing agent and a ROS. The results show that ZnO NCs are mostly oxidized at alkaline and neutral pH, respectively, and 30- and 5-times stronger signal than the controls. ZnO NPs exhibit almost 18 times (Fig. 3C) and about two times (Fig. 3D) stronger prooxidant activity compared to the control. At pH 8.5, ZnO-SiO<sub>B</sub> and ZnO-SiO<sub>A</sub> NPs expressed mild prooxidant effects, less than three times compared to the control signal (Fig. 3C). At pH 7.4, ZnO-SiO<sub>A</sub> provokes three times higher oxidation than ZnO-SiO<sub>B</sub> and the control (Fig. 3D). SiO<sub>2</sub> NPs demonstrate an extremely light prooxidant effect at both tested pH media.

#### • System III

The O<sub>2</sub><sup>·-</sup> generation in this system is believed to follow the chemical scheme of Nishikimi et al.<sup>30, 31</sup>



At alkaline tested conditions, ZnO NCs exhibit the strongest oxidation as their signal is 24 times higher than the control. ZnO NPs demonstrate almost two times stronger prooxidant activity than the control (Fig. 3E). The other tested synthesized NMs exhibit obvious antioxidant effects against the generated O<sub>2</sub><sup>·-</sup> radicals in the system 60 to 80% (Fig. 3E). The registered antioxidant activity is not

**Table 3.** Correlation coefficients between the sensitivity of chosen bacterial strains toward the antimicrobial effect of ZnO, ZnO NCs, ZnO-SiO<sub>A</sub>, and ZnO-SiO<sub>B</sub> NMs tested by spot diffusion and chemiluminescent assays.

Microorganism	System 1 pH 8.5	System 1 pH 7.4	System 2 pH 8.5	System 2 pH 7.4	System 3 pH 8.5	System 3 pH 7.4
<i>E. coli</i>	0.717	0.814	0.895	0.145	0.954	0.969
<i>BL21DE</i>						
<i>B. cereus</i>	0.921	0.970	0.996	0.496	0.998	0.814
<i>NBIMCC1095</i>						
<i>S. epidermidis</i>	0.797	0.879	0.943	0.266	0.984	0.932
<i>ATCC 12228</i>						

observed at pH 7.4 for all types of NPs. At physiological pH and provoked by the  $O_2^{\cdot-}$  radicals, ZnO NPs exhibit the strongest prooxidant activity compared to all tested systems and conditions (Fig. 3F). ZnO NCs show 16 times stronger signal than the control, followed by  $SiO_2$  (almost seven times), ZnO- $SiO_B$  (more than five times), and ZnO- $SiO_A$  (almost two times) (Fig. 3F). It should be noticed that in this ROS-generating system ( $O_2^{\cdot-}$ ),  $SiO_2$  presents a definitive prooxidant activity, which is not observed in the other tested systems.

Table 3 shows the correlation coefficients between the sensitivity of the chosen bacterial strains toward the antimicrobial effect of ZnO NPs, ZnO NCs, ZnO- $SiO_A$ , and ZnO- $SiO_B$  NPs tested by spot diffusion and chemiluminescent assays (1 mg/mL). Systems 1 and 3 show a strong correlation between the two assays. System 2 introduces a weak correlation in the case of *E. coli* and *S. epidermidis* and moderate correlation in the case of *B. cereus* at pH 7.4 despite the same system showing a strong correlation at pH 8.5. This confirms that the luminescent assay can be successfully applied at pH 8.5 for evaluating antimicrobial activity using System 2.

Nanosized ZnO's internalization and mechanistic activity depend on their physicochemical properties such as shape, size, charge, and surface.<sup>32</sup> Therefore, different shapes and sizes of ZnO NMs were synthesized by controlling the preparation conditions. Although the growth mechanism of NMs was extensively studied, the actual mechanism remains unknown. The general mechanism is believed to depend on solvent and growth conditions. Generally, alcohol group is extremely important in contributing the unoccupied oxygen to  $Zn^{2+}$  to form ZnO.<sup>33</sup> Then, small crystalline nuclei are formed by Ostwald ripening in a supersaturated reaction solution, followed by particle growth, and then large nanoparticles grow at the expense of small NPs.<sup>34</sup>

Moreover, by showing ZnO NCs' morphology in our experiment, Figure 1, these NMs look similar to agglomerates of small spheres. The growth mechanism of this form of ZnO NMs could be subject to the oriented attachment, a recent non-classical theory of crystal growth based on the repeated merging of adjacent particles on lattice-matched crystal facets; this is supported by TEM imaging (Figure 1B, inset).<sup>34</sup> Many research groups reported the preparation of ZnO aggregates;<sup>16</sup> however, the newly synthesized ZnO NCs in our experiment are well-packed clusters with high stability. XRD confirms the formation of hexagonal (wurtzite) structure of all synthesized ZnO NMs determined by the JCPDS card no. 01-080-3002, and no other phases were observed.

Based on our antibacterial test, it is clear that the  $SiO_2$  NPs and ZnO- $SiO_A$  were fully safe at concentrations up to 3 mg/mL, while all other investigated materials showed bactericidal effects at a higher concentration than 3 mg/mL. All tested bacterial *E. coli*, *Bacillus cereus*, and *S. epidermidis* showed high sensitivity toward ZnO NPs at 3

mg/mL. Both *E. coli* and *S. epidermidis* were inhibited at 1.5 mg/mL. Meanwhile, lower concentrations of ZnO NPs, however, were safe on all tested bacteria. It is worthy to notice that coating this nanomaterial with silica renders it completely safe for the bacteria at all concentrations. This could be attributed to the complete isolation of ZnO from the surrounding media by silica, which prevents Zn ions leakage from the particles, in addition to the safe action of silica on bacteria.<sup>35</sup> On the contrary, ZnO- $SiO_B$  shows higher toxicity compared to the naked silica particles. This could be attributed to the incomplete shielding of ZnO by silica in this case, which afforded a chance for ZnO leakage from these particles. Moreover, by referring to TEM images, ZnO- $SiO_B$  shows some aggregation that can increase the antibacterial action.<sup>28</sup> However, ZnO NCs demonstrated the strongest antibacterial effect if used in concentrations of 3 mg/mL and less. The mechanism that gives the advantage to ZnO NCs over ZnO NPs when the ZnO NC attaches to the cell membrane, it breaks down under the physiological conditions to its constituent of small spherical particles that duplicate and magnify the effect of ZnO NCs compared to one of the ZnO NPs. The most sensitive of all three tested bacteria were *Bacillus cereus* compared to *E. coli* and *S. epidermidis*, as shown in Table 2.

Our results are consistent with other studies that have reported the bactericidal effect of ZnO NMs. A few proposed mechanisms are the penetration of the NMs that release  $Zn^{2+}$ . Smaller NPs possibly penetrate cells, and hence they have a greater impact.  $Zn^{2+}$  would react with proteins, peptides, and amino acids, probably with phosphates and carbonates too, which will suppress many important cellular activities inside bacteria (active transport, metabolism, and enzyme activity), ultimately inducing the cell death.<sup>9</sup>

Others suggested that the antibacterial activity is not attributed to generated  $O_2^{\cdot-}$  rather than  $H_2O_2$ , with electrons and  $H^+$ .  $H_2O_2$  penetrates the membrane of bacteria, damaging its content such as proteins, lipids, and amino acids, causing cell death.<sup>12</sup> Moreover, we suggest that the outstanding antibacterial effect of ZnO NCs could be related to the random orientation of its cluster bars. We believe it is the same observation with the random-oriented ZnO nanoarrays (ROZN) outlined by Wang et al. who attributed the superior bactericidal effect of ROZN to cell membrane injury.<sup>36</sup>

Chemiluminescent assay results demonstrate the superiority of ZnO NCs over the rest of the tested NMs. One explanation could be that ZnO NCs are composed of small ZnO NPs, as shown in TEM images, which provide a slow release of ZnO for long periods, leading to a stronger effect on bacterial strains. In system I, the tested NPs are oxidized by the generated ROS in Fenton's system (Fig. 3) that could explain the observed anti-inflammatory and antibacterial properties of those materials in the living systems. At physiological pH 7.4 (Fig. 3B), almost the same effects are registered but at much lower levels because of the

change of pH of the media to a lower value. The achieved results from system II are confirmative on the stability of the tested newly synthesized NMs against  $\text{H}_2\text{O}_2$  as a typical strong oxidant, also generated in the living systems as part of their nonspecific inflammation reaction. In system III, ZnO NCs were susceptible to oxidation, followed by  $\text{SiO}_2$ , ZnO- $\text{SiO}_\text{B}$ , and ZnO- $\text{SiO}_\text{A}$ . Note that, in this ROS-generating system ( $\text{O}_2^{\cdot-}$ ),  $\text{SiO}_2$  presents a definitive prooxidant activity, unobserved in the other tested systems.

A detailed correlation analysis was performed of the sensitivity of the selected bacterial strains toward the antimicrobial effect of ZnO NPs, ZnO NCs, ZnO- $\text{SiO}_\text{A}$ , and ZnO- $\text{SiO}_\text{B}$  NPs, tested by the spot diffusion and chemiluminescent assays (1 mg/mL; Table 3). System I and III show a full positive correlation between the two assays. This is confirmative on the assumptions that  $\cdot\text{OH}$ ,  $\cdot\text{OOH}$ , and  $\text{O}_2^{\cdot-}$  radicals are part of the antimicrobial mechanism of the tested ZnO and its derived materials. System II introduces  $\text{H}_2\text{O}_2$  as a ROS and a strong oxidant. The correlation between system II and the spot-diffusion assay was moderate at pH 7.4; however, the correlation was strong at pH 8.5. This confirms that only reactions at pH 8.5 can be tested and followed to obtain reliable results on prooxidant, antimicrobial and bactericidal effects applying the chemiluminescent assay. The strength of the correlation coefficient follows the relationship level as perfect, strong, moderate, weak, and zero to the  $\pm$  values of 1.0, 0.7–0.9, 0.4–0.6, 0.1–0.3, and 0.<sup>37</sup> All achieved results are confirmative of the role of these ROS in the bactericidal effect in living systems. Although there are structural differences between Gram-positive and Gram-negative bacteria cell membranes, ZnO NMs show a strong effect on both types of bacteria, which depicts the broad spectrum of ZnO NMs effect.<sup>38</sup>

## 4. Conclusions

In this study, the different forms of newly synthesized ZnO NMs were prepared and tested against Gram-negative and Gram-positive bacteria. The agar diffusion test confirmed that ZnO NCs presented the best antimicrobial activity, while  $\text{SiO}_2$  and ZnO- $\text{SiO}_\text{A}$  NPs demonstrated no antibacterial activity. All NMs, except  $\text{SiO}_2$ , exhibit mild to strong prooxidant properties in the Fenton's system to generate ROS. ZnO NCs are a powerful oxidant. This could be explained by assuming that ZnO NCs are composed of small units of ZnO NPs that provide a slow release of ZnO for long periods, which leads to a stronger effect on bacterial strains.  $\text{SiO}_2$  is unsusceptible to oxidation by ROS.

The results achieved for both media demonstrate that all tested NMs are susceptible to oxidation by  $\text{H}_2\text{O}_2$ , a typical strong oxidant, also generated in the living systems as part of their nonspecific inflammation reaction. ZnO NCs and ZnO NPs exhibit strong oxidation in the alkaline tested conditions in system III. All other tested NMs ( $\text{SiO}_2$ ,

ZnO- $\text{SiO}_\text{A}$ , and ZnO- $\text{SiO}_\text{B}$ ) exhibit pronounced 60%–80% antioxidant effects on the generated  $\text{O}_2^{\cdot-}$  radicals in the system. The registered antioxidant activity is not observed at pH 7.4 for any newly synthesized materials.

ZnO shows the strongest prooxidant activity compared to all the tested systems. The prooxidant effect is observed for all other materials too.  $\text{SiO}_2$  presents a definitive prooxidant activity, which is not observed in other systems. The correlation analysis on the sensitivity of the chosen bacterial strains toward the antimicrobial effect of ZnO NPs, ZnO- $\text{SiO}_\text{A}$ , and ZnO NCs tested using the spot-diffusion and chemiluminescent assays is highly confirmative on the role of these ROS ( $\cdot\text{OH}$ ,  $\cdot\text{OOH}$ ,  $\text{H}_2\text{O}_2$  and  $\text{O}_2^{\cdot-}$ ) in the bactericidal effect in living systems. Thus, ZnO NCs are an important antibacterial agent that could be an emergent replacement of traditional antibiotics.

## Funding

The Joint Research Project between The Institute of Biophysics and Biomedical Engineering, Bulgarian Academy of Sciences, Bulgaria and The Academy of Scientific Research and Technology (ASRT) and Nanotechnology and Advanced Materials Central Lab, Agricultural Research Centre, Egypt entitled “Biological activity of Nanocomposites materials with potential medical and microbiology application”. Project “Clean Technologies for Sustainable Environment – Waters, Waste, Energy for Circular Economy”, Ministry of Education and Science, Bulgaria, Contract Number: BG05M2OP001-1.002-0019.

## 5. References

1. B. Khameneh, R. Diab, K. Ghazvini and B. S. Fazly Bazzaz, *Microb. Pathog.* **2016**, *95*, 32–42. DOI:10.1016/j.micpath.2016.02.009
2. R. Y. Pelgrift and A. J. Friedman, *Adv. Drug Delivery Rev.* **2013**, *65*, 1803–1815. DOI:10.1016/j.addr.2013.07.011
3. N. Y. Lee, W. C. Ko and P. R. Hsueh, *Front. Pharmacol.* **2019**, *10*, 1–10.
4. G.-X. He and L.-W. Xue, *Acta Chim. Slov.* **2021**, *68*, 567–574. DOI:10.17344/acsi.2020.6333
5. L. Wang, C. Hu and L. Shao, *Int. J. Nanomed.* **2017**, *12*, 1227–1249. DOI:10.2147/IJN.S121956
6. A. Sirelkhatim, S. Mahmud, A. Seeni, N. H. M. Kaus, L. C. Ann, S. K. M. Bakhori, H. Hasan and D. Mohamad, *Nano-Micro Lett.* **2015**, *7*, 219–242. DOI:10.1007/s40820-015-0040-x
7. H. Y. Qian, *Acta Chim. Slov.* **2021**, *63*, 638–644. DOI:10.17344/acsi.2021.6656
8. SCCS (Scientific Committee on Consumer Safety), Addendum to the Opinion SCCS/1489/12 on Zinc oxide (nano form), **2014**, 1–13.
9. H. Mohd Yusof, R. Mohamad, U. H. Zaidan and N. A. Abdul Rahman, *J. Anim. Sci. Biotechnol.* **2019**, *10*, 57.

- DOI:10.1186/s40104-019-0368-z
10. J. Jiang, J. Pi and J. Cai, *Bioinorg. Chem. Appl.* **2018**, *2018*, 1062562–1062562. DOI:10.1155/2018/1062562
  11. M. A. Ansari, H. M. Khan, A. A. Khan, A. Sultan and A. Azam, *Appl. Microbiol. Biotechnol.* **2012**, *94*, 467–477. DOI:10.1007/s00253-011-3733-1
  12. L. Gabrielyan, A. Hovhannisyanyan, V. Gevorgyan, M. Ananyan and A. Trchounian, *Appl. Microbiol. Biotechnol.* **2019**, *103*, 2773–2782. DOI:10.1007/s00253-019-09653-x
  13. L. Palanikumar, S. N. Ramasamy and C. Balachandran, *IET Nanobiotechnol.* **2014**, *8*, 111–117. DOI:10.1049/iet-nbt.2012.0008
  14. D. Bartczak, M. O. Baradez, S. Merson, H. Goenaga-Infante and D. Marshall, *J. Phys.: Conf. Ser.* **2013**, *429*. DOI:10.1088/1742-6596/429/1/012015
  15. F. Mohd Omar, H. Abdul Aziz and S. Stoll, *Sci. Total Environ.* **2014**, *468–469*, 195–201. DOI:10.1016/j.scitotenv.2013.08.044
  16. K. Sahu, S. kuriakose, J. Singh, B. Satpati and S. Mohapatra, *J. Phys. Chem. Solids* **2018**, *121*, 186–195. DOI:10.1016/j.jpcs.2018.04.023
  17. E. G. Pantohan, R. T. Candidato, Jr. and R. M. Vequizo, *IOP Conf. Ser.: Mater. Sci. Eng.* **2015**, *79*, 6. DOI:10.1088/1757-899X/79/1/012024
  18. R. K. Dutta, B. P. Nenavathu, M. K. Gangishetty and A. V. R. Reddy, *Colloids and Surfaces B: Biointerfaces* **2012**, *94*, 143–150. DOI:10.1016/j.colsurfb.2012.01.046
  19. B. Abebe, E. A. Zereffa, A. Tadesse and H. C. A. Murthy, *Nanoscale Research Letters* **2020**, *15*, 190. DOI:10.1186/s11671-020-03418-6
  20. E. L. Pavlova and V. M. Savov, *Biochemistry (Moscow)* **2006**, *71*, 861–863. DOI:10.1134/S0006297906080062
  21. K. Faulkner and I. Fridovich, *Free Radical Biol. Med.* **1993**, *15*, 447–451. DOI:10.1016/0891-5849(93)90044-U
  22. E. L. Pavlova, R. D. Toshkovska, T. E. Doncheva and I. A. Ivanova, *Arch. Microbiol.* **2020**, *202*, 1873–1880. DOI:10.1007/s00203-020-01902-2
  23. G. Simonelli and E. L. Arancibia, *J. Mol. Liq.* **2015**, *211*, 742–746. DOI:10.1016/j.molliq.2015.07.075
  24. H. A. Elshoky, E. Yotsova, M. A. Farghali, K. Y. Farroh, K. El-Sayed, H. E. Elzorkany, G. Rashkov, A. Dobrikova, P. Borisova, M. Stefanov, M. A. Ali and E. Apostolova, *Plant Physiol. Biochem.* **2021**, *167*, 607–618. DOI:10.1016/j.plaphy.2021.08.039
  25. N. M. Shamhari, B. S. Wee, S. F. Chin and K. Y. Kok, *Acta Chim. Slov.* **2018**, *65*, 578–585. DOI:10.17344/acsi.2018.4213
  26. D. Das, Y. Yang, J. S. O'Brien, D. Breznán, S. Nimesh, S. Bernatchez, M. Hill, A. Sayari, R. Vincent and P. Kumarathan, *J. Nanomater.* **2014**, *2014*, 176015.
  27. R. A. Howe, J. M. Andrews and f. t. B. W. P. o. S. Testing, *J. Antimicrob. Chemother.* **2012**, *67*, 2783–2784. DOI:10.1093/jac/dks391
  28. A. Klančnik, S. Piskernik, B. Jeršek and S. S. Možina, *J. Microbiol. Methods* **2010**, *81*, 121–126. DOI:10.1016/j.mimet.2010.02.004
  29. M. M. Tarpey, D. A. Wink and M. B. Grisham, *Am. J. Physiol. Regul. Integr. Comp. Physiol.* **2004**, *286*, R431–R444. DOI:10.1152/ajpregu.00361.2003
  30. J. T. Hancock, R. Desikan and S. J. Neill, *Biochem. Soc. Trans.* **2001**, *29*, 345–349. DOI:10.1042/bst0290345
  31. M. Nishikimi, N. Appaji Rao and K. Yagi, *Biochem. Biophys. Res. Commun.* **1972**, *46*, 849–854. DOI:10.1016/S0006-291X(72)80218-3
  32. A. Happy, M. Soumya, S. Venkat Kumar and S. Rajeshkumar, *Chem.-Biol. Interact.* **2018**, *286*, 60–70. DOI:10.1016/j.cbi.2018.03.008
  33. R. Razali, A. K. Zak, W. H. A. Majid and M. Darroudi, *Ceram. Int.* **2011**, *37*, 3657–3663. DOI:10.1016/j.ceramint.2011.06.026
  34. D. Cao, S. Gong, X. Shu, D. Zhu and S. Liang, *Nanoscale Res. Lett.* **2019**, *14*, 210. DOI:10.1186/s11671-019-3038-3
  35. F. Book, M. T. Ekvall, M. Persson, S. Lönnerud, T. Lammel, J. Sturve and T. Backhaus, *NanoImpact* **2019**, *13*, 100–111. DOI:10.1016/j.impact.2019.01.001
  36. X. Wang, F. Yang, W. Yang and X. Yang, *Chem. Commun.* **2007**, 4419–4421. DOI:10.1039/b708662h
  37. H. Akoglu, *Turkish J. Emerg. Med.* **2018**, *18*, 91–93. DOI:10.1016/j.tjem.2018.08.001
  38. A. Ali, S. Ambreen, R. Javed, S. Tabassum, I. ul Haq and M. Zia, *Mater. Sci. Eng. C* **2017**, *74*, 137–145. DOI:10.1016/j.msec.2017.01.004



## Povzetek

Nanomateriali na osnovi cinkovega oksida (ZnO) nudijo nekaj obetavnih protibakterijskih učinkov. V okviru te študije je bila sintetizirana nova oblika ZnO, imenovana »ZnO palčke nanogrozdov« (angl. ZnO nanocluster bars, NC). Pripravljeni in okarakterizirani so bili ZnO NC, nanodelci ZnO (NP), ZnO, prevlečen s silicijevim dioksidom (ZnO-SiO<sub>A</sub>, ZnO-SiO<sub>B</sub>) in SiO<sub>2</sub> nanodelci, pri čemer je bila testirana tudi njihova protimikrobna in prooksidantna aktivnost. Prooksidantno aktivnost vseh nanomaterialov je bila preučevana glede na reakcije oksidacije s prostimi radikali (pH 7,4 in pH 8,5) v kemiluminiscentnih modelnih sistemih. Vsaka oblika na novo sintetiziranih nanomaterialov ZnO je pokazala edinstveno obnašanje, ki je v Fentonovem sistemu zajemalo vse od blagih do močnih prooksidativnih lastnosti. ZnO NP in ZnO NCs so pokazali močne protibakterijske učinke, ZnO-SiO<sub>A</sub> NPs pa niso pokazali nobene protibakterijske aktivnosti, ki bi predstavljala biokompatibilnost. Vse testirane NM so bile tudi podvržene oksidaciji s H<sub>2</sub>O<sub>2</sub>. Pri ZnO NC in ZnO NPs se je zgodila močna oksidacija v O<sub>2</sub><sup>-</sup> generatorskem sistemu pri pH 8,5. Medtem ko so SiO<sub>2</sub>, ZnO-SiO<sub>A</sub> and ZnO-SiO<sub>B</sub> izkazovali izrazite 60–80 % antioksidativne učinke, so SiO<sub>2</sub> NP delovali kot dokončni prooksidant, česar v drugih testih niso opazili. ZnO NC so močno oksidirani, ob predpostavki, da ZnO NC zagotavljajo počasnejše sproščanje ZnO, kar vodi v močnejši učinek na bakterijske seve. ZnO NC so torej pomembno protibakterijsko sredstvo, ki bi lahko nadomeščalo tradicionalne antibiotike.



Except when otherwise noted, articles in this journal are published under the terms and conditions of the Creative Commons Attribution 4.0 International License

## **DRUŠTVENE VESTI IN DRUGE AKTIVNOSTI**

## **SOCIETY NEWS, ANNOUNCEMENTS, ACTIVITIES**

### **Vsebina**

54. Mednarodna kemijska olimpijada .....	S75
Koledar važnejših znanstvenih srečanj s področja kemije in kemijske tehnologije .....	S81
Navodila za avtorje .....	S84

### **Contents**

54. International Chemistry Olympiad .....	S75
Scientific meetings – Chemistry and chemical engineering.....	S81
Instructions for authors .....	S84



## 54. Mednarodna kemijska olimpijada

(Univerza Nankai, Tianjin, Kitajska)

Andrej Godec

UL, FKKT

Na Fakulteti za kemijo in Kemijsko tehnologijo v Ljubljani se je od 10. 7. do 18. 7. 2022 tednu odvijala 54. mednarodna kemijska olimpijada. To je tekmovanje srednješolcev v znanju kemije, vsako državo pa zastopa ekipa štirih najboljših. Priprave potekajo na Fakulteti za kemijo in kemijsko tehnologijo v Ljubljani, pri organizaciji dogodka pa sodelujemo z Zvezo za tehnično kulturo Slovenije. Mentorja ekipe sta dr. Berta Košmrlj in dr. Andrej Godec. V pripravi na to olimpijado so sodelovali tudi dr. Marta Počkaj, dr. Darko Dolenc, pomagali pa so še Martin Rihtaršič, Vid Kermelj in dr. Damjan Jan Pavlica.

Letošnjo olimpijado je organizirala Kitajska, zaradi epidemioloških razmer v tej državi pa je potekala na daljavo. Našo državo so zastopali dijaki **Dane Jemc** (Gimnazija Škofja Loka), **Matej Nastran** (Gimnazija Škofja Loka), **Nina Cankar** (Gimnazija Kranj) ter **Patrik Potočnik** (Gimnazija Škofja Loka).

Letošnje olimpijade se je sicer udeležilo 326 dijakov iz 84 držav. Naši dijaki so dosegli odličen rezultat: Dane, Matej, in Patrik so dobili bronasto medaljo, Nina pa častno omembo. ČESTITKE!

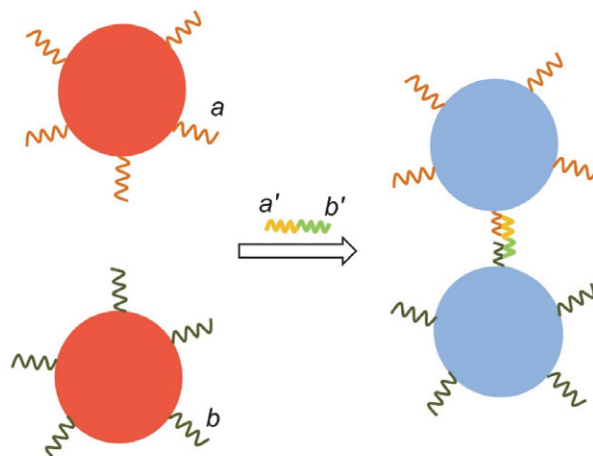


Slovenska ekipa na 54. Mednarodni kemijski olimpijadi: Dane, Patrik, Nina in Matej. Foto: Aljoša Seljak.

Na tekmovanju je bilo letos 9 teoretičnih nalog, za reševanje pa je sicer na voljo 5 ur časa. Naloge na olimpijadi so izjemno težke, tako da se dijaki udeležujejo priprav, slovensko ekipo pa izberemo na treh nacionalnih izbirnih testih.

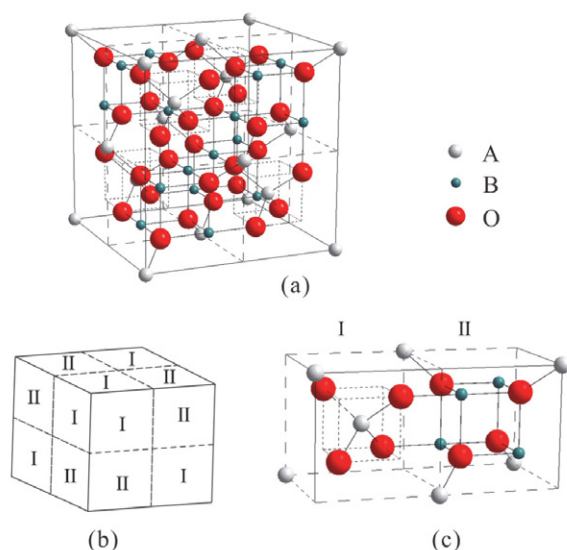
Seveda letošnje naloge niso mogle zaobiti epidemije, saj so hitre in enostavne metode za zgodnje odkrivanje

COVID-19 so nujno potrebne. Ena izmed obetavnih metod je detekcija s pomočjo nanodelcev zlata. Nanodelci zlata se zaradi njihovega visokega molskega ekstinkcijskega koeficienta (molske absorptivnosti) pogosto uporabljajo kot vidni odčitki na testnih lističih. Barvni izgled nanodelcev zlata je povezan z njihovo velikostjo in razpršenostjo. V splošnem velja, da večji kot so nanodelci zlata, bolj rdečkasta je njihova barva. Ko se nanodelci združijo, se barva spremeni iz rdeče v modro. Ko površino nanodelcev zlata modificiramo z dvema vrstama enoverzičnih fragmentov nukleinske kisline *a* in *b*, se nanodelci zlata v prisotnosti tarčne nukleinske kisline (*a'* *b'*) združijo. Pri tem se v nekaj minutah spremeni barva iz rdeče v modro (slika). Na osnovi tega bi lahko zaznavali prisotnost tarčnih nukleinskih kislin, značilnih za koronavirus, v vzorcih.



Tema prve naloge je bila opisana detekcija tarčnih nukleinskih kislin: dijaki so okarakterizirali spekter navedenih spojin, izračunali molarni ekstinkcijski koeficient raztopine nanodelcev zlata, ter na koncu še na osnovi podatkov izračunali koncentracijo virusne nukleinske kisline v originalnem vzorcu brisa žrela.

Druga naloga je bila povezana z glazuro. Črn glaziran porcelan je vrsta kitajskega porcelana, ki je bila še posebej priljubljena v času dinastij Tang in Song pred približno 1000 leti. Tovrstni keramični izdelki kot glavno barvilo vsebujejo železove okside, ki jih zmešajo z ostalimi prehodnimi kovinami, da dobijo različne temne odtenke, kot so kostanjeva, temno rjava ali črna barva. Črni glaziran porcelan je še danes na Kitajskem precej priljubljen. Tipična



črna glazura je sestavljena iz Fe-vsebujočih oksidov s spinelno strukturo. Spinelni oksidi imajo splošno formulo  $AB_2O_4$  in njihova struktura je naslednja:  $O^{2-}$  ioni tvorijo kubični najgostejši sklad, v katerem kationi vrste A zasedajo eno osmino tetraedričnih praznin, kationi B pa eno polovico oktaedričnih praznin (slika).

Črno keramično glazuro, ki ima spinelno strukturo, lahko pripravimo s praženjem  $Fe_2O_3$  in  $Cr_2O_3$  v določenem razmerju v reduktivni atmosferi. Ko  $Fe_2O_3$  in  $Cr_2O_3$  reagirata v masnem razmerju 63.6 : 36.4, se popolnoma spremenita v čisto stehiometrično spojino.

Dijaki so morali okarakterizirati osnovno celico v takšnih spinelnih strukturah; del naloge pa je bil posvečen še vlogi kroma. Spremenljiva valenca kroma namreč ni pomembna samo za proizvodnjo pigmentov, ampak tudi za katalizo. Tipičen Philipsov katalizator za polimerizacijo etena je sestavljen iz kromovega oksida, nanesenega na porozen nosilec, kot je npr. amorfen silicijev dioksid. Dijaki so morali zapisati elektronsko konfiguracijo d elektronov  $Cr(II)$  iona v takšnem katalizatorju, in izračunati energijo stabilizacije kristalnega polja CFSE) ter magnetni moment  $\mu$  za  $Cr(II)$  ion.

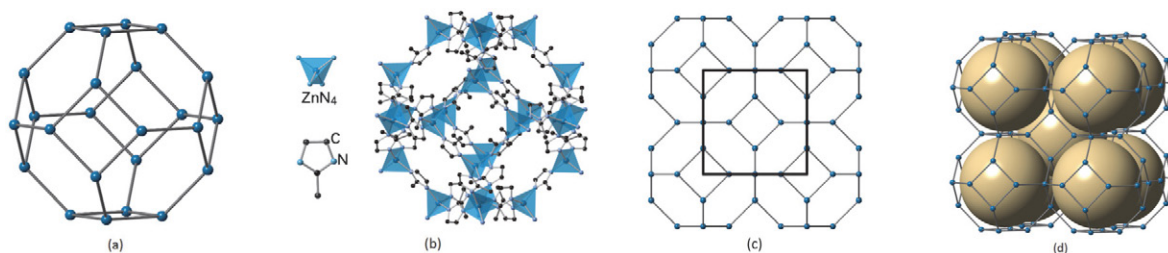
Tema tretje naloge je bilo zajemanje in pretvorba ogljikovega dioksida. Tehnologija direktnega zajema zraka

(DAC, ang. direct air capture), ki naj bi omogočila odstranitev  $CO_2$  direktno iz zraka, je obetavna. Osnova metode DAC je mokro spiranje z alkalno raztopino hidroksida (običajno  $NaOH$ ), v kateri se absorbira zračni  $CO_2$  do vrednosti  $pH \approx 10$ . Porabljen sorbent se regenerira z dodatkom kalcijevega hidroksida. Bela oborina, ki nastane, razpade pri  $700^\circ C$ , pri čemer nastane  $CO_2$  in še ena bela snov. Na koncu lahko pridobimo kalcijev hidroksid z hidracijo. Ta proces je energetsko zelo zahteven. ( $H_2CO_3 : Ka_1 = 4.5 \times 10^{-7}$ ,  $Ka_2 = 4.7 \times 10^{-11}$ ). Nedolgo nazaj pa so razvili elektrokemijski proces za regeneracijo alkalne raztopine, uporabljane v postopku mokrega spiranja za DAC. Čist plinast  $CO_2$  bi lahko ponovno pridobili in shranili ali uporabili naprej. Proces je osnovan na elektrokemijskem sistemu za recikliranje  $H_2$  (HRES; ang.  $H_2$ -recycling electrochemical system), elektrokemijska celica pa vsebuje dve ionoselektivni membrani. Dijaki so morali zapisati in okarakterizirati vse navedene kemijske procese, mehanizme prenosa kationov v celici, ter izračunati hitrost nastajanja  $CO_2$ .

Zeolitno-imidazolatna ogrodja ZIF so podskupina organskih ogrodij MOF in so tudi obetavni materiali za zajemanje in uporabo  $CO_2$ . Strukture ZIF-ov so podobne strukturam zeolitov. Zanje so značilna 3D ogrodja s tetraedrično koordiniranimi kovinskimi ioni (npr.  $Zn^{2+}$ ,  $Co^{2+}$ ), ki so premoščeni z imidazolatnim ionom ( $Im^-$ ) ali njegovimi derivati.

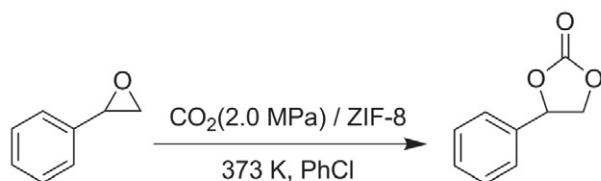
ZIF-8 je predstavnik ZIF-ov s sodalitim (SOD) ogrodjem, prikazanim na sliki. ZIF-8 je prvi pripravil kitajski znanstvenik Xiao-Ming Chen s sodelavci pri reakciji  $Zn^{2+}$  z 2-metilimidazolum ( $CH_3(C_3N_2H_3)$ ,  $HmIm$ ) (produkt so sprva poimenovali MAF-4). ZIF-8 kristalizira v kubičnem sistemu s parametrom osnovne celice  $a = 1.632$  nm (faza brez topila). Efektivni premer pore, ki je prikazana s kroglo na sliki, znaša 1.16 nm. (slika 4)

Dijaki so morali okarakterizirati osnovno celico tega materiala, izračunati notranjo površino por ter poroznost materiala. ZIF-8 lahko igra tudi vlogo katalizatorja pri pretvorbi  $CO_2$  v kemikalije z visoko dodano vrednostjo. Eden izmed najbolj obetavnih načinov za fiksiranje  $CO_2$  je priprava cikličnih karbonatov s cikloadicijo. Spodaj je prikazan primer:



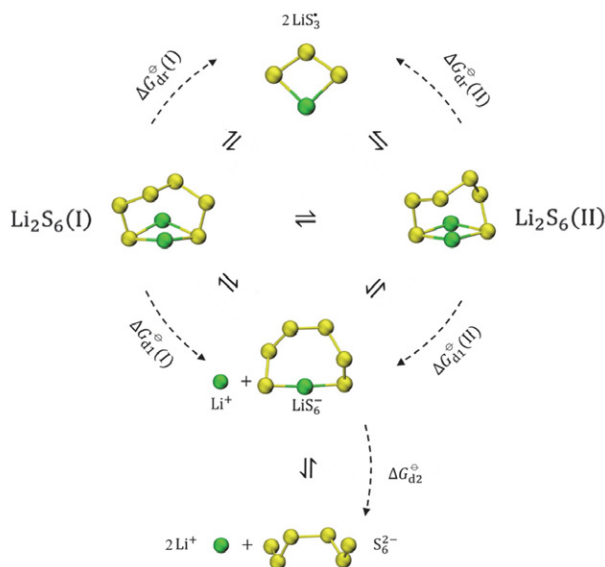
**Slika 4:**

(a) Topologija SOD kletke; (b) SOD kletka v ZIF-8, sestavljenem iz  $Zn^{2+}$  (v središčih tetraedrov) in imidazolnih ionov (H atomi so zaradi jasnosti prikaza izpuščeni); (c) Ogrodje SOD z označeno osnovno celico (kvadrat); (d) Nekaj por v ZIF-8 je poudarjenih z navideznimi krogli.



Dijaki so morali zapisati intermediate pri takšni reakciji, ter tudi urejeno enačbo za to reakcijo.

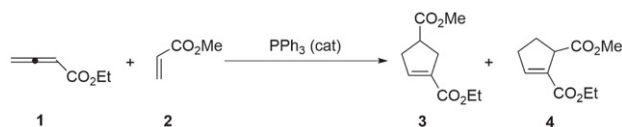
Četrta naloga je bila na temo žvepla, najprej elementarnim, in potem v obliki spojine pirit ( $\text{FeS}_2$ ), ki je surovina pri industrijski proizvodnji elementarnega žvepla. S segrevanjem nastaja žveplo, pa tudi manjše količine plina  $\text{SO}_2$  in še česa. Z merjenjem količin tega plina lahko zasledujemo potek reakcije; dijaki so morali izračunati izkoristek oziroma predvideti izgube žvepla v piritu v obliki stranskih produktov. Razen tega je naloga obravnavala tudi drugačno uporabo žvepla. Litij – žveplovna baterija ima visoko teoretično energijsko gostoto, ki presega konvencionalno Li-ion baterijo. Neto reakcijo v litij – žveplovni bateriji lahko poenostavljeno napišemo takole:  $16 \text{ Li} + \text{S}_8 \rightarrow 8 \text{ Li}_2\text{S}$ . Žveplo je katoda, kovinski litij pa je aktivni material anode pri praznjenju baterije. Dijaki so morali zapisati elektrodne reakcije v tej bateriji, izračunati mase aktivnih elektrodnih materialov, ter izračunati, koliko časa deluje in koliko bolje je to od litij-ionske baterije. V litij – žveplovih baterijah se med praznjenjem  $\text{S}_8$  ne reducira direktno do  $\text{Li}_2\text{S}$ , ampak postopoma preko reakcij, pri katerih nastajajo različni topni litijevi polisulfidi ( $\text{Li}_2\text{S}_n$ ,  $n = 3-8$ ). Ti litijevi polisulfidi lahko difundirajo na anodo in tam povzročijo korozijo, kar pomeni izgubo aktivnega elektrodnega materiala. Ta pojav imenujemo »shuttle učinek«. Teoretične študije kažejo, da dva konformera s primerljivima energijama,  $\text{Li}_2\text{S}_6(\text{I})$  in  $\text{Li}_2\text{S}_6(\text{II})$  soobstajata v 1,2-dimetoksietanu (DME), ki je običajno topilo in elektrolit v litij-žveplovih baterijah. Disociacija  $\text{Li}_2\text{S}_6$  v DME je prikazana spodaj:



Dijaki so morali okarakterizirati korozijo anode, predvideti s pomočjo termodinamskih podatkov, kje se nahaja ravnotežje, izračunati disociacijsko konstanto  $\text{Li}_2\text{S}_6$  v DME (1,2-dimetoksietan (DME) je običajno topilo in elektrolit v litij-žveplovih baterijah), ter redoks potencial litija v tem topilu.

Peta naloga je bila povezana z onesnaževanjem ozračja. Dušikovi oksidi (vključno  $\text{N}_2\text{O}$ ,  $\text{NO}$ ,  $\text{NO}_2$ ,  $\text{N}_2\text{O}_4$  in še drugi, kar skupaj napišemo kot  $\text{NO}_x$ ) so eni od glavnih onesnaževalcev zraka. Povzročijo lahko probleme, kot so ozonska luknja, kisel dež, fotokemijski smog, in efekt tople grede. Zato moramo kontrolirati emisije in pretvorbe  $\text{NO}_x$ , da bi izboljšali kvaliteto zraka. Dijaki so raziskali oksidacijo  $\text{NO}$  v  $\text{NO}_2$  preko reakcije  $2\text{NO} + \text{O}_2 \rightarrow 2\text{NO}_2$ . Izračunali so hitrost te reakcije, ter s termodinamskimi podatki ovrednotili smer poteka reakcije ter položaj ravnotežja. V drugem delu naloge pa so preučevali načine za zmanjšanje emisij  $\text{NO}_x$ . En način za zmanjšanje emisij  $\text{NO}_x$  je oksidacija  $\text{NO}$  v  $\text{NO}_2$  in nato absorpcija nastalega  $\text{NO}_2$  z absorbenti. Vendar pa je zaradi nizkih koncentracij  $\text{NO}$  v izpuštih njegova spontana oksidacija v atmosferi prepočasna, da bi zadostila zahtevam industrije. Zato se za pospešitev te reakcije uporabljajo trdni katalizatorji. Oksidacija  $\text{NO}$  na površini specifičnega katalizatorja (**CatX**) poteka po zapletenem mehanizmu; predpostavili so, da se  $\text{NO}$ ,  $\text{NO}_2$  in  $\text{O}$  (iz disociacije  $\text{O}_2$ ) adsorbirajo v eni plasti, in da so vsa adsorpcijska mesta za adsorpcijo teh vrst enakovredna. Deleži pokritosti površine katalizatorja  $\theta$  so označeni kot  $\theta_{\text{NO}}$ ,  $\theta_{\text{NO}_2}$  in  $\theta_{\text{O}}$ . Dijaki so morali izpeljati zvezo med deležem pokritosti in konstanto reakcijskih hitrosti, ter izpeljati izraz za hitrost reakcije na začetku.

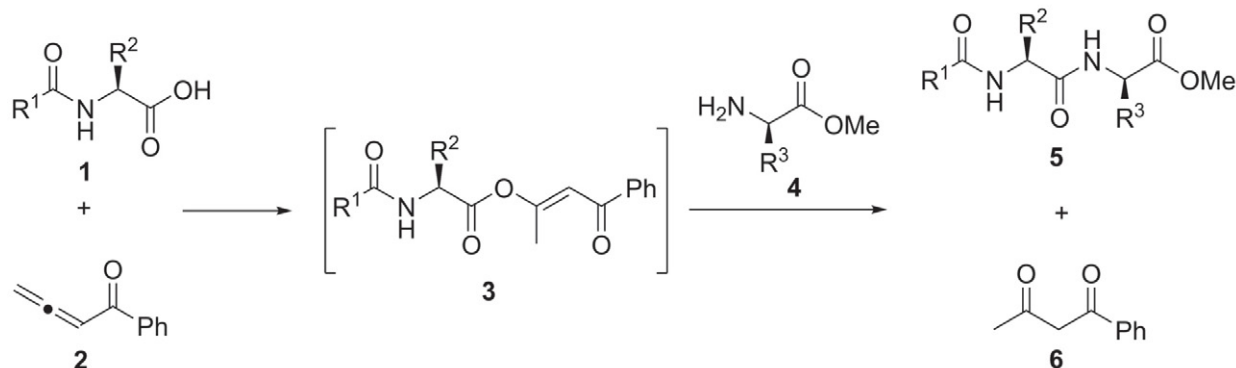
Šesta naloga je bila o fosfinih. Kiralne fosfine pogosto uporabljajo kot kiralne ligande pri katalizi s prehodnimi kovinami. V zadnjih dvajsetih letih se je močno razvilo področje organokatalize, med drugim so odkrili sintezne poti, kjer se uporablja nukleofilni fosfinski katalizator. Med temi je najbolj znana Lu-jeva (3+2) cikloadicija, ki jo je razvil kitajski znanstvenik Xiyan Lu. Naprimer etil aleoat **1** in metil akrilat **2** dajeta pri katalizi s trifenilfosfinom dva ciklopentenska derivata: **3** (večinski produkt) in **4** (manjšinski produkt).



Pri tej nalogi so morali dijaki dopolniti reakcijske sheme za to reakcijo in določiti stereokemijo vmesnih spojin.

Tema sedme naloge je bila sinteza kompleksnih peptidov in proteinov. Spajanje karboksilne in aminske skupine, da nastane peptidna vez, je osnovna reakcija pri sintezi peptidov in proteinov. Alenon **2** lahko uporabimo za aktivacijo karboksilne kisline **1** pod milimi reakcijskimi pogoji, pri čemer nastane intermediat **3**. Ta potem reagira z aminom **4** in daje amid **5** z dobrim izkoristkom. Pri tem nastane tudi stranski produkt **6**.





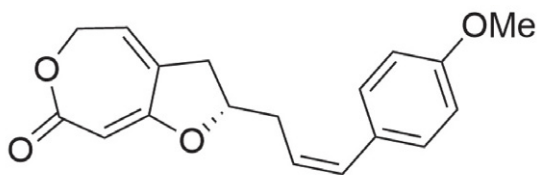
Na podoben način kot alenon lahko aktivira karboksilno kislino tudi *N*-etinil-*N*-metil-*p*-toluensulfonamid. Dijaki so morali najprej za oba primera narisati strukture spojin pri teh reakcijah in prikazati stereokemijo na vsakem od stereocentrov. S tem, ko peptidna veriga raste, postaja tvorba amidnih vezi vedno težja. Za sintezo proteinov zato klasične kondenzacijske metode niso uporabne. Pri prvi sintezi kristaliničnega govejega insulina so razvili metodo, temelječo na kemiji acilhidrazina. S tem so dosegli zahtevno spajanje dveh peptidov z nastankom amidne vezi med njima. Tudi za to reakcijo so morali dijaki narisati strukture spojin. Poleg sinteze iz aminokislin lahko znanstveniki uporabijo modifikacijo obstoječih proteinov. Na verigi proteina je več reaktivnih mest, kot so aminske, karboksilne in tiolne skupine. Najbolj nukleofilna je tiolna skupina in je zato najbolj reaktivna do elektrofilnih reagentov, kot je *N*-fenilmaleimid, na katerega se adira z Michaelovo adicijo. Tudi za ta primer so morali dijaki dopolniti reakcijsko shemo.

Osmo naloga je imela naslov Čudežni kiralni spiro katalizator. Kiralne spojine so med drugim pomembne za človeško zdravje. Več kot 50 % zdravil, ki so trenutno v klinični uporabi, je čistih posamičnih enantiomerov kiralnih spojin. Sinteza kiralnih molekul v enantiomerno obogateni obliki je velik izziv. Skupina profesorja Qilin Zhou-ja na nankaiski univerzi je razvila vrsto visoko aktivnih kiralnih spiro-katalizatorjev. Ti so dvignili učinkovitost asimetrične sinteze na novo raven in se široko uporabljajo v farmacevtski proizvodnji. Ti katalizatorji dosegajo enantiomerni presežek do 99,9 % in se uporabljajo v zelo majhnih količinah, celo do 0,00002 mol%. Dijaki so v nalogi dopolnili reakcijsko shemo za sintezo teh spojin, in uporabo kiralnega spiro katalizatorja Ir-SpiroPAP za asimetrično totalno sintezo diterpena mulinanskega tipa.

Zadnja, deveta naloga, pa je bila totalna sinteza kapitlaktona. Rastlina *Curculigo capitulata*, ki raste na južnem Kitajskem, se že dolgo uporablja v tradicionalni kitajski medicini za zdravljenje mnogih bolezni. Iz korenin te rastline so izolirali spojino kapitlakton.



Mentorice in mentorji ter dijaki slovenske, madžarske in ukrajinske ekipe na letošnji olimpijadi. Naša ekipa: Andrej (glavni mentor, 1. z leve), Dane, Nina ter Matej (8., 9. ter 10. z leve), in Berta (mentorica, 11. z leve).



Capitulactone (**1**)

Njena struktura z absolutno konfiguracijo je bila določena z uporabo spektroskopskih podatkov in totalne sin-

teze. Sintezo **1** so začeli z jodiranjem kupilnega 4-bromoveratrola. Reakcija poteka preko več intermediatov, dijaki pa so morali tudi tukaj dopolniti reakcijsko shemo sinteze.

Letošnja olimpijada je bila posebna, saj smo v goste povabili še madžarsko in ukrajinsko ekipo. Obe sta prišli v soboto, 9.7.2022, in preživel dneve do tekmovanja v druženju z našimi dijakinjami in dijaki ter na izletih. Na sliki so vse tri ekipe z mentoricami in mentorji, slika pa je bila narejena takoj po otvoritvi olimpijade v nedeljo, 10.7.

Takšno obliko dogodka so omogočile Fakulteta za kemijo in kemijsko tehnologijo, madžarsko ministrstvo za notranje zadeve, Zveza za tehnično kulturo Slovenije, Slovensko kemijsko društvo ter zavod Bunker. Vsem se iskreno zahvaljujemo za pomoč pri dogodku, ki je lep primer tega, da se da z meddržavnim sodelovanjem preseči trenutne politične in epidemiološke razmere, ter omogočiti sodelujočim izkušnjo »normalne« olimpijade.

Naslednje leto bo olimpijada v Švici, upajmo, da takrat v živo.

*Tekst in foto: Andrej Godec*



# KOLEDAR VAŽNEJŠIH ZNANSTVENIH SREČANJ S PODROČJA KEMIJE IN KEMIJSKE TEHNOLOGIJE

## SCIENTIFIC MEETINGS – CHEMISTRY AND CHEMICAL ENGINEERING

### 2022

#### October 2022

---

- 5 – 7                    7 MS FOOD DAY  
Florence, Italy  
Information: <https://www.spettrometriadiamassa.it/Congressi/7MS-FoodDay/index.html>
- 14                      CHEMISTRY AND CHEMICAL TECHNOLOGY 2022  
Kaunas, Lithuania  
Information: <https://cct-conference.ktu.edu/>
- 16 – 21                SCHOOL AND CONFERENCE ON ANALYSIS OF DIFFRACTION DATA IN REAL SPACE  
Grenoble, France  
Information: <https://workshops.ill.fr/event/306/>
- 12 – 14                CHEMICAL RESEARCH IN FLANDERS – CHEMISTRY CONFERENCE FOR YOUNG  
SCIENTISTS 2022  
Blankenberge, Belgium  
Information: <https://crf-chemcys.be/>
- 21 – 22                XIV CONFERENCE OF CHEMISTS, TECHNOLOGISTS AND ECOLOGISTS OF THE  
REPUBLIC OF SRPSKA  
Banja Luka, Bosnia and Herzegovina  
Information: <https://savjetovanje.tf.unibl.org/>
- 23 – 26                31<sup>ST</sup> INTERNATIONAL SYMPOSIUM ON THE CHEMISTRY OF NATURAL PRODUCTS  
AND 11<sup>TH</sup> INTERNATIONAL CONGRESS ON BIODIVERSITY (ISCNP31 & ICOB11)  
Naples, Italy  
Information: <https://www.iscnp31-icob11.org/index.php>
- 23 – 26                ENERGY, ENVIRONMENT & DIGITAL TRANSITION  
Milano, Italy  
Information: <https://www.aidic.it/e2dt/>
- 23 – 25                5<sup>th</sup> CryoNET SYMPOSIUM  
Copenhagen, Denmark  
Information: <https://eventsignup.ku.dk/cryonet2022>

#### November 2022

- 8 – 11                    SOLUTIONS IN CHEMISTRY 2022  
Sveti Martin na Muri, Croatia  
Information: <https://solutionsinchemistry.hkd.hr/>

- 6 – 11 EMBO PRACTICAL COURSE: VOLUME ELECTRON MICROSCOPY BY AUTOMATED SERIAL SEM  
Lausanne, Switzerland  
Information: <https://meetings.embo.org/event/21-serial-sem>

**December 2022**

- 5 4<sup>TH</sup> EUROPEAN FORUM ON NEW TECHNOLOGIES - CHEMICAL ENGINEERING AS APPLIED IN MEDICINE  
Paris, France  
<https://efce.info/4th+European+Forum+on+New+Technologies.htm>
- 5 – 8 ENVIRONMENTAL MEETING ON ENVIRONMENTAL CHEMISTRY 2022 – EMEC22  
Ljubljana, Slovenia  
Information: <https://www.emec22.com/>

**2023****January 2023**

- 1 EUROPEAN FOOD CHEMISTRY CONGRESS XXI – EuroFoodChem XXI  
Belgrade, Serbia  
Information: <http://horizon2020foodentwin.rs/eurofoodchemxxi/>

**March 2023**

- 20 – 23 VIII INTERNATIONAL CONGRESS “ENGINEERING, ENVIRONMENT AND MATERIALS IN PROCESS INDUSTRY  
Jahorina, Bosnia and Hercegovina  
Information: <https://eem.tfzv.ues.rs.ba/>

**February 2023**

- 8 – 11 EMBO WORKSHOP IN SITU STRUCTURAL BIOLOGY: FROM CRYO-EM TO MULTI-SCALE MODELLING  
Heidelberg, Germany  
Information: <https://www.embl.org/about/info/course-and-conference-office/events/iss23-01/>

**July 2023**

- 2 – 6 FEZA 2023 – 9<sup>TH</sup> CONFERENCE OF THE FEDERATION OF THE EUROPEAN ZEOLITE ASSOCIATIONS  
Portorož-Portorose, Slovenia  
Information: <https://feza2023.org/en/>
- 7 – 11 9<sup>TH</sup> EUCHEMS CHEMISTRY CONGRESS (ECC9)  
Dublin, Ireland





# Acta Chimica Slovenica

## Author Guidelines

### Submissions

Submission to ACSi is made with the implicit understanding that neither the manuscript nor the essence of its content has been published in whole or in part and that it is not being considered for publication elsewhere. All the listed authors should have agreed on the content and the corresponding (submitting) author is responsible for having ensured that this agreement has been reached. The acceptance of an article is based entirely on its scientific merit, as judged by peer review. There are no page charges for publishing articles in ACSi. The authors are asked to read the Author Guidelines carefully to gain an overview and assess if their manuscript is suitable for ACSi.

### Additional information

- Citing spectral and analytical data
- Depositing X-ray data

### Submission material

Typical submission consists of:

- full manuscript (PDF file, with title, authors, abstract, keywords, figures and tables embedded, and references)
- supplementary files
  - **Full manuscript** (original Word file)
  - **Statement of novelty** (Word file)
  - **List of suggested reviewers** (Word file)
  - **ZIP file containing graphics** (figures, illustrations, images, photographs)
  - **Graphical abstract** (single graphics file)
  - **Proposed cover picture** (optional, single graphics file)
  - **Appendices** (optional, Word files, graphics files)

Incomplete or not properly prepared submissions will be rejected.

### Submission process

Before submission, authors should go through the checklist at the bottom of the page and prepare for submission.

Submission process consists of 5 steps.

#### Step 1: Starting the submission

- Choose one of the journal sections.
- Confirm all the requirements of the **checklist**.
- Additional plain text comments for the editor can be provided in the relevant text field.

#### Step 2: Upload submission

- Upload full manuscript in the form of a Word file (with title, authors, abstract, keywords, figures and tables embedded, and references).

#### Step 3: Enter metadata

- First name, last name, contact email and affiliation for all authors, in relevant order, must be provided. Corresponding author has to be selected. Full postal address and phone number of the corresponding author has to be provided.

- **Title and abstract** must be provided in plain text.
- Keywords must be provided (max. 6, separated by semicolons).
- Data about contributors and supporting agencies may be entered.
- **References** in plain text must be provided in the relevant text field.

#### Step 4: Upload supplementary files

- Original Word file (original of the PDF uploaded in the step 2)
- **List of suggested reviewers** with at least five reviewers with two recent references from the field of submitted manuscript must be uploaded as a Word file. At the same time, authors should declare (i) that they have no conflict of interest with suggested reviewers and (ii) that suggested reviewers are experts in the field of the submitted manuscript.
- All **graphics** have to be uploaded in a single ZIP file. Graphics should be named Figure 1.jpg, Figure 2.eps, etc.
- **Graphical abstract image** must be uploaded separately
- **Proposed cover picture** (optional) should be uploaded separately.
- Any additional **appendices** (optional) to the paper may be uploaded. Appendices may be published as a supplementary material to the paper, if accepted.
- For each uploaded file the author is asked for additional metadata which may be provided. Depending of the type of the file please provide the relevant title (Statement of novelty, List of suggested reviewers, Figures, Graphical abstract, Proposed cover picture, Appendix).

#### Step 5: Confirmation

- Final confirmation is required.

### Article Types

**Feature Articles** are contributions that are written on Editor's invitation. They should be clear and concise summaries of the author's most recent work written with the broad scope of ACSi in mind. They are intended to be general overviews of the authors' subfield of research but should be written in a way that engages and informs scientists in other areas. They should contain the following (see also general guidelines for article structure below): (1) an introduction that acquaints readers with the authors' research field and outlines the important questions for which answers are being sought; (2) interesting, novel, and recent contributions of the author(s) to the field; and (3) a summary that presents possible future directions. Manuscripts should normally not exceed 40 pages of one column format (font size 12, 33 lines per page). Generally, experts who have made an important contribution to a specific field in recent years will be invited by the Editor to contribute a **Feature Article**. Individuals may, however, send a proposal (of no more than one page) for a **Feature Article** to the Editor-in-Chief for consideration.

**Scientific articles** should report significant and innovative achievements in chemistry and related sciences and should exhibit a high level of originality. They should have the following structure:

1. Title (max. 150 characters),
2. Authors and affiliations,
3. Abstract (max. 1000 characters),
4. Keywords (max. 6),
5. Introduction,
6. Experimental,
7. Results and Discussion,
8. Conclusions,
9. Acknowledgements,
10. References.

The sections should be arranged in the sequence generally accepted for publications in the respective fields and should be successively numbered.

**Short communications** generally follow the same order of sections as Scientific articles, but should be short (max. 2500 words) and report a significant aspect of research work meriting separate publication. Editors may decide that a Scientific paper is categorized as a Short Communication if its length is short.

**Technical articles** report applications of an already described innovation. Typically, technical articles are not based on new experiments.

## Preparation of Submissions

**Text** of the submitted articles must be prepared with Microsoft Word. Normal style set to single column, 1.5 line spacing, and 12 pt Times New Roman font is recommended. Line numbering (continuous, for the whole document) must be enabled to simplify the reviewing process. For any other format, please consult the editor. Articles should be written in English. Correct spelling and grammar are the sole responsibility of the author(s). Papers should be written in a concise and succinct manner. The authors shall respect the ISO 80000 standard [1], and IUPAC Green Book [2] rules on the names and symbols of quantities and units. The Système International d'Unités (SI) must be used for all dimensional quantities.

**Graphics** (figures, graphs, illustrations, digital images, photographs) should be inserted in the text where appropriate. The captions should be self-explanatory. Lettering should be readable (suggested 8 point Arial font) with equal size in all figures. Use common programs such as MS Excel or similar to prepare figures (graphs) and ChemDraw to prepare structures in their final size. Width of graphs in the manuscript should be 8 cm. Only in special cases (in case of numerous data, visibility issues) graphs can be 17 cm wide. All graphs in the manuscript should be inserted in relevant places and **aligned left**. The same graphs should be provided separately as images of appropriate resolution (see below) and submitted together in a ZIP file (Graphics ZIP). Please do not submit figures as a Word file. In **graphs**, only the graph area determined by both axes should be in the frame, while a frame around the whole graph should be omitted. The graph area should be white. The legend should be inside the graph area. The style of all graphs should be the same. **Figures and illustrations** should be of sufficient quality for the printed version, i.e. 300 dpi minimum. **Digital images and photographs** should be of high quality (minimum

250 dpi resolution). On submission, figures should be of good enough resolution to be assessed by the referees, ideally as JPEGs. High-resolution figures (in JPEG, TIFF, or EPS format) might be required if the paper is accepted for publication.

**Tables** should be prepared in the Word file of the paper as usual Word tables. The captions should appear above the table and should be self-explanatory.

**References** should be numbered and ordered sequentially as they appear in the text, likewise methods, tables, figure captions. When cited in the text, reference numbers should be superscripted, following punctuation marks. It is the sole responsibility of authors to cite articles that have been submitted to a journal or were in print at the time of submission to ACSi. Formatting of references to published work should follow the journal style; please also consult a recent issue:

1. J. W. Smith, A. G. White, *Acta Chim. Slov.* **2008**, *55*, 1055–1059.
2. M. F. Kemmere, T. F. Keurentjes, in: S. P. Nunes, K. V. Peinemann (Ed.): *Membrane Technology in the Chemical Industry*, Wiley-VCH, Weinheim, Germany, **2008**, pp. 229–255.
3. J. Levec, Arrangement and process for oxidizing an aqueous medium, US Patent Number 5,928,521, date of patent July 27, **1999**.
4. L. A. Bursill, J. M. Thomas, in: R. Sersale, C. Collola, R. Aiello (Eds.), *Recent Progress Report and Discussions: 5th International Zeolite Conference*, Naples, Italy, 1980, Gianini, Naples, **1981**, pp. 25–30.
5. J. Szegezdi, F. Csizmadia, Prediction of dissociation constant using microconstants, [http://www.chemaxon.com/conf/Prediction\\_of\\_dissociation\\_constant\\_using\\_microconstants.pdf](http://www.chemaxon.com/conf/Prediction_of_dissociation_constant_using_microconstants.pdf), (assessed: March 31, 2008)

Titles of journals should be abbreviated according to Chemical Abstracts Service Source Index (CASSI).

## Special Notes

- Complete characterization, **including crystal structure**, should be given when the synthesis of new compounds in crystal form is reported.
- Numerical **data should be reported with the number of significant digits corresponding to the magnitude** of experimental uncertainty.
- **The SI system of units and IUPAC recommendations** for nomenclature, symbols and abbreviations should be followed closely. Additionally, the authors should follow the general guidelines when citing spectral and analytical data, and depositing crystallographic data.
- **Characters** should be correctly represented throughout the manuscript: for example, 1 (one) and l (ell), 0 (zero) and O (oh), x (ex), D7 (times sign), B0 (degree sign). Use Symbol font for all Greek letters and mathematical symbols.
- The rules and recommendations of the **IUBMB** and the **International Union of Pure and Applied Chemistry (IUPAC)** should be used for abbreviation of chemical names, nomenclature of chemical compounds, enzyme nomenclature, isotopic compounds, optically active isomers, and spectroscopic data.
- **A conflict of interest** occurs when an individual (author, reviewer, editor) or its organization is in-

volved in multiple interests, one of which could possibly corrupt the motivation for an act in the other. Financial relationships are the most easily identifiable conflicts of interest, while conflicts can occur also as personal relationships, academic competition, etc. **The Editors** will make effort to ensure that conflicts of interest will not compromise the evaluation process; potential editors and reviewers will be asked to exempt themselves from review process when such conflict of interest exists. When the manuscript is submitted for publication, **the authors** are expected to disclose any relationships that might pose potential conflict of interest with respect to results reported in that manuscript. In the Acknowledgement section the source of funding support should be mentioned. The statement of disclosure must be provided as Comments to Editor during the submission process.

- **Published statement of Informed Consent.** Research described in papers submitted to ACSi must adhere to the principles of the Declaration of Helsinki (<http://www.wma.net/e/policy/b3.htm>). These studies must be approved by an appropriate institutional review board or committee, and informed consent must be obtained from subjects. The Methods section of the paper must include: 1) a statement of protocol approval from an institutional review board or committee and 2), a statement that informed consent was obtained from the human subjects or their representatives.
- **Published Statement of Human and Animal Rights.** When reporting experiments on human subjects, authors should indicate whether the procedures followed were in accordance with the ethical standards of the responsible committee on human experimentation (institutional and national) and with the Helsinki Declaration of 1975, as revised in 2008. If doubt exists whether the research was conducted in accordance with the Helsinki Declaration, the authors must explain the rationale for their approach and demonstrate that the institutional review body explicitly approved the doubtful aspects of the study. When reporting experiments on animals, authors should indicate whether the institutional and national guide for the care and use of laboratory animals was followed.
- To avoid conflict of interest between authors and referees we expect that not more than one referee is from the same country as the corresponding author(s), however, not from the same institution.
- Contributions authored by **Slovenian scientists** are evaluated by non-Slovenian referees.
- Papers describing **microwave-assisted reactions** performed in domestic microwave ovens are not considered for publication in *Acta Chimica Slovenica*.
- *Manuscripts that are **not prepared and submitted** in accord with the instructions for authors are not considered for publication.*

## Appendices

Authors are encouraged to make use of supporting information for publication, which is supplementary material (appendices) that is submitted at the same time as the manuscript. It is made available on the Journal's

web site and is linked to the article in the Journal's Web edition. The use of supporting information is particularly appropriate for presenting additional graphs, spectra, tables and discussion and is more likely to be of interest to specialists than to general readers. When preparing supporting information, authors should keep in mind that the supporting information files will not be edited by the editorial staff. In addition, the files should be not too large (upper limit 10 MB) and should be provided in common widely known file formats to be accessible to readers without difficulty. All files of supplementary materials are loaded separately during the submission process as supplementary files.

## Proposed Cover Picture and Graphical Abstract Image

**Graphical content:** an ideally full-colour illustration of resolution 300 dpi from the manuscript must be proposed with the submission. Graphical abstract pictures are printed in size 6.5 x 4 cm (hence minimal resolution of 770 x 470 pixels). Cover picture is printed in size 11 x 9.5 cm (hence minimal resolution of 1300 x 1130 pixels)

Authors are encouraged to submit illustrations as candidates for the journal Cover Picture\*. The illustration must be related to the subject matter of the paper. Usually both proposed cover picture and graphical abstract are the same, but authors may provide different pictures as well.

\* The authors will be asked to contribute to the costs of the cover picture production.

### Statement of novelty

Statement of novelty is provided in a Word file and submitted as a supplementary file in step 4 of submission process. Authors should in no more than 100 words emphasize the scientific novelty of the presented research. Do not repeat for this purpose the content of your abstract.

### List of suggested reviewers

List of suggested reviewers is a Word file submitted as a supplementary file in step 4 of submission process. Authors should propose the names, full affiliation (department, institution, city and country) and e-mail addresses of five potential referees. Field of expertise and at least two references relevant to the scientific field of the submitted manuscript must be provided for each of the suggested reviewers. The referees should be knowledgeable about the subject but have no close connection with any of the authors. In addition, referees should be from institutions other than (and countries other than) those of any of the authors. Authors declare no conflict of interest with suggested reviewers. Authors declare that suggested reviewers are experts in the field of submitted manuscript.

## How to Submit

Users registered in the role of author can start submission by choosing USER HOME link on the top of the page, then choosing the role of the Author and follow the relevant link for starting the submission process. Prior to submission we strongly recommend that you familiarize yourself with the ACSi style by browsing the journal, particularly if you have not submitted to the ACSi before or recently.

## Correspondence

All correspondence with the ACSi editor regarding the paper goes through this web site and emails. Emails are sent and recorded in the web site database. In the correspondence with the editorial office please provide ID number of your manuscript. All emails you receive from the system contain relevant links. **Please do not answer the emails directly but use the embedded links in the emails for carrying out relevant actions.** Alternatively, you can carry out all the actions and correspondence through the online system by logging in and selecting relevant options.

## Proofs

Proofs will be dispatched via e-mail and corrections should be returned to the editor by e-mail as quickly as possible, normally within 48 hours of receipt. Typing errors should be corrected; other changes of contents will be treated as new submissions.

## Submission Preparation Checklist

As part of the submission process, authors are required to check off their submission's compliance with all of the following items, and submissions may be returned to authors that do not adhere to these guidelines.

1. The submission has not been previously published, nor is it under consideration for publication in any other journal (or an explanation has been provided in Comments to the Editor).
2. All the listed authors have agreed on the content and the corresponding (submitting) author is responsible for having ensured that this agreement has been reached.
3. The submission files are in the correct format: manuscript is created in MS Word but will be **submitted in PDF** (for reviewers) as well as in original MS Word format (as a supplementary file for technical editing); diagrams and graphs are created in Excel and saved in one of the file formats: TIFF, EPS or JPG; illustrations are also saved in one of these formats. The preferred position of graphic files in a document is to embed them close to the place where they are mentioned in the text (See **Author guidelines** for details).
4. The manuscript has been examined for spelling and grammar (spell checked).
5. The **title** (maximum 150 characters) briefly explains the contents of the manuscript.
6. Full names (first and last) of all authors together with the affiliation address are provided. Name of author(s) denoted as the corresponding author(s), together with their e-mail address, full postal address and telephone/fax numbers are given.
7. The **abstract** states the objective and conclusions of the research concisely in no more than 150 words.
8. Keywords (minimum three, maximum six) are provided.
9. **Statement of novelty** (maximum 100 words) clearly explaining new findings reported in the manuscript should be prepared as a separate Word file.
10. The text adheres to the stylistic and bibliographic requirements outlined in the **Author guidelines**.
11. Text in normal style is set to single column, 1.5 line spacing, and 12 pt. Times New Roman font is

recommended. All tables, figures and illustrations have appropriate captions and are placed within the text at the appropriate points.

12. Mathematical and chemical equations are provided in separate lines and numbered (Arabic numbers) consecutively in parenthesis at the end of the line. All equation numbers are (if necessary) appropriately included in the text. Corresponding numbers are checked.
13. Tables, Figures, illustrations, are prepared in correct format and resolution (see **Author guidelines**).
14. The lettering used in the figures and graphs do not vary greatly in size. The recommended lettering size is 8 point Arial.
15. Separate files for each figure and illustration are prepared. The names (numbers) of the separate files are the same as they appear in the text. All the figure files are packed for uploading in a single ZIP file.
16. Authors have read **special notes** and have accordingly prepared their manuscript (if necessary).
17. References in the text and in the References are correctly cited. (see **Author guidelines**). All references mentioned in the Reference list are cited in the text, and vice versa.
18. Permission has been obtained for use of copyrighted material from other sources (including the Web).
19. The names, full affiliation (department, institution, city and country), e-mail addresses and references of five potential referees from institutions other than (and countries other than) those of any of the authors are prepared in the word file. At least two relevant references (important recent papers with high impact factor, head positions of departments, labs, research groups, etc.) for each suggested reviewer must be provided. Authors declare no conflict of interest with suggested reviewers. Authors declare that suggested reviewers are experts in the field of submitted manuscript.
20. Full-colour illustration or graph from the manuscript is proposed for graphical abstract.
21. **Appendices** (if appropriate) as supplementary material are prepared and will be submitted at the same time as the manuscript.

## Privacy Statement

The names and email addresses entered in this journal site will be used exclusively for the stated purposes of this journal and will not be made available for any other purpose or to any other party.

ISSN: 1580-3155

---

## Koristni naslovi

---

Slovensko kemijsko društvo  
Slovenian Chemical Society



**Slovensko kemijsko društvo**

[www.chem-soc.si](http://www.chem-soc.si)

e-mail: [chem.soc@ki.si](mailto:chem.soc@ki.si)

---



**Wessex Institute of Technology**

[www.wessex.ac.uk](http://www.wessex.ac.uk)

---



**SETAC**

[www.setac.org](http://www.setac.org)

---



**European Water Association**

<http://www.ewa-online.eu/>

---



**European Science Foundation**

[www.esf.org](http://www.esf.org)

---



**European Federation of Chemical Engineering**

<https://efce.info/>

---



**I U P A C**

INTERNATIONAL UNION OF  
PURE AND APPLIED CHEMISTRY

**International Union of Pure and Applied Chemistry**

<https://iupac.org/>

---

---

## Novice evropske zveze kemijskih društev EuChemS najdete na:

---

 **EuChemS**  
European Chemical Society

**Brussels News Updates**

<http://www.euchems.eu/newsletters/>

---



**DONAU LAB** Ljubljana  
Member of LPPgroup

 **BINDER**

**Best conditions for your success**



**Komore za testiranje baterij**

**Vakuumski sušilniki**

**Klimatske komore**



Donau Lab d.o.o., Ljubljana  
Tbilisijska 85  
SI-1000 Ljubljana  
[www.donaulab.si](http://www.donaulab.si)  
[office-si@donaulab.com](mailto:office-si@donaulab.com)





# Razvoj in inovacije za globalno uspešnost

Znanje, kreativnost zaposlenih in inovacije so ključnega pomena v okolju, kjer nastajajo pametni premazi skupine KANSAI HELIOS. Z rešitvami, ki zadostijo široki paleti potreb, kontinuiranim razvojem ter s kakovostnimi izdelki, Helios predstavlja evropski center za inovacije in poslovni razvoj skupine Kansai Paint.

Part of  **KANSAI  
PAINT**

[www.helios-group.eu](http://www.helios-group.eu)

 **KANSAI  
HELIOS**  
Designing Excellence





MAGNEZIJ Krka 300

MAGNEZIJ Krka 400



BODITE **ŠE BOLJ**  
NEUSTAVLJIVI

**Magneziju Krka 300** se je pridružil **Magnezij Krka 400**,  
ki vsebuje **več magnezija** in tako še bolj pripomore k:

- ✓ zmanjševanju utrujenosti in izčrpanosti,
- ✓ normalnemu delovanju mišic.

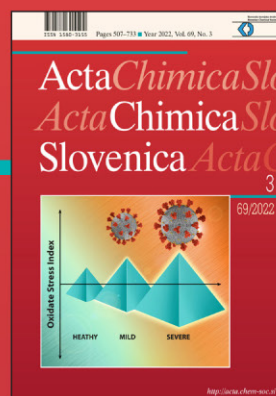




# Acta Chimica Slovenica

## Acta Chimica Slovenica

In many diseases, the ratio of oxidants to antioxidants is disturbed. This condition is also expressed differently depending on the severity of the disease. COVID-19 is one such example (page 564).



Year 2022, Vol. 69, No. 3

